

Tensor network techniques for strongly correlated systems

Simulating the quantum many-body wavefunction
in zero, one, and two dimensions



Benedikt Bruognolo

München 2017

Tensor network techniques for strongly correlated systems

Simulating the quantum many-body wavefunction
in zero, one, and two dimensions

Dissertation

an der Fakultät für Physik
der Ludwig-Maximilians-Universität München

vorgelegt von

Benedikt Bruognolo
aus München

2017

Erstgutachter: Prof. Jan von Delft

Zweitgutachter: Prof. Frank Pollmann

Datum der Abgabe: 06.07.2017

Datum der mündlichen Prüfung: 11.08.2017

Abstract

Many enthralling phenomena in condensed matter physics arise from the interplay of strong quantum correlations induced by many-body interactions. However, the numerical treatment of such strongly correlated quantum systems is inherently complex due to the presence of an exponentially large number of degrees of freedom. Tensor networks techniques provide a compelling framework to systematically reduce this complexity problem and to obtain efficient, yet accurate, representations of quantum many-body wavefunctions.

The present thesis employs two different types of tensor networks, matrix product states (MPS) and infinite projected entangled-pair states (iPEPS), to shed light on a number of intriguing topics in zero-, one- and two-dimensional quantum many-body systems.

We first explore the quantum critical properties of bosonic quantum impurity models, a specific class of zero-dimensional quantum systems consisting of a small spin degree of freedom coupled to a bosonic environment. To gain numerical access to the quantum critical points, we rely on a recently developed MPS algorithm that efficiently deals with the large bosonic state space. The study of a generalized spin-boson model with two competing environments reveals highly nontrivial quantum critical behavior in the form of a breakdown of the quantum-to-classical correspondence. Furthermore, we also uncover universal features of the quantum critical wavefunction in the one-bath spin-boson model and develop a new type of Wilson chain representation for quantum impurity models. These so-called “open” Wilson chains allow for the incorporation of missing bath modes, crucial to faithfully reproduce the critical properties of the spin-boson model at finite temperatures.

The second range of topics concern the evaluation of spectral properties in one-dimensional many-body systems. Employing MPS-based real-time evolution and Chebyshev expansions, we calculate the dynamic spin-structure factor of two effective spin- $\frac{1}{2}$ models governing the low-energy properties of the materials Cs_2CoCl_4 and $\text{Cu}_3(\text{CO}_3)_2(\text{OH})_2$. Our results reveal an intriguing interplay of thermal and quantum fluctuations that impacts the excitation spectrum in both materials. On a technical level, we also propose a symmetry-enhanced version of the minimally entangled typical states (METTS) algorithm designed for the study of spectral quantities at finite temperature. Moreover, we present zero-temperature calculations for the local density of states in an interacting quantum point contact, supporting the validity of a functional RG approach that aims towards the resolution of the 0.7 anomaly.

The last part of this thesis focusses on the application of tensor network techniques to strongly correlated systems in two spatial dimensions. Relying on density-matrix purification and METTS to encode thermal fluctuations, we demonstrate that the MPS framework represents a viable tool to determine finite-temperature properties of highly-frustrated spin systems down to low temperatures. Moreover, we propose a METTS protocol for detecting the critical temperature of finite-temperature phase transitions in the presence of frustration. Finally, we present the first fermionic iPEPS simulations that exploit a variety of non-abelian symmetries, leading to a significant performance boost of the algorithm. By incorporating non-abelian spin- and flavor symmetries, we explore the possibility of treating complex multi-band models with iPEPS and provide promising initial results for a two-band Hubbard model.

Zusammenfassung

Der Ursprung vieler faszinierender Phänomene in der Festkörperphysik beruht auf starken Quantenkorrelationen, die von der Wechselwirkung zwischen Elektronen hervorgerufen werden. Die Komplexität solcher Wechselwirkungseffekte erschwert die numerische Beschreibung dieser Phänomene signifikant. Um die exponentiell große Anzahl an Freiheitsgraden in Vielteilchensystemen zu reduzieren, kann man auf sogenannte Tensor-Netzwerk-Techniken zurückgreifen. Diese Methoden ermöglichen eine genaue und gleichermaßen effiziente Beschreibung der Wellenfunktion eines Quantenvielteilchensystems.

Die vorliegende Dissertation untersucht mit Hilfe zweier Klassen von Tensor-Netzwerken, sogenannter “matrix product states” (MPS) und “infinite projected entangled-pair states” (iPEPS), eine Reihe spannender Themen in niederdimensionalen Quantensystemen.

Der erste Teil dieser Arbeit beschäftigt sich mit den kritischen Quanteneigenschaften von bosonischen Störstellenmodellen. Diese Modelle beschreiben typischerweise kleine lokale Quantensysteme (z.B. einfache Spin-Freiheitsgrade), die im Kontakt mit einer makroskopischen Umgeben stehen. Um direkten Zugang zu den Phasenübergängen in solcher Systeme zu erhalten, verwenden wir eine neuartige MPS-Technik, die die effiziente Beschreibung des großen Zustandsraums der bosonischen Umgebung ermöglicht. Mit dieser Methode untersuchen wir das kritische Verhalten eines verallgemeinerten Spin-Boson-Modells mit zwei Bädern. Unsere Resultate unterstreichen, dass in diesem System das Korrespondenzprinzip zwischen klassischen und Quantenphasenübergängen verletzt wird. Darüber hinaus decken wir universelle Eigenschaften der kritischen Wellenfunktion im Spin-Boson-Modell auf. Außerdem entwickeln wir eine neuartige Darstellung der Wilson-Kette, die es uns ermöglicht, fehlende Badmoden zu berücksichtigen, welche für die korrekte Beschreibung der kritischen Eigenschaften im Spin-Boson-Modell bei endlicher Temperature entscheidend sind.

Das zweite Themengebiet umfasst die dynamischen Eigenschaften eindimensionaler Vielteilchensysteme. Unter anderem untersuchen wir dabei den dynamischen Spin-Strukturfaktor in zwei unterschiedlichen Spin- $\frac{1}{2}$ -Modellen, die zur Beschreibung der Materialeigenschaften von Cs_2CoCl_4 and $\text{Cu}_3(\text{CO}_3)_2(\text{OH})_2$ entwickelt wurden. Das Zusammenspiel von thermischen und quantenmechanischen Fluktuationen lässt sich durch MPS-Techniken abbilden, die auf Realzeit- und Chebyshev-Entwicklungen basieren. Darüber hinaus entwickeln wir eine Variante des “minimally entangled typical thermal states” (METTS) Algorithmus, welche bei der Berechnung dynamischer Größen erlaubt, die Symmetrieeigenschaften eines Systems effizient auszunutzen. Außerdem beschäftigen wir uns mit der Simulation der lokalen Zustandsdichte in einem Quantenpunktkontakt unter Einfluss von Elektron-Elektron- Wechselwirkung. Dabei finden wir gute Übereinstimmung mit Ergebnissen einer funktionalen Renormierungsgruppe, welche auf die Beschreibung der sogenannten 0.7-Anomalie in Quantenpunktkontakten ausgerichtet ist.

Der letzte Teil dieser Dissertation zielt auf die Anwendung von Tensor-Netzwerk-Techniken in zweidimensionalen Quantensystemen ab. Einerseits etablieren wir eine Reihe von MPS-Methoden, die die Beschreibung von thermischen Effekten in stark frustrierten Spinsystemen auch bei niedrigen Temperaturen zulassen. Unter anderem entwickeln wir dabei ein METTS Protokoll, welches uns erlaubt, die kritische Temperatur eines thermischen Phasenübergangs quantitativ korrekt zu bestimmen. In einer weiteren Studie präsentieren wir Ergebnisse einer

fermionischen iPEPS Simulation, die explizit eine Reihe nichtabelscher Symmetrien ausnutzt und damit die Effizienz dieses numerischen Zugangs stark verbessert. Dies erlaubt es uns, iPEPS erstmals auf komplexe Mehrband-Modelle anzuwenden. Das Potential dieser Methode wird durch erste vielversprechende Ergebnisse für ein Zweiband-Hubbard-Modell mit Lochdotierung unterstrichen.

Publications

This dissertation is based on the following journal articles, listed in chronological order

- P1** *Two-bath spin-boson model: Phase diagram and critical properties*
B. Bruognolo, A. Weichselbaum, C. Guo, J. von Delft, I. Schneider, and M. Vojta
Sec. 3.1 / [arXiv:1410.3821](#) *Phys. Rev. B* **90**, 245130 (2014)
- P2** *Symmetric Minimally Entangled Typical Thermal States*
B. Bruognolo, J. von Delft, and A. Weichselbaum
Sec. 4.2 / [arXiv:1506.03336](#) *Phys. Rev. B* **92**, 115105 (2015)
- P3** *Dynamic structure factor of the spin- $\frac{1}{2}$ XXZ chain in a transverse field*
B. Bruognolo, A. Weichselbaum, J. von Delft, and M. Garst
Sec. 4.1 / [arXiv:1606.03294](#) *Phys. Rev. B* **94**, 085136 (2016)
- P4** *Anatomy of quantum critical wave functions in dissipative impurity problems*
Z. Blunden-Codd, S. Bera, **B. Bruognolo**, N.-O. Linden, A. W. Chin, J. von Delft,
A. Nazir, and S. Florens
Sec. 3.2 / [arXiv:1608.00799](#) *Phys. Rev. B* **95**, 085104 (2017)
- P5** *Open Wilson chains for quantum impurity models: Keeping track of all bath modes*
B. Bruognolo, N.-O. Linden, F. Schwarz, S.-S. B. Lee, K. Stadler, A. Weichselbaum,
M. Vojta, F. B. Anders, and J. von Delft
Sec. 3.3 / [arXiv:1611.05291](#) *Phys. Rev. B* **95**, 121115(R) (2017)
- P6** *Spin fluctuations in the 0.7-anomaly in quantum point contacts*
D. Schimmel, **B. Bruognolo**, and J. von Delft
Sec. 4.3 / [arXiv:1703.02734](#) to appear in *Phys. Rev. Lett.* (2017)
- P7** *Matrix product state techniques for two-dimensional systems at finite temperature*
B. Bruognolo, Z. Zhu, S. R. White, E. M. Stoudenmire
Sec. 5.1 / [arXiv:1705.05578](#) submitted to *SciPost Physics*

Acknowledgement

I am deeply grateful to my advisor Jan von Delft for giving me the wonderful opportunity to pursue my PhD in his group and for introducing me to the field of tensor networks. In many ways, he has been the ideal advisor, finding the perfect balance between providing me with a lot of academic freedom and still being always approachable and offering his guidance and invaluable support, whenever needed.

I am also very grateful to Andreas Weichselbaum, who patiently taught me the technicalities and details of computational condensed matter physics and who's QSpace library represents the backbone for the results of this work. I learned a lot from his deep knowledge of tensor networks and from our numerous discussions.

I would like to thank Frank Pollmann for coreferring this thesis.

I appreciated very much to be engaged in collaborations with Frithjof Anders, Zach Blunden-Codd, Soumya Bera, Alex Chin, Serge Florens, Markus Garst, Seung-Sup Lee, Nils-Oliver Linden, Ahsan Nazir, Dennis Schimmel, Imke Schneider, Frauke Schwarz, Katharina Stadler, Miles Stoudenmire, Matthias Vojta, Steve White, and Zhenyue Zhu. In addition, I learned a lot from interesting discussions with Thomas Baker, Philipp Corboz, Chia-Min Chung, Seung-Sup Lee, Wei Li, Matthias Punk, Lode Pollet, Sid Parameswaran, Alex Wolf, and many other colleagues at the Arnold Sommerfeld Center. Thanks to Frauke and Kathi for tolerating me as their office mate all this time, and special thanks to Frauke for many discussions on tensor networks, quantum mechanics, undergraduate math, and many other topics.

A part of the work on this thesis was done in the group of Steve White at UC Irvine. I would like to thank him and the members of his group for their hospitality. I'm particularly thankful for the opportunity to work with Zhenyue, Steve and Miles on the finite-temperature MPS project. Moreover, I would like to thank Tom and his friends, as well as Chia-Min, and Sid for many joint beers and coffees, and for showing me around beautiful southern California.

I am deeply grateful to Madeleine, my family, and my friends for their support and for enriching my life in innumerable ways.

Financial support from the German Research Foundation (DFG) through the SFB 631 and the Cluster of Excellence "Nanosystems Initiative Munich" (NIM), as well as from the BaCaTeC Initiative is acknowledged.

In memory of my loving grandparents, Ilse and Adolf Wedl

Contents

Abstract	i
Publications	v
Acknowledgement	vii
1 Introduction	1
1.1 Effective models for strongly correlated systems	2
1.1.1 Hubbard model	2
1.1.2 Heisenberg model	3
1.1.3 Spin-boson model	4
1.2 Numerical approaches for strongly correlated systems	4
1.3 This thesis	6
2 Tensor network techniques	7
2.1 Overview	7
2.2 Entanglement	8
2.2.1 Local Hamiltonians and correlations	8
2.2.2 Ground-state entanglement and area laws	9
2.3 Diagrams	11
2.3.1 Numerical scaling	12
2.4 Matrix product states	13
2.4.1 Basics and calculus	13
2.4.2 NRG	24
2.4.3 DMRG	26
2.4.4 Time evolution	30
2.4.5 Finite-temperature	34
2.4.6 Spectral methods	38
2.5 Infinite projected entangled-pair states	45
2.5.1 Properties of PEPS and iPEPS	45
2.5.2 Contractions	48
2.5.3 Expectation value	58
2.5.4 Optimization	59
2.6 Fermionic tensor networks	69
2.6.1 Fermionization rules	70
2.6.2 MPS	72
2.6.3 PEPS and iPEPS	73
2.7 Symmetries	76

2.7.1	Abelian and non-abelian symmetries	77
2.7.2	Symmetric tensor networks	78
3	Quantum criticality in bosonic quantum impurity models	81
3.1	Two-bath spin-boson model: Phase diagram and critical properties	83
3.2	Anatomy of quantum critical wave functions in dissipative impurity problems	104
3.3	Open Wilson chains for quantum impurity models	115
4	Spectral features of one-dimensional quantum systems	133
4.1	Dynamic structure factor of the spin- $\frac{1}{2}$ XXZ chain in a transverse field	135
4.2	Symmetric minimally entangled typical thermal states	147
4.3	Spin fluctuations in the 0.7-anomaly in quantum point contacts	164
4.3.1	Technical details of the DMRG implementation	178
5	Extending the range of two-dimensional tensor network techniques	179
5.1	Matrix product state techniques for two-dimensional systems at finite temperature	181
5.2	Fermionic iPEPS simulations with non-abelian symmetries	211
5.2.1	iPEPS with non-abelian symmetries	211
5.2.2	One-band t - J model	215
5.2.3	Two-band Hubbard model	218
5.2.4	Three-flavor Hubbard model	223
6	Conclusion and outlook	226
	Appendix	229
	Bibliography	234

Introduction

The emergence of quantum mechanics in the 20th century marks one of the most remarkable accomplishments of physics. Quantum mechanics fundamentally changed the way physicists think about the world. Its laws and their implications still constantly challenge our understanding and catch us by surprise. Quantum mechanics also revolutionized our daily lives by catalyzing numerous technical advancements, from the development of semiconductor electronics, which nowadays form the building blocks of our mobile phones and computers, to the fabrication of lasers, which have become an invaluable toolkit for medicine and industry.

In principle, the theory of quantum mechanics can be directly applied to solids and materials, as its underlying physical laws accurately guide the behavior of electrons and atoms [Dir28]. Clearly this is easier said than done. Though it is known how to write down the guiding mathematical equations for complicated materials consisting of a large number of atoms, the inherent complexity of the solution requires creative and intelligent approximations.

The properties of a condensed matter system are fully encoded in the famous Schrödinger equation,

$$\hat{H}|\psi\rangle = E|\psi\rangle, \tag{1.1}$$

with the Hamiltonian \hat{H} describing the microscopic interactions of the individual particles in the material, $|\psi\rangle$ representing the many-body wavefunction, an eigenstate of \hat{H} , and E the corresponding eigenenergy.

Solving Eq. (1.1) in the presence of interactions poses a fundamental and complex challenge. To get some perspective about the degree of complexity: the exact numerical solution for a tiny nanoscale piece of material would already require a computer with a hard disk containing more bits than atoms present in the entire universe. Aiming for the exact solution of the many-body problem with brute force is therefore a futile task.

This was also recognized by the pioneers of modern condensed matter physics, who instead relied on approximative and effective theories to tackle the Schrödinger equation. The most famous examples include Bloch's nearly-free electron model [AM05] and Landau's Fermi-liquid theory [Lan59]. The common rationale behind these approaches is the assumption that the properties of the interacting system can be adequately described in a single-particle picture with interactions only entering at a perturbative level. Although their approximative nature only accounts for weak quantum correlations, effective theories have proven to be highly successful in the description of solids. Band theory explains a vast variety of physical properties of solids such as electrical resistivity or optical absorption. Fermi-liquid theory is even capable to capture the occurrence of conventional superconductivity, a fascinating phase of matter featuring, above all, a vanishing electrical resistivity and the expulsion of interior magnetic fields.

However, effective theories fail to explain many experimental discoveries in the last decades including Mott insulators [IFT98], high- T_c superconductivity [Dag94, A⁺97], frustrated quantum magnetism [Ram94, Bal10], the fractional quantum Hall effect [Sto99], or quantum critical phases of matter [Sac01], just to name a few. These fascinating phenomena arise in a specific class of materials and solid-state devices, where, often due to spatial confinement, the inter-particle interactions are strongly enhanced and become comparable or larger than the kinetic energy. Strong interactions induce extensive quantum correlations in the system which ultimately give rise to these intriguing quantum effects and phases of matter.

At the same time, the descriptive power of effective theories is strongly undermined in the context of strongly correlated materials, since the presence of strong interactions leads to a breakdown of any perturbative ansatz. In order to faithfully describe strongly correlated systems, the full many-body wavefunction has to be taken into account. Clearly, this requires alternative approaches to solve the Schrödinger equation from a numerical perspective. Recent years have seen unprecedented efforts in the development of methods to resolve the many-electron problem, and this is also the core topic of this thesis.

In the remainder of this chapter, we give a brief introduction to the most important effective models for the low-dimensional electron and spin systems related to the work presented in this thesis, before diving into the details of how to numerically solve Eq. (1.1) in the presence of many-body interactions. Finally, we provide a short summary of the structure of this thesis.

1.1 Effective models for strongly correlated systems

Dealing with the full many-body wavefunction is a vastly difficult task and, despite recent progress in many different directions, physicists are not yet in shape to simulate the full Schrödinger equation for realistic models of strongly correlated materials. Therefore, we adopt a strategy common in the community and study effective Hamiltonians defined on lattices. These effective Hamiltonians contain significantly less degrees of freedom and are designed such that they (ideally) capture the crucial aspects of the full Hamiltonian (e.g., the low-energy properties). *A priori*, there is no guarantee that an effective model suffices to generate a specific physical phenomena observed in an experiment. But even from examining the “wrong” effective Hamiltonian, we can draw conclusions about the importance of individual terms for the emergence of specific physical properties.

1.1.1 Hubbard model

The Hubbard model is considered the paradigm for strongly correlated electron systems and allows for the description of a variety of strongly correlated phenomena [Hub63]. In two spatial dimensions, it represents the “simplest” model showing a transition from a metallic to a Mott-insulating ground state at half filling [Sca06]. In addition, it is also believed to capture important aspects of high- T_c superconductors in the presence of hole doping.

The one-band Hubbard model on a square lattice with nearest-neighbor hopping t and onsite Coulomb repulsion U is defined by the following Hamiltonian,

$$\hat{H} = -t \sum_{\langle ij \rangle, \sigma} (\hat{c}_{i\sigma}^\dagger \hat{c}_{j\sigma} + \hat{c}_{j\sigma}^\dagger \hat{c}_{i\sigma}) + U \sum_i \hat{c}_{i\uparrow}^\dagger \hat{c}_{i\uparrow} \hat{c}_{i\downarrow}^\dagger \hat{c}_{i\downarrow}, \quad (1.2)$$

with $\hat{c}_{i\sigma}^\dagger$ and $\hat{c}_{i\sigma}$ being the fermionic creation and annihilation operators with spin $\sigma \in \{\uparrow, \downarrow\}$ on lattice site i , and $\langle ij \rangle$ indexing all nearest-neighbor pairs of sites in the lattice. The local Fock space of the model is four-dimensional, with sites either being empty, occupied by a single electron of either spin species, or doubly occupied. For small U , the system

shows metallic behavior. With increasing interaction strength $U \geq t$, double occupancy, and thereby also the mobility of the electrons, is strongly suppressed. At half filling, the system moves into a Mott-insulating ground state for $U > U_c$, where each site contains a single localized electron. Superconducting d-wave order and striped states are observed at finite hole doping.

The full many-body solution of the 2D Hubbard model represents one of the big challenges in the field of strongly correlated systems. Despite many attempts by various analytical and numerical approaches, no consensus has been reached for a long time regarding the details of the phase diagram. Recently, important progress has been reported [LAB⁺15, ZCC⁺17], and it seems that we are on the brink of controlling the physics of the Hubbard model, at least in the case of the standard single-band formulation (1.2). Yet, this only represents the initial step towards the understanding of many strongly correlated materials. Real materials often feature multiple interacting low-energy bands. Their description requires effective models that are multi-band extensions of the Hubbard model. In these cases, much work remains to be done, since only very few unbiased numerical tool can deal with these complex systems.

1.1.2 Heisenberg model

The Heisenberg model is another famous example of an effective model for strongly correlated systems that describes the magnetic properties of many materials [Hei28]. It can be derived from the Hubbard model in the infinite U limit at half filling, where every site contains exactly one electron and hopping is completely suppressed. In this limit, the low-energy physics of the Hubbard model can be described by replacing the electrons with a dynamic spin degree of freedom on every site. The Heisenberg Hamiltonian is obtained by expanding the Hamiltonian (1.2) in powers of t/U and keeping only the leading term,

$$\hat{H} = J \sum_{\langle ij \rangle} \hat{\mathbf{S}}_i \hat{\mathbf{S}}_j, \quad (1.3)$$

with antiferromagnetic coupling $J \sim t^2/U$ and spin operators $\hat{\mathbf{S}}_i$. The ground state of this seemingly simple model favors antiparallel spin order on neighboring sites. Yet, the model can exhibit a variety of different phases depending on the underlying lattice geometry. Some lattices induce frustration which strongly suppresses magnetic order, leading to exotic phases of matter such as spin liquids [Bal10].

The many-body solution of the Heisenberg model is extremely relevant from several points of view. First of all, Heisenberg models and their extensions excellently describe the magnetic properties in a huge variety of strongly correlated materials, especially in those with a one- or two-dimensional lattice structure [PF10]. In addition, Heisenberg models play an important role in the development of fundamental theoretical concepts such as topology in condensed matter physics [Hal83a, Hal83b]. From a numerical perspective, Heisenberg models are under much better control than their fermionic counterparts, at least on nonfrustrated lattices [Man91]. The situation is less ideal for lattice models with geometrical induced frustration, where methodological progress is still required to resolve many illusive questions in the context of frustrated magnetism [Bal10]. The most prominent example is the controversy about the spin-liquid nature of the spin- $\frac{1}{2}$ Heisenberg model on the Kagome lattice [YHW11, DMS12, HZOP16, LXC⁺17].

1.1.3 Spin-boson model

Another category of effective models for strongly correlated systems are so-called quantum impurity models, where a small interacting quantum system consisting of only a few degrees of freedom is (strongly) coupled to an effective environment. Impurity models arise in a

number of different situations. First of all, they represent realistic models for solid state devices such as quantum dots or nano-junctions, which either feel the dissipative effects due to the presents of an environmental quantum system, or pass an electrical current from one reservoir to another [BCP08]. Moreover, quantum impurity models are highly relevant for the realistic description of strongly correlated materials in the context of dynamical mean-field theory and its generalizations [GKKR96, KSH⁺06]. Finally, and most importantly for the work of this thesis, these models play an integral role for the understanding of quantum criticality [Voj06].

One of the most famous quantum impurity models is the spin-boson model [LCD⁺87], consisting of a spin- $\frac{1}{2}$ degree of freedom linearly coupled to a bath of non-interacting bosonic particles. Its Hamiltonian is defined as

$$\hat{H} = -\frac{1}{2}\Delta\hat{\sigma}_x + \frac{1}{2}\hat{\sigma}_z\left[\epsilon + \sum_k t_k(\hat{b}_k + \hat{b}_k^\dagger)\right] + \sum_k \omega_k \hat{b}_k^\dagger \hat{b}_k, \quad (1.4)$$

where $\hat{\sigma}_i$ are Pauli matrices, while ϵ and Δ denote the bias and the tunnel splitting of the impurity spin, respectively. t_k describes the coupling strength of the spin to a particular bosonic bath mode k , which is characterized by energy ω_k and the corresponding annihilation and creation operators $\hat{b}_k, \hat{b}_k^\dagger$.

Despite many numerical and analytical attempts, the quantum critical properties of the spin-boson model have been subject to controversy for a long time [BTV03, Voj03, Voj06, AF09, WRVB09]. At first sight, this seems odd as the structure of the model does not appear to be very complex. However, it turns out to be inherently difficult to obtain the full many-body solution, in particular in the context of strong spin-bath coupling. Only recent methodological progress could settle this longstanding open issue [GWvDV12]. Yet, many questions arising in related systems, such as two-bath spin-boson model or the Bose-Fermi Kondo model [GI05], remain open.

1.2 Numerical approaches for strongly correlated systems

Dealing with the Schrödinger equation of a strongly correlated system is extremely challenging from a numerical perspective. To be more precise, the complexity for obtaining an exact numerical solution of an interacting many-body system grows exponentially with system size. The key challenge for any numerical method is therefore to circumvent or reduce this exponential scaling in system size.

The most straightforward way of tackling the many-body wavefunction numerically is to generate the full many-body Hamiltonian of the system and use *exact diagonalization* (ED) to obtain all or a subset of its eigenvectors [WF08]. In this approach, the exponential scaling hits with full force as the complexity to perform the full diagonalization scales $\sim \mathcal{O}(d^{3N})$, where N represents the number of sites in the lattice system and d is the local dimension per site (e.g., $d = 2$ for a spin- $\frac{1}{2}$ model). In case one is only interested in zero-temperature physics, one can ease this scaling by exploiting a Lanczos algorithm that only targets the ground state of the system [Lan50]. In addition, ED can be extended to larger systems by making use of Hamiltonian symmetries and specific basis setups before using finite-size scaling to extrapolate to the thermodynamic limit. Nevertheless, the method is restricted to fairly small systems $\mathcal{O}(10)$ limiting its applicability especially in the context of many-body systems with long correlation lengths.

Another set of approaches with a long history in condensed matter physics are *series expansion techniques*, which expand a specific quantity in terms of a power series of one or more parameters [OHZ06]. Historically, high-temperature series expansions (HTSE) for classical models gave the first indication of universal properties of phase transitions. In the last decades HTSE have also been applied to quantum systems. In addition, series

expansion techniques were expanded to zero-temperature properties based on a perturbative ansatz (“perturbative $T = 0$ series expansions”) in the 1980s [GS00]. In addition, these series have been extended to also treat excitations [Gel96] and multi-particle expansions [TMH⁺00, ZHS⁺01]. The main limitation of these techniques is achieving high enough expansion orders to get the quantity of interest converged. This is particularly difficult at or below a thermal phase transition and for strongly correlated ground-state phases, where long-ranged correlations dominantly determine the physical properties of a system.

The most powerful and widely applied numerical methods for strongly correlated systems are *quantum Monte-Carlo* (QMC) techniques [SK86, GML⁺11, FMNR01]. The common idea of these QMC methods is to solve the quantum many-body problem stochastically, e.g., by sampling the partition function of the full interacting system. For a vast number of systems, QMC can be implemented highly efficiently, so that one is able to treat very large system sizes of hundreds of sites or even directly working in the thermodynamic limit with only polynomial cost scaling. For most frustrated magnets and models of itinerant fermions, however, QMC techniques are plagued by the so-called sign problem [TW05] (though there are notable exceptions in special cases [HS00, KPS⁺13, HCD⁺16, ADP16]). In these cases, the computation time of the algorithms grows exponentially with the system size.

A possible route for circumventing the limitations of these methods is offered by a different category of numerical tools to tackle the many-body problem, namely so-called *tensor network techniques* [Sch11, Eis13, Orú14b]. Tensor networks (TN) build on the common idea to parametrize the wavefunction of a quantum many-body system in terms of a set of interconnected tensors. Although these ansatzes by construction only work efficiently (i.e., with polynomial cost scaling) for a specific set of lowly-entangled states in the Hilbert space, they turn out to be excellent representations of many physical wavefunctions of strongly correlated systems, including in particular ground states and other low-energy states, as well as thermal Gibbs states.

Tensor network techniques were pioneered by the introduction of the density matrix renormalization group (DMRG) [Whi92, Whi93], an algorithm for obtaining ground states in the form of matrix product states (MPS), which is highly efficient for one-dimensional systems. Following the success of MPS techniques, other families of tensor networks have been proposed that are better suited for 2D systems [VC04] and critical phenomena [Vid07].

Compelling features of TN include the absence of a sign problem, their non-perturbative character, and their ability to treat large system sizes. Of course, tensor network approaches are not free from limitations. However, the nature of these limitations is substantially different from those of other methods in the fields. Instead of dealing with, for example, a sign problem, TN are only limited by the amount of entanglement in the many-body wavefunction. Tensor network approaches therefore significantly extend the range of strongly correlated systems that are numerically accessible.

The concept of tensor networks is highly relevant for the work presented in this thesis from two distinct perspectives. TN represent an ideal tool for the various physical topics considered from a practical perspective, since their flexibility and competitiveness gives us access to a variety of static and dynamic observables of interest. At the same time, parts of our work contribute to the technical development of specific tensor network algorithms.

1.3 This thesis

This thesis covers a broad spectrum of topics in low-dimensional many-body systems which are subject to strong quantum correlations. The recurrent theme in all of these topics represents the application and advancement of different tensor network techniques. Specifically, we relied on numerical algorithms based on matrix product states (MPS) and infinite projected-entangled pair states (iPEPS) to obtain all results presented in this thesis.

Thus we present a discussion of the full range of MPS and iPEPS techniques employed in this work in chapter 2, before applying them to various models in subsequent chapters.

As a first application, we explore quantum critical properties of bosonic quantum impurity models in chapter 3. Employing a highly flexible DMRG algorithm, we extensively study a generalized spin-boson model with two baths that features fascinating critical properties in the form of a breakdown of the quantum-to-classical correspondence [Sec. 3.1]. Moreover, our MPS simulations also provide new insight into universal properties of the critical wavefunction of the one-bath spin-boson model [Sec. 3.2]. Finally, we propose a new type of Wilson chain mapping designed to incorporate missing bath modes, which are crucial to faithfully reproduce critical properties of the spin-boson model at finite temperatures [Sec. 3.3].

In Chapter 4 we deal with the evaluation of spectral properties in one-dimensional many-body systems. Employing MPS-based real-time evolution and Chebyshev expansions, we calculate the different components of the dynamic spin-structure factor in an effective spin- $\frac{1}{2}$ model governing the low-energy properties of the materials Cs_2CoCl_4 [Sec. 4.1]. We focus on the vicinity of the Ising quantum phase transition which is driven by an external magnetic field. It reveals interesting new features in the spectra of spin-spin correlators, which could guide potential future neutron scattering experiments on this compound. Moreover, we propose a symmetry-enhanced version of the minimally entangled typical states (METTS) algorithm designed for the study of spectral quantities at finite temperature [Sec. 4.2]. Using METTS we explore the excitation spectrum of an effective spin-ladder model for the natural material azurite $\text{Cu}_3(\text{CO}_3)_2(\text{OH})_2$, which features a prominent magnetization plateau at $\frac{1}{3}$ of the total magnetization under the application of an external magnetic field. Moreover, we present zero-temperature calculations for the local density of states in an interacting quantum point contact; our results are consistent with those from a functional RG approach that aims towards the resolution of the so-called 0.7 anomaly in quantum point contacts [Sec. 4.3].

The topic of chapter 5 concerns extending the range of tensor network techniques for two-dimensional many-body systems. First, we demonstrate that finite-temperature MPS algorithms can be adopted to 2D models, yielding competitive results in comparison to other state-of-the-art methods [Sec. 5.1]. To this end, we apply a combination of density-matrix purification and METTS to access the finite-temperature phase diagram of the spin- $\frac{1}{2}$ triangular Heisenberg model over a wide range of temperatures. Moreover, we propose a METTS protocol for detecting the critical temperature of finite-temperature phase transitions that also leads to reliable results in the presence of frustration. Furthermore, we present the first fermionic iPEPS simulations that exploit a variety of non-abelian symmetries [Sec. 5.2]. In this way, we are able to substantially increase the performance of the algorithm, allowing for the treatment of fermionic systems up to a bond dimension $D = 24$ on a square lattice. This technical progress renders a variety of complex models numerically accessible. In particular, we present some promising initial results for the three-flavor and the two-band Hubbard model by incorporating both non-abelian spin- and flavor symmetries of the underlying Hamiltonian.

Tensor network techniques

In this methods chapter, we elaborate on the various tensor network (TN) techniques that form the building blocks for the work performed in this thesis. After a brief overview [Sec. 2.1], we discuss the fundamental basis of all TN representation, the area law of the entanglement entropy [Sec. 2.2]. In addition, we introduce a diagrammatic language in Sec. 2.3 that greatly facilitates discussions on details of TN algorithms. Further details of the MPS and iPEPS follow in Sec. 2.4 and 2.5, respectively.

2.1 Overview

Tensor network techniques build on the common idea to parametrize the wavefunction of a quantum many-body system in terms of a set of interconnected tensors. Remarkably, these formulations can still capture the important aspects of physical wavefunctions such as ground states or thermal Gibbs states with high accuracy, despite neglecting the vast majority of the full Hilbert space [Eis13]. By now, tensor networks have been recognized as a natural representation of quantum many-body states and represent one of the most current and exciting branches of computational condensed matter physics.

The most prominent type of tensor networks are so-called matrix product states (MPS), one-dimensional TN representations consisting of an array of tensors. Matrix product states are the basis of some of the most powerful numerical algorithms for one-dimensional (1D) quantum systems, such as the density matrix renormalization group (DMRG), a variational method developed to determine ground-state properties of 1D systems [Whi92, Whi93, Sch05]. Other examples include the time-evolving block decimation (TEBD) [Vid04], as well as various extensions of DMRG for dynamical properties [DKSV04, WF04, HWvD10], and finite temperatures [VGRC04, ZV04, FW05, Whi09], to name only a few. The unprecedented success of these techniques in 1D is strongly linked to the entanglement structure of many physical wavefunctions, which is fully captured by an MPS representation [see Sec. 2.2].

Another important class of tensor networks is the family of projected entangled-pair states (PEPS) [VC04], the natural generalization of the MPS ansatz to higher spatial dimensions. A PEPS consist of a set of high-ranked tensors which are spanned along the physical directions of the corresponding lattice system. PEPS form the basis of many important algorithms for two-dimensional (2D) quantum lattice models such as the PEPS- and the iPEPS approach [JOV⁺08], the tensor renormalization group [LN07, GLW08], or tensor network renormalization [EV15, Eve17]. As in the case of MPS, these tensor networks satisfy specific entanglement properties, and thus can faithfully approximate ground-state wavefunctions of many effective models for strongly correlated systems in 2D.

While the tensor structures of MPS and PEPS mimic the underlying lattice, there are also tensor networks which include extra “holographical” dimensions in addition to the physical

ones. The underlying system typically undergoes some type of rescaling or renormalization along this additional dimensions, for instance to take into account different energy or length scales. The most prominent example of this class of TN is the multi-scale entanglement renormalization ansatz (MERA), a tree tensor network (i.e., a TN without loops) that represents the fundament of the so-called entanglement renormalization algorithm. MERA is capable to faithfully reproduce the entanglement structure of critical systems in 1D and 2D [Vid07, EV09].

Over the last 25 years, tensor network algorithms continuously added to the advancement of the field of strongly correlated systems by providing answers to long-standing open questions, such as the precise measurement of the Haldane spin gap in the spin-1 Heisenberg chain [WH93], or the observation of various novel spin-liquid states in frustrated spin models [YHW11, DMS12], just to name two examples. Their versatility and flexibility also opened up various new research directions towards understanding nonequilibrium, finite-temperature and topological properties of low-dimensional quantum systems. Without suffering from a sign problem and with their non-perturbative character, TN methods currently present one of the most promising approaches to tackle the “hard” open problems in the context of two-dimensional correlated systems such as single- and multi-band Hubbard and t - J models, arising in the context of unconventional superconductivity [LAB⁺15, ZCC⁺17]. Beyond condensed matter, tensor networks keep generating impact on a conceptual level in other fields of science, ranging from high-energy physics [Orú14a] to machine learning [SS16, CCX⁺17, LYCS17].

2.2 Entanglement

Why do tensor network techniques work? Remarkably, the answer to this question can be phrased in a compact way citing two sentences of Ref. [Eis13] (p. 3, p. 10):

“Many natural quantum lattice models have ground states that are little, in fact very little entangled in a precise sense. [...] In the end, the reason for tensor network methods to provide such powerful tools is rooted in the fact that natural ground state satisfy the area law [for the entanglement entropy] (or small violations thereof).”

To understand these statements more deeply, we have to take a closer look at the notions of entanglement and area law in the context of a quantum many-body system. To this end, we mostly follow the reviews Ref. [ECP10, Eis13] throughout this section.

2.2.1 Local Hamiltonians and correlations

Many strongly correlated minimal models for strongly correlated electron systems arise from local Hamiltonians on a lattice \mathcal{L} . In other words, such local Hamiltonians can be decomposed as

$$\hat{H} = \sum_{k \in \mathcal{L}} \hat{h}_k, \quad (2.1)$$

with \hat{h}_k being a local few-body operator including only terms from a somewhat local sub-cluster k of the lattice \mathcal{L} . Without providing a mathematically rigid definition of locality here, \hat{h}_k typically only consists of operators located on nearest- or next-to-nearest-neighbor sites on \mathcal{L} . Paradigmatic examples of such Hamiltonians are the Heisenberg or the Hubbard model.

Since we typically target ground-state and low-energy physics in the scope of this work, one may wonder how the locality of the Hamiltonian is reflected in the ground-state properties

of such a system. A straightforward measure for locality are two-point correlation functions, which are expected to decay with increasing lattice distance due to the local nature of the interactions terms. Indeed, this can be observed in the corresponding ground-state wavefunctions.

In gapped models, which are characterized by a finite energy gap separating the ground state and the first excited state in the thermodynamic limit, correlation functions show a so-called “clustering of correlations”, i.e., they always decay exponentially with increasing lattice distance. In this case, one can define the correlation length ξ as the length scale on which correlations effectively drop to zero [HK06].

In contrast, correlations behave differently in models without an energy gap (so-called gapless or critical models). Inherited from the locality of the Hamiltonian, these models still exhibit a decay of correlation functions with increasing lattice distance. However, this is no longer an exponential but rather an algebraic decay [Eis13].

2.2.2 Ground-state entanglement and area laws

Originally introduced in quantum information theory, entanglement measures have emerged as highly useful concepts in condensed matter physics as well. It turns out that ground-state entanglement represents a more general measurement of locality than studying the decay of two-point correlation functions. Entanglement theory for quantum many-body systems, and at its core the area laws, provide a fundamental explanation for the success of tensor network methods (i.e., why these approaches work with a polynomial cost scaling in many cases).

Now considering some gapped quantum lattice model, how can we measure the entanglement of a particular pure state such as the ground state of the system? To this end, we separate the lattice \mathcal{L} into a subregion \mathcal{C} and its complement \mathcal{D} . Then we form the reduced density matrix $\rho_{\mathcal{C}} = \text{Tr}_{\mathcal{D}}(\rho)$ of subregion \mathcal{C} by taking the trace over an orthonormal basis in \mathcal{D} . The entanglement content of the pure state shared between regions \mathcal{C} and \mathcal{D} can be characterized by the von-Neumann entropy

$$S(\rho_{\mathcal{C}}) = -\text{Tr}(\rho_{\mathcal{C}} \log_2 \rho_{\mathcal{C}}). \quad (2.2)$$

If correlations between subregions \mathcal{C} and \mathcal{D} are present in the wavefunction, then the entropy is nonzero and positive. Only if \mathcal{C} and \mathcal{D} form a product state it follows that $S(\rho_{\mathcal{C}}) = 0$ and consequently no entanglement is shared between the two subregions [BDSW96]. Note that $S(\rho_{\mathcal{C}})$ is a unique measure of the entanglement content in a pure state [DHR02]; for mixed states (e.g., in case of ground-state degeneracy) $S(\rho_{\mathcal{C}})$ has to be replaced by other Renyi-entropies [Eis13].

The crucial question concerns the scaling of $S(\rho_{\mathcal{C}})$ with the size $|\mathcal{C}|$ of the subregion \mathcal{C} . Naively, one would expect that the amount of entanglement scales extensively with the size of \mathcal{C} or, in other words, with its volume,

$$S(\rho_{\mathcal{C}}) = \mathcal{O}(|\mathcal{C}|). \quad (2.3)$$

This is correct for the vast majority of states in the Hilbert space. For a small subset of states including the low-energy sector and, in particular, the ground state of a gapped system, however, this statement does not hold. These states satisfy the so-called *area law for the entanglement entropy* [Has07], indicating the amount of entanglement scales rather with the size of the boundary $|\partial\mathcal{C}|$ than with $|\mathcal{C}|$,

$$S(\rho_{\mathcal{C}}) = \mathcal{O}(|\partial\mathcal{C}|). \quad (2.4)$$

While the area law has only been strictly proven for gapped systems with unique ground states in one spatial dimension, there exists a lot of evidence that it also holds for higher

dimensional gapped systems [PEDC05, CE06, ECP10]. In contrast, for gapless models the entanglement entropy of the ground state scales differently and violates the area law. Typically one finds logarithmic corrections $S(\rho_C) = \mathcal{O}(\log(|\mathcal{C}|))$ that grows much more weakly as compared to a volume scaling [ECP10]. Table 2.1 summarizes the entanglement scaling for 1D and 2D systems subject to this thesis.

Scaling of $S(\rho_C)$	1D	2D
non-critical / gapped	const	L
critical / gapless	$\log(L)$	$L \log(L)$

Table 2.1: Scaling of entanglement for different system types in one and two dimensions. The volume of region \mathcal{C} is given by L in 1D and by L^2 in 2D (see Fig. 2.1 for illustration).

In consequence, low-energy states of local Hamiltonians are in general significantly less entangled than one would naively expect. Whereas the vast majority of pure states in the Hilbert space follow a volume scaling of the entanglement entropy, natural ground states fall into the very small subset of states that satisfy the area law (or only weakly violate it).

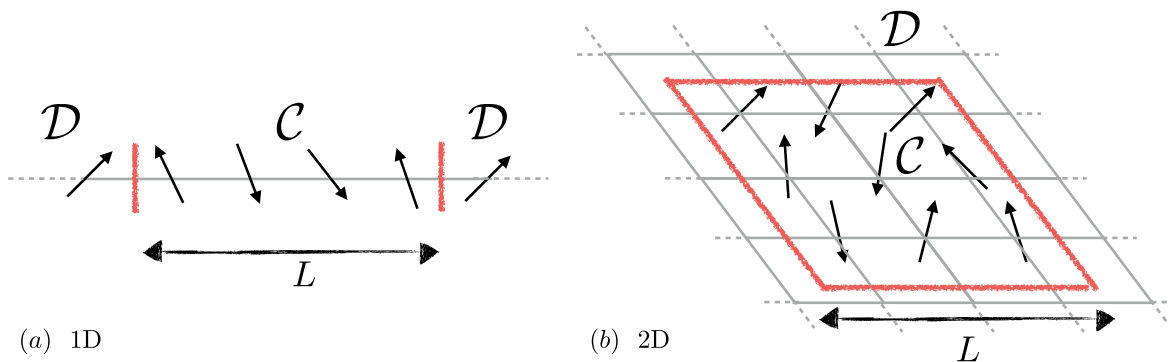


Figure 2.1: Illustration of subregion \mathcal{C} and \mathcal{D} required to obtain the entanglement entropy $S(\rho_C)$ in one- and two dimensions. The volume of region \mathcal{C} is given by L in 1D and by L^2 in 2D.

This observation is crucial for the applicability of the two classes of tensor networks considered in this work. Matrix product states in one dimension and projected entangled-pair states in two dimensions both satisfy the corresponding area laws [VWPGC06]. Thus both descriptions are ideally suited for the representation of a ground state in a gapped lattice model. In other words, one can perform a numerical simulation to find this TN representation based only on a polynomial cost scaling with respect to system size. We emphasize that the same statement does not hold for TN representations of arbitrary pure states following the volume law. In this case, one ends up with an exponential cost scaling leading to a numerically unfeasible task. The success of tensor network techniques is therefore strongly tied to the presence of an area law for the considered quantum states.

2.3 Diagrams

As implied by their name, tensor network techniques typically involve a large number of tensors of various rank that are iteratively manipulated. These manipulation steps may vary in their complexity and, for example, include matrix multiplication, or decomposition techniques such as singular value or eigenvalue decompositions. In order to simplify the lengthy mathematical expressions which describe these steps and typically involve large sums over multiple indices, we heavily rely on using a diagrammatic representation for tensor network states. Analogous to the role of Feynman diagrams in quantum field theories, these tensor network diagrams are pictorial representation of mathematical expressions and help a great deal grasping the essence a TN algorithm. Since we are extensively employing this pictorial language in the rest of this thesis, we here give a brief summary of our conventions together with an explanation on how to understand these diagrams in the following.

Each TN diagram consists of one or multiple extended objects (squares, circles, ...), which are connected by lines. Objects and lines represent tensors and indices, respectively. In the following, we give a few simple examples.

A rank-1 tensor (or vector) A can be labeled by a single index α and has the following diagrammatic representation

$$A_\alpha = \overset{\alpha}{\text{---}} \textcircled{A} . \quad (2.5)$$

The number of values that the index α can take on is called its dimension. Analogously, a matrix or rank-2 tensor A consists of two indices α, β ,

$$A_{\alpha\beta} = \overset{\alpha}{\text{---}} \textcircled{A} \text{---} \overset{\beta}{\text{---}} . \quad (2.6)$$

Note that in both cases, the lines are not connected to anything else. Such open lines in the diagrammatic language indicate that the corresponding indices are not summed over. In contrast, the next expression illustrating a matrix multiplication

$$\sum_{\beta} A_{\alpha\beta} B_{\beta\gamma} = \overset{\alpha}{\text{---}} \textcircled{A} \text{---} \textcircled{B} \text{---} \overset{\gamma}{\text{---}} , \quad (2.7)$$

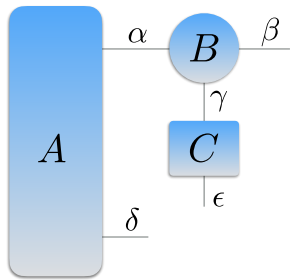
involves the sum over the common index β of A and B . The corresponding line connects the matrix A with B and has no open end, which automatically implies that one carries out the contraction over β .

For the special case of the unit matrix we use a diagram showing only a single line without any box,

$$\mathbb{1}_{\alpha\alpha'} = \textcircled{\mathbb{1}} = \text{---} \begin{array}{c} \alpha \\ \text{---} \\ \alpha' \end{array} . \quad (2.8)$$

In addition to the simple expression shown above, we often have to deal with diagrams

containing multiple sums and open indices, such as

$$\sum_{\alpha, \gamma} A_{\alpha\delta} B_{\alpha\beta\gamma} C_{\gamma\epsilon} =$$

(2.9)

It holds generally true, that the diagrammatic representation becomes more beneficial, the more complex the expression and the larger the number of tensors involved since the logic of reading and understanding these diagrams remains the same.

For more evolved topics, such as fermionic TN descriptions and symmetric TNs, the diagrams will contain extra features. We will introduce these features in detail at the appropriate parts of this thesis.

2.3.1 Numerical scaling

Most tensor network algorithms have no unique implementation prescription. For example, there are multiple ways to perform the contraction of a tensor network, e.g., by carrying out individual contractions in a different order (this is a generalization of associativity of matrix multiplications). Note that such a general contraction is always carried out pairwise, involving only two tensors of the TN at once. The contraction order matters a lot since it is strongly linked to the numerical efficiency of a TN algorithm. Whether a TN application is run using $\mathcal{O}(D^4)$ or $\mathcal{O}(D^8)$ operations strongly influences the applicability of the method. The difference between the two cost scalings could mean that one can study more complex or larger systems in order of magnitudes shorter times.

Here we briefly discuss how to read off the cost scaling from a tensor network diagram, which is actually a quite simple procedure. For a given contraction of two arbitrary tensors, we count the dimensions of all open indices of the two tensors as well as those of the indices that are contracted over. The product of these numbers leads to the number of operators necessary to perform this specific contraction.

Let us consider as a simple example the matrix multiplication in Eq. (2.7), where we assume for $\alpha, \beta = 1, \dots, D$ and $\gamma = 1, \dots, \tilde{D}$. Performing the matrix multiplication and contracting over β then requires $\mathcal{O}(D^2 \tilde{D})$ operations, following the logic described above.

For the second example shown in Eq. (2.9) we assume that $\alpha, \beta, \delta = 1, \dots, D$ and $\gamma, \epsilon = 1, \dots, d$. The first contraction of tensors A and B over the index α then scales $\mathcal{O}(D^3 d)$. Contracting the resulting tensor AB with C leads to a scaling $\mathcal{O}(D^2 d^2)$ (note that the index α disappears after the first contraction).

Examples how to perform TN contractions in a more efficient order will be given numerous times in the rest of this chapter. The rationale behind the given contraction orders is always the cost scaling introduced here.

2.4 Matrix product states

In this part we introduce matrix product states (MPS) as the simplest type of the tensor network representation for quantum many-body states. Matrix product states form effective one-dimensional tensor networks which are able to satisfy the area law in 1D. Thus MPS are a natural representation of low-energy states in an 1D many-body systems.

Historically, the concept of MPS appeared several times independently in the literature, and on top of this in languages different from tensor network states [PWKH99]. Most importantly for the context of this work, the introduction of the density matrix renormalization group (DMRG) by Steve White [Whi92, Whi93] in the early 1990s is responsible for the broad popularity of MPS techniques today. Independently, the concept of MPS emerged around the same time in the literature of mathematical physics [AKLT87] and mathematics [FNW92].

The success of DMRG in finding ground-state wavefunctions of 1D quantum systems is strongly linked to its underlying MPS structure and the area law, although the MPS foundation of DMRG was noticed only years after its invention [OR95, DMDNS98]. Expressing DMRG, and also the numerical renormalization group (NRG), explicitly in the language of MPS has triggered many methodological extensions such as time evolution [WF04, Vid04, DKSV04] or finite temperature [ZV04, VGRC04, FW05, WvD07, Whi09]. By now DMRG and its MPS extensions represent the most powerful numerical framework for one-dimensional quantum systems and have proven to be competitive in two dimensions as well [SW12, BZWS17].

In this section we present the basic properties and operations of the MPS framework. In addition, we provide a short discussion of the most important MPS techniques that are crucial for the work of this thesis. In particular, we discuss the MPS formulation of NRG [Sec. 2.4.2] and DMRG in and [Sec. 2.4.3], respectively, as well as its extensions to calculate dynamical [Sec. 2.4.4] and finite-temperature properties [Sec. 2.4.5]. In this way we summarize the complete set of methodological approaches in a single section. However, we note that especially the more advanced topics of this section have some overlap with the method sections of the publications included in this thesis. For a more detailed introduction to MPS techniques we refer to the excellent reviews [VMC08, Sch11, Eis13] and [CKN⁺16] for matrix product operators.

2.4.1 Basics and calculus

Here we introduce the structure of matrix product states and some basic MPS operations that form the basis for more complex MPS-based algorithms discussed below. Parts of the discussion are adapted from the reviews [VMC08, Sch11]. For compactness and clarity, however, we put more emphasize on the diagrammatic formulations of the algorithmic steps.

For the purpose of this section, we consider a one-dimensional quantum system with N sites. Any generic many-body wavefunction $|\psi\rangle$ of such a model can be expressed in terms of the local Fock space $|\sigma_1\rangle|\sigma_2\rangle\dots|\sigma_N\rangle$ and a rank- N tensor $\Psi_{\sigma_1\sigma_2\dots\sigma_N}$

$$|\psi\rangle = \sum_{\sigma_1\sigma_2\dots\sigma_N} \Psi_{\sigma_1\sigma_2\dots\sigma_N} |\sigma_1\rangle|\sigma_2\rangle\dots|\sigma_N\rangle. \quad (2.10)$$

Obviously, this generic representation suffers from an exponential system-size scaling, which is reflected in the fact that the number of entries in $\Psi_{\sigma_1\sigma_2\dots\sigma_N}$ is equal to the total Hilbert space d^N . The local dimension d describes the total number of quantum states per site. Typical values are $d = 2$ for a spin- $\frac{1}{2}$ system or spinless fermions, $d = 3$ for spin-1, and $d = 4$ for spinful fermions.

The essential idea of an MPS representation is to avoid the exponential scaling in Ψ by decomposing this large tensor into a set of N rank-3 tensors,

$$|\psi\rangle = \sum_{\substack{\sigma_1 \sigma_2 \dots \sigma_N \\ \alpha_1 \alpha_2 \dots \alpha_{N-1}}} A_{1\alpha_1}^{[\sigma_1]} A_{\alpha_1 \alpha_2}^{[\sigma_2]} \dots A_{\alpha_{N-1} 1}^{[\sigma_N]} |\sigma_1\rangle |\sigma_2\rangle \dots |\sigma_N\rangle \quad (2.11)$$

Each $A_{\alpha_{j-1}\alpha_j}^{[\sigma_j]}$ has two “virtual” or “bond” indices α_j, α_{j-1} that connect the tensor to its counterparts on the two neighboring sites, as well as one physical index σ_j corresponding to the local Hilbert space of site j . For finite systems with open boundary conditions (which we assume throughout this section), the indices at the ends of the chain, i.e., first index A_1 and second index of A_N , only run over a single value referring to the vacuum state. From the structure of Eq. (2.11) it becomes apparent that the coefficients for a fixed set of physical indices are build from a product of matrices – hence, the name “matrix product state”.

For the purpose of clarity, we also depict the diagrammatic representations of a generic A tensor A_j

$$A_{\alpha\beta}^{[\sigma_j]} = \begin{array}{c} \alpha \quad \beta \\ \circlearrowleft A_j \circlearrowright \\ | \sigma_j \rangle \end{array} \quad (2.12)$$

as well as the diagrammatic version of Eq. (2.11)

$$\begin{array}{c} \psi \\ \text{---} \\ | \sigma_1 \rangle | \sigma_2 \rangle | \sigma_3 \rangle \dots | \sigma_{N-1} \rangle | \sigma_N \rangle \end{array} = \begin{array}{c} \circlearrowleft A_1 \circlearrowright \quad \circlearrowleft A_2 \circlearrowright \quad \circlearrowleft A_3 \circlearrowright \quad \dots \quad \circlearrowleft A_{N-1} \circlearrowright \quad \circlearrowleft A_N \circlearrowright \\ | \sigma_1 \rangle \quad | \sigma_2 \rangle \quad | \sigma_3 \rangle \quad \dots \quad | \sigma_{N-1} \rangle \quad | \sigma_N \rangle \end{array} \quad (2.13)$$

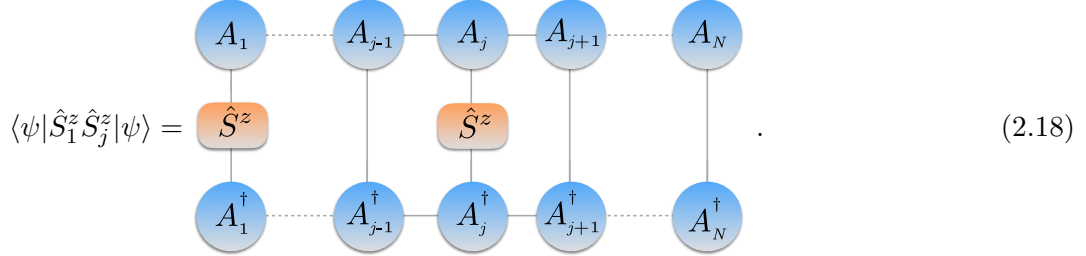
To avoid the exponential scaling of the number of coefficients in $|\psi\rangle$, the sizes of the A tensors are typically restricted by an upper cutoff dimension D for the bond indices. In this way, the total number of coefficients in the MPS representation of $|\psi\rangle$ increases only polynomially with system size. In numerical simulations the bond dimension D then acts as the only control parameter for the accuracy of the calculation.

Of course, the size restriction of the A tensors affects the types of states that can be accurately described by the corresponding MPS. D imposes an upper bound on the entanglement that can be captured by an MPS representation of $|\psi\rangle$. Specifically for any subset \mathcal{C} of consecutive sites, it can easily be shown that $S(\rho_{\mathcal{C}}) \leq 2(\log(D))$. The entanglement entropy of the MPS is therefore bounded from above by a constant in the number of sites N [Eis13]. This means that the entanglement scaling of an MPS with system size is equivalent to the scaling of a ground state of a gapped 1D system. In other words, the MPS satisfies the area law in one dimension and is therefore particularly well suited to represent such a ground state. Note that for a critical ground state with $\log(N)$ correction to the area law, the bond dimension D has to be increased linearly with system size to maintain the same accuracy.

Moreover, many operations from the simple computation of expectation values, to variational ground-state search via DMRG, or real- and imaginary-time evolution can be implemented extremely efficiently in the MPS framework. In the rest of this section, we cover basic MPS calculus including the canonical forms and matrix product operators (MPO) before discussing the more advanced algorithms further below.

Expectation value

The measurement of static observables such as magnetization or two-point correlation functions follows along the same lines as an overlap calculation, as illustrated by the following example,

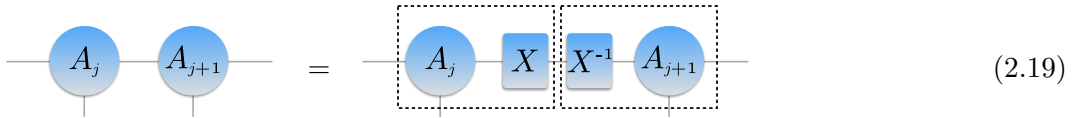


$$\langle \psi | \hat{S}_1^z \hat{S}_j^z | \psi \rangle = \text{TN} \quad (2.18)$$

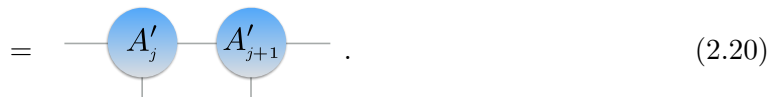
To evaluate this TN, \hat{S}_1^z and \hat{S}_j^z can be applied locally while employing the efficient contraction pattern of Eq. (2.17). Note that the calculation of local observables can be further simplified by exploiting orthonormal state spaces, as discussed in the next section.

Gauge and canonical form

A key aspect contributing to the efficiency of many MPS application is the fact that no MPS representation for a given state $|\psi\rangle$ is unique. Instead, a gauge degree of freedom exists on every virtual index of the A tensors [VMC08]. It has no effect on the physical wavefunction and can be probed simply by inserting an identity XX^{-1} on the bond index connecting two A tensors,

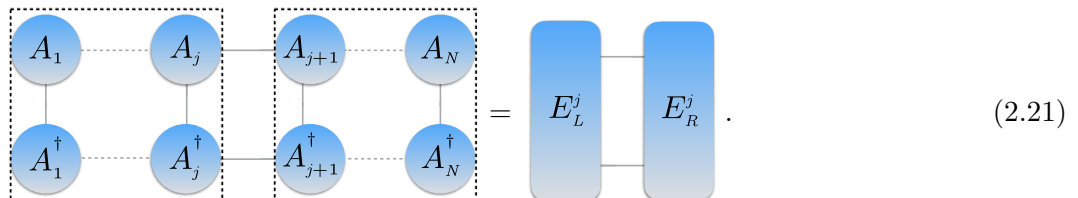


$$A_j - A_{j+1} = \boxed{A_j \ X \ X^{-1} \ A_{j+1}} \quad (2.19)$$



$$= A'_j - A'_{j+1} \quad (2.20)$$

How can we exploit this MPS property in practice? Consider the overlap of a generic MPS with respect to a specific bond j connecting tensors A_j and A_{j+1} . Contracting the entire tensor network with respect to this specific bond, we obtain the environmental tensor. In any MPS application, the environmental tensor factorizes into a left and a right part $E^j = E_L^j \otimes E_R^j$ separated by the bond j ,



$$\text{TN} = E_L^j \otimes E_R^j \quad (2.21)$$

Now we employ two *independent* eigenvalue decompositions to generate $E_L^j = X_j X_j^\dagger$ and $E_R^j = Y_j Y_j^\dagger$, in order to find a gauge for the bond in which both environmental tensors form

identities, $E_L \rightarrow E'_L = \mathbb{1}$, $E_R \rightarrow E'_R = \mathbb{1}$,

$$\begin{aligned}
 E_L^j E_R^j &= \begin{array}{c} X_j \quad Y_j \quad X_j^{-1} \quad X_j \quad Y_j \quad Y_j^{-1} \quad Y_j \\ X_j^\dagger \quad Y_j^\dagger \quad X_j^\dagger \quad X_j^{\dagger-1} \quad X_j^\dagger \quad Y_j^\dagger \quad Y_j^{\dagger-1} \quad Y_j^\dagger \end{array} \\
 &= \begin{array}{c} X_j \quad X_j^{-1} \quad X_j \quad Y_j \quad Y_j^{-1} \quad Y_j \\ X_j^\dagger \quad X_j^{\dagger-1} \quad X_j^\dagger \quad Y_j^\dagger \quad Y_j^{\dagger-1} \quad Y_j^\dagger \end{array} \\
 &= \begin{array}{c} \beta \quad \gamma \\ \circlearrowleft Q_j \quad \circlearrowright \\ \beta' \quad \gamma' \\ \circlearrowright Q_j^\dagger \quad \circlearrowleft \end{array} = \begin{array}{c} \beta \\ \circlearrowleft Q_j \\ \beta' \end{array} = \mathbb{1}_{\beta\beta'} .
 \end{aligned} \tag{2.22}$$

This illustrates that the gauge degree of freedom can be used to orthonormalize effective block state spaces associated with individual bonds (here indices β, γ). This very useful property is crucial for the efficiency and accuracy of MPS algorithms.

Left-canonical form.— To fully exploit the gauge freedom in calculations, one can systematically construct an MPS with orthonormal bases on every bond index. Such representations are called *canonical* forms of an MPS. For instance, an MPS can be brought into a *left-canonical* form by gauging all A tensors such that they obey

$$\sum_{\alpha\sigma_j} \vec{A}_{\alpha\beta}^{[\sigma_j]} \vec{A}_{\alpha\beta'}^{[\sigma_j]^\dagger} = \begin{array}{c} \beta \\ \circlearrowleft \vec{A}_j \\ \beta' \end{array} = \mathbb{1}_{\beta\beta'} , \tag{2.23}$$

where the arrow indicates the left-canonical form. In practice, this can be achieved starting from the first site and systematically generating X_j for each bond j , inserting $X_j^{-1}X_j$ and updating $\vec{A}_j = A_j X_j^{-1}$, $A'_{j+1} = X A_{j+1}$ before moving to bond $j + 1$ and repeating the procedure.

An alternative route to construct a left-canonical MPS is based on an exact singular value decomposition (SVD). For a generic, non-quadratic matrix A a SVD decomposition yields $A = USV^\dagger$, where S is a positive-defined diagonal matrix containing the singular value spectrum of A , the unitary matrix U has orthogonal columns (i.e., $U^\dagger U = \mathbb{1}$), and second unitary V^\dagger has orthogonal rows ($V^\dagger V = \mathbb{1}$).

Again one starts with the first bond $j = 1$ and subsequently performs

$$\begin{aligned}
 A_j A_{j+1} &= U S V^\dagger A_{j+1} = U \boxed{S V^\dagger A_{j+1}} \\
 &= \vec{A}_j A'_{j+1} ,
 \end{aligned} \tag{2.24}$$

keeping all D states in the SVD and refraining from any truncation that could alter the wavefunction. Repeating this for all $N - 1$ bonds in the MPS, one ends up with a fully left-canonical version

$$|\psi\rangle = \begin{array}{c} \xrightarrow{A_1} \xrightarrow{A_2} \xrightarrow{A_3} \cdots \xrightarrow{A_{N-1}} A_N \\ \downarrow \quad \downarrow \quad \downarrow \quad \downarrow \quad \downarrow \end{array} .$$

Right-canonical form. – Analogously, one can bring the MPS into a *right-canonical* form, where all A tensors satisfy

$$\sum_{\beta\sigma_j} \overleftarrow{A}_{\alpha\beta}^{[\sigma_j]} \overleftarrow{A}_{\alpha'\beta}^{[\sigma_j]\dagger} = \begin{array}{c} \xleftarrow{A_j} \\ \downarrow \\ \xleftarrow{A_j^\dagger} \\ \downarrow \\ \alpha' \end{array} = \begin{array}{c} \left. \right) \\ \downarrow \\ \left. \right) \\ \downarrow \\ \alpha \end{array} = \mathbb{1}_{\alpha\alpha'} . \quad (2.25)$$

Again, there exist two options for the construction of a right-canonical MPS, both starting from the last bond of the system $j = N$. One can either systematically generate Y_j for each bond j , insert $Y_j^{-1}Y_j$ and update $A'_j = A_j Y_j$, $\overleftarrow{A}_{j+1} = Y_j^{-1} A_{j+1}$ before moving to bond $j - 1$ and repeating this procedure.

Alternatively, one can also rely on subsequent exact SVDs starting from A_N ,

$$\begin{array}{c} \xrightarrow{A_j} \xrightarrow{A_{j+1}} \\ \downarrow \quad \downarrow \end{array} = \begin{array}{c} \xrightarrow{A_j} \quad U \quad S \quad V^\dagger \\ \downarrow \quad \downarrow \quad \downarrow \quad \downarrow \end{array} = \begin{array}{c} \boxed{\xrightarrow{A_j} \quad U \quad S} \quad V^\dagger \\ \downarrow \quad \downarrow \quad \downarrow \quad \downarrow \end{array} \\ = \begin{array}{c} \xleftarrow{A'_j} \xleftarrow{A_{j+1}} \\ \downarrow \quad \downarrow \end{array} . \quad (2.26)$$

After repeating this procedure on all $N - 1$ bonds, the resulting MPS is brought into its right-canonical representation,

$$|\psi\rangle = \begin{array}{c} A_1 \quad \xleftarrow{A_2} \quad \xleftarrow{A_3} \quad \cdots \quad \xleftarrow{A_{N-1}} \quad \xleftarrow{A_N} \\ \downarrow \quad \downarrow \quad \downarrow \quad \downarrow \quad \downarrow \end{array} .$$

Mixed-canonical form. – In practice, it is very convenient to work with MPS representations that mix left- and right-canonical A matrices. For example, one can gauge all A tensors to left and right of site j in left- and right-canonical form, respectively, leading to

$$|\psi\rangle = \begin{array}{c} \xrightarrow{A_1} \cdots \xrightarrow{A_{j-1}} \quad A_j \quad \xleftarrow{A_{j+1}} \cdots \xleftarrow{A_N} \\ \downarrow \quad \downarrow \quad \downarrow \quad \downarrow \quad \downarrow \end{array} . \quad (2.27)$$

In this form A_j denotes the “orthonormal center” of the MPS, as all bases to the left and right of site j are orthogonalized.

This representation is particularly helpful for MPS techniques that involve subsequent “sweeping” procedures from one end of the chain to the other, such as MPS compression, time evolution or DMRG itself, as illustrated in the following. But even the evaluation of local observables can be drastically simplified by choosing a convenient MPS representation.

We illustrate this for the example of measuring the nearest-neighbor two-point correlation $\langle \psi | \hat{S}_j^z \hat{S}_{j+1}^z | \psi \rangle$,

$$(2.28)$$

Instead of performing an overlap calculation for the entire MPS, one only has to work with the tensors around the orthonormal center in the mixed-canonical form.

Reduced density matrix and entanglement entropy

Although we have already briefly discussed the entanglement properties of MPS above, we are now equipped to explicitly compute the entanglement entropy via the reduced density matrix. To this end, we consider a mixed-canonical MPS representation with the orthonormal center shifted to bond j . This results in a diagram equivalent to Eq. (2.22) with a bond matrix Q_j connected to two orthonormal basis sets.

Now we split the system at this particular bond j so that we obtain a left block \mathcal{C} and a right block \mathcal{D} . To calculate the block entanglement at the cut, we have to generate the reduced density matrix $\rho_{\mathcal{C},\mathcal{D}}$ of either one of the blocks. For example, the reduced density matrix of block \mathcal{D} is generated by tracing out \mathcal{C} ,

$$(2.29)$$

Diagonalizing $\rho_{\mathcal{D}}$, we obtain the corresponding eigenvalues $\rho_{\mathcal{D}}^\alpha$ ($\alpha = 1, \dots, D$) and are therefore able to compute the von Neumann entropy

$$S(\rho_{\mathcal{D}}) = - \sum_{\alpha} \rho_{\mathcal{D}}^\alpha \log(\rho_{\mathcal{D}}^\alpha), \quad (2.30)$$

as an entanglement measure [see Sec. 2.2]. Per construction, the number of eigenvalues of $\rho_{\mathcal{D}}$ is bounded by the bond dimension D , explicitly illustrating that the MPS is able to capture a maximum entanglement $S(\rho_{\mathcal{D}}) = \mathcal{O}(\log(D))$.

DMRG and other MPS-based algorithms typically approximate the MPS representation of a quantum state iteratively, truncating along the way to keep the bond dimension feasibly small. The appropriate truncation criterion is based on discarding the smallest contribution $\rho_{\mathcal{D}}^\alpha < \epsilon \ll 1$ to the reduced density matrix. In other words, one tries to retain only those states in the Hilbert space that have a significant contribution to $|\psi\rangle$ while discarding irrelevant orthogonal many-body states.

Note that the eigenspectrum of $\rho_{\mathcal{D}}$ is equivalent to the squared singular value spectrum s_j^2 obtained from an SVD decomposition of $Q_j = USV^\dagger$. Hence, one can directly truncate on the level of the SVD spectrum instead of using the eigenspectrum of $\rho_{\mathcal{D}}$. In MPS-based applications the truncation is typically implemented based on the singular value spectrum.

Global compression

Compressing an MPS $|\psi'\rangle$ with a large bond dimension D' to an MPS $|\psi\rangle$ with fewer coefficients $D < D'$ represents a very common task in many MPS-based applications. This operation becomes necessary, for example, after the addition of two MPS (see Sec. 4.3 of Ref. [Sch11]) or the application of a matrix product operator to an MPS (see next section), as one ends up with an MPS with enlarged bond dimension in both cases.

The most accurate approach for compressing an MPS builds on a variational procedure [VMC08, Sch11] (sometimes denoted “fitting”) that minimizes the norm

$$\| |\psi'\rangle - |\psi\rangle \|^2 = \langle \psi' | \psi' \rangle + \langle \psi | \psi \rangle - \langle \psi' | \psi \rangle - \langle \psi | \psi' \rangle \quad (2.31)$$

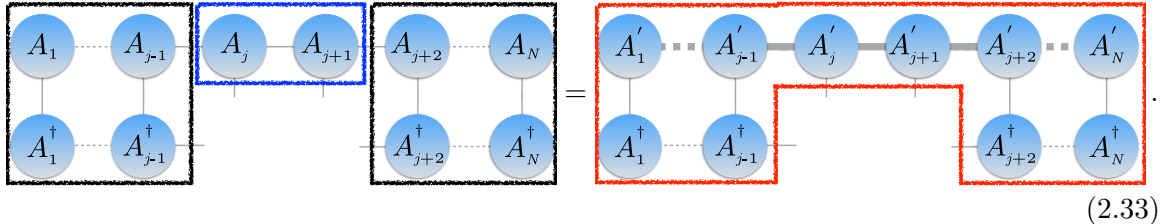
with respect to the new state $|\psi\rangle$. The minimization of Eq. (2.31) in terms of N A -tensors poses a highly non-linear optimization problem. However, it can be tackled iteratively by optimizing either a single or two neighboring A tensors at once while keeping the rest of the wavefunction constant. Thereby it is reduced to a bilinear optimization problem. Repeating this procedure site by site, one sweeps multiple times through the entire chain and eventually ends up with a converged MPS representation for $|\psi\rangle$ after a few sweeps.

In this section, we focus on the two-site variant of the fitting procedure. This numerically more stable formulation is less likely to get stuck in local minima during the optimization process and allows the dynamic modification of the bond dimension D based on the entanglement present in the state.

In order to find the optimal pair of tensors $A_j A_{j+1}$ that minimizes Eq. (2.31), we form the partial derivative of (2.31) with respect to $A_j^\dagger A_{j+1}^\dagger$,

$$\frac{\partial}{\partial (A_j^\dagger A_{j+1}^\dagger)} \left(\langle \psi | \psi \rangle - \langle \psi | \psi' \rangle \right) \stackrel{!}{=} 0, \quad (2.32)$$

which leads to the following diagrammatic expression,

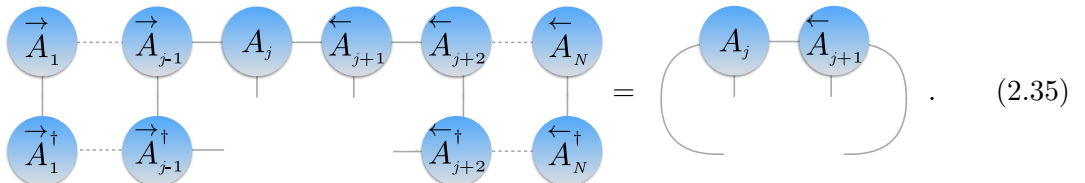


$$(2.33)$$

Note that the line thickness illustrates the larger bond dimension D' of $|\psi'\rangle$. By interpreting the parts of the diagram surrounded by the blue, red and black boxes as vectors x and b , as well as matrix C , respectively, Eq. (2.33) can be reformulated as system of linear equation

$$\boxed{C} \boxed{q} = \boxed{b}. \quad (2.34)$$

The resulting vector q represents the optimal combination of $A_j A_{j+1}$ and can be obtained by using, e.g., a conjugate gradient method. However, one can simplify the system of linear equations significantly by exploiting the mixed-canonical form of $|\psi\rangle$. By shifting the orthonormal center to either of the two sites j or $j+1$, the right-hand side of Eq. (2.33) can be transformed to,



$$(2.35)$$

Thus, it follows that the matrix $C = \mathbb{1}$ so that the solution to Eq. (2.125) can easily be found by contracting out the TN on the right-hand side of Eq. (2.33)

$$\begin{array}{c} \begin{array}{cccccc} \vec{A}'_1 & \vec{A}'_{j-1} & A'_j & \vec{A}'_{j+1} & \vec{A}'_{j+2} & \vec{A}'_N \\ \vdots & \vdots & \vdots & \vdots & \vdots & \vdots \end{array} \\ \begin{array}{cccccc} \vec{A}'^\dagger_1 & \vec{A}'^\dagger_{j-1} & & \vec{A}'^\dagger_{j+2} & \vec{A}'^\dagger_N & \\ \vdots & \vdots & & \vdots & \vdots & \end{array} \end{array} = \begin{array}{c} \boxed{Q_{j,j+1}} \\ \vdots \end{array} \quad (2.36)$$

To restore A_j and A_{j+1} from $Q_{j,j+1}$, we perform an SVD and shift the orthonormal center to the next site (here $j + 1$),

$$\begin{array}{c} \boxed{Q_{j,j+1}} \\ \vdots \end{array} = \begin{array}{c} \boxed{\text{SVD}} \\ \vdots \end{array} = \begin{array}{c} U \\ \vdots \end{array} \begin{array}{c} S \\ \vdots \end{array} \begin{array}{c} V^\dagger \\ \vdots \end{array} \\ = \begin{array}{c} \vec{A}_j \\ \vdots \end{array} \begin{array}{c} A_{j+1} \\ \vdots \end{array} \quad (2.37)$$

A dynamic truncation of the singular value spectrum can be implemented at this step by keeping not a fixed number of D singular values but rather retaining all states larger than some small threshold ϵ_{SVD} . In this way one can directly control the accuracy of the compressed MPS representation $|\psi\rangle$. This procedure is repeated sequentially for every neighboring pair of sites in the system. The convergence can be monitored by evaluating Eq. (2.31) after every full sweep and the number of total sweeps performed can be adapted accordingly.

An important criterion for fast convergence is the starting state $|\psi\rangle$ for this variational algorithm. Typically, a good choice is to reorthonormalize $|\psi'\rangle$ in the beginning while keeping only D states during each SVD.

Matrix product operators

We stated in the beginning of Sec. 2.4 that any generic many-body wavefunction can be reformulated as an MPS by decomposing the coefficient tensor $\Psi_{\sigma_1\sigma_2\dots\sigma_N}$ into N different A tensors. Along the same lines, one can take any arbitrary operator \hat{O} and represent it as a matrix product operator (MPO) [VGRC04, McC07, VMC08, Sch11, CKN⁺16],

$$\begin{aligned} \hat{O} &= \sum_{\substack{\sigma'_1\sigma'_2\dots\sigma'_N \\ \sigma_1\sigma_2\dots\sigma_N}} O_{\sigma'_1\sigma'_2\dots\sigma'_N}^{\sigma_1\sigma_2\dots\sigma_N} |\sigma_1\rangle|\sigma_2\rangle\dots|\sigma_N\rangle\langle\sigma'_1|\langle\sigma'_2|\dots\langle\sigma'_N| \\ &= \sum_{\substack{\sigma'_1\sigma'_2\dots\sigma'_N \\ \sigma_1\sigma_2\dots\sigma_N}} O_{\sigma'_1}^{\sigma_1} O_{\sigma'_2}^{\sigma_2} \dots O_{\sigma'_N}^{\sigma_N} |\sigma_1\rangle|\sigma_2\rangle\dots|\sigma_N\rangle\langle\sigma'_1|\langle\sigma'_2|\dots\langle\sigma'_N|. \end{aligned} \quad (2.38)$$

Again one decomposes a large coefficient tensor $O_{\sigma'_1\sigma'_2\dots\sigma'_N}^{\sigma_1\sigma_2\dots\sigma_N}$ into a set of N smaller tensors O_j (for an excellent review on efficient MPO construction see [CKN⁺16]).

In general, these O tensors are rank-4 (again with the exception of O_1, O_N for systems with open boundaries) since each tensor features two physical indices σ_j, σ'_j instead of just one in case of the A tensors of the MPS. The diagrammatic representation of an MPO closely follows the MPS diagrams. For example, the diagrammatic version of Eq. (2.38) has the form

$$\begin{array}{c} \langle\sigma'_1| \langle\sigma'_2| \langle\sigma'_3| \dots \langle\sigma'_{N-1}| \langle\sigma'_N| \\ \hat{O} \\ |\sigma_1\rangle |\sigma_2\rangle |\sigma_3\rangle \dots |\sigma_{N-1}\rangle |\sigma_N\rangle \end{array} = \begin{array}{c} \langle\sigma'_1| \langle\sigma'_2| \langle\sigma'_3| \dots \langle\sigma'_{N-1}| \langle\sigma'_N| \\ O_1 O_2 O_3 \dots O_{N-1} O_N \\ |\sigma_1\rangle |\sigma_2\rangle |\sigma_3\rangle \dots |\sigma_{N-1}\rangle |\sigma_N\rangle \end{array} \quad (2.39)$$

The MPO tensors describe sets of many-body operators acting on sections of the system with their precise form encoded in the MPO bond index. In case of an exact operator representation, the MPO bond dimension D_{MPO} at a certain bond j thus can be related to the number of operator terms with support on both sites of j .

Many MPO-based applications can be performed in close analogy to the MPS formalism. For instance, the calculation of an expectation value involving an operator represented as MPO,

$$\langle \psi | \hat{O} | \psi \rangle = \begin{array}{ccccccccc} & \textcircled{A_1} & \cdots & \textcircled{A_{j-1}} & \textcircled{A_j} & \textcircled{A_{j+1}} & \cdots & \textcircled{A_N} & \\ & | & & | & | & | & & | & \\ \langle \psi | \hat{O} | \psi \rangle = & \textcircled{O_1} & \cdots & \textcircled{O_{j-1}} & \textcircled{O_j} & \textcircled{O_{j+1}} & \cdots & \textcircled{O_N} & \\ & | & & | & | & | & & | & \\ & \textcircled{A_1^\dagger} & \cdots & \textcircled{A_{j-1}^\dagger} & \textcircled{A_j^\dagger} & \textcircled{A_{j+1}^\dagger} & \cdots & \textcircled{A_N^\dagger} & \end{array}, \quad (2.40)$$

can be carried out efficiently along the same lines as the MPS expectation value and overlap calculations discussed above. Note that an MPO does not increase the performance of MPS-based algorithms in terms of cost scaling (typically they rather generate a tiny overhead). However, MPOs significantly reduce the complexity of MPS codes and are therefore highly convenient for practitioners.

Another common task involves the application of an MPO to an MPS without directly calculating the overlap. This arises for example in the context of using an MPO representation for time evolution [Sec. 2.4.4] or when computing spectral functions in the CheMPS scheme [Sec. 2.4.6]. To this end, one performs a set of local contractions $O_j A_j$ leading to a new MPS with bond dimension DD_{MPO} . This MPS is then compressed in a subsequent step by employing the fitting procedure introduced above,

$$\begin{array}{l} \hat{O}|\psi\rangle = \\ \begin{array}{ccccccccc} \textcircled{A_1} & \textcircled{A_2} & \textcircled{A_3} & \cdots & \textcircled{A_{N-1}} & \textcircled{A_N} \\ | & | & | & & | & | \\ \textcircled{O_1} & \textcircled{O_2} & \textcircled{O_3} & \cdots & \textcircled{O_{N-1}} & \textcircled{O_N} \\ | & | & | & & | & | \end{array} \\ = \\ \begin{array}{ccccccccc} \textcircled{A_1^O} & \textcircled{A_2^O} & \textcircled{A_3^O} & \cdots & \textcircled{A_{N-1}^O} & \textcircled{A_N^O} \\ | & | & | & & | & | \end{array} \\ \stackrel{\text{MPS compression}}{=} \\ \begin{array}{ccccccccc} \textcircled{A'_1} & \textcircled{A'_2} & \textcircled{A'_3} & \cdots & \textcircled{A'_{N-1}} & \textcircled{A'_N} \\ | & | & | & & | & | \end{array} \end{array}. \quad (2.41)$$

Analogous to the MPS representation, an MPO also carries a gauge degree of freedom which can be utilized to construct a canonical representation. It is typically not necessary to canonize an MPO that has an exact representation, which is the case for many local Hamiltonians. Thus we refrain from discussing this step in more detail. However, note that the canonical representation is highly important for the compression of an otherwise unfeasible large MPO representation [HMS17], which can arise in the context of quantum chemistry Hamiltonians [CKN⁺16].

To conclude the discussion on matrix product operators, we illustrate how a simple local Hamiltonian \hat{H} is easily encoded in an MPO representation., we consider the spin- $\frac{1}{2}$ transverse-field Ising model with nearest-neighbor interactions only as a simple example,

$$\hat{H} = J \sum_j \hat{S}_j^z \hat{S}_{j+1}^z + h_x \sum_j \hat{S}_j^x, \quad (2.42)$$

which of course represents an abbreviation for a sum of tensor products in this form,

$$\hat{H} = J\hat{S}_1^z \otimes \hat{S}_2^z \otimes \mathbb{1} \otimes \mathbb{1} \dots + \mathbb{1} \otimes J\hat{S}_2^z \otimes \hat{S}_3^z \otimes \mathbb{1} \dots + \dots \quad (2.43)$$

In order to find the MPO representation of \hat{H} , we have to keep in mind that each MPO tensor O_j only acts on the local Hilbert space at site j , whereas the product of all O tensors generates the global Hilbert space. The structure of the Hamiltonian (e.g., which operator has to be coupled to which to generate a specific interaction term) is fully encoded in the bond dimension of the O tensors. Contracting over all bond indices of the MPO should result in the original expression of the Hamiltonian (2.43).

To simplify the construction of the MPO for a system with a generic number of sites, we first consider a two-site version of Eq. (2.43). Its Hamiltonian can be easily encoded in two operator-valued vectors,

$$\hat{H} = O_1 O_2 = \begin{pmatrix} \mathbb{1} & h_x \hat{S}_1^x & J \hat{S}_1^z \end{pmatrix} \cdot \begin{pmatrix} h_x \hat{S}_2^x \\ \mathbb{1} \\ \hat{S}_2^z \end{pmatrix} = h_x (\hat{S}_1^x \otimes \mathbb{1} + \mathbb{1} \otimes \hat{S}_2^x) + J \hat{S}_1^z \otimes \hat{S}_2^z \quad (2.44)$$

Expanding the system to three sites, the additional terms can be generated by inserting an operator-valued matrix O_2 at site 2,

$$\begin{aligned} \hat{H} &= O_1 O_2 O_3 = \begin{pmatrix} \mathbb{1} & h_x \hat{S}_1^x & J \hat{S}_1^z \end{pmatrix} \cdot \begin{pmatrix} \mathbb{1} & h_x \hat{S}_2^x & J \hat{S}_2^z \\ 0 & \mathbb{1} & 0 \\ 0 & \hat{S}_2^z & 0 \end{pmatrix} \cdot \begin{pmatrix} h_x \hat{S}_3^x \\ \mathbb{1} \\ \hat{S}_3^z \end{pmatrix} \\ &= h_x (\hat{S}_1^x \otimes \mathbb{1} \otimes \mathbb{1} + \mathbb{1} \otimes \hat{S}_2^x \otimes \mathbb{1} + \mathbb{1} \otimes \mathbb{1} \otimes \hat{S}_3^x) \\ &\quad + J (\hat{S}_1^z \otimes \hat{S}_2^z \otimes \mathbb{1} + \mathbb{1} \otimes \hat{S}_2^z \otimes \hat{S}_3^z) \\ &= h_x (\hat{S}_1^x + \hat{S}_2^x + \hat{S}_3^x) + J (\hat{S}_1^z \hat{S}_2^z + \hat{S}_2^z \hat{S}_3^z). \end{aligned} \quad (2.45)$$

Constructing the MPO for larger system sizes is now straightforward. Whereas the boundary tensors O_1, O_N are represented by the two operator-valued vectors of the form already shown in Eq. (2.47), the structure of all “bulk” tensors O_j for sites $j = 2, \dots, N - 1$ emerges from O_2 in Eq. (2.45),

$$O_1 = \begin{pmatrix} \mathbb{1} & h_x \hat{S}_1^x & J \hat{S}_1^z \end{pmatrix}, \quad O_j = \begin{pmatrix} \mathbb{1} & h_x \hat{S}_j^x & J \hat{S}_j^z \\ 0 & \mathbb{1} & 0 \\ 0 & \hat{S}_j^z & 0 \end{pmatrix}, \quad O_N = \begin{pmatrix} h_x \hat{S}_N^x \\ \mathbb{1} \\ \hat{S}_N^z \end{pmatrix}. \quad (2.46)$$

Thus, we conclude that the original Hamiltonian (2.43) can be encoded exactly in an MPO representation with a fairly compact MPO bond dimension $D_{\text{MPO}} = 3$.

As already noted above, D_{MPO} is related to the number of interaction terms which are “sliced” by a specific bond j . Studying for instance an extended Ising model including next-to-nearest-neighbor interaction terms,

$$\hat{H} = J_1 \sum_j \hat{S}_j^z \hat{S}_{j+1}^z + J_2 \sum_j \hat{S}_j^z \hat{S}_{j+2}^z + h_x \sum_j \hat{S}_j^x, \quad (2.47)$$

we end up with an MPO representation with $D_{\text{MPO}} = 4$. In addition to the terms already encoded in (2.46), one also has to account for the J_2 terms that require to be handed over from site j to $j + 2$. This leads to an additional row and column entry in the bulk MPO tensors to track this intermediate state over site $j + 1$,

$$O_j = \begin{pmatrix} \mathbb{1} & h_x \hat{S}_j^x & J_1 \hat{S}_j^z & J_2 \hat{S}_j^z \\ 0 & \mathbb{1} & 0 & 0 \\ 0 & \hat{S}_j^z & 0 & 0 \\ 0 & 0 & \mathbb{1} & 0 \end{pmatrix} \quad (2.48)$$

Therefore, MPO representations of Hamiltonians with longer-ranged interactions typically require a larger D_{MPO} and hence demand more numerical resources. However, there exist important exceptions that can be brought into a compact MPO form. One type of systems are models with exponentially decaying interaction terms $J(x) = Je^{-Cx}$ which are highly relevant in quantum-chemistry applications [CKN⁺16]. Another important class of models are quantum impurity models in the so-called “star geometry” [Sec. 2.4.2]. We refrain from a detailed discussion of these special cases since these cases are not explicitly considered in this thesis.

2.4.2 NRG

Wilson’s numerical renormalization group (NRG) represents a powerful tool for a specific class of zero-dimensional quantum many-body system [Wil75, KmWW80, BCP08]. These so-called quantum impurity models consist of a small interacting quantum system (the impurity) coupled to one (or multiple) non-interacting baths (sometimes also referred to as leads, bands, or reservoirs). The impurity typically resembles a quantum dot or a localized spin degree of freedom while the bath can either consists of bosonic (e.g., phonons, magnons, ...) or fermionic particles (e.g., conduction band electrons). With NRG it is possible to obtain quasi-exact numerical results down to exponentially small energy scales and to resolve both static quantities, such as the dot occupancy, or dynamic observables, such as the conductance or more generally the entire impurity spectral function.

Originally developed in the context of the Kondo model [Wil75], NRG by now has been applied to a vast number of impurity models and yielded quantitatively reliable results for many question, ranging from quench dynamics [AS05, THC⁺11, LHH⁺11] to transport through nanostructures [BZH⁺03, KSGG⁺11]. Moreover, NRG also represents a powerful tool in the context of dynamical mean-field theory (DMFT) [GKKR96, KSH⁺06], where it recently has been shown that the method can also treat complex multi-band models [SYvD⁺15] and can potentially help to provide answers to many open issues regarding real materials.

Decades after its invention, and around the same time when DMRG was reformulated in the MPS language, researchers in Munich realized that NRG can also be naturally expressed in the MPS framework [VWS⁺05, WVS⁺09]. This insight not only helped to improve NRG on a technical level [WvD07, Wei11, Wei12b], it also lead to many DMRG-based applications to impurity models [WVS⁺09, SWvD08, HWvD10, GWvDV12, GAS⁺13, GTV⁺14, WMPS14, BWG⁺14, BLS⁺17].

Three of our publications included in this thesis follow along this path, in particular focusing on bosonic impurity models [BWG⁺14, BCBB⁺17, BLS⁺17] (see chapter 3). Thus we here give a brief introduction to the most important aspects of NRG. For more technical details we refer to the extensive review in Ref. [BCP08].

Quantum impurity model

In our discussion, we focus on one of the paradigmatic quantum impurity models and consider the single impurity Anderson model (SIAM) [And61]. This model was introduced by Phil Anderson in the early 1960s to describe magnetic impurities in metals. Today it is also employed in the context of quantum dot physics. The Hamiltonian of the SIAM consists of three contributions; \hat{H}_{imp} describes the impurity part; \hat{H}_{cpl} contains the coupling terms between impurity and fermionic bath; and \hat{H}_{bath} includes the non-interacting bath

Hamiltonian. Put together, the full Hamiltonian of the SIAM has the following form,

$$\hat{H}_{\text{SIAM}} = \underbrace{\sum_{\sigma=\uparrow\downarrow} \epsilon_d \hat{d}_\sigma^\dagger \hat{d}_\sigma + U \hat{d}_\downarrow^\dagger \hat{d}_\downarrow \hat{d}_\uparrow^\dagger \hat{d}_\uparrow}_{\hat{H}_{\text{imp}}} + \underbrace{V_k \sum_{k\sigma} (\hat{d}_\sigma^\dagger \hat{c}_{k\sigma} + h.c.)}_{\hat{H}_{\text{cpl}}} + \underbrace{\sum_{k\sigma} \epsilon_{k\sigma} \hat{c}_{k\sigma}^\dagger \hat{c}_{k\sigma}}_{\hat{H}_{\text{bath}}}, \quad (2.49)$$

where \hat{d}_σ and $\hat{c}_{k\sigma}$ are the annihilation operators of an electron with spin σ acting on the impurity and on a bath state with momentum k , respectively. ϵ_d is a local energy shift of the impurity level, U is the Coloumb repulsion between two impurity electrons with opposite spin, $\epsilon_{k\sigma}$ is the energy of the individual electron bath states, and V_k describes the k -dependent coupling strength between impurity and bath.

The effects of the bath on the static and dynamic properties of the impurity can be fully characterized by a function containing both the coupling V_k as well as the density of states in the bath. This so-called hybridization function $\Gamma(\omega)$ [BCP08] is defined as

$$\Gamma(\epsilon) = \pi \sum_k V_k^2 \delta(\epsilon - \epsilon_k) \equiv \pi \rho(\epsilon) V^2(\epsilon), \quad (2.50)$$

where the last equality represents a continuum description.

Logarithmic discretization

The first prerequisite step to make the model tractable with NRG is to switch from momentum to an energy representation. This is achieved by replacing the continuous bath spectrum by a discrete set of energy levels.

NRG requires a *logarithmic discretization scheme* that has only poor resolution at high energies but resolves the low energy spectrum close to the fermi energy very accurately. On the one hand, this enables one to capture important low-energy features of quantum-impurity models (e.g., the Kondo peak). On the other hand, the logarithmic energy grid is required for the NRG to work properly as it guarantees *energy-scale separation*. Without this feature, the NRG truncation is bound to fail.

Wilson chain mapping

The second prerequisite step is to map the discretized version of the original Hamiltonian (2.49) to a semi-infinite tight-binding chain of the form,

$$\hat{H}'_{\text{SIAM}} = \hat{H}_{\text{imp}} + V \sum_{\sigma} (\hat{d}_\sigma^\dagger \hat{f}_{0\sigma} + h.c.) + \sum_{\sigma, n=0}^{\infty} [t_n (\hat{f}_{n\sigma}^\dagger \hat{f}_{n+1\sigma} + h.c.) + \epsilon_n \hat{f}_{n\sigma}^\dagger \hat{f}_{n\sigma}], \quad (2.51)$$

where the impurity couples only to the first site of the non-interacting chain representation for the bath. One crucial feature of such a “Wilson chain” is that the hopping elements t_n decay at an exponential rate, $t_n \propto \Lambda^{-n/2}$ with $\Lambda > 1$. Therefore, one can consider a truncated version of Eq. (2.49) with only N bath sites in practice. N is chosen such that all relevant energy scales for a particular calculation are captured by the truncated chain.

The standard procedure to perform the chain mapping is extensively discussed in the literature (see Ref. [BCP08]). Note that we recently introduced an alternative construction for a generic Wilson chain Hamiltonian (2.51) that offers a number of technical advantages [BLS⁺17] [see Sec. 3.3 for more details].

Iterative diagonalization

The NRG protocol iteratively diagonalizes Wilson chain Hamiltonians of the type (2.51) starting from a very short subset of the full chain (e.g., only the impurity and the first bath site) for which all eigenstates can still be computed exactly. In each subsequent NRG step, an additional bath site is added to the subsystem and the full diagonalization is repeated for the enlarged system. Since this procedure becomes quickly unfeasible when working in the full Hilbert space, NRG typically retains only the lowest D eigenstates to perform the next iteration step.

The practicability of this truncation scheme is strongly linked to the previously mentioned concept of energy-scale separation, which applies to models of the type Eq. (2.51) that feature exponentially decaying energy scales along the chain. It assumes that lower energy scales will only lead to negligible corrections of the spectrum at high energies. This fully justifies the NRG procedure treating high-energy contributions at earlier iterations with coarser energy resolution, while proceeding with the low-energy sector on to subsequent iterations. Only these states interact with the additional low-energy contributions added through the sites at later iterations.

MPS representation

As it turns out, the NRG protocol naturally leads to an MPS representation [WVS⁺09, Wei12b]. This can be easily demonstrated by studying the NRG iteration after having already performed N steps. At this point, we have already obtained the D lowest energy eigenstates $|s_N\rangle$ for the modified version of the Hamiltonian in Eq. (2.51) with only N bath sites. For the next iteration $N + 1$ we add another bath site and diagonalize the expanded Hamiltonian in the combined basis of the old eigenstates $|s_N\rangle$ and the additional bath states $|\sigma_{N+1}\rangle$. The new set of eigenstates $|s_{N+1}\rangle$ can be constructed from these states using a unitary transformation A_N ,

$$|s_{N+1}\rangle = \sum_{s_N \sigma_{N+1}} A_{s_N s_{N+1}}^{[\sigma_{N+1}]} |s_N\rangle |\sigma_{N+1}\rangle. \quad (2.52)$$

The tensor A_N has exactly the same structure as the left-canonical A tensors that were used as building blocks of an MPS above. Based on this observation, NRG can be fully reformulated in terms of the MPS framework.

This insight led to technical improvements [WvD07, Wei11, Wei12b] and new applications [THC⁺11, LHH⁺11] in NRG itself. In addition, it also provided the basis for applying DMRG-like approaches to quantum impurity models while borrowing central concepts of the NRG protocol (e.g., rescaling) [WVS⁺09, SWvD08, HWvD10, GWvDV12, GAS⁺13, GTV⁺14, WMPS14, BWG⁺14, BLS⁺17]. Since parts of this thesis are entirely based on performing this NRG-enhanced DMRG on bosonic quantum impurity models, we conclude that the MPS formulation of NRG represents one of the central building blocks of our work.

2.4.3 DMRG

While NRG proved to be highly successful in the context of quantum impurity models, it failed miserably when it was naively applied to real-space models in 1D, such as standard Heisenberg or Hubbard models. The reason for the breakdown of NRG is rather obvious in hindsight, as these systems no longer feature any energy-scale separation rendering the NRG truncation invalid [WN92]. To overcome these shortcomings, Steve White developed the density matrix renormalization group (DMRG) in the early 1990s [Whi92, Whi93], a variational algorithm designed to obtain the ground-state wavefunction of an one-dimensional quantum system. Similar to NRG, it is based on a series of local updates performed iteratively. However, instead of retaining the low-energy part of the Hilbert space, DMRG

is based on a different truncation scheme retaining those states which contribute the most weight to the spectrum of the reduced density matrix.

Nowadays, DMRG and its extensions towards dynamics and finite temperatures have become the most powerful numerical toolbox for one-dimensional quantum many-body systems and also proved to be an asset towards the understanding of strongly correlated models in two dimensions [Sch05, Sch11, SW12]. The success of DMRG is strongly linked to the fact that, already in its original formulation, it implicitly operated on an MPS structure targeting states that obey the area law of the entanglement entropy. The explicit connection to matrix product states was discovered years after the invention of the algorithm [OR95, DMDNS98], giving a belated explanation for why DMRG works so well in 1D (and also why it has a harder time dealing with 2D systems). More importantly, the MPS framework gave rise to many powerful extensions such as time-dependent DMRG [WF04, Vid04, DKSV04] [Sec. 2.4.4] or finite-temperature DMRG [ZV04, VGRC04, FW05, Whi09] [Sec. 2.4.5].

Since we applied ground-state DMRG in five publications included in this thesis [BWG⁺14, BWvDG16, BCB⁺17, BLS⁺17, SBvD17], we present a short summary of the DMRG algorithm explicitly formulated in terms of MPS below, which is partly adapted from Ref. [Sch11]. Moreover, we briefly comment on DMRG applications for 2D quantum lattice models.

DMRG algorithm

The goal of the algorithm is to variationally obtain an approximation of the ground state within a set of MPS with some maximum bond dimension D . To this end, we need to find the MPS $|\psi_0\rangle$ that minimizes the energy,

$$\min_{\{A\}} [E_0] = \frac{\langle \psi_0 | \hat{H} | \psi_0 \rangle}{\langle \psi_0 | \psi_0 \rangle}. \quad (2.53)$$

Given a generic Hamiltonian in MPO form and a random MPS representation as starting state, we reformulate the minimization problem in Eq. (2.53) into a constrained optimization problem using a Lagrangian multiplier λ ,

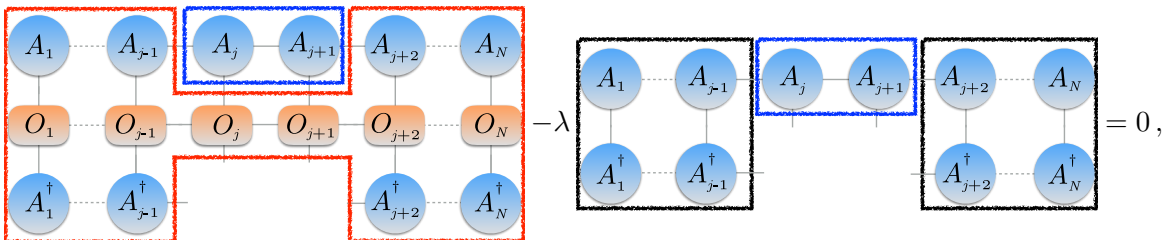
$$\langle \psi_0 | \hat{H} | \psi_0 \rangle - \lambda \langle \psi_0 | \psi_0 \rangle. \quad (2.54)$$

Eq. (2.54) represents a highly non-linear optimization problem which cannot be solved directly. The key idea of DMRG is to employ an iterative optimization instead that works only locally on one or two A tensors of $|\psi_0\rangle$. This simplifies the non-linear optimization problem and one ends up with a set of well-defined eigenvalue problems.

In the following, we consider the two-side formulation of DMRG and vary two neighboring A tensors at once, while keeping all others fixed. For a given bond j , the optimal pairs $A_j A_{j+1}$ is found by extremizing Eq. (2.54) with respect to $A_j^\dagger A_{j+1}^\dagger$,

$$\frac{\partial}{\partial (A_j^\dagger A_{j+1}^\dagger)} \left(\langle \psi_0 | \hat{H} | \psi_0 \rangle - \lambda \langle \psi_0 | \psi_0 \rangle \right) \stackrel{!}{=} 0. \quad (2.55)$$

Taking this partial derivative leads to



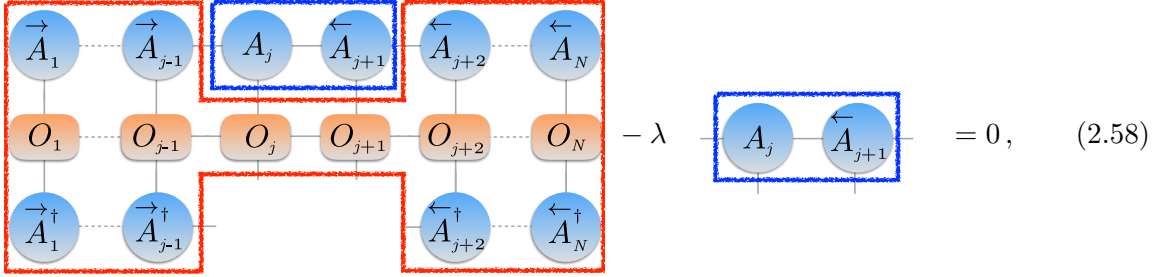
$$(2.56)$$

which represents a surprisingly simple generalized eigenvalue problem of the form

$$\hat{H} \boxed{q} - \lambda \boxed{N} \boxed{q} = 0. \quad (2.57)$$

The local Hilbert space for this two-side update has the size $D^2 d^2$, which is typically too large to be solved fully. But since \hat{H} and N are both Hermitian operators, and because we are only interested in the lowest eigenvalue, one can employ standard iterative eigensolvers based on Lanczos or Davidson algorithms [Lan50, Dav75, Arb12]. Nevertheless, it can be challenging to obtain the numerical solution of this generalized eigenvalue problem in case N is badly conditioned.

Since we exclusively consider systems with open boundary conditions in this thesis, we are able to significantly simplify Eq. (2.56) by exploiting the canonical MPS representation of $|\psi_0\rangle$. To this end, we always gauge the MPS such that its orthonormal center is located on one of the two A tensors surrounding bond j , which is about to be updated. In this way Eq. (2.56) transforms to



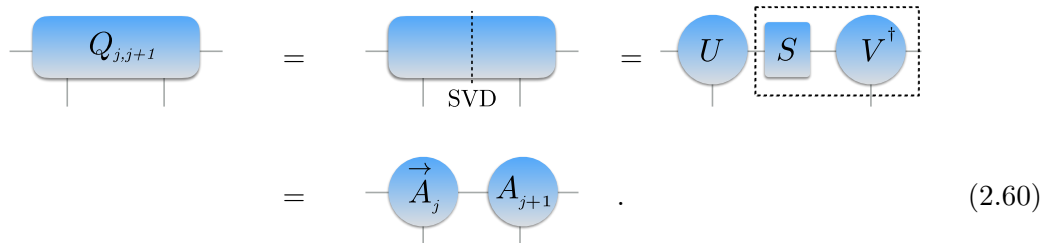
$$- \lambda \boxed{A_j \leftarrow A_{j+1}} = 0, \quad (2.58)$$

which now represents a standard eigenvalue problem,

$$\hat{H} \boxed{q} - \lambda \boxed{q} = 0. \quad (2.59)$$

In contrast to the generalized eigenvalue problem (2.57), the lowest-eigenvalue solution to Eq. (2.59) is numerically more stable and can easily be obtained by an iterative eigensolver.

After generating the optimal two-site tensor $Q_{j,j+1} = q$ that locally minimizes the energy from a Lanczos or Davidson algorithm, we have to restore the original form of the MPS and move to the bond including a new pair of sites (either $j+1$ and $j+2$ or $j-1$ and j) to repeat the procedure. In practice, this is achieved by performing a singular value decomposition and shifting the orthonormal center to the next site (here shown for $j+1$),



$$Q_{j,j+1} = \text{SVD} = U \boxed{S} V^\dagger = \boxed{\vec{A}_j \leftarrow A_{j+1}}. \quad (2.60)$$

Note that the SVD spectrum contains Dd states in this two-side formulation of the algorithm. To keep the bond dimension feasibly small, we have to employ a truncation criterion on the SVD spectrum. Either we keep a fixed number of the D largest singular values or we retain all states corresponding to singular values larger than some threshold accuracy ϵ_{SVD} .

As we have already discussed above in context of the entanglement entropy, truncating the SVD spectrum is equivalent to a truncation criterion based on the spectrum of the

reduced density matrix $\rho_{A,B}$, where A and B label the two blocks of the systems left and right of bond j . This illustrates that the procedure described above exactly mimics White’s original idea that “one should keep the most significant eigenstates of the block density matrix” [Whi93].

We conclude this part with some additional comments on DMRG. First of all, the variational procedure described above is systematically repeated for all pairs of sites in the system. Typically one performs sweeps that start from the first two sites of the chain, move to the last pair of sites in the system, and back to the first pair. These sweeps are repeated multiple times until the ground-state energy (or some other observable) converges. One can monitor the convergence by tracking the variance of the energy calculated at each site j during a single sweep, and stopping the algorithm when its value drops below a certain threshold. For numerical efficiency it is crucial to iteratively update the building blocks of the Hamiltonian matrix and store them separately for each j to be able to recycle them in the next sweep (see [Sch11] for details).

DMRG can also be formulated in terms of a single-site optimization procedure, where one varies only a single A tensor at once. Although the numerical cost of this algorithm are roughly reduced by a factor d in comparison its two-site counterpart, the single-site formulation of DMRG has some substantial disadvantages. First of all, the sizes of the A tensors in the standard single-site formulation are fixed throughout the entire optimization procedure (since a maximum number of D states occur in the SVD spectrum in the single-site version of Eq. (2.60)). Therefore, one cannot increase the number of kept states D on the fly, which often becomes necessary in practice to obtain sufficient numerical accuracy. Moreover, the procedure is much more likely to get stuck in local minima due to the drastically smaller part of the Hilbert space that is variationally accessible. This is particularly worrisome if the implementation explicitly exploits Hamiltonian symmetries, since one is neither able to eliminate contribution from irrelevant symmetry sectors nor to add relevant sectors missing in the initial state [see Sec. 2.7 for details on symmetric TN]. There are a number of fixes for the shortcomings of single-site DMRG, such as introducing a noise term during each update [Whi05, HMSW15]. In our DMRG implementation, however, we refrain from using noise terms and generically work in a slight reformulation of the two-site version where we project onto a central bond matrix before performing the update [McC07].

DMRG for two-dimensional system

Though DMRG is tailored to one-dimensional systems, where its underlying MPS ansatz satisfies the area law, the method also provides important insight when applied to two-dimensional lattice models with frustration or itinerant fermions [WC07, SW12], where other methods such as QMC are very limited. For instance, DMRG uncovered the spin-liquid ground state of the Kagome Heisenberg model [YHW11, DMS12] (although the specific spin-liquid nature is still heavily under debate [HZOP16, LXC⁺17]). Most recently, DMRG in combination with other numerical methods led to a consensus regarding the existence of stripe order in the underdoped Hubbard model [ZCC⁺17]. Despite the 1D tensor network structure of DMRG that ultimately limits the accessible system sizes, its major advantages in the context of these complex systems are its numerical stability, the flexibility of the algorithmic setup and the access to the full ground-state wavefunction [SW12].

To employ DMRG on a 2D model, one has to map the two-dimensional lattice structure onto an effective 1D geometry suitable for an MPS description (see Fig. 2.2 for illustration). As a consequence, interaction terms that are short-ranged on the 2D lattice can become long-ranged in the effective 1D Hamiltonian. Thus some local correlations of the 2D wavefunction obtain a non-local character in the MPS representation as well, since they have to be carried across multiple intermediate bonds along the MPS path. This already indicates that an MPS working in two dimensions is not able to capture the clustering of correlation locally and, in

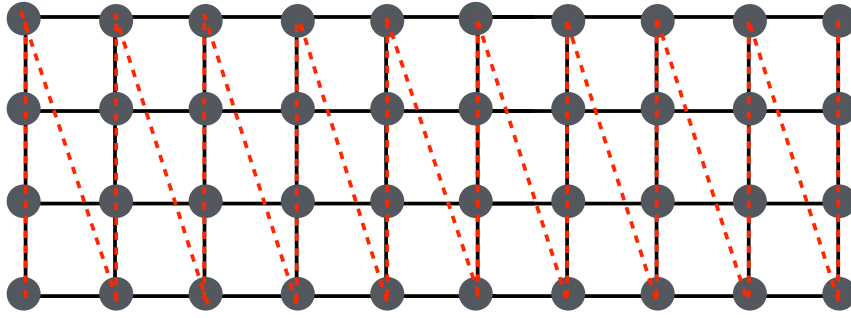


Figure 2.2: Example of square lattice cluster for 2D-DMRG calculation. The dashed red line indicates the quasi-one-dimensional MPS path through the cluster.

consequence, is also not suited to reproduce the 2D area law.

In practice, this means that the efficiency of 2D-DMRG significantly deteriorates and the formerly polynomial cost scaling with system size in 1D is lost (albeit not completely). One ends up with an “easy” dimension transverse to the MPS path (the length), where large system sizes can still be efficiently simulated, and a “hard” dimension parallel to the MPS path (the width). This direction poses a challenge to DMRG, as the number of states kept in the MPS must be increased exponentially with respect to the width in order to work with constant accuracy [SW12]. This limits its application to systems with a moderate width (typically up to width-12 for spin systems, and up to width-6 for spinful fermions) and makes a cylindrical setup most convenient (i.e., enforcing periodic boundary conditions for the width, and open boundary conditions for the length). In the future, we expect that other TN representations more suitable to the lattice geometry such as PEPS [see Sec. 2.5] will supersede DMRG.

In the meantime, however, DMRG still obtains a lot of relevant information working on the accessible system sizes due to the accuracy of the MPS truncation and the numerical stability of the DMRG algorithm. Moreover, one can exploit a number of algorithmic tricks such as cluster subtraction, tailored boundary conditions, pinning fields, and mixed real- and momentum space representations [MZMP16, EWN17], as well as careful finite-size scaling to further enhance the results [SW12].

Although we not directly rely on 2D-DMRG for the work presented in this thesis, we extensively employ the MPS representation for two-dimensional systems in another context. In our publication [BZWS17] [see Sec. 5.1], we show that the finite-temperature extensions of DMRG are highly versatile tools applied to 2D models, recycling many ideas originating from 2D-DMRG. In addition, we illustrate in this manuscript how to minimize finite-size effects by means of numerical linked-cluster expansions [RBS06, RBS07]—a tool that could become useful to other TN applications in the future.

2.4.4 Time evolution

Arguably one of the most important extensions of ground-state DMRG is its time-dependent formulation [WF04, Vid04, DKSV04, Sch11]. It enables one to simulate the action of the time-evolution operator $e^{-i\hat{H}t}$ to an MPS representation of a generic many-body wavefunction $|\psi\rangle$. Thus, this formalism introduces the capability to study an extensive variety of dynamical features within the MPS framework, going far beyond “just” extracting static ground-state physics with standard DMRG. A non-exhaustive list of applications includes the simulation of local and global quenches [KSZ05, DdSHMF⁺08], the calculation of dynamic correlators [WF04, WA08, Bar13], the approximation of steady states in dissipative

systems [DTD⁺09, Dal14, BL14], as well as finite-temperature techniques (based on the imaginary-time-evolution operator $e^{-\beta\hat{H}}$) [ZV04, VGRC04, FW05, Whi09].

In this section, we discuss how to perform an MPS-based time evolution and, in particular, how to construct a suitable approximation for the time-evolution operator $e^{-i\hat{H}t}$. For systems with short-ranged interactions this can be achieved by means of a standard Trotter-Suzuki decomposition, while schemes for systems with long-ranged interactions are more involved. Time evolution techniques for systems with both short- and long-ranged interactions have been heavily employed in four publications included in this thesis [BvDW15, BWvDG16, SBvD17, BZWS17] [see Secs. 4.2, 4.1, 4.3, and 5.1].

Systems with short-ranged interactions

Before performing any real- or imaginary-time evolution, we have to think about how to encode the time-evolution operator in a way feasible for standard MPS techniques. In a first naive attempt, one could recall the power series for the exponential,

$$e^{-i\hat{H}t} = \sum_n \frac{(i\hat{H}t)^n}{n!}, \quad (2.61)$$

and try to find an MPO representation of this sum. However, this quickly leads to an MPO with unfeasibly large bond dimension D_{MPO} and by truncating the series, the result is not unitary.

For Hamiltonians with two-site interaction terms only, there is a simpler and more elegant approximation for the time evolution operator. This amounts to decomposing the time-evolution operator $e^{-i\hat{H}t}$ into a product of M small time steps $\tau = t/M$, and then splitting the operator for a full time step τ into a product of local operators

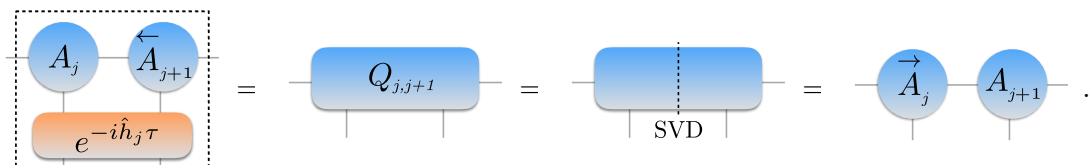
$$e^{-i\hat{H}\tau} \approx \prod_{j=1}^{N_b} e^{-i\hat{h}_j\tau} + \mathcal{O}(\tau^2), \quad (2.62)$$

with $\hat{H} = \sum_j \hat{h}_j$. \hat{h}_j describes the local interaction term acting on bond j , and N_b labels the total number of bonds in the system.

These so-called Suzuki-Trotter decompositions are in general very accurate approximations of the time-evolution operator, since they conserve important symmetries of the system dynamics [HS05]. The only error source originates from the non-commutativity of neighboring bond operators and scales with τ^2 in Eq. (2.62), where a first-order Trotter decomposition has been used. This ‘‘Trotter error’’ can be dealt with by using a higher-order decomposition [HS05] or a smaller time step τ . In practice, one can often employ a second-order decomposition without adding extra numerical costs,

$$\begin{aligned} e^{-i\hat{H}\tau} &\approx \prod_{j=1}^{N_b} e^{-i\hat{h}_j\tau/2} \prod_{j=N_b}^1 e^{-i\hat{h}_j\tau/2} + \mathcal{O}(\tau^3) \\ &= e^{-i\hat{h}_1\tau/2} e^{-i\hat{h}_2\tau/2} e^{-i\hat{h}_3\tau/2} \dots e^{-i\hat{h}_3\tau/2} e^{-i\hat{h}_2\tau/2} e^{-i\hat{h}_1\tau/2} + \mathcal{O}(\tau^3). \end{aligned} \quad (2.63)$$

The Trotter scheme is particularly favorable when treating Hamiltonians with nearest-neighbor interactions only. In this case, the individual Trotter gates all act on neighboring pairs of A tensors in the MPS so that a typical gate $e^{-i\hat{h}_j\tau}$ can be directly applied to bond j before performing a truncation to restore the MPS representation,



$$(2.64)$$

Thus, the full $e^{-i\hat{H}\tau}$ can be applied to $|\psi(t=0)\rangle$ during a single forward and backward sweep through the system while truncating the MPS on the fly. The evolution over the full time period t follows from repeating this procedure M times.

The above discussed scheme is usually called tDMRG in the literature [Sch11]. However, there also exists a slight variation that is mathematically equivalent but handles the truncation procedure differently. This variation (sometimes denoted tMPS [Sch11]) combines all interaction terms corresponding to even and odd numbered bonds respectively, i.e., $\hat{H} = \hat{H}_e + \hat{H}_o$. Note that all terms in one group commute with each other, but that the terms in \hat{H}_e generally do not commute with the ones in \hat{H}_o . The second-order Suzuki-Trotter decomposition for the time-evolution operator can then be expressed as

$$e^{-i\hat{H}\tau} = e^{-i\hat{H}_e\tau/2} e^{-i\hat{H}_o\tau} e^{-i\hat{H}_e\tau/2} + \mathcal{O}(\tau^3). \quad (2.65)$$

In this scheme, one typically constructs an MPO for each $e^{-i\hat{H}_{o,e}\tau/2}$ and applies the MPOs for a full time step before truncating the enlarged MPS using the fitting algorithm [Sec. 2.4.1]. In principle, this scheme is cleaner since the MPS is only truncated after every full time step and not on the fly (as in the tDMRG scheme). But this comes at the price of significantly higher numerical costs as the bonds of all A tensors are blown up by a factor d^2 .

Note that the terms tDMRG, tMPS and a third variant, the time-evolving block decimation (TEBD) [Vid04], are often used loosely in the literature, despite the subtle numerical differences of the approaches. In other words, people might state that they employ tMPS while, in reality, they use tDMRG. In the end, this is nothing worrisome as systematic deviations of the three approaches are almost always negligible.

Systems with longer-ranged interactions

A Trotter-based scheme for time evolution is not generally applicable to models with long-ranged interactions that for example arise in the context of 2D-DMRG [see Sec. 2.4.3]. In these cases, one has to rely on modified approaches to efficiently decompose the time-evolution operator. In this section, we present two particularly versatile methods, a Trotter variant using swap gates and a recently introduced MPO-based approach, which have been applied in our publication [BZWS17] [see Sec. 5.1] in the context of studying finite-temperature effects in 2D systems.

Suzuki-Trotter with swap gates.— Generally, Trotter-based time evolution does not work for systems with long-ranged interactions. However, a modified Trotter algorithm can be applied if interactions are restricted to two-body terms. To this end, one has to introduce the concept of swap gates.

A swap gate switches the states of two identical sites and thus helps to modify the MPS in such a way that a non-local Trotter gate can be applied locally [SW10]. In the context of bosons or spins, it has the simple definition

$$S_{jj+1} = \delta_{\sigma_j, \sigma_{j+1}} \delta_{\sigma_{j+1}, \sigma_j} = \begin{array}{c} |\sigma_j\rangle \quad |\sigma_{j+1}\rangle \\ \text{---} S_{jj+1} \text{---} \\ |\sigma_{j+1}\rangle \quad |\sigma_j\rangle \end{array} \quad (2.66)$$

(for fermions one may have to include additional minus signs) and can easily applied to a

pair of A tensors employing a subsequent SVD to restore the MPS representation,

$$= \text{SVD} = \dots \quad (2.67)$$

Consider some non-local bond operator $e^{-i\hat{h}_j\tau/2}$ originating from a generic Suzuki-Trotter decomposition (2.62) acting on sites i and l . Nearest-neighbor swap gates can modify the MPS in a way that this bond operator can be applied locally: the MPS is modified by a first set of swap gates $S_{l-2,l-1} \dots S_{i+1,i+2} S_{i,i+1}$ so that site i is moved to the position of site $l-1$. Then we can apply the bond operator $e^{-i\hat{h}_j\tau/2}$ locally, before a second set of swap gates $S_{i,i+1} S_{i+1,i+2} \dots S_{l-2,l-1}$ moves site i back to its original position.

This scheme conserves the accuracy of the Suzuki-Trotter decomposition and, at the same time, can handle two-body interactions of any range. Nevertheless, its efficiency is strongly range-dependent. For the example of a rectangular 2D cluster, the number of swaps scales roughly quadratically with the width of the system. Since each additional swap requires an additional singular value decomposition computation, the method can become inefficient for wide systems. In the context of systems considered in [BZWS17], however, we found that the method outperforms the MPO-based scheme, presented in the following.

MPO decomposition.— An alternative strategy relies on MPO approximations of the evolution operator $e^{-i\hat{H}\tau}$ that can naturally include long-ranged interaction terms. An MPO-based time evolution is especially favorable for systems with different types of long-ranged interactions, such as exponentially decaying terms which cannot be captured nicely in terms of two-site gates but, nevertheless, can be encoded efficiently in the MPO representation of the Hamiltonian [CKN⁺16]. Although such systems are not considered in this thesis, an MPO-based approach could conceivably have better efficiency than the Trotter plus swap gate approach when working on large 2D clusters.

An appealing feature of the approach of Ref. [ZMK⁺15] is the enhanced error control in comparison to established MPO approximations, such as a simple Euler step or its Runge-Kutta and Krylov extensions. The key insight of Ref. [ZMK⁺15] is to improve the simple Euler step by a local version of the Runge-Kutta stepper

$$1 + i\tau \sum_x \hat{H}_x \rightarrow \prod_x (1 + i\tau \hat{H}_x). \quad (2.68)$$

While the error remains $\mathcal{O}(\tau^2)$ in both cases, the first-order terms are now applied to any set of bonds in parallel. Therefore, the error of this approximation scales as $\mathcal{O}(Nt^2)$ rather than $\mathcal{O}(N^2\tau^2)$ in the case of the simple Euler stepper. This results in a constant error with system size for intensive quantities. In addition, the approach in Ref. [ZMK⁺15] yields a very compact MPO representation making it appealing in terms of efficiency and implementation. The actual time evolution is carried out by applying the MPO to an MPS using standard tools, such as the fitting approach [VC04]. Note that one can combine two complex time steps to further reduce the scaling of the error per step to $\mathcal{O}(\tau^3)$.

Other methods.— Recent years have seen interesting developments regarding time evolution algorithms in systems with long ranged interactions. In addition to the two approaches discussed here, other suitable techniques include the time-dependent variational principle [HCO⁺11] or a recently introduced series-expansion thermal tensor network [CLCL17] (the latter, so far, only works for imaginary-time evolution). At the moment, these approaches

coexist independently and, due to the inherent technical complexity, a practitioner typically picks the one most suitable to his problem and implementation framework. It remains an open question whether there exists a “best practice” approach amongst these schemes. Hence, a detailed benchmarking of these various time evolution techniques including different systems and both real- and imaginary time would be extremely helpful and is left for future work.

Exponential wall

The time evolution of an MPS is associated with two systematic error sources. We have already encountered the Trotter error as an example of the first category that, more generally, includes all errors originating from the decomposition of the time-evolution operator. Usually this error source can be controlled by using a higher-order decomposition or smaller time steps, and is therefore no fundamental bottleneck.

The second error source stems from the iterative truncation of the enlarged bond dimensions arising in the MPS due to the application of $e^{-i\hat{H}\tau}$. This error is more fundamental as it exponentially increases in time [GKSS05]. The underlying reason is that the entanglement of the time-evolved MPS is typically no longer bounded by the area law. Instead it can be shown that, in the worst case, the entanglement entropy during an out-of-equilibrium evolution grows linearly in time $S(t) \leq S(0) + ct$ [CC05, SWVC08]. The constant c is system dependent and related to the individual propagation speed of an excitation in the system. To compensate a linear growth of entanglement, the bond dimension of the MPS has to be increased exponentially with time in order to maintain the same level of accuracy.

Most out-of-equilibrium MPS simulations (e.g., following a global quench) are bound to encounter this “exponential wall” issue at some point in time. In other words, they are numerically feasible only up to some maximum time t_{\max} , where the accessible numerical resources are no longer sufficient for an accurate MPS representation of $|\psi(t)\rangle$.

The exact value of t_{\max} of course strongly depends on model and simulation specifics. In many cases one is able to reach sufficiently long time scales to extract the relevant information for a specific question. In addition, there are a number of technical tricks to substantially extend the accessible time scales (see Sec. 2.4.6 for some examples in the context of calculating spectral functions). In other situations, for instance in the context of local quenches [EP07] or for the time evolution of many-body-localized states [BPM12], one can observe weaker entanglement growth over time (e.g., only on a logarithmic scale) and thus is able to reach significantly larger values of t_{\max} .

2.4.5 Finite-temperature

Equilibrium thermal properties of quantum systems are fully encoded in the thermal density matrix

$$\hat{\rho}_T = \frac{1}{Z_T} e^{-\beta\hat{H}}, \quad (2.69)$$

where Z_T is the thermal partition function and $\beta = 1/T$ the inverse temperature. It is well-known from numerical evidence that the thermal density matrix also has a faithful MPS representation for short-ranged 1D quantum systems. More recently, this observation has been verified on a formal level: remarkably, it can even be proven that $\hat{\rho}_T$ follows an area law [Bar17]. With numerous time-evolution algorithms available [Sec. 2.4.4], this allows for the efficient computation of the thermal density matrix by means of imaginary-time evolution.

Finite-temperature extensions of DMRG include the purification (or ancilla) method [ZV04, VGRC04, FW05] and the METTS (minimally entangled typical thermal state) algorithm [Whi09, SW10]. There are also transfer-matrix approaches for finite temperature

using MPS [Shi97, WX97], though we do not discuss them further. The purification method directly computes the thermal density matrix using imaginary-time evolution techniques—the approach works well for high temperatures but the cost to reach lower temperatures grows rapidly. To address the limitations of the purification method, the METTS algorithm blends imaginary time evolution with Monte Carlo sampling, enabling a less costly pure-state formalism.

Since three publications included in this thesis are based on or develop enhancements for both finite-temperature extensions [BvDW15, BWvDG16, BZWS17] [see Secs. 4.2, 4.1, and 5.1], we provide an introduction to purification and METTS before concluding with a brief comparison. This section follows in part the methods section of our publications [BvDW15, BZWS17].

Density-matrix purification

Building on the ideas of purification, Refs. [ZV04, VGRC04, FW05] showed how to efficiently represent a thermal density matrix in an MPS framework. To this end, an auxiliary (or ancilla) space A is introduced as a copy of the physical Hilbert space P . The auxiliary sites can be interpreted as a heat bath thermalizing the physical sites. Using the construction of an enlarged Hilbert space $\mathcal{H} = P \otimes A$, it is possible to construct the thermal density matrix from a pure state

$$|\psi_T\rangle = \begin{array}{ccccccc} \textcircled{A_1^P} & \textcircled{A_1^A} & \textcircled{A_2^P} & \textcircled{A_2^A} & \dots & \textcircled{A_N^P} & \textcircled{A_N^A} \\ | & | & | & | & & | & | \\ |\sigma_{P,1}\rangle & |\sigma_{A,1}\rangle & |\sigma_{P,2}\rangle & |\sigma_{A,2}\rangle & & |\sigma_{P,N}\rangle & |\sigma_{A,N}\rangle \end{array} \quad (2.70)$$

by tracing out the pure state's auxiliary degrees of freedom:

$$\hat{\rho}_T = \text{Tr}_A |\psi_T\rangle\langle\psi_T| = \begin{array}{ccccccc} \textcircled{A_1^{P\dagger}} & \textcircled{A_1^{A\dagger}} & \textcircled{A_2^{P\dagger}} & \textcircled{A_2^{A\dagger}} & \dots & \textcircled{A_N^{P\dagger}} & \textcircled{A_N^{A\dagger}} \\ | & | & | & | & & | & | \\ \textcircled{A_1^P} & \textcircled{A_1^A} & \textcircled{A_2^P} & \textcircled{A_2^A} & \dots & \textcircled{A_N^P} & \textcircled{A_N^A} \\ | & | & | & | & & | & | \end{array} \quad (2.71)$$

Starting at infinite temperature ($\beta = 0$), the purified state can be easily constructed as a product state of maximally entangled pairs of one physical and one auxiliary site,

$$|\psi_\infty\rangle = \frac{1}{d^N} \prod_j \left(\sum_\sigma |\sigma_P\rangle |\sigma_A\rangle \right). \quad (2.72)$$

To make a measurement at some finite temperature $T = 1/\beta$, one evolves $|\psi_\infty\rangle$ in imaginary time up to $\beta/2$,

$$\begin{aligned} \hat{\rho}_T &= \frac{1}{Z_T} e^{-\beta\hat{H}} = \frac{1}{Z_T} e^{-\beta(\hat{H}_P \otimes \mathbb{1}_A)/2} \underbrace{\hat{\rho}_\infty Z_\infty}_{\mathbb{1}} e^{-\beta(\hat{H}_P \otimes \mathbb{1}_A)/2} \\ &= \frac{Z_\infty}{Z_T} \text{Tr}_A \left[e^{-\beta(\hat{H}_P \otimes \mathbb{1}_A)/2} |\psi_\infty\rangle\langle\psi_\infty| e^{-\beta(\hat{H}_P \otimes \mathbb{1}_A)/2} \right]. \end{aligned} \quad (2.73)$$

The Hamiltonian used for time evolution is just the one defining the original problem, and acts as the identity on the ancillary space. Note also that the normalization factor $Z_\infty/Z_T = \langle\psi_T|\psi_T\rangle$. An arbitrary static observable \hat{O} can then be evaluated by computing the overlap $\langle\psi_T|\hat{O}|\psi_T\rangle$, tracing out the auxiliary degrees of freedom. For the evaluation of dynamic observables we refer to Sec. 2.4.6.

METTS

The minimally entangled typical thermal state algorithm (METTS) represents an alternative to purification [Whi09, SW10]. Instead of constructing the full density matrix, METTS generates a set of typical states $|\phi_\sigma\rangle$ satisfying

$$e^{-\beta\hat{H}} = \sum_{\sigma} P_{\sigma} |\phi_{\sigma}\rangle\langle\phi_{\sigma}|, \quad (2.74)$$

with P_{σ} denoting the probability, for a given β , of measuring the system in $|\phi_{\sigma}\rangle$. Starting from any orthonormal basis $\{|\sigma\rangle\}$, it can easily be shown that the following definition generates a set of states in agreement with typicality condition of Eq. (2.74),

$$|\phi_{\sigma}\rangle = \frac{1}{\sqrt{P_{\sigma}}} e^{-\beta\hat{H}/2} |\sigma\rangle, \quad P_{\sigma} = \langle\sigma|e^{-\beta\hat{H}}|\sigma\rangle. \quad (2.75)$$

Exploiting the freedom in the choice of the orthonormal basis $\{|\sigma\rangle\}$, the METTS approach starts from a set of classical product states (CPS) of the form $|\sigma\rangle = |\sigma^1\rangle|\sigma^2\rangle\dots|\sigma^N\rangle$. These states represent the natural choice for a typical ensemble at infinite temperature, where the system should behave classically. Since their entanglement entropy starts out exactly zero and grows slowly during the imaginary-time evolution, they can typically be represented efficiently as MPS (hence the notion ‘‘minimally entangled’’).

A thermal measurement of an arbitrary static observable O can be computed as

$$\langle\hat{O}\rangle_T = \frac{1}{Z_T} \sum_{\sigma} P_{\sigma} \langle\phi_{\sigma}|\hat{O}|\phi_{\sigma}\rangle. \quad (2.76)$$

Sampling the METTS ensemble randomly according to the probability distribution P_{σ}/Z_T , this expectation value can be evaluated by taking the ensemble average of $\langle\phi_{\sigma}|\hat{O}|\phi_{\sigma}\rangle$.

To construct a METTS sample $\{|\phi_{\sigma}\rangle\}$ with the correct probability distribution, a Markov chain of CPS $|\sigma\rangle$ is generated. This is done in a way that obeys detailed balance, which guarantees reproducing the probability distribution P_{σ}/Z_T . The sampling algorithm can be set up sequentially. To this end, one starts from an arbitrary CPS $|\sigma\rangle$ and conducts what is called a *thermal step*:

- (i) A single METTS $|\phi_{\sigma}\rangle$ is generated by evolving the CPS in imaginary time and normalizing it.
- (ii) A measurement of all local degrees of freedom is performed by projecting (or collapsing) $|\phi_{\sigma}\rangle$ into a new CPS $|\sigma'\rangle$ with probability $p_{\sigma'\sigma} = |\langle\sigma'|\phi_{\sigma}\rangle|^2$. The transition probabilities obey detailed balance $p_{\sigma'\sigma}P_{\sigma} = p_{\sigma\sigma'}P_{\sigma'}$ by construction.

The thermal step is then repeated with the newly generated CPS to generate a METTS. By construction, the correct distribution is recovered as a fixed point of this procedure. To eliminate any artificial bias caused by the choice of the initial random CPS, the first few thermal steps are neglected when measurements are performed.

We refer to Ref. [SW10] for details on the sampling algorithm and techniques to minimize autocorrelation effects. Note that the original METTS algorithm is not compatible with the implementation of symmetries [Sec. 2.7]. To fix this shortcoming, we introduced a symmetric sampling protocol for dynamic properties in our publication [BvdW15] [see Sec. 4.2]. Recently, a more generalized sampling procedure allows a symmetric sampling also for static observables [BB17].

Applicability

Both finite-temperature methods are highly complimentary since they work best in opposite limits [BvdW15, BB15].

Purification is highly accurate and efficient at high temperatures as it does not require any statistical sampling. However, the full thermal density matrix becomes much more costly to represent as a tensor network at low temperatures in comparison to the cost of representing low-lying energy eigenstates or the pure states encountered in the METTS algorithm. To be more explicit, the bond dimension of $|\psi_T\rangle$ at low temperatures can scale quadratically with the bond dimension necessary to represent the ground-state wavefunction of the corresponding system. This is not very limiting in standard 1D models, where purification can work well even for dynamic properties on the time- and temperature scales of interest. For more complex models including the application to 2D clusters of moderate size performed in our publication [BZWS17], however, the MPS representation of the density matrix quickly reaches the numerically feasible limits due to the additional entanglement in the system.

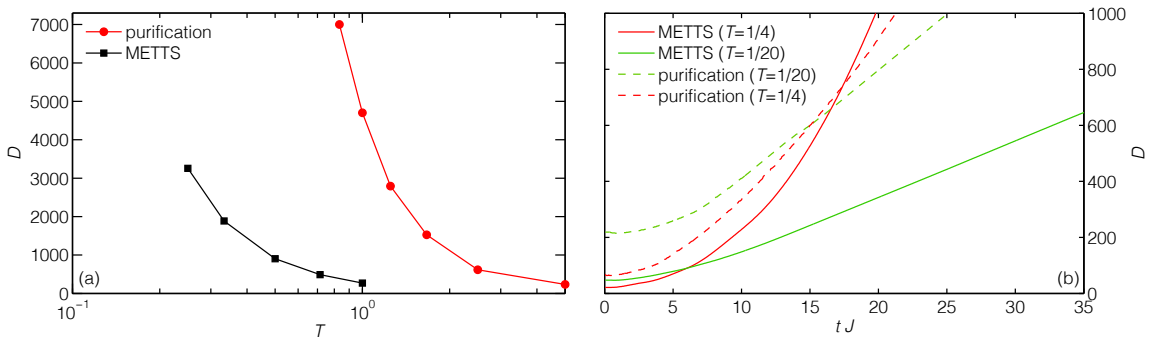


Figure 2.3: Required MPS bond dimension for representing the purified density matrix in comparison to a METTS ensemble (maximum bond dimension of sample shown) illustrating complementary of both finite-temperature methods. (a) For the spin- $\frac{1}{2}$ triangular lattice Heisenberg model on a width-4 cylinder, METTS reaches significantly lower temperatures than accessible with purification (reprint from our publication [BZWS17]) (b) For simulating the finite-temperature dynamics of a spin- $\frac{1}{2}$ Heisenberg model on a 1D chain, METTS is able to reach longer time scales at low temperatures $T = 1/20$. Purification becomes more efficient at $T = 1/4$, where the MPS representation of the density matrix for times $t > 15$ requires a smaller bond dimension than a single METTS (bond dimension D is dynamically truncated in both cases according to the SVD spectrum; reprint from our publication [BvdW15]).

In contrast, the METTS algorithm scales similarly to the ground-state DMRG algorithm [SW10], allowing it to reach significantly lower temperatures. This feature pays off in different contexts:

- for 2D clusters, it enables us to access relevant temperature regimes out of reach of purification. We illustrate this for the example of the spin- $\frac{1}{2}$ triangular lattice Heisenberg model on a width-4 cylinder shown in Fig. 2.3(a), where METTS is able to resolve temperature regimes down to $T = 0.25J$, whereas purification is restricted to $T > 0.8J$.
- for simulating dynamic properties of 1D systems at low temperatures. This is shown for a spin- $\frac{1}{2}$ Heisenberg model on a 1D chain in Fig. 2.3(b), where the real-time evolution of the METTS is able to reach a significantly larger maximum time t_{\max} in comparison to purification for low temperatures $T = 1/20$ (green lines).

On the other hand, METTS is less efficient than purification for higher temperatures, due to the extra sampling overhead and large entanglement growth during real-time evolution (see for example the $T = 1/4$ data (red lines) in Fig. 2.3(b), where, after a while, simulating the density matrix becomes numerically less expensive than representing a single METTS).

2.4.6 Spectral methods

Comparing properties of the ground-state wavefunction obtained from a theoretical model with actual experimental systems poses a big challenge. Experiments have to be cooled down to low enough temperatures to diminish effects from thermal fluctuations and, at the same time, samples have to be extremely clean so that disorder only plays a minor role.

Experimentalists have, however, comparatively easy access to dynamical quantities of quantum many-body systems employing spectroscopy techniques (e.g., ARPES, photon-emission spectroscopy, or neutron scattering). So-called dynamic spin structure factors $\mathcal{S}^{\alpha\beta}(k, \omega)$ represent examples for such spectral observables in a wide class of spin materials. These dynamical spin-spin correlation functions reveal for instance information about the nature of low-energy excitations and, for the case of a 1D model, are defined as

$$\mathcal{S}^{\alpha\beta}(k, \omega) = \sum_j e^{-ikj} \left[\int_{-\infty}^{\infty} dt e^{i\omega t} \langle \hat{S}_j^\alpha(t) \hat{S}_0^\beta \rangle \right], \quad (2.77)$$

where $\hat{S}_j^\alpha(t)$ is a spin- $\frac{1}{2}$ operator in the Heisenberg picture with $\alpha = x, y, z$, and the sum extends over sites j of the one-dimensional lattice with unit lattice spacing.

This section discusses how to obtain spectral functions of the type (2.77) in the MPS framework; it is partly based on the appendices of our publication [BWvDG16]. In particular, we focus on the two most competitive methods, real-time evolution plus Fourier transformation [WF04, WA08], and an MPS-based Chebyshev expansion (CheMPS) [HWM⁺11] working directly in the frequency domain. Both approaches are integral for our work as we employed both tDMRG and CheMPS in three publications included in this thesis [BvDW15, BWvDG16, SBvD17] [see Secs. 4.2, 4.1, and 4.3].

For the sake of completeness, note that there are also other frequency-domain algorithms based on continued fraction expansion [Hal95], as well as the correction-vector method [RPK⁺96, KW99] and its more efficient formulation, the dynamical density matrix renormalization group (DDMRG) [Jec02]. Despite the high accuracy of especially DDMRG, all of these formulations have the severe drawback that each frequency point requires a separate calculation, leading to very high numerical costs. In contrast, tDMRG and CheMPS obtain the full frequency spectrum in a single calculation, making them the methods of choice for the vast majority of applications.

The content of this sections includes some technical notes on both CheMPS and tDMRG, before addressing the question which of the two methods is most efficient for computing spectral functions. To gain some insight into this open question, we adapted a detailed comparison for a spin- $\frac{1}{2}$ chain model at zero temperature from appendix 3 of our publication [BWvDG16] [see also Sec. 4.1]. It turns out that both approaches are very compatible on a general scale. In particular, we observe that entanglement growth towards resolving lower energy scales affects the two methods in a very similar manner.

Real-time evolution with Fourier transform

Generically, correlation functions in the frequency domain can always be computed from their time-domain counterparts employing a Fourier transform. The latter can be obtained with the help of MPS-based time-evolution techniques discussed in Sec. 2.4.4 in real time, both at zero and finite temperature. We briefly elaborate on the most important aspects of this procedure for the example of the dynamic spin-structure factor in Eq. (2.77).

Zero temperature. – To evaluate the zero-temperature structure factor by means of real-time evolution, we first have to determine the time-dependent ground-state correlators

$$\mathcal{S}^{\alpha\beta}(j, t) = e^{iE_0 t} \langle \psi_0 | \hat{S}_j^\alpha e^{-i\hat{H}t} \hat{S}_0^\beta | \psi_0 \rangle \quad (2.78)$$

for various times t and distances j . To this end, we initialize the ground state $|\psi_0\rangle$ employing standard DMRG before we apply a local excitation \hat{S}_0^β in the middle of the chain (labeled with $j_M = 0$) to generate $|\phi\rangle = \hat{S}_0^\beta|\psi_0\rangle$. $|\phi\rangle$ is the initial state for the real-time evolution, $|\phi(t)\rangle = e^{-i\hat{H}t}|\phi\rangle$, which can be carried out with standard MPS-based techniques [Sec. 2.4.4].

Finite temperatures.— The above approach can be generalized with minor modifications to calculate finite-temperature correlators

$$\mathcal{S}^{\alpha\beta}(j, t, T) = \langle\psi_T|e^{i\hat{H}t}\hat{S}_j^\alpha e^{-i\hat{H}t}\hat{S}_0^\beta|\psi_T\rangle. \quad (2.79)$$

In this case, the local excitation \hat{S}_0^β is no longer applied to the ground state $|\psi_0\rangle$ but rather to a thermal state $|\psi_T\rangle$, which either represents the purified density matrix or one state of an ensemble of METTS, depending on the chosen finite-temperature algorithm (see Sec. 2.4.5 for details on finite-temperature techniques). Since the evolution operator acting on the bra can no longer be factored out as a phase factor, one has to carry out two independent real-time evolutions, $|\phi(t)\rangle = e^{-i\hat{H}t}\hat{S}_0^\beta|\psi_T\rangle$ and $|\Phi(t)\rangle = e^{-i\hat{H}t}|\psi_T\rangle$ and evaluate $\mathcal{S}^{\alpha\beta}(j, t, T) = \langle\Phi(t)|\hat{S}_j^\alpha|\phi(t)\rangle$ accordingly.

Entanglement growth.— While the excitation in the beginning acts locally and affects only a small region in the middle of the chain, it spreads in both directions of the chain over time. This leads to an entanglement growth during the real-time evolution, which typically requires the bond dimension of the MPS to be exponentially increased towards longer time scales in order to maintain constant accuracy (see discussion in Sec. 2.4.4). This effectively restricts the accessible time scale to some maximum time t_{\max} , the value of which strongly depends on the specific model and parameter regime.

There exist a set of techniques to further extend t_{\max} to longer time scales. For instance, one can exploit time translational invariance $\langle\hat{S}_j^\alpha(t)\hat{S}_0^\beta\rangle = \langle\hat{S}_j^\alpha(t/2)\hat{S}_0^\beta(-t/2)\rangle$ [Bar13, KK16]. In this setup, one can effectively double t_{\max} by performing two independent real-time evolutions for bra and ket. However, note that in the context of (2.77) this requires to carry out the time evolution individually for each two-point correlator $\langle\hat{S}_j^\alpha(t)\hat{S}_0^\beta\rangle$, which significantly increases the numerical costs.

In the context of finite-temperature simulations, where thermal fluctuations add additional entanglement during the real-time evolution restricting t_{\max} further (rule of thumb: increasing T leads to decreasing t_{\max}), one can exploit the extra degrees of freedom provided by the purification framework to reduce the entanglement growth. While time-evolving the physical state space, one can apply an arbitrary unitary on the auxiliary states. Choosing this auxiliary unitaries appropriately can remove entanglement from the auxiliary Hilbert space leading to a more efficient MPS representation of the purified density matrix. For example, Ref. [KBM12] found that, at high temperatures, using the physical Hamiltonian and applying a backward time evolution to the auxiliary states is an excellent choice. More general strategies already exist [Bar13] and people currently work on systematically constructing the optimal unitary for arbitrary temperatures [HP17].

Postprocessing.— The finite-time limit puts a constraint on the resolution of the spectral functions in frequency space. In order to remove artificial finite-time oscillations in the spectra, one needs to include some sort of broadening when performing the Fourier transform to frequency space.

Typically, a Gaussian filter $\exp[-\eta^2 t^2]$ or Lorentzian filter $\exp[-\eta|t|]$ is included in the time integral in Eq. (2.78) where η is dependent on t_{\max} . Employing the Gaussian filter, the resulting spectral functions contain the exact spectral features convolved with a Gaussian $\exp[-\omega^2/(2W^2)]$, with a frequency resolution $W = \sqrt{2}\eta$. Thus spectral features below W cannot be resolved faithfully.

In some cases, linear prediction represents an alternative to perform the Fourier transform without having to include artificial broadening, and thus retaining more spectral information from the time series [WA08, BSW09]. The idea is to extrapolate from the existing numerical data towards longer time scales. Similar to other extrapolation techniques, linear prediction should not be applied blindly and, in our experience, results should be carefully inspected. According to literature [BSW09, GTV⁺14], linear prediction is considered to work in a stable manner if the results are insensitive to modifications of various numerical parameters of the extrapolation. However, we found that this statement is not generically true. Especially for models with multiple time scales, linear prediction can fool practitioners by producing stable results already on short time scales that cannot possibly capture the full range of physical features (e.g., because t_{\max} is still well below some physically relevant time scale). Thus one has to be sure that the MPS-based time evolution has already captured all relevant time scales before trusting the results of linear prediction.

Finally, we also comment on the second Fourier transform appearing in Eq. (2.78) shifting from real to momentum space. (Depending on the spectral function of interest, this transform might not even be necessary.) In general, there are two different approaches to perform this transform.

The procedure described above using a local excitation attempts to mimic the infinite system with full reflection symmetry with respect to the middle of the chain. Nevertheless, we work on a finite-sized chain so that the transformation is restricted to discrete momenta $k = 2\pi j/N$ ($k = 0, 1, \dots, N-1$) (neglecting here the open boundaries). In this case, it is possible to also include a Gaussian filter to minimize numerical artifacts [BKL⁺11] (yet, this is typically only necessary for very small chains).

An alternative way to perform the Fourier transform is to directly apply a momentum-space operator $\hat{S}_k^\alpha = \sqrt{\frac{2}{N+1}} \sum_{j=1}^N \sin\left(\frac{j\pi k}{N+1}\right) \hat{S}_j^\alpha$ that acts globally on the full system and already properly accounts for the open boundary conditions (note the $N+1$ factor in the denominator).

However, in practice it is advisable to employ the first approach for two reasons. First of all, time-evolving a local excitation generates significantly less entanglement (and thus reaches larger t_{\max}) than evolving a global momentum-space excitation. Secondly, finite-size effects can be controlled more conveniently in this setup as well. System-size effects corrode spectral functions mainly for times when the excitation hits the open ends of the chain and is reflected back into the bulk. This time scale can directly be monitored by studying $\langle \hat{S}_j^\alpha(t) \hat{S}_0^\beta \rangle$ so that one can modify the length N if necessary. Performing a similar check with the momentum-space operator \hat{S}_k^α is not possible, as the excitation feels the open ends of the chain from the beginning of the real-time evolution.

CheMPS

Recently, an MPS-based Chebyshev expansion technique (CheMPS) has been successfully established as a competitive alternative to tDMRG [HWM⁺11, GTV⁺14, TPH14, WMPS14, BS14]. It evaluates dynamic correlators directly in frequency space avoiding the Fourier transform required in any real-time approach. Here we briefly elaborate on the most important technical aspects of this algorithm.

Zero temperature.— Considering again the dynamic spin-structure factor in Eq. (2.78), CheMPS directly computes this correlator in frequency space,

$$\mathcal{S}^{\alpha\beta}(j, \omega) = \langle \psi_0 | \hat{S}_j^\alpha \delta(\omega - \hat{H} + E_0) \hat{S}_0^\beta | \psi_0 \rangle. \quad (2.80)$$

Its key idea is to expand the δ -function in Eq. (2.80) in terms of Chebyshev polynomials of the first kind, T_n . To ensure the convergence of the Chebyshev expansion, the Hamiltonian

has to be rescaled such that its support is fully contained in the interval $[-1, 1]$. One way to achieve this is to use a linear mapping $\hat{H}' = (\hat{H} - E_0)/a - b$, $\omega' = \omega/a - b$ with the two rescaling factors a, b chosen properly.

After appropriate rescaling, the correlator in Eq. (2.80) can be represented with Chebyshev coefficients

$$\mu_n(j) = \langle \psi_0 | \hat{S}_j^\alpha T_n(H') \hat{S}_0^\beta | \psi_0 \rangle, \quad (2.81)$$

leading to

$$\mathcal{S}^{\alpha\beta}(j, \omega) = \frac{1}{a} \sum_{n=0}^{N_{\text{Che}}} w_n(\omega') \mu_n(j) T_n(\omega'), \quad (2.82)$$

with $w_n(\omega) = (2 - \delta_{n0})/(\pi\sqrt{1 - \omega^2})$. The numerically demanding part is to determine the Chebyshev coefficients $\mu_n(j)$. To this end, one exploits the recursion relations of the Chebyshev polynomials to iteratively generate the Chebyshev vectors

$$|t_n\rangle = 2\hat{H}'|t_{n-1}\rangle - |t_{n-2}\rangle, \quad (2.83)$$

$$|t_0\rangle = \hat{S}_0^\beta |\psi_0\rangle, \quad |t_1\rangle = \hat{H}'|t_0\rangle. \quad (2.84)$$

Thus by storing only three MPS per expansion step, we can iteratively evaluate the Chebyshev coefficients $\mu_n(j)$ by computing overlaps of the type $\mu_n(j) = \langle \psi_0 | \hat{S}_j^\alpha |t_n\rangle$ for all values of j on the finite chain. In terms of MPS techniques, this requires the efficient addition and compression of two MPS in every step of the iteration using the fitting algorithm [Sec. 2.4.1].

Analogous to real-time evolution, it is typically more convenient to carry out the Fourier transform from real- to momentum-space after completing the expansion, instead of applying momentum-space operator \hat{S}_k^β to the starting state. In this way, only a single calculation is required to obtain the spectrum at various momenta. Moreover, a local perturbation \hat{S}_0^β leads to a significantly reduced entanglement growth during the expansion.

The entanglement growth observed for $|t_n\rangle$ at higher expansion orders is caused by the repeated application of the Hamiltonian \hat{H} to the MPS and is necessary from a physical point of view to represent the spreading of the local excitation in real space over time. This results in a roughly exponentially growing demand on the numerical resources in order to store and manipulate Chebyshev vectors. Therefore, the expansion is limited to some finite order N_{Che} , at which the computational costs “hit the exponential wall” (very similar to real-time evolution). The finite-order cut off introduces numerical artifacts in the dynamic correlators, which can be removed by including coefficients g_n of a broadening kernel in Eq. (2.82), which smear out the higher order terms and generate a smooth spectrum. Alternatively, it is also possible to determine the full resolvent function in Eq. (2.80) for a nonzero value of η [BS14] or, in some cases, to avoid broadening at all by means of linear prediction [GTV⁺14] (yet, linear prediction should be employed very carefully, as discussed above).

Ref. [WJMS15] showed that the details of the rescaling procedure clearly affect the efficiency of the calculation. It is usually most efficient to map the support of the spectral function close to the lower boundary of the interval $[-1, 1]$, where the zeros of the individual Chebyshev polynomials are densely distributed. This can be achieved by using a “ $b = 1$ ” setup, which is in the following distinguished from the “ $b = 0$ ” setup, where the support of the spectral function lies at the center of $[-1, 1]$.

Finite-temperatures. – In combination with density-matrix purification [Sec. 2.4.5], CheMPS is also capable to determine finite-temperature spectral functions of the form

$$\mathcal{S}^{\alpha\beta}(j, \omega) = \langle \psi_T | \hat{S}_j^\alpha \delta(\omega - \hat{\mathcal{L}}) \hat{S}_0^\beta | \psi_T \rangle, \quad (2.85)$$

where $\hat{\mathcal{L}} = \hat{H}_P \otimes \mathbb{1}_A - \mathbb{1}_P \otimes \hat{H}_A$ denotes the Liouville operator governing the dynamics of the purified density matrix $|\psi_T\rangle \in \mathcal{H}_P \otimes \mathcal{H}_A$ [TMPH14]. Thus the zero-temperature CheMPS algorithm discussed above can also be applied at finite temperatures in a straightforward manner, simply by replacing the ground state with the purified density-matrix and employing the Chebyshev iteration with $\hat{\mathcal{L}}$ instead of the Hamiltonian \hat{H} .

Despite the analogy, finite-temperature CheMPS has one subtle but severe drawback compared to its zero-temperature formulation. The spectral width of the Liouvillian is twice as large as the width of the Hamiltonian, reducing the resolution of CheMPS significantly. Moreover, the rescaling procedure is restricted to a less flexible setup (one of the parameters has always to be set to zero, $b = 0$. See discussion above). Thus the low-energy part of the spectrum cannot be shifted towards the boundaries of the rescaled spectrum $[-1, 1]$, where the individual Chebyshev polynomials are densely distributed and therefore give a much better resolution.

It is also possible to combine CheMPS with METTS, but for technical reasons this turned out to be very inefficient [BvdW15].

tDMRG vs. CheMPS at zero temperature

Although CheMPS has been frequently applied in practice [TRS13, GTV⁺14, TMPH14, WMPS14, BS14, HKM15, RP16, KTF⁺16, THP⁺16], no conclusive answer has yet been presented to the question whether it provides a computationally more efficient framework than real-time evolution. Here we attempt to shed some light on this question and present a detailed comparison for a specific spin- $\frac{1}{2}$ XXZ model governing the magnetic properties of the material Cs_2CoCl_4 . The discussion follows appendix 3 of our publication [BWvDG16] [see also Sec. 4.1].

The low-energy model for Cs_2CoCl_4 is described by the Hamiltonian

$$\hat{H} = \sum_j J \left[(\hat{S}_j^x \hat{S}_{j+1}^x + \hat{S}_j^y \hat{S}_{j+1}^y) + \Delta \hat{S}_j^z \hat{S}_{j+1}^z - h \hat{S}_j^x \right], \quad (2.86)$$

with coupling $J/k_B \approx 3$ K and $\Delta \approx 0.12$ adapted to the properties of Cs_2CoCl_4 [BGS⁺13]. The system features an Ising quantum phase transition at the dimensionless critical field $h_c \approx 1.56$.

In the following, we compare the numerical efficiency of the two methods, tDMRG and CheMPS, in the context of the present model for a system with $N = 100$ spins directly at quantum criticality, $h = 1.56$ and $T = 0$. Starting by placing an excitation in the middle of the chain, we take $\hat{S}_0^\beta |\psi_0\rangle$ as the initial state for both the real-time evolution and the Chebyshev expansion. The CheMPS simulation is carried out in two setups: one with $b = 0$ in the linear mapping and $N_{\text{Che}} = 4800$ iterations, another with $b = 0.995$ and $N_{\text{Che}} = 2100$ iterations. We modify the bond dimension of each MPS by retaining all singular values up to $\epsilon_{\text{SVD}} = 10^{-4}$ in every Trotter step as well as any Chebyshev iteration Eq. (2.83) during the entire calculation.

Fig. 2.4 displays the corresponding evolution of the excitation with time, $\langle \hat{S}_j^z(t) \hat{S}_0^z \rangle$, and iteration order, $\mu_n(j) = \langle \psi_0 | \hat{S}_j^\alpha | t_n \rangle$, respectively. In all cases, the initially localized excitation spreads out in real space, showing the typical light-cone structure. We clearly observe that finite-size reflections are not present up to the maximum time $t_{\text{max}} = 60$ in the tDMRG simulation [Fig. 2.4(a)]. The same applies to the CheMPS results of the $b = 0$ setup in Fig. 2.4(b). Following the literature, the final iteration corresponds to an effective time scale $t \sim N_{\text{Che}}/a \approx 60$, which is equivalent to the maximum time of the tDMRG reference calculation. However, the excitation in (b) is already spread out significantly further in the system than at the end of the tDMRG calculation. This deviation becomes even more apparent studying the $b = 0.995$ setup in (c), which in principle should evolve according to

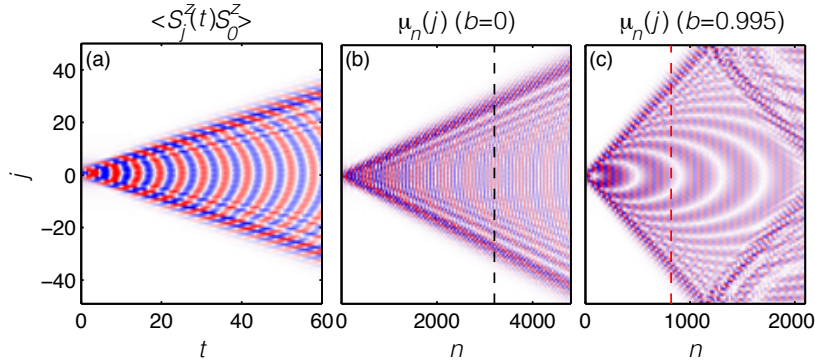


Figure 2.4: Evolution of the excitation over (a) time $\langle \hat{S}_j^z \hat{S}_0^z(t) \rangle$ and (b),(c) iteration order $\mu_n(j) = \langle \psi_0 | \hat{S}_j^z | t_n \rangle$. Reprinted from our publication [BWvDG16].

the same effective time scale as the rescaling factor a is unchanged. In reality, the excitation has already reached the boundary of the system after $n \approx 1100$ iterations. Reflections at both boundaries become strongly visible for higher iterations. This suggests that the effective time scale of $t^* = 60$ is already reached with significantly fewer iterations in the $b = 0.995$ setup, which is in agreement with the findings of Ref. [WJMS15].

Hence, we conclude that only $n^* < at_{\max}$ CheMPS iterations have to be carried out in order to obtain spectral data with comparable accuracy as in the reference tDMRG simulation. This is illustrated in Fig. 2.5(a), where the local spectral function $\langle \hat{S}_0^z \hat{S}_0^z \rangle(\omega)$ obtained from tDMRG and CheMPS data is displayed. We use only the first n^* moments of the respective CheMPS calculation and a Jackson kernel in the Chebyshev reconstruction to mimic both the maximum time cut off and the Gaussian broadening in the Fourier transform of the real-time data, choosing n^* such that the agreement with the reference data is best. These iterations n^* are indicated by the dashed vertical lines in Figs. 2.4(b) and (c). As one would intuitively expect, the excitation is spread over approximately the same distance after these n^* iterations as in the tDMRG calculation at t_{\max} .

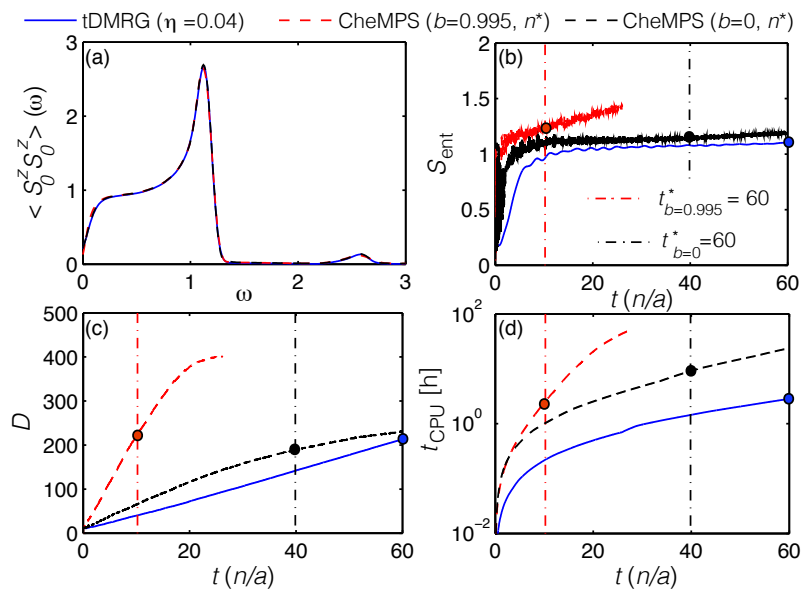


Figure 2.5: (a) Local spectral function $\langle \hat{S}_0^z \hat{S}_0^z \rangle(\omega)$ obtained from tDMRG and CheMPS for the spin- $\frac{1}{2}$ model for Cs_2CoCl_4 with $N = 100$ spins directly at the phase boundary for $h = 1.56$ and $T = 0$. (b)-(d) Comparison of entanglement entropy S_{ent} , bond dimension D , and cumulative CPU time t_{CPU} . Reprinted from our publication [BWvDG16].

Thus we can restrict our efficiency analysis to the first $n \leq n^*$ iterations in order to conduct a reasonable comparison to tDMRG. Figs. 2.5(b)-(d) show the entanglement entropy, bond dimension and accumulated CPU time, respectively. The tDMRG data is plotted in real-time units t , whereas the CheMPS results are displayed with a rescaled iteration number n/a for better comparability. Again, the dashed vertical lines indicate the iteration n^*/a of interest. First of all, we note that the Chebyshev vectors at n^* in both setups are slightly more entangled than the time-evolved MPS [Fig. 2.5(b)], although this is not reflected in the respective bond dimensions at n^* or t_{\max} , respectively: The final time-evolved MPS has a bond dimension $D = 213$, the corresponding Chebyshev vectors in the $b = 0$ and $b = 0.995$ setup carry a somewhat comparable number of many-body states ($D = 188$ and $D = 218$, respectively). This indicates that both methods require very similar amounts of numerical resources in order to reproduce the same spectral information. A comparison of CPU times further confirms this, as tDMRG and $b = 0.995$ CheMPS require almost the identical amount of total CPU-time, namely $t_{\text{CPU}} = 2.8$ hours on a 8-core machine. The CheMPS calculation in the $b = 0$ setup takes approximately three times longer due to the larger number of iterations necessary to reach the same time scale.

We have conducted this study only for a single model and set of parameters, thus we cannot provide an unambiguous answer to whether a spectral function is best represented in terms of Fourier modes or Chebyshev functions. However, we learned here that both methods are affected by the dynamical entanglement growth in a very similar matter. Therefore, it seems rather unlikely that one method can significantly outperform the other. Our analysis would have to be extended to other parameters and systems in order to give a fully conclusive answer. For instance, we expect that tDMRG outperforms CheMPS at finite T , since (i) the Liouvillian formulation of CheMPS requires a factor a twice as large as in the $T = 0$ setup; (ii) the more efficient $b = 1$ setup, which aims to shift the support of the spectral function close to the lower boundary of the rescaled interval $[-1, 1]$, might not be appropriate if finite temperatures shift the support to higher energies; (iii) CheMPS offers no counterpart to exploiting time-translation invariance, which allows us to effectively double the maximum time scale in the tDMRG setup [Bar13]. On the other hand, CheMPS might be the preferred choice for zero-temperature calculations in models with long-ranged interactions, where a Trotter-based time evolution is no longer feasible.

2.5 Infinite projected entangled-pair states

In addition to MPS, this thesis builds on a second type of tensor network representation for quantum many-body states, the so-called projected entangled-pair states (PEPS) [VC04]. These TN states represent the natural generalization of the MPS ansatz to higher spatial dimensions. Like their 1D counterparts, they satisfy the area law, rendering them ideal tools for the simulation of low-energy states in two-dimensional many-body systems on arbitrary lattice geometries.

This type of tensor network can be constructed by considering a system where each site shares a maximally entangled state with each nearest-neighbor site along some virtual degree of freedom. By applying a linear map to each site, one can project locally into the subspace of each site (one “projects entangled pairs”) generating a tensor network of PEPS [VC04]. The class of PEPS includes also another type of tensor network states for higher spatial dimension. These so-called tensor product states represent generalizations of 2D AKLT states and show up even earlier in the literature [HOA99, ON00, NMG04].

Many TN algorithms to simulate many-body states in 2D are based on the PEPS representation. In this work, we only consider the PEPS method extended to translationally invariant systems, the so-called iPEPS (infinite PEPS) ansatz [JOV⁺08] which is capable to obtain ground-state wavefunctions in the thermodynamic limit. But there exist numerous other methods based on PEPS including the tensor renormalization group (TRG) [LN07, GLW08], the second renormalization group (SRG) [XJC⁺09], the higher-order tensor renormalization group [XCQ⁺12], tensor network renormalization [EV15, Eve17], DMRG-like ground-state optimization [Cor16b, VHCV16] and promising extensions to excited states by means of tangent space methods [VMVH15].

Tensor network techniques based on MPS play a dominant role for simulating 1D quantum systems, as elaborated on extensively in the last section. Despite many interesting developments, PEPS has not yet reached the same standing in the context of frustrated and fermionic 2D systems. This is mostly due to the technical complexity of the algorithm, especially in the context of fermions [COBV10]. Nevertheless, the approach has recently proven its competitiveness and, for instance, provided a number of new insights for underdoped Hubbard [ZCC⁺17] and t - J models [CWVT11, CRT14, Cor16a], for spin- $\frac{1}{2}$ [MCHW17, LXC⁺17] and spin-1 Kagome-Heisenberg models [LLW⁺15], as well as for the Shastry-Sutherland model [CM13, CM14]. At the same time, PEPS is still in its infancy and there is much room for technical improvements that will further boost the method. While currently on par with 2D-DMRG, we expect that PEPS-based methods will become the most powerful TN approaches for 2D systems in the near future.

In this section we discuss the most important aspects of the PEPS representation and give a thorough introduction to the iPEPS algorithm, that has been employed to obtain the results in Sec. 5.2. In particular, we discuss how to perform contractions [Sec. 2.5.2], and tensor optimization based on imaginary-time evolution [Sec. 2.5.4] including the gauge fixing for iPEPS [LCBn14, PBT⁺15]. For a more general introduction to PEPS, we refer to the reviews [Eis13, Orú14b, Orú14a].

2.5.1 Properties of PEPS and iPEPS

Here, we discuss the PEPS construction and some basic properties of this TN representation, following in parts Refs. [COBV10] and [Orú14b]. Special focus is put on the diagrammatic PEPS representation that forms the basis for sketching the more complex steps of the algorithm further below. We mostly adopt the diagrammatical TN representation of Ref. [COBV10], specifically to enable a consistent discussion of fermionic PEPS in Sec. 2.6. Moreover, we introduce a translationally invariant PEPS formulation, the so-called infinite PEPS (iPEPS) [JOV⁺08], to perform simulations directly in the thermodynamic limit.

While easily generalizable to other lattice geometries, we restrict our discussion to *bosonic* many-body systems on a square lattice in the following [for the fermionic extension see Sec. 2.6]. We start from a generic many-body wavefunction $|\psi\rangle$ living on a 3×3 cluster (see Fig. 2.6 for illustration, especially regarding the site labeling) that generically can be expressed in terms of the local Fock space $|\sigma_y^x\rangle$ and a rank-9 tensor $\Psi_{\sigma_1^1 \sigma_2^1 \dots \sigma_3^3}$,

$$|\psi\rangle = \sum_{\sigma_1^1 \sigma_2^1 \dots \sigma_3^3} \Psi_{\sigma_1^1 \sigma_2^1 \dots \sigma_3^3} |\sigma_1^1\rangle |\sigma_2^1\rangle \dots |\sigma_3^3\rangle. \quad (2.87)$$

The integer indices x and y enumerate sites in the horizontal and vertical direction, and the local or physical index $\sigma_y^x \in 1, \dots, d$ labels states in the local Hilbert space at site $\mathbf{r} = (x, y)$. The number of coefficients in Ψ is given by d^9 and obviously grows exponentially with system size in this representation. Analogous to the MPS framework in 1D, the key idea of the PEPS representation is to circumvent the exponential scaling in system size by decomposing Ψ into a set of nine M tensors,

$$|\psi\rangle = \sum_{\substack{\sigma_1^1 \sigma_2^1 \dots \sigma_3^3 \\ \alpha_1 \alpha_2 \dots \alpha_6 \\ \gamma_1 \gamma_2 \dots \gamma_6}} M_{\alpha_1 \gamma_1}^{[\sigma_1^1]} M_{\alpha_2 \gamma_1 \gamma_2}^{[\sigma_2^1]} \dots M_{\alpha_6 \gamma_6}^{[\sigma_3^3]} |\sigma_1^1 \sigma_2^1 \dots \sigma_3^3\rangle. \quad (2.88)$$

To this end, one introduces a set of virtual or bond indices, α_i for horizontal bonds and γ_i for vertical bonds, that connect each M tensor to its counterparts on up to four neighboring sites, according to the lattice geometry. The diagrammatic representation can be easily generalized from the MPS framework by introducing the diagram for a rank-4 “bulk” tensor

$$M_{\alpha\beta\gamma\rho}^{[\sigma_y^x]} = \begin{array}{c} \gamma \\ \circlearrowleft M_y^x \\ \rho \\ \alpha \\ |\sigma_y^x\rangle \end{array}. \quad (2.89)$$

The boundary tensors of a finite-size PEPS contain fewer legs. Since we focus on the translationally invariant formulation of PEPS below, we refrain from a detailed discussion of various boundary conditions and the corresponding tensors [LCBn14].

In general, the number of M tensors in the PEPS representation is equal to the number of sites in the system, e.g., for a quadratic case this results in $N = L \times L$ tensors. Starting from Eq. (2.89), the diagrammatic representation of the full wavefunction $|\psi\rangle$ in Eqs. (2.87) and (2.88) follows immediately,

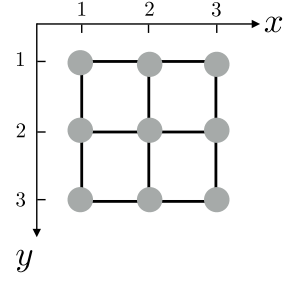
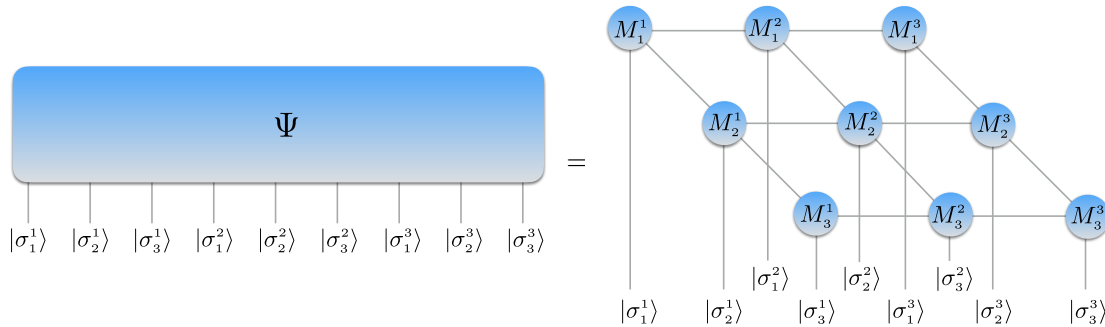


Figure 2.6: Illustration of 3×3 square cluster.

(2.90)

As in the case of MPS, one limits the dimension of the bond indices of each PEPS tensor to some upper cutoff dimension D , in order to restrict the exponential scaling of the coefficients in $|\psi\rangle$ with respect to system size.¹ Thus adding an additional site (or row/column of sites) only leads to a polynomial increase of the coefficients in the wavefunction. In numerical practice, D is used as a control parameter for the numerical accuracy. It is typically restricted to $D \leq 8-16$, depending on the model and lattice geometry, because for larger values the numerical costs become unfeasibly high.

Restricting the bond dimension of the M tensors comes at the price that only a subset of states can efficiently be represented by a PEPS, since D also limits the maximum amount of entanglement that can be captured by the construction. In particular, the entanglement entropy for any block of sites \mathcal{C} with length L (see Fig. 2.1 for illustration) is bounded by $S_{\mathcal{C}} = \mathcal{O}(L \log(D))$. Fortunately, this is perfectly in line with the area law of the entanglement entropy in 2D, which is fully satisfied by a PEPS representation. Hence, PEPS are ideally suited to approximate low-energy states including the ground state of local gapped Hamiltonians in two dimensions. Although this statement cannot yet be put on such a mathematically rigorous foundation as 1D, it is strongly supported by numerical evidence [Eis13].

Moreover, the PEPS representation has the remarkable property that, in contrast to MPS, it is capable to faithfully represent algebraically decaying correlation functions, which are characteristic for gapless models [see Sec. 2.2]. This can easily be shown for the example of the partition function of the 2D Ising model [VWPGC06]. Therefore, the PEPS ansatz is in principle able to also treat critical ground-state wavefunctions. In practice, however, this does not help substantially in the context of 2D quantum criticality (the above mentioned example deals with classical and not quantum criticality). Based on the quantum-to-classical correspondence, one would require a 3D PEPS construction to faithfully approximate a critical 2D quantum system. Thus, in reality PEPS faces the same challenges in the context of gapless 2D systems as MPS treating critical 1D models: Both TN frameworks may obtain results ranging from excellent to moderate quality depending on the “severeness” of the area-law violation in a particular system [Orú14b].

Infinite PEPS

For finite-size PEPS simulations, each M tensor is typically chosen to be different (similar to MPS applications for finite systems). Alternatively, it is possible to exploit the translational invariance of a system and directly work in the thermodynamic limit (of course, this approach also works for MPS [McC08], but is not considered in this thesis). In this way, finite-size and boundary effects can be completely eliminated.

In order to construct an infinite PEPS (iPEPS) [JOV⁺08], we first choose a fixed unit cell of a certain size, which is periodically repeated over the entire infinitely large lattice geometry. The size of the fundamental unit cell directly translates into the number of different M tensors required for the iPEPS representation. For instance, one can impose

¹In principle, each state of the full Hilbert space can be represented by such a PEPS ansatz with arbitrary large values of D . In the literature this property is sometimes referred to as “PEPS are dense” [Orú14b].

strict translational invariance and choose a unit cell of size 1×1 ,

The resulting iPEPS representation of $|\psi\rangle$ then requires only a single M tensor.

However, ordered ground states often break translational invariance to some degree. An iPEPS ansatz of type (2.91) cannot capture this behavior. Therefore, it is advisable to relax the translational invariance to some extent by choosing a larger unit cell. For example, the following ansatz is fully compatible with an antiferromagnetic ground-state order using two different M tensors in a 2×2 unit cell:

In principle, unit-cells of arbitrary size can be considered, e.g.,

The numerical costs scale linearly with the number of tensors in the unit cell, meaning that large unit cells become numerically expensive. A natural guideline to evaluate which unit-cell sizes should be considered in a simulation is to remember that the unit cell should be compatible with the actual ground-state order. Otherwise, one does not obtain the actual ground state from an iPEPS calculation. Instead, one ends up with the lowest-energy state for the system constrained to the corresponding unit-cell geometry and therefore restricted to specific orders.

When studying systems with competing low-energy orders, the flexible unit-cell setup of the iPEPS algorithm actually becomes a big advantage. By probing different unit cells, one is capable to stabilize wavefunctions with competing orders independently. Comparing the energies obtained from the corresponding simulations, one may then determine which order survives in the ground state of the system [CWVT11, CRT14].

2.5.2 Contractions

To extract local observables, perform overlaps, or to actually optimize the tensors, the (i)PEPS framework requires contracting an (infinitely) large tensor network. This turns

out to be much more challenging than in context of MPS where, for example, overlaps can be evaluated exactly with only polynomial costs in system size. For a PEPS tensor network, however, the calculation of an exact overlap represents an exponentially hard problem [SWVC08] and cannot be performed efficiently. Fortunately, there exist a variety of approximative schemes to deal with this issue.

In this section, we mainly focus on the corner transfer matrix method (CTM) [NO96, OV09] that is particularly well suited for iPEPS applications on square-lattice geometries. Alternatively, it is also possible to rely on an infinite MPS technique for the purpose of this work [JOV⁺08, Vid07, OV08]. Other contraction schemes based on renormalization ideas, such as the tensor renormalization group [LN07, GLW08], or tensor network renormalization [EV15, Eve17], do have some technical disadvantages (e.g., environmental recycling [PMV15, PBT⁺15] is not possible, and difficulties arise when calculating longer-ranged correlators, ect.), rendering them unsuitable for our purposes.

Before discussing the details of the CTM scheme for evaluating the scalar product $\langle \psi | \psi \rangle$, we first have to introduced the diagrammatic representation for the conjugated version $M_y^{x\dagger}$ of a generic M tensor. As in the case of MPS, the diagram is obtained by considering the mirror image of (2.89) in horizontal direction with respect to the physical index [COBV10],

$$M_{\alpha\beta\gamma\rho}^{[\sigma_y^x]\dagger} = \begin{array}{c} \langle \sigma_y^x | \\ \rho \\ \circlearrowleft M_y^{x\dagger} \\ \gamma \\ \alpha \end{array} \beta = M_{\rho\gamma\beta\alpha}^{*[\sigma_y^x]}. \quad (2.94)$$

In this way, we are able to conserve the graphical order of the sites previously imposed also on the bra level (this will become relevant in the context of fermions in Sec. 2.6). The corresponding diagram of $\langle \psi |$ for the 3×3 square-lattice toy model follows directly from Eq. (2.94),

$$\begin{array}{c} \langle \sigma_1^1 | \quad \langle \sigma_1^2 | \quad \langle \sigma_1^3 | \quad \langle \sigma_2^1 | \quad \langle \sigma_2^2 | \quad \langle \sigma_2^3 | \quad \langle \sigma_3^1 | \quad \langle \sigma_3^2 | \quad \langle \sigma_3^3 | \\ \hline \Psi^\dagger \end{array} = \begin{array}{c} \langle \sigma_1^1 | \quad \langle \sigma_2^1 | \quad \langle \sigma_3^1 | \quad \langle \sigma_1^2 | \quad \langle \sigma_2^2 | \quad \langle \sigma_3^2 | \quad \langle \sigma_1^3 | \quad \langle \sigma_2^3 | \quad \langle \sigma_3^3 | \\ \hline \begin{array}{c} M_3^{1\dagger} \quad M_3^{2\dagger} \quad M_3^{3\dagger} \\ M_2^{1\dagger} \quad M_2^{2\dagger} \quad M_2^{3\dagger} \\ M_1^{1\dagger} \quad M_1^{2\dagger} \quad M_1^{3\dagger} \end{array} \end{array}. \quad (2.95)$$

We also present a distinct representation for the so-called reduced m tensor, which is obtained

by tracing over the joint physical index of $M_y^{x\dagger} M_y^x$,

$$\begin{aligned}
 m_y^x(\alpha\alpha')(\beta\beta')(\gamma\gamma')(\rho\rho') &= \sum_{\sigma_y^x} M_{\rho\gamma\beta\alpha}^{[\sigma_y^x]\dagger} M_{\alpha'\beta'\gamma'\rho'}^{[\sigma_y^x]} = \\
 &= \begin{array}{c} \gamma' \\ \alpha' \quad M_y^x \quad \beta' \\ \rho \\ \alpha \quad M_y^{x\dagger} \quad \beta \\ \gamma \end{array} \\
 &= \begin{array}{c} \gamma' \\ \alpha' \quad M_y^x \quad \beta' \\ \rho \\ \alpha \quad M_y^{x\dagger} \quad \beta \\ \gamma \end{array} \\
 &= \begin{array}{c} (\gamma\gamma') \\ (\alpha\alpha') \quad m_y^x \quad (\beta\beta') \\ (\rho\rho') \end{array}, \quad (2.96)
 \end{aligned}$$

where the double indices (e.g., $(\alpha\alpha')$) have dimension D^2 , as indicated by their increased line thickness. In the second line, we redrew the lines representing indices γ and ρ in such a way that pairs of corresponding primed and unprimed indices match up. This diagrammatically performed “index bending” exploits the non-uniqueness of the graphical representation for a tensor network [COBV10]. This modification is completely trivial for bosonic iPEPS but will add additional complications in the context of fermions [see Sec. 2.6].

To reduce the complexity of the TN diagrams appearing in the following, we introduce a modified version of the conjugate tensor that automatically accounts for the index bending discussed in Eq. (2.96):

$$\begin{array}{c} \gamma' \\ \alpha' \quad M_y^{x\dagger} \quad \beta' \\ \rho \\ \alpha \quad M_y^{x\dagger} \quad \beta \\ \gamma \end{array} = \begin{array}{c} \gamma' \\ \alpha' \quad \bar{M}_y^{x\dagger} \quad \beta' \\ \rho \\ \alpha \quad \bar{M}_y^{x\dagger} \quad \beta \\ \gamma \end{array}. \quad (2.97)$$

This distinction may seem unnecessary at this point, since $\bar{M}_y^{x\dagger}$ and $M_y^{x\dagger}$ are mathematically equivalent objects in the context of bosons. However, this does no longer hold for fermionic systems [c.f. Eq. (2.149)]. Therefore, we emphasize the importance of this modification already here.

The scalar product $\langle\psi|\psi\rangle$ for this simple example is obtained by contracting all physical

and virtual index of the nine m tensors,

$$\begin{aligned}
 \langle \psi | \psi \rangle &= \text{Diagram 1} \\
 &\stackrel{(2.97)}{=} \text{Diagram 2} \\
 &= \text{Diagram 3}
 \end{aligned}
 \tag{2.98}$$

Note that the second step ($\stackrel{*}{=}$) also exploits the non-uniqueness of the diagrammatic representation by employing a number of so-called “jump-moves” [COBV10]. In these operations, it is possible to drag a line over a tensor without changing the corresponding TN. Again, this modification is trivial in context of bosonic PEPS, but nontrivial for fermionic PEPS [see Sec. 2.6].

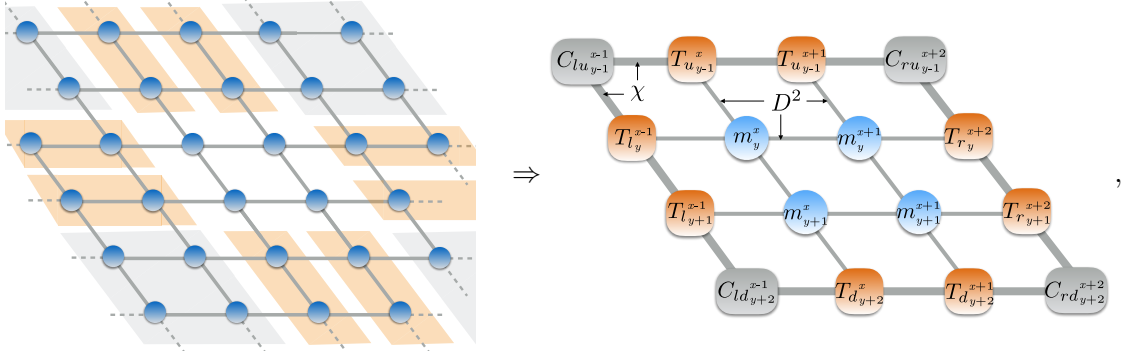
Studying the small tensor networks in Eq. (2.98), it becomes obvious that the exact contraction of the expression scales exponential with system sizes. No matter in which order one decides to contract the tensors, i.e., which “contraction pattern” one uses, one always generates an object with a number of open indices scaling with L (here $L = 3$).

Corner transfer matrix scheme

Since it is not possible to perform the exact calculation of a scalar product efficiently in the PEPS nor in the iPEPS framework, one has to rely on approximative approaches. A particularly powerful contraction scheme is based on ideas of the corner transfer matrix (CTM) renormalization group [NO96]. The ideas were later adapted by Orus and Vidal [OV09] in the context of quantum systems to efficiently evaluate an iPEPS tensor network.

The key insight of the approach is to represent the infinitely large tensor network by a small number of tensors, zooming into a 1×1 or 2×2 window of sites (in general, this might be only a subset of the full unit cell, which in general has the size $L_x \times L_y$). The rest of the system, the so-called “environment”, is represented by a set of corner matrices C and

transfer tensors T . This is illustrated for the 2×2 subset embedded in the environment in the following,



where the environmental tensor network is represented by a set of four corner matrices ($C_{lu}, C_{ld}, C_{ru}, C_{rd}$ with subscripts denoting the spatial location, i.e., l, r, u, d stand for left, right, up, down, respectively) and eight transfer tensors (two tensors for each direction, T_l, T_r, T_u, T_d , respectively). In this representation, a new set of virtual indices is introduced connecting tensors of the environment only. As we discuss below, the dimension χ of these indices acts as additional parameter controlling the accuracy of the environmental approximation (reasonable choices are $\chi \geq D^2$).

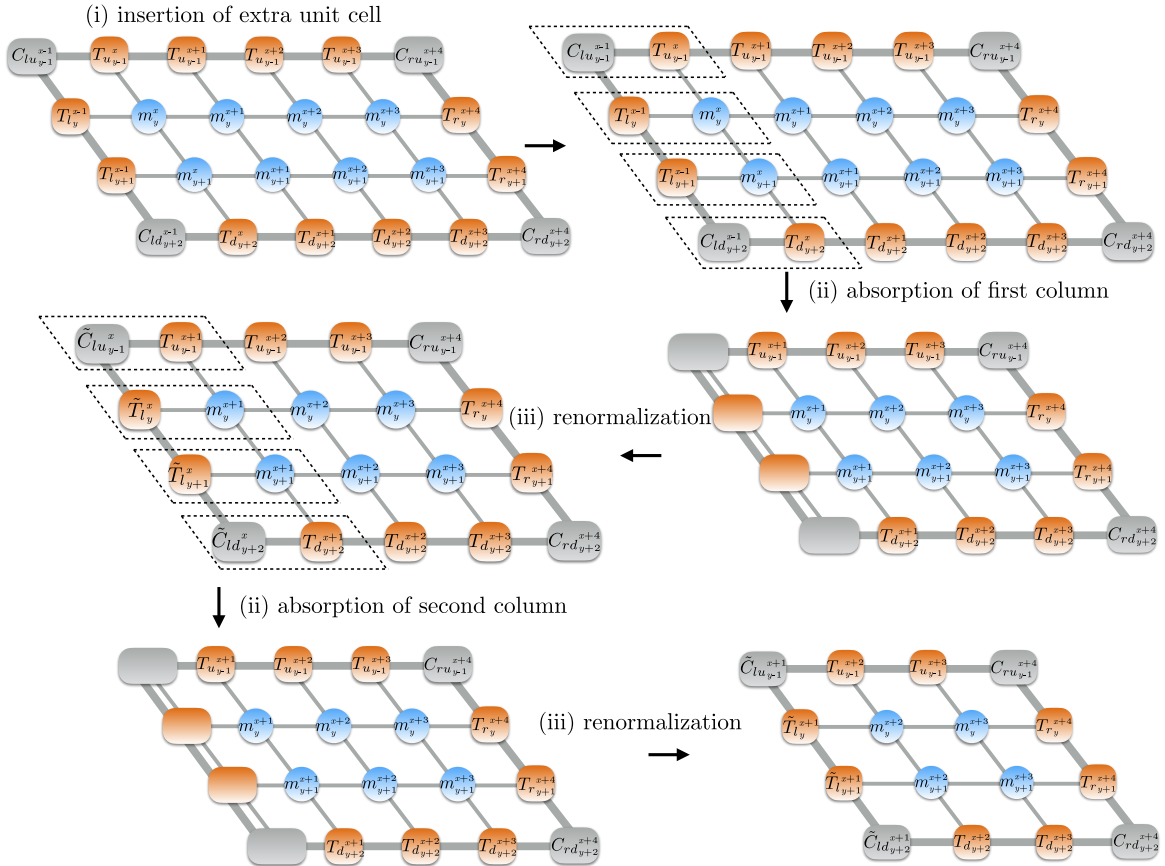


Figure 2.7: CTM coarse graining move to the left lattice direction: (i) extra unit cell is first inserted, and then column-wise integrated into the left part of the environment by performing two subsequent (ii) absorption and (iii) renormalization steps.

CTM protocol.— The environmental tensors are obtained from performing directional

coarse graining moves in each direction of the lattice. Each coarse graining move consists of three different steps: (i) *insertion* of extra unit cell; (ii) *absorption* of single row or column of the unit-cell tensors into the set of the environment in one lattice direction, leading to an enlarged environmental bond dimension χD^2 ; (iii) *renormalization* (or truncation/compression) of the enlarged environmental tensors to their original size. Steps (ii) and (iii) are repeated until the inserted unit cell has been fully absorbed into the set of environmental tensors in the one particular direction. Next, an additional unit cell is inserted next to the original unit cell in one of the other directions, and the move is carried out with respect to another direction of the lattice. A full coarse graining step is completed after one move into each of the four lattice directions (left, right, top, bottom) has been performed.

In the following, we illustrate this procedure for an iPEPS representation with a 2×2 unit cell, using four M tensors that all have the property $M_y^x = M_y^{x+2} = M_{y+2}^x = M_{y+2}^{x+2}$. A directional move to the left then includes the steps illustrated in Fig. 2.7.

Note that the extra unit cell has been inserted horizontally (this is also the case for a move to the right). Moreover, two absorption and renormalization steps are carried out, at the end of which the inserted unit cell has been fully integrated into the left part of the environment. This set of operations yields an updated set of environmental tensors for the direction of the coarse graining step.

In the following, we also sketch in Fig. 2.8 a coarse graining move towards the top of the lattice.

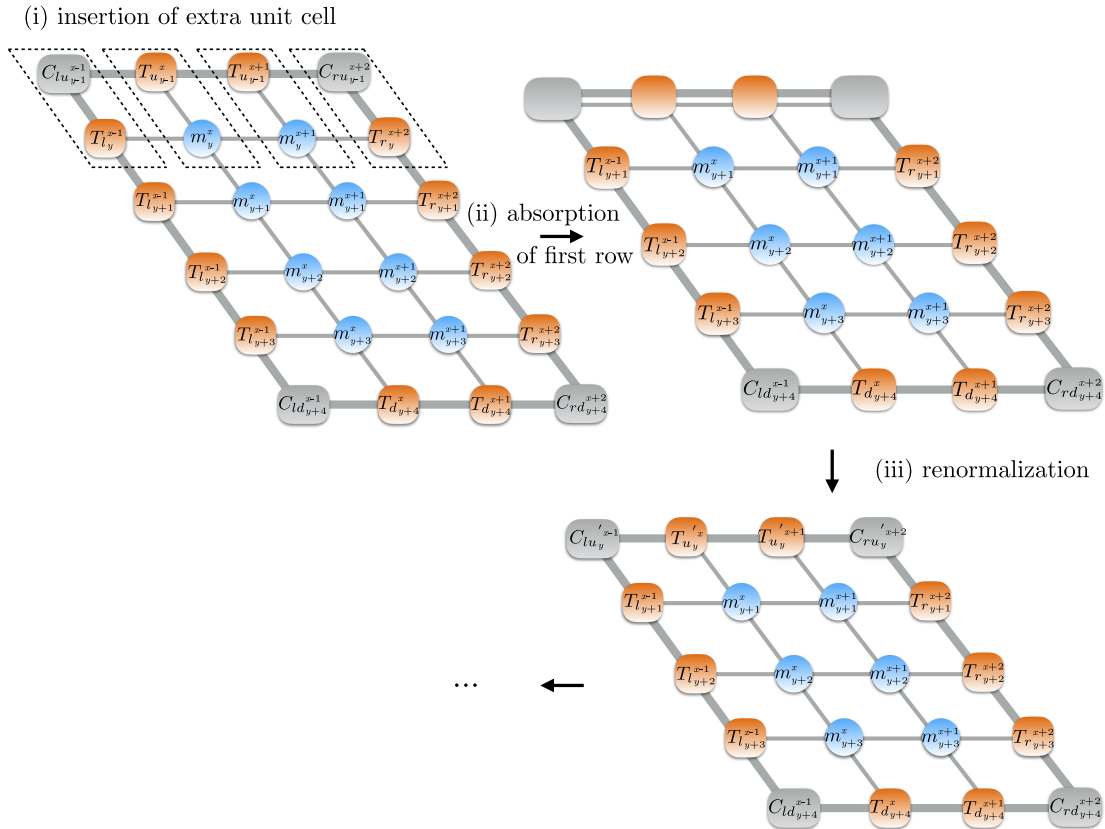


Figure 2.8: CTM coarse graining move to the top of the lattice: (i) extra unit cell is first inserted, and then row-wise integrated into the upper part of the environment by performing two subsequent (ii) absorption and (iii) renormalization steps (only first step is shown).

In this case, the unit cell is inserted vertically. Then we follow the same protocol as for the left move. Only the direction of the absorption and renormalization steps differs. After

also carrying out these coarse graining moves with respect to the other two lattice directions, a full coarse graining step has been completed. The full cycle is typically repeated multiple times depending on the correlation length in the system. In gapped systems already a few full steps may be sufficient to obtain converged results. Especially for critical wavefunctions, however, the number of cycles required to reach convergence in local observables can significantly increase.

Renormalization.— In addition to the number of steps performed, the convergence of the results also strongly depends on the implementation of the renormalization step, which truncates the environmental tensors after the absorption step. The renormalization is crucial for the performance of the CTM scheme. However, its implementation details are not very straightforward, and currently there seems to be ample room for future improvement. The ambiguity of implementation details is mostly caused by the lack of an exact canonical representation for a PEPS TN, which implies that there is no obvious optimal way of performing the truncation (in contrast to an MPS tensor network, which can be truncated optimally even in the context of translationally invariant systems [OV08]).

We tested a number of different renormalization schemes. One corresponds to the directional updated scheme of Ref. [OV09], which we found to work well only in the context of very homogenous wavefunctions. This method takes only small subsets of the environment into account and implicitly assumes full translational invariance when generating the projectors (or isotropies) to perform the truncation. This ultimately yields a very biased truncation pattern for inhomogeneous systems, where this method is bound to fail.

The second approach is based on the original CTMRG [NO96] and was first employed by Ref. [CJV10] in the context of iPEPS. In this case, the full environment is taken into account in each truncation step which presents a crucial advantage for simulating inhomogeneous states. On the other hand, it is severely limited by machine precision, making it unstable for large values of environmental bond dimension χ . This is far from ideal since it is desirable to use χ as additional control parameter.

To overcome these shortcomings, Ref. [CRT14] introduced a third CTM variant that shows strongly improved convergence properties in comparison to the original CTMRG scheme and, at the same time, overcomes the inhomogeneity issues of the directional updated scheme. In the following, we sketch how to obtain the projectors used to reduce the sizes of the environmental tensors after an absorption step in the left direction, following Ref. [CRT14]. The protocol works similarly for the other spatial directions of the lattice.

In the first step, we enforce two cuts in the tensor network consisting of the 2×2 unit-cell subset embedded in the effective environment as follows

(2.99)

Our goal is to obtain projectors (or isotropies) that are inserted after an absorption step at a specific bond to “project” (or truncate/compress) the enlarged environmental Hilbert space $D^2\chi$ back to its original size χ . In this example, we specifically aim for the projectors to be inserted into the two bonds split by the left cut.² To this end, we contract the two upper

²Analogously, we could use (2.99) to obtain the projectors for the two split bonds on the right. This becomes necessary when performing a CTM move into the right direction of the lattice.

and lower parts of the tensor network, leading to rank-4 tensors Q_u and Q_d . By applying a singular value (or QR) decomposition to both of these tensors, we obtain

$$\begin{array}{c} Q_u \\ \hline Q_d \end{array} \xrightarrow{\text{SVD}} \begin{array}{c} U_u \quad S_u \quad V_u^\dagger \\ U_d \quad S_d \quad V_d^\dagger \end{array} = \begin{array}{c} R_u \quad V_u^\dagger \\ R_d \quad V_d^\dagger \end{array} \quad (2.100)$$

The product $R_u R_d$ is then subjected to an additional SVD where only the χ largest singular values are kept,

$$\begin{array}{c} R_u \\ R_d \end{array} \xrightarrow{\text{SVD}} \begin{array}{c} U \\ S \\ V^\dagger \end{array} \approx \begin{array}{c} R_u^{-1} \\ S^{-1} \\ R_d^{-1} \end{array} \quad (2.101)$$

Using the inverse matrices R_u^{-1} and R_d^{-1} , we generate the projectors P_y^x, \tilde{P}_y^x that are inserted at the left cut of the tensor network (2.99).

$$\begin{array}{c} R_d \\ R_d^{-1} \\ R_u^{-1} \\ R_u \end{array} \approx \begin{array}{c} R_d \\ V \\ \sqrt{S^{-1}} \\ \sqrt{S^{-1}} \\ U^\dagger \\ R_u \end{array} = \begin{array}{c} \tilde{P}_y^x \\ P_y^x \end{array} \quad (2.102)$$

The protocol is repeated for the entire row of the unit cell to be absorbed into the environment during this particular coarse graining step (i.e., L_y times). In our example of an 2×2 unit cell, we therefore also obtain P_{y+1}^x and \tilde{P}_{y+1}^x (or alternatively P_{y-1}^x and \tilde{P}_{y-1}^x due to translational invariance) by considering the tensor network and repeating the procedure sketched above,

$$\begin{array}{c} C_{lu}^{x-1} \quad T_{u_y}^x \quad T_{u_y}^{x+1} \quad C_{ru_y}^{x+2} \\ T_{l_{y+1}}^{x-1} \quad m_{y+1}^x \quad m_{y+1}^{x+1} \quad T_{r_{y+1}}^{x+2} \\ \text{cut} \quad \text{cut} \\ T_{l_{y+2}}^x \quad m_{y+2}^x \quad m_{y+2}^{x+1} \quad T_{r_{y+2}}^{x+2} \\ C_{ld_{y+3}}^{x-1} \quad T_{d_{y+3}}^x \quad T_{d_{y+3}}^{x+1} \quad C_{rd_{y+3}}^{x+2} \end{array} \Rightarrow \begin{array}{c} \tilde{P}_{y+1}^x \\ P_{y+1}^x \end{array} = \begin{array}{c} \tilde{P}_{y-1}^x \\ P_{y-1}^x \end{array} \quad (2.103)$$

Now we are fully equipped to renormalize the entire set of environmental tensor which are

subject to truncation during an absorption step to the left,

What has been achieved is a scheme that compressed the bond dimensions of the environmental tensors along the left row in a way that encodes information from the full environment. Thus we can appropriately deal with translational symmetry breaking in the iPEPS wavefunction. At the same time, this procedure leads to numerically stable results since we can eliminate spurious parts of the SVD spectrum during the intermediate SVD decompositions in Eq. (2.100) by discarding very small singular values (e.g., $< 10^{-7}$). This helps to reduce the influence of numerical noise in the subsequent steps.

Nevertheless, it is not clear whether this protocol represents the optimal way to perform the truncation during the CTM procedure. Going forward, alternative renormalization algorithms exploiting the gauge fixing of a TN could further improve the stability [Wei17]. However, finding *the* optimal truncation procedure might not be possible due to the lack of a true canonical form in the iPEPS framework.

Larger unit cells.— Following Ref. [CWVT11], the CTM scheme can also deal with rectangular unit cells of arbitrary sizes containing $L_x \times L_y = N$ different M tensors, where the relative position of each tensor in the unit cell is labeled by its coordinate $\mathbf{r} = (x, y)$. To this end, we assign one set of corner matrices and transfer tensors to *each* coordinate, requiring a total number of $4N$ corner matrices and $4N$ transfer tensors to be stored independently. We illustrate this approach for a 3×2 unit cell in Fig. 2.9. After initialization (see below), the environmental tensors are then iteratively updated by performing coarse graining moves in all four lattice directions, as outlined above. However, an entire CTM cycle now includes L_x coarse graining steps to the left and right, respectively, as well as L_y coarse graining steps to the top and L_y to the bottom of the lattice. Note that using a larger zooming window is not an option, since the numerical costs quickly become unfeasible.

Initialization.— While covering the coarse graining procedure to obtain the converged environmental tensors, we have not yet discussed the initialization of the CTM scheme. In principle, one could start from an arbitrary set of corner matrices and transfer tensors. However, choosing a completely random set can significantly increase the number of coarse graining steps required for obtaining a stable environment TN and sometimes even cause numerical instabilities. In practice, we found that optimal convergence is achieved by starting from an environmental tensor set formed by the corresponding M_y^x tensors and their conjugates, which previously have been generated by means of ground-state optimization

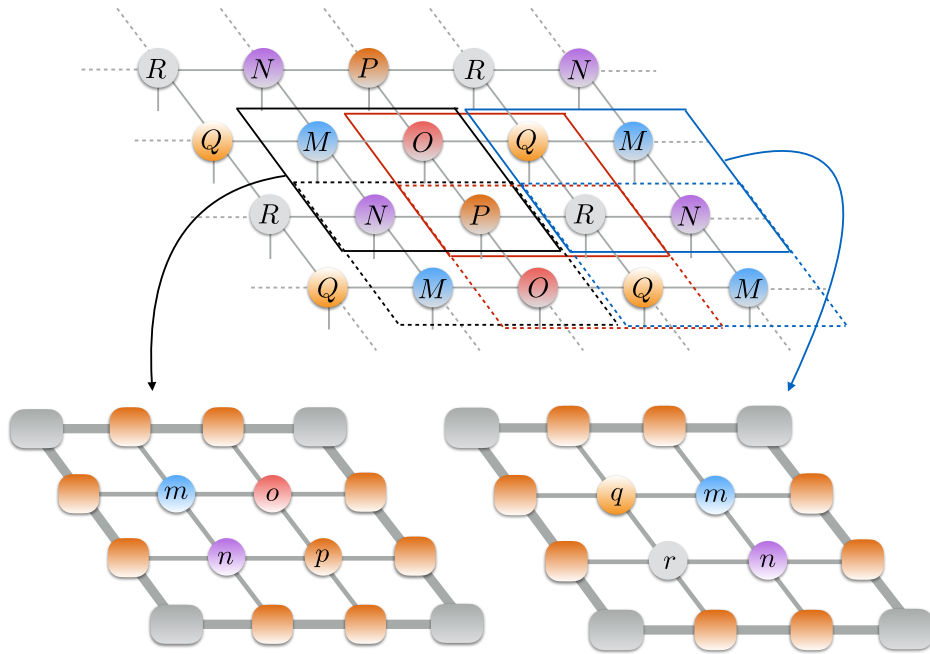


Figure 2.9: A unit cell of size 3×2 consists of six different M tensors (here denoted M, N, O, P, Q , and R). For each of the six relative coordinates in the unit cell, we have to obtain a 2×2 CTM representation (indicated by the solid and dashed squares, and explicitly illustrated for two examples). Therefore, the CTM scheme here requires storing 24 corner matrices and 24 transfer tensors in total.

[see Sec. 2.5.4]. We illustrate this initialization procedure for two examples,

$$\begin{array}{c} \text{C}_{\text{Id}_y}^x \end{array} = \begin{array}{c} \text{M}_y^x \\ \text{M}_y^{x\dagger} \end{array}, \quad \begin{array}{c} \text{T}_y^x \end{array} = \begin{array}{c} \text{M}_y^x \\ \text{M}_y^{x\dagger} \end{array}. \quad (2.105)$$

Effective contraction pattern.— The numerical costs of implementing the square-lattice CTM scheme presented above scales as $\mathcal{O}(D^6\chi^3)$, with the iPEPS bond dimension D and the environmental bond dimension χ . Note that these costs are equivalent to those of the infinite MPS method from Ref. [JOV⁺08]. Assuming that $\chi = \mathcal{O}(D^2)$, we end up with a total cost scaling of $\mathcal{O}(D^{12})$ for the iPEPS algorithm.

The underlying assumption behind this cost scaling is that all contractions are carried out as efficiently as possible, which forces us to pay some attention to the contraction patterns. In particular, we cannot directly work with the reduced tensors m_y^x , but rather need to perform contractions involving M_y^x and its conjugate $M_y^{x\dagger}$ sequentially.

This is illustrated below for contracting a part of the diagram in Eq. (2.99). First consider

the case explicitly using the reduced tensor m_y^x ,

$$(2.106)$$

Counting the involved indices in the dashed box, it becomes clear that the last contraction step scales rather unfavorably as $\mathcal{O}(D^8\chi^2)$.

If we want to achieve the optimal scaling $\mathcal{O}(D^6\chi^2d)$ in this step, we have to contract over M_y^x and $M_y^{x\dagger}$ sequentially,

$$(2.107)$$

The same applies to contraction orders of other TN such as, for example, the one shown in Eq. (2.104) and many others. It pays off to constantly pay attention and ensuring that the optimal contraction pattern is used when implementing an iPEPS algorithm. Otherwise, the backlash of an inefficient iPEPS implementation will quickly become apparent, since simulations with moderate to large D will not be feasible.

Note that the most expensive steps of the CTM algorithm occur when generating the projectors. To obtain the tensor Q_u and in Eq. (2.100), for instance, one has to perform the following contracting,

$$(2.108)$$

which always yields a cost scaling of $\mathcal{O}(\chi^3D^6)$ which cannot be reduced further.

2.5.3 Expectation value

The CTM scheme enables us to evaluate observables within the iPEPS framework. For this case, we consider a simple two-site observable $\hat{O}_{(x,y)}^{(x+1,y)}$ which, for example, represents a spin-spin correlation function acting on neighboring sites. To compute an approximation

for the expectation value $\langle \hat{O}_{(x,y)}^{(x+1,y)} \rangle = \langle \psi | \hat{O}_{(x,y)}^{(x+1,y)} | \psi \rangle / \langle \psi | \psi \rangle$, we represent the environment of the two contiguous sites $\mathbf{r} = (x, y)$ and $\mathbf{r}' = (x, y + 1)$ in terms of the corner matrices and transfer tensors encountered in the last section,

$$\begin{aligned}
 \langle \psi | \hat{O}_{(x,y)}^{(x+1,y)} | \psi \rangle_{\chi} &= \\
 &= \\
 &=
 \end{aligned}
 \tag{2.109}$$

The final contraction of tensor network, consisting of the six environmental tensors E_1, \dots, E_6 and the two M tensors and its conjugates, can be carried out efficiently. It produces an approximation of $\langle \psi | \hat{O}_{(x,y)}^{(x+1,y)} | \psi \rangle \approx \langle \psi | \hat{O}_{(x,y)}^{(x+1,y)} | \psi \rangle_{\chi}$ which is generally expected to deviate from the exact value due to the non-exact representation of the full tensor network. The correct value of $\langle | \hat{O}_{(x,y)}^{(x+1,y)} | \rangle \approx \langle \psi | \hat{O}_{(x,y)}^{(x+1,y)} | \psi \rangle_{\chi} / \langle \psi | \psi \rangle_{\chi}$ should be recovered in the limit $\chi \rightarrow \infty$.

In practice, one evaluates Eq. (2.109) for a number of different values of $\chi = 10, 20, \dots, 100, 150, \dots$ until the observable shows no more significant dependence on χ . The required value for χ to obtain converged results strongly varies depending on the physical properties of the corresponding system and the employed iPEPS bond dimension D .

2.5.4 Optimization

An iPEPS is an ideal representation for the ground-state wavefunction of a local Hamiltonian on a two-dimensional lattice. Having addressed the contraction issue by means of the CTM scheme [see previous Sec. 2.5.2], the remaining open question concerns finding the ground-state iPEPS representation given some Hamiltonian \hat{H} with only nearest-neighbor interactions. (Albeit technical more complicated, iPEPS can also treat longer-ranged interactions, for more details see Ref. [CJV10, CM13].)

Here we follow the strategy proposed in the original iPEPS formulation [JOV⁺08] and rely on imaginary time evolution to target the ground state,

$$|\psi_0\rangle = \lim_{\tau \rightarrow \infty} \frac{e^{-\tau \hat{H}} |\psi\rangle}{\|e^{-\tau \hat{H}} |\psi\rangle\|}. \quad (2.110)$$

The imaginary-time evolution for iPEPS works along the same lines as the standard time-evolution algorithms for MPS [see Sec. 2.4.4]. Thus, the time-evolution operator $e^{-\tau \hat{H}}$ is decomposed by means of a Suzuki-Trotter decomposition,

$$e^{-\hat{H}\tau} \approx \prod_{j=1}^{N_b} e^{-\hat{h}_{y,y'}^{x,x'}\tau} + \mathcal{O}(\tau^2), \quad (2.111)$$

where $\hat{h}_{y,y'}^{x,x'}$ describes the local interaction terms acting on a pair of nearest-neighbor sites in the unit cell, and $\hat{H} = \sum_{\langle(x,y),(x',y')\rangle} \hat{h}_{y,y'}^{x,x'}$. These two-site gates $e^{-\hat{h}_{y,y'}^{x,x'}\tau}$ are subsequently applied to the corresponding pairs of M tensors, M_y^x and $M_{y'}^{x'}$. As in the case of MPS, the resulting tensor has to be truncated accordingly to restore the original form of the iPEPS representation.

In the MPS framework, the truncation can be implemented in an optimal way using the canonical form of the MPS and employing a single singular value decomposition. In the context of iPEPS, this step turns out to be more evolved. Due to the lack of an exact canonical form for the iPEPS, one has to rely on approximative techniques to account for the effects of the environment when employing the truncation. This can be done using several different optimization schemes, such as the *simple update* [JWX08] and the *full update* [JOV⁺08]. We discuss both of these approaches extensively in the rest of this section.

Although not employed in the context of this thesis, we also note that two groups recently introduced alternative optimization schemes, which do not rely on imaginary time evolution [Cor16b, VHCV16]. Instead, they implement a DMRG-style energy minimization procedure,

$$\min_{\{M_y^x\}} [E_0] = \frac{\langle \psi_0 | \hat{H} | \psi_0 \rangle}{\langle \psi_0 | \psi_0 \rangle}. \quad (2.112)$$

The major technical challenge of these newly developed schemes is to find an approximative, yet accurate, representation for the full Hamiltonian \hat{H} . Ref. [Cor16b] achieves this based on a modified CTM scheme, while Ref. [VHCV16] builds on MPS techniques. In addition, it is still unclear how to optimally translate the local update performed on a pair of tensors to the iPEPS representation in the infinite system. Despite these issues, both variational optimization techniques already obtain very impressive results, illustrating that the iPEPS formalism will continuously improve and become more competitive in the near future.

Bond projection

In this work, we only consider the optimization via imaginary-time evolution based on two-site Trotter gates, which implies that we constantly have to update two neighboring M tensors at once (i.e., there is no one-site version of this algorithm). Hence, it is essential to perform the tensor updates as efficiently as possible. Treating the full M tensors in this context turns out to be numerically very inefficient (i.e., numerical costs of $\mathcal{O}(D^{12})$ in the context of the full update). Hence, it is always advisable to perform the tensor update on two subtensors with lower rank which are easily obtained by a bond projection [LvDX12], leading to a significant cost reduction (i.e., $\mathcal{O}(D^6 d^3)$ [PBT⁺15]). Note that this scheme does

not introduce further approximations since the two-site Trotter gate only changes properties of the corresponding bond but leaves the remaining bonds of the iPEPS tensors unchanged.

The bond projection is obtained by performing two exact SVD (or QR) decompositions, as illustrated in the following

$$\begin{aligned}
 & \begin{array}{c} \text{---} \circlearrowleft M_y^x \text{---} \\ | \sigma_y^x \rangle \\ \text{---} \circlearrowright M_y^{x+1} \text{---} \\ | \sigma_y^{x+1} \rangle \end{array} = \begin{array}{c} \text{---} \circlearrowleft M_y^x \text{---} \\ | \sigma_y^x \rangle \\ \text{---} \circlearrowright M_y^{x+1} \text{---} \\ | \sigma_y^{x+1} \rangle \end{array} = \begin{array}{c} \text{---} \circlearrowleft \text{---} \\ \text{---} \circlearrowright \text{---} \end{array} \begin{array}{c} \text{---} \circlearrowleft \text{---} \\ \text{---} \circlearrowright \text{---} \end{array} \\
 & = \begin{array}{c} \text{---} \circlearrowleft X_y^x \text{---} \\ | \sigma_y^x \rangle \\ \text{---} \circlearrowright v_y^x \text{---} \\ | \sigma_y^x \rangle \\ \text{---} \circlearrowright w_y^{x+1} \text{---} \\ | \sigma_y^{x+1} \rangle \\ \text{---} \circlearrowleft Y_y^{x+1} \text{---} \end{array} . \quad (2.113)
 \end{aligned}$$

The tensor optimization now only affects the subtensors v_y^x and w_y^{x+1} , whereas the remaining bonds are shifted into the subtensors X_y^x and Y_y^x , which can be treated as parts of the environment tensor network during the optimization.

Each tensor update is initialized by applying the corresponding Trotter gate in the bond projection,

$$\begin{aligned}
 e^{-\hat{h}_{y,y}^{x,x+1} \tau} | \psi \rangle & = \begin{array}{c} \text{---} \circlearrowleft M_y^x \text{---} \\ | \sigma_y^x \rangle \\ \text{---} \circlearrowright M_y^{x+1} \text{---} \\ | \sigma_y^{x+1} \rangle \end{array} \\
 & = \begin{array}{c} \text{---} \circlearrowleft X_y^x \text{---} \\ | \sigma_y^x \rangle \\ \text{---} \circlearrowright v_y^x \text{---} \\ | \sigma_y^x \rangle \\ \text{---} \circlearrowright w_y^{x+1} \text{---} \\ | \sigma_y^{x+1} \rangle \\ \text{---} \circlearrowleft Y_y^{x+1} \text{---} \end{array} \\
 & = \begin{array}{c} \text{---} \circlearrowleft X_y^x \text{---} \\ | \sigma_y^x \rangle \\ \text{---} \circlearrowright \tilde{v}_y^x \text{---} \\ | \sigma_y^x \rangle \\ \text{---} \circlearrowright \tilde{w}_y^{x+1} \text{---} \\ | \sigma_y^{x+1} \rangle \\ \text{---} \circlearrowleft Y_y^{x+1} \text{---} \end{array} = | \psi(\tilde{v}, \tilde{w}) \rangle \quad (2.114)
 \end{aligned}$$

The Trotter gate increases the initial bond dimension D of the subtensors v_y^x and w_y^{x+1} . Restoring the original representation exactly yields a pair of enlarged subtensors \tilde{v}_y^x and \tilde{w}_y^{x+1} with bond dimension dD (illustrated by the increased line thickness in Eq. (2.114)). In a next step, we have to find an appropriate truncation scheme to obtain a pair of subtensors v_y^x and w_y^{x+1} with the original bond dimension D to prevent an exponential blowup of the iPEPS tensors.

In the following, we present two different truncation methods: (i) the simple update [JWX08], a numerically very efficient and fast approach which, however, relies on a strong simplification of the environmental tensor network and thus carries out the truncation in a suboptimal way; (ii) the full update scheme [JOV⁺08] which leads to an optimal truncation by incorporating the effects of the entire wavefunction appropriately. However, the full update comes at the price of requiring significantly more numerical resources. For completeness, we also mention the so-called cluster updates [WV11] which can be understood as a

hybrid version of the simple and the full update, taking into account an improved, yet not complete version of the effective environment while truncating.

Simple update

The simple tensor update introduced in Ref. [JWX08] is formulated in a slightly modified iPEPS representation. So far, we only dealt with M tensors located directly at sites of the lattice. For the simple update we put an extra set of tensors on the bonds of the iPEPS tensor network. These tensors, here labeled λ_y^x for horizontal and $\tilde{\lambda}_y^x$ for vertical bonds, are diagonal matrices similar to those used in Vidal's TEBD and iTEBD formulation for time-evolving matrix product states [Vid04, Vid07].

Starting from the standard iPEPS representation that has been adopted in this thesis, so far, it requires only a minor adaption to translate into this modified representation,

$$M_y^x = \Gamma_y^x \begin{matrix} \tilde{\lambda}_{y-1}^{x-1/2} & \lambda_y^{x+1/2} \\ \lambda_y^{x-1/2} & \tilde{\lambda}_y^{x+1/2} \end{matrix}, \quad (2.115)$$

where Γ_y^x in combination with the roots of all four bond tensors yields the original M_y^x tensor.

The key idea of the simplified update is to approximate the full environment of two neighboring sites $\mathbf{r} = (x, y)$ and $\mathbf{r}' = (x + 1, y)$ by only the diagonal tensors surrounding this pair of sites. This procedure is adopted from MPS-based time evolution via the iTEBD algorithm.

To perform the simple update explicitly, we switch first into the bond projection to carry out the optimization more efficiently. We illustrate the projection here explicitly since different tensors are involved in the modified iPEPS representation,

$$\begin{aligned} & \left[\Gamma_y^x \right] \left[\Gamma_{y+1}^x \right] = \left[\tilde{\Gamma}_y^x \right] \left[\tilde{\Gamma}_{y+1}^x \right] \\ & = \left[X_y^x \right] \left[v_y^x \right] \left[w_y^{x+1} \right] \left[Y_y^{x+1} \right]. \quad (2.116) \end{aligned}$$

Now the Trotter gate is applied to the subtensors on the bond adding entanglement and potentially increasing the bond dimension to dD . To obtain the pair of subtensors v_y^x and

w'^{x+1} with the original bond dimension D , the simple update relies on a simple SVD,

$$\begin{aligned}
 & \text{Diagrammatic representation of the simple update step, showing the decomposition of a tensor network into a simple update step.} \\
 & \text{The diagram shows a sequence of equalities:} \\
 & \text{1. A tensor network with } \Gamma_y^x \text{ and } \Gamma_y^{x+1} \text{ tensors connected by a bond with singular value } \lambda_y^x. \text{ A box labeled } e^{-i\hat{h}_{y,y}^{x,x+1}\tau} \text{ is inserted.} \\
 & \text{2. This is equal to a tensor network with } X_y^x, v_y^x, w_y^{x+1}, \text{ and } Y_y^{x+1} \text{ tensors, with a box labeled } e^{-i\hat{h}_{y,y}^{x,x+1}\tau} \text{ below } v_y^x \text{ and } w_y^{x+1}. \\
 & \text{3. This is equal to a tensor network with } X_y^x \text{ and } Y_y^{x+1} \text{ tensors, with a vertical dashed line between them, labeled SVD.} \\
 & \text{4. This is equal to a tensor network with } X_y^x, v'_y{}^x, w'_y{}^{x+1}, \text{ and } Y_y^{x+1} \text{ tensors, with a box labeled } e^{-i\hat{h}_{y,y}^{x,x+1}\tau} \text{ below } v'_y{}^x \text{ and } w'_y{}^{x+1}. \\
 & \text{5. This is equal to a tensor network with } Q_y^x \text{ and } Q_y^{x+1} \text{ tensors connected by a bond with singular value } \lambda'_y{}^x. \\
 & \text{6. This is equal to a tensor network with } Q_y^x \text{ and } Q_y^{x+1} \text{ tensors.} \\
 & \text{The final result is labeled (2.117).}
 \end{aligned}$$

No extra iteration or optimization is required to complete the update (hence, the name “simple” update). The updated diagonal bond matrix λ'^x_y contains the D largest singular values, the optimized subtensors are obtained from $v'^x_y = U$ and $w'^{x+1}_y = V^\dagger$.

To restore the form of the iPEPS tensors from Q^x_y and Q^{x+1}_y , we apply the inverse of the additional bond tensors, which have not been altered by this optimization step,

$$\begin{aligned}
 & \text{Diagrammatic representation of the restoration of the iPEPS tensors.} \\
 & \text{The diagram shows two equalities:} \\
 & \text{1. } \Gamma'_y{}^x = \text{Diagram with } Q^x_y \text{ tensor and additional bond tensors } \lambda^{x-1}_y \text{ and } \lambda^{x-1}_{y-1}. \\
 & \text{2. } \Gamma'_y{}^{x+1} = \text{Diagram with } Q^{x+1}_y \text{ tensor and additional bond tensors } \lambda^{x-1}_{y-1} \text{ and } \lambda^{x-1}_y. \\
 & \text{The final result is labeled (2.118).}
 \end{aligned}$$

The simple update is particularly appealing due to its low complexity and high numerical efficiency; the truncation based on a plain SVD in Eq. (2.117) only scales with $\mathcal{O}(D^3 d^6)$ operations. Yet, the truncation itself cannot be considered optimal in the context of iPEPS. It would have been optimal if we had gauged the surrounding bonds in such a way that they exclusively contain orthonormal basis sets. Unfortunately, this is only possible if the environment is separable, as in the case of MPS or other tensor networks *without loops* [see Sec. 2.4.1]. In fact, one can show that a tensor optimization performed in this way presents an optimal update for an infinite tensor network on a Bethe lattice [LvDX12].

Any iPEPS representation on a standard 2D lattice, however, does feature loops, which means that we cannot separate the environment into two blocks and find a gauge with orthonormal basis sets on all surrounding bonds. Hence, the simple update introduces a systematic error, as it does not properly account for the full environment of the bond during the optimization. The magnitude of this error turns out to be less severe than one might expect. Especially for systems in gapped phases, the simple update leads to excellent results [COBV10]. Moreover, its numerical efficiency often allows simulations with larger bond dimensions compared to the full update; thus it can give access to complex systems which remain out of reach for full-update calculations. Despite its approximative nature, the simple update therefore is a very viable tool for iPEPS, which we have employed extensively in the context of simulating complex extensions of the standard Hubbard model [see Sec. 5.2].

We conclude this section with a few practical comments concerning the implementation of the simple update:

- For a generic unit cell, the simple update is employed sequentially on all bonds in the system. One can easily work with a second-order Trotter decomposition by reversing the application order of the gates in every second step, as shown in Eq. (2.63).
- The normalization of the tensor network can be conveniently achieved on the fly by normalizing the trace of each updated diagonal bond matrix λ_y^x to unity. This procedure leads to a numerically fully stable algorithm.
- To obtain a meaningful representation of the ground state by means of imaginary-time evolution, we start from a random set of tensors and use a fairly large time step $\tau = \mathcal{O}(10^{-1})$. A large initial time step is important since it minimizes the risk of getting stuck in a local energy minimum and, in case of symmetric iPEPS implementation, it enables us to dynamically adapt the symmetry sectors on the bonds (starting from a very small time step, one can get stuck in the initial symmetry configuration and not reach all relevant sectors). To decrease the effect of the Trotter error, we then gradually reduce τ as soon as we observe convergence with respect to the SVD spectra (typically after a few hundred or thousand time steps). After reaching a time step of the order $\mathcal{O}(10^{-5})$, the ground-state wavefunction is typically converged.
- Measurements of observables are performed with the converged iPEPS representation, obtained from the simple update, as input for the CTM scheme. Relying on CTM, this leads to a total numerical cost scaling of $\mathcal{O}(\chi^3 D^6)$, which is, in principle, equivalent to the cost scaling of the full update. In the latter, however, the full environment has to be calculated in every step and not just at the end to perform measurements.

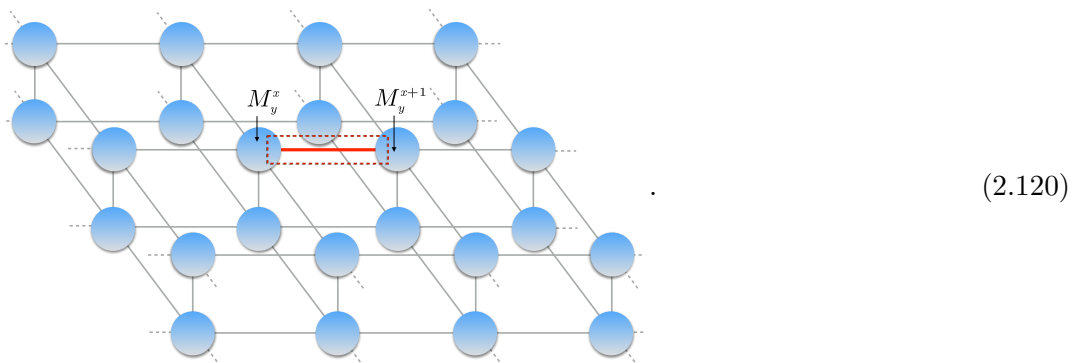
Full update

The full update introduced by Ref. [JOV⁺08] represents the clean and optimal protocol to perform the tensor update during imaginary-time evolution. Its name is derived from the fact that the effects of the entire wavefunction on the bond tensors are considered, including the full environmental TN. The only approximation stems from the non-exact contraction of the environmental TN, which we carry out based on the CTM scheme [see Sec. 2.5.2].

After the application of the Trotter gate in Eq. (2.114), the full update generates the optimized pair of subtensors v_y^x and w_y^{x+1} with bond dimension D by minimizing the squared norm between $|\psi(v', w')\rangle$ and the wavefunction $|\psi(\tilde{v}, \tilde{w})\rangle$ that contains the exact subtensors \tilde{v}_y^x and \tilde{w}_y^{x+1} with enlarged bond dimension dD ,

$$d(\tilde{v}, \tilde{w}, v', w') = \left\| |\psi(v', w')\rangle - |\psi(\tilde{v}, \tilde{w})\rangle \right\|^2. \quad (2.119)$$

To minimize Eq. (2.119) in terms of v_y^x and w_y^{x+1} , we first have to obtain an effective representation of the environment with respect to the bond to be updated (marked red):



This is achieved via the CTM scheme, leading to an approximate representation of the environment in terms of corner matrices and transfer tensors,

Diagram (2.121) illustrates the contraction of corner matrices and transfer tensors. On the left, two horizontal chains of tensors are shown, enclosed in dashed boxes. The top chain consists of $C_{lu_{y-1}^{x-1}}$, $T_{u_{y-1}^x}$, $T_{u_{y-1}^{x+1}}$, and $C_{ru_{y-1}^{x+2}}$. The bottom chain consists of $C_{ld_{y+1}^{x-1}}$, $T_{d_{y+1}^x}$, $T_{d_{y+1}^{x+1}}$, and $C_{rd_{y+1}^{x+2}}$. Vertical lines connect $T_{u_{y-1}^x}$ to $T_{d_{y+1}^x}$ and $T_{u_{y-1}^{x+1}}$ to $T_{d_{y+1}^{x+1}}$. Horizontal lines connect $C_{lu_{y-1}^{x-1}}$ to $C_{ld_{y+1}^{x-1}}$ and $C_{ru_{y-1}^{x+2}}$ to $C_{rd_{y+1}^{x+2}}$. On the right, these are represented by a network of six effective environment tensors E_1 through E_6 connected in a diamond-like structure: E_1 is at the bottom left, E_2 and E_3 are at the top, E_4 is at the top right, E_5 and E_6 are at the bottom right.

As in the case of the simple update, we carry out the tensor update for efficiency reasons in the bond projection, as discussed above. In order to generate the full environment in this representation, we have to account for the subtensors X_y^x and Y_y^{x+1} as well as their conjugates, and multiply them to the effective environment shown in Eq. (2.121), obtaining

Diagram (2.122) shows the full environment E_{full} as a network of six effective environment tensors E_1 through E_6 connected in a diamond-like structure. Four blue circular subtensors are attached to the network: X_y^x and Y_y^{x+1} are connected to the top nodes E_2 and E_3 , while $X_y^{x\dagger}$ and $Y_y^{x+1\dagger}$ are connected to the bottom nodes E_6 and E_5 . The entire structure is equated to a single gray box labeled E_{full} .

In this way, it is possible to represent the cost function (2.119) diagrammatically,

$$\begin{aligned}
 d(\tilde{v}, \tilde{w}, v', w') &= \langle \psi(v', w') | \psi(v', w') \rangle + \langle \psi(\tilde{v}, \tilde{w}) | \psi(\tilde{v}, \tilde{w}) \rangle - \langle \psi(v', w') | \psi(\tilde{v}, \tilde{w}) \rangle \\
 &\quad - \langle \psi(\tilde{v}, \tilde{w}) | \psi(v', w') \rangle \\
 &= \left[\begin{array}{c} \text{Diagram 1} \\ \text{Diagram 2} \end{array} \right] + \left[\begin{array}{c} \text{Diagram 3} \\ \text{Diagram 4} \end{array} \right] - \left[\begin{array}{c} \text{Diagram 5} \\ \text{Diagram 6} \end{array} \right] - \left[\begin{array}{c} \text{Diagram 7} \\ \text{Diagram 8} \end{array} \right].
 \end{aligned}
 \tag{2.123}$$

The diagrams in (2.123) represent the terms of the cost function. Each diagram shows the E_{full} tensor network with specific subtensors attached. Diagram 1 (top left) has $v_y^{\prime x}$ and $w_y^{\prime x+1}$ at the top and $v_y^{\prime x\dagger}$ and $w_y^{\prime x+1\dagger}$ at the bottom. Diagram 2 (top right) has \tilde{v}_y^x and \tilde{w}_y^{x+1} at the top and $\tilde{v}_y^{x\dagger}$ and $\tilde{w}_y^{x+1\dagger}$ at the bottom. Diagram 3 (bottom left) has \tilde{v}_y^x and \tilde{w}_y^{x+1} at the top and $v_y^{\prime x\dagger}$ and $w_y^{\prime x+1\dagger}$ at the bottom. Diagram 4 (bottom right) has $v_y^{\prime x}$ and $w_y^{\prime x+1}$ at the top and $\tilde{v}_y^{x\dagger}$ and $\tilde{w}_y^{x+1\dagger}$ at the bottom.

$d(\tilde{v}, \tilde{w}, v', w')$ is a quadratic function of the tensors $v_y^{\prime x}$ and $w_y^{\prime x+1}$. Thus, the optimized subtensors can be found using an alternating least-square algorithm [JOV⁺08].

To this end, we can first optimize $v_y^{\prime x}$ while keeping $w_y^{\prime x+1}$ fixed. Analogous to the MPS

compression, we form the partial derivative of Eq. (2.123) with respect to $v_y^{\dagger,x}$,

$$\frac{\partial}{\partial v^{\dagger}} d(\tilde{v}, \tilde{w}, v', w') \stackrel{!}{=} 0 \Rightarrow \begin{array}{c} \text{Diagram 1: } E_{\text{full}} \text{ with } v_y^{\prime x} \text{ and } w_y^{\prime x+1} \text{ highlighted in blue boxes. A black box } R \text{ encloses the } v_y^{\prime x} \text{ and } w_y^{\prime x+1} \text{ nodes.} \\ \text{Diagram 2: } E_{\text{full}} \text{ with } \tilde{v}_y^x \text{ and } \tilde{w}_y^{x+1} \text{ highlighted in blue boxes. A red box } S \text{ encloses the } \tilde{v}_y^x \text{ and } \tilde{w}_y^{x+1} \text{ nodes.} \end{array} = \quad (2.124)$$

By interpreting the parts of the diagram surrounded by the blue, red and black boxes as vectors x and b , and a matrix C , respectively, Eq. (2.124) can be reformulated as system of linear equation

$$\boxed{R} \boxed{v'} = \boxed{S}. \quad (2.125)$$

The solution for $v_y^{\prime x}$ is found by inverting R . Using the bond projection, the inversion can be computed exactly with moderate numerical effort $\mathcal{O}(d^3 D^6)$. The full M tensor representation, on the other hand, leads to an unfeasible costs of $\mathcal{O}(D^{12})$ for the exact inversion and $\mathcal{O}(D^8)$ employing approximation methods.

After obtaining the optimized subtensor $v_y^{\prime x}$, we next update $w_y^{\prime x+1}$ while keeping $v_y^{\prime x}$ fixed by forming the partial derivative of Eq. (2.123) with respect to $w_y^{\dagger, x+1}$,

$$\frac{\partial}{\partial w^{\dagger}} d(\tilde{v}, \tilde{w}, v', w') \stackrel{!}{=} 0 \Rightarrow \begin{array}{c} \text{Diagram 1: } E_{\text{full}} \text{ with } v_y^{\prime x} \text{ and } w_y^{\prime x+1} \text{ highlighted in blue boxes. A black box } R \text{ encloses the } v_y^{\prime x} \text{ and } w_y^{\prime x+1} \text{ nodes.} \\ \text{Diagram 2: } E_{\text{full}} \text{ with } \tilde{v}_y^x \text{ and } \tilde{w}_y^{x+1} \text{ highlighted in blue boxes. A red box } S \text{ encloses the } \tilde{v}_y^x \text{ and } \tilde{w}_y^{x+1} \text{ nodes.} \end{array} = \quad (2.126)$$

The solution for $w_y^{\prime x+1}$ is again computed by matrix inversion of R .

This alternation process is repeated until the subtensors $v_y^{\prime x}$ and $w_y^{\prime x+1}$ converge. Monitoring the cost function $d(\tilde{v}, \tilde{w}, v', w')$ after every iteration step i , the convergence is detected by means of a fidelity measure which, following Ref. [PBT⁺15], can be defined as

$$f_d = |d_{i+1} - d_i| / d_0. \quad (2.127)$$

The alternating optimization is stopped in case f_d drops below some small threshold $\epsilon_d = \mathcal{O}(10^{-10})$ while showing no sign of large fluctuations.

Equipped with the converged subtensors $v_y^{\prime x}$ and $w_y^{\prime x+1}$, the original iPEPS form is then restored,

$$\begin{array}{c} \text{Diagram 1: } M_y^{\prime x} \text{ tensor with four legs.} \\ \text{Diagram 2: } X_y^x \text{ tensor with two legs, followed by } v_y^{\prime x} \text{ tensor with two legs.} \\ \text{Diagram 3: } M_y^{\prime x+1} \text{ tensor with four legs.} \\ \text{Diagram 4: } w_y^{\prime x+1} \text{ tensor with two legs, followed by } Y_y^{x+1} \text{ tensor with two legs.} \end{array} = \quad (2.128)$$

so that we can apply the next Trotter gate and repeat the full update optimization.

By accounting for the entire many-body wavefunction of the infinite system, the full update provides an optimization scheme that is free from the systematic error plaguing the simple update. Only the CTM representation of the effective environment induces some approximative character to the algorithm. The high accuracy of the method, however, comes at the price of drastically enhanced numerical costs since the full effective environment, in principle, has to be calculated after the application of every single Trotter gate (i.e., typically thousands of times). Although having the same cost scaling, $\mathcal{O}(\chi^3 D^6)$, this makes the simple update significantly more efficient since the environment has to be calculated only once in the end. Thus, it becomes obvious that calculations with large D in complex systems are often only feasible employing the simple update.

To conclude the section on the full update, we comment on a few technical aspects of the implementation:

- Recently, a more efficient variant of the full update has been proposed [PBT⁺15]. In this so-called fast full update, the full environment is no longer calculated from scratch after the application of every single Trotter gate. Under the assumption that each tensor update only induces small changes to the wavefunction, one can recycle the old environment and include the newly optimized tensors only in subsequent coarse graining moves. This drastically speeds up the process, and we applied it to obtain full-update results for the t - J model in Sec. 5.2.2. However, this full update variant should be applied carefully since it can also induce severe numerical instabilities to the CTM procedure.
- An additional improvement of the full update is given by the recently introduced gauge fixing for iPEPS [LCBn14, PBT⁺15] [see next section 2.5.4]. It strongly enhances and stabilizes the tensor optimization, since it significantly improves the condition number of the matrix R , which needs to be inverted multiple times.
- Another key aspect for the numerical stability is the normalization of the tensor network during (i) the CTM procedure and (ii) after the tensor optimizations. Otherwise one might end up with very small or very large tensors that are sensitive to numerical noise. What we found working best for (i) is to simply scale all CTM tensors in such a way that the absolute value of their largest element is the same (and typically put this element to unity) while checking that the norm $\langle \psi | \psi \rangle$ shows no strong deviations from $\mathcal{O}(1)$. In the context of (ii), we normalize the optimized tensors v' and w' by their norm after each iteration. After restoring the updated M matrices, we also scale their absolute maximum entry to unity.
- Although the full environmental tensor E_{full} should be strictly Hermitian and positive definite, numerical noise during the contraction of the environment might induce small deviations. Thus, we always symmetrize the environment before performing an update, $E_{\text{full}} = (E_{\text{full}} + E_{\text{full}}^\dagger)/2$. Moreover, it is advisable to remove any small negative eigenvalues of E_{full} to work with the positive-definite approximation [LCBn14].
- For further speedup and higher stability, it is very useful not to start the full-update procedure from a completely random set of iPEPS tensors. Instead, we obtain the best results by initializing the full update with tensors previously optimized in a simple-update simulation.

Gauge fixing

As we discussed extensively in Sec. 2.4.1, the gauge degree of freedom on the bond indices can be efficiently exploited to generate a canonical representation in the context of MPS. Through the correct gauge, the effective environment of a specific bond, or rather its tensor network

representation, can be replaced by identity matrices, ensuring numerical precision and stability of the MPS framework. This scheme only works for MPS because the environmental tensor network is separable, such that left and right block can be gauged independently. In the case of PEPS and iPEPS, the environment no longer factorizes into different blocks, due to the presence of loops in the tensor network. In other words, cutting the TN at a single bond does not yield a bipartition of the system (as in the case of MPS), and therefore no full canonical PEPS or iPEPS representation exists.

Nevertheless, it is still possible to exploit the gauge degree of freedom on the bonds to improve the stability of the algorithm. Inspired by the 1D gauging protocol, Lubasch, Cirac, and Bañuls [LCBn14] recently introduced a gauge-fixing for finite PEPS calculations that was later adapted in the context of iPEPS by Ref. [PBT⁺15]. It yields a significantly better conditioned effective environment and thus strongly improves the stability of the tensor optimization during the full update.

The gauge protocol [LCBn14] starts from the effective environment in the bond projection (2.122) which, after symmetrization, is subject to an eigenvalue decomposition,

$$\begin{array}{c} \text{---} \\ | \\ \text{---} \end{array} E_{\text{full}} \begin{array}{c} \text{---} \\ | \\ \text{---} \end{array} = \begin{array}{c} \text{---} \\ | \\ \text{---} \end{array} \begin{array}{c} W \\ \epsilon \\ W^\dagger \end{array} \approx \begin{array}{c} \text{---} \\ | \\ \text{---} \end{array} \begin{array}{c} W \\ \epsilon_+ \\ W^\dagger \end{array} = \begin{array}{c} \text{---} \\ | \\ \text{---} \end{array} \begin{array}{c} Z \\ Z^\dagger \end{array} . \quad (2.129)$$

During this process, we neglect the contributions from small negative eigenvalues to restore the positivity of E_{full} . Next we independently apply a QR and LQ decomposition to the tensor Z ,

$$\begin{array}{c} \text{---} \\ | \\ \text{---} \end{array} Z = \begin{array}{c} \text{---} \\ | \\ \text{---} \end{array} Q_R \begin{array}{c} \text{---} \\ | \\ \text{---} \end{array} R = \begin{array}{c} \text{---} \\ | \\ \text{---} \end{array} L \begin{array}{c} \text{---} \\ | \\ \text{---} \end{array} Q_L , \quad (2.130)$$

and insert two identities LL^{-1} and $R^{-1}R$, into the left and right bond indices of the effective environment, respectively. This yields a renormalized pair of subtensors \bar{v}_y^x and \bar{w}_y^{x+1} and a modified environment \bar{E}_{full} :

$$\begin{array}{c} \text{---} \\ | \\ \text{---} \end{array} \begin{array}{c} L \\ L^{-1} \\ L^{-1\dagger} \\ L^\dagger \end{array} \begin{array}{c} v_y^x \\ E_{\text{full}} \\ v_y^{x\dagger} \end{array} \begin{array}{c} w_y^{x+1} \\ R \\ R^{-1} \\ R^{-1\dagger} \\ w_y^{x+1\dagger} \end{array} \begin{array}{c} \text{---} \\ | \\ \text{---} \end{array} = \begin{array}{c} \text{---} \\ | \\ \text{---} \end{array} \begin{array}{c} \bar{v}_y^x \\ \bar{E}_{\text{full}} \\ \bar{v}_y^{x\dagger} \end{array} \begin{array}{c} \bar{w}_y^{x+1} \\ \bar{w}_y^{x+1\dagger} \end{array} \begin{array}{c} \text{---} \\ | \\ \text{---} \end{array} . \quad (2.131)$$

Moreover, one also has to apply the inverse L^{-1} , R^{-1} to the subtensors X_y^x and Y_y^{x+1} , respectively, so that the full M tensors can be restored properly after the tensor update [c.f. Eq. (2.128)],

$$\begin{array}{c} \text{---} \\ | \\ \text{---} \end{array} \bar{X}_y^x = \begin{array}{c} \text{---} \\ | \\ \text{---} \end{array} \begin{array}{c} X_y^x \\ L^{-1} \end{array} , \quad \begin{array}{c} \text{---} \\ | \\ \text{---} \end{array} \bar{Y}_y^{x+1} = \begin{array}{c} \text{---} \\ | \\ \text{---} \end{array} \begin{array}{c} R^{-1} \\ Y_y^{x+1} \end{array} . \quad (2.132)$$

2.6 Fermionic tensor networks

For the tensor network representations discussed so far, we implicitly restricted our discussion to bosonic quantum many-body models. However, the most challenging and interesting open questions with respect to the physics of strongly correlated systems involve fermions. Especially in two dimensions, the t - J model, the Hubbard model, and its multi-band extensions continuously attract lots of attention, since they are believed to play an important role for understanding of high-Tc superconductivity and quantum criticality. Due to the lack of alternative approaches (QMC is particularly limited by the sign problem in this context), much hope is set on tensor network techniques to treat these complex fermionic models under controlled conditions.

TN representations can incorporate fermionic statistics in any spatial dimension, and several different approaches have been developed for its efficient implementation, being mathematically all equivalent [CV09, CEVV10, COBV10, BPE09, PBE10, KSVC10, SLZZ09]. The most useful point of view for practitioners is taken by Refs. [CV09] and [COBV10], which fully implements the fermionic exchange rules in terms of modifications to the tensor network diagrams. In the following, we briefly review the main ingredients for fermionic tensor networks, mostly following [COBV10] (although not with the same formal rigor, to keep the presentation compact), and discuss a few examples of fermionic TNs in the context of MPS [Sec. 2.6.2] and iPEPS [Sec. 2.6.3]. We refer to Sec. 5.2 for technical details on the fermionic iPEPS implementation in combination with non-abelian symmetries.

For simplicity, we focus on a lattice of spinless fermions with a local Hilbert space dimension $d = 2$ on every site (though everything can easily be generalized to fermions with $d > 2$ [COBV10]). The fermionic statistic of this model is typically treated at the level of operators, specifically by the anticommutation relations of the fermionic annihilation and creation operators $\hat{c}_j, \hat{c}_j^\dagger$,

$$\hat{c}_j^\dagger \hat{c}_{j'} + \hat{c}_j \hat{c}_{j'}^\dagger = \delta_{jj'} \quad \hat{c}_j \hat{c}_{j'} + \hat{c}_j \hat{c}_{j'} = 0. \quad (2.133)$$

In addition, one always imposes some fermionic ordering of the sites, such that a fully occupied state on the lattice containing N sites can be expressed by means of second quantization using the vacuum state $|0_1\rangle|0_2\rangle \dots |0_N\rangle$ and an ordered sequence of creation operators,

$$|1_1\rangle|1_2\rangle \dots |1_N\rangle = \hat{c}_1^\dagger \hat{c}_2^\dagger \hat{c}_3^\dagger \dots \hat{c}_N^\dagger |0_1\rangle|0_2\rangle \dots |0_N\rangle. \quad (2.134)$$

Starting from the techniques discussed in the context of bosonic systems, how can we incorporate the fermionic statistic into the framework of tensor networks? One possibility is to employ a Jordan-Wigner transformation to represent the fermionic operators in terms of Pauli matrices. In this way, the fermionic operator \hat{c}_j is expressed in terms of bosonic operators in a non-local form, which can be described by a so-called *Jordan-Wigner string* acting on all sites $j' < j$ that appear “earlier” in the fermionic order of Eq. (2.134) [Wei12b]. These strings can be treated efficiently in the MPS framework, where it is always possible to choose the fermionic order j equivalent to the position of a site in the MPS chain mapping. However, it leads to severe complications in the context of PEPS, where two nearest-neighbor sites $\mathbf{r} = (x, y)$ and $\mathbf{r}' = (x + 1, y)$ on the lattice might appear far apart in terms of their fermionic order j and j' [COBV10].

To retain the “locality” of the iPEPS algorithm as well, we here adopt a different approach for the treatment of fermionic statistic in the tensor network language. This formulation builds on two simple “fermionization” rules discussed below, that were pioneered in the context of fermionic MERA by Refs. [CV09] and [CEVV10], and later adapted to the PEPS and iPEPS framework [COBV10].

2.6.1 Fermionization rules

Parity conservation

Fermionic systems typically preserve the *parity* of the particle number, i.e., whether a system contains an even or an odd number of fermions. This \mathbb{Z}_2 parity symmetry enables us to define wavefunctions and operators in terms of a well-defined parity quantum number p , resulting in a block structure in the tensor network [see Sec. 2.7 for more details on symmetries]. For $p = 1$ or -1 the corresponding state contains an even or odd number of fermions, respectively.

The first fermionization rule enforces parity conservation in a TN representation. To this end, all tensors have to be chosen to be parity preserving. Taking a generic element of some M tensor as example, it means that

$$M_{\alpha\beta\gamma\rho}^{[\sigma_y^x]} = 0 \quad \text{if} \quad p(\alpha)p(\beta)p(\gamma)p(\rho)p(\sigma_y^x) = -1, \quad (2.135)$$

with $p(\alpha) \in \{-1, 1\}$ describing the parity of the state labeled by the index α [COBV10]. This immediately has the consequence that operators changing the parity number of a state, such as \hat{c}_j have to carry an additional index (see below).

Parity conservation does not directly capture the fermionic statistic. However, it is crucial in order to track the fermionic signs, since we are able to distinguish states containing an even or odd number of fermions.

Fermionic swap gates

The second fermionization rule of [CV09] incorporates the fermionic statistic into the tensor network formalism. It implies that each line crossing in the TN is replaced by a fermionic swap gate,

$$\hat{S}_{\beta'\alpha'}^{\alpha\beta} = \delta_{\alpha\beta'}\delta_{\beta\alpha'}S(\alpha, \beta) = \begin{array}{c} \alpha \quad \beta \\ \quad \blacklozenge \\ \alpha' \quad \beta' \end{array}, \quad (2.136)$$

with $S(\alpha, \beta) = -1$ if $p(\alpha) = p(\beta) = -1$ and $S(\alpha, \beta) = 1$ otherwise.

Why do the swap gates mimic the anticommutation relations of the fermions? Each line of the TN diagrams corresponds to a fermionic degree of freedom carrying either physical (site indices) or virtual particles (bond indices). Any line crossing then corresponds to a particle exchange [CV09]. The implication of such an exchange depends on the nature of the particles. In the case of bosons such a swap is a trivial operation and, hence, can be omitted in practice. In the context of other particles, such as fermions, the underlying particle statistic does yield non-trivial consequences. For instance, additional factors of -1 have to be multiplied to the tensor network when swapping two states with odd fermionic parity number.

Thus, the fermionic statistic of any tensor network can be captured by adding swap gates of type (2.136) to the diagrammatic representation. As a prerequisite, one has to be able to read out the parity of every index in the TN (hence, the first rule).

We emphasize that the fermionization rules can be readily implemented into any standard bosonic TN algorithm *without* altering the leading numerical costs, since the swap gates can typically be absorbed into a single tensor [CV09]. All steps can be performed completely analogously. In our iPEPS implementation we are even able to recycle most parts of the code for bosonic systems by adding swap gates at the appropriate lines.

Fermionic operators

Another prerequisite to capture the fermionic statistic in a TN representation relates to the proper definition of local fermionic operators. Consider a generic two-site operator \hat{O}_{ij} which acts on sites i and j , with $j > i$ not necessarily labeling contiguous sites in terms of the imposed fermionic order. Applied to a generic wavefunction, the resulting TN diagram contains a number of fermionic swap gates (illustrated in detail for MPS and iPEPS below). The impact of these gates to the wavefunction can be interpreted as swapping the physical index of site i such that it becomes contiguous to j with respect to the fermionic order. But this alone does not fully account for the fermionic statistic. In addition, the fermionic order of the local two-site Hilbert space generated by sites i and j has to be properly incorporated on the level of the operators, which leads to factors of -1 for some matrix elements.

While easily generalizable to arbitrary systems [COBV10], we illustrate this briefly for the simple example of spinless fermions, where the operator is expanded in the two-site basis $|\sigma_i\sigma_j\rangle = (c_i^\dagger)^{\sigma_i}(c_j^\dagger)^{\sigma_j}|0_i0_j\rangle$, with $\sigma_j \in \{0, 1\}$:

$$\hat{O} = \sum_{\substack{\sigma'_i\sigma'_j \\ \sigma_i\sigma_j}} O_{\sigma_i\sigma_j}^{\sigma'_i\sigma'_j} |\sigma_i\sigma_j\rangle \langle \sigma'_i\sigma'_j|. \quad (2.137)$$

The coefficients $O_{\sigma_i\sigma_j}^{\sigma'_i\sigma'_j}$ are given by

$$O_{\sigma_i\sigma_j}^{\sigma'_i\sigma'_j} = \langle \sigma_i\sigma_j | \hat{O} | \sigma'_i\sigma'_j \rangle = \langle 0_i0_j | (\hat{c}_i)^{\sigma_i} (\hat{c}_j)^{\sigma_j} \hat{O} (\hat{c}_i^\dagger)^{\sigma'_i} (\hat{c}_j^\dagger)^{\sigma'_j} | 0_i0_j \rangle. \quad (2.138)$$

If the operator describes a pairing term, $\hat{O} = \hat{c}_i\hat{c}_j$, the only non-vanishing coefficient is

$$O_{0_i0_j}^{1_i1_j} = \langle 0_i0_j | \hat{c}_i\hat{c}_j\hat{c}_i^\dagger\hat{c}_j^\dagger | 0_i0_j \rangle = -1. \quad (2.139)$$

A standard hopping term $\hat{O} = \hat{c}_i^\dagger\hat{c}_j$ also has only a single nonzero element,

$$O_{1_i0_j}^{0_i1_j} = \langle 0_j'0_j | \hat{c}_i\hat{c}_i^\dagger\hat{c}_j\hat{c}_j^\dagger | 0_i0_j \rangle = 1. \quad (2.140)$$

We conclude this part with an additional comment on operators that change the parity of a state, such as $\hat{O} = \hat{c}_j$. The first fermionization rule restricts our TN description to parity preserving tensors, as defined in Eq. (2.135). Naively, this would imply that simple annihilation or creation operators could not be properly described by fermionic TNs, since their tensor representation does not conserve fermionic parity. However, any parity changing tensor can be represented by a parity conserving tensor just by adding an additional single-valued index δ with $p(\delta) = -1$ [COBV10]. For instance, the diagrammatic form \hat{c}_j is then given by

$$(\hat{c}_j)_{\sigma_j,\delta}^{\sigma'_j} = \begin{array}{c} \sigma'_j \\ | \\ \textcircled{\hat{c}_j} \\ | \\ \sigma_j \end{array} \overset{\delta}{\text{---}}, \quad (2.141)$$

where the red line indicates that δ only runs over a single value. This representation ensures that the only nonzero element $(\hat{c}_j)_{0_j,\delta}^{1_j}$ now satisfies Eq. (2.135):

$$p(1_j)p(0_j)p(\delta) = (-1)(+1)(-1) = 1. \quad (2.142)$$

2.6.2 MPS

In the context of matrix product states, the simulation of fermions is straightforward for most systems since it is always possible to choose the fermionic order equivalent to the order of chain sites in the MPS mapping.

For Hamiltonians with nearest-neighbor interactions only, the introduced fermionization rules are basically not even required to fully account for the fermionic statistic, as one can treat the fermionic signs purely on the level of local operators. Let us consider a nearest-neighbor correlator representing a typical component of such a Hamiltonian,

$$\langle \psi | \hat{c}_3^\dagger \hat{c}_4 | \psi \rangle = \text{Diagram} \quad (2.143)$$

Note that not a single line crossing appears in this TN diagram, implying the complete absence of any swap gate. The fermionic signs only enter on the operator level, as described above.

The situation becomes only slightly more complicated in the context of non-local quantities, i.e., for Hamiltonians with longer-ranged interactions or for the measurement of non-local correlators. For example, the TN corresponding to the evaluation of a non-local real-time correlator, which we already encountered in discussion on spectral functions [see Sec. 2.135], has the form

$$\langle \psi | e^{i\hat{H}t} \hat{c}_5^\dagger e^{-i\hat{H}t} \hat{c}_2 | \psi \rangle = \text{Diagram} \quad (2.144)$$

First of all, note that the extra third index of the operators \hat{c}_2 is merged with the one of \hat{c}_5^\dagger (as the resulting operator is parity preserving). Moreover, the extra indices are crucial to capture the correct fermionic sign structure, since they introduce a number of swaps with the local site indices of the MPS. Furthermore, one is able to simplify the application of the swap gates, since the extra operator index carries only a single value with odd parity. This allows for the replacement of the swap gates by a parity operator \hat{P} that only acts on the local physical sites [COBV10],

$$\text{Diagram} = \text{Diagram} \quad (2.145)$$

By applying \hat{P} to the physical index of an A tensor, all local states carrying an odd number of fermions simply get multiplied by -1 , while other states with even parity remain unaffected. Thus, the string can be replaced by a set of locally acting parity operators. This turns out to be equivalent to an alternative formulation of fermionization in the context of MPS purely working on the operator level [Wei12b].

2.6.3 PEPS and iPEPS

The full strength of the fermionization rules presented above becomes apparent in the context of PEPS and iPEPS representations. Here, alternative formulations on the operator level [Wei12b] quickly restrict the feasibility of the implementation. In the following, we briefly describe how to obtain the diagrammatic PEPS representation for a given fermionic order, and discuss some examples of fermionic iPEPS networks highlighting some important practical issues. For a more extensive derivation and additional details on fermionic iPEPS we refer to Ref. [COBV10].

PEPS

To enter this discussion, we return to our finite-size PEPS example on a 3×3 square-lattice cluster used in the beginning of Sec. 2.5.1, keeping in mind that each site is labeled according to its coordinate in space $\mathbf{r} = (x, y)$ so that the local basis states are denoted by $|\sigma_y^x\rangle$. In addition, we now have to decide on a specific fermionic order and add a label j running from 1 to 9 to each site in the system, $|\sigma_{y,j}^x\rangle$ (the red color of the fermionic index acts as guide for the eyes). Thus, a specific state in the Fock space can be expressed as

$$|\sigma_{1,1}^1\rangle|\sigma_{2,2}^1\rangle\dots|\sigma_{3,9}^3\rangle = (\hat{c}_1^\dagger)^{\sigma_1^1}(\hat{c}_2^\dagger)^{\sigma_2^1} \dots (\hat{c}_9^\dagger)^{\sigma_3^3}|0_{1,1}^1\rangle|0_{1,2}^1\rangle\dots|0_{1,9}^3\rangle \quad (2.146)$$

Diagrammatically, this ordering *always* corresponds to the order in which the open indices of the wavefunction $|\psi\rangle$ are drawn, and directly affects the specific appearance of the PEPS TN,

We emphasize that a different fermionic order automatically leads to a different diagrammatic representation, where the swap gates potentially act on a different set of indices. In this work, we only consider the fermionic zig-zag order of Eq. (2.147) which (i) can also easily be applied to an infinite lattice system in the framework of iPEPS and (ii) enables us to recycle all bosonic iPEPS diagrams depicted in Sec. 2.5.1. For an explicit example of imposing another fermionic order, see Ref. [COBV10].

After obtaining the proper diagrammatic form of the PEPS, all subsequent operations follow in complete analogy from the bosonic case. The only additional feature are the swap gates, which are put on every line crossing. For instance, an overlap calculation $\langle\psi|\psi\rangle$, derived in Eq. (2.98) for the bosonic PEPS by performing a number of jump moves, is

carried out similarly for a fermionic system,

$$\langle \psi | \psi \rangle = \text{[Diagrammatic representation of the overlap]} \quad (2.148)$$

To reduce the complexity of the diagram, we again introduced a modified representation $\bar{M}_y^{x\dagger}$ of the conjugate tensors in the second step of Eq. (2.148). In contrast to the bosonic case, where $\bar{M}_y^{x\dagger}$ and $M_y^{x\dagger}$ are mathematically equivalent objects [see Eq. (2.97)], we emphasize that $\bar{M}_y^{x\dagger}$ here includes two fermionic swap gates that are absorbed into the tensor, according to

$$\text{[Diagrammatic definition of } \bar{M}_y^{x\dagger} \text{]} \quad (2.149)$$

iPEPS

Considering fermions in an infinite lattice system, the protocol of imposing a zig-zag fermionic order on the lattice can be adopted in a very straightforward manner [COBV10]. In hindsight, we already implied this kind of ordering when drawing the iPEPS diagrams in Sec. 2.5.1. The extensions from the bosonic to the fermionic case is easily achieved by the presence of the fermionic swap gates at line crossings.

In most iPEPS applications, the modified definition of the conjugate tensor $\bar{M}_y^{x\dagger}$ (2.149) and the fermionic version of the reduced tensor m_y^x

$$\text{[Diagrammatic definition of } m_y^x \text{]} \quad (2.150)$$

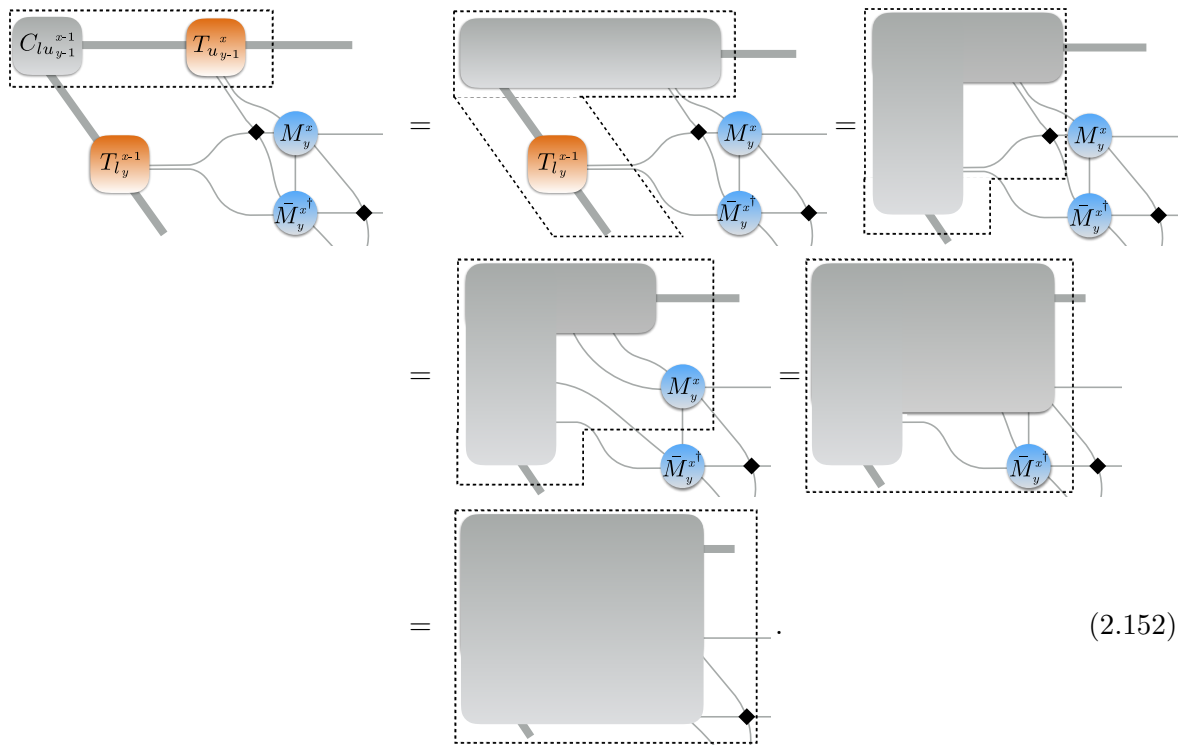
simplify the algorithm by a great deal. For instance, the calculation of an overlap $\langle \psi | \psi \rangle$ can even be represented diagrammatically without any swap gates present,

$$\text{[Diagrammatic representation of the overlap without swap gates]} \quad (2.151)$$

(2.151)

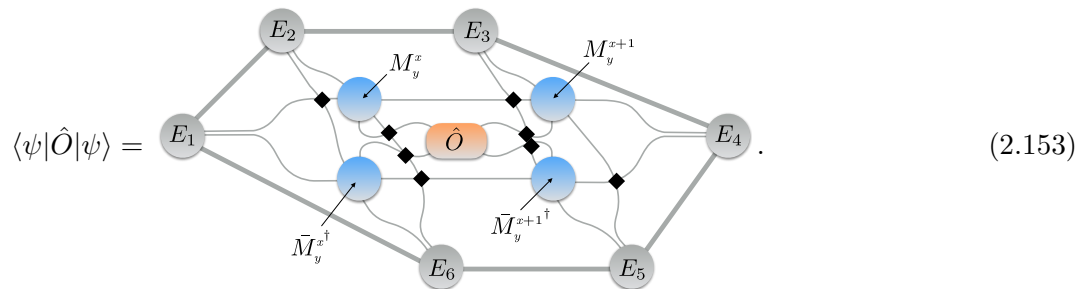
In principle, this would also enable us to carry out the coarse graining steps in the CTM calculation exactly in the same way as in bosonic iPEPS in terms of the reduced m tensors. To perform the algorithm with an efficient cost scaling, however, the M tensors and their conjugates have to be kept separated [see Sec. 2.5.2]. This typically leads to the presence of four additional swap gates for each site (only two when using $\bar{M}_y^{x\dagger}$).

The strategy of incorporating the swap gates appearing in a TN is to absorb them into one single tensor [CV09]. Depending on the TN, this is not always possible in the very first contraction step. Nevertheless, every swap gate can typically be absorbed at some intermediate contraction step. We illustrate this procedure for the contraction of parts of the CTM environment,



(2.152)

Swap gates also appear in the context of tensor optimization and the evaluation of a two-site operator, such as,



(2.153)

We conclude this section by pointing out the modifications to the full-update protocol in the context of fermions. Again, most of the steps are exactly the same as in the bosonic version of the algorithm. In particular, the actual tensor optimization does not contain any swap gates due to the absence of line crossings in Eq. (2.123). However, the initialization slightly differs since one has to account for the presence of swap gates when performing the bond

projection,

$$\begin{aligned}
 & \text{---} \bigcirc_{M_y^x} \text{---} \bigcirc_{M_y^{x+1}} \text{---} = \text{---} \bigcirc_{\text{SVD}} \text{---} \bigcirc_{\text{SVD}} \text{---} \\
 & = \text{---} \bigcirc_{X_y^x} \text{---} \text{---} \text{---} \text{---} \text{---} \bigcirc_{Y_y^{x+1}} \text{---} \quad (2.154)
 \end{aligned}$$

Importantly, the swap gate acts differently on the conjugate tensors, so that the conjugate subtensors have to be generated by two independent SVD or QR decompositions,

$$\begin{aligned}
 & \text{---} \bigcirc_{\bar{M}_y^{x\dagger}} \text{---} \bigcirc_{\bar{M}_y^{(x+1)\dagger}} \text{---} = \text{---} \bigcirc_{\text{SVD}} \text{---} \bigcirc_{\text{SVD}} \text{---} \\
 & = \text{---} \bigcirc_{X_y^{x\dagger}} \text{---} \text{---} \text{---} \text{---} \text{---} \bigcirc_{Y_y^{(x+1)\dagger}} \text{---} \quad (2.155)
 \end{aligned}$$

The tensor network representation of the effective environment also contains an additional set of swap gates,

$$E_{\text{full}} = \text{---} \bigcirc_{E_1} \text{---} \bigcirc_{E_2} \text{---} \bigcirc_{E_3} \text{---} \bigcirc_{E_4} \text{---} \bigcirc_{E_5} \text{---} \bigcirc_{E_6} \text{---} \quad (2.156)$$

Whereas the tensor optimization does not differ from the bosonic formulation, the restoration of the actual iPEPS representation after the update works in a slightly modified way,

$$\text{---} \bigcirc_{X_y^x} \text{---} \text{---} \text{---} \text{---} \text{---} \bigcirc_{\tilde{M}_y^x} \text{---} = \text{---} \bigcirc_{M_y^x} \text{---} \quad (2.157)$$

Compared to the bosonic case in Eq. (2.128), we have to account for the additional swap gate.

2.7 Symmetries

Symmetries are one of the core concepts of physics and, in particular, of condensed matter physics. Systems, states and phases are characterized by their underlying symmetry structure, and phase transitions are often linked to a change in symmetry.

In the context of tensor networks, symmetries also have a decisive impact. First of all, the incorporation of symmetries of a system at the level of the TN representation typically leads to significant numerical benefits. This has been extensively exploited in NRG from the very beginning [Wil75] and was later also adapted in DMRG simulations [SN97, MG02]

and, more recently, also at the level of MERA [SPV10, SPV11, SV12, SV13] and iPEPS [BCOT11, LLW⁺15, Wei12a], and helped gaining insights into systems that previously were not traceable by conventional calculations. Second, symmetric tensor networks also revealed conceptual connections to other fields such as quantum gravity [Orú14a], though the latter is not relevant for the work of this thesis. Here we treat symmetric tensor networks solely from the perspective of numerical algorithms.

We performed symmetry-enhanced TN simulations in four publications included in this thesis [BWG⁺14, BvDW15, SBvD17, BZWS17], as well as in chapter 5.2 in the context of fermionic iPEPS, exploiting both abelian and non-abelian symmetries of various Hamiltonians by means of the QSpace tensor library [Wei12a]. Thus, we here briefly present a short discussion of the core concepts of symmetric tensor networks, adapting parts of our publication [BvDW15]. For a more thorough introduction to the topic we refer to the reader to Ref. [Wei12a] and [SV12].

2.7.1 Abelian and non-abelian symmetries

Strongly correlated systems feature a large number of different symmetries, categorized in distinct symmetry groups \mathcal{S} and characterized by some conserved quantities. We have already encountered the fermionic \mathbb{Z}_2 parity symmetry. Another common symmetry category are abelian $U(1)$ symmetries, for example related to the conservation of the total particle number or the magnetization in a spinful system. In addition, there also exist more complex non-abelian symmetries. The most common non-abelian symmetry encountered in condensed matter systems is the $SU(2)$ spin symmetry connected to the conservation of the total spin. Another example is the particle-hole symmetry often present in Hubbard-type systems at half filling. More complex non-abelian symmetries include $SU(N)$ flavor symmetries or symplectic symmetries (for more details see [Wei12a]).

How does the incorporation of symmetries at the level of a tensor network lead to numerical benefits? Generally speaking, the symmetry-induced selection rules cause a large number of matrix elements to be exactly zero, thus bringing the Hamiltonian into a block-diagonal structure and subdividing tensors into well-defined symmetry sectors. Keeping only the nonzero elements, we can achieve tremendous improvement in speed and accuracy in numerical simulations by the incorporation of symmetries. In the context of non-abelian symmetries, the nonzero data blocks are not independent of each other and can be further compressed using the Clebsch-Gordan algebra for multiplet spaces.

Starting from a Hamiltonian featuring a specific symmetry, how can we construct a symmetric TN representation for a specific state of this system? The key idea is to generate both virtual and physical state spaces in terms of symmetry eigenstates. Following the notation of Ref. [Wei12a], we label the state space in terms of the symmetry eigenbasis $|qn; q_z\rangle$, where the quantum label q denotes the irreducible representation of the symmetry group \mathcal{S} of the Hamiltonian \hat{H} . Every symmetry generator \hat{S}_α satisfies $[\hat{H}, \hat{S}_\alpha] = 0$. Hence, all states in a given Hilbert space corresponding to a certain q -label are combined into a symmetry block q . The label n identifies a particular multiplet within the specific symmetry block q . The internal multiplet label q_z resolves the internal structure of the corresponding multiplet. In the context of abelian symmetries the Clebsch-Gordan structure becomes trivial, hence the q_z labels take the role of q labels. Note that this notation can be easily generalized to the treatment of multiple symmetries [Wei12a].

To further clarify the notation, we consider the example of the isotropic spin- $\frac{1}{2}$ Heisenberg model, $\hat{H} = \sum_{\langle ij \rangle} \hat{\mathbf{S}}_i \hat{\mathbf{S}}_j$, which features a $SU(2)_{\text{spin}}$ symmetry, $\mathcal{S} = SU(2)_{\text{spin}}$. We make the usual choice of basis in which the z component of the spin operator, \hat{S}_z is diagonal and label a general spin multiplet by $|q, q_z\rangle \equiv |S, S_z\rangle$. The spin multiplet label can take the values $q = 0, \frac{1}{2}, 1, \frac{3}{2}, \dots$, while the internal multiplet label, corresponding to the z component of the

spin, is restricted to $q_z \in \{-q, -q + 1, \dots, +q\}$.

2.7.2 Symmetric tensor networks

The building blocks of tensor networks, the tensors themselves, connect different state spaces, both virtual and physical, associated with the legs of the tensors. Consider the simplest non-trivial example of a rank-3 tensor A , which fuses two state spaces with abelian symmetry, $|ql\rangle$ and $|q'm\rangle$, into a third, $|q''n\rangle$. This operation can be expressed as

$$|q''n\rangle = \sum_{ql} \sum_{q'm} (A_{q'q''}^{[q]})_{mn}^{[l]} |q'm\rangle |ql\rangle. \quad (2.158)$$

In contrast to the non-symmetric case, the A tensor carries now an additional q -label for each of the indices l, m, n . From a numerical perspective this introduces additional bookkeeping effort. At the same time, the symmetry-specific selection rules enforce that a large number of elements of A are exactly zero (for the example of U(1) particle conservation, the selection rule takes the form $q'' = q + q'$). Keeping only the nonzero elements leads to sparse tensor structures and, hence, results in significant computational speed-up and reduced memory requirements.

We illustrate the same example in the context of non-abelian symmetries, where the state now carry an additional internal multiplet label and are given by $|ql; q_z\rangle$, $|q'm; q'_z\rangle$, and $|q''n; q''_z\rangle$. The states within a specific multiplet are fully defined by the generalized Clebsch-Gordan coefficients of the specific symmetry. In this description, the elements of the A tensor factorize into a set of reduced matrix elements and the coefficients in the Clebsch-Gordan space,

$$|q''n; q''_z\rangle = \sum_{qlq_z} \sum_{q'mq'_z} (A_{q'q''}^{[q]})_{mn}^{[l]} \cdot C_{q'_z q'_z}^{[q_z]} |q'm; q'_z\rangle |ql; q_z\rangle, \quad (2.159)$$

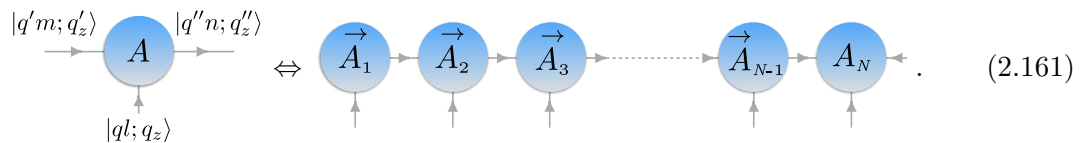
with the Clebsch-Gordan coefficients $C_{q'_z q'_z}^{[q_z]} = \langle qq'; q_z q'_z | q''; q''_z \rangle$ [Wei12a]. This allows one to further compress the nonzero data blocks of the tensors, further reducing the numerical requirements (although adding significant bookkeeping effort). Analogously, elements of some operator \hat{O} acting in a symmetric state space $|ql; q_z\rangle$ can be expressed in a decomposed form exploiting the Wigner-Eckart theorem,

$$\langle q'l'; q'_z | \hat{O}_{\tilde{q}_z} | ql; q_z \rangle = (O_{qq'}^{[\tilde{q}]})_{ll'}^{[1]} \cdot C_{q_z q'_z}^{[\tilde{q}_z]}, \quad (2.160)$$

in terms of Clebsch-Gordan coefficients $C_{q_z q'_z}^{[\tilde{q}_z]}$ and reduced matrix elements $(O_{qq'}^{[\tilde{q}]})_{ll'}^{[1]} = \langle q'l' | \hat{O}_{\tilde{q}} | ql \rangle$ [Wei12a].

With the definition of symmetric tensors and operators in Eqs. (2.159) and (2.160), respectively, we are ready to set up a tensor network consisting of several symmetric A tensors, which naturally leads as to a symmetric MPS representation. By construction, the symmetric MPS guarantees that the corresponding wavefunction conserves the underlying symmetry.

The corresponding tensor diagrams come with two additional features,



$$\begin{array}{c} |q'l'; q'_z \\ \rightarrow \\ \textcircled{A} \\ \uparrow \\ |ql; q_z \end{array} \begin{array}{c} |q''n; q''_z \\ \rightarrow \end{array} \Leftrightarrow \begin{array}{c} \textcircled{A_1} \\ \uparrow \\ \textcircled{A_2} \\ \uparrow \\ \textcircled{A_3} \\ \uparrow \\ \dots \\ \textcircled{A_{N-1}} \\ \uparrow \\ \textcircled{A_N} \\ \uparrow \end{array} \begin{array}{c} \rightarrow \\ \rightarrow \\ \rightarrow \\ \dots \\ \rightarrow \\ \rightarrow \end{array}. \quad (2.161)$$

First of all, notice that each physical and virtual index is now accompanied by an arrow. In this way, we specify the *incoming* and *outgoing* indices, i.e., which (group of) state spaces

are fused into which, according to Eq. (2.159). Note that the choice of the arrow directions changes depending on the context. As shown in Eq. (2.161), the directions are typically chosen such that they point towards the orthonormal center of the MPS. Moreover, we also point out the presence of an extra index to the right of A_N in the MPS representation (2.161). As in the non-symmetric case, this index only runs over a single value. In the context of a symmetry implementation, however, this label carries a multiplet label and determines the global quantum numbers of the wavefunction. In this way, we can directly target different symmetry states in the system. For example in case of a $SU(2)_{\text{spin}}$ symmetry, it is possible to project the last index to the singlet multiplet ($S = 0$), the triplet multiplet ($S = 1$), or to any higher spin multiples. Ref. [DMS12] employed this procedure to determine the spin gap of the Kagome Heisenberg model by means of the energy difference of these two states.

Building on the fusing rules for different state spaces in Eq. (2.159), we are also able to generate symmetric tensor networks consisting of higher-ranked tensors. This can be easily understood from the perspective of contracting multiple A tensors to some larger-ranked object. The resulting tensor then represents a combination of several state spaces. Setting up a symmetric PEPS tensor network, for example, follows exactly this pattern leading to the following diagrammatic representations,

$$\Leftrightarrow \quad (2.162)$$

As in the case of symmetric MPS, the symmetrized M tensors contain additional arrows on the index lines to indicate which state spaces are incoming and outgoing. We have some freedom in fixing the direction of these arrows and some choices might be more convenient to implement than others (we comment on this issue in the context of iPEPS in Sec. 5.2). Again, the extra index of M_3^3 determines the global symmetry state of a specific PEPS representation. Of course, the symmetric PEPS also guarantees that the corresponding quantum state is symmetric, i.e., forms a well-defined symmetry multiplet.

We conclude this section with some general remarks on symmetries in tensor network implementations. The biggest and most obvious benefit relates to the numerical efficiency gains in tensor networks caused by two features of the symmetric TN. First of all, the symmetry-induced block structure leads to compact and sparse tensors and allows for a block-by-block calculation of tensor contractions and tensor decompositions. This speedup typically supersedes the numerical overhead caused by the additional bookkeeping efforts. Second, repeated iteration steps occurring in many TN applications often involve carrying out a basic modification of a set of tensors over and over. Hence, it can be advantageous to compute such a step only once and store the result to recycle it in a later step of the algorithm. The newest version of the QSpace tensor network library exploits this feature very successfully, recycling Clebsch-Gordan coefficients repeatedly in the context of non-abelian symmetries. In this way, every Clebsch-Gordan coefficient encountered during such calculations is only computed once and then saved to a library for future reuse, leading to significant efficiency gains, especially for symmetries featuring large multiplet spaces such as $SU(N > 2)$ [Wei12a].

The benefits of symmetric TN implementations have been widely recognized among practitioners. The incorporation of abelian symmetries has become a standard feature of many

MPS implementations. Non-abelian symmetries are also commonly exploited in NRG and DMRG simulations, at least on the level of $SU(2)$ [MG02]. Progress has also been made in the context of higher-dimensional tensor networks such as MERA or PEPS, where recent applications explicitly demonstrated the potential of both abelian and non-abelian symmetries [SV12, Wei12a, LLW⁺15]. Without the numerical benefits of symmetric TN implementations, many systems would still remain inaccessible to DMRG, NRG, or iPEPS techniques, and we expect that symmetric TN simulations will play a decisive role in tackling complicated 2D models such as multi-flavor models. In this context, we present some preliminary results of iPEPS calculations for extended Hubbard models carried out with QSpace in Sec. 5.2. We emphasize that QSpace represents a unique tool for performing simulations of this type, since it is capable of turning on and off a variety of different abelian and non-abelian symmetries, including arbitrary combinations of $U(1)$, \mathbb{Z}_n , $SU(N \lesssim 5)$, as well as $Sp(2N \lesssim 8)$ symmetries.

However, one should also keep in mind that symmetric TN introduce certain constraints on the wavefunction. For instance, certain phases feature ground states that spontaneously break a symmetry conserved by the Hamiltonian of the system (for example, the Néel-ordered ground state breaks $SU(2)$ symmetry in the square lattice Heisenberg model). Performing a fully symmetric TN simulation in such a parameter regime can require a “more expensive” tensor network representation (i.e., a larger bond dimension) than a simulation based on a non-symmetric TN wavefunction [SV13].

Quantum criticality in bosonic quantum impurity models

Paradigmatic quantum impurity models such as the Kondo or the Anderson model describe small quantum systems coupled to an environment consisting of electronic charge carriers. In many experimental setups, however, noise and dissipation effects are predominantly mediated by phonons or polarons. The influence of these charge-neutral particles on a small interacting system can be captured by a different class of impurity models where the environment is represented by large number of bosonic degrees of freedom.

Among these bosonic impurity models, the spin-boson model [LCD⁺87] probably represents the most famous example [see Sec. 1.1.3]. It has been applied to a variety of problems in physics, chemistry, and biology such as the study of electron transfer processes in biomolecules [MS85], noisy qubits [MSS01, MOL⁺99], and cold-atom quantum dots [RFZ⁺05, OSLH08]. In recent years, the spin-boson model also attracted much attention in the context of quantum criticality [BTV03, Voj03, Voj06, GWvDV12], which also represents the main motivation for the work performed in this chapter.

Bosonic quantum impurity models can only be solved exactly in a handful of special cases, since the large number of particles in the bath induce a high degree of complexity. Instead, one has to rely on numerical tools to obtain results beyond perturbative approximations. In general, the numerical renormalization group (NRG) [see Sec. 2.4.2] represents one of the most powerful and efficient methods to accurately treat a quantum impurity model. In the case of bosonic systems, however, NRG suffers from two substantial flaws that greatly limit its applicability. The first relates to the truncation of the bosonic Hilbert space during the iteration procedure. The second is even more fundamental, and arises from the faulty Wilson chain mapping in context of an asymmetric bath spectral functions.

Both of these issues can be overcome with an NRG-enhanced DMRG procedure in the MPS framework. In parts, this highly effective approach was introduced by Ref. [GWvDV12] to resolve the truncation problem of the bosonic Hilbert space by means of a variational basis optimization. Employing this highly flexible algorithm, we extensively study a generalized spin-boson model with two baths that features fascinating critical properties [Sec. 3.1]. Interestingly, it turns out that this model violates the quantum-to-classical correspondence, a principle guiding the vast majority of all quantum phase transitions. Moreover, our MPS simulations also provide new insight into the properties of the critical wavefunction of the standard spin-boson model [Sec. 3.2]. Finally, we resolve the second major flaw of bosonic NRG in Sec. 3.3 by proposing a completely new type of Wilson chain mapping. These so-called open Wilson chains (OWC) allow for the incorporation of missing bath modes, crucial to faithfully reproduce finite-temperature properties in bosonic impurity models.

Our work in this chapter represents a substantial leap forward in the numerical treatment

of bosonic quantum impurity models and adds to the understanding of quantum criticality in these systems. Especially the OWC construction also opens access to addressing truly new physics, since it provides, for example, a systematic recipe to incorporate dissipative effects and treat complex multi-channel impurity models.

3.1 Two-bath spin-boson model: Phase diagram and critical properties

The following article [BWG⁺14] presents a detailed study of the critical properties of an extended spin-boson model. Interestingly, the additional second bath does not necessarily yield an enhancement of the effective dissipation. Instead, the competition of the two baths coupled to the impurity spin can induce frustration, which catalyzes fascinating critical properties in this system.

Our work is based on extensive numerical simulations by means of MPS techniques, which are further supported by renormalization group calculations. Both, the variational optimization of the bosonic state space as well as the implementation of an additional $U(1)_{\text{bath}}$ symmetry turn out to be crucial in order to accurately study the critical points. In particular, we find a critical intermediate-coupling phase which is bounded by a continuous quantum phase transition that violates the quantum-to-classical correspondence. Our results indicate that this system presents, in a sense, the simplest quantum model violating this guiding principle of quantum criticality.

P1 *Two-bath spin-boson model: Phase diagram and critical properties*

B. Bruognolo, A. Weichselbaum, C. Guo, J. von Delft, I. Schneider, and M. Vojta
Phys. Rev. B **90**, 245130 (2014)

Two-bath spin-boson model: Phase diagram and critical properties

Benedikt Bruognolo,¹ Andreas Weichselbaum,¹ Cheng Guo,¹ Jan von Delft,¹ Imke Schneider,² and Matthias Vojta³

¹Physics Department, Arnold Sommerfeld Center for Theoretical Physics, and Center for NanoScience, Ludwig-Maximilians-Universität, Theresienstraße 37, 80333 München, Germany

²Physics Department and Research Center OPTIMAS, Technische Universität Kaiserslautern, 67663 Kaiserslautern, Germany

³Institut für Theoretische Physik, Technische Universität Dresden, 01062 Dresden, Germany

(Received 17 October 2014; revised manuscript received 28 November 2014; published 18 December 2014)

The spin-boson model, describing a two-level system coupled to a bath of harmonic oscillators, is a generic model for quantum dissipation, with manifold applications. It has also been studied as a simple example for an impurity quantum phase transition. Here, we present a detailed study of a U(1)-symmetric two-bath spin-boson model, where two different components of an SU(2) spin $\frac{1}{2}$ are coupled to separate dissipative baths. Nontrivial physics arises from the competition of the two dissipation channels, resulting in a variety of phases and quantum phase transitions. We employ a combination of analytical and numerical techniques to determine the properties of both the stable phases and the quantum critical points. In particular, we find a critical intermediate-coupling phase which is bounded by a continuous quantum phase transition which violates the quantum-to-classical correspondence.

DOI: [10.1103/PhysRevB.90.245130](https://doi.org/10.1103/PhysRevB.90.245130)

PACS number(s): 05.30.Jp, 05.10.Cc

I. INTRODUCTION

Impurity models, describing small quantum systems coupled to one or multiple baths of bosons or fermions, have seen a lot of activity over the last years, for a variety of reasons: (i) Impurity models display a rich phenomenology, including local Fermi-liquid and non-Fermi-liquid behavior [1,2], phase transitions and quantum criticality [3,4], as well as interesting properties far from equilibrium [5]. (ii) Impurity models can often be simulated by numerical means more efficiently than lattice models [6,7], such that, on the one hand, high-accuracy numerical results can guide analytical approaches and, on the other hand, analytical concepts can be readily tested numerically. A particularly interesting branch is nonequilibrium physics where quantum impurity models have served a test bed for methodological developments. (iii) Impurity models find realizations in diverse settings such as dilute magnetic moments in bulk solids [8,9], electrons in quantum dots coupled to leads [10,11], quantum bits in a dissipative environment [12], and charge-transfer processes in organic molecules [13]. The design of impurity models in cold-atom systems provides further means of manipulating and detecting impurity phenomena [14,15].

The spin-boson model (SBM1 in the following) is a simple paradigmatic model for quantum dissipative systems [16]. It describes a two-level system, i.e., a spin $\frac{1}{2}$, which is coupled to both a bath of harmonic oscillators and a transverse field. While the field induces tunneling (i.e., delocalization) between the two states, the oscillator bath causes friction and impedes tunneling. For gapless baths, characterized by a power-law spectral density $J(\omega) \propto \omega^s$ with $0 < s \leq 1$, this competition results in a quantum phase transition between a delocalized and a localized phase which has been studied extensively [17–28]. As has been shown both analytically and numerically [21–23,25–28], this quantum phase transition obeys the so-called quantum-to-classical correspondence: It is equivalent to the thermal phase transition of a classical Ising chain with long-ranged interactions falling off as $1/r^{1+s}$ where r is the distance between two classical spins [29–31].

In this paper, we consider the generalization of the spin-boson model to two baths ($i = x, y$ below) [32–34], dubbed SBM2. It is described by $\hat{\mathcal{H}} = \hat{\mathcal{H}}_s + \hat{\mathcal{H}}_{\text{cpl}} + \hat{\mathcal{H}}_{\text{bath}}$ with

$$\hat{\mathcal{H}}_s = -\vec{h} \cdot \frac{\vec{\sigma}}{2}, \quad (1a)$$

$$\hat{\mathcal{H}}_{\text{cpl}} = \sum_{i=x,y} \sum_q \lambda_{qi} \frac{\sigma_i}{2} (\hat{a}_{qi} + \hat{a}_{qi}^\dagger), \quad (1b)$$

$$\hat{\mathcal{H}}_{\text{bath}} = \sum_{i=x,y} \sum_q \omega_q \hat{a}_{qi}^\dagger \hat{a}_{qi}. \quad (1c)$$

The two-level system (or quantum spin, with $\sigma_{x,y,z}$ being the vector of Pauli matrices) is coupled both to an external field \vec{h} and, via σ_x and σ_y , to two independent bosonic baths, whose spectral densities $J_i(\omega) = \pi \sum_q \lambda_{qi}^2 \delta(\omega - \omega_q)$ are assumed to be of the same power-law form

$$J_i(\omega) = 2\pi \alpha_i \omega_c^{1-s} \omega^s, \quad 0 < \omega < \omega_c, \quad (2)$$

where $\omega_c = 1$ defines the unit of energy used throughout the paper. For a symmetric coupling to identical bath, i.e., $\alpha = \alpha_x = \alpha_y$, and $h_x = h_y = 0$ the model displays a U(1) symmetry, corresponding to a rotation of the impurity spin about its z axis combined with corresponding bath-mode rotation. In addition, the model features a separate Z_2 symmetry for $h_z = 0$, corresponding to $\sigma_z \leftrightarrow -\sigma_z$.

The model SBM2 is governed not only by the competition between the local field, which tends to point the spin in the \vec{h} direction, and the dissipative bath effects, but also by a competition between the two baths, as an oscillator bath which couples to σ_i tends to localize the spin in i direction. As a result, the combined dissipative effect of both baths in SBM2 can be smaller than that of one bath alone (in a sense which will become clear in the course of the paper), an effect which has been dubbed “frustration of decoherence” [34]. In practical realizations of SBM2, the two baths can be two different sources of dissipation influencing a quantum bit [34,35] or two spin-wave modes which couple to a magnetic impurity in a magnet [36,37].

The model SBM2 is of particular theoretical interest because it displays a nontrivial intermediate-coupling (i.e., critical) phase, characterized by partial screening of the impurity degree of freedom corresponding to a fractional residual moment [i.e., a residual entropy S_{imp} with $\exp(S_{\text{imp}}/k_B)$ not an integer] [3,38], not unlike in the two-channel Kondo state [2,39,40]. The existence of this critical phase, originally deduced by perturbative RG arguments [32,33,37], was recently confirmed numerically [24]. The latter study, performed using a variational matrix-product-state (VMPS) approach, also revealed that the critical phase is unstable at large couplings, resulting in a complex phase diagram.

It is the purpose of this paper to study the physics of SBM2 in some detail, extending the results published in Ref. [24], with particular focus on the quantum phase transitions occurring in this model. To this end, we combine VMPS calculations with analytical renormalization-group and scaling approaches. Our implementation of VMPS, including the use of the U(1) symmetry and an optimized boson basis, enables highly accurate studies of quantum critical behavior.

A. Summary of results

We have used VMPS to determine quantitative phase diagrams for the U(1)-symmetric version of SBM2 as function of the bath exponent s , the dissipation strength α , and the transverse field h_z . For $0 < s < 1$ and finite h_z , there is always a transition between a delocalized (DE) and a localized (LO) phase (Fig. 1) with the LO phase spontaneously breaking the model's U(1) symmetry. There is no localization for $s = 1$ (not shown) [34]: this is qualitatively different from the behavior of the standard single-bath spin-boson model (SBM1) and reflects the frustration of decoherence mentioned above. For $h_z = 0$ the critical (CR) phase emerges, existing for $s^* < s < 1$ and small α .

Based on numerical and analytical results for the quantum critical behavior, we conclude that the transition between the DE and LO phases, controlled by a fixed point labeled QC2 in

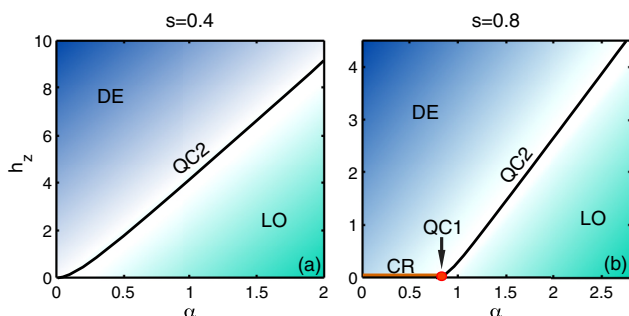


FIG. 1. (Color online) Quantitative phase diagrams of SBM2 for $s = 0.4$ (a) and $s = 0.8$ (b). For a bath exponent $s < s^* \approx 0.76$ in (a), the SBM2 ground state is either in a delocalized (DE) or localized (LO) phase depending on coupling strength α and magnetic field h_z ; the corresponding quantum phase transition is controlled by the critical fixed point QC2. For larger $s > s^*$ in (b), an additional critical phase (CR) emerges at $h_z = 0$ and small couplings. The quantum phase transition between LO and CR is controlled by a different critical fixed point QC1.

the body of the paper, is in the universality class of the classical XY chain with $1/r^{1+s}$ interactions, i.e., obeys a quantum-to-classical correspondence. In particular, $s = \frac{1}{2}$ corresponds to the upper-critical dimension for this transition, with mean-field behavior found for $s < \frac{1}{2}$.

In contrast, the transition between CR and LO, controlled by a different fixed point QC1, does not appear to obey a quantum-to-classical correspondence. Its exponents fulfill hyperscaling relations for $h_z = 0$, but hyperscaling is violated in the presence of a transverse field. We propose how to construct a critical field theory which should ultimately enable an analytical understanding of this conceptually interesting nonclassical transition.

B. Outline

The body of the paper is organized as follows. In Sec. II, we introduce the employed VMPS method. In particular, we discuss both the variational choice of bosonic basis states and the implementation of the U(1) symmetry into the algorithm. Section III describes the phase diagram of the U(1)-symmetric SBM2, together with the main characteristics of the stable phases. The subsequent Sec. IV analyzes the numerical findings in terms of renormalization-group flow and discusses the resulting quantum critical points. Section V is devoted to analytical approaches to the critical phenomena of SBM2, using the toolbox of field theory and epsilon expansion. In particular, we highlight that QC2 is expected to follow the quantum-to-classical correspondence while QC1 is not. In Sec. VI, we show numerical results for critical properties of SBM2. We will extract numerous critical exponents as function of the bath exponent s , confirming the analytical expectations. The concluding Sec. VII will highlight open problems as well as connections to other impurity and lattice problems. In addition, the physics of SBM2 with broken U(1) symmetry will be quickly discussed. Technical details are relegated to various appendices.

II. VMPS METHOD

We start by describing the numerical VMPS approach which we employed to study SBM2. This extends the corresponding presentation in Ref. [41]. In particular, the explicit implementation of the U(1) symmetry, which we found crucial to obtain accurate critical exponents, is a novel ingredient here.

A. Discretization and Wilson chain mapping

Since both bosonic baths of SBM2 are noninteracting and gapless, it is possible to transfer the concept of energy-scale separation frequently employed in numerical renormalization group (NRG) [6,7,42,43]. To this end, the spectral functions of the baths are logarithmically discretized. Then, the Hamiltonian is mapped on a semi-infinite tight binding chain, a so-called Wilson chain.

The choice of a logarithmic coarse graining of the spectral function J_i is motivated by the fact that the study of critical behavior requires exponentially small energy scales. To resolve these scales appropriately, a logarithmic coarse graining is necessary since it yields an exponentially enhanced low-energy resolution compared to a linear or power-law discretization.

Assuming the spectral function J_i of each bosonic bath has a nonzero contribution for energies $\omega \in]0, \omega_c]$, with $\omega_c = 1$ being an upper cutoff frequency, we introduce a dimensionless discretization parameter $\Lambda > 1$ which defines a set of intervals with discretization points [6,7,18,44]

$$\begin{aligned} \omega_0^z &= \omega_c \quad (m = 0), \\ \omega_m^z &= \omega_c \Lambda^{-m+z} \quad (m = 1, 2, 3, \dots), \end{aligned} \quad (3)$$

with $z \in [0, 1]$ an arbitrary shift. Averaging over different z uniformly distributed in $[0, 1]$ is referred to as z averaging. Considering a symmetric coupling of the impurity to two identical baths and using $z = 0$ for simplicity, the discretized Hamiltonian is represented by

$$\hat{\mathcal{H}}_{\text{bath}} = \sum_{i=x,y} \sum_{m=0}^{\infty} \left[\xi_m \hat{a}_{mi}^\dagger \hat{a}_{mi} + \gamma_m \frac{\sigma_i}{2} (\hat{a}_{mi} + \hat{a}_{mi}^\dagger) \right], \quad (4)$$

with \hat{a}_{mi} being a discrete bosonic state at energy ξ_m and coupling strength γ_m to the impurity spin. For general $J(\omega)$ one has [44]

$$\gamma_m^2 = \int_{\omega_{m+1}}^{\omega_m} J(\omega) d\omega, \quad (5a)$$

$$\xi_m = \gamma_m^{-2} \int_{\omega_{m+1}}^{\omega_m} \omega J(\omega) d\omega. \quad (5b)$$

Employing the improved z -averaging scheme of Žitko and Pruschke to reduce discretization artifacts [45], the explicit expressions for the parameters for general z are given by [41]

$$\xi_0^z = \left[\frac{1 - \Lambda^{z(1+s)}}{(1+s) \ln \Lambda} - z + 1 \right]^{\frac{1}{1+s}} \quad (m = 0), \quad (6a)$$

$$\xi_m^z = \left[\frac{\Lambda^{-(s+1)(m+z)} (\Lambda^{1+s} - 1)}{(1+s) \ln \Lambda} \right]^{\frac{1}{1+s}} \sim \omega_m^z \quad (m > 0),$$

$$\gamma_0^z = \sqrt{\frac{2\pi\alpha}{1+s} (1 - \Lambda^{-z(1+s)})} \quad (m = 0), \quad (6b)$$

$$\gamma_m^z = \sqrt{\frac{2\pi\alpha}{1+s} (\Lambda^{1+s} - 1) \Lambda^{-(m+z)(1+s)}} \sim (\omega_m^z)^{\frac{s+1}{s}} \quad (m > 0).$$

Following the standard NRG protocol, the discretized Hamiltonian in Eq. (4) is mapped using an exact unitary transformation onto a semi-infinite tight-binding chain, dubbed Wilson chain, with the impurity coupled to the open end only. The resulting Hamiltonian including $(N + 1)$ bosonic sites is given by $\hat{\mathcal{H}}_N \cong \hat{\mathcal{H}}_s + \hat{\mathcal{H}}_{\text{cpl}} + \hat{\mathcal{H}}_{\text{bath}}^{(N)}$ with

$$\hat{\mathcal{H}}_{\text{cpl}} = \sum_{i=x,y} \sqrt{\frac{\eta_0}{\pi}} \frac{\sigma_i}{2} (\hat{b}_{0i} + \hat{b}_{0i}^\dagger), \quad (7a)$$

$$\hat{\mathcal{H}}_{\text{bath}}^{(N)} = \sum_{i=x,y} \left[\sum_{k=0}^N \epsilon_k \hat{n}_{ki} + \sum_{k=0}^{N-1} (t_k \hat{b}_{ki}^\dagger \hat{b}_{(k+1)i} + \text{H.c.}) \right], \quad (7b)$$

with the operator $\hat{n}_{ki} = \hat{b}_{ki}^\dagger \hat{b}_{ki}$ counting the number of bosons of bath i on chain site k . Each bosonic site represents a harmonic oscillator at frequency $\epsilon_k \sim \Lambda^{-k}$ that is coupled to its nearest neighbors by the hopping amplitude $t_k \sim \Lambda^{-k}$. Assuming identical baths, $\eta_0 = \int J(\omega) d\omega$ describes the overall coupling between a bath and impurity. Note that the impurity spin now couples to a single bosonic degree of

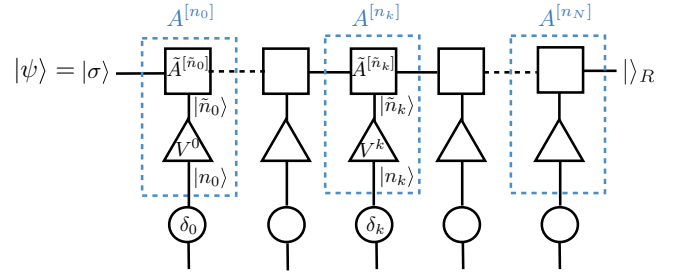


FIG. 2. (Color online) Schematic diagram of $|\psi\rangle$ in Eq. (8) using the OBB representation with explicit bosonic shift. The first index of $A^{[n_0]}$ and the last index of $A^{[n_N]}$ link to the impurity and the right-vacuum state $|\rangle_R$, respectively (for details see text).

freedom per bath located at $k = 0$, i.e., the first site of a bosonic tight-binding chain (see also Fig. 2). Their combined local Hamiltonian is given by $\hat{\mathcal{H}}_0$.

B. VMPS optimization with OBB

The steps remaining in the NRG procedure would involve an iterative diagonalization by adding one site at a time and a subsequent truncation of the high-energy states of the system, keeping only the D lowest-lying energy eigenstates. However, the bosonic nature of the model complicates the NRG approach drastically. Employing NRG, it is required to truncate the infinite-dimensional local bosonic Hilbert spaces on site k to manageable number of d_k states. Thus, *a priori*, NRG is not able to take into account the growing oscillator displacements $\hat{x}_{ki} = 1/\sqrt{2}(\hat{b}_{ki} + \hat{b}_{ki}^\dagger)$ occurring in the system's localized phase. This restricts its application to the delocalized phase. Already at the phase boundary, in combination with the inherent mass-flow error [26], this leads to non-mean-field results for the critical exponents of SBM1 in the regime $s < \frac{1}{2}$ [23,25].

To resolve the issue of bosonic state space truncation, Guo *et al.* [24] proposed a variational matrix-product-state (VMPS) approach involving an optimized boson basis (OBB) [46], that allows an accurate numerical study of the entire phase diagram in the (generalized) spin-boson model. Since we heavily used this method for the numerical results presented here for SBM2, we briefly outline the concept of this powerful approach [41].

The starting point of the variational procedure is setting up an initially random many-body state $|\psi\rangle$ of the truncated Wilson chain described by $\hat{\mathcal{H}}_N$ [having $(N + 1)$ sites in total] in the language of matrix-product-states (MPS) [47]:

$$|\psi\rangle = \sum_{\sigma=\uparrow,\downarrow} \sum_n (A^{[n_0]} A^{[n_1]} \dots A^{[n_N]})_{\sigma} |\sigma\rangle |n\rangle, \quad (8)$$

where $|\sigma\rangle = |\uparrow\rangle, |\downarrow\rangle$ are the eigenstates of σ_x and the states $|n\rangle = |n_0, \dots, n_N\rangle$ represent the boson-number eigenstates of the truncated Fock space, i.e., $\hat{n}_{ki} |n\rangle = n_{ki} |n\rangle$ with $n_{ki} = 0, \dots, d_k - 1$. Combining the state spaces of both chains in Eqs. (7a) and (7b) to supersites, $n_k = (n_{kx}, n_{ky})$ should be interpreted as a combined index of the x and y chains. Each $A^{[n_k]}$ forms a $D \times D$ matrix with elements $(A^{[n_k]})_{\alpha\beta}$, except for $A^{[n_0]}$ and $A^{[n_N]}$ connecting to local impurity and vacuum states, respectively, as indicated in Fig. 2 further discussed in the following. Using standard MPS methods, we optimize $|\psi\rangle$

by iteratively varying one $A^{[n_k]}$ at a time in order to find an appropriate representation of the ground state of $\hat{\mathcal{H}}_N$.

The main advantage of VMPS is the possibility to change the local basis during the stepwise optimization process, while NRG in principle requires the local basis to be fixed *a priori* before starting to diagonalize. To exploit this, we implement the OBB using two key features:

(1) *Effective local basis.* A basis transformation V is introduced with $V^\dagger V = \mathbb{I}$, which maps the local harmonic oscillator basis $|n_k\rangle$ onto a smaller effective basis $|\tilde{n}_k\rangle$ on each site k ,

$$|\tilde{n}_k\rangle = \sum_{n_k=0}^{d_k-1} V_{\tilde{n}_k, n_k} |n_k\rangle \quad (\tilde{n}_k = 0, \dots, \tilde{d}_k - 1), \quad (9)$$

with d_k and \tilde{d}_k denoting the size of the original and effective bases, respectively. Merging V into the A tensors on each bosonic site, the structure of $A^{[n_k]}$ in Eq. (8) is then given by

$$A_{\alpha, \beta}^{[n_k]} = \sum_{\tilde{n}_k=0}^{\tilde{d}_k-1} \tilde{A}_{\alpha, \beta}^{[\tilde{n}_k]} V_{\tilde{n}_k, n_k}. \quad (10)$$

Nevertheless, from an efficiency point of view, it is desirable to keep the separate structure of \tilde{A} and V , where $\tilde{A}^{[\tilde{n}_k]}$ links the effective bosonic basis to the left and right parts of the chain, while V maps the original to the effective local basis. The local optimization procedure for each site thus splits into two steps: at first, V is updated and in this process the optimal effective local basis set $|\tilde{n}_k\rangle$ is determined. Then, we optimize $\tilde{A}^{[\tilde{n}_k]}$ using the new local basis states and move to the next site. Note that with the introduction of the OBB a second adjustable dimension \tilde{d}_k besides the bond dimension D exists. Treating \tilde{A} and V as separate structures, both dimensions are fixed before the start of the ground-state optimization. If a dynamical adjustment of the bond dimensions is required, one has to switch to a two-side optimization procedure or variants of these, which is numerically more expensive [47]. This is for example necessary when enforcing explicit symmetry conservation. In practice, this implementation makes an increase of the size of the local basis sets from $d_k \approx 10$ to $d_k \lesssim 10^4$ possible, while using typically $\tilde{d}_k \lesssim d_k$ below.

(2) *Oscillator shifts.* Moreover, in the localized phase we incorporate an oscillator shift in the Hamiltonian to take the oscillator displacement into account. The oscillator coordinates $\hat{x}_{ki} = 1/\sqrt{2}(\hat{b}_{ki} + \hat{b}_{ki}^\dagger)$ are shifted by their equilibrium value $\langle \hat{x}_{ki} \rangle$ [21] to be determined self-consistently in a variational setting, such that OBB captures the quantum fluctuations near the shifted coordinate $\hat{x}'_{ki} = \hat{x}_{ki} - \langle \hat{x}_{ki} \rangle$. This is achieved by formulating the shift δ_{ki} as unitary transformation acting on the Hamiltonian itself. With

$$\hat{U}(\delta_{ki}) = e^{\frac{\delta_{ki}}{2}(\hat{b}_{ki}^\dagger - \hat{b}_{ki})}, \quad (11)$$

the shifted local bosonic operators \hat{b}'_{ki} and \hat{b}'_{ki}^\dagger are

$$\hat{b}'_{ki} \equiv \hat{U}^\dagger(\delta_{ki}) \hat{b}_{ki} \hat{U}(\delta_{ki}) = \hat{b}_{ki} + \frac{\delta_{ki}}{\sqrt{2}}. \quad (12)$$

By the application of $\hat{U}(\delta_{ki})$ we automatically shift \hat{x}_{ki} by δ_{ki} ,

$$\hat{x}'_{ki} = \frac{1}{\sqrt{2}}(\hat{b}'_{ki} + \hat{b}'_{ki}^\dagger) = \hat{x}_{ki} + \delta_{ki}. \quad (13)$$

After processing the local optimization procedure, we calculate the mean displacement $\langle \hat{x}_{ki} \rangle$. By setting $\delta_{ki} = -\langle \hat{x}_{ki} \rangle$ and replacing \hat{b}_{ki} with the displaced \hat{b}'_{ki} , the shift is included exactly on the Hamiltonian level $\hat{U}^\dagger(\delta_{ki}) \hat{\mathcal{H}}_N(\{\hat{b}_{ki}\}) \hat{U}(\delta_{ki}) = \hat{\mathcal{H}}_N(\{\hat{b}'_{ki}\}) = \hat{\mathcal{H}}_N(\{\hat{b}_{ki}\}, \{\delta_{ki}\})$. Afterwards, the optimization of the current site is repeated in the shifted local bosonic basis until $\langle \hat{x}_{ki} \rangle$ converges, before moving to the next site.

The implementation of an OBB with shifted oscillator modes allows us to simulate an effective local basis that would require a local dimension of $d_k^{\text{eff}} \approx 10^{10}$ in the nonshifted basis, while the actual shifted basis can be kept small, $d_k \lesssim 10^2$. In addition, since the variational procedure determines the optimal shift δ_{ki} for each site of the Wilson chain individually, the exponential growth of $\langle \hat{x}_{ki} \rangle \propto \Lambda^k$ with increasing iteration number k no longer represents a barrier for the method.

Working in the Wilson chain setup with an exponentially decreasing energy scale, it is advantageous to replicate the NRG rescaling procedure in the iterative VMPS procedure in order to avoid losing numerical accuracy towards higher iterations. Therefore, when optimizing $A^{[n_k]}$, we rescale the Hamiltonian in the local picture by a factor Λ^k to ensure that optimization can take place on the effective energy scale $\sim \omega_c$.

Employing standard VMPS methods, we determine the convergence of $|\psi\rangle$ by calculating the variance of the (unscaled) energy E_k^0 of the ground state calculated at each site k . The iterative optimization procedure is stopped once $\text{std}(E_k^0)/\bar{E}^0 < \epsilon$, using double precision accuracy $\epsilon = 10^{-15}$ with $N = 50, \Lambda = 2$ and thus $\epsilon_{N-1} \sim \Lambda^{-N-1} = 10^{-15}$. The resulting state $|\psi\rangle$ is considered to be a reliable approximation of the system's ground state given $\hat{\mathcal{H}}_N$. When computing systems where the effective energy resolution drops below double precision, the relevance of numerical noise as a perturbation to $\hat{\mathcal{H}}_N$ should be double-checked by additionally studying the energy-flow diagrams.

Most results shown in this paper have been obtained using parameters $\Lambda = 2, N = 50, \tilde{d}_k = 24$, unless noted otherwise.

C. U(1) symmetry

Considering the case with symmetric coupling $\alpha_x = \alpha_y$, and no in-plane magnetic fields $h_x = h_y = 0$, the system exhibits an Abelian U(1) symmetry: The Hamiltonian is invariant under simultaneous rotation of the impurity spin and the bosonic baths in the xy plane by an arbitrary angle ϕ , leading to a twofold degeneracy of the resulting ground state. A rotation of this type is described by a unitary operator $\hat{U}(\phi)$:

$$|\psi\rangle \rightarrow \underbrace{e^{i\phi\hat{S}}}_{\equiv \hat{U}(\phi)} |\psi\rangle, \quad (14)$$

where \hat{S} is the generator of the continuous U(1) symmetry, given by

$$\hat{S} = \frac{1}{2}\sigma_z + i \sum_k (\hat{b}_{ky}^\dagger \hat{b}_{kx} - \hat{b}_{kx}^\dagger \hat{b}_{ky}), \quad (15)$$

with $[\hat{S}, \hat{\mathcal{H}}] = 0$. In the form of Eq. (15), however, the symmetry operation \hat{S} involves a hopping between the two baths in the local bosonic state spaces, which poses a serious impediment for the numerical implementation of the symmetry due to truncation of the bosonic state space. Essentially,

the discrete quantum number associated with the symmetry requires a diagonal representation. Hence, it is useful to apply a canonical transformation in order to bring \hat{S} in a diagonal form in the spinor space of $\hat{b}^\dagger \equiv (\hat{b}_x^\dagger, \hat{b}_y^\dagger)$. This leads to

$$\tilde{S} = \frac{1}{2}\sigma_z + \sum_k (\tilde{b}_{ky}^\dagger \tilde{b}_{ky} - \tilde{b}_{kx}^\dagger \tilde{b}_{kx}). \quad (16)$$

Note that this transformation also alters the coupling term in the Hamiltonian. In this form, the symmetry sectors are characterized by the z component of the impurity spin and the difference in the bosonic occupation number in both baths in contrast to the hopping term of Eq. (15), allowing an exact symmetry implementation in the VMPS procedure in the presence of a truncated bosonic state space [48].

Given a simultaneous eigenstate $|q\rangle$ of \hat{S} and \mathcal{H} , the application of the generator results in

$$\tilde{S}|q\rangle = q|q\rangle \quad \text{with} \quad q = \frac{1}{2}\sigma_z + \tilde{N}_y - \tilde{N}_x, \quad (17)$$

where $\tilde{N}_i = \sum_k \tilde{b}_{ki}^\dagger \tilde{b}_{ki}$ is the total number of bosons occupying the Wilson chain of the individual baths and σ_z is the spin component in the z direction. Given any ground state $|G\rangle$, it follows that one may obtain another ground state via $e^{i\phi\tilde{S}}|G\rangle$. Noting that the ground state comes with a symmetric distribution of boson numbers ($\tilde{N}_x = \tilde{N}_y$), we conclude that q should be chosen to be $\pm\frac{1}{2}$:

$$\tilde{S}|G_{q=\pm 1/2}\rangle = \pm\frac{1}{2}|G_{q=\pm 1/2}\rangle, \quad (18)$$

$$\hat{\mathcal{H}}|G_{q=\pm 1/2}\rangle = E_g|G_{q=\pm 1/2}\rangle, \quad (19)$$

where E_g is the ground-state energy. Hence, the ground state is doubly degenerate. The expectation values $\langle\sigma_x\rangle$ and $\langle\sigma_y\rangle$ evaluated using the ground states $|G_{\pm 1/2}\rangle$ are zero by symmetry. How to reconstruct the magnetization of the symmetry-broken ground state, which is a linear superposition within $|G_{q=\pm 1/2}\rangle$, is described in Appendix D.

It turns out that the U(1) symmetry implementation cannot be combined with the shifted OBB. Employing a continuous shift δ_{ki} to the bosonic creation and annihilation operators via Eqs. (12) leads to additional terms of the form $\delta_{ki}(\tilde{b}_{ki} + \tilde{b}_{ki}^\dagger)$ in the symmetry generator. These linear corrections add non-diagonal elements to \tilde{S} , precluding an explicit implementation of the U(1) symmetry in the way indicated above. This limits the application of symmetry-enforced VMPS effectively to the parameter regime $\frac{1}{2} < s < 1$, in which the bosonic state space truncation error does not spoil the calculations of physical quantities such as critical exponents (see Appendix C for more details). Here, the U(1) symmetry implementation is necessary to accurately access the ultra-low-energy behavior governing the critical phenomena of the model (see Sec. VI for details). Note that all results of Ref. [24] are in agreement with the data presented in the following.

D. Energy-flow diagrams

When VMPS is applied to a Wilson-chain Hamiltonian such as Eq. (7), it is possible to generate an energy-level-flow diagram akin to the ones of NRG. To this end, we calculate the eigenvalues E_k of the left-block Hamiltonian $\hat{\mathcal{H}}_L^k$ in each iteration $k < N$ when sweeping from the left

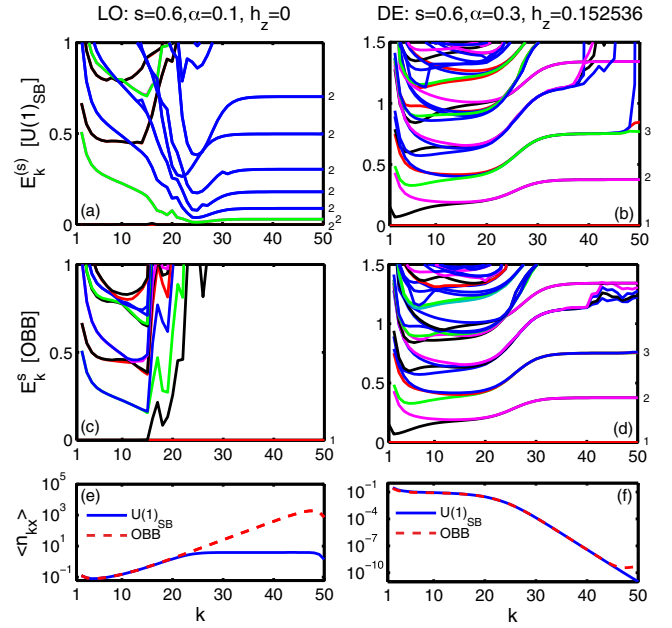


FIG. 3. (Color online) Characteristic VMPS energy-flow diagrams for SBM2 with $s = 0.6$ in two phases for different values of α and h_z . k parametrizes the running energy scale according to $\omega = \omega_c \Lambda^{-k}$. While in the two upper panels the flow is generated using the symmetry-enforced VMPS, the center panels show diagrams generated by employing the shifted OBB. The energy levels flow to a localized fixed point in (a) and (c) and to a delocalized fixed point in (b) and (d) with degenerate (nondegenerate) ground-state space, respectively. The degeneracy of each state is indicated by the numbers to the right side of each curve. The colors in (a) and (b) decode the symmetry label q of each energy level [black and red for $q = \pm 1/2$, green and purple for $q = \pm 3/2$, and blue for $q \geq 5/2$; matching colors are used in panels (c) and (d)]. Panels (e) and (f) display the corresponding occupation numbers $\langle n_{kx} \rangle$ [Eq. (22)].

to the right end of the Wilson chain truncated to N sites. Multiplied with the proper rescaling factor Λ^k , the spectrum $E_s^{(k)}$ relative to the ground-state energy $E_0^{(k)} = 0$ corresponds to the rescaled eigenspectrum determined in a NRG step. The energy flow of excited states is not as smooth as using NRG since our variational procedure focuses on optimizing the global ground state of the system only. However, it can be systematically improved by incorporating symmetries of the model and keeping more states.

Energy-flow diagrams contain information about the fixed points of the impurity model, as illustrated in Fig. 3 for SBM2, where the upper panels [3(a) and 3(b)] are generated by enforcing the U(1) symmetry while for the center panels [3(c) and 3(d)] a shifted OBB is employed in the VMPS procedure. The flow towards a localized fixed point with a twofold-generated ground state is depicted in the left panels of Fig. 3. Only the usage of OBB accounts for the exponential growth of bosonic occupation numbers in the localized phase [cf. Fig. 3(e)]. The energy flow in (c) is distorted when introducing the bosonic shift on the Wilson chain since energy-scale separation is effectively broken due to the exponential growth in local bosonic occupation. The ground-state degeneracy is conserved, however, when enforcing the symmetry in the

VMPS optimization 3(a). In case the system moves towards a delocalized fixed point with a single ground state at the end of the Wilson chain, both methods generate flow diagrams of similar quality [cf. Figs. 3(b) and 3(d)] since no bosonic shift is necessary to appropriately describe the system's ground state. Hence, energy-scale separation remains intact in this case. In the particular example of Figs. 3(b) and 3(d), the intermediate fixed point visible at earlier iterations corresponds to the critical fixed point QC2 discussed in Sec. IV B.

In addition to determining the system's phase or the convergence of the numerical data, flow diagrams can be used to extract information about the effective energy scales characterizing the crossover between fixed points. For example, the transition from the critical to the DE fixed point is governed by the low-energy scale $T^* \approx \omega_c \Lambda^{-k^*}$, with $k^* \approx 25$ for the parameters used in Figs. 3(b) and 3(d).

III. PHASES AND PHASE DIAGRAM

In this section, we describe the phase diagram of the U(1)-symmetric SBM2, together with the main characteristics of the stable phases.

A. Observables

The most important observables for SBM2 employed in this study are the static magnetization

$$M_\alpha = \frac{1}{2} \langle \sigma_\alpha \rangle \quad (\alpha \equiv x, y, z) \quad (20)$$

and the corresponding susceptibility

$$\chi_\alpha = \lim_{h \rightarrow 0} \frac{\partial M_\alpha}{\partial h_\alpha} \quad (\alpha \equiv x, y, z). \quad (21)$$

In the case of U(1) symmetry, we distinguish $\chi_{xy} \equiv \chi_{x,y}$ and χ_z as well as $M_{xy} \equiv M_{x,y}$ and M_z . We will also monitor the occupation numbers of the bath modes of the discretized Wilson chain

$$\langle n_{ki} \rangle = \langle \hat{b}_{ki}^\dagger \hat{b}_{ki} \rangle \quad (22)$$

with $i = x, y$.

B. Stable phases and trivial fixed points

We start with an overview on the stable phases numerically found for SBM2. The description is augmented by an assignment of the corresponding RG fixed points (which are trivial with the exception of the critical phase), with their locations specified in terms of renormalized values of the coupling constants α and h_z .

1. Free-spin or local-moment phase (F)

An asymptotically free spin is controlled by the free-spin (F) fixed point, corresponding to vanishing dissipation $\alpha = 0$ and $h_z = 0$. The ground state is doubly degenerate, and the susceptibility follows $\chi(T) = 1/(4T)$ for all field directions.

2. Localized or strong-coupling phase (LO)

For large dissipation, the system enters a phase with spontaneously broken U(1) symmetry, controlled by the localized (LO) fixed point. LO is located at $\alpha = \infty$ and $h_z = 0$.

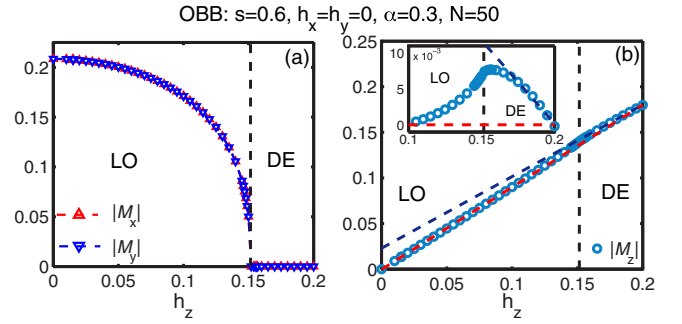


FIG. 4. (Color online) Behavior of the magnetization near the LO–DE transition. The order parameter M_{xy} is driven to zero by increasing h_z past the critical value $h_{z,c}$, indicated by the dashed line (a). Correspondingly, the slight kink in the transverse-field response of M_z at the LO–DE transition in (b) indicates the expected higher-order singularity. The dashed lines are guide to the eye. The inset shows a zoom into the data in panel (b), with the red dashed guide subtracted. We note that the numerics tends to spontaneously favor ordered states with $|M_x| = |M_y|$, as these are the least entangled states.

The bath-oscillator displacements are strongly coupled to the impurity spin, which develops a $T = 0$ expectation value in an arbitrary fixed direction in the xy plane [Fig. 4(a)]. This phase is stable for finite (small) transverse field h_z in which case the expectation values of the impurity describe a canted spin [Fig. 4(b)].

Since the symmetry-broken phase exists at $T = 0$ only, its associated finite- T susceptibility is expected to be Curie-like, albeit with a classical prefactor [37] $\chi_{xy}(T) = 1/(12T)$.

3. Delocalized or polarized phase (DE)

For dominant transverse field, the impurity spin is polarized along the z axis and asymptotically decoupled from the bath. This situation is controlled by the delocalized (DE) fixed point, located at $h_z = \infty$ and $\alpha = 0$. The ground state is unique, the in-plane magnetizations M_x and M_y vanish [Fig. 4(a)], and all susceptibilities are finite.

4. Critical phase (CR)

The nontrivial feature of SBM2 is the existence of a stable critical phase. This is reached for nonzero (but not too large) dissipation strength α and $h_z = 0$ in a certain range of bath exponents s . It is controlled by an intermediate-coupling fixed point, not unlike the celebrated two-channel Kondo fixed point [2,39,40]. In this phase, the expectation value of the impurity moment vanishes, but its temporal correlations decay with a fractional power law. This translates into nonlinear response functions with fractional exponents, as shown in Fig. 5(b).

In contrast to assumptions based on early RG work [32,33] (see also Sec. V A), the critical phase is *not* stable for all dissipation strengths α [Fig. 5(a)] and does not even exist for bath exponents $s < s^*$, with a critical value $s^* \approx 0.76 \pm 0.01$.

We note that the critical nature of the CR phase implies significant finite-size effects for the magnetization, as discussed in Appendix B.

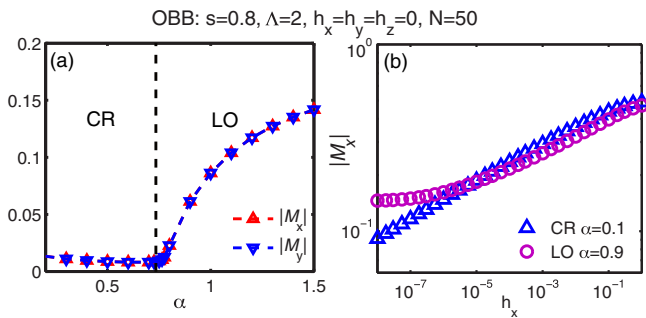


FIG. 5. (Color online) Order parameter near the CR–LO transition (a) for different couplings α and (b) response to finite h_x at two points in CR and LO phase. The small but finite magnetization in the CR phase in panel (a) is caused by finite-size effects as discussed in Appendix B.

C. Numerical determination of phase boundaries

In order to study the critical phenomena of SBM2, it is necessary to accurately determine the phase boundaries, i.e., to numerically calculate the critical coupling α_c and the critical transverse field $h_{z,c}$, which define the location of the LO–CR and LO–DE transitions.

In our experience, the most accurate and efficient way to calculate α_c and $h_{z,c}$ is to distinguish the phases by the characteristic behavior of the bosonic occupation numbers $\langle n_{ki} \rangle$ on the Wilson chain. The average occupation of boson modes increases towards the end of the Wilson chain in the localized phase, while it decreases in both critical and delocalized phases. Moreover, right at the phase boundary (i.e., at criticality) the occupation numbers stay almost constant throughout the chain, except for a sharp decay at the end due to choosing a finite N for the Wilson chain. This characteristic behavior, illustrated in Fig. 6, can be used to determine the phase boundaries with high accuracy. We have thus adopted this approach throughout to determine the precise values of α_c and $h_{z,c}$ involved in the results described in Sec. VI. The accessible accuracy depends on the length N of the Wilson chain. Specifically the calculation of α_c or h_z up to a decimals

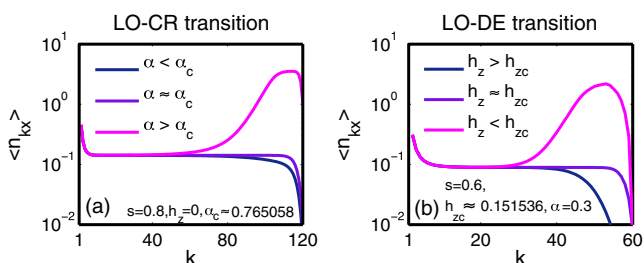


FIG. 6. (Color online) Characteristic behavior of the bosonic occupation numbers on the Wilson chain near QC1 (a) and QC2 (b). In both cases, the occupation numbers stay almost constant throughout the chain directly at the phase boundary, while increasing towards the end of the chain in the localized phase. In the delocalized and critical regimes, we observe a steady decay.

requires a minimal chain length [24]

$$N \propto \nu \frac{\ln(10)}{\ln \Lambda}, \quad (23)$$

where ν is the correlation-length exponent. Thus, for regions in the phase diagram where ν becomes larger we have to increase the length of the Wilson chain, making calculations numerically more demanding.

Note that the numerically determined values of α_c and $h_{z,c}$ depend on the simulation parameters. Especially the logarithmic discretization shifts their values from those expected for a continuum environment. Therefore, α_c and $h_{z,c}$ deviate slightly for different choices of Λ (typically the specific values vary up to within 1%). This, however, does not affect the numerical results for critical exponents [7,41].

IV. RENORMALIZATION-GROUP FLOW AND QUANTUM PHASE TRANSITIONS

In this section, we use the insights gained in Sec. III to deduce the qualitative RG flow of SBM2. The discussion will primarily be made in the language and coupling constants of the original Hamiltonian (1). A more complete discussion of RG beta functions is given in Sec. V.

A. Qualitative RG flow

We start by rephrasing our numerical findings in RG language while referring to the qualitative RG flow diagrams in Fig. 7. For $h_z = 0$, the model SBM2 displays three phases: F, CR, and LO. For $s \geq 1$, the free-spin phase F is the only stable phase, i.e., even large dissipation does not overcome the quantum fluctuations arising through the two-bath coupling. This can be contrasted with the physics of SBM1 where, in the Ohmic case $s = 1$, large dissipation can overcome the quantum fluctuations induced by a finite tunneling term (h_z) leading to localization: this distinction reflects the frustration of decoherence in SBM2. For $s < 1$, F is unstable against any finite α , whereas the localized phase LO is stable for sufficiently large α . Finally, the critical phase CR only exists for $s^* < s < 1$ and small values of α .

A transverse field $h_z \neq 0$ destabilizes F for any s and drives the system into the DE phase. CR is unstable against any finite h_z as well. In contrast, LO is stable and hence requires a critical h_z to be destroyed.

This collection allows us to construct the qualitative RG flow diagrams for the ranges of bath exponents $0 < s < s^*$, $s^* < s < 1$, and $s \geq 1$, as shown in Fig. 7. We also note that the system is always localized for $-1 < s \leq 0$ provided that $\alpha \neq 0$.

In addition to the CR fixed point corresponding to the critical phase, there are two further critical fixed points, QC1 and QC2, which control the quantum phase transitions of SBM2. These are described in more detail in the next section.

B. Intermediate-coupling fixed points

For $h_z = 0$, there are two fixed points at intermediate coupling, namely, CR and QC1, with QC1 controlling the transition between CR and LO. Both intermediate-coupling fixed points are unstable w.r.t. finite h_z . Both fixed points

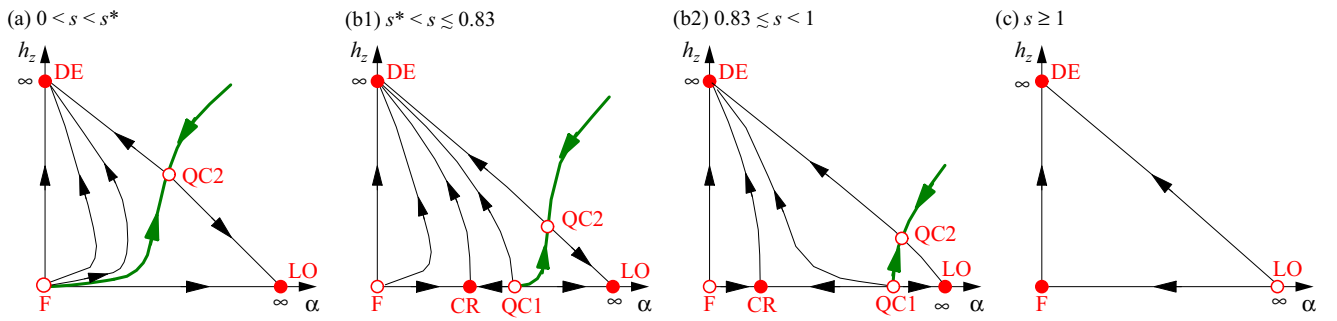


FIG. 7. (Color online) Qualitative RG flow diagrams of the U(1)-symmetric SBM2 model in a plane spanned by the dissipation strength α and the transverse field h_z , as deduced from the VMPS results and supported by the analytical considerations of Sec. V. Filled (open) dots denote stable (unstable) RG fixed points; the heavy line is the separatrix corresponding to the DE–LO transition. Qualitatively distinct behavior is found for the bath-exponent ranges (a) $0 < s < s^* \approx 0.76$, (b) $s^* < s < 1$, and (c) $s \geq 1$. The panels (b1) and (b2) illustrate the evolution of both location and relevant-operator dimensions of the fixed points CR and QC1, i.e., $\nu > \nu'$ of QC1 in regime (b1) while $\nu < \nu'$ of QC1 in regime (b2) (for details see text).

only exist for $s^* < s < 1$, and it is interesting to discuss their location upon variation of the bath exponent s : As will be shown analytically in Sec. V, CR moves towards F as $s \rightarrow 1^-$ whereas QC1 moves towards LO in the same limit, in the fashion characteristic of a lower critical dimension.

In contrast, as $s \rightarrow s^{*+}$, both CR and QC1 approach each other, merging at $s = s^*$, and disappear for $s < s^*$. This merging of two intermediate-coupling fixed points leads to rather unusual behavior, with the phase boundary of LO jumping upon variation of s across s^* .

For finite h_z , a transition can be driven between DE and LO, which is controlled by QC2. QC2 moves towards LO as $s \rightarrow 1^-$, again in a manner of a lower critical dimension. This is consistent with the fact that the localized phase ceases to exist for $s > 1$. In the limit $s \rightarrow 0^+$, QC2 approaches DE, such that DE becomes unstable w.r.t. finite α for $s \leq 0$, reflecting that the system is always localized.

C. Critical exponents

The quantum phase transitions of SBM2 can be characterized by standard critical exponents [49]. For a transition which can be accessed by varying α (at fixed h_z), with the transition point at $\alpha = \alpha_c$, the following exponents can be defined from the zero-temperature order parameter M_{xy} and its conjugate field h_{xy} :

$$M_{xy}(\alpha, h_{xy} = 0) \propto (\alpha - \alpha_c)^\beta, \quad (24)$$

$$M_{xy}(\alpha = \alpha_c, h_{xy}) \propto h_{xy}^{1/\delta}. \quad (25)$$

Transitions which occur at finite h_z can also be driven by varying h_z at fixed α ; correspondingly, the exponent β may be defined via $M_{xy} \propto (h_{z,c} - h_z)^\beta$ as well. In contrast, for $h_z = 0$ transitions, h_z takes a role different from $(\alpha - \alpha_c)$, as it reduces the symmetry of the model from $U(1) \times Z_2$ to $U(1)$. It is useful to introduce an exponent for the nonlinear response to h_z according to

$$M_z(\alpha = \alpha_c, h_{xy} = 0, h_z) \propto h_z^{1/\delta'}. \quad (26)$$

A correlation-length exponent is defined as usual from the divergence of a correlation length, here equivalent to the

vanishing of a crossover energy T^* according to

$$T^*(\alpha, h_{xy} = 0) \propto |\alpha - \alpha_c|^\nu; \quad (27)$$

note that there is no separate dynamical exponent for the $(0 + 1)$ -dimensional impurity model under consideration, formally $z = 1$. For fixed points located at $h_z = 0$ which are unstable towards finite h_z , we additionally define

$$T^*(\alpha = \alpha_c, h_{xy} = 0, h_z) \propto |h_z|^{\nu'}. \quad (28)$$

The linear-response order-parameter susceptibility diverges at the quantum critical point, in the approach from either smaller α or from finite T , according to

$$\chi_{xy}(\alpha, T = 0) \propto (\alpha_c - \alpha)^{-\gamma}, \quad (29)$$

$$\chi_{xy}(\alpha = \alpha_c, T) \propto T^{-x}. \quad (30)$$

Within the quantum-to-classical correspondence, x is related to the finite-size scaling of the classical model's susceptibility at criticality. One may also consider the dynamic version of the order-parameter susceptibility, which follows a power-law behavior at criticality

$$\chi_{xy}(\alpha = \alpha_c, \omega) \propto \omega^{-y}, \quad (31)$$

corresponding to power-law autocorrelations of the impurity spin in time. The exponent y contains the same information as the usually defined anomalous exponent η , with $y \equiv 2 - \eta$. At the critical points of SBM2 (and other spin models with long-ranged interactions), $\eta = 2 - s$ (equivalently, $y = s$) is believed to be an exact relation (see also Sec. V).

Due to the anisotropic nature of the spin fluctuations, different power laws arise for the z -component susceptibility:

$$\chi_z(\alpha = \alpha_c, T) \propto T^{-x'}, \quad (32)$$

$$\chi_z(\alpha = \alpha_c, \omega) \propto \omega^{-y'}, \quad (33)$$

Finally, it is also useful to introduce exponents which describe the location of the DE–LO phase boundary at small h_z . For $0 < s < s^*$, this phase boundary is connected to the $\alpha = h_z = 0$ point, and we define

$$h_{z,c} \propto \alpha^\psi. \quad (34)$$

In contrast, for $s^* < s < 1$, the DE–LO boundary terminates at the CR–LO transition located at $\alpha = \alpha_c$ and $h_z = 0$, and we use

$$h_{z,c} \propto (\alpha - \alpha_c)^\psi. \quad (35)$$

D. Scaling

The exponents introduced above can be related to each other via scaling relations, following textbook strategy [49]. The standard scaling relations do hold:

$$\beta \delta = \beta + \gamma, \quad (36)$$

$$\gamma = (2 - \eta)v \equiv yv. \quad (37)$$

The exact result $y = s$ then implies

$$\gamma = sv. \quad (38)$$

For critical points with hyperscaling, additional scaling relations apply, which involve spatial dimensionality d :

$$2\beta + \gamma = vd, \quad (39)$$

$$\delta = \frac{d + 2 - \eta}{d - 2 + \eta}. \quad (40)$$

Furthermore, hyperscaling implies $x = y$. For $d = 1$ and using the exact result $y = s$, the hyperscaling relations can be converted into

$$x = s, \quad (41)$$

$$\beta = \gamma \frac{1-s}{2s} = v \frac{1-s}{2}, \quad (42)$$

$$\delta = \frac{1+s}{1-s}. \quad (43)$$

For critical points of SBM2 with $h_z = 0$, the scaling hypothesis underlying hyperscaling can be extended to include the dependence on h_z [in addition to that on $(\alpha - \alpha_c)$, h_{xy} , and T]. This then yields additional hyperscaling relations: $x' = y'$ and

$$v' = 1 + \frac{1}{\delta'}, \quad (44)$$

$$\delta' = \frac{1+x'}{1-x'}. \quad (45)$$

(see Appendix A for a derivation).

We recall that hyperscaling, which is of general interest because it implies simple and powerful scaling relations which can be applied in analyzing both experimental and numerical data, usually holds for phase transitions below their upper critical dimension. Hyperscaling is spoiled by the existence of dangerously irrelevant variables in the critical theory; the most important example here is the quartic coupling of a (classical) ϕ^4 theory in dimensions $d > 4$.

V. EPSILON EXPANSIONS AND CRITICAL BEHAVIOR

We now describe analytical approaches to the critical-point properties of SBM2, utilizing the field-theoretic toolbox with renormalization-group and epsilon-expansion techniques.

A. Expansion around F: CR phase

The free-impurity fixed point F is characterized by a doubly degenerate impurity at $\alpha = 0, h_z = 0$. Tree-level power counting yields the scaling dimensions (recall that $\alpha \propto \lambda_{qi}^2$)

$$\dim[\alpha] = 1 - s, \quad (46)$$

$$\dim[h_z] = 1. \quad (47)$$

1. DE–LO phase boundary

From the scaling dimensions one can immediately read off the asymptotic behavior of the flow trajectories leaving the F fixed point $h_z \propto \alpha^{1/(1-s)}$. This also applies to the DE–LO separatrix in the exponent range $0 < s < s^*$, yielding the phase-boundary exponent according to Eq. (34) as

$$\psi = \frac{1}{1-s}. \quad (48)$$

2. RG analysis

Now, we turn to a RG analysis of the flow of α at $h_z = 0$. Given that the dissipation is a marginal perturbation at $s = 1$, this is akin to a standard epsilon expansion with $\epsilon = 1 - s$, which can give reliable results for small $(1 - s)$. Straightforward perturbation theory, along the lines of Refs. [33,37,38], yields the two-loop beta function [33,50]

$$\beta(\alpha) = (1-s)\alpha - \alpha^2 + \alpha^3. \quad (49)$$

This beta function indicates the existence of an infrared-stable fixed point at

$$\alpha^* = (1-s) + (1-s)^2 + \mathcal{O}[(1-s)^3] \quad (50)$$

and $h_z = 0$; this is the CR fixed point. Its properties can be obtained in a double expansion in α and $(1-s)$. The exact result $x = y = s$ follows from the diagrammatic structure of the susceptibility [37] or, alternatively, from a Ward identity [33]. From this, we have

$$1/\delta = \frac{1-s}{1+s} \quad (51)$$

as above. The z -component correlator requires an explicit computation, with the two-loop result [33]

$$1 - y' = 2(1-s) + (1-s)^2 + \mathcal{O}[(1-s)^3]. \quad (52)$$

The remaining exponents involving the h_z response can be calculated from the hyperscaling relations (44) and (45), with the result

$$1/v' = s - \frac{(1-s)^2}{2} + \mathcal{O}[(1-s)^3], \quad (53)$$

$$1/\delta' = 1 - s + \frac{3(1-s)^2}{2} + \mathcal{O}[(1-s)^3]. \quad (54)$$

We point out that the RG flow towards the CR fixed point is rather slow because the leading irrelevant operator, its prefactor

being $(\alpha - \alpha^*)$, has a small scaling dimension of $\omega = 1 - s$. Therefore, quickly converging numerical results are best obtained using a bare coupling close to α^* [50].

3. Disappearance of CR for $s < s^*$

It is interesting to note that the beta function in Eq. (49) displays *two* nontrivial fixed points at $\alpha_{1,2}^* = 1/2 \pm \sqrt{1/4 - (1-s)}$. While α_2^* corresponds to the stable CR fixed point of Eq. (50), the infrared-unstable fixed point at α_1^* is outside the range of validity of the epsilon expansion. However, *if* we choose to ignore this restriction, the comparison with the numerical results suggests to associate α_1^* with QC1. Remarkably, α_1^* and α_2^* approach each other upon decreasing s from unity, and the criterion $\alpha_1^* = \alpha_2^*$ yields $s^* = \frac{3}{4}$ which is extremely close to the numerical determined value of $s^* \approx 0.76 \pm 0.01$ where CR and QC1 merge.

While this can be interpreted as a remarkable success of the epsilon expansion (it predicts not only the existence of the CR phase, but also its disappearance for $s < s^*$), we note that this epsilon expansion does not provide means to reliably calculate critical properties of QC1, simply because α_1^* is never small. As we show in the following, the presence (absence) of hyperscaling in a field at CR (QC1) even indicates a qualitative difference between CR and QC1 which is not apparent from this epsilon expansion.

B. Expansion around DE: QC2

It is also possible to devise an expansion around the delocalized fixed point DE, located at $h_z = \infty$, $\alpha = 0$. Such an expansion has been first used in Ref. [19] for SBM1, but the analysis there missed the presence of a dangerously irrelevant operator [the quartic coupling u in Eq. (56)] and erroneously assumed hyperscaling, which led to partially incorrect conclusions [23]. Here, we correct this approach and apply it to SBM2. For convenience we assume equal couplings between the impurity and the different oscillator modes $\lambda_{qi} \equiv \lambda_i$, such that the energy dependence of $J_i(\omega)$ is contained in the density of states of the oscillator modes ω_q , and we have $\alpha_i \propto \lambda_i^2$.

1. Projection

At DE we have a single low-lying impurity level $|\uparrow\rangle$, while $|\downarrow\rangle$ is separated by an energy h_z . Low-energy interaction processes between the impurity and the baths arise in second-order perturbation theory, controlled by the coupling

$$\kappa_i = \lambda_i^2 / h_z. \quad (55)$$

In the low-energy sector (this corresponds to projecting out the $|\downarrow\rangle$ state), the effective theory reads as (assuming from here on $\alpha_x = \alpha_y$ or $\kappa_x = \kappa_y$)

$$\hat{\mathcal{H}}_{\text{eff}} = \hat{\mathcal{H}}_{\text{bath}} + m(\phi_x^2 + \phi_y^2) + u(\phi_x^2 + \phi_y^2)^2 \quad (56)$$

with $m = -\kappa$ and $u = \kappa^2$. We have defined

$$\phi_i = \sum_q (\hat{a}_{qi} + \hat{a}_{qi}^\dagger), \quad (57)$$

and we have omitted higher-order terms in Eq. (56). Figure 8 illustrates how the m and u terms are generated from \mathcal{H} of

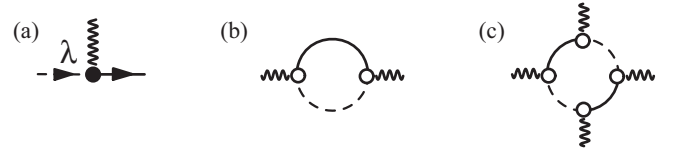


FIG. 8. Feynman diagrams occurring in the perturbation expansion around DE. Full and dashed lines denote the propagators of the $|\uparrow\rangle$ and $|\downarrow\rangle$ impurity states, respectively; the two states are separated by a gap h_z . The wiggly line is the local bath boson $\phi_{x,y}$. (a) Interaction vertex λ . (b) Bilinear ϕ term. (c) Quartic ϕ term.

the original model SBM2; this approach is valid provided that $\lambda \ll h_z, \omega_c$.

2. Local ϕ^4 theory and quantum-to-classical correspondence

The theory $\hat{\mathcal{H}}_{\text{eff}}$ can be understood as a theory for the local bosonic fields $\phi_{x,y}$. Their “bare” propagator arises from $\hat{\mathcal{H}}_{\text{bath}}$ and is given by $G_\phi^{-1}(i\nu_n) = iA_0 \text{sgn}(\nu_n) |\nu_n|^s + A_1$ at low energies, with $A_1 = -2\omega_c/s$ for the power-law spectrum in Eq. (2). The main role of the impurity in $\hat{\mathcal{H}}_{\text{eff}}$ is that of an additional mass term (recall that the impurity spin degree of freedom has been projected out).

Importantly, $\hat{\mathcal{H}}_{\text{eff}}$ in Eq. (56) is identical to a local ϕ^4 theory for an XY-symmetric order-parameter field (ϕ_x, ϕ_y) with long-ranged interactions $\propto 1/\tau^{1+s}$ in imaginary time. It displays a critical point which corresponds to a vanishing ϕ mass. Ignoring the influence of the quartic interaction u , this happens at $m_c = A_1 < 0$; this can alternatively be understood by interpreting m as the strength of a potential scatterer, where $m_c G_\phi(0) = m_c/A_1 = 1$ is the condition for a zero-energy pole of the T matrix. For positive mass, i.e., small κ , $\hat{\mathcal{H}}_{\text{eff}}$ is in a disordered phase corresponding to DE, whereas negative mass drives the system into an ordered phase with spontaneously broken XY symmetry; this can be identified with LO.

Consequently, the critical point of $\hat{\mathcal{H}}_{\text{eff}}$ corresponds to QC2. As the ϕ^4 theory in question is the low-energy theory of a classical XY chain with long-range interactions, we conclude that QC2 obeys a quantum-to-classical correspondence at least if QC2 is located in the small- κ parameter regime where the above mapping to $\hat{\mathcal{H}}_{\text{eff}}$ is valid, i.e., for small s . The critical properties for the classical XY chain are listed in Sec. VD; in particular, mean-field behavior obtains for $s < \frac{1}{2}$.

3. RG analysis

An alternative approach to $\hat{\mathcal{H}}_{\text{eff}}$ is to analyze the flow of the couplings m and u near the DE fixed point by RG means. Power counting w.r.t. the $\lambda = 0$ limit gives

$$\dim[m] = -s, \quad (58)$$

$$\dim[u] = 2s - 1, \quad (59)$$

i.e., m is marginal at $s = 0$ while u is irrelevant. Near $s = 0$ we can follow the flow of m which yields at one-loop order

$$\beta(m) = -sm + m^2. \quad (60)$$

Aside from the stable DE fixed point at $m = 0$ (i.e., $\alpha = 0$), this flow equation displays an infrared unstable fixed point (QC2) at

$$m^* = s + \mathcal{O}(s^2) \quad (61)$$

which controls the transition between the DE and LO phases. Corrections from u only enter at higher orders in s because the initial values obey $u = m^2$. We note that the value of m^* in Eq. (60) is consistent with $m_c = -A_1$ from above. Expanding the RG beta function around the fixed point (61) gives the correlation-length exponent

$$1/\nu = s + \mathcal{O}(s^2), \quad (62)$$

apparently in agreement with the classical mean-field result (65).

One may employ renormalized perturbation theory to calculate critical exponents in a double expansion in m and s . This is, however, complicated by the facts that (i) for many observables of the original model SBM2 one needs to restore the impurity Hilbert space, i.e., undo the elimination of the $|\downarrow\rangle$ state, and (ii) the quartic coupling u is dangerously irrelevant and cannot be neglected. For selected exponents, we have checked that this procedure yields results consistent with Eqs. (66)–(70).

C. Quantum-to-classical mapping of SBM2

One may ask whether a general mapping of SBM2 to a classical statistical-mechanics model exists. Such a mapping, using a Feynman path-integral representation, can indeed be formulated for the single-bath spin-boson model (SBM1) and directly leads to an Ising chain with both long-ranged $1/r^{1+s}$ and short-ranged interactions [16,25].

Here, we sketch what happens when applying the same procedure to SBM2. For simplicity, we restrict ourselves to $\bar{h} = 0$. The Hamiltonian may be written as $\hat{\mathcal{H}} = \hat{\mathcal{H}}_x + \hat{\mathcal{H}}_y + \hat{\mathcal{H}}_{\text{bath}}$ with

$$\begin{aligned} \hat{\mathcal{H}}_i &= \sum_q \lambda_{qi} \frac{\sigma_i}{2} Q_{qi} \quad (i = x, y), \\ \hat{\mathcal{H}}_{\text{bath}} &= \sum_{i=x,y} \sum_q \left(\frac{P_{qi}^2}{2m_q} + \frac{m_q \omega_q^2 Q_{qi}^2}{2} \right). \end{aligned} \quad (63)$$

The Feynman path integral for the partition function can be expressed using eigenstates of σ_x , σ_y , and the oscillator's coordinates. Inserting the identities for the spin variables (those for the oscillator coordinates are standard and do not lead to any complications), it reads as

$$\begin{aligned} Z &= \text{Tr}_{P,Q} \int \mathcal{D}\sigma_x \mathcal{D}\sigma_y \langle \sigma_{xN} | e^{-\epsilon \hat{\mathcal{H}}_x} | \sigma_{yN-1} \rangle \\ &\times \langle \sigma_{yN-1} | e^{-\epsilon \hat{\mathcal{H}}_y} | \sigma_{xN-1} \rangle e^{-\epsilon \hat{\mathcal{H}}_{\text{bath}}} \langle \sigma_{xN-1} | \dots | \sigma_{x0} \rangle, \end{aligned} \quad (64)$$

where N is the number of Trotter slices, $\epsilon = \beta/N$, and $\sigma_{x0} = \sigma_{xN}$. In principle, a classical spin model can now be obtained by integrating out the bath oscillators, which generates long-ranged interactions for the variables coupled to these oscillators. In the case of SBM2, these are both σ_x

and σ_y , such that one ends up with a representation in terms of sets of Ising spins. To rewrite this in terms of a classical spin model requires to express the matrix elements in Eq. (64) as exponentials of classical interactions. Remarkably, the set of matrix elements $\langle \sigma_x | \sigma_y \rangle$ cannot be expressed as $e^{H_c(\sigma_x, \sigma_y)}$ with a classical real Hamiltonian function H_c , i.e., the Feynman path-integral representation of SBM2 leads to an ill-defined classical model with negative Boltzmann weights [51]. Clearly, this problem can be traced back to the noncommutativity of the two spin components which couple to the oscillator baths in SBM2.

We recall, however, that the physics of the QC2 fixed point of SBM2 can be mapped onto that of a classical XY model at least near $s = 0$ (see Sec. VB). Assuming that the character of QC2 does not change fundamentally as a function of s , this implies that a quantum-to-classical correspondence indeed holds for QC2. As will be shown in Sec. VI, our numerical results for the critical behavior near QC2 are perfectly consistent with this assertion.

D. Exponents of classical XY chain

Here, we collect and summarize the available results for critical exponents of the classical XY chain with long-range interactions decaying as $1/r^{1+s}$; these have been discussed in Refs. [29,30]. The classical model has a thermal phase transition for $0 < s < 1$; no ordered phase exists for $s \geq 1$.

For $s < \frac{1}{2}$ and $s \gtrsim \frac{1}{2}$ one may utilize the language of a ϕ^4 theory. Power counting shows that the quartic interaction is marginal for $s = \frac{1}{2}$, such that mean-field behavior attains for $s < \frac{1}{2}$, with

$$1/\nu = s, \quad (65)$$

$$\eta = 2 - s, \quad (66)$$

$$\beta = 1/2, \quad (67)$$

$$\gamma = 1, \quad (68)$$

$$\delta = 3, \quad (69)$$

$$x = 1/2, \quad (70)$$

with hyperscaling being violated.

In the non-mean-field regime $s > \frac{1}{2}$, one can obtain exponents in an expansion in $\epsilon = s - \frac{1}{2}$, with two-loop results as quoted in Ref. [29]:

$$\gamma = 1 + \frac{8}{5}\epsilon - \frac{16}{25} \left(1 - \frac{17\mathcal{A}(1/2)}{5} \right) \epsilon^2 + \mathcal{O}(\epsilon^3), \quad (71)$$

$$\eta = 2 - s, \quad (72)$$

the latter result is believed to be exact to all orders [29,52], and the constant

$$\mathcal{A}(s) = s[\psi(1) - 2\psi(s/2) + \psi(s)] \quad (73)$$

in terms of the digamma function $\psi(x)$, with $\mathcal{A}(1/2) = 2.957$. Hyperscaling holds for $\frac{1}{2} < s < 1$; this allows us to derive the remaining exponents: The correlation-length exponent ν follows from the scaling relation $\gamma = (2 - \eta)\nu$ [Eq. (37)],

while β can be read off from the hyperscaling relation $\beta = \gamma(1-s)/(2s)$ [Eq. (42)], with the results

$$1/\nu = 1/2 + 1/5\epsilon - 3.217\epsilon^2 + \mathcal{O}(\epsilon^3), \quad (74)$$

$$1/\beta = 2 + 24/5\epsilon - 3.269\epsilon^2 + \mathcal{O}(\epsilon^3). \quad (75)$$

Near $s = 1$ RG equations can be derived [30] using a variant of a method proposed by Polyakov [53]; this is similar to an ordered-phase expansion in $(2 + \epsilon)$ dimensions for magnets with short-range interactions. Exponents are formally obtained in an expansion in $(1 - s)$; the one-loop results read as [30]

$$1/\nu = 1 - s + \mathcal{O}[(1 - s)^2], \quad (76)$$

$$\eta = 2 - s, \quad (77)$$

the latter result again believed to be exact to all orders. Using hyperscaling, we obtain the one-loop result for β as

$$\beta = 1/2 + \mathcal{O}[(1 - s)^2]. \quad (78)$$

VI. NUMERICAL RESULTS FOR CRITICAL EXPONENTS

Taking into account the insights gained in the preceding Secs. IV and IV, we now focus on the numerical results obtained for the critical behavior of SBM2. To this end, we employ the VMPS methodology as introduced in Sec. II at the quantum phase transitions QC1 and QC2, as well as in the CR phase to extract various critical exponents.

Our main results are that (i) the transition between LO and DE, controlled by QC2, indeed obeys quantum-to-classical correspondence, i.e., its critical properties are that of a classical XY chain with long-range interactions, and (ii) the transition between CR and LO, controlled by QC1, is of unusual nature, with no quantum-to-classical correspondence and hyperscaling present only at $h_z = 0$.

In the following, we distinguish VMPS results obtained using the shifted OBB (denoted by OBB) from the symmetry-enforced approach [denoted by $U(1)_{\text{SB}}$]. In all calculations, we work with a fixed Wilson discretization parameter $\Lambda = 2$, bond dimension $D = 60$, and local bosonic dimension $d_k = 100$ while varying the chain length N and the effective local dimension $\tilde{d}_k \leq d_k/2$, as denoted in the figures. Since d_k and \tilde{d}_k are set equal for different sites during a single VMPS calculation, we omit the label k in the following. This choice of D and \tilde{d} ensures that we keep all singular values larger than 10^{-5} in our calculation.

A. Transition between LO and DE phase

We start the discussion with the continuous quantum phase transition between the LO and DE phases that is controlled by the critical fixed point QC2. As explained in Sec. V, this transition should correspond to the thermal transition of the XY chain with long-ranged interactions. Here, we show that our numerical results are in excellent agreement with analytical predictions of scaling and epsilon-expansion calculations, listed in Sec. VD, and therefore fully confirm the quantum-to-classical correspondence.

1. Order-parameter exponent β

Accessible only at finite h_z , we drive the transition between the DE and LO phases by varying h_z for fixed α . Hence, the critical exponent β is defined via $M_{xy} \propto (h_{z,c} - h_z)^\beta$ at the phase boundary moving into the LO phase. Figures 9(a) and 9(d) show the corresponding numerical data. The characteristic power-law behavior of the magnetization for fixed $s = 0.4$ close to the critical point on a log-log scale is displayed in Fig. 9(a). The exponent derived from a linear fit to these data, namely $\beta = 0.48 \pm 0.03$, corresponds to the mean-field prediction in Eq. (67) within the error bars. Deviations from power-law behavior at small $|h_z - h_{z,c}|$ can be attributed to a combination of finite chain length $N \leq 80$ and numerical errors of VMPS. Our numerical method generates power-law plots of similar quality for all $s \geq 0.3$; the resulting exponents are collected in Fig. 9(d). These are found to be in excellent agreement with the predictions of the quantum-to-classical mapping. As for the classical XY chain, the exponent assumes its mean-field value $\beta = \frac{1}{2}$ for $0 < s < \frac{1}{2}$, while it follows the two-loop RG results in Eq. (75) for $s = \frac{1}{2} + \epsilon$. In the limit of $s \rightarrow 1^-$, β shows the tendency to approach the value $\frac{1}{2}$, consistent with Eq. (78). The growing shifts in the localized phase, in combination with the decreasingly low-energy scale necessary to precisely access the critical point, prevent our numerics to extract accurate results for β in the deep sub-Ohmic regime ($s \leq 0.3$). The second issue (decreasingly low-energy scale) also applies in the limit $s \rightarrow 1^-$.

2. Response exponent δ

As defined in Eq. (25), δ can be extracted from the response at criticality of the order parameter M_{xy} to an external magnetic field. Figure 9(b) displays the typical power-law scaling of the magnetization at the critical point. The deviations at small h_x are again related to finite system size and numerical artifacts. Determining δ from power-law fitting over six decades for fixed $s = 0.4$, we find it to be in accordance with the mean-field predictions of the quantum-to-classical mapping $\delta_{\text{MF}} = 3$. Although the deep sub-Ohmic regime $s < 0.3$ is again not accurately accessible for our VMPS approach, the collected results for $s \geq 0.3$ depicted in Fig. 9(e) strongly support the validity of quantum-to-classical mapping: for $s < \frac{1}{2}$, δ approaches its mean-field value of $\delta_{\text{MF}} = 3$, while for $\frac{1}{2} < s < 1$ it clearly follows the hyperscaling relation in Eq. (43).

3. Correlation-length exponent ν

The definition of the correlation-length exponents ν in Eq. (27) involves a crossover energy scale T^* that can easily be derived using the VMPS energy-flow diagrams introduced in Sec. IID. To this end, we determine the site on the Wilson chain k^* where the flow starts to significantly deviate from the characteristically smooth flow at the critical point. This approach is illustrated in Fig. 10, where two typical energy flows inside the localized phase close to QC2 are displayed. In the beginning, the system resides at the critical fixed point (smooth energy flow), then a transition to the localized fixed point occurs. This crossover is indicated by the red bar corresponding to the iteration k^* . It is defined by the point

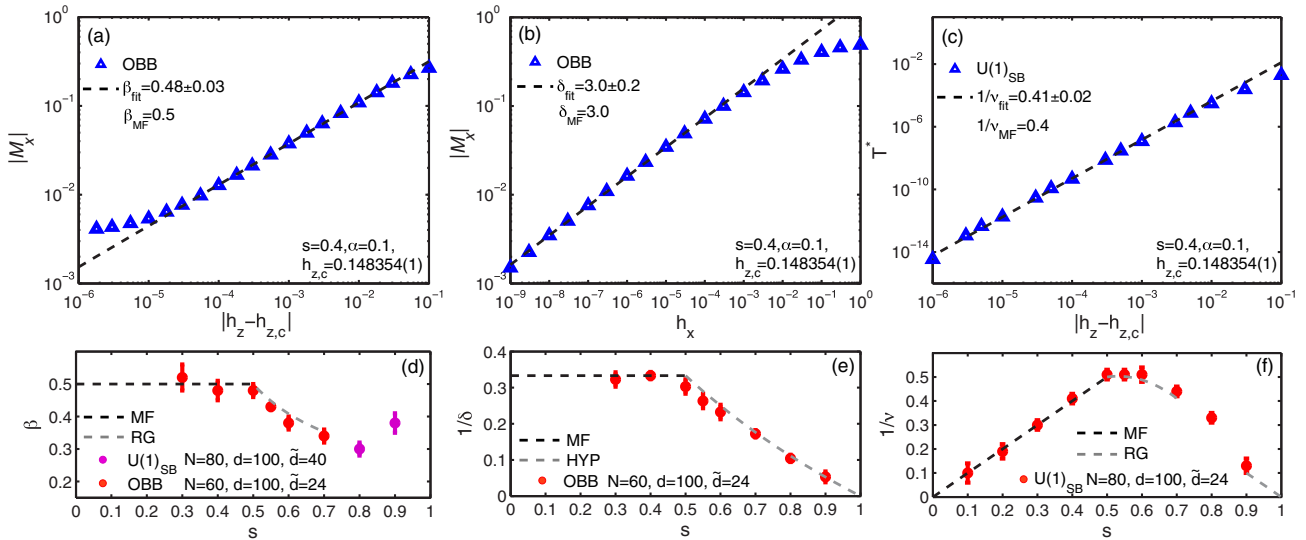


FIG. 9. (Color online) VMPS results for critical exponents β , δ , and ν at the LO-DE quantum phase transition. Analogous to Fig. 12, the upper panels (a)–(c) display the calculated VMPS results for the order parameter and the crossover scale close to/at the critical point for $s = 0.4$, respectively. The s -dependent behavior of the critical exponents β , δ , and ν obtained from the respective power-law fits is illustrated in lower panels (d)–(f). In addition, these panels contain the corresponding predictions of the classical XY model (dashed lines), which we find to be in excellent agreement with the numerical data.

where the first-excited energy level drops below $E < 0.05$ in rescaled energy units.

The crossover energy scales T^* determined from such an analysis are collected in Fig. 9(c) for fixed $s = 0.4$ and $\alpha = 0.1$ close to the phase transition. The power-law scaling of T^* over several orders allows us to extract ν with high accuracy. Studying the s dependence in Fig. 9(f), we again find excellent agreement with the classical XY model: ν closely follows the mean-field prediction [Eq. (65)] for $0 < s < \frac{1}{2}$ (black dashed line), and also agrees with the perturbative RG calculations near $s = \frac{1}{2}$ [Eq. (74)] and $s = 1$ [Eq. (76)]. As a further check, we analyze the validity of the hyperscaling relation (42) involving both β and ν by usage of our numerical results. Figure 11(a) shows that the numerically extracted

exponents obey hyperscaling for $\frac{1}{2} < s < 1$ but clearly violate the respective relation in regime $s < \frac{1}{2}$, as expected by quantum-to-classical correspondence.

B. Transition between LO and CR phases

Next, we consider the second continuous quantum phase transition of SBM2 between LO and CR phases, which is controlled by the critical fixed point QC1. In this case, the quantum-to-classical correspondence is presumably violated (see Sec. V C), and no analytical predictions for the critical exponents are available.

1. Order-parameter exponent β

The transition between CR and LO phases can be driven by varying α at $h_z = 0$ and $s^* < s < 1$. Hence, β is defined

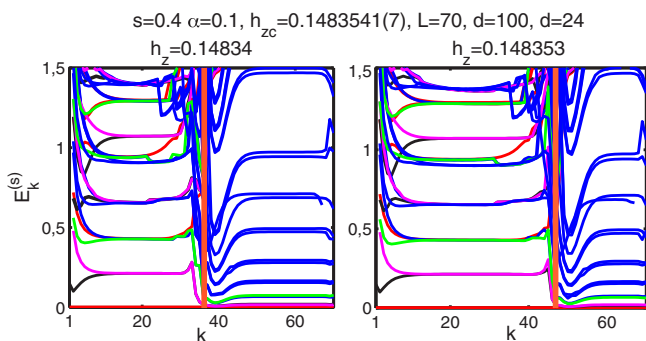


FIG. 10. (Color online) Energy-level-flow diagrams for $s = 0.4$ in the LO close to the LO-DE transition. The smooth behavior in the first iterations reflects the characteristics of the critical fixed point, while the bending and jumps in the lines suggest that the system flows to the localized fixed point. The red bar indicates the characteristic iteration k^* of the transition that is used to calculate the low-energy scale T^* . By tuning h_z close to its critical value, k^* moves towards higher iterations.

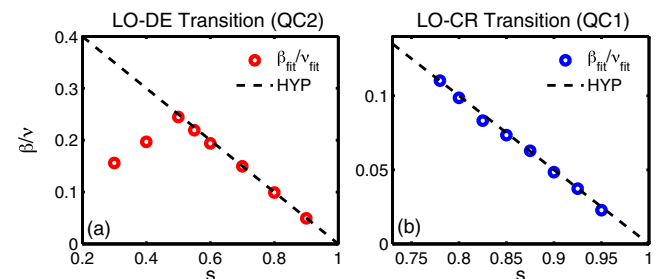


FIG. 11. (Color online) Hyperscaling relation (42) involving exponents β and ν at QC1 (a) and QC2 (b) with the numerical data (dots) is compared to the exact results (dashed line). We find excellent agreement with the theory at QC1 for all values of $s^* < s < 1$ as well as for $\frac{1}{2} < s < 1$ at QC2. As expected by quantum-to-classical mapping, the numerical data confirm that hyperscaling (HYP) fails at QC2 below $s < \frac{1}{2}$.

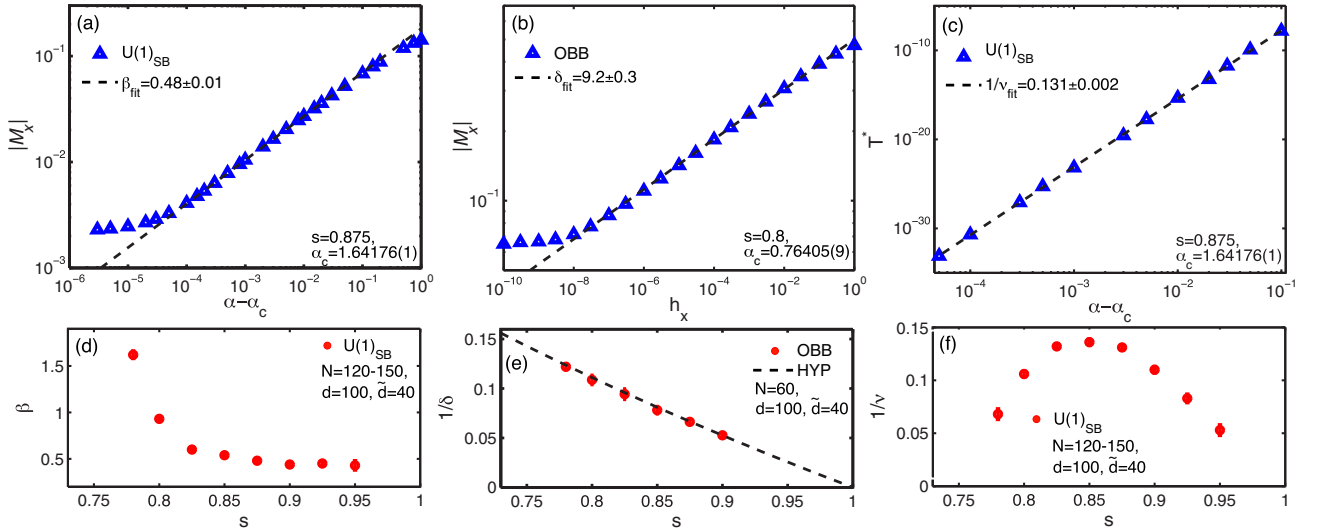


FIG. 12. (Color online) VMPS results for critical exponents β , δ , and ν at the LO–CR quantum phase transition. In (a) the power-law scaling of the order parameter in the vicinity of the critical point is displayed for fixed $s = 0.875$, whereas the fitted values of β are collected for various s in (d). Panel (b) shows similar VMPS data for the order parameter at the critical point w.r.t. an increasing h_x for fixed $s = 0.8$, which we use to extract the exponent δ . Its overall s dependence is illustrated in (e), which is in accordance with hyperscaling equation (43) (dashed line). In addition, (c) depicts the crossover energy scale T^* close to the transition, which relates to the exponent ν for the correlation length which shows an overall s dependence according to panel (f).

according to Eq. (24) with the corresponding numerical data displayed in Figs. 12(a) and 12(d). Figure 12(a) depicts the scaling of M_x close to α_c for fixed $s = 0.875$ on a log-log scale, where a power-law behavior is apparent over more than three decades, with an exponent $\beta = 0.48 \pm 0.01$. Figure 12(d) shows the dependence of β on the bath exponent s gained from power-law scaling fits with similar quality as Fig. 12(a). We find increasing values of $\beta > 1$ for $s \rightarrow s^*$, while in the limit of $s \rightarrow 1^-$ our VMPS calculations suggest that β approaches the value $\frac{1}{2}$. Furthermore, we are able to show that β in combination with ν satisfies the hyperscaling relation in Eq. (42), as illustrated in Fig. 11(b).

Note that the extraction of β is particularly complicated for QC1 since this transition comes with a large exponent ν for the correlation length, on which we elaborate below. This property relates to a low-energy scale required to resolve α_c appropriately Eq. (23), a precondition to obtain a solid power-law scaling of the order parameter M_x . Such calculations involving large chain lengths ($N > 100$) become extremely sensitive to artificial symmetry breaking caused by numerical noise. Therefore, the use of the symmetry-enforced VMPS is essential in this parameter regime, for performance and accuracy reasons. In particular, the application of OBB fails for energy scales significantly below double precision accuracy since the small “perturbations” introduced by a shifted basis grow exponentially for later Wilson shells, and hence break the energy-scale separation on the Wilson chain. This should not affect the validity of our results since a shifted basis is not strictly required for $\frac{1}{2} < s < 1$ (see Appendix C).

2. Response exponents δ and δ'

For a transition at $h_z = 0$, it is possible to extract both exponents δ and δ' via the order parameter’s response to a

magnetic field according to Eqs. (25) and (26), respectively. Focusing first on δ , Figs. 12(b) and 12(e) illustrate the results of our VMPS calculations. Again, Fig. 12(b) shows the typical response of the magnetization to an increasing h_x at the critical point for $s = 0.8$. The robust power-law scaling over more than six decades allows us to extract $\delta = 9.2 \pm 0.3$ with high accuracy. The data collected from OBB calculations with different values of s in Fig. 12(e) indicate that δ closely follows the hyperscaling relation in Eq. (43).

In contrast to δ , we find the exponent δ' , corresponding to the h_z response, to be completely independent of the bath exponent s , having $\delta' = 1$ for all s at the LO–CR transition (not shown).

3. Correlation-length exponent ν

As described above, the crossover energy scale T^* characterizing the LO–CR transition is obtained by studying energy-flow diagrams close to the phase boundary. Figure 12(c) displays the extracted T^* for fixed $s = 0.875$ and $h_z = 0$, with clear power-law scaling being apparent over several decades. This allows us to extract ν with high accuracy by fitting. Figure 12(f) shows the s dependence of the exponent ν . Our results suggest that ν diverges both in the limit $s \rightarrow s^{*+}$ and $s \rightarrow 1^-$, in a manner reminiscent of the approach to a lower critical dimension. We have verified that the exponent ν is identical for both sides of the transition, i.e., independent of whether QC1 is approached from the LO or from the CR phase.

Generally, the computed values of ν take large values for the entire range of bath exponents. As previously discussed, this causes our VMPS calculations to require large chains ($N > 100$) in order to access the ultra-low-energy scales needed to accurately determine α_c .

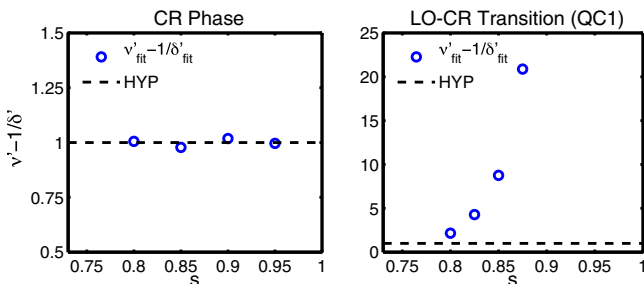


FIG. 13. (Color online) Hyperscaling relation (44) involving exponents ν' and δ' in the CR phase (a) and at LO–CR critical point (b). The numerical results (dots) are in reasonable agreement with the hyperscaling relation (dashed line) in the CR phase (a). At QC1, however, hyperscaling appears to be violated. Note that the dots show $\nu' - 1$, as we find that $\delta' = 1$ for all s .

4. Correlation-length exponent ν' , absence of hyperscaling, and field instability of QC1

A finite h_z applied at the zero-field critical coupling $\alpha_c(h_z = 0)$ places the system into the DE phase. The characteristic crossover scale T^* obtained from the energy-flow diagrams determines the critical exponent ν' , which only diverges in the limit $s \rightarrow 1^-$ but not for $s \rightarrow s^{*+}$, in contrast to ν . Most importantly, δ' and ν' in combination do not obey the hyperscaling relation (44), as illustrated in Fig. 13(b). Hence, our results suggest that QC1 obeys hyperscaling properties only in the absence of a transverse field h_z . The underlying reason for this exotic critical behavior is not understood.

We note that the values for ν' can be read off from Fig. 13(b) as $\delta' = 1$ for all s . They imply that $\nu > \nu'$ for $s^* < s \lesssim 0.83$ while $\nu < \nu'$ for $0.83 \lesssim s < 1$, i.e., the role of the leading relevant operator at QC1 changes at $s \approx 0.83$ [see Fig. 7(b)].

We have also investigated the flow *along* the separatrix between DE and LO at small h_z , in order to verify that QC1 is unstable along this separatrix, which implies that any finite-field transition is controlled by QC2. To this end, we first identify the stable energy-flow patterns corresponding QC1 and QC2 by placing the system at criticality for $h_z = 0$ (QC1) and sizable h_z (QC2) (see Fig. 14). Second, we study the energy-flow diagrams for parameters sets at criticality and

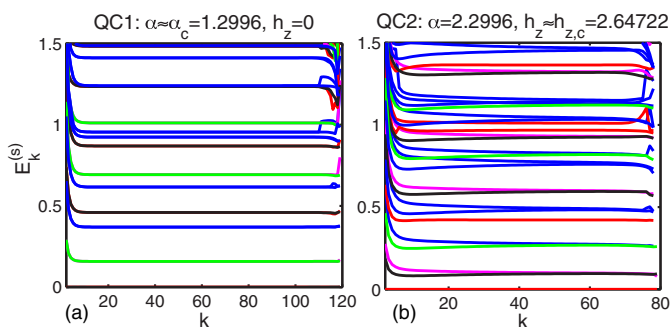


FIG. 14. (Color online) Energy-flow diagrams at QC1 (a) and QC2 (b). The two critical fixed points can be distinguished by noting the twofold ground-state degeneracy at QC1 that disappears at QC2 introducing a finite h_z .

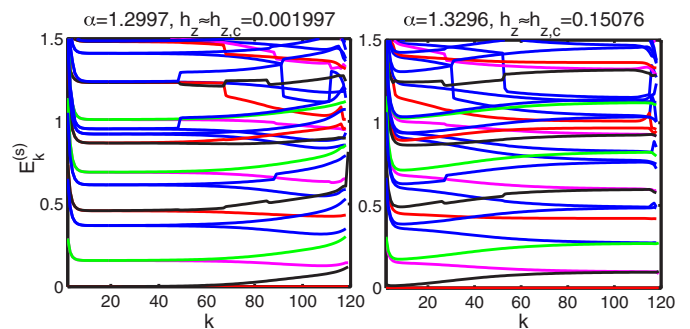


FIG. 15. (Color online) Two energy-flow diagrams for parameters located on the critical separatrix with small h_z , i.e., close to QC1. In both cases, the level energies clearly flow from QC1 at high energies to QC2 at low energies, thus confirming the instability of QC1.

very small h_z . As displayed in Fig. 15, we observe a clear flow from QC1 at high energies to QC2 at lower energies, thus confirming the schematic RG flow diagram in Fig. 7(b).

C. CR phase

We supplement the analysis of the critical phenomena of SBM2 by briefly elaborating on the properties of the impurity spin in the CR phase. Although an abridged version of the results has already been presented elsewhere [41], this section completes the picture and also includes a discussion on the validity of hyperscaling inside the CR phase.

1. Response exponents δ and δ'

The RG calculations around the free-spin fixed point, presented in Sec. V A, predict a nonlinear scaling of the magnetization in the CR phase [see Eqs. (51) and (54)]. Our numerical data confirm this nonlinear response, as illustrated in Figs. 16(a) for δ and in 16(b) for δ' at different values of s , α chosen close to the CR fixed point α^* . We find a clear power-law scaling over several decades. The extracted values for δ in Fig. 16(d) are perfectly consistent with the hyperscaling result (51), while those for δ' in Fig. 16(e) are in good agreement with the perturbative results for $s \rightarrow 1^-$. The small deviations of the numerical data from the RG calculations for larger values of $(1 - s)$ are expected since the higher-order contributions in Eq. (54) become more important.

2. Correlation-length exponent ν' and field instability of CR

The energy-flow diagrams (not shown) confirm that the CR phase is unstable w.r.t. a finite transverse field h_z , i.e., applying any finite h_z places the system into the DE phase. The corresponding crossover scale $T^*(h_z)$ between the CR and DE fixed points allows us to extract the correlation-length exponent ν' (28). The collected results for different s are displayed in Figs. 16(c) and 16(f), with ν' being in fair agreement with perturbative prediction in Eq. (53).

In contrast to QC1, where the hyperscaling relation (44) is not met by the numerical data, ν' and δ' obey hyperscaling in the critical phase, as depicted in Fig. 13(a).

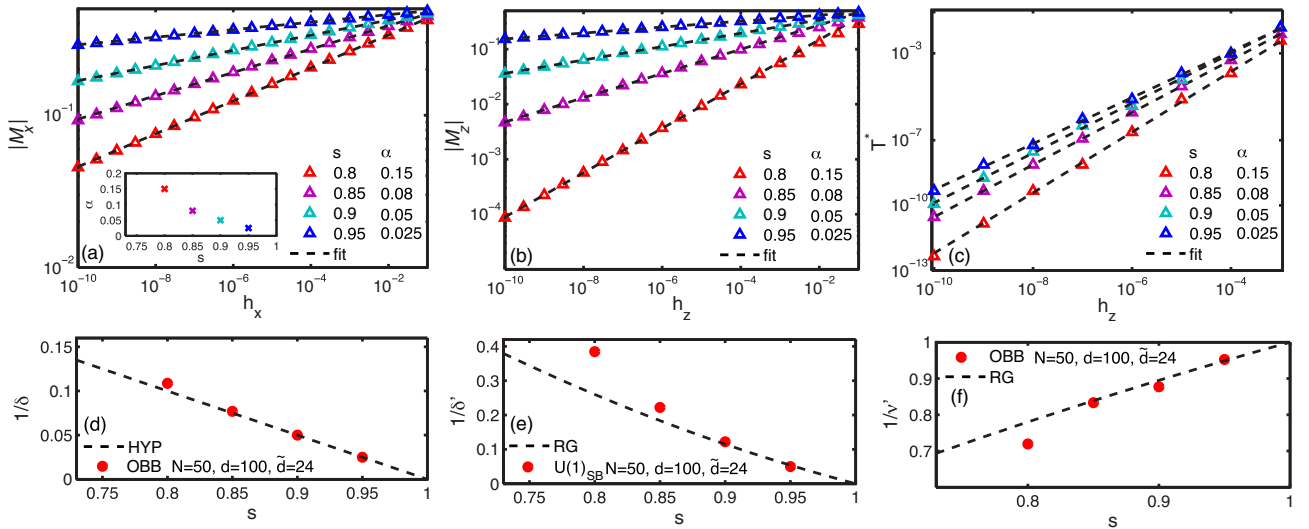


FIG. 16. (Color online) VMPS results for critical exponents δ , δ' , and ν' inside the CR phase for various s , with α chosen close to the CR fixed point α^* [$\alpha(s)$ displayed in inset of panel (a)]. The magnetization shows nonlinear behavior in response to h_x (a) and h_z (b). The exponents δ and δ' extracted from the power-law scaling are in good agreement with perturbative RG from Eqs. (51) and (54) in the limit of $s \rightarrow 1^+$, as illustrated in panels (d) and (e). The same applies for ν' computed from the vanishing crossover energy scale T^* in panel (c), which agrees with the RG prediction (53) for large values of the bath exponent s (f).

D. Phase-boundary exponent ψ

We have determined the location of the DE–LO phase boundary for small h_z , in order to extract the expected power-law behavior. Sample results for $s < s^*$, where the phase boundary starts at $\alpha = 0$, are shown in Fig. 17(a); they are in essentially perfect agreement with the analytical result $\psi = 1/(1-s)$ (48).

For $s^* < s < 1$, the phase boundary starts at the zero-field CR–LO transition at $\alpha = \alpha_c$, and thus determining ψ requires an accurate knowledge of α_c and is therefore rather time consuming. Sample results are in Fig. 17(b). A hyperscaling-based guess would be $\psi = \nu/\nu'$ which we find approximately fulfilled for $s = 0.825$ and 0.85 , but violated for $s = 0.875$. (Recall that the hyperscaling relation between ν' and δ' is violated as well.)

VII. CONCLUSIONS

Using the variational matrix-product-state approach, we have numerically determined the phase diagram of the U(1)-symmetric two-bath spin-boson model (SBM2), which is characterized by the phenomenon of frustration of decoherence. Our detailed study of the quantum phase transitions of SBM2, using both numerical and analytical techniques, has revealed that the transition between the localized and delocalized phases, accessed at finite transverse field, is in the universality class of the XY spin chain with long-ranged interactions and thus obeys a quantum-to-classical correspondence.

In contrast, the zero-field critical (intermediate-coupling) phase and its transition to the localized phase do not have a classical counterpart. Our numerical results for the critical exponents can serve as a guide for developing an analytical theory of the latter transition. Given that the relevant critical fixed point (QC1) approaches the localized fixed point (LO) as $s \rightarrow 1^-$, we believe that an expansion around LO akin to an expansion in $(2 + \epsilon)$ dimensions for classical magnets should be able to access the properties of QC1; this task is left for future work.

We recall that the analysis in this paper has been restricted to the model SBM2 with symmetric couplings, i.e., two identical baths and $\alpha_x = \alpha_y$. For asymmetric couplings, with finite $\Delta\alpha = \alpha_y - \alpha_x$, the behavior of the model is driven towards that of the one-bath model SBM1. Naturally, the LO phase now displays spontaneous Ising order, with the impurity spin localized in direction of the stronger coupled bath. Further, the CR phase is unstable against any finite $\Delta\alpha$. The rich and interesting crossover physics of SBM2 in the presence of small symmetry breaking is beyond the scope of this paper and will be discussed elsewhere.

Interesting open questions concern the finite-temperature behavior of SBM2, specifically the quantum critical finite- T

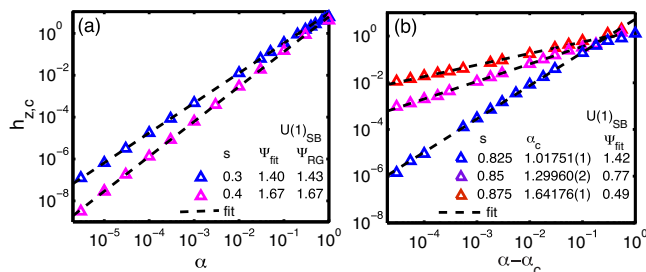


FIG. 17. (Color online) Numerical results for the DE–LO phase boundary at small h_z for selected values of the bath exponent s , obtained by U(1)_{SB} with $N = 50, \bar{d}_k = 24$ (a) and $N = 120, \bar{d}_k = 40$ (b). (a) Regime of $s < s^*$ where $h_{z,c} \propto \alpha^\psi$. (b) Regime of $s^* < s < 1$ where $h_{z,c} \propto (\alpha - \alpha_c)^\psi$. The power-law fits to determine the phase-boundary exponent ψ are shown by dashed lines.

susceptibilities and the residual entropy, as well as its equilibrium and nonequilibrium dynamics. Generalizations to three bosonic baths as well as combined fermionic and bosonic baths would be interesting as well. The former is linked to the problem of impurity spins in quantum critical magnets [32,37], and both occur in self-consistent single-site solutions for certain lattice models, e.g., in the large- N -based theory of a gapless spin liquid [54] and in more general extensions of dynamical mean-field theory [55].

In the quest for nontrivial quantum critical behavior, we believe that SBM2 presents, in a sense, the simplest quantum model violating the quantum-to-classical correspondence: It lives in $(0+1)$ dimensions and is constructed solely from bosonic degrees of freedom. Our analysis reveals that the violation of the quantum-to-classical correspondence is rooted in the noncommutativity of the spin components coupled to the two baths; this property of a quantum spin can also be rephrased as a spin Berry phase. We note that quantum phase transitions in quantum impurity models with *fermionic* baths frequently behave nonclassically, with the pseudogap Kondo and Anderson models [56,57] being well-studied examples. Here, the absence of a quantum-to-classical correspondence can be traced back to fermionic “signs,” i.e., exactly integrating out the fermionic bath is only possible at the expense of working with a fermionic impurity, which has no classical analog.

ACKNOWLEDGMENTS

We thank A. Alvermann, S. Florens, S. Kirchner, K. Ingersent, Q. Si, A. Schiller, and T. Vojta for helpful discussions. This research was supported by the Deutsche Forschungsgemeinschaft through the Excellence Cluster “Nanosystems Initiative Munich”, Grants No. SFB/TR 12, SFB 631, No. WE4819/1-1 (AW), and No. FOR 960, by the German-Israeli Foundation through Grant No. G-1035-36.14, and the NSF through Grant No. PHY05-51164.

APPENDIX A: SCALING HYPOTHESIS FOR QC1

Here, we sketch the use of the scaling hypothesis to deduce hyperscaling relations for QC1. The standard homogeneity law for the critical contribution to the free energy implies the scaling form

$$F_{cr}(\alpha, h_x, h_z, T) = T f_1(\Delta\alpha/T^a, h_x/T^b, h_z/T^c) \quad (\text{A1})$$

[recall that the problem at hand is effectively $(0+1)$ dimensional]. Here, $\Delta\alpha = \alpha - \alpha_c$ and h_z correspond to two operators which drive the system away from criticality, and f_1 is a scaling function. The definitions of the correlation-length exponents in Eqs. (27) and (28) lead to the identifications $a = 1/\nu$ and $c = 1/\nu'$.

Taking the derivative of Eq. (A1) w.r.t. h_x yields

$$M_x = T^{1-b} f_2(\Delta\alpha/T^a, h_x/T^b, h_z/T^c) \quad (\text{A2})$$

which can be cast into the forms

$$M_x = (\Delta\alpha)^{(1-b)/a} f_3(T^a/\Delta\alpha, T^b/h_x, T^c/h_z) \quad (\text{A3})$$

and

$$M_x = h_x^{(1-b)/a} f_4(T^a/\Delta\alpha, T^b/h_x, T^c/h_z). \quad (\text{A4})$$

Upon taking the limit $T \rightarrow 0$ in Eq. (A3), one deduces the order-parameter exponent as $\beta = (1-b)/a$; similarly Eq. (A4) yields $1/\delta = (1-b)/b$ or $b = \delta/(1+\delta)$. Using $a = 1/\nu$ then leads to $\beta = \nu/(1+\delta)$ which is consistent with the hyperscaling relations (42) and (43). Taking the second derivative of Eq. (A1) w.r.t. h_x yields χ_x and facilitates the identification $1-2b = -x$. Together with $b = \delta/(1+\delta)$ this yields $\delta = (1+x)/(1-x)$, consistent with the relations (41) and (43).

In full analogy, taking the derivative of Eq. (A1) w.r.t. h_z yields $1/\delta' = (1-c)/c$ or $c = \delta'/(1+\delta')$. Using $c = 1/\nu'$ finally gives $\nu' = 1/\delta' + 1$ which is Eq. (44). Taking the second derivative w.r.t. h_z yields $1-2c = -x'$ and then $\delta' = (1+x')/(1-x')$ which is Eq. (45). The hyperscaling relations (44) and (45) can also be applied in the CR phase where h_z corresponds to a relevant operator as well. Note that the nature of the exponent pair (ν, δ) is different from that of (ν', δ') : ν parametrizes the scaling dimension of $\Delta\alpha$ at criticality and δ the nonlinear response to a field conjugate to the order parameter. In contrast, ν' and δ' correspond to the scaling dimension of and the nonlinear response to the *same* field h_z .

APPENDIX B: FINITE-SIZE EFFECTS

As the numerical computations are done for finite Wilson chains, it is worth discussing finite-size effects arising from a finite chain length N . The most important effect of finite N is to induce a gap $\bar{\Delta}$ in the bath spectrum which scales as $\bar{\Delta} \propto \Lambda^{-N}$. While this gap has no effect in the DE phase, as its fixed point corresponds to $\alpha = 0$, it prevents true spontaneous symmetry breaking in the LO phase. However, this does not affect our calculations because, with increasing N , the finite correlation length induced by $\bar{\Delta}$ increases faster than the system size, such that the finite-size system “looks” ordered in the LO phase once N is sufficiently large.

Most problematic are finite-size effects in the CR phase. Here, $M = 0$ in the infinite-system limit, but a bath gap induces a finite residual magnetic moment scaling as [37] $M \propto \bar{\Delta}^{(1-x)/2}$, with x defined in Eq. (30). Indeed, our VMPS calculations in Fig. 5 find a small but finite magnetization. Figure 18 supports that M_x indeed vanishes in infinite-system

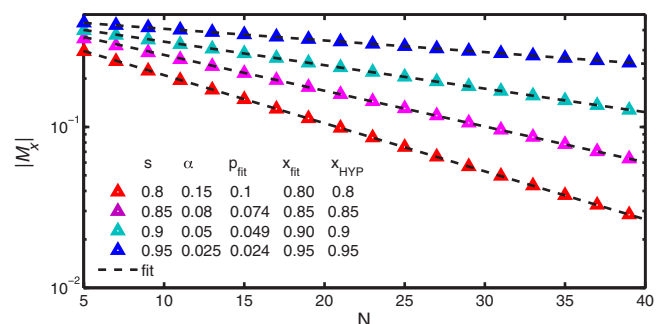


FIG. 18. (Color online) Finite-size scaling of M_x for different points close to the CR fixed point α^* . We observe that the magnetization decreases exponentially with system size. The small value of the decay exponent p results in a notable finite-size effects even for large systems [U(1)_{SB} with $N = 60, \bar{d}_k = 24$].

limit as

$$M_x \propto L^{-p} \propto (\Lambda^{-N})^p = e^{-\ln(\Lambda)pN}, \quad (\text{B1})$$

with the system size $L \sim \Lambda^N$ on a Wilson chain. Given that the exponent p governing the decrease of M_x is very small, the order parameter remains finite even for very large systems.

The fit exponent p allows us to extract the value of the exponent x in the CR phase according to $p = (1 - x)/2$. The values for x obtained in this way are indicated in Fig. 18 and are consistent with the hyperscaling result $x = s$ (see Sec. IV D). We note that a direct measurement of x at the various critical points is not easily possible using the present numerics, as (i) the variational approach is designed for $T = 0$ only, and (ii) the mass-flow problem [26] would prevent an accurate approach to critical points using chains of different length.

APPENDIX C: INFLUENCE OF TRUNCATION ERROR ON CRITICAL EXPONENTS

As numerical artifacts play an increasingly important role close to the critical phase, we found it to be essential to enforce the conservation of the U(1) symmetry when trying to access the critical properties of QC1 and QC2 for large bath exponents $s > 0.8$. Since the symmetry incorporation excludes employing a shifted OBB-VMPS calculation, it is fair to ask whether the bosonic truncation error corrupts the presented results of the critical exponent β .

Careful analysis revealed a similar situation as in the SBM1 [25], where the resulting critical exponents are only affected by the truncation error in the regime $s < \frac{1}{2}$. In the same fashion, Hilbert-space truncation in the SBM2 only influences the behavior of critical properties for $s < \frac{1}{2}$, as illustrated in Fig. 19. Comparing the scaling of the magnetization to

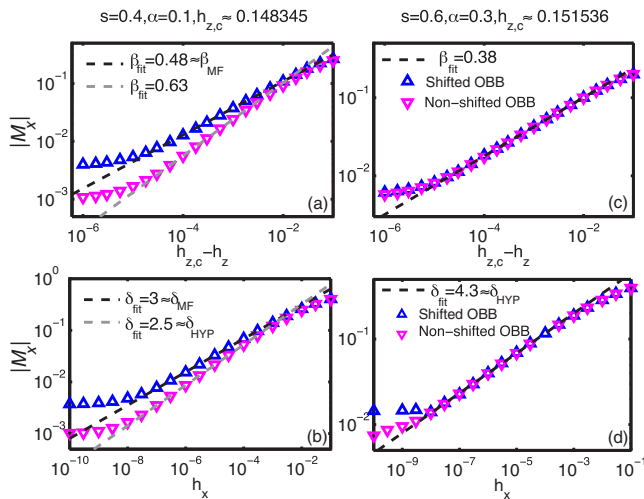


FIG. 19. (Color online) Influence of Hilbert-space truncation on critical exponents β and δ employing VMPS with (blue) and without shifted OBB (purple). Choosing $s = 0.4 < \frac{1}{2}$ in panels (a) and (b), we observe considerable deviations between both types of VMPS calculations where the mean-field prediction for β and δ is only obtained with a shifted OBB. In the case of $s > \frac{1}{2}$, both methods lead to similar results, as illustrated in panels (c) and (d) for the exponent $s = 0.6$ [OBB with $N = 60, \tilde{d}_k = 24$].

determine β and δ using VMPS calculations with and without shifted OBB reveals the characteristic difference between $s < \frac{1}{2}$ and $s > \frac{1}{2}$. In Figs. 19(a) and 19(b), we observe significant deviations between both types of calculations for $s = 0.4$. Employing the shifted OBB method, the resulting critical exponents are in good agreement with the mean-field predictions $\beta_{\text{MF}} = \frac{1}{2}$ and $\delta_{\text{MF}} = 3$, while VMPS calculations without shift lead to considerable deviations from the mean-field values. In contrast, considering a larger bath exponent $s = 0.6$, we clearly obtain the same results for both types of VMPS calculations, as illustrated in Figs. 19(c) and 19(d). Thus, for the evaluation of critical exponents we conclude the following: the shifted OBB is only strictly necessary for small bath exponents $s < \frac{1}{2}$, whereas for $s > \frac{1}{2}$ VMPS calculations with and without shifted OBB work equally well.

APPENDIX D: CALCULATION OF THE MAGNETIZATION IN THE U(1)-SYMMETRIC IMPLEMENTATION

The ground state of SBM2 in the LO phase with $h_x = h_y = 0$ exhibits a continuous degeneracy due to the inherent rotational symmetry, which was elaborated on in Sec. II C. When not enforcing the U(1) symmetry, the final ground state of a VMPS calculation spontaneously breaks this U(1) symmetry, while maximizing magnetization $M_x = M_y$ in the x and y directions in the localized phase (note that this is the least entangled state).

In contrast, for a U(1)-symmetric implementation, these expectation values vanish by construction. However, it is possible to attach a well-defined symmetry label ($q = \pm \frac{1}{2}$) to the numerical ground state. The two resulting states $|G_{\pm 1/2}\rangle$ form an orthonormal pair, which can be used to construct the space of all (symmetry-broken) ground states. By symmetry, the expectation value $\langle G_q | \sigma_{i=x,y} | G_{q'} \rangle$ evaluated using only one symmetry eigenstate $q = q'$ gives zero. To reconstruct the magnetization of the “original,” symmetry-broken ground state, we have to calculate the magnetization using nondiagonal elements $q \neq q'$ of the above-defined expectation value.

In general, this can be accomplished in two different ways. The simple but numerically expensive variant is to use two VMPS runs to obtain $|G_{+1/2}\rangle$ and $|G_{-1/2}\rangle$ separately for the same parameters and explicitly calculate $\langle G_{+1/2} | \sigma_{i=x,y} | G_{-1/2} \rangle$. Alternatively, we may borrow a concept of NRG that allows us to use only a single VMPS to determine the magnetization for a system with arbitrary Wilson chain length $0 < k < N$. Starting with the right-orthogonalized representation of either $|G_{+1/2}\rangle$ or $|G_{-1/2}\rangle$, we construct and diagonalize the left-block Hamiltonian $\hat{\mathcal{H}}_L^k$. After projecting into the subspace of the two lowest-lying energy states $|s_k\rangle$, with $s_k \in \{0, 1\}$,

$$|s_k\rangle = \sum_{n_1 \dots n_n} (A^{[\sigma]} A^{[n_1]} \dots A^{[n_n]})_s |n_1, n_2, \dots, n_n\rangle, \quad (\text{D1})$$

we explicitly determine all matrix elements $(M_i)_{s_k s'_k}^{[n]} \equiv \langle s_k | \sigma_{i=x,y} | s'_k \rangle_n$ of the magnetization. The eigenvalues of the 2×2 matrix $M_i^{[n]}$ give the two possible values of the magnetization of the system with chain length k in the ground state $\langle \sigma_{i=x,y} \rangle / 2 = \pm M_i$. Therefore, the plain thermal average

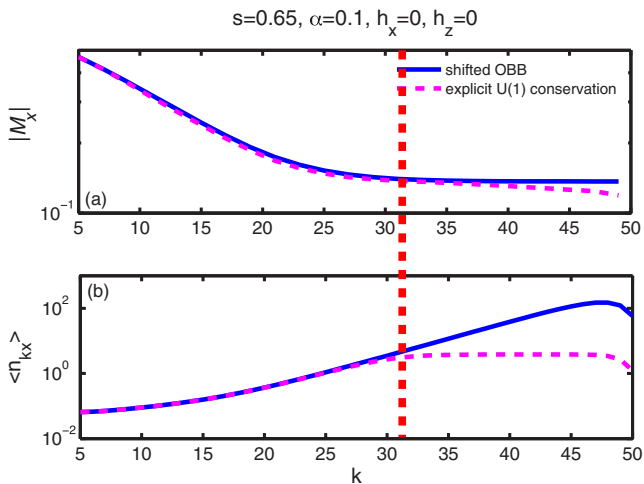


FIG. 20. (Color online) Influence of bosonic truncation error. Studying the finite-size scaling effects of the impurity magnetization in the localized phase, we clearly observe in (a) that the symmetry implementation is accompanied by a further downbending induced by reaching the maximum bosonic occupation numbers towards larger iterations.

without spontaneous symmetry breaking would result in zero magnetization.

Independently of how the magnetization is calculated, we face an additional challenge regarding the Hilbert-space

truncation error in the context of explicit symmetry implementation. Studying the finite-size scaling of the magnetization in the localized regime, we expect M_x to saturate at a finite value after an initial decay when moving towards larger systems. As illustrated in Fig. 20(a), our VMPS data for M_x indeed saturates as expected when symmetry is not enforced (solid line).

However, when employing the symmetry implementation we observe a further decrease (dashed line) after the saturation to an intermediate plateau. Considering the behavior of the bosonic occupation numbers on the Wilson chain in Fig. 20(b), we attribute this effect with the Hilbert-space truncation error. The difference between solid and dashed lines sets in once the bosonic occupation numbers $\langle n_{kx} \rangle$ for the symmetry-enforced implementation, where a shifted OBB cannot be used, begin to saturate [Fig. 20(b), dashed line], whereas those for non-symmetry-enforced implementation, for which a shifted OBB can be used, do not yet saturate [Fig. 20(b), solid line]. To circumvent this systematic error, we extract M_x not at the end of the chain but choose an iteration N^* right before $\langle n_{kx} \rangle$ saturates (indicated by the red dashed line in Fig. 20). At N^* , the magnetization from the symmetry-enforced code clearly agrees with a VMPS calculation using a shifted bosonic basis.

As indicated in the previous section, this approach is only appropriate for bath exponents $s > \frac{1}{2}$. For smaller values of s , it is absolutely necessary to employ VMPS with the shifted OBB scheme in order to capture the correct physical properties of the system.

-
- [1] A. C. Hewson, *The Kondo Problem to Heavy Fermions* (Cambridge University Press, New York, 1993).
 [2] P. Nozières and A. Blandin, *J. Phys. (Paris)* **41**, 193 (1980).
 [3] M. Vojta, *Philos. Mag.* **86**, 1807 (2006).
 [4] D. E. Logan, A. P. Tucker, and M. R. Galpin, *Phys. Rev. B* **90**, 075150 (2014).
 [5] A. Rosch, J. Paaske, J. Kroha, and P. Wölfle, *Phys. Rev. Lett.* **90**, 076804 (2003).
 [6] K. Wilson, *Rev. Mod. Phys.* **47**, 773 (1975).
 [7] R. Bulla, T. Costi, and T. Pruschke, *Rev. Mod. Phys.* **80**, 395 (2008).
 [8] W. J. de Haas, J. de Boer, and G. J. van den Berg, *Physica (Amsterdam)* **1**, 1115 (1934).
 [9] T. A. Costi, L. Bergqvist, A. Weichselbaum, J. von Delft, T. Micklitz, A. Rosch, P. Mavropoulos, P. H. Dederichs, F. Mallet, L. Saminadayar, and C. Bäuerle, *Phys. Rev. Lett.* **102**, 056802 (2009).
 [10] S. M. Cronenwett, T. H. Oosterkamp, and L. P. Kouwenhoven, *Science* **281**, 540 (1998).
 [11] D. Goldhaber-Gordon, H. Shtrikman, D. Mahalu, D. Abusch-Magder, U. Meirav, and M. A. Kastner, *Nature (London)* **391**, 156 (1998).
 [12] Y. Makhlin, G. Schön, and A. Shnirman, *Rev. Mod. Phys.* **73**, 357 (2001).
 [13] A. Garg, J. N. Onuchic, and V. Ambegaokar, *J. Chem. Phys.* **83**, 4491 (1985).
 [14] J. Bauer, C. Salomon, and E. Demler, *Phys. Rev. Lett.* **111**, 215304 (2013).
 [15] Y. Nishida, *Phys. Rev. Lett.* **111**, 135301 (2013).
 [16] A. J. Leggett, S. Chakravarty, A. T. Dorsey, M. P. A. Fisher, A. Garg, and W. Zwerger, *Rev. Mod. Phys.* **59**, 1 (1987).
 [17] S. K. Kehrein and A. Mielke, *Phys. Lett. A* **219**, 313 (1996).
 [18] R. Bulla, N.-H. Tong, and M. Vojta, *Phys. Rev. Lett.* **91**, 170601 (2003).
 [19] M. Vojta, N.-H. Tong, and R. Bulla, *Phys. Rev. Lett.* **94**, 070604 (2005).
 [20] K. Le Hur, P. Doucet-Beaupré, and W. Hofstetter, *Phys. Rev. Lett.* **99**, 126801 (2007).
 [21] A. Alvermann and H. Fehske, *Phys. Rev. Lett.* **102**, 150601 (2009).
 [22] A. Winter, H. Rieger, M. Vojta, and R. Bulla, *Phys. Rev. Lett.* **102**, 030601 (2009).
 [23] M. Vojta, N.-H. Tong, and R. Bulla, *Phys. Rev. Lett.* **102**, 249904(E) (2009).
 [24] C. Guo, A. Weichselbaum, J. von Delft, and M. Vojta, *Phys. Rev. Lett.* **108**, 160401 (2012).
 [25] M. Vojta, *Phys. Rev. B* **85**, 115113 (2012).
 [26] M. Vojta, R. Bulla, F. Güttge, and F. B. Anders, *Phys. Rev. B* **81**, 075122 (2010).
 [27] A. W. Chin, J. Prior, S. F. Huelga, and M. B. Plenio, *Phys. Rev. Lett.* **107**, 160601 (2011).
 [28] M. F. Frenzel and M. B. Plenio, *New J. Phys.* **15**, 073046 (2013).
 [29] M. E. Fisher, S. K. Ma, and B. G. Nickel, *Phys. Rev. Lett.* **29**, 917 (1972).
 [30] J. M. Kosterlitz, *Phys. Rev. Lett.* **37**, 1577 (1976).
 [31] E. Luijten and H. W. J. Blöte, *Phys. Rev. B* **56**, 8945 (1997).

- [32] A. M. Sengupta, *Phys. Rev. B* **61**, 4041 (2000).
- [33] L. Zhu and Q. Si, *Phys. Rev. B* **66**, 024426 (2002); G. Zaránd and E. Demler, *ibid.* **66**, 024427 (2002).
- [34] A. H. Castro Neto, E. Novais, L. Borda, G. Zaránd, and I. Affleck, *Phys. Rev. Lett.* **91**, 096401 (2003); E. Novais, A. H. Castro Neto, L. Borda, I. Affleck, and G. Zarand, *Phys. Rev. B* **72**, 014417 (2005).
- [35] D. V. Khveshchenko, *Phys. Rev. B* **69**, 153311 (2004).
- [36] V. N. Kotov, J. Oitmaa, and O. Sushkov, *Phys. Rev. B* **58**, 8500 (1998).
- [37] M. Vojta, C. Buragohain, and S. Sachdev, *Phys. Rev. B* **61**, 15152 (2000).
- [38] M. Kircan and M. Vojta, *Phys. Rev. B* **69**, 174421 (2004).
- [39] N. Andrei and C. Destri, *Phys. Rev. Lett.* **52**, 364 (1984).
- [40] A. M. Tsvelick and P. B. Wiegmann, *Z. Phys. B Condens. Matter* **54**, 201 (1984).
- [41] Supplemental Material to Ref. [24].
- [42] A. Weichselbaum, F. Verstraete, U. Schollwöck, J. I. Cirac, and J. von Delft, *Phys. Rev. B* **80**, 165117 (2009).
- [43] H. Saberi, A. Weichselbaum, and J. von Delft, *Phys. Rev. B* **78**, 035124 (2008).
- [44] R. Bulla, H.-J. Lee, N.-H. Tong, and M. Vojta, *Phys. Rev. B* **71**, 045122 (2005).
- [45] R. Žitko and T. Pruschke, *Phys. Rev. B* **79**, 085106 (2009).
- [46] C. Zhang, E. Jeckelmann, and S. R. White, *Phys. Rev. Lett.* **80**, 2661 (1998).
- [47] U. Schollwöck, *Ann. Phys. (NY)* **326**, 96 (2011).
- [48] A. Weichselbaum, *Ann. Phys. (NY)* **327**, 2972 (2012).
- [49] N. Goldenfeld, *Lectures on Phase Transitions and the Renormalization Group* (Westview Press, Boulder, CO, 1992).
- [50] Technically, the RG treatment requires the introduction of a renormalized running coupling. Its initial value is determined by the bare coupling and suitable powers of the ultraviolet cutoff scale, with details depending on the RG scheme. In our case, the cutoff is $\omega_c = 1$, and we can identify the initial value of the running coupling with the bare coupling.
- [51] T. Vojta (private communication).
- [52] M. Suzuki, *Prog. Theor. Phys.* **49**, 424 (1973); **49**, 1106 (1973); **49**, 1440 (1973).
- [53] A. M. Polyakov, *Phys. Lett. B* **59**, 79 (1975).
- [54] S. Sachdev and J. Ye, *Phys. Rev. Lett.* **70**, 3339 (1993).
- [55] Q. Si, S. Rabello, K. Ingersent, and J. L. Smith, *Nature (London)* **413**, 804 (2001); *Phys. Rev. B* **68**, 115103 (2003).
- [56] D. Withoff and E. Fradkin, *Phys. Rev. Lett.* **64**, 1835 (1990).
- [57] M. Vojta and L. Fritz, *Phys. Rev. B* **70**, 094502 (2004); L. Fritz and M. Vojta, *ibid.* **70**, 214427 (2004).

3.2 Anatomy of quantum critical wave functions in dissipative impurity problems

In the following article [BCBB⁺17], we investigate for the first time the detailed structure of many-body wavefunctions at a quantum critical point, using complementary numerical simulations based on a coherent-state expansion as well as MPS techniques.

Our extensive calculations demonstrate some salient features that are likely generic in other classes of quantum critical states, such as a universal decay of entanglement between an impurity and its bath, as well as strong fluctuations of the order parameter when the wavefunction is decomposed into a large set of classical-like configurations.

These results are relevant for a variety of physical fields, such as quantum critical matter, open quantum systems, strongly correlated materials, theoretical quantum optics, and circuit-QED.

P4 *Anatomy of quantum critical wave functions in dissipative impurity problems*

Z. Blunden-Codd, S. Bera, **B. Bruognolo**, N.-O. Linden, A. W. Chin, J. von Delft, A. Nazir, and S. Florens

[Phys. Rev. B 95, 085104 \(2017\)](#)

Anatomy of quantum critical wave functions in dissipative impurity problemsZach Blunden-Codd,^{1,2} Soumya Bera,³ Benedikt Bruognolo,^{4,5} Nils-Oliver Linden,⁴ Alex W. Chin,⁶
Jan von Delft,⁴ Ahsan Nazir,¹ and Serge Florens⁷¹*Photon Science Institute & School of Physics and Astronomy, University of Manchester, Oxford Road, Manchester M13 9PL, United Kingdom*²*Department of Physics, Imperial College London, London SW7 2AZ, United Kingdom*³*Max-Planck-Institut fuer Physik Komplexer Systeme, 01187 Dresden, Germany*⁴*Physics Department, Arnold Sommerfeld Center for Theoretical Physics, and Center for NanoScience, Ludwig-Maximilians-Universität, Theresienstrasse 37, 80333 München, Germany*⁵*Max-Planck-Institut ur Quantenoptik, Hans-Kopfermann-Strasse 1, 85748 Garching, Germany*⁶*Theory of Condensed Matter Group, University of Cambridge, J. J. Thomson Avenue, Cambridge, CB3 0HE, United Kingdom*⁷*Institut Néel, CNRS and Université Grenoble Alpes, F-38042 Grenoble, France*

(Received 7 August 2016; published 2 February 2017)

Quantum phase transitions reflect singular changes taking place in a many-body ground state; however, computing and analyzing large-scale critical wave functions constitutes a formidable challenge. Physical insights into the sub-Ohmic spin-boson model are provided by the coherent-state expansion (CSE), which represents the wave function by a linear combination of classically displaced configurations. We find that the distribution of low-energy displacements displays an emergent symmetry in the absence of spontaneous symmetry breaking while experiencing strong fluctuations of the order parameter near the quantum critical point. Quantum criticality provides two strong fingerprints in critical low-energy modes: an algebraic decay of the average displacement and a constant universal average squeezing amplitude. These observations, confirmed by extensive variational matrix-product-state (VMPS) simulations and field theory arguments, offer precious clues into the microscopics of critical many-body states in quantum impurity models.

DOI: [10.1103/PhysRevB.95.085104](https://doi.org/10.1103/PhysRevB.95.085104)**I. INTRODUCTION**

The understanding of critical phenomena in classical mechanics owes a great deal to the spatial representation of critical states, whereby the order parameter experiences statistical fluctuations on all length scales due to a diverging correlation length [1,2] at the critical temperature. This scale invariance property was the starting point for one of the most powerful tools in theoretical physics, the renormalization group, which allowed rationalization of classical criticality in terms of trajectories in the space of coupling constants [3]. Today, one frontier of research in critical phenomena lies in the quantum realm, where criticality may govern some of the most fascinating and complex properties found in strongly correlated materials or cold atoms [4,5]. One very fruitful approach is to consider quantum criticality in light of an effective classical theory in higher dimensions [5], combining spatial and temporal fluctuations within the path integral formalism. Quantum phase transitions are then probed through physical response functions that display a diverging correlation length in space-time. However, this point of view does not provide a full picture of the physics at play, especially since quantum criticality pertains to a singular change in a many-body ground state. Developing wave-function-based approaches to strong correlations is indeed a blossoming field, ranging from quantum chemistry [6] to quantum information [7,8], so that hopes are high that quantum critical states may be rationalized in a simpler way.

Our aim in this article is to directly study the quantum critical wave function of a simple toy model, the sub-Ohmic spin-boson Hamiltonian, and to unveil some salient fingerprints of criticality in its ground state. In this standard model, to be described in further detail below, a single quantized spin

interacts with a continuum of bosonic modes, with a spectrum of coupling constants that vanishes with a power law $s < 1$ at low energy. For this purpose, we shall use a combination of two numerically exact wave-function-based methods for quantum impurity models: a variational matrix-product-state approach (VMPS) [8–11] and the coherent-state expansion (CSE) [12–15]. VMPS is an abbreviation for the variational matrix-product-state (MPS) formulation of the density matrix renormalization group (DMRG), which has been established as a very powerful and flexible technique, also in the context of bosonic impurity models [11,16,17], and will be used as a reference. Its all-purpose character makes it hard, however, to rationalize the precise content of the wave function in simple physical terms. For this reason, we implement the CSE variationally, which amounts to expanding environmental states of the bath onto a discrete set of classical-like configurations, namely, coherent states of the bosonic states in the bath. (Note that an infinite discrete set is enough to ensure completeness of the coherent-state basis [18].) Thus, crucial aspects of quantum criticality can be directly inferred by reading-off the various superpositions of oscillator displacements that parametrize the set of coherent states.

For a given spin orientation of the impurity, we find that the distribution of displacements within the CSE wave function displays an emergent symmetry (between positive and negative values) in the critical domain. This implies that the average displacement decays to zero for low-energy critical modes, with a universal exponent controlled by the dynamical susceptibility. This behavior reflects the absence of spontaneous symmetry breaking and the fact that the magnetization order parameter directly couples to the bosonic displacement field. Hence the displacements of the oscillators in the critical many-body wave function vanish in average

at low energy. In addition, the CSE wave function indicates that the distribution of displacements admits a finite width at the quantum critical point (although its mean value vanishes algebraically for critical modes, as mentioned above). This observation translates physically the wide fluctuations of the order parameter that take place in the quantum critical regime in absence of ordering. At the level of the critical wave function, these effects amount to a finite average squeezing amplitude of the quantum critical modes (averaged over a logarithmic energy interval), which we show from field theory arguments to take a constant universal value.

For the spin-boson model, we demonstrate that both the MPS and CSE methodologies converge to the same results, both away from and at the critical point. We find that the number of coherent states required to capture quantum critical behavior on a reasonable energy range (at least three decades) is relatively large, of the order of a hundred. For this reason, recent investigations of the sub-Ohmic model with variational CSEs using fewer states [19,20] failed to grasp the critical exponents found in large-scale VMPS calculations [16,17]. In contrast to the usual Kondo problem associated with the Ohmic spin-boson model, the sub-Ohmic case is indeed governed by two energy scales in its delocalized phase, namely, the renormalized tunneling amplitude and the mass of a soft bosonic collective mode which drives the transition. Capturing the critical softening requires careful and extensive numerical simulations, as we shall show by benchmarking the VMPS and CSE against each other.

The paper is organized as follows. In Sec. II, we present the spin-boson model, its discretization on a Wilson energy mesh, and the variational solution of its many-body wave function using both MPS and CSE representations. The wave function obtained by CSE is displayed to guide physical intuition in the rest of the paper. Section III develops the necessary analytical work that relates the dynamical critical exponent of the spin susceptibility to two important features of the wave function: the average displacement of the environmental state and the average width (or squeezing amplitude). This allows us to elucidate the different behaviors of the wave function in both the noncritical delocalized phase and at the quantum critical point. Finally, Sec. IV shows numerical results from the VMPS and CSE approaches, finding excellent agreement between each other, as well as with analytical predictions. Appendix A provides details on our hierarchical algorithm devised to solve the CSE in a fast and reliable way.

II. GROUND-STATE WAVE FUNCTION OF THE SUB-OHMIC SPIN-BOSON MODEL

A. Model

Our study will be based on the spin-boson Hamiltonian [4,21–24] with Δ the quantum Larmor frequency of a two-level system described by Pauli matrices $\vec{\sigma}$:

$$H = \frac{\Delta}{2} \sigma_x - \frac{\sigma_z}{2} \sum_k g_k (a_k^\dagger + a_k) + \sum_k \omega_k a_k^\dagger a_k. \quad (1)$$

The bosonic spectrum assumes a pure power law with exponent $0 \leq s \leq 1$ up to a sharp high-energy cutoff ω_c ($\omega_c = 1$ in all

our numerical computations):

$$J(\omega) \equiv \sum_k \pi g_k^2 \delta(\omega - \omega_k) = 2\pi \alpha \omega_c^{1-s} \omega^s \theta(\omega) \theta(\omega_c - \omega). \quad (2)$$

The Ohmic case ($s = 1$) can be realized in the context of waveguide QED [25–28] by coupling a superconducting qubit to a high-impedance transmission line consisting of a uniform Josephson junction array. In principle, a precise tailoring of the capacitance network could allow the sub-Ohmic regime to be realized as well. In terms of quantum critical phenomena [29–33], the sub-Ohmic model with $0 \leq s < 1$ presents a continuous quantum phase transition at a critical coupling α_c between a localized phase (with $\langle \sigma_z \rangle \neq 0$ for $\alpha > \alpha_c$) and a symmetric phase (with $\langle \sigma_z \rangle = 0$ for $\alpha \leq \alpha_c$), which will be our focus.

B. Wilson discretization

The bosonic bath $J(\omega)$ is discretized in a logarithmic fashion using a Wilson parameter $\Lambda > 1$, first on the highest energy window close to the cutoff $[\Lambda^{-1}\omega_c, \omega_c]$, and then iteratively on successive decreasing energy intervals $[\omega_{n+1}, \omega_n]$ with $\omega_n = \Lambda^{-n} \omega_c$ [16,29,30]. This leads to the so-called star Hamiltonian, which involves the direct coupling of the spin to all bosonic modes (and not to a single site within an extended bosonic chain):

$$H_{\text{star}} = \frac{\Delta}{2} \sigma_x - \frac{1}{2} \sigma_z \sum_{n=0}^{+\infty} \frac{\gamma_n}{\sqrt{\pi}} [a_n^\dagger + a_n] + \sum_{n=0}^{+\infty} \xi_n a_n^\dagger a_n. \quad (3)$$

The impurity coupling strength reads

$$\gamma_n^2 = \int_{\omega_{n+1}}^{\omega_n} d\omega J(\omega) = 2\pi \alpha \frac{1 - \Lambda^{-(s+1)}}{s+1} \omega_c^2 \Lambda^{-n(s+1)}, \quad (4)$$

and the typical energy ξ_n in each Wilson shell is

$$\xi_n = \frac{1}{\gamma_n^2} \int_{\omega_{n+1}}^{\omega_n} d\omega \omega J(\omega) = \frac{s+1}{s+2} \frac{1 - \Lambda^{-(s+2)}}{1 - \Lambda^{-(s+1)}} \omega_c \Lambda^{-n}. \quad (5)$$

Note that the continuum limit is only recovered for $\Lambda \rightarrow 1$ and an infinite number of Wilson shells. However, in practice $\Lambda = 2$ will be used in the following, and 50 sites will be used for both the MPS and the CSE variational calculations. This standard choice of parameters offers a good compromise between energy resolution and numerical costs, but our techniques can be pushed in principle to smaller Λ values.

C. Variational matrix-product-states approach

One very successful approach that enables direct access to the ground-state wave function of a low-dimensional quantum system is the density matrix renormalization group (DMRG) [9,10]. Though originally developed in the context of one-dimensional real-space systems, the matrix-product-state formulation of this variational method (VMPS) has been established as indispensable tool also in the context of quantum impurity models [8,11,16,17].

Its application to the spin-boson model works as follows. First, the star Hamiltonian H_{star} is mapped on a truncated

Wilson chain, where the spin- $\frac{1}{2}$ impurity is coupled to a length- N tight-binding chain model whose hopping matrix elements decrease exponentially with site number k . Next, one initializes a random MPS for the Wilson chain Hamiltonian,

$$|\psi\rangle = \sum_{\sigma, \mathbf{m}} A^{[\sigma]} A^{[m_0]} A^{[m_1]} \dots A^{[m_N]} |\sigma\rangle |\mathbf{m}\rangle, \quad (6)$$

where $|\uparrow\rangle, |\downarrow\rangle$ represents the σ_z eigenstates of the impurity and $|\mathbf{m}\rangle = |m_0\rangle \dots |m_N\rangle$ describes boson number eigenstates in a truncated Fock basis, i.e., $\hat{m}_k |\mathbf{m}\rangle = m_k |\mathbf{m}\rangle$, with $m_k = 0, 1, \dots, d_k - 1$. The wave-function coefficient is split into a product of tensors $A^{[\dots]}$, which are iteratively varied with respect to the energy for finding the best approximation for the ground-state wave function. If the parameters such as the bond dimension D and the Fock-space dimension d_k are chosen appropriately large, the algorithm converges the MPS to a numerically quasixact representation of the ground-state wave function. In practice, we use an optimal boson basis [16,17] mapping the local Fock basis $|m_k\rangle$ to a smaller, effective bosonic basis $|\tilde{m}_k\rangle$ for efficiency reasons. Good convergence is ensured for the delocalized phase and at the quantum critical point for $D = 60$, $d_k = 100$, and $\tilde{d}_k = 16$.

D. Coherent-state expansion

1. General methodology

More recently, an alternative representation of bosonic environmental wave functions was proposed [12,13] based on a simple physical picture of the energy landscape in terms of classical-like configurations. These are parametrized by multimode coherent states, $|\pm f^{(m)}\rangle = e^{\pm \sum_k f_k^{(m)} (a_k^\dagger - a_k)} |0\rangle$, with $f_k^{(m)}$ the displacement of mode k for the m th variational coherent state. Note that the index k labels momentum, while the index $m = 1 \dots M_{cs}$ represents an optimal choice of a set of discrete coherent states which embodies a complete basis for an infinite number of coherent states, $M_{cs} \rightarrow \infty$ [18]. The expansion for the many-body ground-state wave function |GS) reads

$$|\text{GS}\rangle = \sum_{m=1}^{M_{cs}} [p_m |f^{(m)}\rangle |\uparrow\rangle + q_m |h^{(m)}\rangle |\downarrow\rangle], \quad (7)$$

with the normalization $\langle \text{GS} | \text{GS} \rangle = 1$. Here, p_m and q_m characterize the weight of the different coherent-state components within the ground-state wave function for each spin orientation. The discrete sum over the index m can thus be interpreted as an optimal discretization of the multidimensional integral involved in the standard overcomplete Glauber-Sudarshan representation [18] in terms of continuously varying displacement functions. We find in practice that the coherent-state representation does not show signs of this overcompleteness once the wave function is developed on a discrete sum of coherent states, as in Eq. (7), and if the number of coherent states M_{cs} is typically much less than the number of states in the Hilbert space required to capture the ground state (which corresponds to the usual application of the method). There is, of course, a trivial redundancy when reshuffling the indices m of the set of coherent states for a given solution, but apart from this, we usually find a single global minimum in the variational procedure (although the local minima tend

to cluster in energy when more and more states are added). Thus, the full many-body ground state of the spin-boson model can be interpreted physically based on the optimal variational state, a path that we will follow here. We have also developed a hierarchical algorithm for the optimization of the systematic variational state (7), see Appendix A.

For the spin-boson model without any magnetic field along σ_z and in absence of spontaneous symmetry breaking (which occurs for $\alpha > \alpha_c$), the system obeys a \mathbb{Z}_2 symmetry, so that the parameters for the ground state satisfy exactly $p_m = -q_m$ and $f_k^{(m)} = -h_k^{(m)}$ for all k and m . This method was thoroughly tested for the Ohmic spin-boson model ($s = 1$) [12,13], where extremely rapid convergence was established for a moderate number of coherent states $M_{cs} \lesssim 10$, unless one considers the deep Kondo regime where $\alpha \rightarrow 1$.

2. Full many-body wave function

We show in Fig. 1 typical wave functions obtained with the CSE near the quantum critical point (for two bath exponents $s = 0.3$ and $s = 0.8$). Here the set of displacements $f_n^{(m)}$ for each oscillator mode a_n^\dagger is plotted versus the frequency ω_n of the mode, with $m = 1 \dots M_{cs}$ the index in the expansion (the corresponding weights p_m are shown in the Appendix). In both plots, the critical domain lies roughly for frequencies in the range $10^{-4} < \omega_n < 10^{-2}$, which shows two striking observations. First, the distribution of displacements looks very symmetric between positive and negative values of the set of $f_n^{(m)}$, both in the critical regime, and in the region of runaway

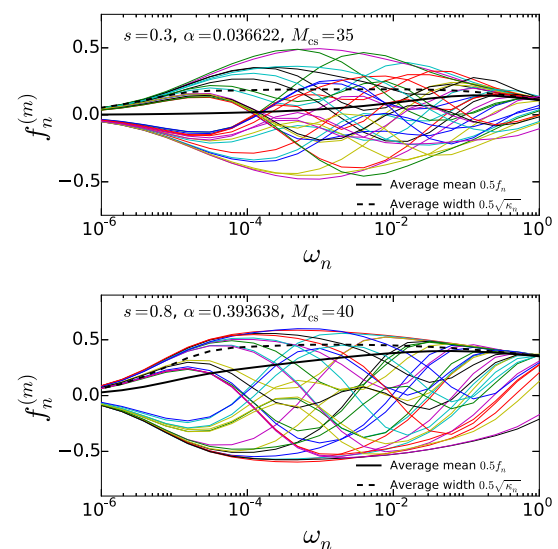


FIG. 1. Nearly critical wave functions from the CSE for the case $s = 0.3$ (upper panel) and $s = 0.8$ (lower panel), represented by the set of displacements $f_n^{(m)}$ with $m = 1 \dots M_{cs}$ given by the thin full lines. Thick full lines show the average mean displacement $0.5 f_n$, and thick dashed lines the average width $0.5\sqrt{\kappa_n}$. The critical regime is identified in the range $10^{-4} < \omega_n < 10^{-2}$ by a constant plateau in κ_n , which reflects the clearly wide distribution of the displacements associated to the classical-like configurations of the CSE. For frequencies $\omega \ll 10^{-4}$, the wave function is no more critical and the displacements collapse onto a single curve, so that the distribution narrows, and κ_n goes to zero.

flow $\omega_n < 10^{-4}$ at lower energy. This symmetry is clearly not obeyed for the high-energy modes near the cutoff. Because the displacement operator directly couples to the order parameter σ_z in the Hamiltonian (1), this symmetry nicely reflects the absence of spontaneous symmetry breaking at the critical point. This observation can be substantiated mathematically by defining, from the star Hamiltonian (3), the average f_n of the displacement fields in mode n (see Sec. III for a thorough discussion):

$$f_n \equiv \langle (a_n^\dagger + a_n)\sigma_z \rangle \\ = 2 \sum_{m,m'}^{MCS} p_m p_{m'} \langle f^{(m)} | f^{(m')} \rangle (f_n^{(m)} + f_n^{(m')}). \quad (8)$$

The absence of spontaneous symmetry breaking, both at the critical point and in the whole delocalized phase, translates in the fact that the average value f_n vanishes for $\omega_n \rightarrow 0$. However, the set of displacements in the noncritical domain ($\omega_n < 10^{-4}$) obey a trivial symmetry, as all displacements collapse on a single curve. In contrast, the displacements in the critical range $10^{-4} < \omega_n < 10^{-2}$ keep fluctuating, showing a finite width of the distribution. This width κ_n can be defined as follows:

$$\kappa_n \equiv \langle (a_n^\dagger + a_n)^2 \rangle - 1 \\ = 2 \sum_{m,m'}^{MCS} p_m p_{m'} \langle f^{(m)} | f^{(m')} \rangle (f_n^{(m)} + f_n^{(m')})^2. \quad (9)$$

This plateau in κ_n , seen in the critical domain, has for origin the strong quantum fluctuations that take place at criticality due to an order parameter that is nearly but not quite localized. Alternatively, the width κ_n can be interpreted as a squeezing parameter for the mode a_n^\dagger .

Having clarified the physics at play in the wave function itself, we will study these two coarse-grained quantities f_n (average) and κ_n (width), which capture mathematically the distribution of classical configurations in the wave function. This study will rely not only on the CSE variational state, but also on VMPS calculations for benchmark, and on analytical field theory calculations, which we present now.

III. ANALYTICAL INSIGHTS INTO VARIOUS WAVE-FUNCTION PROPERTIES

We establish in this section a set of exact analytical results for various wave-function properties, both in the noncritical and in the critical regimes. The properties that we will consider concern the average displacement of the bath oscillators, as well as their squeezing amplitude, which can be interpreted as the variance of the oscillator displacements. These two quantities thus give interesting information on the structure of the environmental wave function.

A. Average displacement

1. General formula

Owing to the linear coupling between σ_z and the oscillator displacement operator $(a_k^\dagger + a_k)$, correlations are established between the spin degree of freedom and its bosonic environ-

ment. Due to the symmetry properties of Hamiltonian (1), the ground-state wave function can be written generically as $|\text{GS}\rangle = |\uparrow\rangle|\Psi_\uparrow\rangle - |\downarrow\rangle|\Psi_\downarrow\rangle$, where $|\Psi_\downarrow\rangle = \hat{P}|\Psi_\uparrow\rangle$, with the parity operator $\hat{P} = \exp(i\pi \sum_k a_k^\dagger a_k)$. Thus, except for the trivial noninteracting case $\alpha = 0$ where the environmental wave function is in the bare vacuum, the qubit does not factorize from its environment. The manner in which correlations in $|\Psi_\uparrow\rangle$ penetrate the bath states can be viewed equally as properties of a screening cloud [15,28]. One goal of this paper is to illustrate the behavior of this screening cloud in the sub-Ohmic model, both away from and at the quantum critical point. Since the environmental wave function $|\Psi_\uparrow\rangle$ is a complicated object, the simplest measure of the cloud resides in the average displacement f_k that is obeyed by a given but arbitrary mode a_k^\dagger within this state. This quantity is defined as $f_k \equiv \langle (a_k^\dagger + a_k)\sigma_z \rangle$, where the average is taken with respect to the full many-body ground state $|\text{GS}\rangle$. The average displacement f_k thus gives information on how strong the order parameter fluctuates at the energy scale ω_k .

Now, we would like to show that this average displacement can be related exactly to the spin-spin equilibrium correlation function, defined in imaginary time as

$$\chi(\tau) = \langle \text{GS} | T_\tau \frac{\sigma_z(\tau) \sigma_z(0)}{2} | \text{GS} \rangle, \quad (10)$$

with T_τ the standard time-ordering operator, so that $T_\tau A(\tau)B(0) = \theta(\tau)A(\tau)B(0) + \theta(-\tau)B(0)A(\tau)$. The imaginary-time evolved operators read $A(\tau) = e^{H\tau} A e^{-H\tau}$. For the purpose of computing f_k , let us introduce the mixed correlation function between the spin and the displacement operator associated to a given bosonic k mode:

$$G_{z,k}(\tau) \equiv \langle \text{GS} | T_\tau [a_k^\dagger(\tau) + a_k(\tau)] \sigma_z(0) | \text{GS} \rangle, \quad (11)$$

so that $f_k = G_{z,k}(0^+)$. Taking the time derivative in Eq. (11), one gets the equations of motion:

$$\frac{\partial^2}{\partial \tau^2} G_{z,k}(\tau) = \omega_k^2 G_{z,k}(\tau) - 4g_k \omega_k \chi(\tau). \quad (12)$$

Now, going to zero temperature (but the formula below applies as well to finite temperature using discrete Matsubara frequencies), with $G(i\omega) = \int_{-\infty}^{+\infty} dt G(\tau) e^{i\omega t}$, one obtains the exact relation:

$$G_{z,k}(i\omega) = \frac{4g_k \omega_k}{\omega^2 + \omega_k^2} \chi(i\omega). \quad (13)$$

Going back to the time domain, one finds the connection between the average displacement of the environmental wave function (the screening cloud) and the local spin susceptibility:

$$f_k = \int \frac{d\omega}{2\pi} G_{z,k}(i\omega) = 4g_k \omega_k \int \frac{d\omega}{2\pi} \frac{1}{\omega^2 + \omega_k^2} \chi(i\omega). \quad (14)$$

From this equation, previous knowledge obtained for spin dynamics of the sub-Ohmic model [29,30,33] will allow us to make exact predictions for the average displacement characterizing the screening cloud.

2. Asymptotic behavior of the average displacement

A change of variable in Eq. (14) gives

$$f_k = 4g_k \int \frac{dx}{2\pi} \frac{1}{x^2 + 1} \chi(i\omega_k x), \quad (15)$$

so that the small-momentum behavior of f_k is determined by the low-energy scaling of the spin-spin correlation function [29,30,33], which reads $\chi(i\omega) \simeq 1/(m_R + B_s|\omega|^s)$, with $B_s = 4\alpha\omega_c^{1-s} \int dx x^{s-1}/(1+x^2)$. Here m_R is the renormalized mass, which is finite in the delocalized phase ($\alpha < \alpha_c$) and vanishes at the quantum critical point. Thus, two scaling laws are established in the limit $k \rightarrow 0$:

$$f_k \simeq \frac{2g_k}{m_R} \text{ for } \alpha < \alpha_c, \quad (16)$$

$$f_k \simeq \frac{4A_s}{B_s} \frac{g_k}{|\omega_k|^s} \text{ for } \alpha = \alpha_c, \quad (17)$$

where $A_s = \int (dx/2\pi)x^{-s}/(1+x^2)$. Let us now specialize to the case of the Wilson energy discretization on the grid $\omega_n = \omega_c \Lambda^{-n}$, in which case ω_k is replaced by $\xi_n \propto \Lambda^{-n} \propto \omega_n$ and g_k by $\gamma_n/\sqrt{\pi} \propto \Lambda^{-n(s+1)/2} \propto \omega_n^{(s+1)/2}$. We thus find the following low-energy scaling laws of the average displacement for the modes obeying the Wilson energy discretization:

$$f_n \propto \omega_n^{(1+s)/2} \text{ for } \alpha < \alpha_c, \quad (18)$$

$$f_n \propto \omega_n^{(1-s)/2} \text{ for } \alpha = \alpha_c. \quad (19)$$

The noncritical modes thus follow a different and faster power law than the critical ones, a result that we shall confirm from our numerics in Sec. IV. In fact, our low-frequency analysis allows us to extract the exact prefactor of the critical average displacement. At $\alpha = \alpha_c$, we find

$$f_n = \frac{\sqrt{2}(s+2)^s (1 - \Lambda^{-(s+1)})^{s+\frac{1}{2}} \tan \frac{\pi s}{2}}{\pi \sqrt{\alpha} \omega_c^{\frac{1-s}{2}} (s+1)^{s+\frac{1}{2}} (1 - \Lambda^{-(s+2)})^s} \omega_n^{\frac{1-s}{2}}. \quad (20)$$

The prefactor is clearly nonuniversal, as a dependence in the frequency cutoff ω_c is present.

B. Average width (squeezing amplitude)

1. General formula

Generalizing the previous results, we define the average intramode squeezing amplitude as $\kappa_k \equiv \langle (a_k^\dagger + a_k)^2 \rangle - 1$, such that it is exactly zero for a vacuum state. Following the previous methodology, we introduce the intermode Green's function of the displacement field of the bosonic modes:

$$G_{k,q}(\tau) \equiv \langle \text{GS} | T_\tau [a_k^\dagger(\tau) + a_k(\tau)] [a_q^\dagger(0) + a_q(0)] | \text{GS} \rangle. \quad (21)$$

Applying the time derivative twice provides exact equations of motion, which lead to the following formula in the Matsubara domain:

$$G_{k,q}(i\omega) \equiv G_k^0(i\omega)\delta_{k,q} + g_k g_q G_k^0(i\omega)G_q^0(i\omega)\chi(i\omega), \quad (22)$$

where $G_k^0(i\omega) = 2\omega_k/(\omega^2 + \omega_k^2)$. This gives the exact equation relating the average squeezing parameter to the dynamical

spin-spin susceptibility:

$$\kappa_k = \int \frac{d\omega}{2\pi} G_{k,k}(i\omega) - 1 = 4g_k^2 \omega_k^2 \int \frac{d\omega}{2\pi} \frac{1}{(\omega^2 + \omega_k^2)^2} \chi(i\omega). \quad (23)$$

Again, knowledge of the spin dynamics will give information on the average squeezing parameter for the ground-state wave function.

2. Asymptotic behavior of the average squeezing

Similar to our analysis of the average displacement, a change of variable in Eq. (23) gives

$$\kappa_k = \frac{4g_k^2}{\omega_k} \int \frac{dx}{2\pi} \frac{1}{(x^2 + 1)^2} \chi(i\omega_k x), \quad (24)$$

resulting in the following low-energy leading-order behavior of the average squeezing amplitude:

$$\kappa_k \simeq \frac{g_k^2}{m\omega_k} \text{ for } \alpha < \alpha_c, \quad (25)$$

$$\kappa_k \simeq \frac{4C_s}{B_s} \frac{g_k^2}{|\omega_k|^{1+s}} \text{ for } \alpha = \alpha_c, \quad (26)$$

where $C_s = \int (dx/2\pi)x^{-s}/(1+x^2)^2$. In the case of the Wilson energy discretization on the grid $\omega_n = \omega_c \Lambda^{-n}$, we get the explicit scaling laws for the average squeezing amplitude:

$$\kappa_n \propto \omega_n^s \text{ for } \alpha < \alpha_c, \quad (27)$$

$$\kappa_n = \text{const. for } \alpha = \alpha_c.$$

We find a constant and universal (cutoff independent) value of κ_n at the quantum critical point, as a precise computation of the constant value for $\alpha = \alpha_c$ reads

$$\kappa_n = \frac{(s+2)^{s+1} (1 - \Lambda^{-(s+1)})^{s+2} \tan \frac{\pi s}{2}}{\pi (s+1)^{s+1} (1 - \Lambda^{-(s+2)})^{s+1}}. \quad (28)$$

Since the average displacement f_n vanishes at low energy, this means that the distribution of displacements of the critical wave function is very broad, reflecting the strong fluctuations of the order parameter at the quantum critical point. We stress that κ_n , defined as (10), strictly vanishes in the continuum limit $\Lambda \rightarrow 1$ but that it remains finite when integrated over a logarithmic energy mesh.

IV. NUMERICAL RESULTS

A. General scaling behavior

We start by presenting general VMPS calculations, allowing us to outline the scaling behavior and the quantum criticality of the sub-Ohmic spin-boson model. We shall consider two different values of the bath spectral density throughout the paper, $s = 0.3$ and $s = 0.8$. The former corresponds to the case where the quantum phase transition is of mean-field type, while the latter case is associated to an interacting fixed point [29–32]. We stress beforehand that both the average displacement f_n and average squeezing amplitude κ_n are exactly related to the dynamical susceptibility from Eqs. (14) and (23), so that their scaling behavior as a function

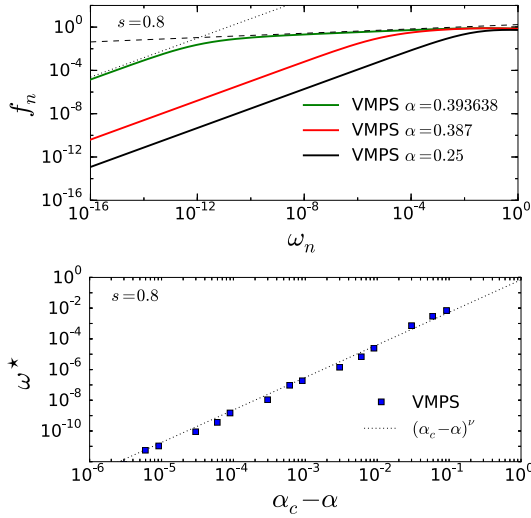


FIG. 2. The upper panel shows the average displacement $f_n = \langle (a_n^\dagger + a_n)\sigma_z \rangle$ from the VMPS calculation at $s = 0.8$, for three values of $\alpha = 0.25, 0.387, 0.393638$. (The last value is very close to the quantum critical interaction strength α_c .) The dotted line denotes the noncritical scaling $f_n \propto \omega_n^{(1+s)/2}$ for $\omega \ll \omega^*$, while the dashed line indicates the expected critical behavior $f_n \propto \omega_n^{(1-s)/2}$ for $\omega^* \ll \omega \ll \omega_c$. The crossover scale ω^* between the two scaling behaviors is shown in the lower panel for a large selection of α values, allowing us to extract the correlation length exponent $\nu \simeq 0.47$ for $s = 0.8$. This value is quite different from the mean-field result $\nu_{\text{MF}} = 1/s = 1.25$, because the system lies below its upper critical dimension [29,30].

of momenta, both in the noncritical and critical regimes, is determined by a trivial s -dependent exponent.

However, nontrivial exponents in the interacting case $0.5 < s < 1$ will show up in the α dependence of the correlation length ξ that is defined by the spatial extent up to which quantum critical fluctuations penetrates within the bath states. More precisely, the correlation length is given by an inverse energy $\xi = 1/\omega^*$, where ω^* is such that quantum critical behavior is established for $\omega^* \ll \omega_k \ll \omega_c$. (This regime sets in only if α is quite close to α_c .) This correlation length behaves as $\xi \propto |\alpha_c - \alpha|^{-\nu}$, with the exponent $\nu_{\text{MF}} = 1/s$ in the mean-field regime $0 < s < 1/2$. This can be gathered from the low-energy behavior $\chi(i\omega) \simeq 1/(m_R + B_s|\omega|^s)$ and the absence of singular vertex corrections at mean-field level, giving the renormalized mass $m_R \propto \alpha_c - \alpha$. However, ν assumes nontrivial values given by a classical long-range Ising model [29,30] for the interacting regime $1/2 < s < 1$. This behavior is illustrated in the lower panels of Figs. 2 and 3. Thus, both the average displacement and average squeezing amplitude (not shown here) encode nontrivial exponents for $1/2 < s < 1$, but only due to the divergent correlation length $\xi = 1/\omega^*$. These observations can be also summed up by scaling laws:

$$f_n = \omega_n^{(1-s)/2} F(\omega_n/\omega^*), \quad (29)$$

$$\kappa_n = K(\omega_n/\omega^*), \quad (30)$$

with $F(x), K(x) \propto 1$ for $x \gg 1$, and $F(x), K(x) \propto x^s$ for $x \ll 1$. This general scaling behavior of the average displacement

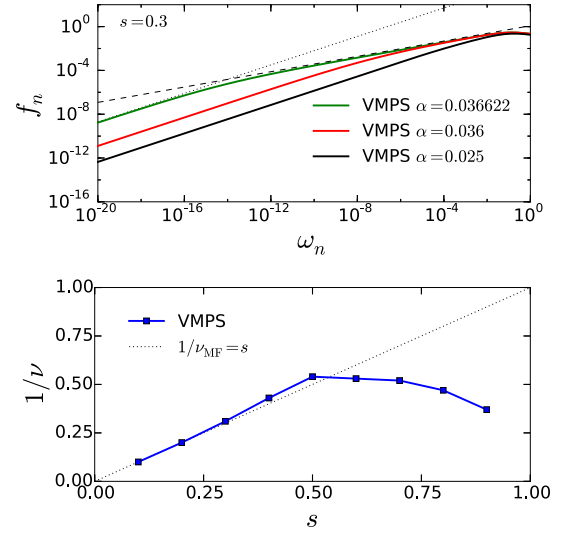


FIG. 3. The upper panel shows, similarly to Fig. 2, the average displacement, but now for $s = 0.3$, with $\alpha = 0.0326, 0.036, 0.036622$. (The last value is very close to the quantum critical point.) The dotted line shows the noncritical scaling $f_n \propto \omega_n^{(1+s)/2}$, while the dashed line indicates the expected critical quantum behavior $f_n \propto \omega_n^{(1-s)/2}$. The lower panel shows the extracted correlation length exponent ν for various values of s , which assumes the mean-field prediction $\nu_{\text{MF}} = 1/s$ only for $0 < s < 1/2$.

is illustrated in the upper panel of Fig. 2 for $s = 0.8$ and in the upper panel of Fig. 3 for $s = 0.3$. We find indeed that our VMPS data exhibits the expected noncritical and critical scaling laws, respectively $f_n \propto \omega_n^{(1+s)/2}$ for $\alpha \ll \alpha_c$ (dotted line) and $f_n \propto \omega_n^{(1-s)/2}$ for $\alpha = \alpha_c$ (dashed line). We now turn to a more detailed analysis, with a comparison to our analytical predictions, and with the numerics from the coherent-state expansion.

B. Noncritical regime

Let us now investigate the noncritical regime, which is established either for $\alpha \ll \alpha_c$ at all frequencies, or for $\alpha \simeq \alpha_c$ but for $\omega \ll \omega^*$. Focusing first on the average displacement, we consider in Fig. 4 the two cases $s = 0.3$ and $s = 0.8$ for values of α that are sufficiently away from α_c so that critical behavior is not triggered. The comparison between the fully converged VMPS data and CSE at increasing number M_{cs} of coherent states shows that the CSE converges very quickly in this simplest noncritical regime. In addition, the CSE captures the exact leading behavior of the average displacement, $f_n \propto \omega_n^{(1+s)/2}$, already for $M_{\text{cs}} = 1$ (the so-called Silbey-Harris theory [34–36]), since the variational equation gives $f_k = (g_k/2)/(\omega_k + \Delta_R) \propto g_k/\Delta_R$ for $k \rightarrow 0$, in agreement with the exact result (16). Note that the quantum critical scaling $f_n \propto \omega_n^{(1-s)/2}$ is not apparent in this plot because the α value is too far away from α_c .

Turning to the average squeezing amplitude, we find excellent agreement of our converged CSE results to the expected noncritical scaling behavior $\kappa_n \propto \omega_n^s$ (see Fig. 5). However, we observe a much slower convergence of the CSE for the average squeezing amplitude as compared to

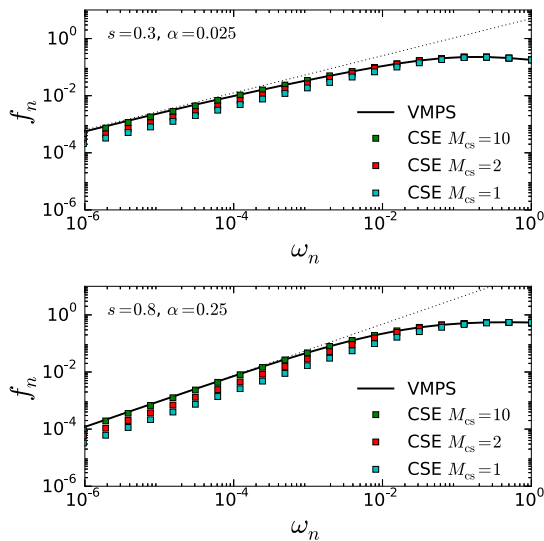


FIG. 4. Average displacement f_n of mode a_n^\dagger in the noncritical regime ($\alpha \ll \alpha_c$) for two values of the bath spectra, $s = 0.3$ (top panel, with $\alpha = 0.025$) and $s = 0.8$ (bottom panel, with $\alpha = 0.25$). The full black line denotes the fully converged VMPS results, while the colored symbols show the CSE at increasing number of coherent states, $M_{cs} = 1, 2, 10$ (bottom to top). A dotted line denotes the expected $f_n \propto \omega_n^{(1+s)/2}$ behavior in the noncritical regime.

the computation of the average displacements in Fig. 4, especially regarding the low-energy modes. This behavior can be understood from the Silbey-Harris theory at $M_{cs} = 1$, which predicts incorrectly $\kappa_n = (f_n)^2 \propto \omega_n^{1+s}$ instead of the exact noncritical scaling $\kappa_n \propto \omega_n^s$. This disagreement is not

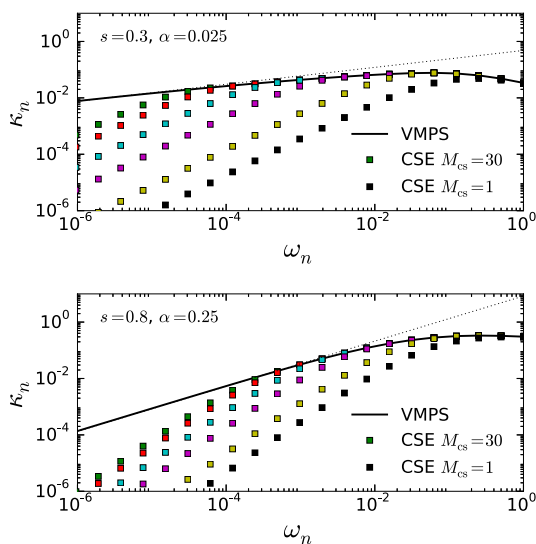


FIG. 5. Average squeezing amplitude κ_n of mode a_n^\dagger in the noncritical regime ($\alpha \ll \alpha_c$) for two values of the bath spectra, $s = 0.3$ (top panel, with $\alpha = 0.025$) and $s = 0.8$ (bottom panel, with $\alpha = 0.25$). The full black line denotes the fully converged VMPS results, while the colored symbols show the CSE at increasing number of coherent states, $M_{cs} = 1, 2, 5, 10, 20, 30$ (bottom to top). A dotted line denotes the expected $\kappa_n \propto \omega_n^s$ behavior in the noncritical regime.

fully a surprise, because the Silbey-Harris theory is based on a single coherent state and is tailored to address at best the displacement and not necessarily the squeezing amplitude. As a matter of fact, one can prove from the explicit form of the displacements [13] at arbitrary M_{cs} values that the incorrect scaling behavior $\kappa_n \propto \omega_n^{1+s}$ at vanishing ω_n is found for any finite value of M_{cs} , which is also clear from Fig. 5. Only in the strict limit $M_{cs} \rightarrow \infty$ is the correct noncritical scaling obeyed down to zero energy. Nevertheless, if one focuses on a reasonable energy range (typically a few decades), the correct noncritical scaling behavior is well captured for both the average displacement and the average squeezing amplitude in our CSE computations. This analysis illustrates the general fact that systematic variational calculations may lead to the rapid convergence of some physical observables but not of others. This problem is particularly severe near quantum critical points, because the deviations concern asymptotically low energy modes, which occupy a tiny fraction of the total ground-state energy.

C. Critical regime

We now consider the quantum critical point, where the dissipation strength $\alpha = \alpha_c$ is such that the correlation length $\xi = 1/\omega^*$ diverges. In practice we fine tune $\alpha_c - \alpha$ to more than seven digits so that ξ is larger than 10^{10} , as can be seen from the VMPS data of Fig. 2. The coherent-state expansion offers, alternatively, a more pictorial view of the quantum critical wave function, which can be fully represented by a set of classical-like displacement configurations, as shown previously in Fig. 1.

While the average critical displacement $f_n \propto \omega_n^{(1-s)/2}$ vanishes (with the expected exponent) at low energy, we showed analytically in Eq. (28) that the average squeezing amplitude $\kappa_n = \langle (a_n^\dagger + a_n)^2 \rangle - 1$ is constant at the quantum critical point. Thus κ_n can be viewed as the average fluctuation of the displacements within the many-body wave function. Therefore we conclude that $\kappa_n \gg (f_n)^2$ at the quantum critical point, which reflects the strong fluctuations of the order parameter. This expected physical picture is very clear in Fig. 1: in the intermediate energy range $10^{-4} < \omega < 10^{-2}$, the distribution of displacements is nearly symmetric around zero, and thus almost vanishes on average. (This behavior is more pronounced for $s = 0.3$ than for $s = 0.8$ because the average displacement vanishes as $\omega_n^{(1-s)/2}$.) In contrast, the width of the distribution of displacements has roughly a constant value in the critical domain. Away from the critical domain, namely, for very low frequencies $\omega \ll \omega^*$, the distribution of the classical-like configurations becomes very narrow as all displacements collapse onto the same curve. Thus the average squeezing amplitude should vanish, with the noncritical scaling behavior $\kappa_n \propto \omega_n^s$. However, due to the finite size of the coherent-state basis set used here, we find for this computation the different behavior $\kappa_n \propto \omega_n^{1+s}$ as discussed previously.

Let us finally check in more detail the precise scaling behavior of the critical average displacement in Fig. 6. Again we find excellent convergence of the CSE to the VMPS curves, and we are able to match quantitatively the expected scaling law Eq. (20), including the analytic prefactor F_s in front of

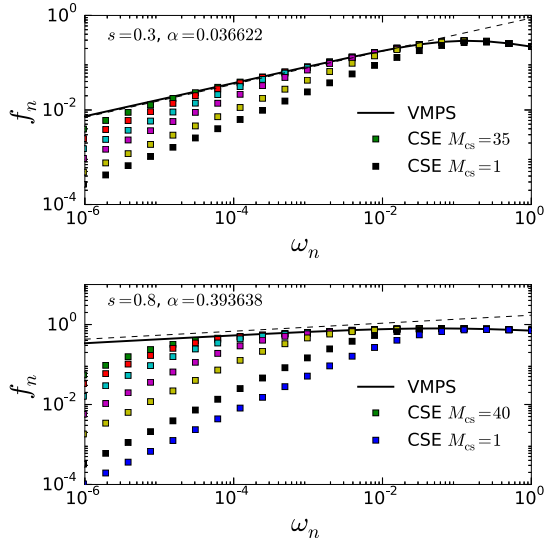


FIG. 6. Average displacement f_n of mode a_n^\dagger at the critical point ($\alpha = \alpha_c$) for two values of the bath spectra, $s = 0.3$ (top panel, with $\alpha = 0.036622$) and $s = 0.8$ (bottom panel, with $\alpha = 0.393638$). The full black line denotes the fully converged VMPS results, while the colored symbols show the CSE at increasing number of coherent states, $M_{cs} = 1, 2, 5, 10, 20, 35$ (bottom to top) for $s = 0.3$ and $M_{cs} = 1, 2, 5, 10, 20, 30, 40$ for $s = 0.8$. A dashed line denotes the expected $f_n \simeq F_s \omega_n^{(1-s)/2}$ scaling behavior in the critical regime, including the analytical prefactor F_s given in Eq. (20).

the power law $\omega_n^{(1-s)/2}$. Due to the construction of the CSE based on coherent states, one sees again that any truncation to finite M_{cs} produces an incorrect scaling $f_n \propto \omega_n^{(1+s)/2}$ at

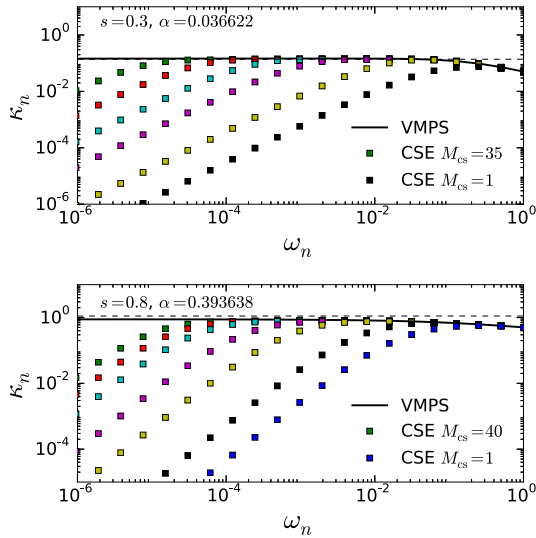


FIG. 7. Average squeezing amplitude κ_n of mode a_n^\dagger at the critical point ($\alpha = \alpha_c$) for two values of the bath spectra, $s = 0.3$ (top panel, with $\alpha = 0.036622$) and $s = 0.8$ (bottom panel, with $\alpha = 0.393638$). The full black line denotes the fully converged VMPS results, while the colored symbols show the CSE at increasing number of coherent states, $M_{cs} = 1, 2, 5, 10, 20, 35$ (bottom to top) for $s = 0.3$ and $M_{cs} = 1, 2, 5, 10, 20, 30, 40$ for $s = 0.8$. A dashed line denotes the expected universal constant value of κ_n given by Eq. (28) in the critical regime.

vanishing energy. But the correct power law is typically obeyed on several decades for a moderate numerical effort. The same type of behavior is also found in the critical average squeezing amplitude κ_n , which shows the expected constant plateau (see Fig. 7) and that matches the analytical prediction of Eq. (28) nicely. We have assessed the general prediction of the power-law dependence of the critical average displacement $f_n \propto \omega_n^{(1-s)/2}$ by fitting the low-energy tails of our converged data for a wide selection of the bath exponent s in the range $0 < s < 1$. We found that the critical exponent $(1-s)/2$ is very well obeyed, both in the mean field and interacting regimes, with an accuracy of a few percent. This reflects the peculiarity of the spin-boson model, which does not present anomalous exponents in the spin-spin correlation function [29,30,33], even below its upper critical dimension.

V. CONCLUSION

We have investigated physical properties of ground-state wave functions in a simple model of quantum criticality, the sub-Ohmic spin-boson Hamiltonian. For this purpose, a combination of variational matrix product states and an extensive coherent-state expansion has been performed and compared very precisely. The coherent-state approach allows a direct representation of many-body wave functions in terms of a collection of classical-like trajectories associated to a set of displacements. Focusing on the quantum critical regime, the wave function displays a nearly symmetric distribution of displacements at low energy. However its width, related to a squeezing amplitude of the low-energy modes defined on a logarithmic energy interval, remains finite with a universal value. This behavior strikingly reflects the wide fluctuations of the order parameter at the quantum critical point in absence of spontaneous symmetry breaking, in analogy with strong statistical fluctuations near classical phase transitions. Detailed analytical predictions have been made using exact field theory results, which match very well all the obtained numerical data, both in the noncritical and critical regimes. Similar analysis should be possible for various extensions of the dissipative impurity model, such as the two-bath case [16,17], which presents new classes of interacting fixed points. It should be applicable also to fermionic models, both with impurities or with bulk interactions, using a similar decomposition of the many-body wave function in terms of a distribution of one- or two-body phase shifts [37].

ACKNOWLEDGMENTS

We thank H. Baranger, N. Roch, and I. Snyman for useful discussions. S.F., A.N., A.W.C., and Z.B.C. acknowledge funding from the CNRS PICS contract ‘‘StrongCircQED’’ (No. 191148). A.N. and Z.B.C. are also supported by The University of Manchester and the EPSRC. A.W.C. acknowledges support from the Winton Programme for the Physics of Sustainability. B.B. and J.v.D. are supported by the DFG through the Excellence Cluster ‘‘Nanosystems Initiative Munich,’’ Contract No. SFB/TR 12, SFB 631.

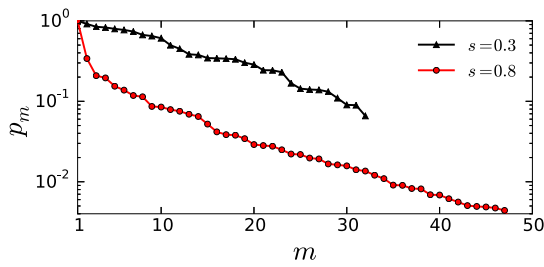


FIG. 8. Weights p_m of the coherent state $|f^{(m)}\rangle$ in the coherent-state expansion (7), as a function of index m , for $s = 0.3$ (triangles) and $s = 0.8$ (circles), with the same parameters as in Fig. 1. The fast exponential decay of the weights illustrates the hierarchical structure of the CSE.

APPENDIX: HIERARCHICAL ALGORITHM FOR THE CSE

We present here a new algorithm for finding the many-body ground state (7) of the spin-boson model (1), which radically improves the methodology developed previously in Refs. [12] and [13], allowing us to incorporate a large number M_{cs} of coherent states. This new scheme, devised to optimize efficiently the energy functional, is based only on fast local minimization routines. Indeed, while global minimization routines such as simulated annealing can give the most reliable estimates, they do not scale favorably in the case of a large number of variational parameters. However, blind application of local routines, for instance, L-BFGS or conjugate gradients [38], do not guarantee convergence to the lowest energy minimum. Hence, physical insight must be used as a guide to implement a fast and reliable local optimization method.

Here, we use the fact that the coherent-state decomposition (7) is an expansion that displays a hierarchical structure. Indeed, our simulations demonstrate that the weight p_M of a newly added coherent state is typically smaller than the majority of the weights p_m of the preceding states. This hierarchical structure is clearly apparent in Fig. 8.

This feature is exploited as follows in our numerical implementation. The algorithm starts with the solution for

a single coherent state (the so-called Silbey-Harris ansatz) with $M_{\text{cs}} = 1$, which is reliably obtained by a local routine, providing a first estimate of $f_k^{(1)}$. Then the energy is minimized for $M_{\text{cs}} = 2$ with two coherent states, using the previously determined $f_k^{(1)}$ as an initial guess, $f_k^{(2)} = 0$, and $p_2 = p_1/2$. Both displacements (and their corresponding weights) are then optimized together. The algorithm continues in the same manner by increasing M_{cs} by one unit at a time and using the previous displacements and weights as an initial guess for the next minimization stage. For completeness, we give below all the required analytical expressions used in our simulations.

1. Explicit form of the energy functional

We focus here on the case of \mathbb{Z}_2 symmetry, so that the averaged Hamiltonian from the systematic variational state (7) reads

$$\begin{aligned} \langle H \rangle = & -\Delta \sum_{n,m=1}^{M_{\text{cs}}} p_n p_m \langle f^{(n)} | -f^{(m)} \rangle \\ & + \sum_{n,m=1}^{M_{\text{cs}}} p_n p_m \langle f^{(n)} | f^{(m)} \rangle \sum_q 2\omega_q f_q^{(n)} f_q^{(m)} \\ & - \sum_{n,m=1}^{M_{\text{cs}}} p_n p_m \langle f^{(n)} | f^{(m)} \rangle \sum_q g_q (f_q^{(n)} + f_q^{(m)}). \end{aligned} \quad (\text{A1})$$

The overlaps obey the usual coherent-state algebra (all displacements $f_q^{(n)}$ and weights p_n are real in the ground state), namely, $\langle f^{(n)} | f^{(m)} \rangle = e^{-(1/2) \sum_q (f_q^{(n)} - f_q^{(m)})^2}$. The minimization is performed on the energy $E = \langle H \rangle / \mathcal{N}$ with the norm $\mathcal{N} = \langle \text{GS} | \text{GS} \rangle = 2 \sum_{n,m=1}^{M_{\text{cs}}} p_n p_m \langle f^{(n)} | f^{(m)} \rangle$.

2. Energy gradients

Standard optimization routines gain a huge computing advantage by using an explicit expression for the gradient of the function to be minimized. We thus provide here the gradients with respect to the weight p_M and displacement $f_k^{(M)}$:

$$\frac{\partial E}{\partial p_M} = \frac{2}{\mathcal{N}} \sum_{n=1}^{M_{\text{cs}}} p_n \left\{ -\Delta \langle f^{(n)} | -f^{(M)} \rangle + \langle f^{(n)} | f^{(M)} \rangle \left[\sum_q [2\omega_q f_q^{(n)} f_q^{(M)} - g_q (f_q^{(n)} + f_q^{(M)})] - 2E \right] \right\}, \quad (\text{A2})$$

$$\begin{aligned} \frac{\partial E}{\partial f_k^{(M)}} = & \frac{2p_M}{\mathcal{N}} \sum_{n=1}^{M_{\text{cs}}} p_n \left\{ \Delta \langle f^{(n)} | -f^{(M)} \rangle (f_k^{(n)} + f_k^{(M)}) + \langle f^{(n)} | f^{(M)} \rangle (2\omega_k f_k^{(n)} - g_k) \right. \\ & \left. + \langle f^{(n)} | f^{(M)} \rangle (f_k^{(n)} - f_k^{(M)}) \left(\sum_q [2\omega_q f_q^{(n)} f_q^{(M)} - g_q (f_q^{(n)} + f_q^{(M)})] - 2E \right) \right\}. \end{aligned} \quad (\text{A3})$$

- [1] S.-K. Ma, *Statistical Mechanics* (World Scientific, Singapore, 1985).
 [2] D. J. Amit, *Field Theory, the Renormalization Group, and Critical Phenomena* (World Scientific, Singapore, 2005).
 [3] K. G. Wilson, *Rev. Mod. Phys.* **55**, 583 (1983).

- [4] *Understanding Quantum Phase Transitions*, edited by Lincoln D. Carr (Taylor and Francis, Boca Raton, FL, 2010).
 [5] S. Sachdev, *Quantum Phase Transitions* (Cambridge University Press, Cambridge, UK, 1999).
 [6] R. J. Bartlett and M. Musiał, *Rev. Mod. Phys.* **79**, 291 (2007).
 [7] F. Verstraete, J. I. Cirac, and V. Murg, *Adv. Phys.* **57**, 143 (2008).

- [8] U. Schollwoeck, *Ann. Phys. (NY)* **326**, 96 (2011).
- [9] S. R. White, *Phys. Rev. Lett.* **69**, 2863 (1992).
- [10] U. Schollwöck, *Rev. Mod. Phys.* **77**, 259 (2005).
- [11] A. Weichselbaum, F. Verstraete, U. Schollwöck, J. I. Cirac, and J. von Delft, *Phys. Rev. B* **80**, 165117 (2009).
- [12] S. Bera, S. Florens, H. U. Baranger, N. Roch, A. Nazir, and A. W. Chin, *Phys. Rev. B* **89**, 121108(R) (2014).
- [13] S. Bera, A. Nazir, A. W. Chin, H. U. Baranger, and S. Florens, *Phys. Rev. B* **90**, 075110 (2014).
- [14] N. Gheeraert, S. Bera, and S. Florens, [arXiv:1601.01545](https://arxiv.org/abs/1601.01545).
- [15] S. Florens and I. Snyman, *Phys. Rev. B* **92**, 195106 (2015).
- [16] C. Guo, A. Weichselbaum, J. von Delft, and M. Vojta, *Phys. Rev. Lett.* **108**, 160401 (2012).
- [17] B. Bruognolo, A. Weichselbaum, C. Guo, J. von Delft, I. Schneider, and M. Vojta, *Phys. Rev. B* **90**, 245130 (2014).
- [18] K. E. Cahill, *Phys. Rev.* **138**, B1566 (1965).
- [19] N. Zhou, L. Chen, D. Xu, V. Chernyak, and Y. Zhao, *Phys. Rev. B* **91**, 195129 (2015).
- [20] L. Duan, S. He, and Q.-H. Chen, [arXiv:1412.6343](https://arxiv.org/abs/1412.6343).
- [21] A. J. Leggett, S. Chakravarty, A. T. Dorsey, M. P. A. Fisher, A. Garg, and W. Zwerger, *Rev. Mod. Phys.* **59**, 1 (1987).
- [22] U. Weiss, *Quantum Dissipative Systems* (World Scientific, Singapore, 1993).
- [23] M. Vojta, *Philos. Mag.* **86**, 1807 (2006).
- [24] K. Le Hur, *Ann. Phys. (NY)* **323**, 2208 (2008).
- [25] K. Le Hur, *Phys. Rev. B* **85**, 140506 (2012).
- [26] M. Goldstein, M. H. Devoret, M. Houzet, and L. I. Glazman, *Phys. Rev. Lett.* **110**, 017002 (2013).
- [27] B. Peropadre, D. Zueco, D. Porras, and J. J. García-Ripoll, *Phys. Rev. Lett.* **111**, 243602 (2013).
- [28] I. Snyman and S. Florens, *Phys. Rev. B* **92**, 085131 (2015).
- [29] R. Bulla, N.-H. Tong, and M. Vojta, *Phys. Rev. Lett.* **91**, 170601 (2003).
- [30] R. Bulla, H. J. Lee, N. H. Tong, and M. Vojta, *Phys. Rev. B* **71**, 045122 (2005).
- [31] A. Winter, H. Rieger, M. Vojta, and R. Bulla, *Phys. Rev. Lett.* **102**, 030601 (2009).
- [32] M. Vojta, R. Bulla, F. Güttge, and F. Anders, *Phys. Rev. B* **81**, 075122 (2010).
- [33] A. Freyn and S. Florens, *Phys. Rev. B* **79**, 121102 (2009).
- [34] V. J. Emery and A. Luther, *Phys. Rev. B* **9**, 215 (1974).
- [35] R. Silbey and R. A. Harris, *J. Chem. Phys.* **80**, 2615 (1984).
- [36] A. W. Chin, J. Prior, S. F. Huelga, and M. B. Plenio, *Phys. Rev. Lett.* **107**, 160601 (2011).
- [37] I. Snyman and S. Florens (unpublished).
- [38] W. W. Hager and H. Zhang, *SIAM J. Optimiz.* **23**, 2150 (2013).

3.3 Open Wilson chains for quantum impurity models

In the following publication [BLS⁺17], we introduce a new type of Wilson chain to represent a quantum impurity model which resolves a fundamental problem, open since the original work of Wilson himself. Whereas the standard construction neglects the effect of all truncated bath modes, our open Wilson chain (OWC) setup enables us for the first time to systematically keep track of these modes. To this end, each site is coupled to a separate effective bath of its own, representing a subset of truncated bath modes. This allows us to take them into account explicitly, albeit approximatively, in numerical calculations, whereas previously they were simply ignored altogether.

This strategy allows us to cure the so-called mass-flow problem that can arise when using standard Wilson chains to treat impurity models with asymmetric bath spectral functions at finite temperature. We demonstrate this for the strongly subohmic spin-boson model at quantum criticality where a solution to the mass-flow has been a longstanding open issue. For the first time we can directly study the energy RG flow towards a Gaussian critical fixed point, employing state-of-the-art techniques based on MPS. Remarkably, our method produces even *quantitatively correct* results in perfect agreement with analytic predictions from a controlled perturbative RG.

Our results are highly relevant for a variety of physical fields such as quantum critical matter, open quantum systems, strongly correlated materials, and non-equilibrium dynamics. Apart from the fact that a new category of impurity models with a Gaussian fixed point becomes numerically accessible, the OWC setup also opens access to addressing truly new physics. For instance, it paves the way to the solution of multi-channel impurity models with off-diagonal couplings relevant for multi-impurity models and DMFT applications involving spin-orbit coupling. In addition, our work sets the scene for incorporating dissipative effects as required for nonequilibrium situations leading to an entirely different category of new physics to be studied.

P5 *Open Wilson chains for quantum impurity models: Keeping track of all bath modes*
B. Bruognolo, N.-O. Linden, F. Schwarz, S.-S. B. Lee, K. Stadler, A. Weichselbaum,
M. Vojta, F. B. Anders, and J. von Delft
[Phys. Rev. B 95, 121115\(R\) \(2017\)](#)

Open Wilson chains for quantum impurity models: Keeping track of all bath modes

B. Bruognolo,^{1,2} N.-O. Linden,¹ F. Schwarz,¹ S.-S. B. Lee,¹ K. Stadler,¹ A. Weichselbaum,¹ M. Vojta,³ F. B. Anders,⁴ and J. von Delft¹

¹*Physics Department, Arnold Sommerfeld Center for Theoretical Physics and Center for NanoScience, Ludwig-Maximilians-Universität München, D-80333 München, Germany*

²*Max-Planck-Institut für Quantenoptik, Hans-Kopfermann-Strasse 1, D-85748 Garching, Germany*

³*Institut für Theoretische Physik, Technische Universität Dresden, D-01062 Dresden, Germany*

⁴*Lehrstuhl für Theoretische Physik II, Technische Universität Dortmund, D-44221 Dortmund, Germany*

(Received 22 November 2016; published 31 March 2017)

When constructing a Wilson chain to represent a quantum impurity model, the effects of truncated bath modes are neglected. We show that their influence can be kept track of systematically by constructing an “open Wilson chain” in which each site is coupled to a separate effective bath of its own. As a first application, we use the method to cure the so-called mass-flow problem that can arise when using standard Wilson chains to treat impurity models with asymmetric bath spectral functions at finite temperature. We demonstrate this for the strongly sub-Ohmic spin-boson model at quantum criticality where we directly observe the flow towards a Gaussian critical fixed point.

DOI: [10.1103/PhysRevB.95.121115](https://doi.org/10.1103/PhysRevB.95.121115)

A quantum impurity model describes a discrete set of degrees of freedom, the “impurity”, coupled to a bath of excitations. For an infinite bath this is effectively an *open* system. However, the most powerful numerical methods for solving such models, Wilson’s numerical renormalization group (NRG) [1,2] and variational matrix-product-state (VMPS) generalizations thereof [3–6], actually treat it as *closed*: The continuous bath is replaced by a so-called Wilson chain, a finite-length tight-binding chain whose hopping matrix elements t_n decrease exponentially with site number n , ensuring energy-scale separation along the chain. This works well for numerous applications, ranging from transport through nanostructures [7,8] to impurity solvers for dynamical mean-field theory [9–11]. However, replacing an open by a closed system brings about finite-size effects. Wilson himself had anticipated that the effect of bath modes neglected during discretization might need to be included perturbatively “to achieve reasonable accuracy”, but concluded that “this has proven to be unnecessary” for his purposes (see p. 813 of Ref. [1]). By now, it is understood that finite-size effects often do matter. They hamper the treatment of dissipative effects [12], e.g., in the context of nonequilibrium transport [13] and equilibration after a local quench [14]. Moreover, even in equilibrium, they may cause errors when computing the bath-induced renormalization of impurity properties [15–17]. Indeed, finite-size issues constitute arguably the most serious conceptual limitation of approaches based on Wilson chains.

Here, we set the stage for controlling finite-size effects by constructing “open Wilson chains” (OWCs) in which each site is coupled to a bath of its own. The resulting open system implements energy-scale separation in a way that, in contrast to standard Wilson chains (SWCs), fully keeps track of all bath-induced dissipative and renormalization effects. The key step involved in any renormalization group (RG) approach, namely, integrating out degrees of freedom at one energy scale to obtain a renormalized description at a lower scale, can then be performed more carefully than for SWCs. We illustrate this by focusing on renormalization effects, leaving a systematic treatment of dissipative effects on OWCs for the future.

A SWC is constructed by logarithmically discretizing the bath and tridiagonalizing the resulting discrete bath Hamiltonian to obtain a tight-binding chain, with the impurity coupled to site $n = 0$ [1,2]. Properties at temperature T are calculated using a chain of finite length N_T , chosen such that its smallest energy scale matches the temperature $t_{N_T} \simeq T$ ($k_B = 1$). However, since sites $n > N_T$ are neglected, the contribution of the corresponding truncated bath modes (TBMs) to the renormalization of impurity properties is missing [17]. For example, for a local level linearly coupled to a bath with an asymmetric bath spectrum, this coupling generates a physical shift in the level energy. When this shift is computed using a SWC of length N_T , the result contains a temperature-dependent error. Hence, the use of SWCs generically leads to qualitative errors in the temperature dependence of renormalized model parameters, called the “mass-flow problem” [16,17]. Quantitative errors persist even for $T \rightarrow 0$, when $N_T \rightarrow \infty$, because constructing a SWC actually involves neglecting TBMs at *every* site.

The mass-flow problem is particularly serious when targeting a quantum critical point, where it causes errors for critical exponents describing finite-temperature properties at the critical point. This has been studied in some detail for the dissipative harmonic oscillator (DHO) and the sub-Ohmic spin-boson model (SBM). For both, SWCs are unable to even qualitatively describe the temperature dependence of the local susceptibility $\chi(T)$ at criticality [15–17]. Both involve Gaussian criticality of ϕ^4 type and hence a bosonic mode whose excitation energy vanishes at the critical fixed point. The finite-temperature RG flow in its vicinity cannot be correctly described using finite-length SWCs because the erroneous mass dominates over physical interaction effects. Summarizing, methods based on SWCs produce systematic quantitative errors for all impurity problems with asymmetric baths, and they fail even qualitatively in addressing Gaussian criticality and other phenomena with zero modes.

Here, we show that these issues *can* be addressed using OWCs: The bath coupled to each site of the OWC induces an energy shift for that site that can be computed *exactly* and

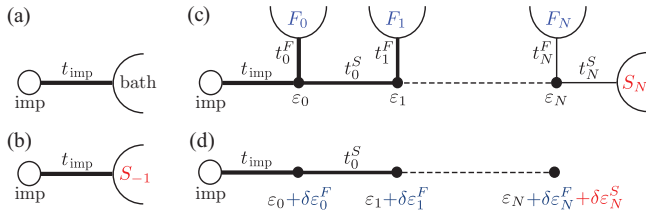


FIG. 1. (a) Impurity model. (b) Initialization. (c) Open Wilson chain (OWC). (d) Renormalized Wilson chain (RWC).

used to define a “renormalized Wilson chain” (RWC). The ground-state properties of a RWC of length N_T mimic the finite- T properties of the original model in a way that is free from mass-flow problems. We demonstrate this explicitly by using VMPS techniques [6] on RWCs to compute $\chi(T)$ for the DHO and SBM. We also compute the energy-level flow of the SBM; it unambiguously reveals flow towards a Gaussian fixed point with a dangerously irrelevant interaction term.

Model. We consider a generic single-band impurity model with Hamiltonian $\mathcal{H} = \mathcal{H}^{\text{imp}}[b^\dagger t_{\text{imp}}] + \mathcal{H}^{\text{bath}}$, where $\mathcal{H}^{\text{bath}}$ describes the bath, and \mathcal{H}^{imp} the impurity and its coupling to the bath via normalized bath operators b^\dagger and b , with coupling constant t_{imp} [Fig. 1(a)]. The free ($t_{\text{imp}} = 0$) dynamics of b^\dagger , generated by $\mathcal{H}^{\text{bath}}$, is encoded in the free retarded correlator $\mathcal{G}^{\text{bath}}(\omega) = \langle\langle b|b^\dagger \rangle\rangle_\omega$, which is uniquely characterized by its spectral function $\mathcal{A}^{\text{bath}}(\omega) = -\frac{1}{\pi} \text{Im} \mathcal{G}^{\text{bath}}(\omega)$. The impurity dynamics is therefore fully determined once \mathcal{H}^{imp} and the “bath spectrum”, $\Gamma^{\text{bath}}(\omega) = |t_{\text{imp}}|^2 \mathcal{A}^{\text{bath}}(\omega)$, have been specified.

Continued-fraction expansion. One well-known way of mapping an impurity model to a chain is to iteratively construct a continued-fraction expansion (CFE) for $\mathcal{G}^{\text{bath}}$ [18]. Our main idea is to do this in a way that *zooms in on low energies* without discarding high-energy information. Our construction involves a sequence of retarded correlators $\mathcal{G}_n^X(\omega)$, with $X = S$ or F , describing the effective “slow” (low-energy) or “fast” (high-energy) bath modes of iteration step n , with spectral functions $\mathcal{A}_n^X(\omega) = -\frac{1}{\pi} \text{Im} \mathcal{G}_n^X(\omega)$ having unit weight $\int d\omega \mathcal{A}_n^X(\omega) = 1$. We initialize our CFE construction with $\mathcal{G}_{-1}^S = \mathcal{G}^{\text{bath}}$ [Fig. 1(b)]. Starting with $n = 0$, we iteratively use \mathcal{G}_{n-1}^S , describing the low-energy modes of the previous iteration, as input to define a new retarded correlator \mathcal{G}_n and its retarded self-energy Σ_n ,

$$\mathcal{G}_n(\omega) = \mathcal{G}_{n-1}^S(\omega) = 1/[\omega - \varepsilon_n - \Sigma_n(\omega)], \quad (1)$$

with $\varepsilon_n = \int d\omega \omega \mathcal{A}_n(\omega)$ [19]. Then we split this self-energy into low- and high-energy parts by writing it as

$$\Sigma_n(\omega) = \Sigma_n^S(\omega) + \Sigma_n^F(\omega), \quad \Sigma_n^X(\omega) = |t_n^X|^2 \mathcal{G}_n^X(\omega). \quad (2)$$

Here, the corresponding retarded correlators $\mathcal{G}_n^{S/F}$ are defined by choosing their rescaled spectral functions $|t_n^{S/F}|^2 \mathcal{A}_n^{S/F}$ to represent the low- and high-energy parts of $\Gamma_n(\omega) = -\frac{1}{\pi} \text{Im} \Sigma_n$, with t_n^X chosen such that \mathcal{A}_n^X has unit weight (see Sec. S-1 A of Ref. [19] for details). To be explicit, we write $\Gamma_n = \Gamma_n^S + \Gamma_n^F$, with $\Gamma_n^X(\omega) = w_n^X(\omega) \Gamma_n(\omega)$. The splitting functions $w_n^{S/F}(\omega)$ are defined on the support of Γ_n , take values in the interval $[0, 1]$, satisfy $w_n^S(\omega) + w_n^F(\omega) = 1$, and have weight predominantly at low/high energies. Then

we write the split bath spectra as $\Gamma_n^X(\omega) = |t_n^X|^2 \mathcal{A}_n^X(\omega)$, with “couplings” t_n^X chosen as $|t_n^X|^2 = \int d\omega \Gamma_n^X(\omega)$, and define new retarded correlators via $\mathcal{G}_n^X(\omega) = \int d\tilde{\omega} \frac{\mathcal{A}_n^X(\tilde{\omega})}{\omega - \tilde{\omega} + i0^+}$, also fixing $\Sigma_n^X(\omega)$ via Eq. (2).

Iterating, using \mathcal{G}_n^S as input to compute new correlators \mathcal{G}_{n+1}^X while retaining the self-energy Σ_n^F , we obtain a sequence of exact CFE representations for $\mathcal{G}^{\text{bath}}$. That of depth 2, e.g., reads

$$\mathcal{G}^{\text{bath}}(\omega) = \frac{1}{\omega - \varepsilon_0 - \Sigma_0^F(\omega) - \frac{|t_0^S|^2}{\omega - \varepsilon_1 - \Sigma_1^F(\omega) - \frac{|t_1^S|^2}{\omega - \varepsilon_2 - \Sigma_2^F(\omega)}}}.$$

To ensure energy-scale separation, we choose $\mathcal{A}_n^X(\omega)$ such that the CFE parameters decrease monotonically, $\max\{|\varepsilon_n|, |t_n^S|\} \leq \max\{|\varepsilon_{n-1}|, |t_{n-1}^S|\}/\Lambda$, with $\Lambda > 1$ [20].

Open Wilson chain. We now use the CFE data $(\varepsilon_n, t_n^X, \mathcal{G}_n^X)$ to represent the original bath in terms of a chain with $N + 1$ sites, each coupled to a bath of its own, and site 0 coupled to the impurity (site -1) [Fig. 1(c)]. This OWC is constructed such that the free ($t_{\text{imp}} = 0$) correlator of site 0 is exactly equal to the depth- N CFE found above, i.e., $\mathcal{G}_0 = \mathcal{G}^{\text{bath}}$, implying that the chain and original bath have the same effect on the impurity.

The key point is that each CFE step of writing $\mathcal{G}_{n-1}^S(\omega)$ in the form $\mathcal{G}_n(\omega) = 1/[\omega - \varepsilon_n - \Sigma_n(\omega)]$ can be implemented on the level of the Hamiltonian: It corresponds to replacing the bath represented by \mathcal{G}_{n-1}^S , say, S_{n-1} , by a new site n , with energy ε_n and normalized site operators f_n^\dagger and f_n , which is linearly coupled to a new bath that generates the self-energy Σ_n . In the present case, the latter is split into low- and high-energy contributions, $\Sigma_n^S + \Sigma_n^F$. We can generate these by linearly coupling the new site with couplings t_n^S and t_n^F to *two* new baths, say, S_n and F_n , via normalized bath operators $b_{S_n}^\dagger, b_{S_n}$ and $b_{F_n}^\dagger, b_{F_n}$, that are governed by bath Hamiltonians \mathcal{H}_n^X chosen such that $\langle\langle b_{X_n}^\dagger | b_{X_n}^\dagger \rangle\rangle_\omega$ equals the $\mathcal{G}_n^X(\omega)$ found above (see Sec. S-1 A of Ref. [19] for details). For the next iteration, we retain the fast bath F_n , but replace the slow bath S_n by a new site $n + 1$ coupled to new baths S_{n+1} and F_{n+1} , etc. This leads to replacing \mathcal{H} by $\mathcal{H}_N^{\text{OWC}} = \mathcal{H}_N^{\text{SWC}} + \mathcal{H}_N^{\text{TBM}}$, with

$$\begin{aligned} \mathcal{H}_N^{\text{SWC}} &= \mathcal{H}_f^{\text{imp}} + \sum_{n=0}^N \varepsilon_n f_n^\dagger f_n + \sum_{n=0}^{N-1} (f_{n+1}^\dagger t_n^S f_n + \text{H.c.}), \\ \mathcal{H}_N^{\text{TBM}} &= \sum_{n=0}^N (b_{F_n}^\dagger t_n^F f_n + \text{H.c.}) + \sum_{n=0}^N \mathcal{H}_n^F \\ &\quad + (b_{S_N}^\dagger t_N^S f_N + \text{H.c.}) + \mathcal{H}_N^S, \end{aligned} \quad (3)$$

and $\mathcal{H}_f^{\text{imp}} = \mathcal{H}^{\text{imp}}[f_0^\dagger t_{\text{imp}}]$. This chain Hamiltonian is depicted schematically in Fig. 1(c). $\mathcal{H}_N^{\text{SWC}}$ has the structure of a SWC, while $\mathcal{H}_N^{\text{TBM}}$ describes the couplings to all fast baths $F_{n \leq N}$, and of the last site N to its slow bath S_N . These “fast and last slow” baths F_n and S_N constitute TBMs, since a SWC neglects them. By instead using an OWC, we can keep track of their influence, namely, to shift, mix, and broaden the eigenstates of those subchains to which they couple. Equation (3), which represents an impurity model in terms of a Wilson chain that

still is a fully open system, is the first main result of this Rapid Communication.

Renormalized Wilson chain. For concrete numerical calculations, we need to approximate an OWC by a RWC that can be treated using standard NRG or VMPS methods, while still including information about the TBMs. To this end, we replace \mathcal{H}^{OWC} by \mathcal{H}^{RWC} [Fig. 1(d)], a Hamiltonian of the same form as \mathcal{H}^{SWC} (without fast or last baths), but with each on-site energy ε_n shifted to

$$\tilde{\varepsilon}_n = \varepsilon_n + \delta\varepsilon_n^F + \delta_{nN} \delta\varepsilon_n^S, \quad \delta\varepsilon_n^X = \text{Re}[\Sigma_n^X(0)]. \quad (4)$$

For the CFE of $\mathcal{G}^{\text{bath}} = \mathcal{G}_{-1}^S = \mathcal{G}_0$, this amounts to replacing the slow and fast self-energies by the real parts of their zero-frequency values [21]. Therefore, $\text{Re}[\Sigma^{\text{bath}}(0)]$, the real part of the zero-frequency self-energy of $\mathcal{G}^{\text{bath}}$, is reproduced correctly [22], irrespective of the length N of the RWC used to calculate $\mathcal{G}^{\text{bath}}$. (Since the imaginary parts of all self-energies are neglected, dissipative effects are not included.) If the original bath spectrum is symmetric, $\Gamma^{\text{bath}}(\omega) = \Gamma^{\text{bath}}(-\omega)$, as often happens for fermionic models, then $\delta\varepsilon_n^{S/F} = 0$. However, for an asymmetric bath function [e.g., $\Gamma^{\text{bath}}(\omega < 0) = 0$, as is the case for bosonic baths], these shifts are in general nonzero.

We will henceforth consider two types of RWCs, labeled by C1 or C2 [23]. A C1 chain includes only fast shifts ($\delta\varepsilon_n^S = 0$); this turns out to lead to results qualitatively similar to those obtained using a SWC constructed by discretizing the original bath logarithmically, as done by Wilson, and tridiagonalizing the bath Hamiltonian $\mathcal{H}^{\text{bath}}$. A C2 chain includes both the fast and slow shifts from Eq. (4), thus correctly reproducing $\text{Re}[\Sigma^{\text{bath}}(0)]$.

Dissipative harmonic oscillator. As a first example, consider a DHO with Hamiltonian $\mathcal{H}_{\text{DHO}}^{\text{imp}} + \mathcal{H}^{\text{bath}}$, where

$$\mathcal{H}_{\text{DHO}}^{\text{imp}} = \Omega a^\dagger a + \frac{1}{2}(a + a^\dagger)[\epsilon + t_{\text{imp}}(b + b^\dagger)] \quad (5)$$

describes an ‘‘impurity’’ oscillator with bare frequency Ω and displacement force ϵ , linearly coupled to a bosonic bath. The bath spectral function has the form

$$\Gamma^{\text{bath}}(\omega) = 2\alpha\omega_c^{1-s}\omega^s, \quad 0 < \omega < \omega_c, \quad (6)$$

where $s > -1$, α characterizes the dissipation strength, and ω_c is a cutoff frequency, henceforth set to unity. This model is exactly solvable. The static impurity susceptibility at temperature T , defined by $\chi(T) = \frac{d\langle a+a^\dagger \rangle_T}{d\epsilon}|_{\epsilon=0}$, turns out to be temperature independent and given by [17] $\chi_{\text{exact}}(T) = 1/\Omega_r$, where $\Omega_r = \Omega + \text{Re}[\mathcal{G}^{\text{bath}}(\omega = 0)]$ can be interpreted as the renormalized impurity frequency, reduced relative to the bare one by the coupling to the bath. It vanishes at the critical coupling $\alpha_c = s\Omega/(2\omega_c)$, beyond which the model becomes unstable.

When $\chi(T)$ is computed numerically for $\alpha < \alpha_c$ using NRG to perform thermal averages on SWCs of length N_T , one does not obtain a constant but a temperature-dependent curve [15–17]. We find the same using NRG on C1-RWCs of length N_T (Fig. 2, circles). The reason is the neglect of the TBMs associated with sites $n > N_T$: Their contribution to the renormalization shift $\text{Re}[\mathcal{G}^{\text{bath}}(\omega = 0)]$ in Ω_r is missing. The approach developed above offers a straightforward cure: We simply compute $\chi(T)$ using C2-RWCs of length N_T , thus incorporating the energy shift induced by the remaining TBMs via

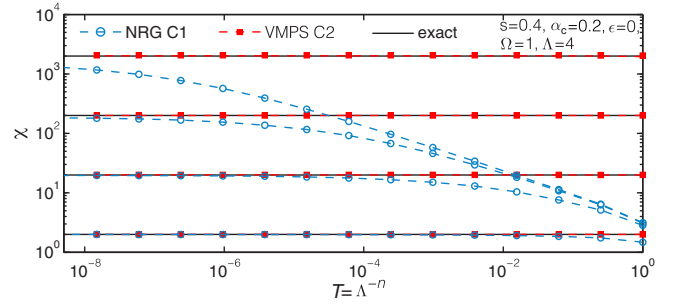


FIG. 2. DHO susceptibility $\chi(T)$ as function of temperature, computed by NRG on C1-RWCs (circles) and by VMPS on C2-RWCs (squares), for $\alpha = 0.1, 0.19, 0.199$, and 0.1999 (from bottom to top). Solid lines show exact results.

the slow-mode shift for site N_T . Since the latter substantially affects the low-energy spectrum, these calculations require VMPS methods (see Secs. S-2 B and S-2 C of Ref. [19] for details). They yield T -independent χ values (Fig. 2, squares), in excellent agreement with the exact ones (Fig. 2, solid lines).

We remark that SWCs constructed using previous discretization schemes [24–26] either strongly over- or underestimate the critical coupling α_c , reflecting the presence of discretization artifacts. In contrast, our C2-RWCs yield α_c values that match the analytic results almost perfectly (see Sec. S-3 D of Ref. [19]). Thus, our RWC construction constitutes a general, new discretization scheme free of the discretization artifacts of previous schemes.

Spin-boson model. Next, we consider the SBM, which is not exactly solvable. In its Hamiltonian $\mathcal{H}_{\text{SBM}}^{\text{imp}} + \mathcal{H}^{\text{bath}}$,

$$\mathcal{H}_{\text{SBM}}^{\text{imp}} = -\frac{1}{2}\Delta\hat{\sigma}_x + \frac{1}{2}\hat{\sigma}_z[\epsilon + t_{\text{imp}}(b + b^\dagger)] \quad (7)$$

describes a spin- $\frac{1}{2}$ ‘‘impurity’’ ($\hat{\sigma}_i$ being Pauli matrices) linearly coupled to a bosonic bath, with $\Gamma^{\text{bath}}(\omega)$ again given by Eq. (6). ϵ and Δ denote the bias and the tunnel splitting of the impurity spin, respectively.

For the *sub-Ohmic* case ($0 < s < 1$), increasing α at zero temperature drives the SBM through a quantum phase transition (QPT) from a delocalized to a localized phase (with $\langle \hat{\sigma}_z \rangle_0 = 0$ or $\neq 0$, respectively). According to a quantum-to-classical correspondence (QCC) argument [15,16,27], this QPT belongs to the same universality class as that of a classical one-dimensional Ising chain with long-ranged interactions [28]. Thus, the critical exponents characterizing the QPT follow mean-field predictions for $s \leq 0.5$ and obey hyperscaling for $0.5 < s < 1$. The QCC predictions were confirmed numerically using Monte Carlo methods [29] or sparse polynomial bases [30].

In contrast, verifying the QCC predictions using NRG turned out to be challenging. Initial NRG studies [15] yielded non-mean-field exponents for $s < 0.5$, but were subsequently [16,17] found to be unreliable, due to two inherent limitations of NRG. The first was a too severe NRG truncation of Hilbert space in the localized phase; it was overcome in Ref. [6] by using a VMPS approach involving an optimized boson basis [31–33] on a SWC, which reproduced QCC predictions for critical exponents characterizing zero-temperature behavior. The second NRG limitation was the mass-flow problem:

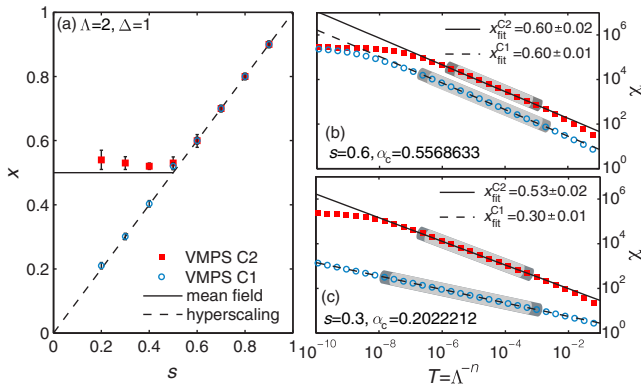


FIG. 3. (a) Critical exponent x for the sub-Ohmic SBM, as a function of s , computed by VMPS using RWCs of type C1 (circles) and C2 (squares). Examples of $\chi(T)$ curves used to extract these exponents are shown in (b) for $s = 0.3$ and (c) for $s = 0.6$. Error bars in (a) are derived by varying the fitting ranges, e.g., as indicated by dark and light shading in (b) and (c).

For exponents describing *finite*-temperature critical behavior at $\alpha = \alpha_c$, it causes NRG on SWCs to yield hyperscaling results not only for $0.5 < s < 1$ (correct) but also for $s < 0.5$ (incorrect). For example, consider the susceptibility $\chi(T) = \frac{d(\delta_z)_T}{d\epsilon} \Big|_{\epsilon=0}$, which scales as $\chi(T) \propto T^{-x}$ at the critical coupling α_c . The QCC predicts $x = 0.5$ for $s < 0.5$ and $x = s$ for $0.5 < s < 1$. In contrast, past NRG calculations yielded $x = s$ throughout the interval $0 < s < 1$ [16,17,24]. We recover the latter behavior if we compute $\chi(T)$ via VMPS calculations on length- N_T C1-RWCs [Fig. 3(a), circles]. In contrast, if we use length- N_T C2-RWCs instead, the results for x [Fig. 3(a), squares] agree well with QCC predictions, showing that the mass-flow problem has been cured.

Critical energy-level flow diagrams. The reason why the sub-Ohmic SBM shows qualitatively different critical behavior for $0.5 < s < 1$ and $s \leq 0.5$ is that the critical fixed point is interacting for the former but Gaussian for the latter [17]. To elucidate the difference, Fig. 4 shows energy-level flow diagrams, obtained by plotting the rescaled lowest-

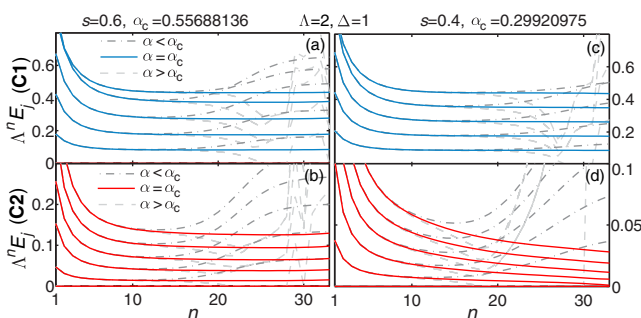


FIG. 4. Energy-level flow diagrams for the sub-Ohmic SBM with $s = 0.6$ (left column) and $s = 0.4$ (right column), computed by VMPS techniques [5,19] on C1-RWCs (top row) and C2-RWCs (bottom row). Dashed lines depict flow to delocalized ($\alpha < \alpha_c$) or localized fixed points ($\alpha > \alpha_c$), and solid lines depict critical flow ($\alpha = \alpha_c$). For the latter, the C2 flow in (d) is characteristic of a Gaussian fixed point.

lying energy eigenvalues of length- N Wilson chains, $\Lambda^N E_j$, as functions of N . For $s = 0.6$ (left column), having an interacting critical fixed point for which mass-flow effects are not relevant, the critical level flows for RWCs of type C1 and C2 are qualitatively similar [Figs. 4(a) and 4(b)], becoming stationary independent of N for large N , in a manner familiar from fermionic NRG.

In contrast, for $s = 0.4$ (right column), having a Gaussian fixed point for which mass-flow effects do matter, the critical C1 and C2 level flows are very different: Whereas the C1 flow becomes stationary [Fig. 4(c)] (an artifact of neglecting slow-mode shifts), the low-lying C2 levels all flow towards zero [Fig. 4(d)], causing the level spacing to decrease towards zero, too. This striking behavior, inaccessible when using SWCs, is characteristic of a Gaussian fixed point: It implies that the fixed-point excitation spectrum contains a zero-energy bosonic mode. Remarkably, our C2-RWCs yield a *quantitatively* correct description of the critical spectral flow for $0 < s < 0.5$: It follows a power law $\Lambda^n E_j \propto \epsilon_n^\kappa$ with $\kappa = (2s - 1)/3$, in perfect agreement with the prediction from controlled perturbative RG for a ϕ^4 -type theory with a dangerously irrelevant quartic coupling (see Sec. S-4 D of Ref. [19]).

Conclusions and outlook. Open Wilson chains are representations of quantum impurity models that achieve energy-scale separation while fully keeping track of the effects of bath modes, by iteratively replacing them by a sequence of separate baths at successively lower-energy scales, one for each chain site. Starting from such a fully open system, the effects of these baths can be included systematically. We have taken the first step in that direction, using the bath-induced energy shift for each site to define a renormalized Wilson chain. Remarkably, this simple scheme is sufficiently accurate to yield renormalized impurity properties free from the long-standing mass flow problem. The next step, namely, integrating out each site's bath more carefully, should lead to a description of dissipative effects on Wilson chains, as required for nonequilibrium situations. For example, the effect of bath F_n on the eigenstates of a length- n subchain could be treated using some simple approximation capable of mixing and broadening the eigenlevels (e.g., an equation-of-motion approach with a decoupling scheme). This is left for future work.

Finally, we note that our iterative construction of renormalized Wilson chains constitutes a well-controlled new discretization scheme that offers progress on two further fronts, unrelated to finite-size effects but relevant, e.g., when using NRG or DMRG as impurity solvers for dynamical mean-field theory [9–11,34], or to study multi-impurity models [35]. First, it avoids the discretization artifacts known to arise when conventional schemes [1,24–26] are used to treat strongly asymmetric bath spectra. Second, it can be generalized straightforwardly to treat multiflavor models having non-diagonal bath spectral functions (see Sec. S-1 B of Ref. [19]).

Acknowledgments. We thank Andrew Mitchell for a stimulating discussion on discretizing multiflavor impurity models. This research was supported by the DFG through the Excellence Cluster “Nanosystems Initiative Munich”, SFB/TR 12, SFB 631, SFB 1143 (M.V.), AN 275/8-1 (F.B.A.), and WE4819/2-1 (A.W.).

- [1] K. G. Wilson, *Rev. Mod. Phys.* **47**, 773 (1975).
- [2] R. Bulla, T. A. Costi, and T. Pruschke, *Rev. Mod. Phys.* **80**, 395 (2008).
- [3] H. Saberi, A. Weichselbaum, and J. von Delft, *Phys. Rev. B* **78**, 035124 (2008).
- [4] A. Weichselbaum, F. Verstraete, U. Schollwöck, J. I. Cirac, and J. von Delft, *Phys. Rev. B* **80**, 165117 (2009).
- [5] I. Pizorn and F. Verstraete, *Phys. Rev. Lett.* **108**, 067202 (2012).
- [6] C. Guo, A. Weichselbaum, J. von Delft, and M. Vojta, *Phys. Rev. Lett.* **108**, 160401 (2012); B. Bruognolo, A. Weichselbaum, C. Guo, J. von Delft, I. Schneider, and M. Vojta, *Phys. Rev. B* **90**, 245130 (2014).
- [7] L. Borda, G. Zaránd, W. Hofstetter, B. I. Halperin, and J. von Delft, *Phys. Rev. Lett.* **90**, 026602 (2003).
- [8] A. V. Kretinin, H. Shtrikman, D. Goldhaber-Gordon, M. Hanl, A. Weichselbaum, J. von Delft, T. A. Costi, and D. Mahalu, *Phys. Rev. B* **84**, 245316 (2011).
- [9] R. Bulla, *Phys. Rev. Lett.* **83**, 136 (1999).
- [10] T. Pruschke and R. Bulla, *Eur. Phys. J. B* **44**, 217 (2005).
- [11] K. M. Stadler, Z. P. Yin, J. von Delft, G. Kotliar, and A. Weichselbaum, *Phys. Rev. Lett.* **115**, 136401 (2015).
- [12] A. Rosch, *Eur. Phys. J. B* **85**, 6 (2012).
- [13] F. B. Anders, *J. Phys.: Condens. Matter* **20**, 195216 (2008).
- [14] F. B. Anders and A. Schiller, *Phys. Rev. Lett.* **95**, 196801 (2005). H. E. Türeci, M. Hanl, M. Claassen, A. Weichselbaum, T. Hecht, B. Braunecker, A. Govorov, L. Glazman, A. İmamoğlu, and J. von Delft, *ibid.* **106**, 107402 (2011); C. Latta, F. Haupt, M. Hanl, A. Weichselbaum, M. Claassen, P. Fallahi, S. Faelt, L. Glazman, J. von Delft, H. E. Türeci, and A. İmamoğlu, *Nature (London)* **474**, 627 (2011).
- [15] M. Vojta, N.-H. Tong, and R. Bulla, *Phys. Rev. Lett.* **94**, 070604 (2005).
- [16] M. Vojta, N.-H. Tong, and R. Bulla, *Phys. Rev. Lett.* **102**, 249904(E) (2009).
- [17] M. Vojta, R. Bulla, F. Güttge, and F. Anders, *Phys. Rev. B* **81**, 075122 (2010).
- [18] G. Grosso and G. P. Parravicini, *Adv. Chem. Phys.* **62**, 81 (2007); M. Foulkes and R. Haydock, *J. Phys. C* **19**, 6573 (1986); E. R. Gagliano and C. A. Balseiro, *Phys. Rev. Lett.* **59**, 2999 (1987); Q. Si, M. J. Rozenberg, G. Kotliar, and A. E. Ruckenstein, *ibid.* **72**, 2761 (1994); K. A. Hallberg, *Phys. Rev. B* **52**, R9827(R) (1995).
- [19] See Supplemental Material at <http://link.aps.org/supplemental/10.1103/PhysRevB.95.121115>, which includes Refs. [36–42], for details about the OWC construction, numerical methods used, and additional numerical data.
- [20] If $\Gamma^{\text{bath}}(\omega)$ has power-law form $\propto \omega^s$, we can achieve this by taking the support of \mathcal{A}_n^S and \mathcal{A}_n^F to partition that of $-\frac{1}{\pi}\text{Im}\Sigma_n$ into low- and high-energy regimes [19].
- [21] This choice of $\delta\varepsilon_n^X$ aims to correctly describe low-energy properties, in order to solve the mass-flow problem. More generally, the $\delta\varepsilon_n^X$ may be viewed as fit parameters that optimize the truncated CFE representation of $\mathcal{G}^{\text{bath}}(\omega)$.
- [22] For the single-impurity Anderson model, this guarantees that the height of the zero-temperature Kondo resonance at $\omega = 0$, which is governed solely by $\text{Re}[\Sigma^{\text{bath}}(0)]$, is reproduced correctly, irrespective of the choice of Λ .
- [23] Chains that include neither fast nor slow shifts, $\delta\varepsilon_n^{F,S} = 0$, yield completely incorrect results; see Sec. S-3 of Ref. [19].
- [24] R. Bulla, N.-H. Tong, and M. Vojta, *Phys. Rev. Lett.* **91**, 170601 (2003); R. Bulla, H.-J. Lee, N.-H. Tong, and M. Vojta, *Phys. Rev. B* **71**, 045122 (2005).
- [25] V. L. Campo Jr. and L. N. Oliveira, *Phys. Rev. B* **72**, 104432 (2005).
- [26] R. Žitko and T. Pruschke, *Phys. Rev. B* **79**, 085106 (2009).
- [27] M. Vojta, *Phys. Rev. B* **85**, 115113 (2012).
- [28] M. E. Fisher, S.-k. Ma, and B. G. Nickel, *Phys. Rev. Lett.* **29**, 917 (1972); E. Luijten and H. W. J. Blöte, *Phys. Rev. B* **56**, 8945 (1997).
- [29] A. Winter, H. Rieger, M. Vojta, and R. Bulla, *Phys. Rev. Lett.* **102**, 030601 (2009).
- [30] A. Alvermann and H. Fehske, *Phys. Rev. Lett.* **102**, 150601 (2009).
- [31] C. Zhang, E. Jeckelmann, and S. R. White, *Phys. Rev. Lett.* **80**, 2661 (1998).
- [32] A. Weiße, H. Fehske, G. Wellein, and A. R. Bishop, *Phys. Rev. B* **62**, R747 (2000).
- [33] Y. Nishiyama, *Eur. Phys. J. B* **12**, 547 (1999).
- [34] F. A. Wolf, A. Go, I. P. McCulloch, A. J. Millis, and U. Schollwöck, *Phys. Rev. X* **5**, 041032 (2015).
- [35] A. K. Mitchell and R. Bulla, *Phys. Rev. B* **92**, 155101 (2015); A. K. Mitchell, P. G. Derry, and D. E. Logan, *ibid.* **91**, 235127 (2015).
- [36] A. Weichselbaum and J. von Delft, *Phys. Rev. Lett.* **99**, 076402 (2007).
- [37] L. Borda, *Phys. Rev. B* **75**, 041307 (2007); B. Lechtenberg and F. B. Anders, *ibid.* **90**, 045117 (2014).
- [38] S. R. White, *Phys. Rev. Lett.* **69**, 2863 (1992); *Phys. Rev. B* **48**, 10345 (1993); U. Schollwöck, *Rev. Mod. Phys.* **77**, 259 (2005).
- [39] U. Schollwöck, *Ann. Phys.* **326**, 96 (2011).
- [40] C. Brockt, F. Dorfner, L. Vidmar, F. Heidrich-Meisner, and E. Jeckelmann, *Phys. Rev. B* **92**, 241106 (2015); F. A. Y. N. Schröder and A. W. Chin, *ibid.* **93**, 075105 (2016); F. Dorfner and F. Heidrich-Meisner, *Phys. Rev. A* **93**, 063624 (2016).
- [41] N.-O. Linden, Master's thesis, LMU Munich, 2014.
- [42] H.-J. Lee, R. Bulla, and M. Vojta, *J. Phys.: Condens. Matter* **17**, 6935 (2005).

Open Wilson chains for quantum impurity models: Keeping track of all bath modes

Supplementary material

B. Bruognolo,^{1,2} N.-O. Linden,¹ F. Schwarz,¹ S.-S. B. Lee,¹ K. Stadler,¹
A. Weichselbaum,¹ M. Vojta,³ F. B. Anders,⁴ and J. von Delft¹

¹*Physics Department, Arnold Sommerfeld Center for Theoretical Physics and Center for NanoScience, Ludwig-Maximilians-Universität München, 80333 München, Germany*

²*Max-Planck-Institut für Quantenoptik, Hans-Kopfermann-Str. 1, D-85748 Garching, Germany*

³*Institut für Theoretische Physik, Technische Universität Dresden, 01062 Dresden, Germany*

⁴*Lehrstuhl für Theoretische Physik II, Technische Universität Dortmund, 44221 Dortmund, Germany*

The supplementary material presented below deals with four topics. Section S-1 offers a more detailed discussion of the construction of continued-fraction expansions and open Wilson chains. Section S-2 describes the numerical VMPS techniques used. Section S-3 is devoted to a detailed study of the dissipative harmonic oscillator, in order to benchmark our numerical methods against exact results. Section S-4 describes how the RG flow towards the Gaussian fixed point of the sub-ohmic spin-boson model for $0 < s \leq 0.5$ can be understood using scaling arguments.

S-1. DETAILED DISCUSSION OF CFE AND OWC CONSTRUCTION

Below we supply some technical details involved in the construction of (i) the continued-fraction expansion (CFE) and (ii) the open Wilson chain (OWC) presented in the main text. We begin in Subsection S-1 A with the case of a bath involving only a single flavor of excitations, as discussed in the main text. In Subsection S-1 B, we generalize the construction to a multi-flavor bath having a nondiagonal bath spectrum.

A. Single-flavor bath

(i) *Continued-fraction iteration step.*— We here give some details on the central step of the CFE, which takes a retarded correlator \mathcal{G}_n as input and produces as output a self-energy, split into low- and high-energy contributions.

The input correlator \mathcal{G}_n , being retarded, has the spectral representation $\mathcal{G}_n(\omega) = \int d\bar{\omega} \frac{\mathcal{A}_n(\bar{\omega})}{\omega - \bar{\omega} + i0^+}$, with a spectral function, $\mathcal{A}_n(\omega) = -\frac{1}{\pi} \text{Im} \mathcal{G}_n(\omega)$ that is normalized to unity, $\int d\omega \mathcal{A}_n(\omega) = 1$. If this correlator is represented in the form [Eq. (1)]

$$\mathcal{G}_n(\omega) = \frac{1}{\omega - \varepsilon_n - \Sigma_n(\omega)}, \quad (\text{S1})$$

with $\Sigma_n(\omega)$ analytic in the upper half-plane as required for a retarded self-energy, then the constant in the denominator must be equal to the average energy of the spectral function $\mathcal{A}_n(\omega)$, $\varepsilon_n = \int d\omega \omega \mathcal{A}_n(\omega)$. In the main

text this fact was used, but not explained. To understand its origin, invert Eq. (S1), multiply it by $\mathcal{G}_n(\omega)$, and integrate over frequency:

$$\begin{aligned} \int d\omega \Sigma_n(\omega) \mathcal{G}_n(\omega) &= \int d\omega \left[(\omega - \varepsilon_n) \mathcal{G}_n(\omega) - 1 \right] \\ &= \int d\omega \int d\bar{\omega} \left[\frac{\omega - \varepsilon_n}{\omega - \bar{\omega} + i0^+} - 1 \right] \mathcal{A}_n(\bar{\omega}) \\ &= \int d\bar{\omega} \int d\omega \left[\frac{\bar{\omega} - \varepsilon_n}{\omega - \bar{\omega} + i0^+} \right] \mathcal{A}_n(\bar{\omega}) \\ &= -i\pi \int d\bar{\omega} (\bar{\omega} - \varepsilon_n) \mathcal{A}_n(\bar{\omega}). \end{aligned} \quad (\text{S2})$$

Since both $\mathcal{G}_n(\omega)$ and $\Sigma_n(\omega)$ are by assumption retarded functions and hence analytic in the upper half-plane, the left-hand side of the first line yields zero, as can be seen by closing the integration contour in the upper half-plane. The second line follows from the right-hand side of the first using the spectral representation of \mathcal{G}_n , and the fact that \mathcal{A}_n is normalized to unity. Since the last line, being equal to the first, must equal zero too, it fixes ε_n to the value stated in above (again using the unit normalization of \mathcal{A}_n). Once ε_n has been fixed, the self-energy is fixed, too, by inverting Eq. (S1):

$$\Sigma_n(\omega) = \omega - \varepsilon_n - 1/\mathcal{G}_n(\omega). \quad (\text{S3})$$

To summarize: The fact that the retarded correlator $\mathcal{G}_n(\omega)$ is analytic implies the same for its self-energy $\Sigma_n(\omega)$; this uniquely fixes ε_n and thus also $\Sigma_n(\omega)$ itself, which in turn can be viewed as a correlator with its own self-energy, etc. Thus, the analyticity of $\mathcal{G}_n(\omega)$ guarantees that it is always possible to iteratively construct a CFE for it. The new twist added to this well-known fact in the present work is to zoom in to small energies by splitting the self-energy into slow and fast parts and using only the former as input for the next iteration step.

To explicitly implement this splitting, given by Eq. (2),

$$\Sigma_n(\omega) = \Sigma_n^S(\omega) + \Sigma_n^F(\omega), \quad \Sigma_n^X(\omega) = |t_n^X|^2 \mathcal{G}_n^X(\omega), \quad (\text{S4})$$

we proceed as follows. We split $\Gamma_n(\omega) = -\frac{1}{\pi} \text{Im} \Sigma_n(\omega)$, which may be viewed as the bath spectrum of iteration n , into slow and fast parts, $\Gamma_n = \Gamma_n^S + \Gamma_n^F$, with

$$\Gamma_n^X(\omega) = w_n^X(\omega) \Gamma_n(\omega). \quad (\text{S5})$$

Here the splitting functions $w_n^{S/F}(\omega)$ are defined on the support of Γ_n , take values in the interval $[0, 1]$, satisfy $w_n^S(\omega) + w_n^F(\omega) = 1$, and have weight predominantly at low/high energies. Then we write the split bath spectra as $\Gamma_n^X(\omega) = |t_n^X|^2 \mathcal{A}_n^X(\omega)$, with ‘‘couplings’’ t_n^X chosen as

$$|t_n^X|^2 = \int d\omega \Gamma_n^X(\omega), \quad (\text{S6})$$

to ensure that the new spectral functions $\mathcal{A}_n^X(\omega)$ are normalized to unity. Using them to define new retarded correlators via $\mathcal{G}_n^X(\omega) = \int d\bar{\omega} \frac{\mathcal{A}_n^X(\bar{\omega})}{\omega - \bar{\omega} + i0^+}$, we obtain the desired slow/fast splitting of the self-energy stated above.

Next we describe the choice of splitting functions $w_n^X(\omega)$ used to obtain the numerical results of the main text. Let $I_n^S = [\omega_{S_n}^-, \omega_{S_{n-1}}^+]$ denote the support of the slow spectral function \mathcal{A}_n^S . The bath spectrum for iteration n , $\Gamma_n(\omega) = -\frac{1}{\pi} \text{Im} \Sigma_n(\omega)$, has support on the same interval, say I_n , as the correlator $\mathcal{G}_n = \mathcal{G}_{n-1}^S$, i.e. $I_n = I_{n-1}^S$. To implement the splitting $\Gamma_n = \Gamma_n^S + \Gamma_n^F$, we partition this interval into disjoint slow and fast subranges, $I_n = I_n^S \cup I_n^F$, with $|\omega_{S_n}^\pm| \leq |\omega_{S_{n-1}}^\pm|$, and use corresponding step-form splitting functions:

$$w_n^X(\omega) = \begin{cases} 1 & \text{for } \omega \in I_n^X, \\ \text{otherwise.} & \end{cases} \quad (\text{S7})$$

To ensure energy-scale separation, I_n^S should be chosen such that

$$\max\{|\varepsilon_n|, |t_n^S|\} \leq \max\{|\varepsilon_{n-1}|, |t_{n-1}^S|\} / \Lambda \quad (\text{S8})$$

holds, with $\Lambda > 1$. If the bath spectrum $\Gamma^{\text{bath}}(\omega)$ has a flat or power-law form, a natural choice is $\omega_{S_n}^\pm = \omega_{S_{n-1}}^\pm / \Lambda$. This is the choice used for the numerical work in the main text. However, if $\Gamma^{\text{bath}}(\omega)$ has nontrivial structure, the choices for the subrange boundaries $\omega_{S_n}^\pm$ might have to be fine-tuned to ensure Eq. (S8) at each iteration. More generally, one might also explore using splitting functions $w_n^X(\omega)$ of smoother shape than those of Eq. (S7). The freedom of choice available for ensuring Eq. (S8) is one of the major strengths of the above strategy for generating a CFE.

(ii) *Construction of open Wilson chain.*— Here we provide some details on the construction of the OWC Hamiltonian of $\mathcal{H}_N^{\text{OWC}}$ of Eq. (3). It describes a chain with $N + 1$ sites, each coupled to a bath of its own, and site 0 coupled to the impurity (site -1) [Fig. 1(c)]. It is constructed such that the free ($t_{\text{imp}} = 0$) correlator of site 0 is given by a depth- N CFE, $\mathcal{G}_0 = \mathcal{G}^{\text{bath}}$.

We associate with each pair of correlators $\mathcal{G}_n^{S/F}$ from the CFE two mutually independent baths S_n and F_n . We regard \mathcal{G}_n^X as the free retarded correlator of a normalized bath operator $b_{X_n}^\dagger$, whose dynamics is generated by a bath Hamiltonian \mathcal{H}_n^X , chosen such that $\mathcal{G}_n^X(\omega) = \langle\langle b_{X_n} | b_{X_n}^\dagger \rangle\rangle_\omega$ has the form found via the CFE.

We start our OWC construction by associating bath S_{-1} with the original bath [Fig. 1(b)], setting $\mathcal{H}_{-1}^S =$

$\mathcal{H}^{\text{bath}}$, $b_{S_{-1}}^\dagger = b^\dagger$ and $\mathcal{G}_{-1}^S = \mathcal{G}^{\text{bath}}$, with impurity-bath coupling $t_{-1}^S = t_{\text{imp}}$. We then proceed iteratively, starting with $n = 0$. The central CFE iteration step of writing \mathcal{G}_{n-1}^S in the form of Eq. (1) corresponds, on the level of the Hamiltonian, to replacing the bath S_{n-1} by a new site n [Fig. 1(c)], with energy ε_n and normalized site operator f_n^\dagger , which is linearly coupled to two new baths, S_n and F_n , in such a way that its free ($t_{n-1}^S = 0$) site correlator \mathcal{G}_n equals \mathcal{G}_{n-1}^S [Eq. (1)]. To achieve this, we make the replacements $b_{S_{n-1}}^\dagger \rightarrow f_n^\dagger$ and

$$\mathcal{H}_{n-1}^S \rightarrow \varepsilon_n f_n^\dagger f_n + \sum_X (b_{X_n}^\dagger t_n^X f_n + \text{H.c.}) + \sum_X \mathcal{H}_n^X. \quad (\text{S9})$$

Then $\mathcal{G}_n = \langle\langle f_n | f_n^\dagger \rangle\rangle_\omega$ indeed matches Eq. (1), since the self-energy generated for it by the new baths, $\Sigma_n(\omega) = \sum_X |t_n^X|^2 \mathcal{G}_n^X(\omega)$, agrees with Eq. (2). Since $\mathcal{G}_n = \mathcal{G}_{n-1}^S$, f_n^\dagger and $b_{S_{n-1}}^\dagger$ have the same dynamics, i.e. the new site, bath S_n and bath F_n jointly have the same effect on site $n - 1$ as the previous bath S_{n-1} . Now we iterate: we retain the fast bath F_n , but replace the slow bath S_n by a new site $n + 1$ coupled to new slow and fast baths S_{n+1} and F_{n+1} , etc. After $N + 1$ steps, the initial \mathcal{H} has been replaced by the OWC Hamiltonian $\mathcal{H}_N^{\text{OWC}}$ given in Eq. (3).

The above argument does not require the free Hamiltonians \mathcal{H}_n^X and bath operators $b_{X_n}^\dagger$ to be constructed explicitly. For concreteness we specify them nevertheless:

$$\mathcal{H}_n^X = \sum_q \varepsilon_{qn}^X b_{X_{qn}}^\dagger b_{X_{qn}}, \quad b_{X_n}^\dagger = \sum_q b_{X_{qn}}^\dagger \lambda_{qn}^X. \quad (\text{S10})$$

These involve a set of canonical annihilation and creation operators satisfying $[b_{X_{qn}}, b_{X_{qn}}^\dagger]_\pm = 1$ ($+$ for a fermionic anti-commutator, $-$ for a bosonic commutator). The bath operators b_{X_n} are normalized to satisfy $[b_{X_n}, b_{X_n}^\dagger]_\pm = 1$. The free dynamics of $b_{X_n}^\dagger$, generated by \mathcal{H}_n^X , is characterized by the free retarded correlator and spectral function

$$\mathcal{G}_n^X(\omega) = \sum_q \frac{|\lambda_{qn}^X|^2}{\omega - \varepsilon_{qn}^X + i0^+}, \quad (\text{S11a})$$

$$\mathcal{A}_n^X(\omega) = \sum_q |\lambda_{qn}^X|^2 \delta(\omega - \varepsilon_{qn}^X). \quad (\text{S11b})$$

The bath energies ε_{qn}^X and couplings λ_{qn}^X are assumed such that $\mathcal{G}_n^X(\omega)$ has the form obtained in the CFE.

B. Multi-flavor bath

Next we consider impurity models involving a multi-flavor bath with m_f flavors of excitations, labeled by an index $\nu = 1, \dots, m_f$. We assume that the impurity Hamiltonian $\mathcal{H}_{\text{imp}}[b_\nu^\dagger]$, describing the impurity degrees of freedom and their coupling to the bath, depends on the bath only through m_f bath operators b_ν^\dagger and their conjugates b_ν , not necessarily normalized or orthogonal,

with retarded correlator $\mathcal{G}_{\nu\nu'}^{\text{bath}}(\omega) = \langle\langle b_\nu; b_{\nu'}^\dagger \rangle\rangle_\omega$. We assume that the corresponding bath spectrum,

$$\Gamma_{\nu\nu'}^{\text{bath}}(\omega) = -[\mathcal{G}_{\nu\nu'}^{\text{bath}}(\omega) - \mathcal{G}_{\nu\nu'}^{\text{bath}*}(\omega)]/(2\pi i), \quad (\text{S12})$$

is a specified, Hermitian, positive definite *matrix* function (i.e. for any given ω , the eigenvalues of the matrix are real and non-negative). Together with the form of \mathcal{H}_{imp} , this matrix function fully determines the impurity dynamics. Models of this structure arise in studies of the Kondo compensation cloud [36], when considering multi-impurity situations [34], and in DMFT studies of multi-band lattice models, where $\Gamma_{\nu\nu'}^{\text{bath}}(\omega)$ is constructed iteratively from the impurity spectral function $\mathcal{A}_{\nu\nu'}^{\text{imp}}(\omega)$ computed at the previous DMFT iteration.

If $\Gamma_{\nu\nu'}^{\text{bath}}(\omega)$ can be diagonalized using a frequency-independent unitary transformation, the eigenvalues, say $\Gamma_\nu(\omega)$, constitute m_f hybridization functions that can be discretized independently, using either standard Wilsonian discretization or our RWC discretization scheme. Here we are interested in the more general case that diagonalizing the bath spectrum requires a frequency-dependent unitary transformation, $\Gamma_{\nu\nu'}^{\text{bath}}(\omega) = \sum_{\bar{\nu}} u_{\nu\bar{\nu}}^\dagger(\omega) \Gamma_{\bar{\nu}}(\omega) u_{\bar{\nu}\nu'}(\omega)$. This would be the case, for example, for DMFT studies of a fermionic lattice model with broken band degeneracy and spin-orbit coupling; the corresponding self-consistent impurity model is a multi-band Anderson model involving nondiagonal level-bath couplings, leading to a nondiagonal impurity spectral function.

To treat this situation in Wilsonian fashion, one could write the bath spectrum as $\Gamma_{\nu\nu'}^{\text{bath}}(\omega) = \int d\varepsilon_q \sum_{\bar{\nu}} v_{q\nu\bar{\nu}}^\dagger \delta(\omega - \varepsilon_q) v_{q\bar{\nu}\nu}$, with bath-lead matrix elements $v_{q\nu\nu'} = \sqrt{\Gamma_\nu(\varepsilon_q)} u_{\nu\nu'}(\varepsilon_q)$, and discretize the integral logarithmically (with the implicit assumption that $\Gamma_\nu(\omega)$ and $v_{q\nu\nu'}(\omega)$ change sufficiently slowly with ω that within a discretization interval they may be replaced by constants). We note, though, that the neglect of truncated bath modes is potentially more problematic for multi- than single-flavor models, since $\Gamma_{\nu\nu'}^{\text{bath}}(\omega)$ will generically have matrix elements asymmetric in frequency.

Below we explain how multi-flavor models can alternatively be discretized using a generalization of our RWC construction. (We thank Andrew Mitchell for a stimulating discussion which led to this realization.) The overall strategy is completely analogous to the single-flavor case, but with a flavor index added to all creation and annihilation operators (e.g. $b_{X\nu\nu}^\dagger$), and two flavor indices to all matrix elements (e.g. $t_{\nu\nu'}^X$) and correlators (e.g. $\mathcal{G}_{\nu\nu'}^X$). We will mostly use a compact notation that suppresses these indices and indicates their implicit presence by an underscore, e.g. $\underline{b}_{Xn}^\dagger$, \underline{t}_n^X , $\underline{\mathcal{G}}_n^X$, $(\underline{b}_{Xn}^\dagger \underline{t}_n^X)_{\nu\nu'} = b_{Xn\nu}^\dagger t_{n\nu\nu'}^X$, and $\underline{f}_n^\dagger \underline{\varepsilon}_n \underline{f}_n = \sum_{\nu\nu'} f_{n\nu}^\dagger \varepsilon_{n\nu\nu'} f_{n\nu'}$, etc.

Extracting normalized modes from bath spectrum.— The CFE to be constructed below involves a sequence of bath spectra with matrix structure, generically denoted by $\underline{\Gamma}(\omega)$. Each is a Hermitian, positive definite matrix function, $\underline{\Gamma}(\omega) = \underline{\Gamma}^\dagger(\omega)$. We would like to express such a

function in terms of a Hermitian, positive definite matrix function $\underline{\mathcal{A}}(\omega)$ that is normalized as

$$\int d\omega \underline{\mathcal{A}}(\omega) = \underline{1}, \quad (\text{S13})$$

because such an $\underline{\mathcal{A}}(\omega)$ can be viewed as the spectral function of a set of *orthonormal* bath modes. To this end, we note that the frequency integral $\underline{w} = \int d\omega \underline{\Gamma}(\omega)$ yields a Hermitian, positive definite matrix. (Reason: If two matrices are Hermitian and positive definite, the same is true for their sum, and similarly for an integral of such matrix functions.) The matrix \underline{w} can thus be diagonalized in the form $\underline{w} = \underline{u}^\dagger \underline{d} \underline{u}$, with \underline{u} unitary and \underline{d} diagonal and positive. Then the matrix $\underline{t} = \underline{u}^\dagger \sqrt{\underline{d}} \underline{u}$ can be used to write the bath spectrum in the form

$$\underline{\Gamma}(\omega) = \underline{t}^\dagger \underline{\mathcal{A}}(\omega) \underline{t}, \quad (\text{S14})$$

where both \underline{t} and $\underline{\mathcal{A}}$ are Hermitian and positive definite, while $\underline{\mathcal{A}}$ by construction is normalized as in Eq. (S13). The first moment of $\underline{\mathcal{A}}$ yields a Hermitian matrix, too: $\underline{\varepsilon} = \int d\omega \omega \underline{\mathcal{A}}(\omega)$. In the chain to be constructed below, $\underline{\varepsilon}$ plays the role of an onsite Hamiltonian and \underline{t} that of a nearest-neighbor coupling. If desired, one may make another unitary transformation that diagonalizes either $\underline{\varepsilon}$ or \underline{t} , while leaving the normalization condition (S13) in tact.

Continued-fraction expansion.— As for the one-band case, we aim to iteratively represent $\underline{\mathcal{G}}^{\text{bath}}(\omega)$ in terms of a sequence of continued-fraction expansions that zoom in on low energies. These involve a sequence of Hermitian, positive definite functions, $\underline{\mathcal{A}}_n^X(\omega) = \underline{\mathcal{A}}_n^{X\dagger}(\omega)$. Each is normalized to unity [Eq. (S13)] and can be viewed as the spectral function of a retarded correlator $\underline{\mathcal{G}}_n^X(\omega)$,

$$\underline{\mathcal{A}}_n^X(\omega) = -[\underline{\mathcal{G}}_n^X(\omega) - \underline{\mathcal{G}}_n^{X\dagger}(\omega)]/(2\pi i), \quad (\text{S15})$$

which in turn can be expressed as

$$\underline{\mathcal{G}}_n^X(\omega) = \int d\bar{\omega} \frac{\underline{\mathcal{A}}_n^X(\bar{\omega})}{\omega - \bar{\omega} + i0^+}. \quad (\text{S16})$$

The multi-band CFE construction follows the one-band case, except that all correlators carry underscores to indicate their matrix structure. First we initialize the CFE by expressing the bath spectrum in terms of a normalized spectral function, $\underline{\Gamma}^{\text{bath}}(\omega) = \underline{t}_{\text{imp}}^{S\dagger} \underline{\mathcal{A}}_1^S(\omega) \underline{t}_{\text{imp}}^S$ [cf. (S14)] and compute the corresponding retarded correlator $\underline{\mathcal{G}}_{-1}^S$ via Eq. (S16). Starting with iteration $n = 0$, we then iteratively use $\underline{\mathcal{G}}_{n-1}^S$ as input to define a new retarded correlator $\underline{\mathcal{G}}_n^S$ and its retarded self-energy $\underline{\Sigma}_n$,

$$\underline{\mathcal{G}}_n(\omega) = \underline{\mathcal{G}}_{n-1}^S(\omega) = 1/[\omega \underline{1} - \underline{\varepsilon}_n - \underline{\Sigma}_n(\omega)], \quad (\text{S17})$$

with $\underline{\varepsilon}_n = \int d\omega \omega \underline{\mathcal{A}}_n(\omega)$. Then we split this self-energy into low- and high-energy parts by writing it as

$$\underline{\Sigma}_n = \underline{\Sigma}_n^S + \underline{\Sigma}_n^F, \quad \underline{\Sigma}_n^X(\omega) = \underline{t}_n^{X\dagger} \underline{\mathcal{G}}_n^X(\omega) \underline{t}_n^X. \quad (\text{S18})$$

To be concrete, we achieve this splitting by proceeding as follows. We split $\Gamma_n(\omega) = -[\Sigma_n(\omega) - \Sigma_n^\dagger]/(2\pi i)$, the bath spectrum of iteration n , into slow and fast parts, $\Gamma_n = \Gamma_n^S + \Gamma_n^F$, with

$$\Gamma_{n,\nu\nu'}^X(\omega) = w_{n,\nu\nu'}^X(\omega)\Gamma_{n,\nu\nu'}(\omega) \quad (\text{S19})$$

(no index summation implied here), using symmetric, real matrix functions $w_n^X(\omega)$. Their matrix elements $w_{n\nu\nu'}^{S/F}(\omega)$ are splitting functions that are defined on the support of Γ_n , take values in $[0, 1]$, have weight predominantly at low/high energies, and satisfy $w_{n\nu\nu'}^S(\omega) + w_{n\nu\nu'}^F(\omega) = 1$. (The simplest choice would be $w_n^X(\omega) = w_n^X(\omega)\mathbb{1}$, using the same pair of weighting functions for all matrix elements; but situations may arise where the additional freedom of making different choices for different matrix elements is useful.) Since the splitting functions are symmetric and non-negative, the split spectra Γ_n^X are Hermitian and positive definite matrix functions, too. We can thus express them in terms of normalized spectral functions [Eq. (S14)]:

$$\Gamma_n^X(\omega) = t_n^{X\dagger} \mathcal{A}_n^X(\omega) t_n^X. \quad (\text{S20})$$

Computing the corresponding retarded correlators $\underline{\mathcal{G}}_n^X$ [Eq. (S16)] we obtain the self-energy splitting stated in Eq. (S18). To ensure energy-scale separation, the weighting functions w_n^X should be chosen such that

$$\max\{\|\underline{\varepsilon}_n\|, \|t_n^S\|\} \leq \max\{\|\underline{\varepsilon}_{n-1}\|, \|t_{n-1}^S\|\}/\Lambda \quad (\text{S21})$$

holds, with $\Lambda > 1$, where $\|\cdot\|$ denotes some matrix norm.

Iterating this procedure yields a sequence of CFEs for $\underline{\mathcal{G}}^{\text{bath}}$, in the same fashion as for the one-band case.

Chain representation.— The CFE data $(\underline{\varepsilon}_n, t_n^X, \underline{\mathcal{G}}_n^X)$ can now be used to represent the model in terms of a chain with $N + 1$ sites, each coupled to a bath of its own. The chain is constructed such that the free ($t_{-1}^S = 0$) correlator of the first site ($n = 0$) is given by a dept- N CFE. To this end, we associate each pair of correlators $\underline{\mathcal{G}}_n^{S/F}$ with two mutually independent baths S_n and F_n , and regard each $\underline{\mathcal{G}}_n^X$ as the free retarded correlator of a set of m_f normalized bath operators b_{Xn}^\dagger , whose free dynamics is generated by a bath Hamiltonian \mathcal{H}_n^X , such that $\underline{\mathcal{G}}_n^X(\omega) = \langle\langle b_{Xn} | b_{Xn}^\dagger \rangle\rangle_\omega$. These free bath Hamiltonians and bath operators have the form

$$\mathcal{H}_n^X = \sum_q b_{Xqn}^\dagger \underline{\varepsilon}_{qn}^X b_{Xqn}, \quad b_{Xn}^\dagger = \sum_q b_{Xqn}^\dagger \underline{\lambda}_{qn}^X, \quad (\text{S22})$$

where $\underline{\varepsilon}_{qn}^X$ and $\underline{\lambda}_{qn}^X$ are matrices w.r.t. to the flavor indices. $\underline{\varepsilon}_{qn}^X$ is diagonal and real, and $\underline{\lambda}_{qn}^X$ unitary, normalized such that $[b_{Xn}, b_{Xn}^\dagger]_\pm = \mathbb{1}$. The free bath correlators and spectral functions then have the explicit representations

$$\underline{\mathcal{G}}_n^X(\omega) = \sum_q \underline{\lambda}_{qn}^{X\dagger} [(\omega + i0^+)\mathbb{1} - \underline{\varepsilon}_{qn}^X]^{-1} \underline{\lambda}_{qn}^X, \quad (\text{S23a})$$

$$\underline{\mathcal{A}}_n^X(\omega) = \sum_q \underline{\lambda}_{qn}^{X\dagger} \delta(\omega\mathbb{1} - \underline{\varepsilon}_{qn}^X) \underline{\lambda}_{qn}^X. \quad (\text{S23b})$$

This representation for $\underline{\mathcal{A}}_n^X(\omega)$ shows explicitly that it is a Hermitian, positive definite matrix function.

The iterative OWC construction proceeds as for the single-flavor case, except that all operators, matrix elements and correlators now carry underscores to indicate implicit flavor indices. For example, the generalization of Eq. (S9) now involves the replacements $b_{S_{n-1}}^\dagger \rightarrow \underline{f}_n^\dagger$ and

$$\mathcal{H}_{n-1}^S \rightarrow \underline{f}_n^\dagger \underline{\varepsilon}_n \underline{f}_n + \sum_X (b_{Xn}^\dagger t_n^X \underline{f}_n + \text{H.c.}) + \sum_X \mathcal{H}_n^X. \quad (\text{S24})$$

The final OWC Hamiltonian has the same form as Eq. (3) of the main text, suitably decorated with underscores, and with $\mathcal{H}^{\text{imp}}[f_0^\dagger t_{\text{imp}}]$ as impurity Hamiltonian. Similarly, when moving on to a RWC, the energy shift equation (4) of the main text is decorated by underscores, i.e. we shift the onsite energy matrices $\underline{\varepsilon}_n$ by $\delta\underline{\varepsilon}_n^X$ shifts that should be chosen to optimize the truncated CFE representation of $\underline{\mathcal{G}}^{\text{bath}}$. We expect this step to be more important for multi- than single-flavor models, since $\Gamma_n^X(\omega)$ will generically have matrix elements asymmetric in frequency. If one is interested mainly in correctly reproducing low-energy properties, one could choose $\delta\underline{\varepsilon}_n^X = \text{Re}\Sigma_n^X(\omega = 0)$, as in the main text. Another option would be to view the $\delta\underline{\varepsilon}_n^X$ as fitting parameters, chosen to get the best possible agreement between the depth- n CFE for $\underline{\mathcal{G}}^{\text{bath}}(\omega)$ and its actual form.

S-2. NUMERICAL DETAILS

In this section, we elaborate on the details of the numerical methods employed in the main text. In Subsection S-2 A we briefly review NRG and its limitations in the context of bosonic impurity models. In Subsection S-2 B we discuss the VMPS techniques by which these limitations can be overcome. Finally, in Subsection S-2 C we present a generalized VMPS scheme that simultaneously targets multiple low-energy states on the Wilson chain, which enables us to generate the well-controlled energy-level flow diagrams for the sub-Ohmic spin-boson model (SBM) shown in Fig. 4 of the main text.

A. Bosonic NRG

The numerical renormalization group (NRG) is one of the most powerful tools to numerically evaluate the properties of quantum impurity models [1]. Wilson's formulation of "standard NRG" involves two steps. First, the model is represented in terms of a Wilson chain, i.e. a semi-infinite tight-binding chain whose hopping matrix elements t_n decrease exponentially with n , ensuring energy-scale separation along the chain. In the main text and Sec. S-1, we have described in detail how this is achieved for an RWC; for details on setting up a SWC we refer to Refs. [24] and [2]. Second, the chain is diagonalized iteratively one site at a time, discarding high-energy

states at each step, to yield a set of so-called Wilson shells, where shell N contains the low-lying eigenstates of a finite chain whose last site is labelled N (a “length- N ” chain). These shells can be used to calculate both thermodynamic and dynamical quantities; in particular, we employed the full-density-matrix NRG scheme (fdm-NRG) to evaluate thermal averages of observables in this work [35].

Whereas NRG has been highly successful in the context of fermionic impurity models, its application to bosonic baths has been impeded by two numerical issues, (i) the mass-flow error and (ii) the local Hilbert space truncation. We elaborated on (i) in detail in the main text. We add that NRG cannot be completely cured from the mass flow using the C2-RWC construction, as discussed in more detail in Sec. S-3 below. This is related to the iterative nature of the NRG diagonalization procedure, which does not allow to incorporate any feedback of the slow-mode correction to earlier iterations, in contrast to the variational setup presented in Sec. S-2 B below. Problem (ii) is related to the fact that only a limited number of bosons can be included in an NRG calculation. NRG requires an *a priori* truncation of the infinite-dimensional local bosonic Hilbert space on each site n to a numerically feasible number of d_n bosonic states. For example, for the spin-boson model NRG is therefore not able to accurately deal with the fact that the oscillator displacement occurring in the localized phase grows exponentially along the Wilson chain, which implies that the number of bosons in the standard oscillator representation must increase exponentially, too [16].

In the context of the sub-Ohmic SBM, it has been thoroughly illustrated how the limitations of bosonic NRG can tamper with physical properties. Here, the interplay of these two numerical issues affected a number of critical exponents, causing them to follow hyperscaling instead of mean-field results for $0 < s < 0.5$ [15]. The internal consistency of these NRG results (which were later shown to be incorrect) was so striking that it initially lead to the controversial conclusion, that the quantum-to-classical correspondence breaks down in case of the sub-Ohmic SBM. This subtle “conspiracy of errors” [27] implies that NRG is not fully equipped to deal with bosonic baths, since parts of the phase diagram and, in particular, the impurity quantum phase transition, may not be reliably accessible for the method.

B. VMPS with optimal boson basis

The intrinsic flaws of bosonic NRG can be completely dealt with by employing the strategy of the density matrix renormalization group (DMRG) to treat RWC Hamiltonians [4, 37]. To this end, we use the matrix-product-state (MPS) formulation of DMRG [38], which we refer to as variational matrix-product-state approach (VMPS) in the following [3, 4]. This method can overcome the issue of Hilbert space truncation by using a flex-

ible, shifted optimized boson basis (OBB) [31], as shown in [6, 39]. Moreover, the mass-flow problem can be successfully cured by performing the variational procedure on C2-RWCs, as demonstrated in the main text. We briefly elaborate on the main aspects of the VMPS approach and refer to [6] for technical details.

The goal of the VMPS approach is to efficiently represent the ground state of a Wilson chain with N bath sites in the formalism of matrix-product states [38]. A generic MPS of a bosonic impurity model has the form

$$|\psi\rangle = \sum_{\sigma, \mathbf{m}} A^{[\sigma]} A^{[m_0]} A^{[m_1]} \dots A^{[m_N]} |\sigma\rangle |\mathbf{m}\rangle, \quad (\text{S25})$$

where $|\sigma\rangle$ represents the local space of the impurity (e.g., a spin- $\frac{1}{2}$ degree of freedom) and $\mathbf{m} = |m_0\rangle \dots |m_N\rangle$ describes the local boson number eigenstates in a truncated Fock basis, i.e., $f_n^\dagger f_n |\mathbf{m}\rangle = m_n |\mathbf{m}\rangle$ with $m_n = 0, 1, \dots, d_n - 1$. Starting with a random MPS, the ground state is approximated by iteratively varying the tensors $A^{[\dots]}$ to minimize the energy of the Wilson chain Hamiltonian, sweeping back and forth through the chain until a global energy minimum is reached with sufficient convergence.

One key advantage of VMPS over NRG is the ability to flexibly adapt the local bosonic state basis on each site of the Wilson chain during the optimization process. This concept of an adaptive boson basis enables us, for example, to determine the ground state also in the localized phase of the SBM faithfully, which is not possible in NRG calculations. Our OBB implementation includes two features: First, we introduce an additional basis transformation V with $V^\dagger V = \mathbb{1}$, which maps the local harmonic oscillator basis $|m_n\rangle$ onto a smaller effective basis $|\tilde{m}_n\rangle$ on each site n ,

$$|\tilde{n}_n\rangle = \sum_{m_n=0}^{d_n-1} V_{\tilde{m}_n, m_n} |m_n\rangle \quad (\tilde{m}_n = 0, \dots, \tilde{d}_n - 1). \quad (\text{S26})$$

V can be naturally embedded in the MPS structure and is optimized in an additional local update to determine the best set of local basis states $|\tilde{m}_n\rangle$ for the subsequent update steps [6].

Second, we explicitly incorporate any oscillator displacements occurring in strong-coupling phases when constructing the local boson basis sets. To this end, we shift the oscillator coordinate $\hat{x}_n = \frac{1}{\sqrt{2}}(f_n + f_n^\dagger)$ on each site n by its equilibrium value $\langle \hat{x}_n \rangle$ [30] employing an unitary transformation to the Hamiltonian of the system [6]. $\langle \hat{x}_n \rangle$ can be determined self-consistently in a variational setting. Using such a setup, the OBB is able to capture quantum fluctuations around the shifted coordinate $\hat{x}'_n = \hat{x}'_n - \langle \hat{x}_n \rangle$.

In practice, the shifted OBB not only allows a significant increase of the size of the local basis sets from $d_n \approx \mathcal{O}(10^2)$ to $d_n \lesssim \mathcal{O}(10^4)$ by means of the basis transformation V . In addition, the shifted oscillator basis enables us to account for the exponentially growing oscillator displacements in a numerically quasi-exact

way, which would require a local dimension of up to $d_n^{\text{eff}} \approx (10^{10})$ in a nonshifted basis [6].

An additional advantage of the variational optimization over NRG is the fact that the former typically involves multiple sweeps along the chain, so that information from different parts of the Wilson chain (i.e., from different energy scales) is incorporated during the optimization process. This feedback mechanism is not needed for chains that have energy-scale separation. However, the latter is violated at the last site of a C2-RWC, where the slow-mode energy shift is large enough to affect the nature of the MPS not only on the last site but also on several preceding sites. In contrast to NRG, the VMPS approach is capable of feeding back this slow-mode information from low-energy scales to higher ones during the optimization sweeps, which is key to successfully avoid any mass-flow effects.

Even though the VMPS scheme described above only targets the ground state, it can be used to mimic finite-temperature averages on the Wilson chain, such as the thermal average $\langle a+a^\dagger \rangle_T$ or $\langle \hat{\sigma}_z \rangle_T$ needed to compute the local susceptibility $\chi(T)$ for the DHO or SBM, respectively. To this end, we compute the ground-state expectation value $\langle G|a+a^\dagger|G \rangle_{N_T}$ or $\langle G|\hat{\sigma}_z|G \rangle_{N_T}$ for a length- N_T C2-RWC, where N_T is chosen such that the chain's lowest energy scale matches the temperature, $T \sim \Lambda^{-N_T}$. This works because, for a length- N_T chain, the response of the ground state is calculated for a discrete spectrum whose low-energy excitations have characteristic spacing T . This is the strategy that was used for the VMPS calculations of $\chi(T)$ reported in the main text. A more detailed description of this strategy is given in Sec. S-3 below, devoted to a detailed study of the dissipative harmonic oscillator (DHO). There we compare several different strategies for computing thermal averages and benchmark their results against the exact solution for $\chi(T)$.

An important prerequisite for studying critical properties is a highly accurate determination of the critical coupling α_c . Numerically, it can be found in several ways. First, by determining the α -value at which the susceptibility $\chi(T=0)$ diverges; this was our method of choice in the context of the DHO. Second, by monitoring how the NRG or VMPS energy flow diagrams evolve with α . For the SBM there exist a third option, namely monitoring the behavior of the average boson occupation per site, $\langle m_n \rangle$: at the phase boundary it stays almost constant throughout the chain, but in the delocalized (localized) phase it decreases (increases) towards the end of the Wilson chain. We used the third scheme for the SBM, since it can be automated very easily. C2-chains sometimes required additional fine-tuning, since the slow-mode shift always increases the occupation numbers at the end of the chain.

We end this section with some technical notes. All VMPS ground-state calculations in this work for both DHO and SBM were performed using a 1-site update with fixed bond dimension $D = 60$, $d_n = 100$, and

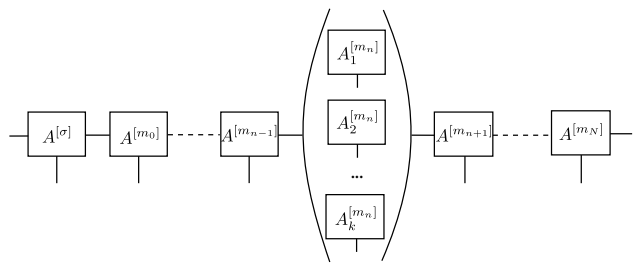


Figure S1. Illustration of mVMPS setup for variationally calculating the m lowest-energy excitation on a Wilson chain.

$\tilde{d}_n = 16$. Convergence was assumed if the change in the chain's ground-state energy dropped below the threshold $|\delta E_G| < 10^{-15}$, which for our longest chains corresponded to $\simeq 0.5$ of the hopping matrix element t_N to the last site. This typically took 10 to 50 sweeps. For the determination of the temperature-dependent susceptibility $\chi(T)$, we performed separate VMPS calculations for each value of T and used a five-point stencil to evaluate the numerical derivative with respect to ϵ . The convergence of the results with respect to all important numerical parameters was checked thoroughly.

C. Multilevel VMPS

The study of energy-level flow during the renormalization procedure is an important part of the NRG toolbox to characterize the fixed-point properties of an impurity model. However, in the presence of the mass-flow error, prominent for a bosonic bath with asymmetric bath spectrum, NRG does not correctly capture the physics of the critical fixed point and the resulting RG flow can no longer be considered reliable. On the other hand, we have already demonstrated that VMPS techniques are able to appropriately deal with mass flow; below we show that they can also be employed to properly access the energy-level flow at quantum critical points.

In its standard formulation, described above, VMPS only targets the ground state and does not have sufficient information about low-lying excited states on the Wilson chain to accurately describe the energy-level flow. In order to go beyond ground-state physics and properly capture the critical energy-level RG flow of multiple low-lying levels, we have implemented a multi-level VMPS (mVMPS) optimization scheme, in the spirit of Ref. [5], that simultaneously targets the lowest k energy eigenstates $|\psi_j\rangle$. A detailed description of our procedure may be found in Sec. 2.3.6 of [40]. Here we just outline the main idea.

Assuming canonical form of the MPS with the center shifted to site n , we define an array $\mathbf{A}^{[m_n]}$ consisting of k tensors $\{A_1^{[m_n]}, A_2^{[m_n]}, \dots, A_k^{[m_n]}\}$ (illustrated in Fig. S1).

For each tensor $A_j^{[m_n]}$, with $j = 1, \dots, k$, the state

$$|\psi_j\rangle = \sum_{\sigma, \mathbf{m}} A^{[\sigma]} A^{[m_0]} \dots A^{[m_{n-1}]} A_j^{[m_n]} A^{[m_{n+1}]} \dots A^{[m_N]} |\sigma\rangle |\mathbf{m}\rangle, \quad (\text{S27})$$

describes one of the k lowest-energy eigenstate of the specified Wilson chain Hamiltonian; the state corresponding to $j = 1$ targets the ground state. The optimization procedure then works as follows: we generate a local Krylov space on site n by subsequent application of the Hamiltonian on each of the k orthonormal states associated with the array $\mathbf{A}^{[m_n]}$. The resulting Hamiltonian \hat{H}_n has a block structure in the Krylov space, with nonzero elements in form of $k \times k$ blocks along the diagonal and the first off-diagonal. Next, we diagonalize the Hamiltonian in the Krylov subspace and construct from its eigenvectors an updated version of the array $\mathbf{A}^{[m_n]}$, each element being orthonormal to the others by construction. To move the orthonormal center of the MPS to the next site ($n + 1$), we form the reduced density matrix $\rho_{n,n+1}^{\text{red},j}$ of each component j by tracing out the rest of the chain and sum them up to form $\rho_{n,n+1}^{\text{red}}$. Similar to the original DMRG formulation, we then diagonalize $\rho_{n,n+1}^{\text{red}}$; keep only the D largest eigenvalues and use the resulting isometry to move the orthonormal center to site $n + 1$. We repeat the optimization procedure, sweeping multiple times through the entire chain. Convergence was assumed when the change in each energy level E_j dropped below the threshold $|\delta E_j| < 10^{-11}$, which for our longest multi-level chains corresponded to $\simeq 10^{-3}$ of the hopping matrix element t_N to the last site. In all mVMPS calculations we used bond dimensions of $D = 100$, $d_n = 40$.

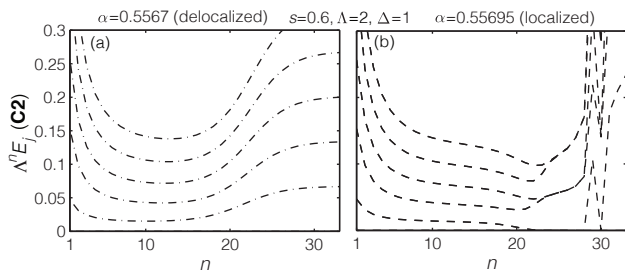


Figure S2. Energy-flow diagrams obtained with mVMPS for the SBM on a C2-RWC. (a) Flow to the delocalized fixed point, characterized by a unique ground state. (b) Flow to the localized fixed point, featuring a doubly degenerated ground-state level. Note that the flow gets distorted deep in the localized regime. This is a signature of the exponentially growing oscillator shifts which cannot be properly dealt with in the mVMPS setup.

To account for the mass flow in the energy-level flow of a length- N RWC system, we conduct a *separate* mVMPS calculation for *every* chain length $N' < N$. This ensures that the k excited states properly take into account the fast- and slow-mode correction at a particular energy scale, which is crucial for correctly describing the critical energy flow at a Gaussian fixed-point. Combining

the results for various lengths and rescaling each set of energies appropriately by a factor $\Lambda^{N'}$, we obtain the energy-flow diagrams in a variational setup.

In addition to the critical fixed-point flows shown in Fig. 3 of the main text, we here present the energy-flow to the stable fixed points in Fig. S2. Panel (a) displays the energy flow to the delocalized fixed point ($\alpha < \alpha_c$), which features a nondegenerate ground state. In contrast, the fixed point flow to the localized fixed point ($\alpha > \alpha_c$) in panel (b) clearly shows a doubly degenerated ground state before getting numerically distorted by the exponentially growing oscillator displacements.

The main goal of our mVMPS calculations was to study the *critical* energy-level flow for the SBM. Since at the critical point the truncation of the bosonic Hilbert space is not problematic, it was not necessary to incorporate the OBB scheme in our mVMPS setup. Doing so would become essential, however, when studying the effects of a local bias, $\epsilon \neq 0$, since then $\langle \hat{\sigma}_z \rangle \neq 0$. In particular, this would be needed if one wishes to compute the static susceptibility $\chi(T)$ using not just the VMPS ground-state expectation value for a length- N_T RWC (as described above), but a thermal average over a shell of low-lying VMPS eigenstates (as done in NRG). We have refrained from attempting such combined mVMPS+OBB computations of $\chi(T)$, since they are numerically expensive, and the ground-state-based scheme worked very well.

S-3. DISSIPATIVE HARMONIC OSCILLATOR

In this section, we perform a systematic study of the properties of RWCs in the context of the exactly solvable DHO, which was briefly introduced in the main text. We compare the RWC and SWC setups in detail with respect to the following issues: iteration details, static susceptibility, and critical coupling α_c .

A. Iteration details

We introduced two types of RWCs in the main text: C1 chains, which include only the fast shifts ($\delta \varepsilon_N^S = 0$), and C2 chains, which contain both slow- and fast-mode shift in Eq. (4). For completeness, we also discuss a third type of RWC to be called C0 chains, which by definition include no energy shifts, i.e. $\delta \varepsilon_n^{S/F} = 0$ in Eq. (4).

We have explored two versions of the RWC iteration scheme, that differ only in the choice of the frequencies $\omega_{S_n}^+$ that define the intervals $I_n^S = [0, \omega_{S_n}^+]$. For version 1, we chose $\omega_{S_n}^+$ in such a manner that the resulting hopping matrix elements t_n^S of the OWC agree with those used by Bulla, Tong and Vojta (BTV), [24] to be called t_n^{BTV} [Eq. (13) of Ref. 24], with relative error below 10^{-3} . (The error could be further reduced, if desired, by using a finer

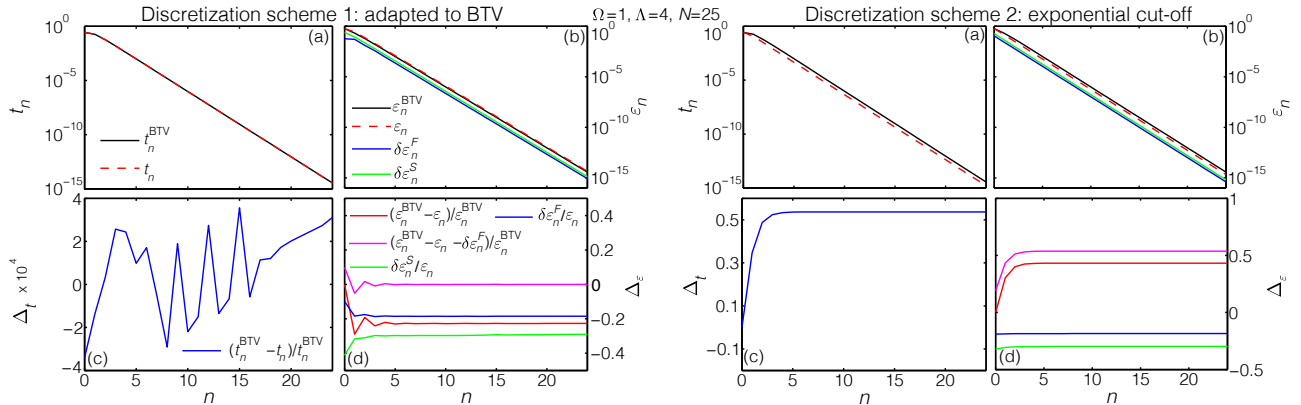


Figure S3. Iteration details: chain parameters. (a-d) Comparison of the Wilson chain parameters t_n and ε_n for $\alpha = 0.199$, obtained using the standard discretization scheme of BTV [24] for $\Lambda = 4$, or using two versions of the RWC-approach described above: for version 1 (left two columns), $\omega_{S,n}^+$ was fine-tuned to ensure that $t_n = t_n^{\text{BTV}}$; for version 2 (right two columns), we simply chose $\omega_{S,n}^+ = \omega_{S,n-1}^+/\Lambda$. (a) t_n^{BTV} used by BTV (black) and our t_n^S (red dashed). (b) The onsite energies $\varepsilon_n^{\text{BTV}}$ (black), our C0 onsite energies ε_n (red dashed), and the shifts $|\delta\varepsilon_n^F|$ (blue) and $|\delta\varepsilon_n^S|$ (green). Evidently, they all scale the same way with n . (c) Relative difference $\Delta_t = (t_n^{\text{BTV}} - t_n^S)/t_n^{\text{BTV}}$ in hopping elements. The noisy structure seen for version 1 (left, note the amplification factor of 10^4) reflects the ω -discretization grid used to represent the bath correlators $\mathcal{G}_n^X(\omega)$ during the OWC construction. (d) Relative differences Δ_ε of various onsite energies: $\Delta_\varepsilon^{\text{C0}} = (\varepsilon_n^{\text{BTV}} - \varepsilon_n)/\varepsilon_n^{\text{BTV}}$ (red); $\Delta_\varepsilon^{\text{C1}} = (\varepsilon_n^{\text{BTV}} - \varepsilon_n - \delta\varepsilon_n^F)/\varepsilon_n^{\text{BTV}}$ (purple); $\Delta_\varepsilon^F = \delta\varepsilon_n^F/\varepsilon_n$ (blue); and $\Delta_\varepsilon^S = \delta\varepsilon_n^S/\varepsilon_n$ (green). For version 1 (left), the relative difference between BTV and C0 energies (no shifts) is quite significant throughout ($\Delta_\varepsilon^{\text{C0}} \simeq 0.2$). The relative difference between BTV and C1 energies (only fast shifts) is significant for early iterations, but becomes small ($\Delta_\varepsilon^{\text{C1}} \lesssim 10^{-3}$) once the iteration scheme reaches self-similarity. For version 2 (right), both $\Delta_\varepsilon^{\text{C0}}$ and $\Delta_\varepsilon^{\text{C1}}$ differ significantly from 0. Both the fast and last slow mode shifts are comparable in magnitude to the bare OWC energies, $\mathcal{O}(\Delta_\varepsilon^{F/S}) = 1$.

frequency grid for representing $\Gamma_n(\omega)$, and more accurately fine-tuning the numerical integration routine used to evaluate the integral that yields t_n^S .) For version 2, we used a plain exponential discretization, $\omega_{S,n}^+ = \omega_{B,n}^+/\Lambda$.

A comparison of the resulting t_n^S , the bare onsite energies ε_n and the shifts $\delta\varepsilon_n^{F/S}$, is shown in Fig. S3. It has two take-home messages: First, all these quantities scale the same way with n and are comparable in magnitude [Figs. S3(a,b)]. In particular, the fast and slow shifts $\delta\varepsilon_n^{F/S}$ are comparable to the bare OWC energies ε_n . Second [Figs. S3(d)], our RWT energies, both $\varepsilon_n + \delta\varepsilon_n^F$ and $\varepsilon_n + \delta\varepsilon_n^F + \delta\varepsilon_n^S$, are in general different from the SWC onsite energies $\varepsilon_n^{\text{BTV}}$ obtained by BTV using standard Wilsonian discretization and tridiagonalization, the relative difference being $\mathcal{O}(1)$. For version 1, however, we note that the relative difference between $\varepsilon_n + \delta\varepsilon_n^F$ and $\varepsilon_n^{\text{BTV}}$ becomes negligible for after a few iterations, but for early ones the difference remains.

Note that we also explored a third discretization scheme similar to version 1, with the difference that we fixed the truncation energies $\omega_{S,n}^+$ such that the resulting hoppings agree with those resulting from the improved logarithmic discretization recently proposed by Zitko and Pruschke (ZP) [26]. This leads to results qualitatively similar to those of version 1, therefore we refrained from including them in the discussion above.

The results in the main text were obtained using version 2. This discretization scheme is particularly appealing due to its accuracy and simplicity. It is more ac-

curate than standard Wilsonian discretization, since by construction it reproduces the hybridization function correctly. The discretization scheme of ZP was devised to achieve this, too, but our scheme turns out to be more accurate, due to its inclusion of TBMs (compare green and red symbols in Fig. S5 below). Our discretization scheme is also simpler to implement than that of ZP, since their chain parameters are found by solving a differential equation, whereas our chain parameters (fixed fully by the energies $\tilde{\varepsilon}_n$ and couplings t_n^S) are found purely by numerical integrations. The accuracy of the latter can be easily controlled by distributing the grid points logarithmically and, in particular, increasing the resolution around the cut-off frequencies $\omega_{S,n}^+$. Note that our discretization scheme offers great flexibility, as one can easily relax the logarithmic discretization in favour of a linear or mixed one (log-linear or linear-log) if high- or low-energy properties need to be taken into account more carefully [4]. (The resulting chain would then have to be treated purely with VMPS methods.)

In addition, we have also examined the retarded self-energies Σ_n^S generated in different iterations n and checked to what extent our chain parameters reproduce the original bath correlator $\mathcal{G}^{\text{bath}}$ [Fig. S4]. (In this context, the two discretization schemes yield qualitatively similar results, so that Fig. S4 only displays version 2.) The main conclusion drawn from the real and imaginary part of Σ_n^S [Figs. S4(a,b)] for the power-law coupling spectrum Γ^{bath} considered here is that the iteration

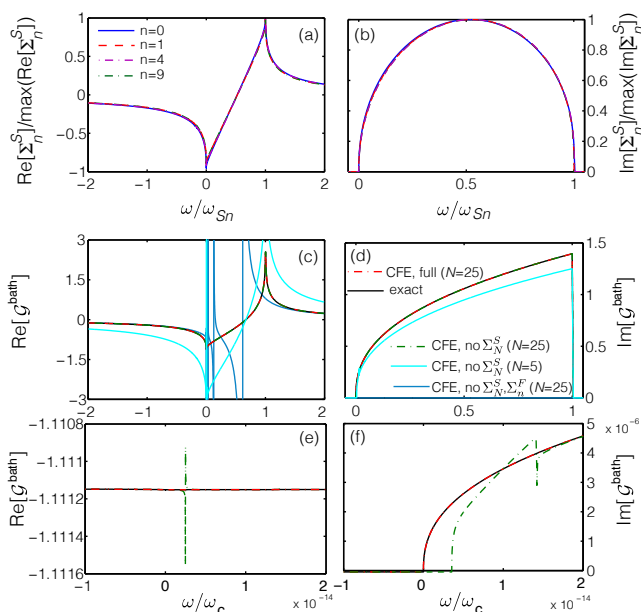


Figure S4. Iteration details: self-energies. (a) $\text{Re}[\Sigma_n^S(\omega)]$ and (b) $\text{Im}[\Sigma_n^S(\omega)]$, plotted vs. $\omega/\omega_{S_n}^+$ for $n = 0, 1, 4, 9$ (different colors), showing that the spectral functions and self-energies have a self-similar structure. (c-f) Various CFE representations of $\mathcal{G}^{\text{bath}} = \mathcal{G}_0$. (c) $\text{Re}[\mathcal{G}^{\text{bath}}(\omega)]$ and (d) $\text{Im}[\mathcal{G}^{\text{bath}}(\omega)]$ vs. ω/ω_c , calculated directly from $\Gamma^{\text{bath}}(\omega)$ (solid black), or from a CFE while including both $\Sigma_n^F(\omega)$ and $\Sigma_n^S(\omega)$ with $N=25$ (dashed red), only $\Sigma_n^F(\omega)$ with $N=5$ (cyan) or $N=25$ (dashed green), or neither of the two with $N=25$ (blue). In the latter case, the absence of any imaginary parts in the CFE causes $\text{Im}[\mathcal{G}^{\text{bath}}(\omega)]$ to vanish and $\text{Re}[\mathcal{G}^{\text{bath}}(\omega)]$ to have divergences. Behavior of (e) $\text{Re}[\mathcal{G}^{\text{bath}}(\omega)]$ and (f) $\text{Im}[\mathcal{G}^{\text{bath}}(\omega)]$ for $\omega \rightarrow 0$ with the same color code as in (c,d). The missing slow-mode term in the CFE using only $\Sigma_n^F(\omega)$ (green) causes discrepancies for both the imaginary and the real part only in the vicinity of $\omega = 0$ illustrating that the effect of slow-mode shifts becomes noticeable only at the lowest energy scale of a Wilson chain, associated with its last site.

scheme has a self-similar structure, in that the shape of $\text{Re}[\Sigma_n^S(\omega)]$ and $\text{Im}[\Sigma_n^S(\omega)]$ vs. ω/ω_{S_n} does not change with n . Moreover, the continued fraction expansion of $\mathcal{G}^{\text{bath}}$ [Figs. S4(c-f)] fully reproduces the original function (black) if both the fast- and last mode contributions $\Sigma_n^{F/S}(\omega)$ are included (dashed red), but if these are neglected (dashed green, cyan, blue), the low-frequency behavior changes significantly.

B. Various averaging schemes

For the VMPS calculations of $\chi(T)$ reported in the main text, we mimicked thermal averages by ground-state expectation values of C2-RWCs of length N_T . However, we have also explored several other averaging

schemes. For the sake of completeness, we briefly describe them here, and in the next section compare their results for the susceptibility of the DHO.

For a RWC of specified length N , we have explored the following ways of calculating ground-state expectation values or thermal averages, distinguished by combinations of the following labels: W stands for *Wilsonian* NRG with energy-based truncation; V for *variational* MPS; G for a ground-state expectation value; and T for a thermal average. For Wilsonian NRG calculations, we denote the eigenstates and -energies of Wilson shell n by $|s\rangle_n^W$ and $E_{s_n}^W$, and by $|G\rangle_n^W$ and $E_{G_n}^W$ for that shell's ground state. For VMPS calculations, we variationally minimize the ground-state expectation value of a length- N RWC in the space of all MPS having specified matrix dimensions. Call the resulting ground state $|G\rangle_N^V$, with energy $E_{G_N}^V$.

We write $\langle \hat{O} \rangle_N^{GZ} = \frac{Z}{N} \langle G | \hat{O} | G \rangle_N^Z$ for a ground-state expectation value of type $Z = W$ or V . We write N_T for the length of a RWC whose smallest excitation energies are comparable to the temperature,

$$\max\{|\tilde{\epsilon}_{N_T}|, |t_{N_T}^S|\} \simeq T, \quad (\text{S28})$$

and $\langle \hat{O} \rangle_{N_T}^{\text{TW}}$ for a thermal average over all Wilson shell states $|s\rangle_{N_T}^W$. We will call this TW-averaging. Thermal averages can also be mimicked using a single state associated with a length- N_T chain, e.g. $\langle \hat{O} \rangle_{N_T}^{GZ} = \frac{Z}{N_T} \langle G | \hat{O} | G \rangle_{N_T}^Z$ (GW- or GV-averaging), because, by the choice of N_T , the characteristic energy spacing for low-energy excitations above such a state is of order T . GW-, TW- and GV-averaging require calculating a separate length- N_T chain for every temperature.

C. Susceptibility

In this section, we compare the various types of RWCs discussed above (C0,C1,C2) and the various averaging schemes by using them to calculate the static susceptibility of the DHO. It is defined by

$$\chi(T) = \lim_{\epsilon \rightarrow 0} \frac{d\langle a + a^\dagger \rangle_T}{d\epsilon}, \quad (\text{S29})$$

where $\langle \dots \rangle_T$ denotes a thermal expectation value. Its form is easily found analytically [17],

$$\chi_{\text{exact}}(T) = \frac{1}{\Omega + \text{Re}(\mathcal{G}^{\text{bath}}(\omega = 0))}, \quad (\text{S30})$$

which, importantly, is independent of temperature.

Alternatively, the static susceptibility can also be calculated via the dynamical correlation function

$$C(\omega) = \frac{1}{2\pi} \int_{-\infty}^{\infty} e^{i\omega t} C(t) dt, \quad (\text{S31})$$

where $C(t) = \frac{1}{2} \langle [(a + a^\dagger)(t), (a + a^\dagger)] \rangle_T$. The integral

$$\chi_{\text{dyn}}(T) = 4 \int_0^{\infty} \frac{C(\omega)}{\omega} d\omega \quad (\text{S32})$$

can analytically be shown to equal the static susceptibility, $\chi(T) = \chi_{\text{dyn}}(T)$, yielding an important consistency check for numerical calculations. Our Wilsonian NRG calculations passed this check for all three types of RWC introduced above (C0, C1, C2), where $\chi(T)$ was calculated by evaluating $\langle \dots \rangle_T$ in Eq. (S29) using a Wilson-shell thermal average $\langle \dots \rangle_{N_T}^{\text{TW}}$, and $\chi_{\text{dyn}}(T)$ was calculated using fdm-NRG [35]. This illustrates the internal consistency of Wilsonian NRG for a given RWC. However, none of these calculations reproduce the exact result (S30). In contrast, the latter *is* reproduced correctly when calculating χ using VMPS on chain type C2, as we now discuss in detail.

Fig. S5 shows $\chi(T)$ for three types of RWC, C0 (blue), C1 (green), and C2 (red), calculated in four different ways, involving either a CFE (solid lines), or a thermal average over Wilson shell N_T (TW, triangles), or two types of expectation values w.r.t. states associated with site N_T (GW, GV), as detailed in the figure caption. We observe the following salient features.

First, all four methods yield mutually consistent results both for C0 and for C1, but not for C2 (all orange data lie on a line, as do all blue data, but not all red data). Thus the methods differ mainly in their treatment of slow last modes, which are absent in C0 and C1, but present in C2.

Second, for C0 (orange), which has the structure of a *standard* Wilson chain without any TBM information included, $\chi_{C0}(T)$ differs from the exact result, χ_{exact} (dashed black line) in two important ways: instead of being T -independent, $\chi_{C0}(T)$ increases with decreasing T , eventually saturating toward a constant value, $\chi_{C0}(0)$; and this constant value disagrees from χ_{exact} . The reason for these failings was identified clearly by VBGA [17]: the neglect of TBMs causes $\text{Re}[\mathcal{G}^{\text{bath}}(0)]$ to be represented incorrectly [as is also clearly visible in Fig. S4(c)]. VBGA called the missing contribution to $\text{Re}[\mathcal{G}^{\text{bath}}(0)]$ a “mass-flow” error (since near a quantum phase transition, it implies an artificial scale-dependent shift of the order-parameter mass).

Third, for C1 (blue), which includes fast but not last slow modes, the T -dependence of $\chi_{C1}(T)$ persists, but its asymptotic low-temperature value agrees with the exact one, $\chi_{C1}(0) = \chi_{\text{exact}}$. Thus, including fast modes is essential to get the asymptotic value right. Indeed, if they are omitted but the slow mode correction included, one obtains curves (not shown) whose $T \rightarrow 0$ limits corresponds to those of C0 curves rather than the exact result.

Fourth, for C2 (red), which includes fast and last slow modes, two methods fully reproduce the T -independent result $\chi_{C2}(T) = \chi_{\text{exact}}$: CFE and GV. Their common feature is that both succeed in fully incorporating the slow-mode contributions to $\text{Re}[\mathcal{G}^{\text{bath}}(0)]$. For the CFE this is guaranteed by construction. For GV-averaging using $|G\rangle_{N_T}^{\text{V}}$, it reflects the ability of the variational MPS scheme to correctly deal with the large energy shift $\delta\varepsilon_{N_T}^{\text{S}}$ at the end of the length- N_T RWC.

Fifth, the other two methods fail to yield a T -independent result even for C2, since, being based on Wilsonian NRG, they fail to properly deal with the last slow shift. TW- and GW-averaging involve, respectively, a thermal average or ground-state expectation value for Wilson shell N_T ; but the slow shift $\delta\varepsilon_{N_T}^{\text{S}}$ on the last site is so large that upon adding it to the chain, some feedback to earlier sites becomes necessary. Since Wilsonian NRG does not allow for such feedback, while a variational MPS approach does (through back and forth optimization sweeps along the chain), TW- and GW-averaging fail, whereas GV-averaging does not. We also note that GW does better (yielding a weaker T -dependence) than TW. Presumably the reason is that the thermal average used by the latter incorporates information from higher-lying Wilson states $|s\rangle_{N_T}^{\text{W}}$, for which the $\omega = 0$ focus of the static approximation works less well than for the shell’s ground state $|G\rangle_{N_T}^{\text{W}}$.

The upshot of the above analysis is that GV-averaging fully meets the challenge of correctly computing $\chi(T)$ for the DHO. Therefore, GV-averaging was the scheme used for the VMPS calculation of $\chi(T)$ reported in Figs. 2 and 3 of the main text.

D. Critical coupling α_c

We now turn our attention a small but very important detail illustrating the power of RWCs to minimize discretization artefacts: the determination of the critical coupling α_c . Its analytical value for the parameters used here is $\alpha_c = 0.2$. Numerically, we determined α_c by monitoring the divergence of the susceptibility, as described at the end of Sec. S-2C.

On a SWC with $\Lambda = 4$, the analytical value is either largely overestimated when using the BTV discretization scheme ($\alpha_c^{\text{BTV}} \approx 0.228$), or underestimated when using the improved ZP discretization ($\alpha_c^{\text{ZP}} \approx 0.1984$); the deviations are due to the missing information of the TBMs in the Wilson chain setup. In Fig. S5, computed for $\alpha = 0.199$, this causes the low-temperature limit of the susceptibilities χ^{BTV} and χ^{ZP} to lie far below or above the analytical value χ_{exact} , respectively. (In fact, χ^{ZP} diverges in that figure because $\alpha = 0.199$ lies above the critical coupling α_c^{ZP} .)

In contrast, the critical coupling obtained for a C2-RWC matches almost perfectly with the analytic result. For our setup, we found $\alpha_c = 0.199998$. It is possible to systematically reduce the deviation from the analytical value of α_c even further by improving the resolution of the frequency grid used to represent $\mathcal{G}_n^{\text{X}}(\omega)$ while constructing a RWC. Once again, this illustrates the power of our RWC construction and points out how missing TBMs can introduce systematic “discretization” artefacts. Correspondingly, we expect that RWCs will turn out to be useful for reducing discretization artefacts also for other dynamic quantities such as local spectral functions.

As α is tuned ever closer to α_c , the VMPS scheme ex-

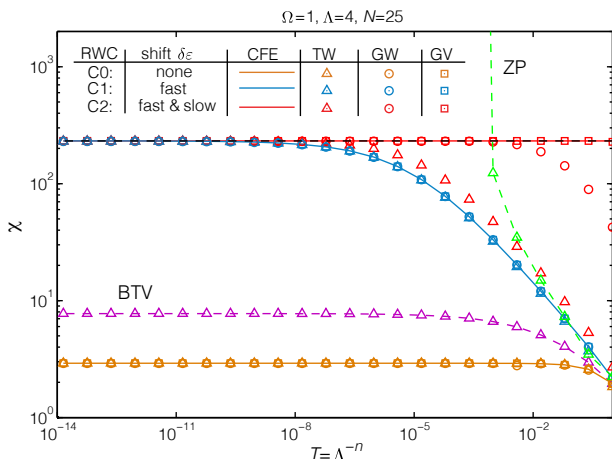


Figure S5. The static susceptibility $\chi(T)$ of the DHO as function of temperature, for $\alpha = 0.199$, $s = 0.4$. The black dashed line gives the exact result χ_{exact} expected from Eq. (S30), the purple and green symbols the results obtained with standard NRG using the discretization scheme of BTM and ZP, respectively. The other data are numerical results for three types of RWC, C0 (orange), C1 (blue), and C2 (red), obtained in four different ways. The first uses a CFE of length N_T to evaluate $\text{Re}[\mathcal{G}_0(0)]$ in Eq. (S30) (CFE, solid lines), while including both $\Sigma_n^S(\omega)$ and $\Sigma_n^F(\omega)$ for C2 (red), only $\Sigma_n^F(\omega)$ (blue), or neither of the two (orange). The second evaluates $\langle \dots \rangle_T$ in Eq. (S29) as thermal average over Wilson shell N_T (TW, triangles). The other two ways approximate $\langle \dots \rangle_T$ by an expectation value taken w.r.t. one of two different single states: the ground state $|G\rangle_{N_T}^W$ of Wilson shell N_T (GW, circles) and the variational ground state $|G\rangle_{N_T}^V$ of a length- N_T chain (GV, squares). In all cases, the derivative $d/d\epsilon$ in Eq. (S29) was evaluated numerically, using several ϵ -values chosen small enough (typically $\ll T$) to ensure that the calculated averages depend linearly on ϵ . TW-, GW- and GV-averages require a separate run for each combination of T and ϵ .

periences increasing convergence problems, resulting in increasing errors for $\chi(0)$. This is not surprising, because the effective potential of the DHO becomes ever shallower the nearer α approaches α_c , where the energy of one mode vanishes. That leads to very large zero-point fluctuations, and a very strong linear response to small values of ϵ . Increasing the VMPS bond dimension to keep more states during the calculation failed to significantly improve $\chi(0)$. We were able to ameliorate this convergence problem to some extent by implementing an optimized boson basis designed to incorporate large bosonic displacements. However, as a matter of principle, this problem will become unmanageable in the limit $\alpha \rightarrow \alpha_c$.

S-4. RG FLOW TOWARDS GAUSSIAN FIXED POINT

In this section, we connect the numerically obtained energy-level diagrams to analytical considerations and

show that the numerical results prove the existence of a Gaussian critical fixed point for the SBM with bath exponents $0 < s \leq 0.5$.

Using a Feynman path-integral representation, the spin-boson model (7) can be shown to be equivalent – in the scaling limit – to the following one-dimensional ϕ^4 theory:

$$\mathcal{S} = \int \frac{d\omega}{2\pi} (m_0 + |\omega|^s) |\phi(i\omega)|^2 + \int d\tau [u_0 \phi^4(\tau) + \bar{\epsilon} \phi(\tau)] \quad (\text{S33})$$

where $\bar{\epsilon}$ is a rescaled bias, and the $|\omega|^s$ term arises from integrating out the oscillator bath with bath exponent s ; this generates a bilinear coupling which is long-ranged in time. m_0 is the (bare) mass of the Ising order parameter ϕ ; an increase of m_0 corresponds to a decrease in the dissipation strength α . Finally, u_0 is the quartic self-interaction. By universality arguments, the same ϕ^4 theory also describes the phase transition of a classical Ising chain with $1/r^{s+1}$ interactions.

Power counting in Eq. (S33) yields the scaling dimensions at criticality:

$$\begin{aligned} \dim[\phi(\tau)] &= (1-s)/2, \\ \dim[u_0] &= 1 - 4\dim[\phi(\tau)] = 2s - 1, \end{aligned} \quad (\text{S34})$$

i.e., the system is above (below) its upper-critical dimension for $s < 0.5$ ($s > 0.5$).

In the following, we focus on the regime $0 < s \leq 0.5$ where the transition is controlled by a Gaussian fixed point. Although the quartic interaction u_0 is irrelevant at criticality, i.e., its fixed-point value is zero, it is required to stabilize the system and it influences observables in a nontrivial fashion, hence it is termed “dangerously irrelevant”. The scaling dimension (S34) implies that the leading-order behavior of the dimensionless renormalized quartic coupling u , defined as $u_0 = \mu^{1-2s}u$ with μ a renormalization energy scale, at criticality is given by

$$u \propto \varepsilon_{\text{uv}}^{1-2s} \quad (\text{S35})$$

with logarithmic corrections present at $s=0.5$, where ε_{uv} is the running ultraviolet cutoff. From this we can expect that the many-body spectrum, i.e., the energy-level flow as described above, displays families of levels whose spacing goes to zero as the cutoff energy ε_{uv} goes to zero. This is in contrast to interacting critical fixed points, here realized for $0.5 < s < 1$ where the renormalized u reaches a finite fixed-point value: This causes the level spacings to approach constant values as $\varepsilon_{\text{uv}} \rightarrow 0$ (see Ref. 41 for a detailed analysis of NRG fixed-point spectra at interacting critical points). Both behaviors are nicely borne out by our numerical results in Figs. 4 and S6.

While the effect of u on many observables can be calculated using (renormalized) perturbation theory, this does not apply to the level spectrum at criticality: For $u = 0$ the spectrum is degenerate (reflecting a bosonic zero mode), such that the effect of u is nonperturbative. This zero-mode physics in the presence of a quartic interaction is captured by the toy-model Hamiltonian for

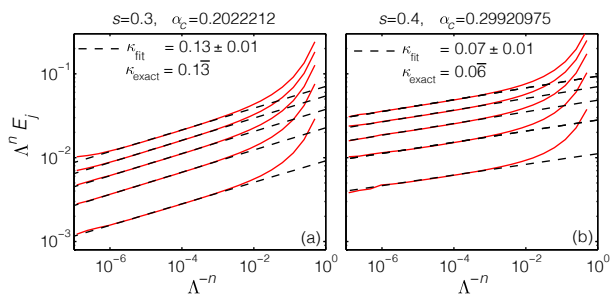


Figure S6. Energy-level flow diagram for the SBM on a C2-RWC obtained for (a) $s = 0.3$ and (b) $s = 0.4$ at the critical point. The dashed lines illustrate the power-law fits employed to extract the exponent κ characterizing the Gaussian fixed point. The numerical results are in excellent agreement with the analytical prediction $\kappa = (1 - 2s)/3$.

a quartic oscillator, $\mathcal{H}_4 = p^2/(2m) + ux^4$ in standard notation. Scaling considerations shows that the eigenenergies of this model obey the exact scaling $e_i \propto u^{1/3}$. Importantly, this toy model, if used with a renormalized

u , describes *renormalized* energy levels.

Let us now connect the behavior of these renormalized energy levels with those generated by NRG. To this end, we note that in NRG the Wilsonian scale $\varepsilon_n \propto \Lambda^{-n}$, which is an infrared cutoff, controls the RG flow in a way analogous to that of the running UV cutoff ε_{UV} in a perturbative RG scheme, as both schemes are designed to describe the renormalized physics at the scale ε_{UV} . Indeed, in an NRG calculation the ultraviolet cutoff at a fixed point is a multiple of the infrared cutoff ε_n . Combining the energy scaling of \mathcal{H}_4 with Eq. (S35), we conclude that the low-lying renormalized energy levels obtained from mVMPS, $\Lambda^n E_j$, scale with the Wilsonian energy scale $\varepsilon_n \propto \Lambda^{-n}$ as

$$\Lambda^n E_j \propto (\Lambda^{-n})^\kappa \quad \text{with } \kappa = (1 - 2s)/3, \quad (\text{S36})$$

characterizing the approach to a Gaussian fixed point. Fig. S6 shows a log-log plot of the energy-level flow for two values of s , together with a power-law fit. We obtain $\kappa = 0.13 \pm 0.01$ for $s = 0.3$ and $\kappa = 0.07 \pm 0.01$ for $s = 0.4$, in excellent agreement with the analytical prediction, which yields $0.4/3 = 0.13$ and $0.2/3 = 0.06$, respectively.

Spectral features of one-dimensional quantum systems

The examination of ground-state wavefunctions yields fascinating information about properties of low-dimensional quantum systems from a theoretical point of view. However, experimentalists have only limited access to the actual ground state of a quantum nanosystem or material as their setups are notoriously plagued by thermal noise and disorder effects. It is therefore highly desirable to establish and improve numerical approaches to study the *dynamical* quantities of a quantum many-body system.

Spectral functions represent a particularly interesting class of dynamic observables which encode various characteristics of a system, ranging from the classification of quantum phases, over the nature of low-energy excitations to equilibrium transport properties. Typical examples are dynamical spin-structure factors of spin materials or local densities of states in electron systems, which both yield helpful insights into nature of the excitation spectrum in a quantum system. Moreover, these observables are directly accessible for experimentalists by means of spectroscopy techniques such as ARPES or neutron scattering.

MPS techniques are particularly well-suited to compute spectral functions of one-dimensional quantum systems [see Sec. 2.4.6]. tDMRG and CheMPS, in particular, are powerful tools capable of extracting spectral information in such models with unprecedented accuracy, despite being ultimately limited by entanglement growth. Approaches based on exact diagonalization or quantum Monte-Carlo cannot be considered as viable alternatives in 1D, as their applicability is either restricted by system size or an ill-defined analytic continuation from the imaginary frequency axis.

In this chapter, we extensively apply tDMRG and CheMPS to obtain spectral properties for several different one-dimensional quantum systems at zero and finite temperatures. First of all, we consider an effective spin- $\frac{1}{2}$ XXZ chain capturing the low-energy properties of the material Cs_2CoCl_4 and study the dynamic spin-structure factors as a function of a transverse magnetic field that drives a Ising quantum phase transition [see Sec. 4.1]. Moreover, we propose a symmetry-enhanced version of the minimally entangled typical states algorithm designed for the study of dynamical quantities at finite temperatures in Sec. 4.2. This algorithm is capable of outperforming other state-of-the-art techniques particularly at low temperatures, which we demonstrate by computing the finite-temperature excitation spectrum of an effective spin-ladder model for the natural mineral azurite $\text{Cu}_3(\text{CO}_3)_2(\text{OH})_2$. Finally, we perform tDMRG calculations extracting the local density of states in an interacting quantum point contact [see Sec. 4.3]. Our quasi-exact numerical results are mainly intended to support the validity of a functional RG technique that aims at resolving the long-standing puzzle of the 0.7 anomaly in the lowest conductance step of this system.

Our work in this chapter provides substantial new information on two very interesting

low-dimensional spin materials. Moreover, it contributes to the advancement of dynamic MPS techniques by (i) benchmarking tDMRG and CheMPS for the first time in the context of spectral functions, and (ii) by notably improving an existing finite-temperature algorithm.

4.1 Dynamic structure factor of the spin- $\frac{1}{2}$ XXZ chain in a transverse field

In the following article [BWvDG16] we consider a spin- $\frac{1}{2}$ XXZ chain with easy-plane anisotropy in a transverse magnetic field. This model describes well the thermodynamic properties of the material Cs_2CoCl_4 in a wide range of temperatures and fields. Employing both tDMRG and CheMPS, we present results of an extensive numerical study of its dynamic structure factor $\mathcal{S}^{\alpha\beta}(k, \omega)$ with a particular focus on the Ising quantum phase transition separating a gapped spin-flop phase and a gapped spin-polarized phase.

Going beyond what is known from mean-field theory and exact results, our study reveals interesting new features in the spectra of the correlators. For example, the transverse correlator \mathcal{S}^{zz} features additional spectral weight at higher energies over the single-particle excitation, which we tentatively attribute to a repulsively bound pair of particles. Moreover, we include a technical section, where we compare the numerical efficiency of real-time evolution to an MPS-based Chebyshev expansion in the present context.

Our work sets the scene for detailed future theoretical and experimental studies of the rich spectral features of the spin- $\frac{1}{2}$ XXZ model. In particular, it would be worthwhile to compare our results to inelastic neutron scattering experiments on the compound Cs_2CoCl_4 . We hope that this work will motivate such an experiment in the near future.

P3 *Dynamic structure factor of the spin- $\frac{1}{2}$ XXZ chain in a transverse field*

B. Bruognolo, A. Weichselbaum, J. von Delft, and M. Garst

Phys. Rev. B 94, 085136 (2016)

Dynamic structure factor of the spin- $\frac{1}{2}$ XXZ chain in a transverse field

Benedikt Bruognolo,¹ Andreas Weichselbaum,¹ Jan von Delft,¹ and Markus Garst^{2,3}

¹*Physics Department, Arnold Sommerfeld Center for Theoretical Physics, and Center for NanoScience, Ludwig-Maximilians-Universität, Theresienstraße 37, 80333 München, Germany*

²*Institut für Theoretische Physik, Universität zu Köln, Zùlpicher Str. 77a, 50937 Köln, Germany*

³*Institut für Theoretische Physik, Technische Universität Dresden, 01062 Dresden, Germany*

(Received 22 June 2016; published 22 August 2016)

The spin- $\frac{1}{2}$ XXZ chain with easy-plane anisotropy in a transverse field describes well the thermodynamic properties of the material Cs_2CoCl_4 in a wide range of temperatures and fields including the region close to the spin-flop Ising quantum phase transition. For a comparison with prospective inelastic neutron scattering experiments on this compound, we present results of an extensive numerical study of its dynamic structure factor $S^{\alpha\beta}(k, \omega)$ using matrix-product-state (MPS) techniques. Close to criticality, the dynamic part of the correlator S^{xx} longitudinal to the applied field is incoherent and possesses a small total weight as the ground state is already close to saturation. The transverse correlator S^{zz} , on the other hand, is dominated by a coherent single-particle excitation with additional spectral weight at higher energies that we tentatively attribute to a repulsively bound pair of particles. With increasing temperature, the latter quickly fades and spectral weight instead accumulates close to zero wave vector just above the single-particle energy. On a technical level, we compare the numerical efficiency of real-time evolution to an MPS-based Chebyshev expansion in the present context, finding that both methods yield results of similar quality at comparable numerical costs.

DOI: [10.1103/PhysRevB.94.085136](https://doi.org/10.1103/PhysRevB.94.085136)

I. INTRODUCTION

A transverse magnetic field applied to a spin- $\frac{1}{2}$ XXZ chain reduces the remaining U(1) spin-rotation symmetry and immediately results in a gapped ground state whose classical analog corresponds to a spin-flop phase with long-range Néel order. Increasing the magnetic field beyond a critical value H_c , this long-range order is lost at a Ising quantum phase transition. Such spin chains govern the magnetic properties of the material Cs_2CoCl_4 in a wide regime of temperatures and fields [1–9]. They effectively emerge from spin- $\frac{3}{2}$ Heisenberg chains attributed to Co^{2+} ions whose tetrahedral environment results in a strong single-ion anisotropy. The latter splits the four levels of each spin- $\frac{3}{2}$ into two doublets, and the low-energy doublet provides an effective spin- $\frac{1}{2}$ degree of freedom. Projecting the Hamiltonian onto this low-energy subspace [8,10], XXZ chains arise with easy-plane anisotropy. The CoCl_4 tetrahedra of neighboring chains are tilted with respect to each other which leads to two different easy planes within a single unit cell, so that only a nonstaggered transversal magnetic field can be applied along the crystallographic b axis. In a recent study [8], it was shown that the thermal expansion and specific heat of Cs_2CoCl_4 below a temperature of approximately 2.5 K and for transverse fields smaller than approximately 3 T can be consistently explained in terms of the spin- $\frac{1}{2}$ XXZ chain Hamiltonian. This parameter range also encompasses the regime of Ising quantum criticality at $\mu_0 H_c \approx 2$ T. At much lower temperatures of approximately 300 mK, the interchain coupling stabilizes three-dimensional long-range order with various different phases as a function of magnetic field [9].

Whereas neutron diffraction experiments on Cs_2CoCl_4 were carried out already more than ten years ago [5], inelastic neutron scattering studies, as far as we know, have not been performed yet. Such an experiment would access the components of the dynamical spin-spin correlation functions

of the XXZ Hamiltonian in a transverse field,

$$S^{\alpha\beta}(k, \omega) = \sum_j e^{-ikj} \left[\int_{-\infty}^{\infty} dt e^{i\omega t} \langle \hat{S}_j^\alpha(t) \hat{S}_0^\beta \rangle \right], \quad (1)$$

where $\hat{S}_j^\alpha(t)$ is a spin- $\frac{1}{2}$ operator in the Heisenberg picture with $\alpha = x, y, z$, and the sum extends over sites j of the one-dimensional lattice with unit lattice spacing. The expectation value is taken with respect to the XXZ Hamiltonian

$$\hat{H} = \sum_j J [(\hat{S}_j^x \hat{S}_{j+1}^x + \hat{S}_j^y \hat{S}_{j+1}^y) + \Delta \hat{S}_j^z \hat{S}_{j+1}^z - h \hat{S}_j^x]. \quad (2)$$

For Cs_2CoCl_4 the parameters were estimated in Ref. [8] to be $J/k_B \approx 3$ K and $\Delta \approx 0.12$. In the following, we exclusively use this value for Δ and measure energies in units of J . The Ising quantum phase transition then occurs at the dimensionless critical field $h_c \approx 1.56$.

The correlation functions (1) have been theoretically investigated before by Caux, Essler, and Löw (CEL) [11] using exact results in combination with a mean-field approximation (MFA). Here, we study these correlators numerically with a quasixact matrix-product-state (MPS) approach as a function of transverse field at zero and finite temperatures T , and we extensively compare to the results of CEL. In particular, we employ the time-dependent adaption of the density matrix renormalization group (tDMRG) [12–14] in the MPS framework to carry out the real-time evolution of the real-space correlators in Eq. (1) before Fourier transforming into momentum and frequency space. The results at finite T are obtained by matrix-product purification [15,16]. For a recent work on the dynamic structure factor of the XXZ chain but with easy-axis anisotropy see Ref. [17].

The main findings of our numerical study are the following. The dynamic part of the correlator S^{xx} longitudinal to the applied field is confirmed to be incoherent close to quantum criticality. Moreover, it possesses a small total weight as the

ground state is already close to saturation. The correlator S^{zz} transverse to the field and longitudinal to the hard axis is dominated by a coherent single-particle excitation close to the critical field in agreement with the findings of CEL. This coherence gets lost with decreasing field as the hybridization with two-particle excitations becomes more and more important. Furthermore, we find additional spectral weight at higher energies that we tentatively ascribe to a repulsively bound pair of particles, which is not anticipated in the MFA of CEL. A finite temperature is expected to destabilize such pairs. Correspondingly, we find that this weight quickly decreases with increasing T , and it is redistributed close to zero wave vector just above the single-particle energy. The interesting and rich physics of repulsively bound particle pairs in the XXZ spin- $\frac{1}{2}$ chain might thus be observable in the spin-spin correlations of the material Cs_2CoCl_4 .

On a technical level, we compare the numerical efficiency of the real-time evolution in the present context to a recently developed MPS-based Chebyshev expansion (CheMPS) [18]. Our main conclusion is that CheMPS produces zero-temperature spectral functions of similar quality as tDMRG at comparable computational costs. Accordingly, the CheMPS setup must appropriately deal with a growing amount of entanglement in the MPS to produce reliable results.

The paper is structured as follows. In Sec. II we briefly review the approximation of CEL used in their computation of the correlators (1) and introduce the two matrix-product-state techniques, tDMRG and CheMPS, employed in our numerical calculations. Our results for the dynamic structure factor are presented in Sec. III and compared to the approximation of CEL. The paper ends with a short discussion in Sec. IV. Technical details on tDMRG and CheMPS, including our comparison of their numerical efficiency, are presented in the Appendix.

II. METHODS

A. Approximation of CEL

The approximation employed by Caux, Essler, and Löw (CEL) [11] involves two steps. First, after a Jordan-Wigner transformation of the Hamiltonian (2) the interaction between Jordan-Wigner fermions is treated within a self-consistent mean-field approximation (MFA). This amounts to solving three coupled nonlinear equations numerically. The validity regime of the MFA was determined by CEL with the help of DMRG calculations of thermodynamic quantities. In a second step, the structure factor (1) is evaluated with respect to the mean-field Hamiltonian, that can be identified with an effective anisotropic XY spin chain. The spin-spin correlator longitudinal to the magnetic field $S^{xx}(k, \omega)$ reduces to a density-density correlation function of Jordan-Wigner fermions that can be straightforwardly computed. The spin-spin correlators transverse to the field $S^{\alpha\beta}(k, \omega)$ with $\alpha, \beta = y, z$ on the other hand, contain Jordan-Wigner strings so that a further approximation is employed. Exact results for the XY spin chain are now exploited to approximate the transverse spin-spin correlator either by the contribution of the two-particle sector at intermediate fields, $h < h_c$, or by the contribution of the single-particle sector at larger fields, $h > h_c$.

CEL also discuss the range of validity of the MFA by comparing thermodynamic quantities to static density matrix

renormalization group (DMRG) calculations. They conclude (for $\Delta = 1/4$) that the MFA should work well for large fields $h \gtrsim 1.5$ whereas for intermediate field strengths $0.5 \gtrsim h \gtrsim 1.5$ it should provide at least qualitatively correct results. It breaks down however in the low-field limit $h \rightarrow 0$.

B. Numerical matrix-product-state techniques

To capture all facets of the interacting model (2) beyond the approximation of CEL, we employ quasiexact numerical simulations in a matrix-product-states (MPS) setup. The MPS framework offers different approaches to evaluate the components of the dynamic structure factor (1) in frequency space. Here, we mostly use the time-dependent adaption of the density matrix renormalization group (tDMRG) [12–14] to evolve the real-space spin-spin correlation function in time. The dynamic spin structure factor in frequency space is then obtained by a subsequent Fourier transform of the real-time data. At zero temperature, we start from the ground state of the system obtained with standard DMRG [19–21] before applying the local perturbation \hat{S}_0^β and evolving the state in real time. To obtain finite-temperature correlators, the initial MPS is chosen to be a thermal state representing the purified density matrix at a certain temperature [15,16]. Details on our tDMRG implementation, the post-processing by means of Fourier transform, and the chosen numerical parameters can be found in Appendix 1. We emphasize that all results presented in Sec. III were obtained using tDMRG.

To conclude this section, we briefly mention a point of technical interest for readers with a numerical MPS background. Recently, an MPS-based Chebyshev expansion technique (CheMPS) has been successfully established as a competitive alternative to tDMRG [18,22–25]. It evaluates dynamic correlators directly in frequency space avoiding the Fourier transform required in any real-time approach. However, it still remains unclear which of the two methods, CheMPS or tDMRG, is more efficient for computing spectral functions. To gain some insight into this open question, we conducted a detailed comparison for the present problem at zero temperature. We found that both methods yield results of similar quality at almost identical computational costs. For an extended discussion of technical details of CheMPS, and a comparison of the performance of tDMRG and CheMPS for the present model system, the reader is referred to the Appendices 2 and 3, respectively.

For completeness, we note that the correction-vector (CV) method can also be employed to calculate the dynamic structure factor at zero temperature [26–29]. However, CV requires individual calculations for each frequency point ω and is therefore not practicable in the context of this work. In comparison, tDMRG and CheMPS are significantly more efficient since these methods can access the entire frequency axis using a single calculation.

III. RESULTS

A. Phase diagram

In order to identify the position of the Ising quantum phase transition of the Hamiltonian (2) we have first considered its ground-state properties. The panels in Fig. 1 illustrate distinct

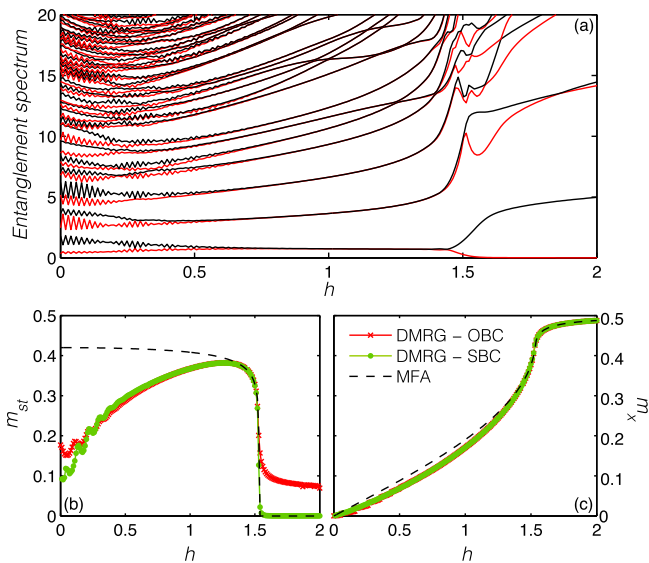


FIG. 1. (a) Entanglement spectrum, (b) staggered per-site magnetization m_{st} , and (c) per-site magnetization m_x along the in-plane field direction as functions of h . To generate the entanglement spectrum, we used a system of $N = 301$ spins with a site-dependent field that linearly increases along the chain. Every other state in the entanglement spectrum is shown in red for better visual contrast. The data in panels (b) and (c) was generated from individual DMRG runs for each h on a system with $N = 100$ spins using both open and smooth boundary conditions (OBC/SBC). The phase transition from the spin-flop to the spin-polarized phase occurs around $h_c \approx 1.56$ beyond which the order parameter m_{st} vanishes.

static features of the different ground state phases. The data in panel (a) represents the entanglement spectrum, which is generated from a single ground-state DMRG calculation [19,20] of a system with $N = 301$ sites while keeping all states associated with singular values larger than $\epsilon_{\text{SVD}} = 10^{-5}$. We chose a site-dependent magnetic field h_j , which is increased in small steps of 0.01 throughout the chain from $h_1 = -0.5$ at the first site to $h_{301} = 2.5$ at the last site.

This setup provides a quick snapshot of the physics of the different phases vs magnetic field along the chain within a single DMRG run and does not require a separate calculation for each value of the magnetic field [30,31]. While finite-size effects in the bulk part of the chain are reduced in this setup leading to a smooth tuning of the spectrum as a function of h , blurred effective finite-size effects are present and depend on the speed of the tuning. In the present case, however, the position of the phase boundary is already in good agreement with the calculations from homogeneous systems in Figs. 1(b) and 1(c).

By cutting the chain on each bond and diagonalizing the reduced density matrix $\hat{\rho}_j$, we obtain the entanglement spectrum ξ_k^j as a function of h from the spectral decomposition ρ_k^j of $\hat{\rho}_j$, i.e., $\xi_k^j = -\log \rho_k^j$. The entanglement spectrum displays a smooth behavior in both the spin-flop and the spin-polarized phase and nicely captures the distinct ground-state degeneracy in the two phases. Whereas the ground state is twofold degenerate in the spin-flop phase $0 < h < h_c$, it is unique within the spin-polarized phase, $h > h_c$.

To locate the critical point quantitatively, we study the order parameter of the system, represented by the staggered magnetization. Since a finite length N breaks translational symmetry, leading to

$$\sum_j \langle \psi_0 | (-1)^j \hat{S}_j^y | \psi_0 \rangle = \sum_j \langle \psi_1 | (-1)^j \hat{S}_j^y | \psi_1 \rangle = 0, \quad (3)$$

we calculate the order parameter using

$$m_{st} = \frac{1}{N} \sum_j \langle \psi_0 | (-1)^j \hat{S}_j^y | \psi_1 \rangle, \quad (4)$$

where $|\psi_0\rangle$ is the ground state and $|\psi_1\rangle$ the first excited state of the system. Figure 1(b) illustrates the dependence of the order parameter on the in-plane field h using both MFA and ground-state DMRG calculations. Both methods nicely agree for larger fields and pinpoint the critical point at $h_c \approx 1.56 \pm 0.01$, without performing any further finite-size scaling. Since the MFA works poorly for small fields, we observe strong deviations between MFA and DMRG within the spin-flop phase—a phenomenon which we will reencounter when calculating the components of the dynamic structure factor in Sec. III B.

We note that the DMRG calculations of m_{st} are plagued by strong finite-size effects when using a standard setup with open boundary conditions (OBC) in the spin-polarized phase, as illustrated by the large finite value of the red curve for $h > h_c$ in Fig. 1(b). The finite-size effects can be significantly reduced for high fields by employing the concept of smooth boundary conditions (SBC) [32,33] in a small region of 10 sites on the edges of the system (blue curve). The idea of SBC is to smoothly decrease the parameters of the Hamiltonian to zero at both ends of the chain to avoid having a sharp and rigid boundary as in the OBC setup. However, finite-size effects for small fields, albeit reduced with SBC, are not completely absent as indicated by the nonzero value of m_{st} at zero field.

Other quantities such as the magnetization per site, $m_x = \frac{1}{N} \sum_j \langle \psi_0 | \hat{S}_j^x | \psi_0 \rangle$, are already well converged in the OBC setup. As illustrated in Fig. 1(c), a nonzero field immediately leads to a finite magnetization which increases monotonically with h . Note that even in the spin-polarized phase at $h > h_c$, the magnetization is not saturated yet due to quantum fluctuations. Full saturation is only reached in the limit of infinitely strong magnetic fields.

B. Dynamic structure factors at $T = 0$

In the following, we present the numerical tDMRG results for various components of the zero-temperature dynamic structure factor and compare them to the approximation of CEL. Numerical details on our tDMRG implementation can be found in Appendix 1 a. We will discuss the contribution S^{zz} longitudinal to the hard axis and transverse to the magnetic field, the contribution S^{xx} longitudinal to the magnetic field, and the spin-flip contribution $S^{+-} = S^{xx} + S^{yy} + i(S^{yx} - S^{xy})$. For our analysis, we choose four representative values of the magnetic field $h = 0.8, 1.4, 1.56, 2$: the first two are located within the spin-flop phase, the third corresponds to the critical field h_c , and the last is located within the polarized phase. We do not consider the limit of zero magnetic field, $h = 0$, as the dynamic structure factor in this case is well known [34,35].

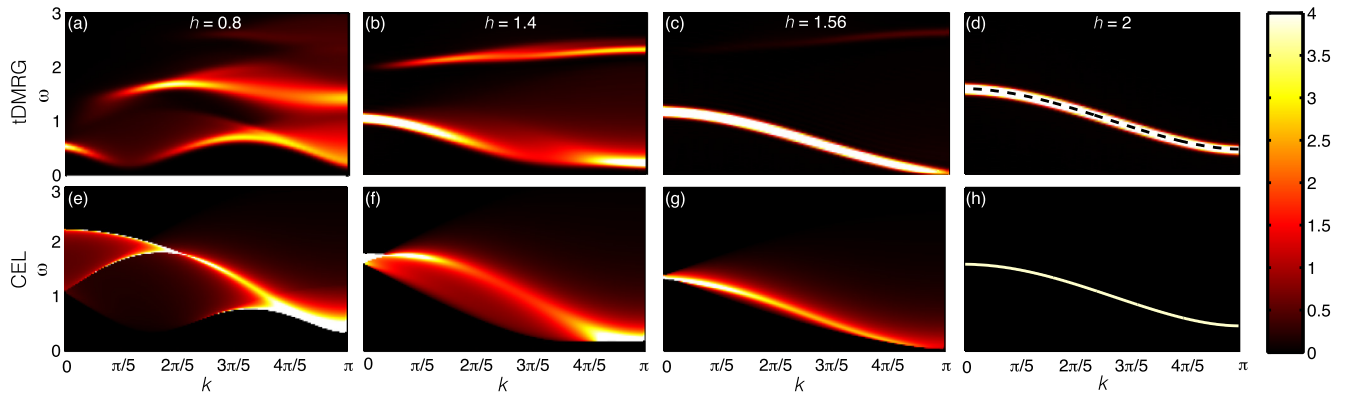


FIG. 2. Dynamic spin structure factor $S^{zz}(k, \omega)$ longitudinal to the hard axis and transverse to the applied magnetic field h , at zero temperature. (a)–(d) show the numerical results of tDMRG [$N = 100$, $t_{\max} = 60$; see Appendix 1 a for details] whereas (e)–(h) display the corresponding CEL approximation with contributions from (e)–(g) the two-particle sector and (h) the one-particle sector only. The system is gapped within the spin-flop phase [(a),(b),(e),(f)] with an incoherent spectrum. The gap closes at the quantum phase transition, (c),(g), at $h_c \approx 1.56$. The gap reopens within the spin-polarized phase, (d),(h), where the spectrum is dominated by a single coherent mode [dashed line in (d)] in excellent agreement with the CEL approximation. In panel (b) a distinct higher-energy branch is visible that is absent in the CEL spectra of panel (f).

1. Transverse dynamic structure factor $S^{zz}(k, \omega)$

The results for the dynamic structure factor $S^{zz}(k, \omega)$ transverse to the applied magnetic field but longitudinal to the hard axis are shown in Fig. 2. The panels in the first row [Figs. 2(a)–2(d)] illustrate our numerical tDMRG calculations, to be compared with the CEL approximation in the panels shown in the second row [Fig. 2(e)–2(h)]. The spectra in the spin-flop phase [Figs. 2(a), 2(b), 2(e), 2(f)] display an incoherent continuum with a gap. The majority of the spectral weight is distributed around $k = \pi$ for $h = 0.8$, but is partly shifted to $k = 0$ as the field strength is increased. At the critical point [Figs. 2(c) and 2(g)], the spectrum becomes gapless at the wave vector $k = \pi$ and is dominated by a single coherent mode, which remains a persistent feature also in the spin-polarized phase [Figs. 2(d) and 2(h)] where the gap opens up again.

This coherent mode is fully captured within the CEL approximation. It possesses a dispersion of the form [11]

$$\omega(k) = \tilde{J}_+ \sqrt{(\cos k + \tilde{h})^2 + \gamma^2 \sin^2 k}, \quad (5)$$

where the parameters \tilde{J}_+ , \tilde{h} , and γ depend on the magnetic field h and obey self-consistent mean-field equations. This dispersion is also shown as a dashed line in Fig. 2(d) with excellent agreement with the tDMRG numerics. At large fields, the magnetization is already close to saturation and the coherent mode essentially corresponds to a single spin-flip excitation.

As expected, the agreement between the tDMRG and the CEL approximation deteriorates with decreasing field. Interestingly, below the critical field even pronounced qualitative differences emerge. At $h = 1.4$ within the spin-flop phase but close to the critical point [Figs. 2(b) and 2(f)], the CEL approximation still captures the low-energy branch qualitatively but it fails to describe the additional branch at higher energies, $\omega > 2$. This higher-energy branch is a distinct feature that is quasicohherent and possesses only a weak

dispersion. It might arise from repulsively bound two-particle states that we will further discuss in Sec. IV.

For even smaller fields, strong deviations between tDMRG and CEL are expected, because the latter is no longer able to describe the low-energy properties of the system, as we have already seen in the study of the order parameter in Sec. III A. For a field $h = 0.8$ [Figs. 2(a) and 2(e)], the higher-energy features visible around $k = 0$ in the CEL spectra appear to be shifted to $k = \pi$ in the tDMRG data. At the same time, the spectral weight around $k = 0$ at low energies is not captured by the CEL approximation.

2. Longitudinal dynamic structure factor $S^{xx}(k, \omega)$

The component $S^{xx}(k, \omega)$ of the dynamic spin structure factor longitudinal to the applied field is shown in Fig. 3. Within the CEL approximation this quantity is related to a density-density correlation function of Jordan-Wigner fermions.

Both the CEL approximation and the tDMRG calculations show that these longitudinal correlations are basically incoherent for any value of the applied magnetic field. Moreover, we find that the correlators exhibit an incommensurable low-energy feature in the spin-flop phase [Figs. 3(a), 3(b), 3(e), 3(f)], reminiscent of the incommensurability of the isotropic XY model in a longitudinal field [36]. The incommensurable wave vector is located near $k = \pi$ (not shown) at small magnetic fields and moves towards $k = 0$ at the quantum phase transition. The incommensurability becomes most apparent in Figs. 3(a) and 3(e) for $h = 0.8$, where the wave vector corresponds to $k \approx 0.8\pi$. This incommensurate low-energy feature is also captured by the CEL approximation, whereas the low-energy branch at $k = \pi$ and the higher-energy excitations again substantially deviate from the tDMRG results at $h = 0.8$. For increasing field, the spectral weight decreases and becomes very small within the spin-polarized phase for all momenta as the magnetization approaches full saturation, which is illustrated by the reduced intensity of $S^{xx}(k, \omega)$ in Figs. 3(c), 3(d), 3(g), and 3(h) [note that their color bars differ]. Similar to the transverse component in Fig. 2(b), the longitudinal

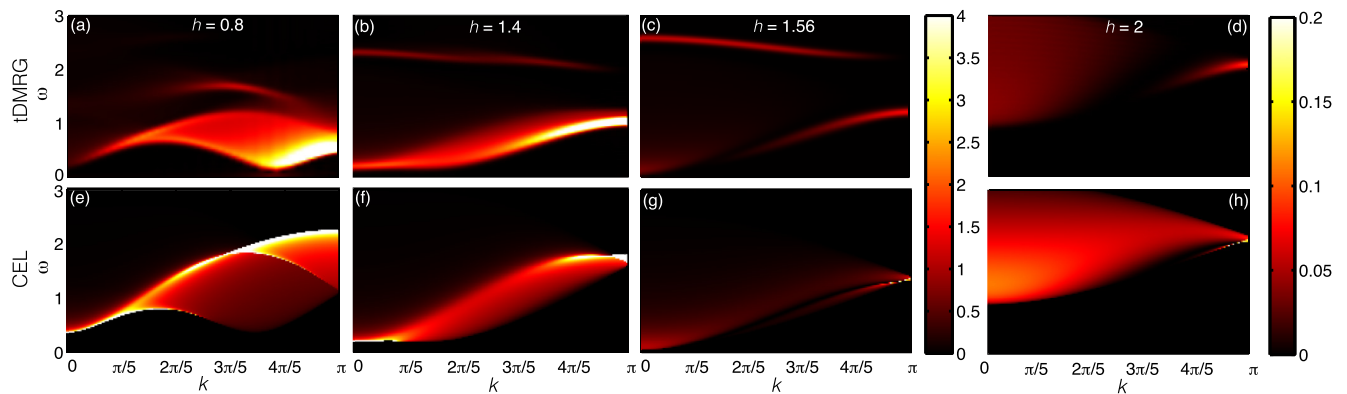


FIG. 3. Dynamic spin structure factor $S^{xx}(k, \omega)$ longitudinal to the applied magnetic field h at zero temperature. (a)–(d) show the numerical results of tDMRG [$N = 100$, $t_{\max} = 60$; see Appendix 1 a for details] whereas (e)–(h) display the corresponding CEL approximation. In the spin-flop phase [(a),(b),(e),(f)] the spectra show weight at low energies located at an incommensurate wave vector which moves towards $k = 0$ at criticality (c),(g). The weight of the spectra (d),(h) substantially decreases within the spin-polarized phase [note the different color scales]. Again, we find that the agreement between the CEL approximation and tDMRG is improving with increasing field strength.

component also exhibits a higher-energy branch in panel Figs. 3(b) and 3(c) that is not captured within the CEL approximation.

3. Spin-flip dynamic structure factor $S^{+-}(k, \omega)$

In Fig. 4 we show tDMRG results for the spin-flip component $S^{+-}(k, \omega)$ of spin operators within the easy plane. At high fields, the spectra are dominated by the coherent single-particle spectrum like the one of the transverse correlator in Fig. 2. In the spin-flop phase at lower fields in Figs. 4(a) and 4(b) we find that most spectral weight is distributed around $k = \pi$.

C. Dynamic structure factor at finite T

We now present an analysis of the temperature dependence of the dynamical structure factor limiting ourselves, however, to a discussion of the transverse component $S^{zz}(k, \omega, T)$ only. The results are obtained using real-time evolution in combination with matrix-product purification [15,16], where an auxiliary copy of the physical Hilbert space is introduced, which adopts the role of a heat bath and effectively doubles

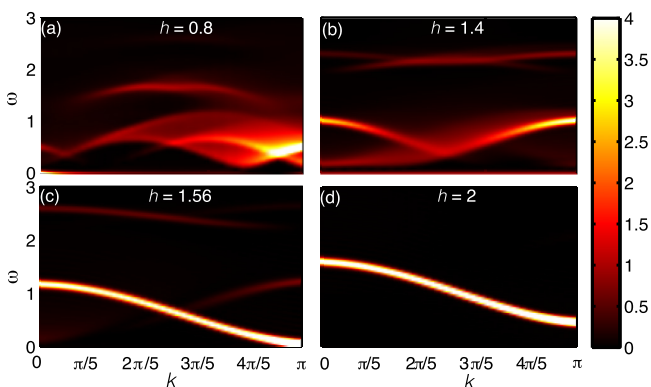


FIG. 4. Dynamic spin structure factor $S^{+-}(k, \omega)$ at $T = 0$ obtained with tDMRG [$N = 100$, $t_{\max} = 60$; see Appendix 1 a for details]. The spectra show the system in (a),(b) the spin-flop phase, (c) at the quantum phase transition, and (d) the spin-polarized phase.

the system size. Starting from a product state consisting of maximally entangled pairs of physical and auxiliary sites, we imaginary-time evolve the system from $T = \infty$ to the desired temperature to obtain the thermal initial state $|\psi_T\rangle$ for the real-time evolution. For numerical details we refer to Appendix 1 b.

Considering the same field values $h = 0.8, 1.4, 1.56, 2$ as in the previous section, we compute $S^{zz}(k, \omega, T)$ at three different temperatures $T = 1, \frac{1}{4}, \frac{1}{12}$, measured in units of J with $k_B = 1$. For these temperatures, the approximation of an effective spin- $\frac{1}{2}$ description for Cs_2CoCl_4 is still justified: the energy gap between the doublets of the original spin- $\frac{3}{2}$ due to the single-ion anisotropy is $\Delta E \approx 4.6$ in the same units [8] so that $T \ll \Delta E$.

Figure 5 displays the numerical results for $S^{zz}(k, \omega, T)$. First, we notice that thermal fluctuations quickly lead to a blurring of the excitation gap in the spin-flop phase [Fig. 5 left two columns]. Already at very small temperatures $\frac{1}{12}$ [Figs. 5(a) and 5(b)], we observe additional spectral weight being distributed around $k \approx \pi$ at $\omega = 0$. Increasing temperature further, the two spectra in the spin-flop phase show quite different behavior. Deep in the spin-flop phase for $h = 0.8$ and $T = \frac{1}{4}$ [Fig. 5(e)], the gap is also washed out around $k \approx 0.2\pi$ and a lot of spectral weight is distributed towards lower energies ω . At high temperatures $T = 1$ [Fig. 5(i)], almost all spectral structures are already washed out. Closer to the phase transition at $h = 1.4$ [Fig. 5(f)], the growing thermal fluctuation predominantly shift spectral weight into the region between the low and higher energy branch. For $T = 1$ [Fig. 5(j)], the two branches have dissolved into a continuum around $k = \pi$, while the gap at $k = 0$ still remains very pronounced. Interestingly, an additional spectral feature seems to arise close to $k = 0$ at slightly higher energies than the low-energy branch as indicated by the arrow. We will offer an interpretation for it in the next section.

At the phase transition, thermal fluctuations cause some interesting new features in the spectrum. First of all, we note that the higher-energy branch becomes more pronounced at finite T while it was barely visible at $T = 0$, Fig. 2(c), and not captured at all within the CEL approximation. We also

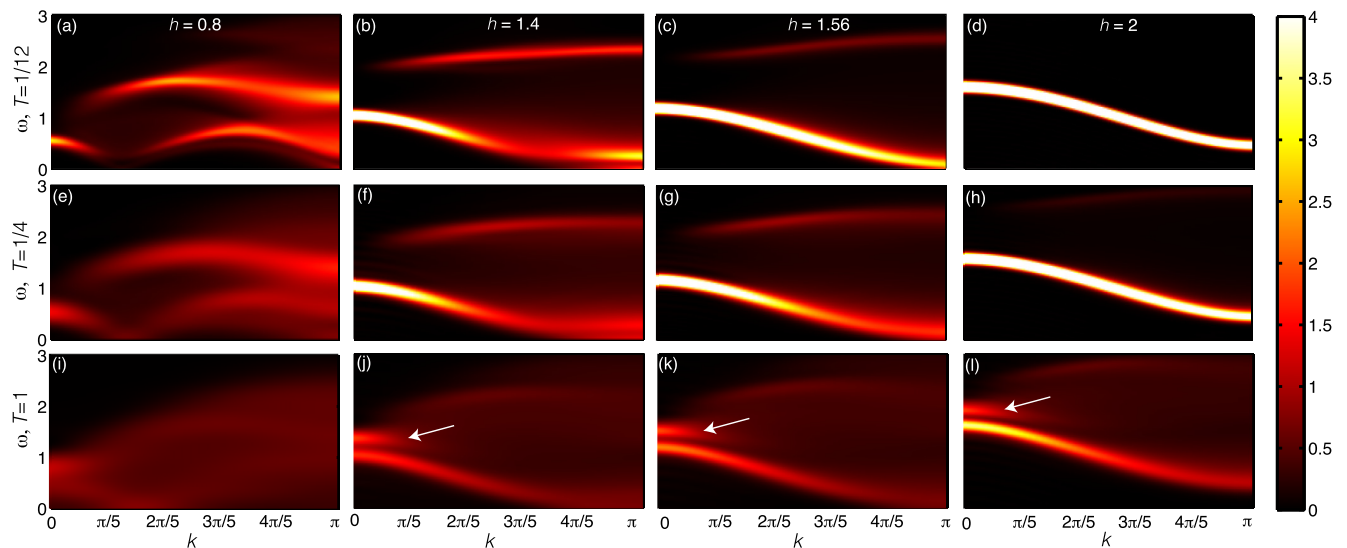


FIG. 5. Dynamic structure factor $\mathcal{S}^{zz}(k, \omega, T)$ transverse to the applied magnetic field for three finite temperatures: (a)–(d) $T = \frac{1}{12}$, (e)–(h) $T = \frac{1}{4}$, and (i)–(l) $T = 1$ obtained with tDMRG [$N = 50$ – 70 , $t_{\max} = 20$ – 60 ; see Appendix 1 b for details]. Analogously to Fig. 2, the spectra show the system in the spin-flop phase (first two columns), at the quantum phase transition (third column), and in the spin-polarized phase (fourth column). At finite T an additional feature appears close to $k = 0$, as indicated by the white arrow.

find that thermal fluctuations strongly redistribute spectral weight between the two branches for increasing temperatures. Moreover, the additional spectral feature close to $k = 0$ found in Fig. 5(j) also appears at the quantum phase transition at $h_c \approx 1.56$ [Fig. 5(k)].

A finite temperature plays only a minor role in the spin-polarized phase at $h = 2$ because the large excitation gap of $\Delta_e \approx 0.5$ suppresses most thermal fluctuations for $T < \Delta_e$ [Figs. 5(d) and 5(h)]. Only for temperatures above the gap, we observe thermal broadening and again the appearance of an additional excitation mode around $k = 0$ [white arrow in Fig. 5(l)].

IV. DISCUSSION

In this work, we performed an extensive numerical study of the dynamic structure factor $\mathcal{S}^{\alpha\beta}(k, \omega)$ of the spin- $\frac{1}{2}$ XXZ model (2) in a transverse field for a particular value of easy-plane anisotropy $\Delta = 0.12$. Employing matrix-product-state calculations, we computed the components of the structure factor at zero and finite temperatures for various values of the transverse field with a particular focus on the Ising quantum phase transition separating a gapped spin-flop phase and a gapped spin-polarized phase at a critical dimensionless field $h_c \approx 1.56$.

Comparing with previous approximate analytical calculations of Caux, Essler, and Löw (CEL) [11] for $T = 0$, we confirmed that at large fields, $h \gtrsim h_c$, the correlator \mathcal{S}^{zz} transverse to the applied field is governed by a coherent single-particle mode, which in the large-field limit basically corresponds to a single spin-flip excitation of the almost polarized chain. At smaller fields, \mathcal{S}^{zz} loses coherence as it becomes dominated by the two-particle continuum. The correlator \mathcal{S}^{xx} longitudinal to the field, on the other hand, is mostly incoherent.

Our numerical study has revealed two distinct features in the dynamic structure factor that deserve special attention: (i) an additional relatively sharp mode located at higher energies $\omega > 2J$ clearly visible in \mathcal{S}^{zz} , see Fig. 2(b), as well as in \mathcal{S}^{xx} , see Figs. 3(b) and 3(c); and (ii) additional weight emerging at finite temperature just above the low-energy branch close to zero wave vector, see white arrow in Fig. 5. In particular, a mode at higher energies $\omega > 2J$ is not anticipated within the mean-field approximation of CEL.

Let us speculate about the origin of these additional features. A possible candidate for (i) the higher-energy mode is a repulsively bound two-particle state, which goes beyond the mean-field approximation. The presence of such a bound state is at least supported from an analysis in the large field limit. In this limit, the ground state is completely polarized and a particle excitation just corresponds to a single spin flip. While a spin flip loses Zeeman energy Jh , it gains twice the bond energy $J/2$ due to the antiferromagnetic alignment with its neighboring spins. This also applies for each spin flip of the two-particle excitation provided that they are separated by at least two sites. If spin flips occupy adjacent sites, however, they gain only half of the bond energy giving rise to an effective repulsive interaction J . In lowest order in $1/h$, this repulsion gives rise to a bound state above the two-particle continuum similar to the doublon in the Hubbard model [37]. At high fields, its weight is probably too small to be observable in the dynamic structure factor, but it might survive at smaller fields, giving rise to the signatures observed in our spectra. The lifetime of this repulsively bound state could be large at small temperatures, as its decay requires the interaction with additional particles in order to release its energy [38–40]. At finite temperatures, the thermal occupation of particles will facilitate the decay, which might explain the fading of the higher-energy mode in the spectra in Fig. 5 with increasing T . It is striking that the signature (ii) close to zero wave vector in the transverse dynamic structure factor \mathcal{S}^{zz} identified by

the white arrow in Fig. 5, which is reminiscent of a Villain mode [41], gains weight with the simultaneous vanishing of the higher-energy mode. It is therefore tempting to speculate that this feature (ii) is associated with the decay of the repulsively bound pair.

It might be worth exploring these spectral features further in future theoretical work. The physics of repulsively bound particle pairs should be particularly transparent in the Ising limit of the XXZ spin- $\frac{1}{2}$ chain for a longitudinal field close to its triple point [42]. On the experimental side, the dynamic structure factor considered in this work might be observable with the help of inelastic neutron scattering experiments on the compound Cs₂CoCl₄. This material thus offers the opportunity to study the rich structure of the dynamic spin-spin correlations of the XXZ spin- $\frac{1}{2}$ chain in a regime where it is not integrable with interesting effects emerging already on the two-particle level. We hope that our study motivates such experiments in the near future.

ACKNOWLEDGMENTS

M.G. acknowledges helpful discussions and an earlier collaboration with O. Breunig and T. Lorenz that motivated this work. B.B. thanks the Tensor-Network group at UCI for their hospitality and in particular S. R. White for pointing out the concept of smooth boundary conditions. This research was supported by the Deutsche Forschungsgemeinschaft through the Excellence Cluster “Nanosystems Initiative Munich”, SFB/TR 12, SFB 631 and WE4819/2-1 (A.W.).

APPENDIX: NUMERICAL DETAILS

This Appendix discusses the numerical methods used to obtain the results presented in the main part of the paper. Sec. 1 deals with tDMRG, Sec. 2 with CheMPS, and Sec. 3 offers a detailed comparison of their efficiency within the context of the present spin- $\frac{1}{2}$ XXZ model.

1. tDMRG

This section elaborates on the details of our tDMRG implementation employed to generate the results for the dynamic structure factor at zero and finite temperatures in the main part of this work.

a. Zero temperature

To evaluate the zero-temperature structure factor by means of real-time evolution, we first have to determine the time-dependent ground-state correlators

$$S^{\alpha\beta}(j,t) = e^{iE_0 t} \langle \psi_0 | \hat{S}_j^\alpha e^{-i\hat{H}t} \hat{S}_0^\beta | \psi_0 \rangle \quad (\text{A1})$$

for various times t and distances j . To this end, we initialize the ground state $|\psi_0\rangle$ in terms of an MPS employing DMRG [19–21] before applying the local perturbation \hat{S}_0^β in the middle of the chain (labeled with $j_M = 0$) to generate $|\phi\rangle = \hat{S}_0^\beta |\psi_0\rangle$. $|\phi\rangle$ is the initial state for the real-time evolution, $|\phi(t)\rangle = e^{-i\hat{H}t} |\phi\rangle$, which is carried out using standard tDMRG techniques [12–14,21]. This amounts to splitting the time-evolution operator $e^{-i\hat{H}t}$ into a product of M small time steps

$\tau = t/M$. For systems with short-ranged interactions, each term $e^{-i\hat{H}\tau}$ is decomposed into a product of local operator via a Suzuki-Trotter decomposition. For Hamiltonians with nearest-neighbor interactions only, such as (2), this results in combining all interaction terms corresponding to even and odd numbered bonds, respectively, i.e., $\hat{H} = \hat{H}_e + \hat{H}_o$. Note that all terms in one group commute with each other but the terms in \hat{H}_e generally do not commute with the ones in \hat{H}_o . The second-order Suzuki-Trotter decomposition for the time-evolution operator then reads

$$e^{-i\hat{H}\tau} = e^{-i\hat{H}_e\tau/2} e^{-i\hat{H}_o\tau} e^{-i\hat{H}_e\tau/2} + \mathcal{O}(\tau^3). \quad (\text{A2})$$

The time evolution is carried out by repeatedly applying the Trotter-decomposed evolution operator to the initial state $|\phi\rangle$. For every (or a subset of) time step(s) we evaluate the two-point correlators $S^{\alpha\beta}(j,t)$ for all possible values of j on the finite chain. In the end, we compute the Fourier transform in time t and real space j to obtain the dynamic structure factor of Eq. (1).

Such calculations are typically affected by two major error sources:

(1) The Trotter decomposition introduces an error of the order $\mathcal{O}(\tau^3)$ because it ignores the noncommutativity of odd and even terms of the Hamiltonian. This so-called Trotter error can be dealt with by using a higher-order decomposition [43] or a smaller time step.

(2) The spreading of the excitation over time causes a growth of entanglement in the state during the time evolution, which typically requires the bond dimension of the MPS to increase exponentially towards longer time scales. This effectively restricts the accessible time scale to some maximum time t_{\max} , the value of which strongly depends on the specific model and parameter regime.

The finite-time limit also puts a constraint on the resolution of the spectral functions in frequency space. In order to remove artificial finite-time oscillations in the spectra, one needs to include some type of broadening when performing the Fourier transform to frequency space. Here we choose to include a Gaussian filter $\exp[-\eta^2 t^2]$ in the time integral in Eq. (1) and choose η dependent on t_{\max} . Hence, the resulting spectral functions contain the exact spectral features convolved with a Gaussian $\exp[-\omega^2/(2W^2)]$, with a frequency resolution $W = \sqrt{2}\eta$. In some cases, linear prediction can be used to avoid the artificial broadening and extract more spectral information from the time series [44,45]. We refrain from employing linear prediction in this work, because we found its results were very sensitive to changes of the regularization parameter and the statistical window on the given time scale for the present model.

The zero-temperature tDMRG calculations in Sec. III B were performed on a chain with open boundary conditions and $N = 100$ spins, which is large enough to prevent any finite-size reflections for the considered time scales. We worked with a second-order Suzuki-Trotter decomposition and used a time step $\tau = 0.05$, which is small enough in the context of the present model that the Trotter error becomes negligible. Moreover, the bond dimension D of the time-evolved MPS $|\phi(t)\rangle$ was chosen adaptively by keeping all singular values larger than $\epsilon_{\text{SVD}} = 10^{-4}$ during the application of the Trotter

gates. We stopped the time evolution at $t_{\max} = 60$ and worked with a broadening parameter $\eta = 0.033$, which corresponds to an energy resolution of $W = \sqrt{2}\eta = 0.047J$ using the Gaussian filter of Ref. [12] in the reconstruction of the dynamic structure factor. In practice, this lead to a maximum bond dimension of $D < 1400$ during the last time step. Furthermore, we note that a setup with smooth boundary conditions, employed in Sec. III A to minimize finite-size effects in static quantities, is not particularly well suited for dynamic calculations. Its decreasing energy scales at the chain's ends introduce a set of low-energy states, which significantly alter the entanglement growth during time evolution.

b. Finite temperatures

The above approach can be generalized with minor modifications to calculate finite-temperature correlators

$$\mathcal{S}^{\alpha\beta}(j, t, T) = \langle \psi_T | e^{i\hat{H}t} \hat{S}_j^\alpha e^{-i\hat{H}t} \hat{S}_0^\beta | \psi_T \rangle. \quad (\text{A3})$$

In this case, the local perturbation \hat{S}_0^β is no longer applied to the ground state $|\psi_0\rangle$ but rather to a thermal state $|\psi_T\rangle$, which either represents the purified density matrix [15] or one state of an ensemble of minimally entangled typical thermal states (METTS) [46,47], depending on the chosen finite-temperature algorithm. Since the evolution operator acting on the bra cannot be factored out as a phase factor anymore, one has to carry out two independent real-time evolutions, $|\phi(t)\rangle = e^{-i\hat{H}t} \hat{S}_0^\beta | \psi_T \rangle$ and $|\Phi(t)\rangle = e^{-i\hat{H}t} | \psi_T \rangle$ and evaluate $\mathcal{S}^{\alpha\beta}(j, t, T) = \langle \Phi(t) | \hat{S}_j^\alpha | \phi(t) \rangle$ accordingly.

The finite-temperature tDMRG calculations in Sec. III C were performed in the purification setup on an open chain of $N = 50\text{--}70$ physical spins (corresponding to a total number of $N_{\text{tot}} = 100\text{--}140$ sites in the purified scheme), where the time scales were again chosen such that no finite-size reflections occurred. We set $\epsilon_{\text{svd}} = 10^{-4}, 10^{-5}$ during the real- and imaginary-time evolution, respectively, and chose a Trotter step of $\tau = 0.05$ in both cases. Since the entanglement of the MPS during time evolution grows much more rapidly the higher the temperature, the accessible time scale varied between $t_{\max} = 60$ for $T = 1/12$ and $t_{\max} = 20\text{--}40$ for $T = 1$.¹ Although thermal broadening dominates at high temperatures on the considered time scale, we nevertheless included a broadening parameter $\eta = 0.05$ in the Fourier transform for consistency.

2. CheMPS

In this section we discuss the basics of CheMPS, which are relevant for the detailed comparison to tDMRG in Appendix 3. With CheMPS we are able to work directly in frequency space and compute dynamic correlators of the

type

$$\mathcal{S}^{\alpha\beta}(j, \omega) = \langle \psi_0 | \hat{S}_j^\alpha \delta(\omega - \hat{H} + E_0) \hat{S}_0^\beta | \psi_0 \rangle. \quad (\text{A4})$$

The CheMPS approach expands the δ -function in Eq. (A4) in terms of Chebyshev polynomials of the first kind, T_n . To ensure the convergence of the Chebyshev expansion, the Hamiltonian has to be rescaled such that its support is fully contained in the interval $[-1, 1]$. One way to achieve this is to use a linear mapping $\hat{H}' = (\hat{H} - E_0)/a - b$, $\omega' = \omega/a - b$ with the two rescaling factors a, b chosen properly.

Reference [48] showed that the details of the rescaling procedure clearly affect the efficiency of the calculation. It is usually most efficient to map the support of the spectral function close to the lower boundary of the interval $[-1, 1]$, where the zeros of the individual Chebyshev polynomials are densely distributed. This can be achieved by using a “ $b = 1$ ” setup, which is in the following distinguished from the “ $b = 0$ ” setup, where the support of the spectral function lies at the center of $[-1, 1]$.

After proper rescaling, the correlator in Eq. (A4) can be represented with Chebyshev coefficients

$$\mu_n(j) = \langle \psi_0 | \hat{S}_j^\alpha T_n(\hat{H}') \hat{S}_0^\beta | \psi_0 \rangle, \quad (\text{A5})$$

leading to

$$\mathcal{S}^{\alpha\beta}(j, \omega) = \frac{1}{a} \sum_{n=0}^{N_{\text{Che}}} w_n(\omega') \mu_n(j) T_n(\omega'), \quad (\text{A6})$$

with $w_n(\omega) = (2 - \delta_{n0})/(\pi\sqrt{1 - \omega^2})$. The numerically demanding part is to determine the Chebyshev coefficients $\mu_n(j)$. To this end, one employs standard MPS techniques and exploits the recursion relations of the Chebyshev polynomials to iteratively generate the Chebyshev vectors

$$|t_n\rangle = 2\hat{H}'|t_{n-1}\rangle - |t_{n-2}\rangle, \quad (\text{A7})$$

$$|t_0\rangle = \hat{S}_0^\beta | \psi_0 \rangle, \quad |t_1\rangle = \hat{H}'|t_0\rangle. \quad (\text{A8})$$

Thus by storing only three MPS per expansion step, we can iteratively evaluate the Chebyshev coefficients $\mu_n(j)$ by computing overlaps of the type $\mu_n(j) = \langle \psi_0 | \hat{S}_j^\alpha |t_n\rangle$ for all values of j on the finite chain. Analogous to real-time evolution, it is typically more convenient to carry out the Fourier transform from real- to momentum-space after completing the expansion, instead of applying momentum-space operator \hat{S}_k^β to the starting state. In this way, only a single calculation is required to obtain the spectrum at various momenta. Moreover, a local perturbation \hat{S}_0^β leads to a significantly reduced entanglement growth during the expansion.

The increase of entanglement stored in $|t_n\rangle$ at higher expansion orders is caused by the repeated application of the Hamiltonian \hat{H} to the MPS and is necessary from a physical point of view to represent the spreading of the local excitation in real space over time. This results in a roughly exponentially growing demand on the numerical resources in order to store and manipulate Chebyshev vectors. Therefore, the expansion is limited to some finite order N_{Che} , at which the computational costs “hit the exponential wall.” The finite-order cutoff introduces numerical artifacts in the dynamic correlators, which can be removed by including coefficients g_n

¹In order to reach these time scales, we applied a backward time evolution on the auxiliary states for $T = 1, \frac{1}{4}$, which significantly reduced the growth of entanglement [50]. Note that we refrained from exploiting time-translation invariance to reach even larger times [51], since it would have required to carry out tDMRG runs individually for each distance j .

of a broadening kernel in Eq. (A6), which smears out the higher order terms and generate a smooth spectrum. Alternatively, it is also possible to determine the full resolvent function in Eq. (A4) for a nonzero value of η [22] or, in some cases, to avoid broadening at all by means of linear prediction [23].

Recently, Ref. [25] expanded CheMPS to determine spectra also at finite temperatures. To this end, they formulated the Chebyshev expansion in terms of a Liouvillian and matrix-product purification. It is also possible to combine CheMPS with METTS, but for technical reasons this turned out to be very inefficient [49].

3. tDMRG vs CheMPS

In the following, we compare the numerical efficiency of the two methods, tDMRG and CheMPS. CheMPS has been frequently applied in practice [22–25,52–55], but no conclusive answer has yet been presented to the question whether it provides a computationally more efficient framework over real-time evolution to simulate spectral functions. Whereas tackling this question in full generality would go beyond the scope of this work, we present below a brief analysis of the efficiency of CheMPS in the present context.

Our main conclusion is that CheMPS produces zero-temperature results of similar quality as tDMRG at comparable computational costs. Accordingly, the CheMPS setup, too, needs to appropriately deal with a growing amount of entanglement in the MPS to produce reliable results.

In order to compare real-time evolution and CheMPS, we have studied the spin- $\frac{1}{2}$ XXZ chain Hamiltonian (2) with $N = 100$ spins directly at quantum criticality $h = 1.56$ and $T = 0$. Starting by placing an excitation in the middle of the chain, we take $\hat{S}_0^\beta |\psi_0\rangle$ as the initial state for both the real-time evolution and the Chebyshev expansion. The CheMPS simulation is carried out in two setups: one with $b = 0$ in the linear mapping, see Appendix 2, and $N_{\text{Che}} = 4800$ iterations, another with $b = 0.995$ and $N_{\text{Che}} = 2100$ iterations. The reference tDMRG calculation uses the data from Fig. 2(c). As previously, we adapt the bond dimension of the MPS by truncating according to $\epsilon_{\text{SVD}} = 10^{-4}$ in every Trotter step as well as any Chebyshev iteration Eq. (A7) during the entire calculation.

Figure 6 displays the corresponding evolution of the excitation with time, $\langle \hat{S}_j^z(t) \hat{S}_0^z \rangle$, and iteration order, $\mu_n(j) = \langle \psi_0 | \hat{S}_j^\alpha | t_n \rangle$, respectively. In all cases, the initially localized excitation spreads out in real-space showing the

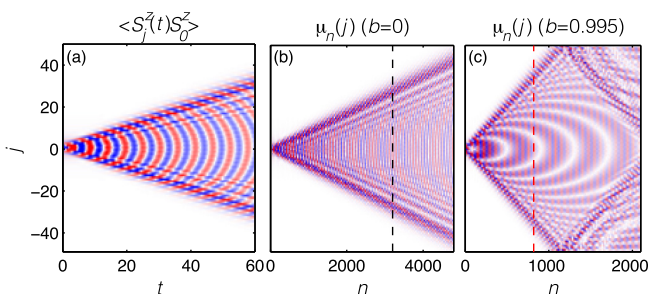


FIG. 6. Evolution of the excitation over (a) time $\langle \hat{S}_j^z(t) \hat{S}_0^z \rangle$ and (b),(c) iteration order $\mu_n(j) = \langle \psi_0 | \hat{S}_j^\alpha | t_n \rangle$.

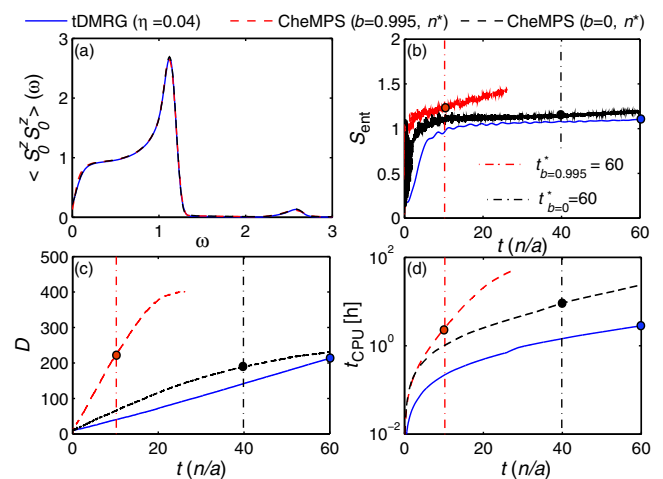


FIG. 7. (a) Local spectral function $\langle \hat{S}_0^z \hat{S}_0^z \rangle(\omega)$ obtained from tDMRG and CheMPS for the spin- $\frac{1}{2}$ model for Cs_2CoCl_4 with $N = 100$ spins directly at the phase boundary for $h = 1.56$ and $T = 0$. (b)–(d) Comparison of entanglement entropy S_{ent} , bond dimension D , and cumulative CPU time t_{CPU} .

typical light-cone structure. We clearly observe that finite-size reflections are not present up to the maximum time $t_{\text{max}} = 60$ in the tDMRG simulation [Fig. 6(a)]. The same applies to the CheMPS results of the $b = 0$ setup in Fig. 6(b). Following the literature, the final iteration corresponds to an effective time scale $t \sim N_{\text{Che}}/a \approx 60$, which is equivalent to the maximum time of the tDMRG reference calculation. However, the excitation in (b) is already spread out significantly further in the system than at the end of the tDMRG calculation. This deviation becomes even more apparent studying the $b = 0.995$ setup in (c), which in principle should evolve according to the same effective time scale as the rescaling factor a is unchanged. In reality, the excitation has already reached the boundary of the system after $n \approx 1100$ iterations. Reflections at both boundaries become strongly visible for higher iterations. This suggests that the effective time scale of $t^* = 60$ is already reached significantly sooner in the $b = 0.995$ setup, which is in agreement with the findings of Ref. [48].

Hence, we conclude that only $n^* < at_{\text{max}}$ CheMPS iterations have to be carried out in order to obtain spectral data with comparable accuracy as in the reference tDMRG simulation. This is illustrated in Fig. 7(a), where the local spectral function $\langle \hat{S}_0^z \hat{S}_0^z \rangle(\omega)$ obtained from tDMRG and CheMPS data is displayed. We use only the first n^* moments of the respective CheMPS calculation and a Jackson kernel in the Chebyshev reconstruction to mimic both the maximum time cutoff and the Gaussian broadening in the Fourier transform of the real-time data, choosing n^* such that the agreement with the reference data is best. These iterations n^* are indicated by the dashed vertical lines in Figs. 6(b) and 6(c). As one would intuitively expect, the excitation is spread over approximately the same distance after these n^* iterations as in the tDMRG calculation at t_{max} .

Thus we can restrict our efficiency analysis to the first $n \leq n^*$ iterations in order to conduct a reasonable comparison to tDMRG. Figures 7(b)–7(d) show the entanglement entropy, bond dimension, and accumulated CPU time, respectively.

The tDMRG data is plotted in real-time units t , whereas the CheMPS results are displayed with a rescaled iteration number n/a for better comparability. Again, the dashed vertical lines indicate the iteration n^*/a of interest. First of all, we note that the Chebyshev vectors at n^* in both setups are slightly more entangled than the time-evolved MPS [Fig. 7(b)], although this is not reflected in the respective bond dimensions at n^* or t_{\max} , respectively: The final time-evolved MPS has a bond dimension $D = 213$, the corresponding Chebyshev vectors in the $b = 0$ and $b = 0.995$ setup carry a somewhat comparable number of many-body states ($D = 188$ and $D = 218$, respectively). This indicates that both methods require very similar amounts of numerical resources in order to reproduce the same spectral information. A comparison of CPU times further confirms this, as tDMRG and $b = 0.995$ CheMPS require almost the identical amount of total CPU-time, namely $t_{\text{CPU}} = 2.8$ hours on a 8-core machine. The CheMPS calculation in the $b = 0$ setup takes approximately three times longer due to the larger number of iterations necessary to reach the same time scale.

We have conducted this study only for a single model and set of parameters, thus we cannot provide an unambiguous

answer to whether a spectral function is best represented in terms of Fourier modes or Chebyshev functions. However, we learned here that both methods are affected by the dynamical entanglement growth in a very similar matter. Therefore, it seems rather unlikely that one method can significantly outperform the other. For this reason, we have only applied one approach, namely tDMRG, to generate the results presented in Secs. III B and III C. Our analysis would have to be extended to other parameters and systems in order to give a fully conclusive answer. For instance, we expect that tDMRG outperforms CheMPS at finite T , since (i) the Liouvillian formulation of CheMPS requires a factor a twice as large as in the $T = 0$ setup; (ii) the more efficient $b = 1$ setup, which aims to shift the support of the spectral function close to the lower boundary of the rescaled interval $[-1, 1]$, might not be appropriate if finite temperatures shift the support to higher energies; (iii) there exists no counterpart to time-translation invariance, which allows us to effectively double the maximum time scale in the tDMRG setup [51]. On the other hand, CheMPS might be the preferred choice for zero-temperature calculations in models with long-ranged interactions, where a Trotter-based time evolution is no longer feasible.

-
- [1] H. Algra, L. de Jongh, H. Blöte, W. Huiskamp, and R. Carlin, *Physica (Amsterdam) B+C* **82**, 239 (1976).
- [2] J. N. McElearney, S. Merchant, G. E. Shankle, and R. L. Carlin, *J. Chem. Phys.* **66**, 450 (1977).
- [3] J. Smit and L. De Jongh, *Physica (Amsterdam) B+C* **97**, 224 (1979).
- [4] P. M. Duxbury, J. Oitmaa, M. N. Barber, A. van der Bilt, K. O. Joung, and R. L. Carlin, *Phys. Rev. B* **24**, 5149 (1981).
- [5] M. Kenzelmann, R. Coldea, D. A. Tennant, D. Visser, M. Hofmann, P. Smeibidl, and Z. Tylczynski, *Phys. Rev. B* **65**, 144432 (2002).
- [6] I. Chatterjee, *J. Magn. Magn. Mater.* **265**, 363 (2003).
- [7] M. Siahatgar and A. Langari, *Phys. Rev. B* **77**, 054435 (2008).
- [8] O. Breunig, M. Garst, E. Sela, B. Buldmann, P. Becker, L. Bohaty, R. Müller, and T. Lorenz, *Phys. Rev. Lett.* **111**, 187202 (2013).
- [9] O. Breunig, M. Garst, A. Rosch, E. Sela, B. Buldmann, P. Becker, L. Bohaty, R. Müller, and T. Lorenz, *Phys. Rev. B* **91**, 024423 (2015).
- [10] R. Toskovic, R. van den Berg, A. Spinelli, I. S. Eliens, B. van den Toorn, B. Bryant, J.-S. Caux, and A. F. Otte, *Nat. Phys.* **12**, 656 (2016).
- [11] J.-S. Caux, F. H. L. Essler, and U. Löw, *Phys. Rev. B* **68**, 134431 (2003).
- [12] S. R. White and A. E. Feiguin, *Phys. Rev. Lett.* **93**, 076401 (2004).
- [13] G. Vidal, *Phys. Rev. Lett.* **93**, 040502 (2004).
- [14] A. J. Daley, C. Kollath, U. Schollwöck, and G. Vidal, *J. Stat. Mech.: Theor. Exp.* (2004) P04005.
- [15] F. Verstraete, J. J. Garcia-Ripoll, and J. I. Cirac, *Phys. Rev. Lett.* **93**, 207204 (2004).
- [16] A. E. Feiguin and S. R. White, *Phys. Rev. B* **72**, 220401(R) (2005).
- [17] Z. Wang, J. Wu, S. Xu, W. Yang, C. Wu, A. K. Bera, A. T. M. Nazmul Islam, B. Lake, D. Kamenskyi, P. Gogoi, H. Engelkamp, A. Loidl, and J. Deisenhofer, [arXiv:1512.01753](https://arxiv.org/abs/1512.01753).
- [18] A. Holzner, A. Weichselbaum, I. P. McCulloch, U. Schollwöck, and J. von Delft, *Phys. Rev. B* **83**, 195115 (2011).
- [19] S. R. White, *Phys. Rev. Lett.* **69**, 2863 (1992).
- [20] U. Schollwöck, *Rev. Mod. Phys.* **77**, 259 (2005).
- [21] U. Schollwöck, *Ann. Phys.* **326**, 96 (2011).
- [22] A. Braun and P. Schmitteckert, *Phys. Rev. B* **90**, 165112 (2014).
- [23] M. Ganahl, P. Thunström, F. Verstraete, K. Held, and H. G. Evertz, *Phys. Rev. B* **90**, 045144 (2014).
- [24] F. A. Wolf, I. P. McCulloch, O. Parcollet, and U. Schollwöck, *Phys. Rev. B* **90**, 115124 (2014).
- [25] A. C. Tiegel, S. R. Manmana, T. Pruschke, and A. Honecker, *Phys. Rev. B* **90**, 060406 (2014).
- [26] S. Ramasesha, S. K. Pati, H. Krishnamurthy, Z. Shuai, and J. Brédas, *Synth. Met.* **85**, 1019 (1997).
- [27] T. D. Kühner and S. R. White, *Phys. Rev. B* **60**, 335 (1999).
- [28] E. Jeckelmann, *Phys. Rev. B* **66**, 045114 (2002).
- [29] E. Jeckelmann, *Prog. Theor. Phys. Suppl.* **176**, 143 (2008).
- [30] Z. Zhu, D. A. Huse, and S. R. White, *Phys. Rev. Lett.* **110**, 127205 (2013).
- [31] Z. Zhu, D. A. Huse, and S. R. White, *Phys. Rev. Lett.* **111**, 257201 (2013).
- [32] M. Vekić and S. R. White, *Phys. Rev. Lett.* **71**, 4283 (1993).
- [33] M. Vekić and S. R. White, *Phys. Rev. B* **53**, 14552 (1996).
- [34] J.-S. Caux and J. M. Maillet, *Phys. Rev. Lett.* **95**, 077201 (2005).
- [35] R. G. Pereira, J. Sirker, J.-S. Caux, R. Hagemans, J. M. Maillet, S. R. White, and I. Affleck, *Phys. Rev. Lett.* **96**, 257202 (2006).
- [36] H.-J. Mikeska and A. K. Kolezhuk, *One-Dimensional Magnetism*, Lecture Notes in Physics Vol. 645 (Springer, Berlin, Heidelberg, 2004), pp. 1–83.
- [37] K. Winkler, G. Thalhammer, F. Lang, R. Grimm, J. Hecker Denschlag, A. J. Daley, A. Kantian, H. P. Büchler, and P. Zoller, *Nature (London)* **441**, 853 (2006).

- [38] N. Strohmaier, D. Greif, R. Jördens, L. Tarruell, H. Moritz, T. Esslinger, R. Sensarma, D. Pekker, E. Altman, and E. Demler, *Phys. Rev. Lett.* **104**, 080401 (2010).
- [39] R. Sensarma, D. Pekker, E. Altman, E. Demler, N. Strohmaier, D. Greif, R. Jördens, L. Tarruell, H. Moritz, and T. Esslinger, *Phys. Rev. B* **82**, 224302 (2010).
- [40] A. L. Chudnovskiy, D. M. Gangardt, and A. Kamenev, *Phys. Rev. Lett.* **108**, 085302 (2012).
- [41] J. Villain, *Physica B* **79**, 1 (1975).
- [42] C. Trippé, F. Göhmann, and A. Klümper, *J. Stat. Mech.* (2010) P01021.
- [43] N. Hatano and M. Suzuki, *Quantum Annealing and Other Optimization Methods*, edited by A. Das and B.K. Chakrabarti (Springer, Berlin, 2005), pp. 37–68.
- [44] S. R. White and I. Affleck, *Phys. Rev. B* **77**, 134437 (2008).
- [45] T. Barthel, U. Schollwöck, and S. R. White, *Phys. Rev. B* **79**, 245101 (2009).
- [46] S. R. White, *Phys. Rev. Lett.* **102**, 190601 (2009).
- [47] M. E. Stoudenmire and S. R. White, *New J. Phys.* **12**, 055026 (2010).
- [48] F. A. Wolf, J. A. Justiniano, I. P. McCulloch, and U. Schollwöck, *Phys. Rev. B* **91**, 115144 (2015).
- [49] B. Bruognolo, J. von Delft, and A. Weichselbaum, *Phys. Rev. B* **92**, 115105 (2015).
- [50] C. Karrasch, J. H. Bardarson, and J. E. Moore, *Phys. Rev. Lett.* **108**, 227206 (2012).
- [51] T. Barthel, *New J. Phys.* **15**, 073010 (2013).
- [52] R. Thomale, S. Rachel, and P. Schmitteckert, *Phys. Rev. B* **88**, 161103 (2013).
- [53] J. C. Halimeh, F. Kolley, and I. P. McCulloch, *Phys. Rev. B* **92**, 115130 (2015).
- [54] A. C. Tiegel, A. Honecker, T. Pruschke, A. Ponomaryov, S. A. Zvyagin, R. Feyerherm, and S. R. Manmana, *Phys. Rev. B* **93**, 104411 (2016).
- [55] R. Rausch and M. Potthoff, *New J. Phys.* **18**, 023033 (2016).

4.2 Symmetric minimally entangled typical thermal states

Finite-temperature spectra typically require excessive amounts of numerical resources since the entanglement growth under real-time evolution is significantly enhanced by thermal fluctuations. In an attempt to tackle this issue, the following publication [BvDW15] for the first time extracts spectral functions at finite temperature with the minimally entangled typical thermal state (METTS) algorithm instead of relying on density-matrix purification [see Sec. 2.4.5].

Since METTS does not explicitly construct the full density matrix but instead works with an ensemble of pure states, we find that it can outperform purification at low temperatures (e.g., reach longer time scales), whereas purification represents the better choice for calculations at high temperatures. In addition, we unfold the full potential of METTS by developing a sampling routine that allows for the explicit incorporation of symmetries during the MPS simulation, something which cannot be achieved in the original formulation of the algorithm. Beyond benchmark calculations for the spin- $\frac{1}{2}$ Heisenberg chain, we employ our symmetry-enhanced METTS approach to study the finite-temperature behavior of an effective spin-ladder model for the natural mineral azurite $\text{Cu}_3(\text{CO}_3)_2(\text{OH})_2$, which features a prominent magnetization plateau at $\frac{1}{3}$ of the total magnetization under the application of an external magnetic field.

P2 *Symmetric Minimally Entangled Typical Thermal States*

B. Bruognolo, J. von Delft, and A. Weichselbaum

Phys. Rev. B **92**, 115105 (2015)

Symmetric minimally entangled typical thermal states

Benedikt Bruognolo, Jan von Delft, and Andreas Weichselbaum

Physics Department, Arnold Sommerfeld Center for Theoretical Physics, and Center for NanoScience, Ludwig-Maximilians-Universität, Theresienstraße 37, 80333 München, Germany

(Received 12 June 2015; published 2 September 2015)

We extend White's minimally entangled typically thermal states approach (METTS) to allow Abelian and non-Abelian symmetries to be exploited when computing finite-temperature response functions in one-dimensional (1D) quantum systems. Our approach, called SYMETTS, starts from a METTS sample of states that are not symmetry eigenstates, and generates from each a symmetry eigenstate. These symmetry states are then used to calculate dynamic response functions. SYMETTS is ideally suited to determine the low-temperature spectra of 1D quantum systems with high resolution. We employ this method to study a generalized diamond chain model for the natural mineral azurite $\text{Cu}_3(\text{CO}_3)_2(\text{OH})_2$, which features a plateau at $\frac{1}{3}$ in the magnetization curve at low temperatures. Our calculations provide new insight into the effects of temperature on magnetization and excitation spectra in the plateau phase, which can be fully understood in terms of the microscopic model.

DOI: [10.1103/PhysRevB.92.115105](https://doi.org/10.1103/PhysRevB.92.115105)

PACS number(s): 71.27.+a, 75.10.Pq

I. INTRODUCTION

The simulation of dynamical quantities in one-dimensional (1D) quantum many-body systems still poses a major challenge for theoretical condensed matter physics, particularly at finite temperature. From an experimentalist's perspective, there is high demand for such calculations for a variety of reasons: (i) Experimental measurements hardly allow to study solely ground-state physics as thermal fluctuations cannot be eliminated altogether. Thus, for a direct comparison with experimental data, it is essential to include temperature in the theoretical modeling. (ii) Technical advances have nowadays drastically enhanced the precision of neutron scattering and electron resonance spectroscopy, which for example allows the measurement of dynamic observables such as momentum-resolved excitation spectra in effective 1D materials with very high resolution [1–6]. (iii) Thermal fluctuations can cause new phenomena, which are not captured by the ground-state physics of the system. Two examples are the sudden emergence of a single spinon dispersion (“Villain mode”) in XXZ-like spin-chain materials [7–9] or the existence of quantum critical phases in various strongly correlated materials [10].

Which numerical tools can be employed to simulate such dynamic observables in a 1D quantum system? At zero temperature, the density matrix renormalization group (DMRG) is the most successful exact numerical method for describing quantum many-body systems regarding their static and dynamic ground-state properties [11,12]. DMRG-based algorithms have also been successfully extended to treat systems at finite temperature, yet the computational efficiency of such approaches is still limited. Exact diagonalization (ED) or quantum Monte Carlo (QMC) [13–15] can only be considered as complementary approaches rather than proper alternatives to DMRG since the applicability of ED is restricted by small system sizes, and that of QMC by the need for performing an ill-defined analytic continuation, and often also by the occurrence of a sign problem. Thus, the simulation of experimentally relevant quantities such as dynamic response functions represents a highly demanding and difficult task for finite-temperature numerics.

Whereas early DMRG approaches for computing finite-temperature response functions for a 1D quantum system

have been based on the transfer matrix renormalization group (TMRG) [16–19], today the most popular method builds on the purification of the density matrix in the matrix-product-state (MPS) formalism [20]. The response functions can then be calculated with high precision by using tDMRG in the real-time realm, and a subsequent Fourier transform also allows the computation of spectral functions [21–27]. Purification can also be combined with a Chebyshev expansion technique to determine finite-temperature spectral functions directly in frequency space [28,29]. Although these methods have been successfully applied to a number of experimental setups, the accessible time scale (or maximal Chebyshev expansion order) and hence the spectral resolution is limited, as the propagation of excitations during the dynamic evolution yields a linear growth of entanglement, leading to an exponential increase in the required numerical resources. In addition, the encoding of mixed states inevitably requires doubling the size of the Hilbert space and introduces additional entanglement between the physical state and its environment, which limits the efficiency of purification simulations towards low temperatures.

An alternative way to compute finite-temperature quantities was recently presented by White in Ref. [30]. Instead of purifying the density matrix, an ensemble of pure states is introduced that are constructed to resemble the typical state of a quantum system at finite temperature. It has been shown that these so-called minimally entangled typical thermal states (METTS) excellently represent the thermal properties of the system of interest. At the same time, they can efficiently be represented in the MPS formalism as their entanglement is very low [30,31]. The METTS approach was originally only used to compute static quantities of spin chains [30,31] and fermions [32]. In the meantime, it has also been applied to simulate finite-temperature quenches [33] and response functions [34].

The numerical effort for constructing a single METTS is comparable to ground-state DMRG since METTS avoids the explicit computation of the density matrix. Since METTS calculations are also easily parallelized, it has originally been considered to be a more efficient finite-temperature formulation than purification. More recently, Ref. [34] showed in a detailed study that this claim cannot generally be supported because the additional statistical error source introduced by

the sampling increases computational costs, especially at high temperatures. Nevertheless, METTS still offers much potential towards the simulations of low-temperature properties of complex models, as long as one does not insist on reducing the statistical error to be as small as the truncation error.

To bring out the full potential of METTS for the calculation of dynamic quantities, this work addresses a severe constraint of the current formulation of the algorithm: the ensemble states cannot be chosen such that they respect inherent *symmetries* of the system and at the same time minimize autocorrelation effects. This drastically increases the numerical resources necessary for computing the real-time evolution of the ensemble states, as the MPS have not been decomposed into symmetry blocks by means of the symmetry-induced selection rules [35–38]. To remedy this problem, we introduce an intuitive and easily implementable extension of White’s approach: starting from a METTS sample of states that are not symmetry eigenstates, we generate a sample of symmetry eigenstates, called SYMETTS. These states allow both simple Abelian and more complex non-Abelian symmetries to be exploited in the computation of dynamic quantities.

As an experimentally relevant application of SYMETTS, we study temperature effects on the $\frac{1}{3}$ magnetization plateau of a generalized diamond chain model, which has been derived as a microscopic model for the natural mineral azurite $\text{Cu}_3(\text{CO}_3)_2(\text{OH})_2$ [39,40]. This material has attracted much attention due to the discovery of a plateau at $\frac{1}{3}$ in the magnetization curve at low temperatures [4,5,39–49]. Via real-time evolution of SYMETTS ensembles, it is possible to obtain highly resolved excitation spectra in the $\frac{1}{3}$ plateau phase for various temperatures. We observe a crossing of monomer and dimer branches with increasing magnetic field, which intuitively explains the effects of finite temperature on the magnetization in the plateau phase.

The paper is organized as follows. In Sec. II, we briefly review the original METTS algorithm and the necessity of choosing a symmetry-breaking collapse routine to generate the ensemble. Section III introduces a METTS formulation based on symmetry eigenstates for models with both Abelian and non-Abelian symmetries. Section IV summarizes benchmark calculations for static and dynamic observables for the spin- $\frac{1}{2}$ XXZ chain. In Sec. V, SYMETTS is employed to study an experimentally relevant microscopic model for the natural mineral azurite. A technical discussion on the combination of SYMETTS with a Chebyshev expansion to directly calculate dynamic correlators in frequency space is relegated to Appendix A. The computational efficiency of SYMETTS in the context azurite is assessed in Appendix B.

II. MINIMALLY ENTANGLED TYPICAL THERMAL STATES

A. METTS calculations thermal quantities

First of all, we review the construction of a METTS sample to approximate a thermal expectation value $\langle \hat{A} \rangle_\beta$ for a general chain model with N sites. To this end, the trace of a thermal expectation value $\langle \hat{A} \rangle_\beta = \text{Tr}[\rho_\beta \hat{A}]$ is expanded in terms of an orthonormal basis $\{|\sigma\rangle\}$ of classical product states (CPS) of the form $|\sigma\rangle = |\sigma^1\rangle|\sigma^2\rangle \dots |\sigma^N\rangle$. Each such

state has an entanglement entropy of exactly zero. Thus, these states represent a natural choice for a basis at infinite temperature, where the system should behave classically. In addition, their entanglement growth under imaginary-time evolution remains comparatively low, hence, the designation “minimally entangled” states. The expectation value of \hat{A} can be written as

$$\begin{aligned} \langle \hat{A} \rangle_\beta &= \frac{1}{Z_\beta} \sum_{\sigma} \langle \sigma | e^{-\beta \hat{H}/2} \hat{A} e^{-\beta \hat{H}/2} | \sigma \rangle \\ &= \frac{1}{Z_\beta} \sum_{\sigma} P_\sigma \langle \phi_\sigma | \hat{A} | \phi_\sigma \rangle, \end{aligned} \quad (1)$$

with the partition function $Z_\beta = \text{Tr}[e^{-\beta \hat{H}}] = \sum_{\sigma} P_\sigma$. The normalized states $|\phi_\sigma\rangle$ represent a set of METTS with corresponding probabilities P_σ , defined as

$$|\phi_\sigma\rangle = \frac{1}{\sqrt{P_\sigma}} e^{-\beta \hat{H}/2} |\sigma\rangle, \quad P_\sigma = \langle \sigma | e^{-\beta \hat{H}} | \sigma \rangle. \quad (2)$$

By sampling the METTS $|\phi_\sigma\rangle$ according to the probability distribution P_σ/Z_β , the calculation of a thermal expectation value can be reformulated into taking the plain average of $\langle \phi_\sigma | \hat{A} | \phi_\sigma \rangle$.

To obtain a METTS sample $\{|\phi_\sigma\rangle\}$ with the correct probability distribution, a Markov chain of CPS $|\sigma\rangle$ is generated. This is done in a way that obeys detailed balance, which guarantees reproducing the probability distribution P_σ/Z_β . The sampling algorithm can be set up sequentially. To this end, one starts from an arbitrary CPS $|\sigma\rangle$ and conducts what is called a *thermal step*:

(i) A single METTS $|\phi_\sigma\rangle$ is generated by evolving the CPS in imaginary time and normalizing it.

(ii) A measurement of all local degrees of freedom is performed by projecting (or collapsing) $|\phi_\sigma\rangle$ into a new CPS $|\sigma'\rangle$ with probability $p_{\sigma'\sigma} = |\langle \sigma' | \phi_\sigma \rangle|^2$. The transition probabilities obey detailed balance $p_{\sigma'\sigma} P_\sigma = p_{\sigma\sigma'} P_{\sigma'}$ by construction.

The thermal step is then repeated with the newly generated CPS to generate a METTS (see Fig. 1 for illustration). By construction, the correct distribution is recovered as a fixed point of this procedure. To eliminate any artificial bias caused by the choice of the initial random CPS, the first few thermal steps are neglected in the calculation of any static observable $\langle \phi_\sigma | \hat{A} | \phi_\sigma \rangle$ or dynamic response function of any static observable $\langle \hat{B}(t) \hat{C} \rangle_\beta$.

By making good choices for the local measurements (see Sec. II B), the sample size M can be chosen surprisingly small to obtain accurate results [$M \sim O(10^2 - 10^3)$].

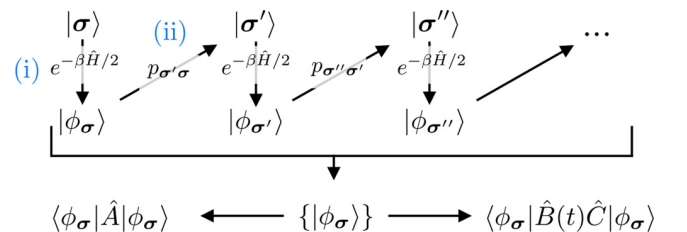


FIG. 1. (Color online) Schematic illustration of the METTS algorithm. For details on how to explicitly evaluate response functions of the type $\langle \hat{B}(t) \hat{C} \rangle_\beta$, see Sec. IV B.

At this point, a comment on accuracy is in order. It was recently pointed out by Ref. [34] that the purification approach drastically outperforms METTS because for fixed total computation time it reaches more accurate results, where the accuracy was judged by comparing to quasiaexact calculations. However, this should not be a surprise since the METTS sampling introduces an additional statistical error source, which generally scales as $\beta^{-1}/\sqrt{M-1}$. Obviously, this prevents a perfect convergence of METTS results towards exact data and limits the efficiency at very high temperatures in comparison to a nonstatistical method. Nevertheless, we believe that METTS offers much potential towards the simulations of low-temperature properties of complex models, as long as one does not insist on pushing the statistical error towards the order of the truncation error.

B. Ergodicity and efficient sampling

Generating a new CPS $|\sigma\rangle$ by collapsing a METTS represents the most crucial step of the sampling algorithms, as a bad choice of measurement basis leads to a drastically increased autocorrelation time [31].

Let us assume that the local Hilbert space of each site j in our chain model is represented by an orthonormal basis $|\sigma_j\rangle$ of size d , $\sigma_j \in \{1, 2, \dots, d\}$. The projective measurement $|\phi_\sigma\rangle \rightarrow |\sigma'\rangle$ can be efficiently carried out site by site by making use of the well-defined orthogonality relations for a MPS, typically starting at one end of the chain (in our case site 1). To this end, the d transition probabilities $p(\sigma_1) = \langle \phi_\sigma | \hat{P}(\sigma_1) | \phi_\sigma \rangle$ are calculated by introducing the projectors $\hat{P}(\sigma_1) = |\sigma_1\rangle\langle\sigma_1|$. Then, one of the d states is chosen with probability $p(\sigma_1)$ by rolling a dice. The state is collapsed by the application of the projector $\hat{P}(\sigma_1)$, and the orthonormal center of the MPS is shifted to the next site, where the collapse process is repeated.

In principle, the orthonormal basis $|\sigma_j\rangle$ on each site j can be chosen arbitrarily. Nevertheless, there are good and bad choices with respect to the sampling efficiency. We illustrate this for the example of the spin- $\frac{1}{2}$ XXZ Heisenberg chain

$$\hat{H} = J \sum_j^N [\hat{S}_j^x \hat{S}_{j+1}^x + \hat{S}_j^y \hat{S}_{j+1}^y + \Delta \hat{S}_j^z \hat{S}_{j+1}^z] + h \sum_j^N \hat{S}_j^z \quad (3)$$

for the isotropic case $J = 1$, $\Delta = 1$, and $h = 0$. This model features a non-Abelian $SU(2)_{\text{spin}}$ symmetry, which can be reduced to an Abelian $U(1)$ symmetry, e.g., by considering the total magnetization S_{tot}^z as a good quantum number. At first sight, the eigenstates of the spin operator \hat{S}_j^z resemble a natural choice for the orthonormal basis set $|\sigma_j\rangle$ since this choice allows the encoding of the projectors in the form of diagonal operators. Moreover, all resulting CPS are eigenstates of $\hat{S}_{\text{tot}}^z = \sum_j^N \hat{S}_j^z$. Therefore, it is possible to directly implement the Abelian $U(1)$ symmetry in the MPS representation resulting in a massive reduction of computational effort.

However, a collapse routine based on measurements along the z axis only (“ z collapse”) leads to a serious problem with ergodicity, as already extensively discussed in Ref. [31]. Subsequently generated CPS are strongly correlated and thus the autocorrelation times are very long, so that the bias arising from the initial random CPS cannot be removed in a few thermal steps. Additionally, CPS generated from subsequent

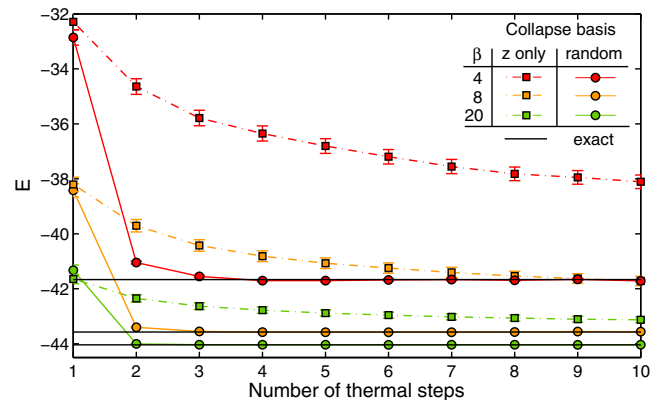


FIG. 2. (Color online) Energy of the spin- $\frac{1}{2}$ Heisenberg chain with $N = 100$ spins for $\beta = 4, 8, 20$. Details on the setup of the imaginary-time evolution can be found in Sec. IV. Starting from an ensemble of 100 randomly generated CPS, we conduct 10 thermal steps with each state and measure the ensemble average of the total energy in each step. The different basis choices for the CPS collapse become apparent in the autocorrelation times. Whereas measuring along the z axis only (squares) leads to strong autocorrelations that prevent the energy to converge towards the exact value (black lines), randomly chosen measurement bases (circles) result in short autocorrelation times of a few thermal steps [31].

thermal steps always have the same total magnetization S_{tot}^z since the z collapse conserves this quantity. It is therefore impossible to cover different S_{tot}^z sectors with the sampling algorithm described above, as one is always stuck in the symmetry sector of the initially chosen CPS.

This issue can be resolved by randomly choosing a different local basis for each site of the chain (“random collapse”). Alternatively, it has been shown that alternating in subsequent thermal steps between two basis sets that are maximally mixed relative to each other, e.g., the eigenstates of \hat{S}^z and \hat{S}^x , also restores ergodicity and covers multiple symmetry sectors of the sample (“maximally mixed collapse”).

We illustrate the failure of the z collapse routine by starting from an ensemble of randomly generated CPS and then conducting 10 thermal steps with each state of the ensemble for three different values of β . After each step, we measure the ensemble average of the total energy, which is displayed in Fig. 2. For comparison, we also calculate the same quantity using the random collapse routine. When choosing a random basis for each CPS collapse (circles), the total energy of the ensemble is already well converged towards the exact value after a few thermal steps because autocorrelations between subsequent CPS are practically absent.

In contrast, when measuring along the z axis only (squares), the total energy is nowhere near its exact value, even after 10 thermal steps. We have discussed the causes of this behavior above: first of all, one can identify strong correlations between subsequent CPS during the application of the z collapse resulting in an increase of autocorrelation time. In addition, each CPS remains in its initial symmetry sector. If the different symmetry sectors are not distributed according to the correct probability distribution at a specific value β (which is very unlikely starting from a random set), the ensemble cannot capture the correct behavior of the system, as the sample is

biased towards specific sectors. This explains why the average energy is not only converging slowly towards the exact value, but rather seems to saturate at a significantly higher value. Thus, a symmetry-conserving collapse routine that is based on measurements in a fixed local basis is clearly impracticable.

If we want to retain the ergodicity of the METTS sample, we are left to choose between the random or the maximally mixed collapse routine. This comes at a price, as the ensemble states cannot be chosen such that they conserve inherent symmetries of the system because both collapse routines clearly require symmetry-breaking measurements. However, the efficient treatment of symmetries is often essential for calculating especially dynamic properties of complex models, such as 1D systems and 2D lattice models with experimental relevance. Since the current METTS setup does not allow Abelian or non-Abelian symmetries to be exploited, it is not suitable for accessing dynamic observables of such complex systems.

In the following, we show how to resolve this fundamental issue by a simple extension of the sampling algorithm that will enable us to systematically build a METTS ensemble based on symmetry eigenstates.

III. SYMMETRIC METTS

A. Symmetries

The matrix-product-state framework allows for a straightforward incorporation of symmetries of the model Hamiltonian [35–38]. Generally speaking, the symmetry-induced selection rules cause a large number of matrix elements to be exactly zero, thus bringing the Hamiltonian into a block-diagonal structure and subdividing tensors into well-defined symmetry sectors. Keeping only the nonzero elements, we can achieve tremendous improvement in speed and accuracy in numerical simulations by the inclusion of symmetries. In the context of non-Abelian symmetries, the nonzero data blocks are not independent of each other and can be further compressed using the Clebsch-Gordan algebra for multiplet spaces. Here, we refrain from discussing this topic at length and refer to Ref. [36] for a detailed review on the treatment of symmetries in tensor network applications.

Following the notation of Ref. [36], we label the state space in terms of the symmetry eigenbasis $|qn; q_z\rangle$, where the quantum labels q denote the irreducible representation of the symmetry group \mathcal{S} of the Hamiltonian \hat{H} . Every symmetry generator \hat{S}_α satisfies $[\hat{H}, \hat{S}_\alpha] = 0$. Hence, all states in a given Hilbert space corresponding to a certain q label are combined into a symmetry block q . The label n identifies a particular multiplet within the specific symmetry block q . The internal multiplet label q_z resolves the internal structure of the corresponding multiplet. In the context of Abelian symmetries, the Clebsch-Gordan structure becomes trivial, hence, the q_z labels take the role of q labels. Note that this notation can be easily generalized to the treatment of multiple symmetries [36].

To further clarify the notation, we consider the example of the isotropic Heisenberg chain in Eq. (3), which features an $SU(2)_{\text{spin}}$ symmetry $\mathcal{S} = SU(2)_{\text{spin}}$. We make the usual choice of basis in which the z component of the spin operator \hat{S}_z is diagonal and label a general spin multiplet by $|q, q_z\rangle \equiv |S, S_z\rangle$. The spin multiplet label can take the

values $q = 0, \frac{1}{2}, 1, \frac{3}{2}, \dots$, while the internal multiplet label, corresponding to the z component of the spin, is restricted to $q_z \in \{-q, -q+1, \dots, +q\}$.

Now, consider a typical MPS scenario, where the wave function $|\psi\rangle$ in the local picture of site j can be represented as

$$|\psi\rangle = \sum_{L\sigma_j R} A_{LR}^{[\sigma_j]} |L\rangle |\sigma_j\rangle |R\rangle. \quad (4)$$

In the presence of symmetries, the physical state space at site j as well as the left and right orthonormal basis states can be written as $|L\rangle \equiv |ql; q_z\rangle$, $|\sigma_j\rangle \equiv |q'm; q'_z\rangle$, $|R\rangle \equiv |q''n; q''_z\rangle$. Hence, symmetry labels can be introduced naturally in the MPS representation. In particular, every leg or bond in the usual diagrammatic depiction of a MPS can be assigned a multiplet label, here q, q' and q'' , e.g.,

$$A_{qq''}^{[q']} = \begin{array}{c} q \\ \bullet \\ q'' \\ | \\ q' \end{array}, \quad (5)$$

B. METTS with symmetry eigenstates

In order to work with a symmetry-conserving METTS ensemble, we reformulate Eqs. (1) and (2) in terms of symmetry eigenstates before introducing an efficient sampling routine (see Sec. III C). In place of the CPS, we introduce a set of symmetry product states (SPS) $|\mathbf{q}\rangle$, that can be considered as symmetrized counterparts of the CPS. A SPS is a MPS with (multiplet) bond dimension one, where each bond represents a single, unique symmetry block q_j , and that block contains just a single multiplet ($n_j = 1$). Thus, the SPS can be fully characterized by a set of N quantum labels $\mathbf{q} = \{q_1, q_2, q_3, \dots, q_N\}$, one label q_j per site/bond j labeling the corresponding symmetry sector. The overall symmetry sector of each SPS $|\mathbf{q}\rangle$ is fully determined by the q label of the last bond q_N .

The simplest example of a SPS for the $SU(2)$ symmetric Heisenberg chain is to combine pairs of neighboring spins to singlets

$$|\mathbf{q}\rangle_{SU(2)} = (|\uparrow_1\rangle|\downarrow_2\rangle - |\uparrow_2\rangle|\downarrow_1\rangle)(|\uparrow_3\rangle|\downarrow_4\rangle - |\uparrow_4\rangle|\downarrow_3\rangle) \dots (|\uparrow_{N-1}\rangle|\downarrow_N\rangle - |\uparrow_N\rangle|\downarrow_{N-1}\rangle). \quad (6)$$

For spin- $\frac{1}{2}$ systems, the quantum labels q correspond to a sequence of $q_j = \frac{1}{2}, 0$ for odd and even bonds, respectively, with a total spin $q_N \equiv S_{\text{tot}} = 0$, as illustrated in Fig. 3(a). Although the (multiplet) dimension on each bond remains one for a non-Abelian SPS, it is no longer a pure product state

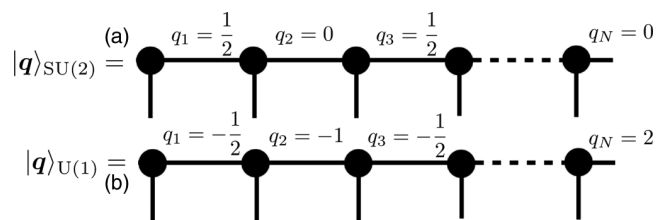


FIG. 3. Schematic illustration of the SPS (a) in Eq. (6) and (b) in Eq. (7).

in the classical sense as the internal multiplet structures can introduce nontrivial entanglement between neighboring sites.

The same formalism also applies for Abelian SPS. Reducing SU(2) to an Abelian U(1) symmetry in the Heisenberg model, e.g., by choosing an anisotropy $\Delta \neq 1$ in Eq. (3) or adding a finite magnetic field in the z direction, and choosing the total spin S_{tot}^z as conserved quantity, a typical SPS takes the form of

$$|\mathbf{q}\rangle_{U(1)} = |\downarrow_1\rangle|\downarrow_2\rangle|\uparrow_3\rangle|\downarrow_4\rangle \dots |\uparrow_N\rangle. \quad (7)$$

In this case, the quantum label q_j represents the sum of all S^z contributions for sites $i \leq j$, i.e., $q_j = \sum_{i \leq j} S_i^z$ as shown in Fig. 3(b). Hence, the total magnetization S_{tot}^z of the SPS is given by the last label q_N . In the Abelian case, a SPS can be understood as a direct product of local symmetry eigenstates of each site, and hence is always represented by a MPS of bond dimension one, much like a classical product state.

Analogously to the CPS basis set $\{|\sigma\rangle\}$, a full set of SPS $\{|\mathbf{q}\rangle\}$ represents a complete orthonormal basis taking into account all possible symmetry sectors of the system. Thus, we can proceed as above and expand the trace of a thermal expectation value $\langle \hat{A} \rangle_\beta = \text{Tr}[\rho_\beta \hat{A}]$ in terms of the symmetry product states $|\mathbf{q}\rangle$:

$$\begin{aligned} \langle \hat{A} \rangle_\beta &= \frac{1}{Z_\beta} \sum_{\mathbf{q}} \langle \mathbf{q} | e^{-\beta \hat{H}/2} \hat{A} e^{-\beta \hat{H}/2} | \mathbf{q} \rangle \\ &= \frac{1}{Z_\beta} \sum_{\mathbf{q}} P_{\mathbf{q}} \langle \phi_{\mathbf{q}} | \hat{A} | \phi_{\mathbf{q}} \rangle. \end{aligned} \quad (8)$$

The normalized states $|\phi_{\mathbf{q}}\rangle$ now represent a set of symmetric METTS (SYMETTS) with probabilities $P_{\mathbf{q}}$ defined in analogy to Eq. (2):

$$|\phi_{\mathbf{q}}\rangle = \frac{1}{\sqrt{P_{\mathbf{q}}}} e^{-\beta \hat{H}/2} |\mathbf{q}\rangle, \quad (9a)$$

$$P_{\mathbf{q}} = \langle \mathbf{q} | e^{-\beta \hat{H}} | \mathbf{q} \rangle. \quad (9b)$$

The thermal expectation value $\langle \hat{A} \rangle_\beta$ is now estimated by sampling SYMETTS $|\phi_{\mathbf{q}}\rangle$ according to the probability distribution $P_{\mathbf{q}}/Z_\beta$. However, we still have to establish how to sample a set of SYMETTS $\{|\phi_{\mathbf{q}}\rangle\}$ according to the correct probability distribution $P_{\mathbf{q}}/Z_\beta$, in a way that ensures ergodicity.

C. Algorithm for efficient sampling

We illustrated in Sec. II B for the spin- $\frac{1}{2}$ Heisenberg chain that a collapse routine purely based on measurements along the z axis, conserving the $U(1)_{\text{spin}}$ symmetry, fails to capture the correct thermal properties of the model. This is due to strong autocorrelation effects and the fact that the symmetry sectors initially are distributed randomly instead of according to the correct probability distribution $P_{\mathbf{q}}/Z_\beta$. From this discussion, we can learn that the SYMETTS sample has to be generated

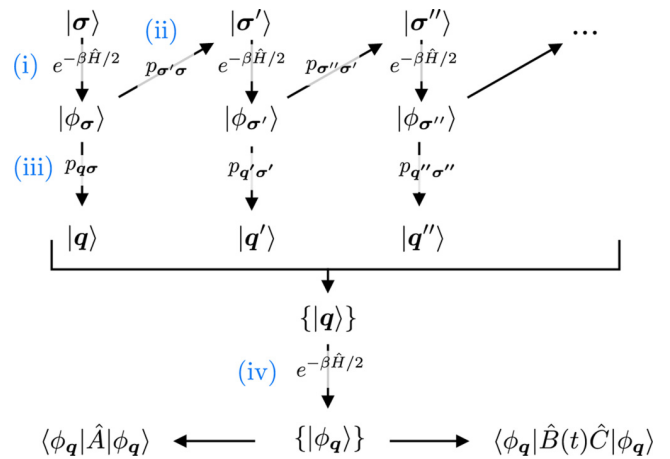


FIG. 4. (Color online) Schematic illustration of the SYMETTS sampling algorithm. For details on how to explicitly evaluate response functions of the type $\langle \hat{B}(t) \hat{C} \rangle_\beta$, see Sec. IV B.

from SPS that already capture the correct distribution of symmetry sectors.¹

This can be achieved by starting from a typical thermal state, which already incorporates all the necessary thermal information. To this end, we extend the METTS sampling algorithm. After the conduction of a thermal step with a nonsymmetric CPS $|\sigma\rangle$ and METTS $|\phi_\sigma\rangle$ using a random or maximally mixed collapse [cf. (i) and (ii) in Sec. II], we employ an additional *symmetrization step*:

(iii) Using a symmetry-conserving collapse routine (described in the following), we collapse $|\phi_\sigma\rangle$ to a SPS $|\mathbf{q}\rangle$ with probability $p_{\mathbf{q}\sigma} = |\langle \mathbf{q} | \phi_\sigma \rangle|^2$. Each collapse generates a SPS according to the correct probability distribution $P_{\mathbf{q}}/Z_\beta$ (thus belonging to one of the relevant symmetry sectors at a given temperature), as long as the nonsymmetric METTS has been sampled according to P_σ/Z_β .

(iv) The resulting SPS $|\mathbf{q}\rangle$ can easily be converted into an MPS with explicit encoded symmetry sectors [36], which is then evolved in imaginary time and normalized to generate the SYMETTS $|\phi_{\mathbf{q}}\rangle$.

The combination of thermal and symmetrization step is then repeated with the newly generated CPS $|\sigma'\rangle$ to create a full SYMETTS sample $\{|\phi_{\mathbf{q}}\rangle\}$, which represents the basis for calculating static or dynamic observables at finite temperature (see Fig. 4 for an illustration). Thus, we ensure that all computed SYMETTS are minimally autocorrelated, as each of them is generated from a different nonsymmetric METTS.

By maximizing the ergodicity of the sample, we face additional computational cost, as we have to generate a full nonsymmetric METTS sample $\{|\phi_\sigma\rangle\}$ as well. In principle, it

¹ It was briefly noted in Ref. [31] that this can already be achieved using a maximally mixed collapse procedure and treating the x basis as an effective z basis. This is possible due to the presence of the $SU(2)_{\text{spin}}$ symmetry in the isotropic model which is effectively reduced to $U(1)$ by this implicit switch of bases. Note that this is not possible in absence of $SU(2)$, e.g., in the anisotropic XXZ model or in the presence of a magnetic field. Hence, this trick cannot be used to exploit the full symmetry of the respective model.

is possible to reduce the number of nonsymmetric METTS by generating a larger number of SPS from each $|\phi_\sigma\rangle$ by repeating the symmetrization step multiple times. However, this may introduce artificial correlations between different SPS generated from the same nonsymmetric METTS. For this reason, we present the SYMETTS algorithm using a formulation that maximizes ergodicity. This limits the applicability of SYMETTS in terms of calculating static observables. In these cases, we would have to work harder than with regular METTS. However, when calculating *dynamic* quantities, generating the SYMETTS sample accounts for only a factor $O(10^{-3})$ or less of the total computation time. Hence, our algorithm ensures that the full potential of SYMETTS towards dynamic applications is guaranteed and no ergodicity problems arise.

D. Collapse routine for non-Abelian symmetries

In this section, we illustrate step (iii) of the SYMETTS sampling for the example of the isotropic spin- $\frac{1}{2}$ Heisenberg chain (3).

In context of $U(1)_{\text{spin}}$, the collapse routine employed in step (iii) simply corresponds to the z collapse discussed in Sec. II B, i.e., measuring along the z axis only. The resulting SPS take the form of direct products of local symmetry eigenstate $|\uparrow\rangle, |\downarrow\rangle$ and are automatically distributed according to the correct probability P_q/Z_β .

However, to exploit the full $SU(2)_{\text{spin}}$ symmetry of the model, the collapse routine has to be adapted in order to generate a SPS ensemble $\{|\mathbf{q}\rangle\}$ of $SU(2)$ eigenstates. For a single SPS, this is achieved by using a nonsymmetric METTS $|\phi_\sigma\rangle$ and sequentially collapsing it into the different eigensectors of the total spin operator \hat{S}^2 .

To this end, we gradually build \hat{S}^2 starting from the left end of the chain. At the first site, the total spin is always $\frac{1}{2}$ as we only consider a single spin, hence after constructing \hat{S}_1^2 no projection is required and the orthonormal center of $|\phi_\sigma\rangle$ can be shifted to the second site. Here, we generate the total spin operator of first and second sites according to

$$\hat{S}_{L,2}^2 = \hat{S}_1^2 + \hat{S}_2^2 + \hat{S}_1\hat{S}_2 + \hat{S}_2\hat{S}_1, \quad (10)$$

with $\hat{S}_j^2 = (\hat{S}_j^x)^2 + (\hat{S}_j^y)^2 + (\hat{S}_j^z)^2$ and the subscript “ $L,2$ ” indicating that we consider the total spin of the left part of the chain up to the second site. Diagonalizing this operator, we obtain the two spin sectors $S_{L,2} = \frac{1}{2} \pm \frac{1}{2} = 0, 1$ corresponding to the singlet and triplet configurations, and the projectors $\hat{P}(S_{L,2})$. We project the second bond of $|\phi_\sigma\rangle$ (and also $\hat{S}_{L,2}^2$) either into singlet or triplet configuration according to the transition probabilities

$$p(S_{L,2}^z) = \langle \phi_\sigma | \hat{P}(S_{L,2}^z) | \phi_\sigma \rangle, \quad (11)$$

and shift the orthonormal center of $|\phi_\sigma\rangle$ to the next site. This procedure is repeated sequentially for every site j of the system. Each time, we construct the spin operator for the left and the local part of the chain according to

$$\hat{S}_{L,j}^2 = \hat{S}_{L,j-1}^2 + \hat{S}_j^2 + \hat{S}_{L,j-1}\hat{S}_j + \hat{S}_j\hat{S}_{L,j-1}, \quad (12)$$

where $\hat{S}_{L,j-1}^2$ denotes the total spin squared of all sites to the left of (and excluding) site j . After diagonalization, the

transition probabilities are calculated and $|\phi_\sigma\rangle$ is projected at bond j into a single spin sector. Just as for the initially considered example, the operator $\hat{S}_{L,j}^2$ always contains only two spin sectors, namely, $S_{L,j} = S_{L,j-1} \pm \frac{1}{2}$. Hence, diagonalization and projections can be carried out very efficiently.

In the end, one obtains an $SU(2)_{\text{spin}}$ symmetric SPS $|\mathbf{q}\rangle$ with probability $p_{\mathbf{q}\sigma} = |\langle \mathbf{q} | \phi_\sigma \rangle|^2$. States of this type are the initial point for setting up the $SU(2)$ symmetric MPS framework [36].

IV. BENCHMARK RESULTS

In this section, we present some benchmark results for our SYMETTS approach applied to both static and dynamic observables of the XXZ Heisenberg model with $N = 100$ spins in the isotropic ($\Delta = 1$, XXX model) and the free-fermion limit ($\Delta = 0$, XX model). As truncation criterion, we choose to keep all singular values above $s_\beta^{\text{tol}} > 10^{-5}$ during the process of imaginary-time evolution, which is carried out using standard tDMRG tools with a second-order Trotter decomposition and a time step $\tau = 0.05$. For the subsequent real-time evolution we adapt only the truncation criterion to $s_{\text{dyn}}^{\text{tol}} = 10^{-4}$. All quantities are expressed in terms of the coupling $J = 1$.

A. Static observables: Thermal energy

First, we discuss some static SYMETTS calculations for the total energy of the isotropic Heisenberg chain (3) with and without finite magnetic field. The data below conclusively show that the slightly modified METTS algorithm above is able to obtain results of similar accuracy as the nonsymmetric METTS sampling at equal sample size M . Of course, this is to be expected since SYMETTS essentially generates the ensemble states analogously to the original algorithm. Nevertheless, this exercise helps to understand the importance of using sample states which are correctly distributed over the relevant symmetry sectors.

To illustrate the method in more detail, Fig. 5 shows $U(1)$ -SYMETTS results resolving the different symmetry sectors entering into the calculation of the thermal energy for four different inverse temperatures. The upper row displays the average energy of each subsample of states characterized by fixed S_{tot}^z . In the middle row, we zoom into a window of order of the temperature around the average energy of the sample. The resulting values for $\langle E \rangle_\beta$ determined by SYMETTS [Eq. (8)] are benchmarked against METTS calculations [Eq. (1)] and quasixact purification data. The thermal average of all SYMETTS subsamples leads to highly accurate results for $\langle E \rangle_\beta$.

For large β , the lowest energy is obtained by the $S_{\text{tot}}^z = 12$ sector, which corresponds to the ground-state symmetry sector of the system. Depending on the temperature, the energy of the neighboring sectors increases more or less steeply. At high temperatures, thermal fluctuations become clearly visible in the thermal energies of the different symmetry sectors. Accordingly, the number of relevant symmetry sectors obtained from the SYMETTS sampling step (ii) is closely related to the temperature. Thermal fluctuations drive the sample states into more “excited” symmetry sectors at high temperatures: the maximum symmetry sector occurring in the $\beta = 4$ simulation corresponds to $S_{\text{tot}}^z = 20$, whereas we find a

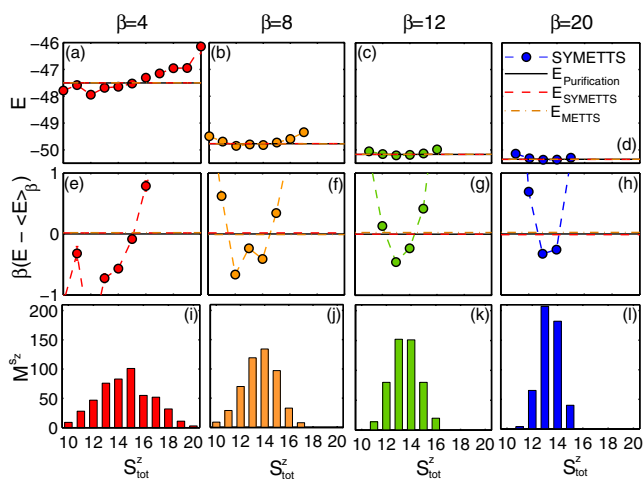


FIG. 5. (Color online) U(1)-SYMETTS sampling of the thermal energy for the isotropic Heisenberg chain with $h = 1$. Panels (a)–(d) in the upper row display the thermal energy of each symmetry sector entering the SYMETTS sample for β ranging between 4 and 20; dashed lines indicate the overall ensemble average $\langle E \rangle_\beta$ determined by SYMETTS. Moreover, a comparison to benchmark calculation based on METTS (dotted lines) and purification (solid lines) is provided. Panels (e)–(h) in the second row show $\beta(E - \langle E \rangle_\beta)$, in order to zoom into an energy window of order of the temperature around $\langle E \rangle_\beta$. Panels (i)–(l) in the last row illustrate the subsample size $M^{S_{\text{tot}}^z}$ of different symmetry sectors for a fixed total sampling size $M = 500$.

maximum of $S_{\text{tot}}^z = 15$ for $\beta = 20$ as the system relaxes more towards the ground state. This behavior is also illustrated by the bottom row of Fig. 5, which shows the subsample size $M^{S_{\text{tot}}^z}$ of each symmetry sector for a fixed total sample size $M = \sum_{S_{\text{tot}}^z} M^{S_{\text{tot}}^z} = 500$. Again, we observe that the distribution of symmetry sectors is broad at high temperatures and becomes narrow for large values of β .

Figure 6 presents results for the thermal energy of the isotropic Heisenberg chain (3) at zero magnetic field, where we can exploit the non-Abelian SU(2) symmetry of the model.

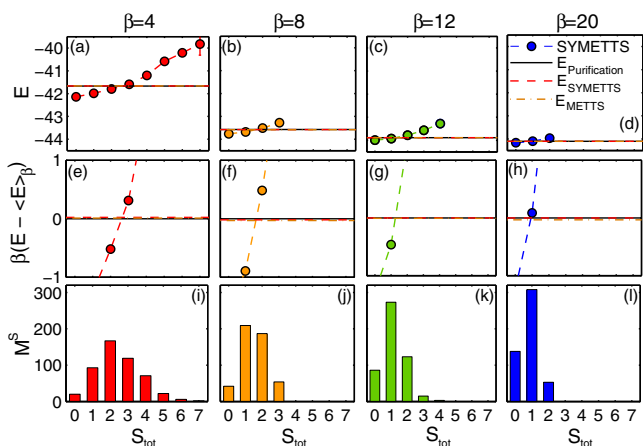


FIG. 6. (Color online) SU(2)-SYMETTS sampling of the thermal energy for the isotropic Heisenberg chain with $h = 0$, using the same layout as Fig. 5.

The layout of the panels and the parameters are chosen in accordance with those in Fig. 5 above. Instead of S_{tot}^z sectors, the SYMETTS are now categorized in terms of the total spin S_{tot} of each SU(2) multiplet in the sample. Again, the upper and middle rows display the average energy of each subsample corresponding to a fixed S_{tot} . The resulting values for $\langle E \rangle_\beta$ determined by SYMETTS [Eq. (8)] are benchmarked against METTS calculations [Eq. (1)] and quasiexact purification data. We find that the overall ensemble average of all SYMETTS subsamples gives a good approximation of the thermal energy of the state also for the non-Abelian sampling routine.

As for the Abelian case, the distribution of different multiplets shown in the last row becomes more narrow towards lower temperatures. Whereas the majority of states at $\beta = 20$ belong to the multiplets $S_{\text{tot}} = 0, 1$, these sectors deplete for higher temperatures and the maximum moves towards $S_{\text{tot}} = 2$ for $\beta = 4$.

B. Dynamic observables: Dynamic spin structure factor

Whereas SYMETTS does not offer any significant computational advantage over the original formulation for computing static observables, its potential is enormous for the calculation of dynamic quantities, such as response functions of the form

$$A_{\beta}^{\hat{B}\hat{C}}(t) = \langle \hat{B}(t)\hat{C} \rangle_{\beta}, \quad \text{with} \quad \hat{B}(t) = e^{i\hat{H}t} \hat{B} e^{-i\hat{H}t}. \quad (13)$$

For such problems, generating the ensemble states represents only a negligible part of the total computational costs. Most computational effort has to be put into the real-time evolution of each state in the sample, as the linearly growing entanglement requires an exponential increase of the bond dimension of the MPS towards longer time scales. Here, SYMETTS offers a great advantage over the existing METTS approach since the symmetry implementation strongly increases the numerical efficiency during the real-time evolution. In addition, the overhead cost of generating both a symmetric and nonsymmetric sample in the SYMETTS sampling (see Sec. III C) can be ignored in almost every case, as it only accounts for a very small fraction [$O(10^{-3})$] of the total computational time. The achievable efficiency gains are completely analogous to the exploitation of symmetries in other MPS applications, such as ground-state DMRG, tDMRG, or iTEBD. For example, the direct implementation of the Abelian U(1) symmetries in spin models can already speed up calculations by about a factor of up to 10 [37,50].² Even larger benefits can be achieved when studying models with multiple Abelian or non-Abelian symmetries.

To simulate a response function using real-time evolution, we follow Ref. [34] and compute for every SYMETTS $|\phi_q\rangle$ in our sample the expectation value

$$\langle \langle |\phi_q\rangle e^{i\hat{H}t} | \hat{B} [e^{-i\hat{H}t} \hat{C} | \phi_q\rangle \rangle \rangle \quad (14)$$

by carrying out two independent real-time evolutions $|\psi_q(t)\rangle = e^{-i\hat{H}t} \hat{C} |\phi_q\rangle$ and $|\phi_q(t)\rangle = e^{-i\hat{H}t} |\phi_q\rangle$ using standard tDMRG. Equation (14) can be evaluated at any intermediate time step t by calculating the overlap for the operator

²See also Appendix B.

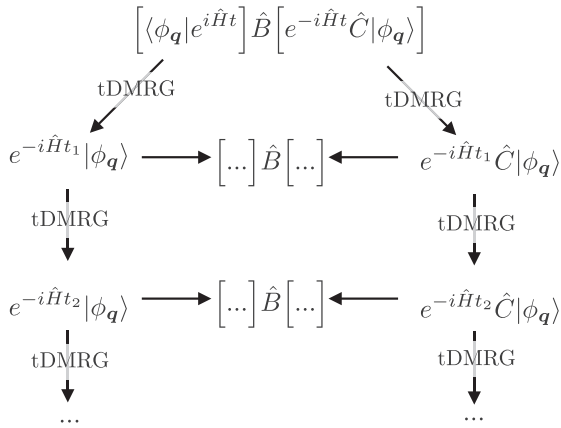


FIG. 7. Schematic illustration of the dynamic calculation with SYMETTS [34].

$\langle \psi_q(t) | \hat{B} | \phi_q(t) \rangle$, as illustrated in Fig. 7. In the end, we take the sample average to obtain a result for the finite-temperature response function.

In principle, there are other options for calculating the real-time evolution of response functions [34]. In this work, we restricted ourselves to the scheme outlined above, as it requires only two tDMRG simulations per sample state to access all intermediate time steps up to the maximally reached time scale t_{\max} .

Instead of studying real-time response functions, here we consider their Fourier transforms, i.e., spectral functions. More particularly, we focus on dynamic spin structure factors $S^{\alpha\beta}(\omega, k)$, which are the Fourier transform of dynamical spin correlation functions. These quantities are of particular experimental relevance, as they can be directly accessed by inelastic neutron scattering experiment. For a benchmark, we compute the dynamic spin structure factor of the XXZ Heisenberg model with open boundaries:

$$S^{\alpha\beta}(k, \omega) = \sum_{ij}^N \frac{\sin(ik) \sin(jk)}{\pi(N+1)} \int dt e^{i\omega t} \langle S_i^\alpha(t) S_j^\beta(0) \rangle. \quad (15)$$

To this end, we define the spin-wave operator $\hat{S}_k^\alpha = \sqrt{\frac{2}{N+1}} \sum_{j=1}^N \sin(\frac{j\pi k}{N+1}) \hat{S}_j^\alpha$ and evaluate $\langle \hat{S}_k^\alpha(t) \hat{S}_k^\beta \rangle_\beta$ via Eq. (14) for a number of intermediate points up to some maximum time t_{\max} . Then, we perform a Fourier transform to frequency space, including a Gaussian broadening $\exp[-4(t/t_{\max})^2]$ in the integral in Eq. (15) to remove artificial oscillations, which are caused by the finite cutoff of the real-time evolution [21]. This means that the exact spectral features are convolved with a Gaussian $\exp[-\omega^2/(2W^2)]$, with a frequency resolution $W = 2\sqrt{2}t_{\max}^{-1}$. In some cases, linear prediction can be used to avoid the artificial broadening and extract more spectral information from the time series [22,23]. However, we found that linear prediction is not reliable in our study of the generalized diamond chain (see Sec. VB). Hence, we refrain from employing linear prediction in this work.

In a first study, we employ our U(1)-SYMETTS approach to extract the dynamic spin structure factor in the limit of $\Delta = 0$. In this case, the XXZ model can be solved exactly

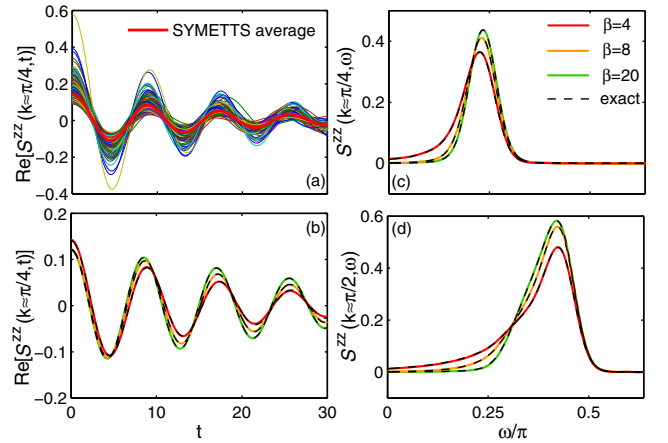


FIG. 8. (Color online) tDMRG calculation for the dynamic spin structure factor of the XX model using $M = 300$ ensemble states. Panel (a) illustrates the time evolution of individual SYMETTS (thin lines) at $\beta = 4$ used to calculate $S^{zz}(\pi/4, t)$ by taking the ensemble average (thick red line). (b) Displays the SYMETTS ensemble average for various inverse temperatures, which is then used to compute the dynamic spin structure factor in frequency space. Panels (c) and (d) show the frequency data obtained from Fourier transform for $k \approx \pi/4$ and $\pi/2$. For all considered inverse temperatures, we find excellent agreement with the exact result (dashed lines).

by mapping the system by a Jordan-Wigner transformation to noninteracting spinless fermions [51,52]. This allows us to exactly evaluate the spin correlation functions $\langle \hat{S}_i^\alpha(t) \hat{S}_j^\beta(0) \rangle$ for arbitrary times and obtain the dynamic spin structure factor by Fourier transformation for direct comparison to the SYMETTS data.

Figure 8(a) displays the real-time evolution of $S^{zz}(\pi/4, t)$ for $\beta = 4$ up to $t_{\max} = 30$, with the thin lines corresponding to individual realization of particular SYMETTS states and the thick red line denoting the ensemble average. The sample averages are collected for different temperatures in Fig. 8(b). After the real-time evolution, we perform a Fourier transform to obtain the dynamic spin structure factor as a function of frequency, as shown in Figs. 8(c) and 8(d) for $k \approx \pi/2$ and $\pi/4$. We find excellent agreement with exact results (dashed lines). A prerequisite for agreement of this quality is that the statistical sampling error, and hence the temperature, is sufficiently small; for the sample size of $M = 300$ used in Fig. 8 the relative error, defined as

$$\delta S = \frac{\sqrt{\int d\omega [S(k, \omega) - S_{\text{exact}}(k, \omega)]^2}}{\sqrt{\int d\omega S_{\text{exact}}(k, \omega)^2}}, \quad (16)$$

varies between $\delta S \approx 1\%$ for $\beta = 4$ and $\delta S \approx 0.3\%$ for $\beta = 20$. We note that the error is approximately proportional to the temperature, which indicates that the dominant contribution is given by the statistical error of the ensemble, which scales as $\sim T/\sqrt{M}$.

Next, we consider an isotropic coupling $\Delta = 1$, which allows us to compute $\hat{S}(k, \omega)$ using SU(2) SYMETTS, since the XXZ Hamiltonian (3) features the full spin symmetry in this case. Figures 9(a) and 9(b) show the results for $k \approx 3\pi/4$

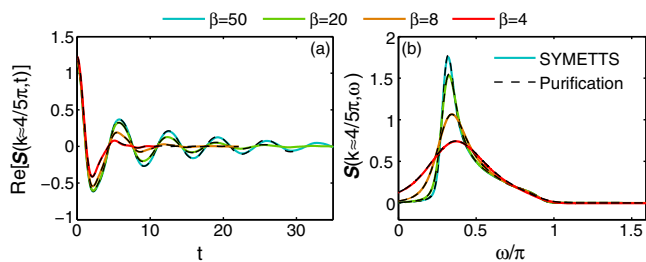


FIG. 9. (Color online) SU(2)-SYMETTS calculation (solid lines) for (a) $\hat{S}(3\pi/4, t)$ and (b) $\hat{S}(3\pi/4, \omega)$ of the isotropic Heisenberg chain using $M = 300$ ensemble states. For all considered inverse temperatures, we find very good agreement with data obtained from matrix-product purification (dashed lines).

in time and frequency space, respectively, in comparison to purification calculations using the same truncation criterion (black dashed lines). The maximum time t_{\max} varies for different temperatures, since we stopped the SYMETTS calculations when a threshold of 1000 states was exceeded by the bond dimension D , which was determined adaptively by keeping all singular values $> 10^{-4}$ (see Fig. 10 and upper panel of Table I for values of t_{\max}). Again, we find excellent agreement for the considered temperature range.

In this context, we briefly discuss the intriguing question whether SYMETTS can reach longer time scales than purification in certain limits. To this end, we study the growth of entanglement during the real-time evolution, which manifests itself in the growing bond dimension of both the average SYMETTS as well as the purified density matrix. Figures 10(a) and 10(b) present SU(2) data for the average maximum multiplet bond dimension \bar{D}^* and the corresponding states space dimension \bar{D} , respectively. We find that an average SYMETTS requires significantly less numerical resources at $\beta = 20, 50$. For such low temperatures, SYMETTS certainly allows to access longer time scales than purification when

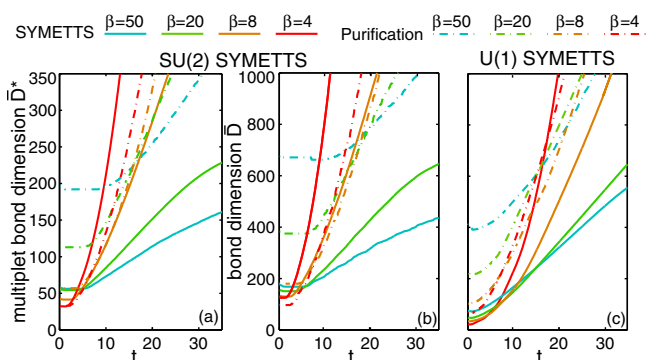


FIG. 10. (Color online) (a) Average multiplet bond dimension \bar{D}^* and (b) the corresponding bond dimension \bar{D} of SU(2) SYMETTS during the calculation of $\hat{S}(3\pi/4, t)$ (solid lines) in comparison to the purified density matrix (dashed lines). In both cases, we keep all singular values $> 10^{-4}$ during real-time evolution. For $\beta = 4, 8$ we include a backwards time evolution of the auxiliary bonds of the purified density matrix, as this leads to a reduction of the entanglement growth [24,53]. (c) Average bond dimension \bar{D} of U(1)-SYMETTS sample during the calculation of $S^{zz}(3\pi/4, t)$ for comparison.

TABLE I. Upper panel: maximum time t_{\max} reached in the simulations shown in Figs. 9 and 10. Lower panel: average multiplet bond dimension \bar{D}^* and corresponding average and maximum bond dimension for SU(2) and U(1) symmetry product states for various temperatures.

t_{\max}	$\beta = 4$	$\beta = 8$	$\beta = 20$	$\beta = 50$
SYMETTS _{SU(2)}	11.2	21.4	>35	>35
Purification _{SU(2)}	18	22	26.1	30.6
SYMETTS _{U(1)}	19.8	31.2	>35	>35
Bond dim.	$\beta = 4$	$\beta = 8$	$\beta = 20$	$\beta = 50$
$\bar{D}_{\text{SU}(2)}^*$	1	1	1	1
$\bar{D}_{\text{SU}(2)}$	4.11	3.08	2.31	1.96
$\max[D_{\text{SU}(2)}]$	16	12	7	5
$\bar{D}_{\text{U}(1)}$	1	1	1	1

fixing the numerically feasible bond dimension to an upper cutoff. Note that due to the presence of the statistical error, this does not imply that SYMETTS is generally more accurate than purification when fixing the total computation time and judging accuracy by comparing to quasixact calculations, as done in Ref. [34]. However, if one does not insist to push the statistical error towards the order of the truncation error, and moreover takes into account parallelizability, SYMETTS offers much potential towards the dynamical description of low-dimensional systems at low temperature. This is already illustrated by the calculations in this section, demonstrating that it is possible to extract the dynamic structure factor with high accuracy using a sample size of only a few hundred states.

On the other hand, SYMETTS is limited to small t_{\max} at high temperatures. Particularly at $\beta = 4$, a single SU(2) SYMETTS on average requires larger bond dimensions \bar{D} than the purified density matrix! This can be attributed to the intrinsic structure of the SU(2) symmetry product states. Although their multiplet dimension D^* is strictly unity at infinite temperature, the SPS already contain some entanglement due to the presence of nontrivial multiplet sectors with internal structure, which lead to a state space dimension $D > 1$. Because of thermal fluctuations, these “excited” multiplet sectors appear more frequently at high temperatures, which is illustrated by the comparison \bar{D}^* and \bar{D} of the corresponding SPS samples in the lower panel of Table I for different temperatures. With these nontrivial multiplets being present in the SPS, the subsequent imaginary- and real-time evolution obviously also induces more entanglement. This explains why \bar{D} of an SU(2) SYMETTS exceeds the bond dimension necessary to represent the purified density matrix already before starting the real-time evolution at $\beta = 4$ [cf. Fig. 10(b)].

This issue is not present in the context of U(1) SYMETTS, where the SPS does not contain any intrinsic entanglement at infinite temperature and thus can still be considered as a classical product state. Thus, the initial \bar{D} is strictly smaller than the bond dimension of the purified density matrix for all temperatures, as shown in Fig. 10(c). Moreover, the increase of \bar{D} at high and intermediate temperatures is slightly less severe than in the SU(2) calculations.

We conclude from this analysis that it is possible for SYMETTS to exploit both Abelian and non-Abelian sym-

metries. In combination with tDMRG, it represents a valuable alternative to computing spectral functions, particularly for low temperatures. In addition, we find that Abelian SYMETTS have favorable entanglement properties over their non-Abelian counterparts at high temperatures. Hence, one should refrain from exploiting non-Abelian SYMETTS in these cases and switch to U(1) SYMETTS or matrix-product purification.

We point out that the METTS algorithm in principle can also exploit time-translational invariance in order to reformulate the response function in terms of $\langle \hat{B}(t/2)\hat{C}(-t/2) \rangle$, which effectively doubles the maximum reachable time scale t_{\max} [25,27,34]. Ideally, the time evolution is then carried out in the Heisenberg picture by evolving \hat{B} and \hat{C} directly in terms of matrix-product operators (MPO) [54], so that it still requires only two tDMRG simulations to access all intermediate time steps. We note that working in the Heisenberg picture is generally considered to be suboptimal for matrix-product purification [27]. However, it seems more appealing for the METTS framework as one could carry out the real-time evolution only once for the MPO and compute the response function by calculating the overlap of the time-evolved MPO and the METTS sample. Thus, the time-evolved MPO could be recycled for arbitrary temperatures. In general, this would imply that the maximum reachable time scale is set by the real-time evolution of the operators. In the pure-state formulation, t_{\max} would then be temperature independent, as temperature only enters through the calculation of the overlaps with the METTS sample. Naturally, this idea enormously profits from the inclusion of symmetries into the METTS language presented here, but is beyond the scope of this paper and will be discussed elsewhere.

Finally, we remark that we have also explored the possibility of combining SYMETTS with a Chebyshev expansion to directly compute spectra in frequency space. However, this approach is computationally more expensive due to technical reasons and therefore not recommendable (see Appendix A for details).

V. GENERALIZED DIAMOND CHAIN MODEL FOR AZURITE

In the following, we demonstrate the efficiency of SYMETTS by studying a more complicated spin-chain model of direct experimental relevance. We focus on the natural mineral azurite $\text{Cu}_3(\text{CO}_3)_2(\text{OH})_2$, which has attracted much attention due to the discovery of a plateau at $\frac{1}{3}$ in the magnetization curve at low temperatures [4,5,39–49]. Some authors proposed that the magnetic properties of this material are well described by a spin- $\frac{1}{2}$ diamond chain formed by the copper atoms with purely antiferromagnetic exchange couplings [42,45,55]. Others suggested a dominant ferromagnetic coupling [4,43,44] and the importance of interchain coupling [46], yet none of them were able to derive a microscopic model for azurite that is able to fully characterize its complex magnetic properties.

Employing a combination of first-principle methods, exact diagonalization, and DMRG, Ref. [39] recently derived a full three-dimensional model which can be mapped to an effective one-dimensional system, namely, a generalized diamond chain model with purely antiferromagnetic couplings, illustrated

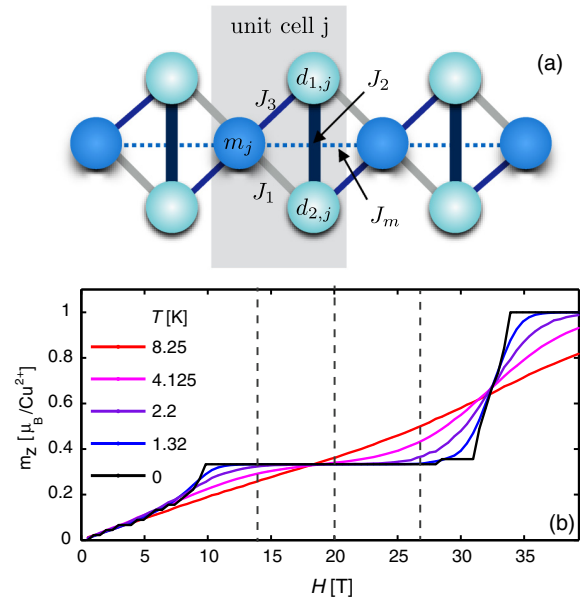


FIG. 11. (Color online) (a) Illustration of the generalized diamond chain model with the antiferromagnetic exchange couplings J_1, J_2, J_3 , and J_m . One unit cell of the system is highlighted by the gray area. (b) Dependence of the magnetization on an external magnetic field H , which we calculated by employing DMRG and SYMETTS at zero and finite temperature, respectively. In all calculations, we keep every singular value larger than the truncation threshold $s^{\text{tol}} = 10^{-5}$ and use a sample size of $M = 1000$. For a system of $N = 90$ spins in total, the emergence of the $\frac{1}{3}$ plateau can be observed for fields in the range of $H_{l,c} \leq H \leq H_{u,c}$. At finite temperatures, the plateau is washed out and the magnetization curve becomes a linear function of H . The vertical dashed lines indicate the parameter choices for our dynamical SYMETTS calculations in Sec. V B.

in Fig. 11(a). One third of the Cu spins (dark blue balls) forms weakly coupled monomers (dashed horizontal lines), whereas the other two thirds (light blue balls) form strongly coupled dimer singlets (heavy vertical lines). The dominant energy scale is determined by the dimer-dimer coupling J_2 . In addition, there are nearest- and third-nearest-neighbor dimer-monomer exchange J_1 and J_3 as well as the monomer-monomer coupling J_m . More precisely, the full Hamiltonian of the generalized diamond chain is defined as

$$\begin{aligned} \hat{H}_0 = & \sum_{j=1}^{N/3} [J_1 \hat{S}_{m,j} \cdot (\hat{S}_{d1,j+1} + \hat{S}_{d2,j}) + J_2 \hat{S}_{d1,j} \cdot \hat{S}_{d2,j} \\ & + J_3 \hat{S}_{m,j} \cdot (\hat{S}_{d1,j} + \hat{S}_{d2,j+1}) + J_m \hat{S}_{m,j} \cdot \hat{S}_{m,j+1}] \\ & - g\mu_B H \sum_{j=1}^{N/3} [\hat{S}_{d1,j}^z + \hat{S}_{d2,j}^z + \hat{S}_{m,j}^z], \end{aligned} \quad (17)$$

with external magnetic field H , Bohr magneton μ_B , and gyromagnetic ratio $g = 2.06$ [56]. N labels the total number of Cu spins in the system, the number of unit cells is therefore given by $N/3$. Note that this model features a $U(1)_{\text{spin}}$ symmetry for finite values of H , which we exploit in our SYMETTS calculations. The value of the couplings has been determined by DFT calculations and small refinements using

experimental data, leading to

$$\begin{aligned} J_1 &= 15.51 \text{ K}, & J_2 &= 33 \text{ K}, \\ J_3 &= 6.93 \text{ K}, & J_m &= 4.62 \text{ K}. \end{aligned} \quad (18)$$

Based on this system, the authors of Ref. [39] managed to derive a full microscopic picture for azurite, that is able to explain a wide number of experimental results. Additional support for the validity of this model is given by Ref. [40], which explores further aspects such as magnetocaloric properties and excitation spectrum. Although Refs. [39,40] also present some selected results for the dynamic spin structure factor using dynamical DMRG (DDMRG), their resolution in the energy ω and the momentum transfer k is limited, since DDMRG is numerically expensive and requires separate calculations for each ω . Moreover, their results are restricted to zero temperature.

We will now illustrate the power of SYMETTS by calculating the excitation spectra in the plateau phase and analyze the influence of magnetic field and temperature on the excitation branches.

A. Magnetization plateau

The most striking feature of azurite is the plateau at $\frac{1}{3}$ in the magnetization curve as a function of a magnetic field applied along the b axis of the crystal lattice [42]. This property can be nicely captured by the generalized diamond chain model, as already demonstrated in Ref. [39] by employing a direct comparison of the magnetization obtained from ground-state DMRG calculations with experimental data. Performing DMRG on an open chain with $N = 90$ spins, we obtain the magnetization plateau at $T = 0$ shown in Fig. 11(b) (black line). For better comparison, we use experimental units in the rest of this section. We find that the plateau phase is bounded by a lower and upper critical field $H_{l,c} \approx 9.8$ T and $H_{u,c} \approx 31.0$ T. Note that the small intermediate steps for $H < H_{l,c}$ and $H = 28.5$ T are artifacts caused by finite-size effects of the chain.

The plateau can be explained by a very intuitive argument [39]. The dominant dimer-dimer exchange coupling J_2 forces the dimer spins into a singlet state, whereas the monomer spins are only weakly coupled by J_m . Therefore, the monomer spins polarize first for a finite magnetic field, whereas the dimers remain in the singlet state for a considerable interval of H . Only at large fields $H > H_{u,c}$, the dimers are arranged in a polarized state. Thus, only $\frac{1}{3}$ of the total spins is aligned in direction of the field at intermediate fields strengths $H_{l,c} \leq H \leq H_{u,c}$, leading to the emergence of the $\frac{1}{3}$ magnetization plateau.

Introducing thermal fluctuations by employing SYMETTS, we observe that the plateau is gradually washed out with increasing temperature. At high temperatures, the quantum mechanical properties of the system are almost erased and the magnetization curve becomes a linear function of the magnetic field. We note that in the plateau phase, the effect of temperature on the magnetization depends strongly on the specific field strength. For values of H significantly smaller than 20 T the magnetization strongly decreases with increasing temperatures. In this case, we expect the change in magnetization to be predominantly caused by the monomers, which have to vacate their fully polarized state. On the other

hand, the monomers cannot contribute to the thermal increase of the total magnetization for $H > 20$ T as they are already fully polarized on the plateau. Here, the thermal fluctuations should predominantly excite the dimers by breaking up their singlet structure. We expect this to be reflected in the excitation spectra on the plateau. We study these next by means of the transverse dynamic spin structure factor, for the three values $H = 14, 20, 27$ T indicated by the vertical dashed lines in Fig. 11(b).

B. Transverse dynamic spin structure factor

We employ U(1) SYMETTS to compute the transverse dynamic spin structure factor of the generalized diamond chain model, which can directly be measured by neutron scattering experiments. Following Ref. [40], the dynamic spin structure factor is defined as

$$S^{xx}(\mathbf{k}, \omega) = \frac{1}{N} \sum_{m,n} e^{ik(\mathbf{R}_i - \mathbf{R}_j)} \left[\int dt e^{i\omega t} \langle \hat{S}_i^x(t) \hat{S}_j^x \rangle \right]. \quad (19)$$

Note that it is important to use the precise positions \mathbf{R}_i of the Cu spins in azurite [57] and the experimentally chosen momentum direction in order to make the data comparable to the experiment in Ref. [4].

We perform all calculations for an open chain of $N = 90$ spins, which allows an accurate resolution of the momentum transfer k along the chain direction. For each k , we average over a SYMETTS sample of 300 states exploiting the U(1)_{spin} symmetry of the model. In comparison to nonsymmetric METTS, U(1) SYMETTS yields a reduction of CPU time by a factor between 4 and 10 for the parameters considered here (see Appendix B for a more detailed assessment). Using a second-order Trotter decomposition, we set the time step $\tau_\beta = \tau_{\text{dyn}} = 0.05J_2^{-1}$ and truncation error $s_\beta^{\text{tol}} = 10^{-5}$, $s_{\text{dyn}}^{\text{tol}} = 5 \times 10^{-4}$ in the imaginary- and real-time evolutions, respectively. We stop the real-time evolution at $t_{\text{max}} = 50J_2^{-1}$ and checked that calculations are not impaired by finite-size reflections on this time scale. This setup leads to a maximum bond dimension $D < 600$ at t_{max} for all the time-evolved SYMETTS considered. To minimize finite-time effects, we here use a Gaussian broadening to perform the Fourier transform, leading to a frequency resolution $W \approx 0.16$ meV. As an alternative route, we had also tested linear prediction, but found that for this model its results were very sensitive to changes of the regularization parameter and the statistical window on the given time scale. Therefore, while in principle after significant further fine tuning, linear prediction may allow a systematic extrapolation to longer time scales to enhance spectral resolution, we did not further pursue this route.

Our results are displayed in Fig. 12. Each column indicates a different magnetic field strength $H = 14, 20, 27$ T and each row corresponds to a different temperature $T = 0, 4, 125, 8.25$ K.

Let us first note that Fig. 12(a) at zero temperature and $H = 14$ T nicely reproduces all features of the DDMRG data used in Ref. [39] for a direct comparison with the experiment in Ref. [4]. We observe a gapped system with a low-energy band dispersing along k , corresponding to the monomer excitations, and a dimer branch at higher energies, whose dispersion is weakened by the competition of J_1 and J_2 [39]. The

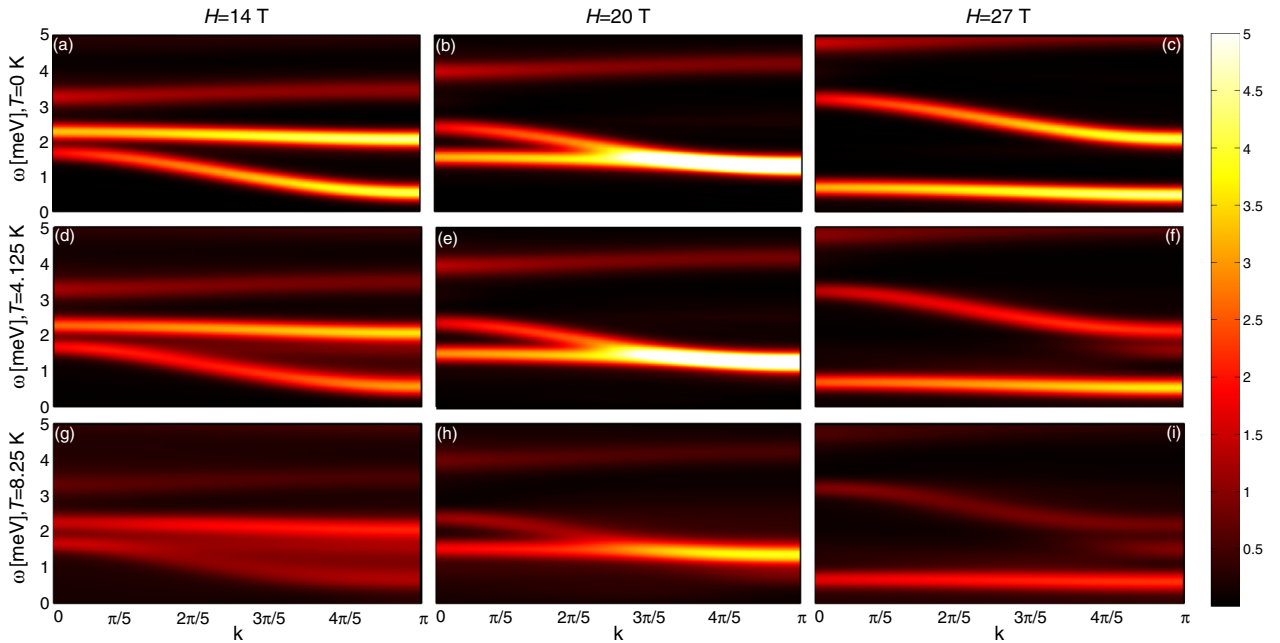


FIG. 12. (Color online) Transverse dynamic spin structure factor $S^{xx}(k, \omega)$ of a generalized diamond chain model for azurite. The intensity is displayed in arbitrary units. Each column indicates a different magnetic field strength, $H = 14, 20, 27$ T, corresponding to distinct points in the $\frac{1}{3}$ plateau phase. The ground state spectra are displayed in panels (a)–(c) in the first row, whereas the panels (d)–(i) show finite-temperature results obtained using tDMRG in combination with U(1) SYMETTS (for details see text).

spectral weight in both branches is mainly distributed around $k = \pi$. Moreover, we find an additional excitation branch at $\omega > 3$ meV with only small spectral weight and almost no dispersion. In the experiment, this branch is shifted towards higher energies (by ~ 1 meV) [4].

Increasing the magnetic field has an effect on the position of both the monomer and dimer bands (but not on their dispersion), which can be understood easily in an intuitive picture. As discussed in Sec. V A, the monomers are fully polarized in the entire plateau phase. Hence, exciting a monomer spin becomes increasingly expensive for larger magnetic fields because a spin flip is penalized by the additional Zeeman energy. Comparing the position of the monomer branch in Figs. 12(a) and 12(c), the shift towards higher energies at $H = 27$ T is fully captured by the change in the Zeeman term $g\mu_B\Delta H \approx 1.6$ meV.

The magnetic field has the reversed effect on the dimer band, which is shifted to lower energies. Again, the effect can be understood using the same line of arguments. Exciting a dimer singlet results in the break off of the singlet structure, allowing the dimer spins to polarize in the direction of H . At larger field strength, each excited dimer spin is therefore rewarded by a factor of $(1/2)g\mu_B\Delta H$ from the Zeeman term. This fully accounts for the shift of the dimer branch to lower energies in Figs. 12(a) and 12(c). At $H = 20$ T, the system is approximately probed in the middle of the plateau phase (cf. Fig. 11). At this point, the band gap reaches a maximum $\Delta E \approx 1$ meV, as the monomer branch has already moved to rather high energies while the dimer band is about to cross it, as illustrated in Fig. 12(b).

Based on this discussion, we can confirm the very distinct effects of temperature on the different points at the $\frac{1}{3}$ plateau

and put the arguments given in Sec. V A on solid ground. For regions of the plateau where the magnetization decreases at finite temperature, the thermal fluctuations primarily excite the monomers as this is energetically favorable. On the other hand, the thermal increase of the magnetization for larger magnetic fields observed in Fig. 11(b) can be understood in terms of the lowering of the dimer excitation energy due to the additional rewards in Zeeman energy, which has the opposite effect on the monomer band.

Figures 12(d)–12(i) displays the evolution of the spin excitations at finite temperature. The thermal broadening effects are strongly visible at $H = 14$ and 27 T, where the low-energy bands are strongly smeared out even at intermediate temperatures. This is expected from the comparatively small band gap at $T = 0$ and Fig. 11(b), which shows strong effects of temperature on the magnetization in this regime. In contrast, thermal fluctuations have a much weaker effect at $H = 20$ T, where the band gap is maximal. Indeed, comparing Figs. 12(b) and 12(e), we see almost no difference in the distribution of the spectral weight. Only Fig. 12(h) shows some thermal broadening, yet no new features arise in the spectrum. Again, this is in good agreement with the robustness of the magnetization for finite temperature in the middle of the plateau, as illustrated in Fig. 12(b). These features become even more prominent when studying cross sections of Fig. 12, i.e., the spin excitations for a specific momentum value. These are displayed in Fig. 13 for $k \approx 4/5\pi$. Again, we observe that the large peaks indicating the monomer and dimer branches are already washed out at intermediate temperatures at the edges of the plateau phase [Figs. 13(a) and 13(c)]. In both cases, thermal fluctuations strongly redistribute spectral weight in-between the two excitation peaks. In contrast, the

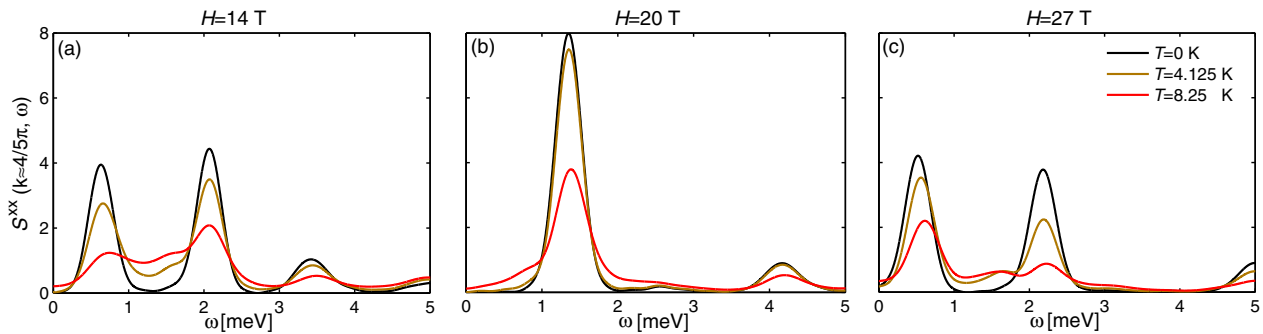


FIG. 13. (Color online) Transverse dynamic spin structure factor $S^{xx}(k, \omega)$ at $k \approx 4\pi/5$ of a generalized diamond chain model for azurite for three different field strengths in the plateau phase. At the edges of the plateau phase [(a) and (c)], the large peaks indicating the monomer and dimer branches are already washed out at intermediate temperatures. Thermal fluctuations redistribute spectral weight in-between the two excitation peaks in these cases. In the middle of the plateau phase (b) thermal broadening is almost not present at $T = 4.125$ K. Only at high temperatures is the height of the combined peak of monomer and dimer excitations significantly reduced.

height of the combined monomer and dimer excitation peaks in the middle of the plateau phase is significantly reduced only at high temperatures [Fig. 13(b)].

To conclude, our finite-temperature study of the spectra of the generalized diamond chain model for azurite fits in nicely with previous work [39,40] and provides new insight in the plateau phase. We observe a crossing of the monomer and dimer branches with increasing magnetic field, which can very intuitively explain the effects of finite temperature on the plateau phase. Testing these features in neutron scattering experiments would provide additional information on the validity of the microscopic model for azurite. Such a study would be particularly enlightening in the context of the results provided by Ref. [5], which showed discrepancies of using an isotropic spin model to describe azurite in the regime of $H < H_{l,c}$, i.e., for fields below the plateau phase.

VI. CONCLUSION

In this work, we have introduced an intuitive and easily implemented extension of the minimally entangled typical thermal state approach of Ref. [30], which allowed us to generate a METTS sample of symmetry eigenstates. We explicitly showed how to construct such a SYMETTS ensemble exploiting both the Abelian $U(1)_{\text{spin}}$ and non-Abelian $SU(2)_{\text{spin}}$ symmetry of spin- $\frac{1}{2}$ Heisenberg chains, without introducing strong autocorrelation effects in-between the ensemble states.

Whereas SYMETTS does not improve the numerical efficiency when calculating static observables as compared to METTS, the benefits of using symmetries come fully to the fore when calculating more complex dynamic quantities such as response functions. Here, most computational effort has to be put into the real-time evolution of each state in the sample and the gains of explicitly exploiting symmetries in the MPS simulations is enormous. We checked the validity of our approach for the dynamic spin structure factors of the XX and XXX Heisenberg chains and found that SYMETTS in principle is able to reach longer time scales than purification at low temperatures.

Moreover, we applied SYMETTS to study the finite-temperature excitation spectra of a generalized diamond chain model for the natural mineral azurite $\text{Cu}_3(\text{CO}_3)_2(\text{OH})_2$.

Focusing on the plateau phase of the system, we found very distinct effects of temperature on the different points at the $\frac{1}{3}$ plateau, which are caused by the Zeeman term shifting the dimer and monomer branches in opposite directions. Our results fit in nicely with previous work [39,40] and provide new insight in the plateau phase.

Interesting questions for future work involve the treatment of fermionic systems, where the symmetric ensemble states could be formulated in terms of a combination of $SU(2)_{\text{charge}}$ and $SU(2)_{\text{spin}}$ symmetries or their Abelian counterparts. For example, SYMETTS could be employed to study finite-temperature density profiles in interacting quantum-point contacts [58]. In this context, it would be particularly interesting to further explore the possibility of combining a real-time evolution to an MPO with local support in the Heisenberg picture, as briefly described at the end of Sec. IV B. In principle, this would simplify combining METTS with the concept of time translational invariance [27] to double the maximum reachable time scale and could be a generally more efficient approach for finite-temperature response functions at low temperatures.

Finally, we note as an outlook that the SYMETTS algorithm may also be entirely based within symmetry eigenstates, in that the nonsymmetric sampling as described in this paper is fully replaced by Metropolis sampling. Based on the weights $P_{\mathbf{q}}$ above, necessarily, this must also include a proposal distribution to switch to neighboring symmetry sectors. To minimize rejection probability, this random walk towards neighboring symmetry sectors can be chosen temperature dependent. By definition, the Metropolis sampling also guarantees detailed balance. And, by rejecting certain higher-energy states, this may lead to reduced spread and hence enhanced convergence of computed observables. In this formulation, SYMETTS would also provide benefits for the calculation of static properties and might allow the finite-temperature treatment of 2D clusters.

ACKNOWLEDGMENTS

We thank F. Schwarz and M. Stoudenmire for insightful discussions. This research was supported by the DFG through the Excellence Cluster ‘‘Nanosystems Initiative Munich’’,

SFB/TR 12, SFB 631 and WE4819/1-1, WE4819/2-1 (A.W.). B.B. also acknowledges financial support from the BaCaTeC Grant No. 15 [2014-2].

APPENDIX A: CHEBYSHEV EXPANSION AND METTS

Chebyshev expansion techniques have been successfully established as an alternative approach for the computation of spectral functions in the context of kernel polynomial methods [59]. More recently, Ref. [29] introduced the Chebyshev expansion in the MPS formalism (CheMPS) to determine spectral properties at zero temperature. Based on this work, CheMPS has been applied to determine signatures of the Majorana fermion in the interacting Kitaev model [60], in the context of the interacting resonating level model [61], and as impurity solver for single- and two-band DMFT calculations in combination with linear prediction [62,63]. In addition, CheMPS has been expanded towards finite-temperature calculations using a Liouvillian in a matrix-product purification framework [28].

The question as to whether CheMPS is the most efficient method for computing spectral functions using MPS methods cannot be generally considered settled, as there is no one-to-one correspondence of CheMPS in its most efficient setup to real-time evolution. Nevertheless, the claim of Ref. [29] that CheMPS is significantly less expensive than tDMRG to obtain the same spectral information can no longer be supported [64]. We have not conducted a systematic comparison of both approaches, but in our experience CheMPS and tDMRG require similar computational effort when aiming for the same spectral resolution and employing an equal truncation criterion at zero temperature. CheMPS, though, offers a significant advantage over tDMRG as it allows better control over the broadening procedure of the spectral data [29,61].

In this context, it is worthwhile to explore the compatibility of SYMETTS and CheMPS. To this end, we start with the Fourier transform of the response function in Eq. (13):

$$\mathcal{A}_\beta^{\hat{B}\hat{C}}(\omega) = \int d\bar{\omega} \langle \delta(\bar{\omega} - \hat{H}) \hat{B} \delta(\omega + \bar{\omega} - \hat{H}) \hat{C} \rangle_\beta. \quad (\text{A1})$$

To compute the response function in this form, we follow Ref. [59] and expand both δ functions in terms of orthogonal Chebyshev polynomials of the first kind $T_m(\omega + \bar{\omega})$ and $T_n(\bar{\omega})$ before integrating over the frequency index $\bar{\omega}$ for every SYMETTS $|\phi_q\rangle$ in our sample. This “double” Chebyshev expansion involves Chebyshev moments of the type $\mu_{mn}^{\hat{B}\hat{C}} = \langle T_m(\hat{H}') \hat{B} T_n(\hat{H}') \hat{C} \rangle_\beta$, where \hat{H}' represents the Hamiltonian with a rescaled spectrum $\omega' \in [-1, 1]$ to ensure the convergence of the Chebyshev recursion. This is usually achieved by using a linear rescaling with the parameters a, b :

$$\hat{H}' = \frac{\hat{H} - b}{a}. \quad (\text{A2})$$

The moments μ_{mn} are determined by calculating a first set of Chebyshev vectors up to the desired expansion order N_{Che} via the recursion relation

$$\begin{aligned} |t_m\rangle &= 2\hat{H}'|t_{m-1}\rangle - |t_{m-2}\rangle, \\ |t_0\rangle &= |\phi_q\rangle, |t_1\rangle = \hat{H}'|t_0\rangle, \end{aligned} \quad (\text{A3})$$

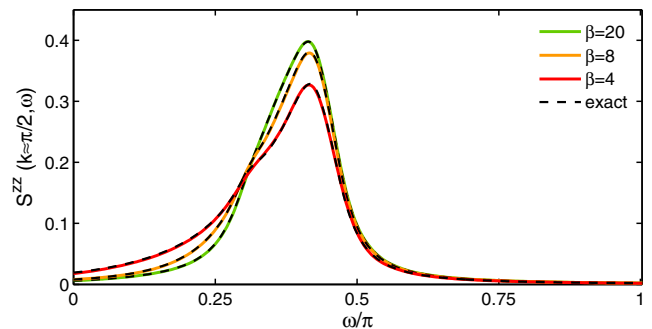


FIG. 14. (Color online) CheMETTS calculation for spin structure factor of the XX model with $N = 50$, $s_{\text{tol}}^{\text{dyn}} = 5 \times 10^{-4}$, $N_{\text{Che}} = 300$, $\eta = 0.1$, and $M = 300$. For all considered inverse temperatures, we find excellent agreement with the exact result. However, note that the required numerical resources clearly exceed those used in Fig. 8, where tDMRG was employed for a system with twice as many spins!

and keeping it in storage. Then, we iteratively obtain a second set of vectors $|\tilde{t}_n\rangle$ using a different starting vector $|\tilde{t}_0\rangle = \hat{C}|\phi_q\rangle$. For each $|\tilde{t}_n\rangle$, we compute the overlap $\mu_{mn} = \langle t_m | \hat{B} | \tilde{t}_n \rangle$ for $m = 0, 1, \dots, N_{\text{Che}} - 1$.

The sample average of the Chebyshev moments is then used to compute the finite-temperature response function in frequency space.

To this end, we work with a finite broadening η instead of the usual kernel approach for $\delta(\omega' + \bar{\omega}' - \hat{H}')$ to remove the artificial “Gibbs” oscillations caused by finite expansion order from the spectral data [61]. Note that the broadening has to be performed for the δ function containing the external frequency index only as $\bar{\omega}'$ is integrated out to obtain the final result. The finite-temperature response function in Eq. (A1) then takes the form

$$\begin{aligned} \mathcal{A}_\beta^{\hat{B}\hat{C}}(\omega) &= \frac{1}{a} \sum_{m,n=0}^{N_{\text{Che}}-1} \mu_{mn} (2 - \delta_{m0}) \\ &\times \int d\bar{\omega}' \frac{1}{\pi \sqrt{1 - \bar{\omega}'^2}} T_m(\bar{\omega}') \alpha_n(z), \end{aligned} \quad (\text{A4})$$

with $z = (\omega' + \bar{\omega}') + i\eta/a$ and α_n given by [61]

$$\alpha_n(z) = \frac{2/(1 + \delta_{n0})}{(z)^{n+1} (1 + \sqrt{z^2 - 1}/z^2)^n \sqrt{1 - 1/z^2}}. \quad (\text{A5})$$

In principle, this approach represents an alternative to the combination of tDMRG plus Fourier transform, which we have applied in the main part of this work. We illustrate this in Fig. 14, where we used U(1) SYMETTS and a double Chebyshev expansion to compute the dynamic spin structure factor of the XX model showing excellent agreement with exact calculations (dashed lines). However, the Chebyshev approach in the METTS formalism involves significantly higher computational costs than the real-time evolution since, in contrast to $T = 0$ CheMPS, (i) the full set of Chebyshev vectors $|t_m\rangle$ has to be stored throughout the entire calculation, and (ii) the number of moments increases from N_{Che} to N_{Che}^2 , also squaring the number of MPS overlaps to be calculated.

Therefore, we conclude that the combination of CheMPS and METTS is not a competitive alternative to real-time

evolution for calculating spectra at finite temperature since the advantage of the more controlled broadening procedure does not outweigh the drastically enhanced numerical costs involved in the double Chebyshev expansion.

APPENDIX B: NUMERICAL EFFICIENCY OF SYMETTS FOR AZURITE

Here, we assess the numerical performance of SYMETTS and the existing METTS approach on an explicit example. We focus on the average cumulative CPU time \bar{t}_{CPU} required to carry out the real-time evolution of one ensemble state up to $t \leq t_{\text{max}} = 50J_2^{-1}$ when determining the dynamic spin structure factor $S^{xx}(k, \omega)$ of azurite in Eq. (19). For simplicity, we choose the same model parameters as in Fig. 13(a), namely $N = 90$, $H = 14$ T, and $k = 4/5\pi$, and in Figs. 15(a) and 15(b) display the resulting average cumulative CPU times for the two temperatures $T = 4.125$ K and 8.25 K. Using the tDMRG setup described in Sec. VB, each calculation was performed on a single core Xeon E5-2670v2 (2.50 GHz) machine with 4GB memory.

The explicit implementation of the U(1) symmetry in the SYMETTS ensemble states clearly enhances the numerical efficiency, resulting in an average reduction of CPU time by a factor of 4 for $T = 4.125$ K in comparison to a nonsymmetric METTS sample [cf. Fig. 15(a)]. The efficiency gain increases to a factor of almost 10 for $T = 8.25$ K in Fig. 15(b) since states with a larger bond dimension profit even more from the exploitation of the spin symmetry. This is illustrated in Figs. 15(c) and 15(d), where we show the average computation time of a *single* time step τ as a function of the average maximum bond dimension \bar{D} . The additional imaginary-time evolution necessary for the generation of the SYMETTS requires on average only 25 and 12 s for $T = 4.125$ and 8.25 K, respectively. Thus, the overhead costs of the generating the SYMETTS sample are clearly negligible compared to the total computation time. In addition to benefits in terms of memory requirement, SYMETTS enables us to reduce the CPU time necessary to compute the dynamic spin structure factor for various

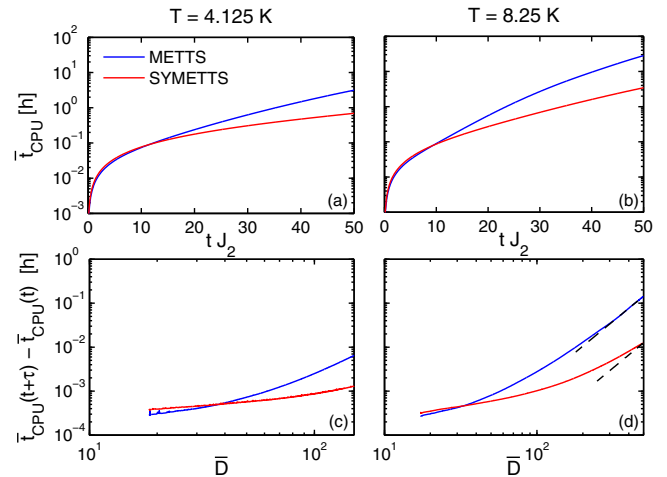


FIG. 15. (Color online) (a), (b) Display the numerical performance of SYMETTS and METTS in terms of the average cumulative CPU time \bar{t}_{CPU} as a function of tJ_2 , when carrying out the real-time evolution to determine the dynamic spin structure factor $S^{xx}(k, \omega)$ of azurite in Eq. (19) using the parameters $N = 90$, $H = 14$ T, and $k = 4/5\pi$. (c), (d) Show the average computation time of a *single* time step τ as a function of \bar{D} . We note that the ensemble states have a $\bar{D} \approx 20$ at both temperatures after the initial imaginary-time evolution. The dashed lines in Fig. 15(d) are guide to the eye illustrating the $\bar{t}_{\text{CPU}} \sim D^3$ scaling of the CPU time for larger bond dimensions. The employed tDMRG setup is described in Sec. VB.

momenta and magnetic fields presented in Fig. 12 from $O(10^6)$ to $O(10^5)$ hours. Consequently, when running 400 CPUs in parallel, SYMETTS generates these data in roughly one week, whereas the same calculation would require almost three months in the original METTS formulation. Note that the factor of 10 gained in numerical efficiency by implementing the U(1) spin symmetry in simple spin-chain models has also been reported in Refs. [37,50] in the context of iTEBD and tDMRG, respectively. Even larger benefits can be achieved when studying models with multiple Abelian or non-Abelian symmetries.

- [1] I. A. Zaliznyak, H. Woo, T. G. Perring, C. L. Broholm, C. D. Frost, and H. Takagi, *Phys. Rev. Lett.* **93**, 087202 (2004).
- [2] I. A. Zaliznyak and S.-H. Lee, *Modern Techniques for Characterizing Magnetic Materials* (Springer, Heidelberg, 2005).
- [3] B. Lake, D. A. Tennant, C. D. Frost, and S. E. Nagler, *Nat. Mater.* **4**, 329 (2005).
- [4] K. C. Rule, A. U. B. Wolter, S. Söllow, D. A. Tennant, A. Brühl, S. Köhler, B. Wolf, M. Lang, and J. Schreuer, *Phys. Rev. Lett.* **100**, 117202 (2008).
- [5] K. C. Rule, D. A. Tennant, J.-S. Caux, M. C. R. Gibson, M. T. F. Telling, S. Gerischer, S. Söllow, and M. Lang, *Phys. Rev. B* **84**, 184419 (2011).
- [6] S. A. Zvyagin, *Low Temp. Phys.* **38**, 819 (2012).
- [7] J. Villain, *Phys. B+C (Amsterdam)* **79**, 1 (1975).
- [8] S. E. Nagler, W. J. L. Buyers, R. L. Armstrong, and B. Briat, *Phys. Rev. B* **28**, 3873 (1983).
- [9] A. J. A. James, W. D. Goetze, and F. H. L. Essler, *Phys. Rev. B* **79**, 214408 (2009).
- [10] S. Sachdev, *Quantum Phase Transitions* (Cambridge University Press, Cambridge, UK, 2001).
- [11] S. R. White, *Phys. Rev. Lett.* **69**, 2863 (1992).
- [12] U. Schollwöck, *Ann. Phys. (NY)* **326**, 96 (2011).
- [13] M. Suzuki, S. Miyashita, and A. Kuroda, *Prog. Theor. Phys.* **58**, 1377 (1977).
- [14] J. E. Hirsch, R. L. Sugar, D. J. Scalapino, and R. Blankenbecler, *Phys. Rev. B* **26**, 5033 (1982).
- [15] A. W. Sandvik and J. Kurkijärvi, *Phys. Rev. B* **43**, 5950 (1991).
- [16] T. Nishino, *J. Phys. Soc. Jpn.* **64**, 3598 (1995).
- [17] R. J. Bursill, T. Xiang, and G. A. Gehring, *J. Phys.: Condens. Matter* **8**, L583 (1996).
- [18] N. Shibata, *J. Phys. Soc. Jpn.* **66**, 2221 (1997).
- [19] X. Wang and T. Xiang, *Phys. Rev. B* **56**, 5061 (1997).

- [20] F. Verstraete, J. J. Garcia-Ripoll, and J. I. Cirac, *Phys. Rev. Lett.* **93**, 207204 (2004).
- [21] S. R. White and A. E. Feiguin, *Phys. Rev. Lett.* **93**, 076401 (2004).
- [22] S. R. White and I. Affleck, *Phys. Rev. B* **77**, 134437 (2008).
- [23] T. Barthel, U. Schollwöck, and S. R. White, *Phys. Rev. B* **79**, 245101 (2009).
- [24] C. Karrasch, J. H. Bardarson, and J. E. Moore, *Phys. Rev. Lett.* **108**, 227206 (2012).
- [25] T. Barthel, U. Schollwöck, and S. Sachdev, [arXiv:1212.3570](https://arxiv.org/abs/1212.3570).
- [26] B. Lake, D. A. Tennant, J.-S. Caux, T. Barthel, U. Schollwöck, S. E. Nagler, and C. D. Frost, *Phys. Rev. Lett.* **111**, 137205 (2013).
- [27] T. Barthel, *New J. Phys.* **15**, 073010 (2013).
- [28] A. C. Tiegel, S. R. Manmana, T. Pruschke, and A. Honecker, *Phys. Rev. B* **90**, 060406 (2014).
- [29] A. Holzner, A. Weichselbaum, I. P. McCulloch, U. Schollwöck, and J. von Delft, *Phys. Rev. B* **83**, 195115 (2011).
- [30] S. R. White, *Phys. Rev. Lett.* **102**, 190601 (2009).
- [31] E. M. Stoudenmire and S. R. White, *New J. Phys.* **12**, 055026 (2010).
- [32] G. Alvarez, *Phys. Rev. B* **87**, 245130 (2013).
- [33] L. Bonnes, F. H. L. Essler, and A. M. Läuchli, *Phys. Rev. Lett.* **113**, 187203 (2014).
- [34] M. Binder and T. Barthel, [arXiv:1411.3033](https://arxiv.org/abs/1411.3033).
- [35] I. P. McCulloch and M. Gulacsi, *Europhys. Lett.* **57**, 852 (2002).
- [36] A. Weichselbaum, *Ann. Phys. (NY)* **327**, 2972 (2012).
- [37] S. Singh and G. Vidal, *Phys. Rev. B* **86**, 195114 (2012).
- [38] S. Singh and G. Vidal, *Phys. Rev. B* **88**, 115147 (2013).
- [39] H. Jeschke, I. Opahle, H. Kandpal, R. Valentí, H. Das, T. Saha-Dasgupta, O. Janson, H. Rosner, A. Brühl, B. Wolf, M. Lang, J. Richter, S. Hu, X. Wang, R. Peters, T. Pruschke, and A. Honecker, *Phys. Rev. Lett.* **106**, 217201 (2011).
- [40] A. Honecker, S. Hu, R. Peters, and J. Richter, *J. Phys.: Condens. Matter* **23**, 164211 (2011).
- [41] H. Kikuchi, Y. Fujii, M. Chiba, S. Mitsudo, and T. Idehara, *Phys. B: Condens. Matter* **329-333**, 967 (2003).
- [42] H. Kikuchi, Y. Fujii, M. Chiba, S. Mitsudo, T. Idehara, T. Tonegawa, K. Okamoto, T. Sakai, T. Kuwai, and H. Ohta, *Phys. Rev. Lett.* **94**, 227201 (2005).
- [43] B. Gu and G. Su, *Phys. Rev. Lett.* **97**, 089701 (2006).
- [44] B. Gu and G. Su, *Phys. Rev. B* **75**, 174437 (2007).
- [45] H.-J. Mikeska and C. Luckmann, *Phys. Rev. B* **77**, 054405 (2008).
- [46] J. Kang, C. Lee, R. K. Kremer, and M.-H. Whangbo, *J. Phys.: Condens. Matter* **21**, 392201 (2009).
- [47] N. Ananikian, H. Lazaryan, and M. Nalbandyan, *Eur. Phys. J. B* **85**, 223 (2012).
- [48] P. T. Cong, B. Wolf, R. S. Manna, U. Tutsch, M. de Souza, A. Brühl, and M. Lang, *Phys. Rev. B* **89**, 174427 (2014).
- [49] J. Richter, O. Krupnitska, T. Krokhumalskii, and O. Derzhko, *J. Magn. Magn. Mater.* **379**, 39 (2015).
- [50] D. M. Kennes and C. Karrasch, [arXiv:1404.3704](https://arxiv.org/abs/1404.3704).
- [51] J. Stolze, A. Nöppert, and G. Müller, *Phys. Rev. B* **52**, 4319 (1995).
- [52] O. Derzhko and T. Krokhumalskii, *Phys. Status Solidi B* **208**, 221 (1998).
- [53] C. Karrasch, J. H. Bardarson, and J. E. Moore, *New J. Phys.* **15**, 083031 (2013).
- [54] I. Pižorn, V. Eisler, S. Andergassen, and M. Troyer, *New J. Phys.* **16**, 073007 (2014).
- [55] H. Kikuchi, Y. Fujii, M. Chiba, S. Mitsudo, T. Idehara, T. Tonegawa, K. Okamoto, T. Sakai, T. Kuwai, and H. Ohta, *Phys. Rev. Lett.* **97**, 089702 (2006).
- [56] H. Ohta, S. Okubo, T. Kamikawa, T. Kunimoto, Y. Inagaki, H. Kikuchi, T. Saito, M. Azuma, and M. Takano, *J. Phys. Soc. Jpn.* **72**, 2464 (2003).
- [57] F. Zigan and H. D. Schuster, *Z. Kristallogr.* **135**, 416 (1972).
- [58] F. Bauer, J. Heyder, E. Schubert, D. Borowsky, D. Taubert, B. Bruognolo, D. Schuh, W. Wegscheider, J. von Delft, and S. Ludwig, *Nature (London)* **501**, 73 (2013).
- [59] A. Weiße, G. Wellein, A. Alvermann, and H. Fehske, *Rev. Mod. Phys.* **78**, 275 (2006).
- [60] R. Thomale, S. Rachel, and P. Schmitteckert, *Phys. Rev. B* **88**, 161103 (2013).
- [61] A. Braun and P. Schmitteckert, *Phys. Rev. B* **90**, 165112 (2014).
- [62] M. Ganahl, P. Thunström, F. Verstraete, K. Held, and H. G. Evertz, *Phys. Rev. B* **90**, 045144 (2014).
- [63] F. A. Wolf, I. P. McCulloch, O. Parcollet, and U. Schollwöck, *Phys. Rev. B* **90**, 115124 (2014).
- [64] F. A. Wolf, J. A. Justiniano, I. P. McCulloch, and U. Schollwöck, *Phys. Rev. B* **91**, 115144 (2015).

4.3 Spin fluctuations in the 0.7-anomaly in quantum point contacts

Quantum point contacts (QPCs) represent one of the elementary building blocks of semiconductor nanostructures. Electronic transport in these narrow and short quasi one-dimensional constriction is subject to conductance quantization, a textbook example of a quantum transport effect, which relates to a step-wise increase of the linear conductance in units of the conductance quantum $G = 2e^2/h$. The regime of the first conductance step is subject to a set of anomalous transport effects going by name of the 0.7 anomaly. In a recent work [BHS⁺13] it has been argued that the 0.7 anomaly originates from an enhanced density of states at the top of the point-contact barrier. This so-called van Hove ridge strongly amplifies the effects of interactions. The following article [SBvD17] studies their impact on dynamical quantities of the QPC.

Most of the calculations have been carried out by a functional renormalization group (fRG) approach on the Keldysh contour that has been developed by the first author of the article, Dennis Schimmel. Since fRG is a perturbative method, we also perform DMRG and tDMRG calculations to verify the validity of the fRG results. In particular, we extract the local density with ground-state DMRG and the local density of states with tDMRG, finding excellent agreement with the fRG data. On a technical level, the treatment of the semi-infinite leads, as well as the strong inhomogeneity of the contact region pose a challenge to DMRG. Moreover, the application of linear prediction [WA08, BSW09] to the spectral data of this model leads to ambiguous results in cases where tDMRG cannot resolve all relevant energy scales.

P6 *Spin fluctuations in the 0.7-anomaly in quantum point contacts*

D. Schimmel, **B. Bruognolo**, and J. von Delft
to appear in Phys. Rev. Lett. (2017)

Spin fluctuations in the 0.7-anomaly in quantum point contacts

Dennis H. Schimmel,¹ Benedikt Bruognolo,^{1,2} and Jan von Delft¹

¹*Physics Department, Arnold Sommerfeld Center for Theoretical Physics, and Center for NanoScience, Ludwig-Maximilians-Universität, Theresienstraße 37, 80333 Munich, Germany*

²*Max-Planck-Institut für Quantenoptik, Hans-Kopfermann-Straße 1, 85748 Garching, Germany*

(Dated: March 9, 2017)

It has been argued that the 0.7 anomaly in quantum point contacts (QPCs) is due to an enhanced density of states at the top of the QPC-barrier (van Hove ridge), which strongly enhances the effects of interactions. Here, we analyze their effect on dynamical quantities. We find that they pin the van Hove ridge to the chemical potential when the QPC is subopen; cause a temperature dependence for the linear conductance that qualitatively agrees with experiment; strongly enhance the magnitude of the dynamical spin susceptibility; and significantly lengthen the QPC traversal time. We conclude that electrons traverse the QPC via a slowly fluctuating spin structure of finite spatial extent.

Quantum point contacts are narrow, one-dimensional (1D) constrictions usually patterned in a two-dimensional electron system (2DES) by applying voltages to local gates. As QPCs are the ultimate building blocks for controlling nanoscale electron transport, much effort has been devoted to understand their behavior at a fundamental level. Nevertheless, in spite of a quarter of a century of intensive research into the subject, some aspects of their behavior still remain puzzling.

When a QPC is opened up by sweeping the gate voltage, V_g , that controls its width, its linear conductance famously rises in integer steps of the conductance quantum, $G_Q = 2e^2/h$ [1, 2]. This conductance quantization is well understood [3] and constitutes one of the foundations of mesoscopic physics. However, during the first conductance step, where the dimensionless conductance $g = G/G_Q$ changes from 0 to 1 (“closed” to “open” QPC), an unexpected shoulder is generically observed near $g \simeq 0.7$. More generally, the conductance shows anomalous behavior as function of temperature (T), magnetic field (B) and source-drain voltage (V_{sd}) throughout the regime $0.5 \lesssim g \lesssim 0.9$, where the QPC is “subopen”. The source of this behavior, collectively known as the “0.7-anomaly”, has been controversially discussed [4–22] ever since it was first systematically described in 1996 [4]. Though no consensus has yet been reached regarding its detailed microscopic origin [10, 22], general agreement exists that it involves electron spin dynamics and geometrically-enhanced interaction effects.

In this paper we further explore the van Hove ridge scenario, proposed in [22]. It asserts that the 0.7 anomaly is a direct consequence of a “van Hove ridge”, i.e. a smeared van Hove peak in the energy-resolved local density of states (LDOS) $\mathcal{A}_i(\omega)$ at the bottom of the lowest 1D subband of the QPC. Its shape follows that of the QPC barrier [22, 23] and in the subopen regime, where the barrier top lies just below the chemical potential μ , it causes the LDOS at μ to be strongly enhanced. This reflects the fact that electrons slow down while crossing the QPC barrier (since the semiclassical velocity of an electron with energy ω at position i is inversely propor-

tional to the LDOS, $\mathcal{A}_i(\omega) \sim v^{-1}$). The slow electrons experience strongly enhanced mutual interactions, with striking consequences for various physical properties.

In this paper, we elucidate their effect on various *dynamical* quantities, which we extract from real-frequency correlation functions computed using the functional Renormalization Group (fRG) on the Keldysh contour [24–27]. We compute (i) the frequency dependence of the LDOS, finding that its maximum is pinned to μ in the subopen regime, indicative of a Coulomb-blockade type behaviour; (ii) the temperature dependence of the linear conductance, finding qualitative agreement with experiment; (iii) the dynamical spin susceptibility $\chi(\omega)$, from which we extract a characteristic time scale t_{spin} for spin fluctuations, and (iv) the time t_{trav} for a quasiparticle to traverse the QPC, which we extract from the single-particle scattering matrix $S(\omega)$. Intermediate interaction strengths suffice to obtain the characteristic 0.7 shoulder at finite temperatures. We find strong links between the ω -dependence of the spin susceptibility, the one-particle S-matrix, and the form of the LDOS. As long as the van Hove ridge is pinned to μ , interactions cause relevant degrees of freedom to slow down, inducing significant increases in both t_{trav} and t_{spin} . Moreover, these two times are comparable in magnitude, implying that a quasiparticle traversing the QPC encounters a quasi-static spin background. This provides a link to other proposed explanations of the 0.7 anomaly [4–18].

Model.—We model the QPC by a smooth potential barrier describing the effective 1D-potential along the transport direction. Information about the channel’s transverse structure is incorporated into space-dependent model parameters. After discretizing the longitudinal position coordinate as $x = ai$, with site index i and lattice spacing a , the model Hamiltonian has the form [22]

$$\mathcal{H} = - \sum_{\sigma,i} \tau_i \left(c_{i+1,\sigma}^\dagger c_{i,\sigma} + \text{h.c.} \right) + \sum_i U_i c_{i\uparrow}^\dagger c_{i\uparrow} c_{i\downarrow}^\dagger c_{i\downarrow}. \quad (1)$$

It describes an infinite tight-binding chain with nearest-neighbor hopping τ_i of quasiparticles with spin $\sigma = \uparrow, \downarrow$ and short-range interactions U_i . The hopping amplitude

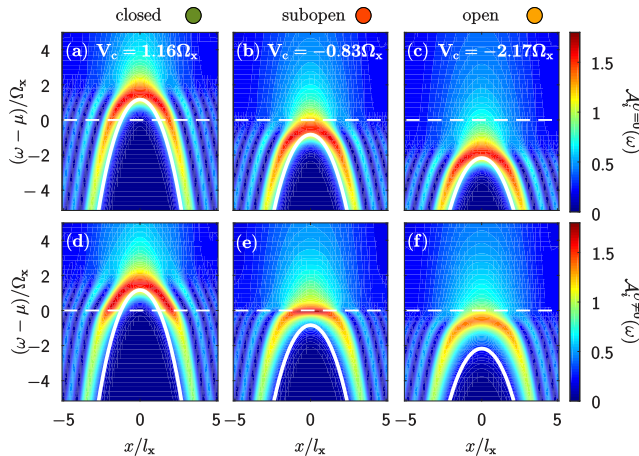


Figure 1. van Hove ridge in the LDOS $\mathcal{A}_i(\omega)$ (color scale) of a non-interacting (upper row) and interacting (lower row) QPC, plotted as function of energy $\omega - \mu$ and position $x = ai$. The thick solid white line depicts the effective bare potential barrier V_i , the thin dashed white line the chemical potential μ . From left to right: closed, subopen and open regimes. With interactions, the Hove ridge is shifted upward and flattened in the (sub-)open regime [compare (b) and (e), (c) and (f)].

τ_i varies smoothly with i , thus creating an effective potential barrier $V_i = -(\tau_i + \tau_{i+1}) + 2\tau$ measured w.r.t. the leads' band bottom -2τ . We choose $U_i \neq 0$ and $\tau_i \neq \tau$ only for $N = 2N' + 1$ sites, symmetric around $i = 0$, that define the extent of the QPC (central region). U_i is constant in the center of the QPC with $U_0 = U$ and drops smoothly to zero as i approaches the edges of the central region at sites $\pm N'$. We tune the hopping such that the effective barrier is symmetric and parabolic near the top, $V_i = \tilde{V}_c - i^2\Omega_x^2/(4\tau)$, where the barrier height \tilde{V}_c mimics the role of gate voltage from experiment, and the curvature Ω_x sets the characteristic length scale $l_x = a\sqrt{\tau/\Omega_x}$ of the QPC. We vary \tilde{V}_c such that the barrier crosses the chemical potential μ . The precise form of U_i and τ_i is given in [28]. The model is solved with the perturbatively-truncated Keldysh-fRG in equilibrium [28]. The plots shown are computed for $\tau = 1$, $U = 0.7\tau$, $\mu = -1.475\tau$, $V_c = \tilde{V}_c - \mu - 2\tau \in [-2.83, 1.83]\Omega_x$, and $\Omega_x \approx 0.03\tau$ [with $\hbar = 1$].

Local density of states.— It has been argued in Ref. [22] that the physics of the QPC is governed by the LDOS, $\mathcal{A}_i(\omega) = -\frac{1}{\pi}\text{Im}G_{ii}^R(\omega)$, where G_{ij}^R is the retarded single-particle Green's function between site i and j . Fig. 1(a-c) shows the bare LDOS $\mathcal{A}_i^{U=0}(\omega)$ of the QPC as a function of site i and frequency ω at three values of the barrier height V_c . The bare LDOS has a maximum just above the band bottom, visible as a red structure, that follows the shape of the effective potential (thick white line). This structure is the bare van Hove ridge discussed in [22], the apex of the which has a maximum value $\sim (\Omega_x\tau)^{-1/2}$, and occurs at an energy $\omega_{\max}(V_c)$ that lies slightly higher than the bare potential maximum V_0 , by an amount $\sim \Omega_x$.

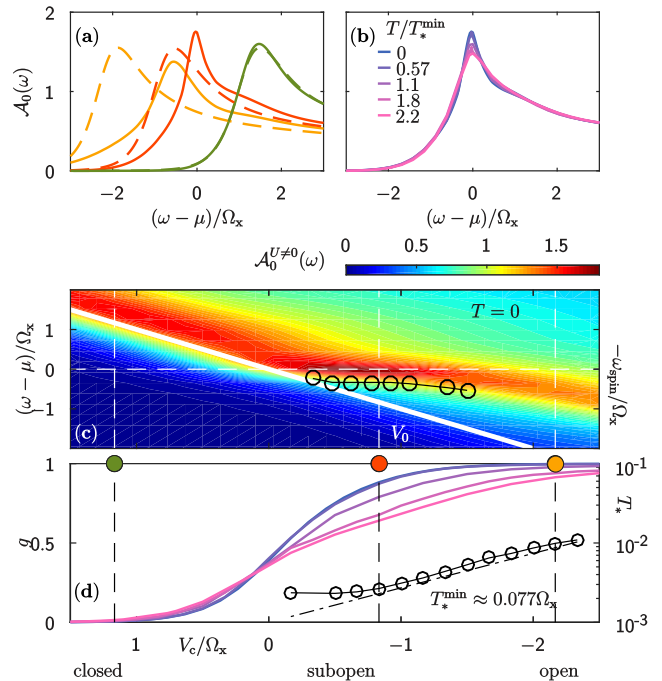


Figure 2. (a) The interacting LDOS (solid lines) and bare LDOS (dashed lines), plotted as function of energy ω for three values of V_c , indicated by dots of corresponding color in (c,d). In the subopen (red) and open (orange) regimes, interactions shift the van Hove peak to larger frequencies, as the barrier height is renormalized. Moreover, in the subopen regime, flattening of the van Hove ridge causes the peak to become sharper and higher. (b) $\mathcal{A}_0(\omega)$ in the subopen regime, for three different temperatures. At larger temperatures, the maximum is lower as weight is shifted into the flanks of the van Hove ridge and redistributed in the band. (c) $\mathcal{A}_0(\omega)$, the interacting LDOS (color scale) at the central site, as function of ω and V_c . The solid white line shows the bare barrier height, V_0 . In the subopen regime the energy of the van Hove ridge maximum, ω_{\max} , is pinned to the chemical potential. The black circles show the characteristic frequency ω_{spin} of the spin susceptibility χ . They clearly follow the LDOS maximum. (d) Conductance g (left axis) for different temperatures, and T_* (circles), as defined in Eq. (2), on a logarithmic scale (right axis). Temperature is measured in units of $T_*^{\min} = \min T_*(V_c)$. As guide to the eye: $0.001 \cdot \exp(-V_c/\Omega_x)$ (dashed-dotted line).

Upon adding interactions, we obtain Fig. 1(d-f), which shows two striking differences to the non-interacting case: In the (sub-)open regime the renormalized van Hove ridge is shifted upwards in energy (ω_{\max} is larger) and becomes flatter spatially. Both of these effects may *qualitatively* be understood by a mean field argument [29, 30]: The slope of the van Hove ridge may be interpreted as reflecting the shape of an effective, renormalized potential barrier, which is shifted upwards relative to the bare barrier by a Hartree-shift proportional to the local electron density. Away from the center, the density is higher, such that the shift is larger, causing the van Hove ridge to become flatter as function of x near its apex, while

becoming narrower and higher as function of ω . This is also seen clearly in Fig. 2(a), which shows the interacting (solid lines) and bare (dashed lines) LDOS $\mathcal{A}_0(\omega)$. The x -flattening and ω -sharpening is most striking in the subopen regime, where the van Hove ridge apex intersects the chemical potential [Fig. 1(e)], because there the interaction-induced effects are largest. We have checked our Keldysh-fRG results against DMRG computations of the system with somewhat different parameters [28], finding good qualitative agreement and, in particular, the same values for ω_{\max} .

The evolution of $\mathcal{A}_0(\omega)$ as V_c is varied is shown in Fig. 2(c). As V_c is lowered, the energy ω_{\max} of the Hove ridge maximum follows the bare barrier top (solid white line) as long as the QPC is closed, then remains *pinned* at the chemical potential throughout the subopen regime to form a plateau-like structure, and finally decreases again only deep in the open regime (compare Fig. 1(d) of [29]). We interpret this plateau-like structure as a precursor of Coulomb blockade behavior, since it arises from the interactions of electrons in a region of limited spatial extent.

Finite temperature.— This structure sheds new light on the temperature dependence of the linear conductance on temperature. When the temperature, T , is increased, the van Hove peak in the LDOS retains its overall shape and is broadened only slightly (for $T \lesssim \Omega_x/10$) [Fig. 2(b)]. At the same time, the first conductance step is flattened out in a characteristic, asymmetric fashion [Fig. 2(d)], in qualitative agreement with experiment (compare Fig. 2(f) of Ref. [22]). This can be understood as follows [22]: Increasing T increases the available phase space for inelastic scattering, thus enhancing interaction effects. Their strength is governed by the LDOS near the chemical potential, which is particularly large *throughout the subopen region*, due to the pinning of ω_{\max} to the chemical potential. Accordingly, interaction-induced backscattering is large in the whole subopen regime, leading to a strong suppression of the conductance [Fig. 2(d)] even into the open regime. At pinch-off, the conductance is slightly increased due to thermal activation.

To quantify the strength of the temperature dependence as function of V_c , we expand the conductance as

$$g(T, V_c) = g(0, V_c) - \frac{T^2}{T_*^2(V_c)} + \mathcal{O}(T^3), \quad (2)$$

as appropriate for a Fermi liquid [22]. The $T_*(V_c)$ values extracted from our finite- T data [see Fig. 2(d), circles] depend roughly exponentially on gate voltage $T_*(V_c) \sim \exp(-V_c/\Omega_x)$ [Fig. 2(d), dashed-dotted line], when the QPC is tuned from subopen to open, reflecting the V_c -dependence of the bare QPC transmission rate [22].

Spin susceptibility.— In the van Hove ridge scenario a key property of a subopen QPC is the presence of “slow spin fluctuations” [22], as advocated also in Ref. [31]. To explore this, we have computed the dynamical equilibrium spin susceptibility

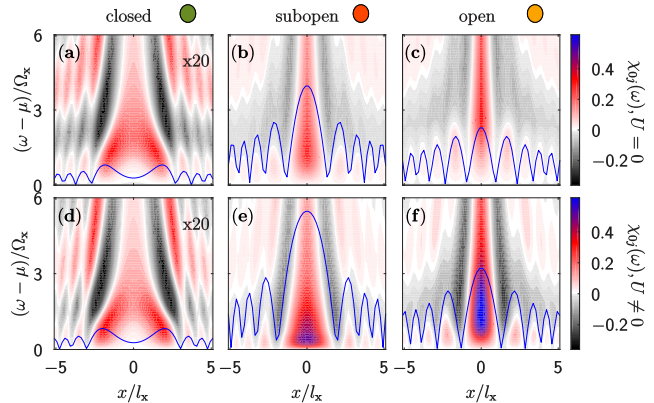


Figure 3. Non-interacting (a-c) and interacting (d-f) dynamical spin susceptibility [multiplied by a factor of 20 in order to be visible in (a) and (d)], for a closed, subopen and open QPC. The blue line shows $|\text{Im}(G_{0i}(\omega = \mu))|$ (a.u.).

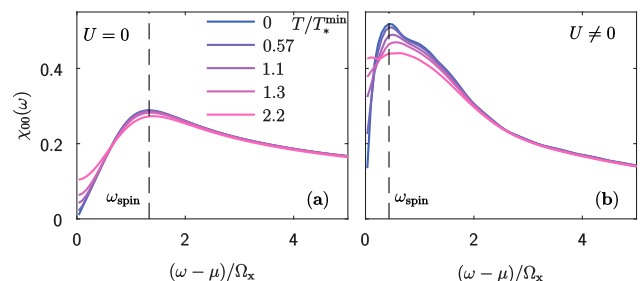


Figure 4. Non-interacting (a) and interacting (b) spin-spin correlations on the central site in the subopen regime at different temperatures, i.e. the blue lines are vertical cuts of Fig. 3(b), (e) through $x = 0$. The dashed black line is at $\omega = \omega_{\text{spin}}$. The shoulder in (b) is due to the LDOS-dependent enhancement of the spin susceptibility due to interactions.

rium spin susceptibility

$$\chi_{ij}(\omega) = \int dt \langle \mathcal{T} S_i^z(t) S_j^z(0) \rangle \exp(i\omega t), \quad (3)$$

where \mathcal{T} denotes time-ordering. In a Fermi liquid, the spin susceptibility is determined by the particle-hole bubble and thus governed by single-particle properties. However, due to the inhomogeneity of the QPC, both the frequency- and position-dependence of the spin susceptibility are non-trivial. For now, we focus on χ_{0j} , shown in Fig. 3, which has the following salient features:

(i) χ_{0j} oscillates with a spatially varying wavelength, which becomes shorter as the QPC is opened or the energy increased. For small frequencies ω the wavelength of these oscillations is determined by the “local Fermi wavelength” λ_F , which can be extracted from $|\text{Im} G_{0j}^R(\mu)|$ (blue line in Fig. 3). In the subopen regime, λ_F is large in the center, where the density is small, such that the sign of the spin susceptibility only changes far away from the center. Thus, an excited spin in the center leads to a rather large cloud (covering a region of $\sim 3l_x$) of co-oriented spins. Away from the QPC the oscillations in χ_{0j} simply follow the Friedel oscillations.

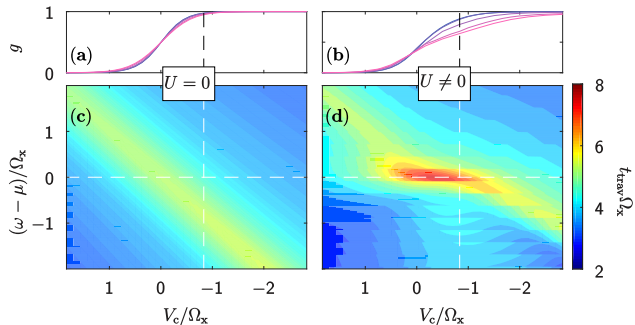


Figure 5. Comparison of non-interacting (a,c) and interacting (b,d) traversal time. (a,b): Conductance g as function of gate voltage V_c , to identify closed, subopen and open regimes. The color code is identical to Fig. 2; (c,d): Traversal time [Eq. (4)] as function of frequency ω and gate voltage V_c . While the traversal time of modes below the barrier is small, these modes have low transmission probability and are irrelevant when determining the timescale of transport.

(ii) On the central site, $\chi_{00}(\omega)$ shows a clear characteristic at a frequency $\omega_{\text{spin}}(V_c)$, whose dependence on V_c follows that of ω_{max} [$-\omega_{\text{spin}}$ is indicated by black circles in Fig. 2(c)]. In general, for small energies, ω_{spin} is set by the distance between the chemical potential and the nearest peak in the LDOS [28].

(iii) The spin susceptibility $\chi_{0i}(\omega)$ is amplified by interactions (Stoner physics) [compare Fig. 3(a-c) and Fig. 3(d-f); also Fig. 4(a) and (b)]. Interactions also amplify the temperature-induced reduction of the spin susceptibility at ω_{spin} [Fig. 4(a,b)]. This effect is of similar strength as the decrease of the LDOS at ω_{max} [Fig. 2(b)].

Traversal time.— The traversal time t_{trav} for a single incident quasiparticle with energy ω to traverse a scattering region can be obtained by a procedure due to Wigner [32], which relates it to the scattering-induced dispersion of the incident wave-packet: It is given by

$$t_{\text{trav}}(\omega) = t_0(\omega) + t_{\text{delay}}(\omega), \quad t_{\text{delay}}(\omega) = 2\partial_\omega \phi(\omega), \quad (4)$$

where $t_0(\omega)$ is the traversal time through the central region with the potential and interactions being turned off, t_{delay} and $\phi(\omega)$ are the delay time and the scattering phase shift due to the potential- and interaction-induced slow-down of the quasiparticles. In our setup $\phi(\omega)$ is the phase of the left-right-component of the zero-temperature single-particle S-matrix,

$$S_{l,r}(\omega) = -2\pi i \tau \rho(\omega) G_{-N',N'}^R(\omega), \quad (5)$$

where $\rho(\omega)$ is the lead density of states at the sites $\pm(N'+1)$ in the absence of the central region and τ is the hopping amplitude there. $|S_{l,r}(\omega)|^2$ yields the transmission probability. Figs. 5(a,b) show the traversal time. Though calculated from a non-local correlation function, its behaviour is strikingly similar to that of the LDOS at the central site, Fig. 2(c). This is consistent with the semiclassical interpretation $\mathcal{A} \sim v^{-1}$: Whenever the

LDOS is large, quasiparticles are slow and thus a large time is required to traverse the QPC.

Interestingly, we find that in the subopen regime the traversal time t_{trav} is of the same order as the characteristic time scale, $t_{\text{spin}} = \frac{2\pi}{\omega_{\text{spin}}}$, associated with spin fluctuations, namely $t_{\text{trav}} \lesssim 8/\Omega_x$ and $t_{\text{spin}} \lesssim 10/\Omega_x$. We note that with our parameters, $t_0 \approx 1.3/\Omega_x$, thus t_{trav} is dominated by the delay time. That t_{trav} and t_{spin} are comparable in magnitude is consistent with a Fermi-liquid description of the system (which underlies the fRG-method used here): The only stable degrees of freedom in a Fermi liquid are dressed electron- and hole-like quasiparticles, and spin fluctuations arise via electron-hole-like excitations. Near the QPC center ($x \lesssim l_x$) the lifetime of spin fluctuations is thus governed by the quasiparticle decay time. Heuristically, this roughly corresponds to t_{trav} , as the region where interaction effects are strongest extends over only few λ_F -oscillations. Though we find no static contributions to the dynamical spin susceptibility at zero magnetic field, the fact that $t_{\text{spin}} \simeq t_{\text{trav}}$, together with the extended spatial structure of the spin susceptibility in the subopen regime, suggests the heuristic view that a quasiparticle traversing the QPC encounters a quasi-static, spatially coherent spin environment.

Conclusions.—Our results allow us to establish contact with two other prominent scenarios that have been proposed to explain the 0.7 anomaly. (i) According to the “spin-polarization scenario”, interactions cause the spin degree of freedom in the QPC to spontaneously polarize, giving rise to a non-zero magnetization even at vanishing magnetic field, $B = 0$ [4–9, 14–18]. (ii) According to the “quasi-localized spin scenario” proposed by Meir and coworkers [13], a subopen QPC hosts a quasi-localized state involving a spin- $\frac{1}{2}$ magnetic moment, causing Kondo-like conductance anomalies [10–13]. At low energies, a quasi-localized spin would be screened, giving rise to Fermi-liquid behavior that includes slow spin fluctuations. These two scenarios thus seem to offer starkly contrasting views of the spin structure in a QPC: (i) spatially extended but static in time, vs. (ii) spatially localized but fluctuating in time. Our work suggests that a view that entails elements of both: the spin structure fluctuates in time, in accord with (ii), but *slowly* – which is compatible with (i) if one is willing to reinterpret “spontaneous polarization” as “slowly fluctuating polarization”. And the spin structure is spatially coherent, in accord with (i), over a region of *finite extent* – which is compatible with (ii) if one is willing to associate a nonzero spatial extent and a finite life-time with the quasi-localized state evoked there. We thus suggest that the controversy between the opposing views (i) and (ii) can be resolved by associating the quasi-localized state evoked in (ii) with the slow electrons of the van Hove ridge, and realizing that these constitute a quasi-static, spatially coherent spin environment, in the spirit of (i), for electrons traversing the QPC. Thus, though the var-

ious scenarios differ substantially in their details (and if one insists on comparing these the controversy will never be put to rest), they can be argued to have a common core: a *slowly fluctuating spin structure of finite spatial extent* in the center of the QPC. Moreover, our work, shows that this spin structure originates naturally from the same interplay of interactions and QPC barrier geometry, encoded in the van Hove ridge, that causes transport properties to be anomalous.

We thank F. Bauer, J. Heyder, Y. Meir and L. Weidinger for useful discussions. BB thanks S. R. White for discussions on the DMRG setup. The authors are supported by the DFG through the Excellence Cluster “Nanosystems Initiative Munich”, SFB/TR 12, SFB 631.

-
- [1] D. A. Wharam, T. J. Thornton, R. Newbury, M. Pepper, H. Ahmed, J. E. F. Frost, D. G. Hasko, D. C. Peacock, D. A. Ritchie, and G. A. C. Jones, *Journal of Physics C: Solid State Physics* **21**, L209 (1988).
- [2] B. J. van Wees, H. van Houten, C. W. J. Beenakker, J. G. Williamson, L. P. Kouwenhoven, D. van der Marel, and C. T. Foxon, *Phys. Rev. Lett.* **60**, 848 (1988).
- [3] M. Büttiker, *Phys. Rev. B* **41**, 7906 (1990).
- [4] K. J. Thomas, J. T. Nicholls, M. Y. Simmons, M. Pepper, D. R. Mace, and D. A. Ritchie, *Phys. Rev. Lett.* **77**, 135 (1996); K. J. Thomas, J. T. Nicholls, N. J. Appleyard, M. Y. Simmons, M. Pepper, D. R. Mace, W. R. Tribe, and D. A. Ritchie, *Phys. Rev. B* **58**, 4846 (1998).
- [5] D. J. Reilly, T. M. Buehler, J. L. O’Brien, A. R. Hamilton, A. S. Dzurak, R. G. Clark, B. E. Kane, L. N. Pfeiffer, and K. W. West, *Phys. Rev. Lett.* **89**, 246801 (2002).
- [6] D. J. Reilly, *Phys. Rev. B* **72**, 033309 (2005).
- [7] P. Jaksch, I. Yakimenko, and K.-F. Berggren, *Phys. Rev. B* **74**, 235320 (2006).
- [8] E. Koop, A. Lerescu, J. Liu, B. van Wees, D. Reuter, A. D. Wieck, and C. van der Wal, *J. Supercond. Nov. Magn.* **20**, 433 (2007).
- [9] L. W. Smith, A. R. Hamilton, K. J. Thomas, M. Pepper, I. Farrer, J. P. Griffiths, G. A. C. Jones, and D. A. Ritchie, *Phys. Rev. Lett.* **107**, 126801 (2011).
- [10] M. J. Iqbal, R. Levy, E. J. Koop, J. B. Dekker, J. P. de Jong, J. H. M. van der Velde, D. Reuter, A. D. Wieck, R. Aguado, Y. Meir, and C. H. van der Wal, *Nature* **501**, 79 (2013).
- [11] B. Brun, F. Martins, S. Faniel, B. Hackens, G. Bachelier, A. Cavanna, C. Ulysse, A. Ouerghi, U. Gennser, D. Mailly, S. Huant, V. Bayot, M. Sanquer, and H. Sellier, *Nature Comm.* **5**, 4290 (2014).
- [12] S. M. Cronenwett, H. J. Lynch, D. Goldhaber-Gordon, L. P. Kouwenhoven, C. M. Marcus, K. Hirose, N. S. Wingreen, and V. Umansky, *Phys. Rev. Lett.* **88**, 226805 (2002).
- [13] Y. Meir, K. Hirose, and N. S. Wingreen, *Phys. Rev. Lett.* **89**, 196802 (2002); K. Hirose, Y. Meir, and N. S. Wingreen, *Phys. Rev. Lett.* **90**, 026804 (2003); A. Golub, T. Aono, and Y. Meir, *Phys. Rev. Lett.* **97**, 186801 (2006); T. Rejec and Y. Meir, *Nature* **442**, 900 (2006).
- [14] T.-M. Chen, A. C. Graham, M. Pepper, I. Farrer, and D. A. Ritchie, *Applied Physics Letters* **93**, 032102 (2008).
- [15] T.-M. Chen, A. C. Graham, M. Pepper, I. Farrer, D. Anderson, G. A. C. Jones, and D. A. Ritchie, *Nano* **10**, 2330 (2010).
- [16] T.-M. Chen, M. Pepper, I. Farrer, G. A. C. Jones, and D. A. Ritchie, *Phys. Rev. Lett.* **109**, 177202 (2012).
- [17] R. M. Potok, J. A. Folk, C. M. Marcus, and V. Umansky, *Phys. Rev. Lett.* **89**, 266602 (2002).
- [18] C.-K. Wang and K.-F. Berggren, *Phys. Rev. B* **54**, R14257 (1996); *Phys. Rev. B* **57**, 4552 (1998).
- [19] A. P. Micolich, *Journal of Physics: Condensed Matter* **23**, 443201 (2011).
- [20] Y. Komijani, M. Csontos, I. Shorubalko, T. Ihn, K. Ensslin, Y. Meir, D. Reuter, and A. D. Wieck, *Eur. Phys. Lett.* **91**, 67010 (2010).
- [21] Y. Chung, S. Jo, D.-I. Chang, H.-J. Lee, M. Zaffalon, V. Umansky, and M. Heiblum, *Phys. Rev. B* **76**, 035316 (2007).
- [22] F. Bauer, J. Heyder, E. Schubert, D. Borowsky, D. Taubert, B. Bruognolo, D. Schuh, W. Wegscheider, J. von Delft, and S. Ludwig, *Nature* **501**, 73 (2013); J. Heyder, F. Bauer, D. Schimmel, and J. von Delft, to be published (2015).
- [23] F. Bauer, J. Heyder, and J. von Delft, *Phys. Rev. B* **89**, 045128 (2014); J. Heyder, F. Bauer, E. Schubert, D. Borowsky, D. Schuh, W. Wegscheider, J. von Delft, and S. Ludwig, *Phys. Rev. B* **92**, 195401 (2015), arXiv:1409.3415 [cond-mat.str-el].
- [24] S. G. Jakobs, M. Pletyukhov, and H. Schoeller, *Phys. Rev. B* **81**, 195109 (2010).
- [25] S. G. Jakobs, M. Pletyukhov, and H. Schoeller, *J. Phys. A: Math. and Theor.* **43**, 103001 (2010).
- [26] C. Karrasch, T. Enss, and V. Meden, *Phys. Rev. B* **73**, 235337 (2006).
- [27] W. Metzner, M. Salmhofer, C. Honerkamp, V. Meden, and K. Schönhammer, *Rev. Mod. Phys.* **84**, 299 (2012).
- [28] See Supplemental Material at [url] for the technical details used in our calculation, which includes Refs. [33–42].
- [29] S. Ihnatsenka and I. V. Zozoulenko, *Phys. Rev. B* **79**, 235313 (2009).
- [30] A. X. Sánchez and J.-P. Leburton, *Phys. Rev. B* **88**, 075305 (2013).
- [31] K. Aryanpour and J. E. Han, *Phys. Rev. Lett.* **102**, 056805 (2009).
- [32] E. P. Wigner, *Phys. Rev.* **98**, 145 (1955).
- [33] U. Schollwöck, *Rev. Mod. Phys.* **77**, 259 (2005).
- [34] S. R. White, *Phys. Rev. Lett.* **69**, 2863 (1992).
- [35] S. R. White, *Phys. Rev. B* **48**, 10345 (1993).
- [36] U. Schollwöck, *Ann. Phys.* **326**, 96 (2011).
- [37] M. Vekić and S. R. White, *Phys. Rev. B* **53**, 14552 (1996).
- [38] M. Vekić and S. R. White, *Phys. Rev. Lett.* **71**, 4283 (1993).
- [39] G. Vidal, *Phys. Rev. Lett.* **93**, 040502 (2004); A. J. Daley, C. Kollath, U. Schollwöck, and G. Vidal, *Journal of Statistical Mechanics: Theory and Experiment* **2004**, P04005 (2004); S. R. White and A. E. Feiguin, *Phys. Rev. Lett.* **93**, 076401 (2004).
- [40] S. R. White and I. Affleck, *Phys. Rev. B* **77**, 134437 (2008).
- [41] T. Barthel, U. Schollwöck, and S. R. White, *Phys. Rev. B* **79**, 245101 (2009).
- [42] A. Weichselbaum, *Ann. Phys.* **327**, 2972 (2012).

Supplementary material

This supplement consists of two parts. In the first, we give the technical details on the model, the fRG- flow equations and the numerics involved. We also argue that the characteristic frequency for spin fluctuations, ω_{spin} , is governed by the distance between the chemical potential and the effective lower band edge, $\omega_{\text{spin}} \simeq \mu - \omega_{\text{max}}$. In the second part, we report on DMRG calculations of the LDOS that we have performed to as an independent check of our fRG predictions. We find good qualitative agreement between both methods.

S-I. MODEL

We use a modified version of Model II of Ref. [22]: In the central region, described by $N = 2N' + 1$ sites, with $i = -N', \dots, N'$, the on-site potential is zero, and the hopping elements vary from site to site according to

$$\tau_j = \tau - \frac{1}{2}\tilde{V}_c \exp\left(-\frac{x_j^2}{1-x_j^2}\right); \quad x_j = \frac{2j+1}{N-1}, \quad (\text{S1})$$

where j runs from $-N'$ to $N'-1$. The on-site interaction in the central region is given by

$$U_i = U_0 \exp\left(-\frac{l_i^6}{1-l_i^2}\right); \quad l_i = \frac{i}{N'+\frac{1}{2}}, \quad (\text{S2})$$

The hopping and interaction Eqs. (S1),(S2) lead to a Hamiltonian

$$\begin{aligned} \mathcal{H} &= -\sum_{\sigma,i} \tau_i \left(c_{i+1,\sigma}^\dagger c_{i,\sigma} + \text{h.c.} \right) + \sum_i \left(U_i c_{i\uparrow}^\dagger c_{i\uparrow} c_{i\downarrow}^\dagger c_{i\downarrow} \right), \\ &=: \sum_{\sigma,i,j} \left(\tilde{H}_{ji}^\sigma c_{j,\sigma}^\dagger c_{i,\sigma} + \text{h.c.} \right) + \sum_i \left(U_i c_{i\uparrow}^\dagger c_{i\uparrow} c_{i\downarrow}^\dagger c_{i\downarrow} \right), \end{aligned} \quad (\text{S3})$$

where we use the tilde to indicate that the indices of the Hamiltonian matrix \tilde{H}^σ run over \mathbb{Z} . \tilde{H}_{ij}^σ is invariant under transposition and parity \mathcal{P} , which we implement as $\mathcal{P} : i \mapsto -i$. We will explicitly assume the presence of these symmetries in the following. Note that for our description of the central region, the effect of the tight-binding leads with hopping τ coupling to sites $-N'$ and N' is fully included in the self-energy contribution

$$\begin{aligned} \Sigma_{\text{lead}ij}^R(\omega) &= (\delta_{i,-N'}\delta_{j,-N'} + \delta_{i,N'}\delta_{j,N'}) \\ &\quad \times \begin{cases} \frac{\omega}{2} \left(1 - \sqrt{1 - \left(\frac{2\tau}{\omega}\right)^2} \right), & |\omega| > 2\tau \\ \frac{\omega}{2} - i\tau \sqrt{1 - \left(\frac{\omega}{2\tau}\right)^2}, & |\omega| < 2\tau, \end{cases} \end{aligned} \quad (\text{S4})$$

$$\Sigma_{\text{lead}ij}^K(\omega) = (1 - 2n_F(\omega))(\Sigma_{\text{lead}ij}^R - \Sigma_{\text{lead}ij}^A). \quad (\text{S5})$$

Here, the superscript $R(K,A)$ denotes the retarded (Keldysh, advanced) component of the self energy and n_F is the Fermi distribution function.

As stated in the main text, we use $U_0 = 0.7\tau$ and $\tilde{V}_c \in [0.44, 0.58]\tau$.

S-II. KELDYSH FRG

The model is solved by employing the functional renormalization group (fRG) [24–27] on the Keldysh-contour to obtain real-frequency information. The flow is truncated perturbatively, i.e. we set the three-particle vertex (and all higher vertices) to zero during the flow and approximate the two-particle vertex by the three usual channels (P , X , and D) [22, 24], assuming a local and static inter-channel mixing (coupled-ladder-approximation). The computation is then exact to second order in the interaction. It may be viewed as extension of the flow used in Ref. [25] to multiple sites (neglecting the $D^{\sigma\bar{\sigma}}$ -channel, which in our case is of order U_0^3) or an extension of the flow used in Ref. [22] to real frequencies. As flow parameter we use an artificial, on-site broadening of the spectrum (c.f. Eq. (S6), and Ref. [24]). This flow parameter respects fluctuation-dissipation theorems, so that in equilibrium it is unnecessary to compute the Keldysh components of the self energy (Σ^K) and the channels (b^P , b^X , b^D). The conventions on the Keldysh-contour used are those of Ref. [25], with the difference that after the Keldysh rotation we use the labels c(lassical) and q(uantum), instead of 2 and 1. In particular, this means that the Keldysh rotation used for the fermions is the same as the one usually used for bosons. We use $\sigma = \uparrow, \downarrow$ to denote spin, and $\bar{\sigma}$ to denote the spin opposite to σ . Letters from the middle of the roman alphabet (i, j) refer to spatial sites, while letters from the beginning of the Greek alphabet (α, β) refer to the Keldysh indices.

A. The Single-Scale Propagator

The flow parameter is determined by the bare retarded Green's function

$$\tilde{G}_{0,\Lambda,\sigma}^R(\omega) = \frac{1}{\omega \mathbb{1} - \tilde{H}^\sigma + i \left(\frac{1}{2}\Lambda\right) \mathbb{1}}, \quad (\text{S6})$$

where \tilde{H}^σ is the non-interacting Hamiltonian matrix extracted from Eq. (S3). Λ is the flow parameter, ranging from ∞ (start of flow) to 0 (end of flow). $\mathbb{1}$ is the unit matrix in the space of the sites, which we will omit from now on. Once the leads have been projected out, we drop the tilde on the restricted Hamiltonian matrix H^σ and the spatial indices then only run from $-N'$ to N' . We use the artificial on-site broadening for all sites (includ-

ing the leads) to avoid artifacts at the transition from the lead to the central region.

The retarded single-scale propagator \tilde{S}^R is

$$\tilde{S}^R(\omega) = \left(\tilde{G} \tilde{G}_0^{-1} \partial_\Lambda \tilde{G}_0 \tilde{G}_0^{-1} \tilde{G} \right)^R = -\frac{i}{2} \tilde{G}_\Lambda^R \cdot \tilde{G}_\Lambda^R, \quad (\text{S7})$$

where we omit the site and spin labels.

After the integration over the leads' degrees of freedom has been performed, the Green's function projected onto the central part acquires an additional self-energy term

$$G_0^{R(\sigma)}(\omega) = \frac{1}{\omega^{(\sigma)} - \mathcal{H}^{(\sigma)} - \Sigma_{\text{lead}}^{(\sigma)}(\omega, \Lambda) + i\Lambda/2}, \quad (\text{S8})$$

where $\omega^{(\sigma)} = \omega + \frac{\sigma}{2}B$ and

$$\Sigma_{\text{lead}ij}^{(\sigma)}(\omega, \Lambda) = \frac{1}{2} \left(\omega^{(\sigma)} + i\frac{\Lambda}{2} - i\sqrt{4\tau^2 - (\omega^{(\sigma)} + i\frac{\Lambda}{2})^2} \right) \times (\delta_{i,-N'}\delta_{j,-N'} + \delta_{i,N'}\delta_{j,N'}). \quad (\text{S9})$$

This self-energy is also reflected in the projected single-scale propagator, which now takes the form

$$\begin{aligned} S^R(\omega) &= (GG_0^{-1}\partial_\Lambda G_0 G_0^{-1}G)^R \\ &= G_\Lambda^R \cdot \left(-\frac{i}{2} + \partial_\Lambda \Sigma_{\text{lead}}(\omega, \Lambda) \right) \cdot G_\Lambda^R. \end{aligned} \quad (\text{S10})$$

For $\Lambda \rightarrow \infty$ the model is exactly solvable and the irreducible part of the full vertex is simply the bare vertex [25]. Since we only consider equilibrium situations in this paper and the flow parameter respects fluctuation-dissipation theorems, the Keldysh Green's function G^K [and single scale S^K] is determined simply via the fluctuation-dissipation theorem

$$G^K = (1 - 2n_F)(G^R - G^A), \quad S^K = (1 - 2n_F)(S^R - S^A). \quad (\text{S11})$$

B. The Vertex

The vertex is assumed to consist *only* of a two-particle contribution. This contribution is approximated by a structure compatible with a decomposition into three channels (with only static and local interchannel feedback). This approximation yields a consistent set of flow equations. We use the following parametrization:

We decompose the 2-particle vertex into three channels, according to

$$\gamma(\omega'_1, \omega'_2; \omega_1, \omega_2) \approx \bar{v} + \varphi^P(\omega_1 + \omega_2) + \varphi^X(\omega_2 - \omega'_1) + \varphi^D(\omega_2 - \omega'_2), \quad (\text{S12})$$

where we have suppressed all indices other than frequency, and primed quantities denote outgoing legs. \bar{v}

denotes the bare vertex. The Keldysh structure is arranged according to the convention

$$\gamma^{\alpha\beta|\gamma\delta} = \begin{pmatrix} (qq|qq) & (qq|cq) & (qq|qc) & (qq|cc) \\ (cq|qq) & (cq|cq) & (cq|qc) & (cq|cc) \\ (qc|qq) & (qc|cq) & (qc|qc) & (qc|cc) \\ (cc|qq) & (cc|cq) & (cc|qc) & (cc|cc) \end{pmatrix}. \quad (\text{S13})$$

The channels are labelled as (the Keldysh structure corresponds to Eqs. (A8,A11,A17) of Ref. [24], while the spatial structure is that of Eq. (S48) of Ref. [22])

$$(\varphi^P)_{(\sigma\bar{\sigma}|\sigma\bar{\sigma}), (ii|jj)}(\Pi) = \begin{pmatrix} 0 & a_{ji}^{P*} & a_{ji}^{P*} & 0 \\ a_{ij}^P & b_{ij}^P & b_{ij}^P & a_{ij}^P \\ a_{ij}^P & b_{ij}^P & b_{ij}^P & a_{ij}^P \\ 0 & a_{ji}^{P*} & a_{ji}^{P*} & 0 \end{pmatrix}^{(\sigma\bar{\sigma})} \quad (\Pi), \quad (\text{S14})$$

$$(\varphi^X)_{(\sigma\bar{\sigma}|\sigma\bar{\sigma}), (ji|ij)}(X) = \begin{pmatrix} 0 & a_{ji}^{X*} & a_{ij}^X & b_{ij}^{X*} \\ a_{ij}^X & b_{ij}^X & 0 & a_{ji}^{X*} \\ a_{ji}^{X*} & 0 & b_{ij}^X & a_{ij}^X \\ b_{ij}^X & a_{ij}^X & a_{ji}^{X*} & 0 \end{pmatrix}^{(\sigma\bar{\sigma})} \quad (X), \quad (\text{S15})$$

$$(\varphi^D)_{(\sigma\sigma|\sigma\sigma), (ij|ij)}(\Delta) = \begin{pmatrix} 0 & a_{ij}^D & a_{ji}^{D*} & b_{ij}^{D*} \\ a_{ij}^D & 0 & b_{ij}^D & a_{ji}^{D*} \\ a_{ji}^{D*} & b_{ij}^D & 0 & a_{ij}^D \\ b_{ij}^D & a_{ji}^{D*} & a_{ij}^D & 0 \end{pmatrix}^{(\sigma\sigma)} \quad (\Delta). \quad (\text{S16})$$

Each channel is labelled by only two spatial indices and one frequency. Conceptually, it can be thought of as the propagator of a Hubbard-Stratonovitch particle of the corresponding channel with retarded (a^P , a^D , and a^{X*}) and Keldysh (b^P , b^D , and b^X) components. From this point of view it is not surprising that in equilibrium the channels satisfy the fluctuation-dissipation theorems (c.f. Eqs. (A10,A13,A19) of Ref. [24]:

$$b_{(ij)}^{P(\sigma\bar{\sigma})}(\Pi) = 2i \coth \left[\beta \left(\frac{\Pi}{2} - \mu \right) \right] \text{Im} a_{(ij)}^{P(\sigma\bar{\sigma})}(\Pi) \quad (\text{S17a})$$

$$b_{(ij)}^{X(\sigma\bar{\sigma})}(X) = -2i \coth \left[\frac{\beta X}{2} \right] \text{Im} a_{(ij)}^{X(\sigma\bar{\sigma})}(X) \quad (\text{S17b})$$

$$b_{(ij)}^{D(\sigma\sigma)}(\Delta) = 2i \coth \left[\frac{\beta \Delta}{2} \right] \text{Im} a_{(ij)}^{D(\sigma\sigma)}(\Delta) \quad (\text{S17c})$$

C. The Flow Equations

When all vertices higher than the 2-particle vertex are set to zero, the resulting truncated flow equations are

(c.f. Eqs. (27,28) of Ref. [24])

$$\begin{aligned}
\frac{d}{d\Lambda} \Sigma_{1'1}^\Lambda &= - \sum_{2'2} \frac{i}{2\pi} \gamma_{1'2'12}^\Lambda S_{22'}^\Lambda \\
\frac{d}{d\Lambda} \gamma_{1'2'12}^\Lambda &= + \sum_{3'4'34} \frac{i}{2\pi} \gamma_{1'2'34}^\Lambda S_{33'}^\Lambda G_{44'}^\Lambda \gamma_{3'4'12}^\Lambda \\
&\quad + \sum_{3'4'34} \frac{i}{2\pi} \gamma_{1'4'32}^\Lambda [S_{33'}^\Lambda G_{44'}^\Lambda + S_{44'}^\Lambda G_{33'}^\Lambda] \gamma_{3'2'14}^\Lambda \\
&\quad - \sum_{3'4'34} \frac{i}{2\pi} \gamma_{1'3'14}^\Lambda [S_{33'}^\Lambda G_{44'}^\Lambda + S_{44'}^\Lambda G_{33'}^\Lambda] \gamma_{4'2'32}^\Lambda.
\end{aligned} \tag{S18}$$

Here, 1, 1' etc. are multi-indices encompassing spin, site and frequency. In the flow of the vertex, each summand corresponds to a single channel. The vertex of each summand will be approximated by the contribution of the corresponding channel for all frequencies and the feedback of the other channels at a specific frequency (2μ for the P-channel, 0 for the X- and D-channels). Inserting the channel decomposition with the above notations into the flow equations, the flow of the self-energy is given by [compare Eqs. (B3,B4) of Ref. [24]]:

$$\begin{aligned}
\partial_\Lambda \Sigma_{(kl)}^{q|c(\sigma)}(\omega) &= -\frac{i}{2\pi} \int d\omega' \left[S_{(lk)}^{c|c(\bar{\sigma})}(\omega') a_{(kl)}^{P(\sigma\bar{\sigma})}(\omega + \omega') + S_{(kl)}^{c|c(\bar{\sigma})}(\omega') a_{(lk)}^{X(\sigma\bar{\sigma})}(\omega' - \omega) - S_{(kl)}^{c|c(\sigma)}(\omega') a_{(kl)}^{D(\sigma\sigma)}(\omega - \omega') \right. \\
&\quad + S_{(lk)}^{q|c(\bar{\sigma})}(\omega') b_{(kl)}^{P(\sigma\bar{\sigma})}(\omega + \omega') + S_{(kl)}^{q|c(\bar{\sigma})}(\omega') b_{(lk)}^{X(\sigma\bar{\sigma})}(\omega' - \omega) - S_{(kl)}^{c|c(\sigma)}(\omega') b_{(lk)}^{D(\sigma\sigma)}(\omega - \omega') \\
&\quad \left. + S_{(lk)}^{c|c(\bar{\sigma})}(\omega') U_k / 2 \delta_{kl} + \sum_m S_{(mm)}^{c|c(\sigma)}(\omega') a_{(km)}^{D(\sigma\sigma)}(0) \delta_{kl} \right]
\end{aligned} \tag{S19}$$

and

$$\begin{aligned}
\partial_\Lambda \Sigma_{(kl)}^{q|q(\sigma)}(\omega) &= -\frac{i}{2\pi} \int d\omega' \left[S_{(lk)}^{c|q(\bar{\sigma})}(\omega') a_{(lk)}^{X(\sigma\bar{\sigma})}(\omega' - \omega) - S_{(kl)}^{c|q(\sigma)}(\omega') a_{(kl)}^{D(\sigma\sigma)}(\omega - \omega') + S_{(lk)}^{q|c(\bar{\sigma})}(\omega') a_{(kl)}^{P(\sigma\bar{\sigma})}(\omega + \omega') \right. \\
&\quad + S_{(lk)}^{c|q(\bar{\sigma})}(\omega') a_{(lk)}^{P^*(\sigma\bar{\sigma})}(\omega' + \omega) + S_{(kl)}^{q|c(\bar{\sigma})}(\omega') a_{(kl)}^{X^*(\sigma\bar{\sigma})}(\omega' - \omega) - S_{(kl)}^{q|c(\sigma)}(\omega') a_{(lk)}^{D^*(\sigma\sigma)}(\omega - \omega') \\
&\quad + S_{(lk)}^{c|c(\bar{\sigma})}(\omega') b_{(kl)}^{P(\sigma\bar{\sigma})}(\omega + \omega') + S_{(kl)}^{c|c(\bar{\sigma})}(\omega') b_{(lk)}^{X(\sigma\bar{\sigma})}(\omega' - \omega) - S_{(kl)}^{c|c(\sigma)}(\omega') b_{(kl)}^{D(\sigma\sigma)}(\omega - \omega') \\
&\quad \left. + \left(S_{(lk)}^{c|q(\bar{\sigma})}(\omega') + S_{(lk)}^{q|c(\bar{\sigma})}(\omega') \right) U_k / 2 \delta_{kl} \right].
\end{aligned} \tag{S20}$$

The flow of the vertex contains two bubbles

$$I_{ab|a'b'}^{pp}(\omega)_{(ij|kl)}^{(\sigma_1\sigma_2)} = \frac{i}{2\pi} \int d\omega' \left[G_{(ik)}^{a|a'(\sigma_1)}(\omega/2 + \omega') S_{(j|l)}^{b|b'(\sigma_2)}(\omega/2 - \omega') + S_{(ik)}^{a|a'(\sigma_1)}(\omega/2 + \omega') G_{(j|l)}^{b|b'(\sigma_2)}(\omega/2 - \omega') \right], \tag{S21}$$

$$I_{ab|a'b'}^{ph}(\omega)_{(ij|kl)}^{(\sigma_1\sigma_2)} = \frac{i}{2\pi} \int d\omega' \left[G_{(ik)}^{a|a'(\sigma_1)}(-\omega/2 + \omega') S_{(j|l)}^{b|b'(\sigma_2)}(\omega/2 + \omega') + S_{(ik)}^{a|a'(\sigma_1)}(-\omega/2 + \omega') G_{(j|l)}^{b|b'(\sigma_2)}(\omega/2 + \omega') \right], \tag{S22}$$

and is given by (compare Eqs. (C3,C6,C9) of Ref. [24])

$$\begin{aligned} \partial_\Lambda(\varphi^P)_{(\bar{\sigma}\bar{\sigma}|\sigma\bar{\sigma})(ij|jj)}^{qq|cq}(\Pi) &= \partial_\Lambda a^{P*}{}_{(ij)}^{(\bar{\sigma}\sigma)}(\Pi) \\ &= \sum_{km} \left(\frac{1}{2} U_k \delta_{ki} + a^{P*}(\Pi)_{(ki)}^{(\bar{\sigma}\sigma)} + \frac{1}{2} U^X{}_{(ki)}^{(\bar{\sigma}\sigma)} \right) \left(I_{cq|cc}^{pp}(\Pi)_{(kk|mm)}^{(\bar{\sigma}\bar{\sigma}|\sigma\bar{\sigma})} + I_{qc|cc}^{pp}(\Pi)_{(kk|mm)}^{(\bar{\sigma}\bar{\sigma}|\sigma\bar{\sigma})} \right) \left(\frac{1}{2} U_j \delta_{jm} + a^{P*}(\Pi)_{(jm)}^{(\bar{\sigma}\sigma)} + \frac{1}{2} U^X{}_{(jm)}^{(\bar{\sigma}\sigma)} \right) \end{aligned} \quad (\text{S23})$$

$$\begin{aligned} \partial_\Lambda(\varphi^X)_{(\bar{\sigma}\bar{\sigma}|\sigma\bar{\sigma})(ji|ij)}^{qq|cq}(X) &= \partial_\Lambda a^{X*}{}_{(ji)}^{(\bar{\sigma}\sigma)}(X) \\ &= \sum_{kl} \left(\frac{1}{2} U_j \delta_{jk} + \frac{1}{2} U^P{}_{(jk)}^{(\bar{\sigma}\sigma)} + a^{X*}{}_{(jk)}^{(\bar{\sigma}\sigma)}(X) \right) \left(I_{qc|cc}^{ph}(X)_{kl|lk}^{(\bar{\sigma}\bar{\sigma}|\sigma\bar{\sigma})} + I_{cc|cq}^{ph}(X)_{kl|lk}^{(\bar{\sigma}\bar{\sigma}|\sigma\bar{\sigma})} \right) \left(\frac{1}{2} U_i \delta_{il} + \frac{1}{2} U^P{}_{(li)}^{(\bar{\sigma}\sigma)} + a^{X*}{}_{(li)}^{(\bar{\sigma}\sigma)}(X) \right) \end{aligned} \quad (\text{S24})$$

$$\begin{aligned} \partial_\Lambda(\varphi^D)_{(\sigma\sigma)(ij|ij)}^{cq|qq}(\Delta) &= \partial_\Lambda a^D{}_{(ij)}^{(\sigma\sigma)}(\Delta) \\ &= - \sum_{kl} \left[\left(-\frac{1}{2} W^D{}_{(ik)}^{(\sigma\sigma)} + a^D{}_{(ik)}^{(\sigma\sigma)}(\Delta) \right) \left(I_{qc|cc}^{ph}(\Delta)_{(lk|kl)}^{(\sigma\sigma|\sigma\sigma)} + I_{cc|cq}^{ph}(\Delta)_{(lk|kl)}^{(\sigma\sigma|\sigma\sigma)} \right) \left(-\frac{1}{2} W^D{}_{(lj)}^{(\sigma\sigma)} + a^D{}_{(lj)}^{(\sigma\sigma)}(\Delta) \right) \right. \\ &\quad \left. + \left(\frac{1}{2} U_i + \frac{1}{2} U^P{}_{(ik)}^{(\bar{\sigma}\bar{\sigma})} + \frac{1}{2} U^X{}_{(ik)}^{(\bar{\sigma}\bar{\sigma})} \right) \delta_{ik} \left(I_{qc|cc}^{ph}(\Delta)_{(lk|kl)}^{(\bar{\sigma}\bar{\sigma}|\bar{\sigma}\bar{\sigma})} + I_{cc|cq}^{ph}(\Delta)_{(lk|kl)}^{(\bar{\sigma}\bar{\sigma}|\bar{\sigma}\bar{\sigma})} \right) \delta_{jl} \left(\frac{1}{2} U_j + \frac{1}{2} U^P{}_{(jl)}^{(\bar{\sigma}\sigma)} + \frac{1}{2} U^X{}_{(jl)}^{(\bar{\sigma}\sigma)} \right) \right] \end{aligned} \quad (\text{S25})$$

$$\begin{aligned} \partial_\Lambda(\varphi^P)_{(\bar{\sigma}\bar{\sigma})(ii|jj)}^{cq|cq}(\Pi) &= \partial_\Lambda b^P{}_{(ij)}^{(\sigma\bar{\sigma})}(\Pi) \\ &= \sum_{km} \left[\left(\frac{1}{2} U_i \delta_{ik} + a^P(\Pi)_{(ik)}^{(\sigma\bar{\sigma})} + \frac{1}{2} U^X{}_{(ik)}^{(\sigma\bar{\sigma})} \right) \left(I_{cc|cc}^{pp}(\Pi)_{(kk|mm)}^{(\sigma\bar{\sigma}|\sigma\bar{\sigma})} + I_{qq|cc}^{pp}(\Pi)_{(kk|mm)}^{(\sigma\bar{\sigma}|\sigma\bar{\sigma})} + I_{cc|qq}^{pp}(\Pi)_{(kk|mm)}^{(\sigma\bar{\sigma}|\sigma\bar{\sigma})} \right) \right. \\ &\quad \times \left(\frac{1}{2} U_j \delta_{jm} + a^{P*}(\Pi)_{(jm)}^{(\sigma\bar{\sigma})} + \frac{1}{2} U^X{}_{(jm)}^{(\sigma\bar{\sigma})} \right) \\ &\quad + b^P(\Pi)_{(ik)}^{(\sigma\bar{\sigma})} \left(I_{qc|cc}^{pp}(\Pi)_{(kk|mm)}^{(\sigma\bar{\sigma}|\sigma\bar{\sigma})} + I_{cc|qc}^{pp}(\Pi)_{(kk|mm)}^{(\sigma\bar{\sigma}|\sigma\bar{\sigma})} \right) \left(\frac{1}{2} U_j \delta_{jm} + a^{P*}(\Pi)_{(jm)}^{(\sigma\bar{\sigma})} + \frac{1}{2} U^X{}_{(jm)}^{(\sigma\bar{\sigma})} \right) \\ &\quad \left. + \left(\frac{1}{2} U_i \delta_{ik} + a^P(\Pi)_{(ik)}^{(\sigma\bar{\sigma})} + \frac{1}{2} U^X{}_{(ik)}^{(\sigma\bar{\sigma})} \right) \left(I_{cc|qc}^{pp}(\Pi)_{(kk|mm)}^{(\sigma\bar{\sigma}|\sigma\bar{\sigma})} + I_{cc|qc}^{pp}(\Pi)_{(kk|mm)}^{(\sigma\bar{\sigma}|\sigma\bar{\sigma})} \right) b^P(\Pi)_{(mj)}^{(\sigma\bar{\sigma})} \right] \end{aligned} \quad (\text{S26})$$

$$\begin{aligned} \partial_\Lambda(\varphi^X)_{ji|ij}^{qq|cc}(X) &= \partial_\Lambda b^X{}_{(ij)}^{(\sigma\bar{\sigma})}(X) \\ &= \sum_{kl} \left[\left(\frac{1}{2} U_k \delta_{kj} + \frac{1}{2} U^P{}_{(kj)}^{(\sigma\bar{\sigma})} + a^X(X)_{(kj)}^{(\sigma\bar{\sigma})} \right) \left(I_{cc|cc}^{ph}(X)_{kl|lk}^{(\sigma\bar{\sigma}|\sigma\bar{\sigma})} + I_{qc|cq}^{ph}(X)_{kl|lk}^{(\sigma\bar{\sigma}|\sigma\bar{\sigma})} + I_{cq|qc}^{ph}(X)_{kl|lk}^{(\sigma\bar{\sigma}|\sigma\bar{\sigma})} \right) \right. \\ &\quad \times \left(\frac{1}{2} U_l \delta_{il} + \frac{1}{2} U^P{}_{(il)}^{(\sigma\bar{\sigma})} + a^{X*}{}_{(li)}^{(\sigma\bar{\sigma})}(X) \right) \\ &\quad + b^X(X)_{(kj)}^{(\sigma\bar{\sigma})} \left(I_{qc|cc}^{ph}(X)_{kl|lk}^{(\sigma\bar{\sigma}|\sigma\bar{\sigma})} + I_{cc|cq}^{ph}(X)_{kl|lk}^{(\sigma\bar{\sigma}|\sigma\bar{\sigma})} \right) \left(\frac{1}{2} U_l \delta_{il} + \frac{1}{2} U^P{}_{(li)}^{(\sigma\bar{\sigma})} + a^{X*}{}_{(li)}^{(\sigma\bar{\sigma})}(X) \right) \\ &\quad \left. + \left(\frac{1}{2} U_j \delta_{jk} + \frac{1}{2} U^P{}_{(jk)}^{(\sigma\bar{\sigma})} + a^X(X)_{(kj)}^{(\sigma\bar{\sigma})} \right) \left(I_{cq|cc}^{ph}(X)_{kl|lk}^{(\sigma\bar{\sigma}|\sigma\bar{\sigma})} + I_{cc|qc}^{ph}(X)_{kl|lk}^{(\sigma\bar{\sigma}|\sigma\bar{\sigma})} \right) b^X(X)_{(il)}^{(\sigma\bar{\sigma})} \right] \end{aligned} \quad (\text{S27})$$

$$\begin{aligned} \partial_\Lambda(\varphi^D)_{(\sigma\sigma)(ij|ij)}^{cc|qq}(\Delta) &= \partial_\Lambda b^D{}_{(ij)}^{(\sigma\sigma)}(\Delta) \\ &= - \sum_{kl} \left[\left(-\frac{1}{2} W^D{}_{ik}^{\sigma\sigma} + a^D{}_{(ik)}^{(\sigma\sigma)}(\Delta) \right) \cdot \left(I_{cc|cc}^{ph}(\Delta)_{(lk|kl)}^{(\sigma\sigma|\sigma\sigma)} + I_{qc|cq}^{ph}(\Delta)_{(lk|kl)}^{(\sigma\sigma|\sigma\sigma)} + I_{cq|qc}^{ph}(\Delta)_{(lk|kl)}^{(\sigma\sigma|\sigma\sigma)} \right) \left(-\frac{1}{2} W^D{}_{(lj)}^{(\sigma\sigma)} + a^{D*}{}_{(jl)}^{(\sigma\sigma)}(\Delta) \right) \right. \\ &\quad + \left(-\frac{1}{2} W^D{}_{(ik)}^{(\sigma\sigma)} + a^D{}_{(ik)}^{(\sigma\sigma)}(\Delta) \right) \left(I_{qc|cc}^{ph}(\Delta)_{(lk|kl)}^{(\sigma\sigma|\sigma\sigma)} + I_{cc|cq}^{ph}(\Delta)_{(lk|kl)}^{(\sigma\sigma|\sigma\sigma)} \right) b^D{}_{(lj)}^{(\sigma\sigma)}(\Delta) \\ &\quad + b^D{}_{(ik)}^{(\sigma\sigma)}(\Delta) \left(I_{qc|cc}^{ph}(\Delta)_{(lk|kl)}^{(\sigma\sigma|\sigma\sigma)} + I_{cc|qc}^{ph}(\Delta)_{(lk|kl)}^{(\sigma\sigma|\sigma\sigma)} \right) \left(-\frac{1}{2} W^D{}_{(lj)}^{(\sigma\sigma)} + a^{D*}{}_{(jl)}^{(\sigma\sigma)}(\Delta) \right) \\ &\quad + \left(\frac{1}{2} U_i \delta_{ik} + \frac{1}{2} U^P{}_{(ik)}^{\bar{\sigma}\bar{\sigma}} + \frac{1}{2} U^X{}_{(ik)}^{\bar{\sigma}\bar{\sigma}} \right) \left(I_{cc|cc}^{ph}(\Delta)_{(lk|kl)}^{(\bar{\sigma}\bar{\sigma}|\bar{\sigma}\bar{\sigma})} + I_{qc|cq}^{ph}(\Delta)_{(lk|kl)}^{(\bar{\sigma}\bar{\sigma}|\bar{\sigma}\bar{\sigma})} + I_{cq|qc}^{ph}(\Delta)_{(lk|kl)}^{(\bar{\sigma}\bar{\sigma}|\bar{\sigma}\bar{\sigma})} \right) \\ &\quad \left. \times \left(\frac{1}{2} U_l \delta_{lj} + \frac{1}{2} U^P{}_{(lj)}^{(\bar{\sigma}\sigma)} + \frac{1}{2} U^X{}_{(lj)}^{(\bar{\sigma}\sigma)} \right) \right] \end{aligned} \quad (\text{S28})$$

The relative signs between the X - and the D -channel stem from the fact that they are related through ex-

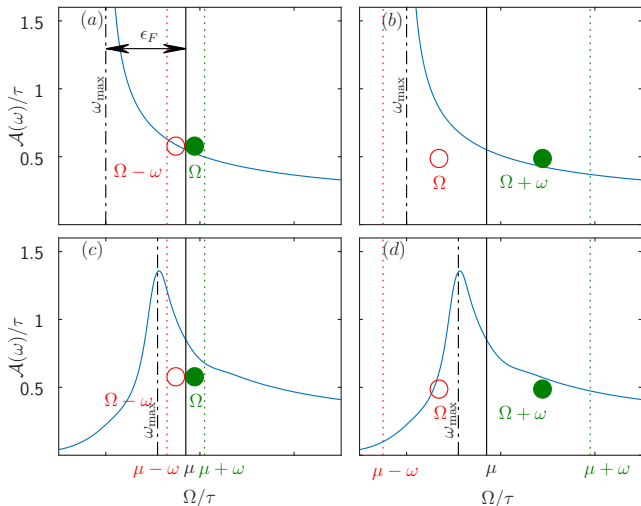


Figure S1. (a,b) LDOS of a non-interacting homogeneous system and (c,d) LDOS at the central site of an interacting QPC in the open regime. The filled (empty) circles show electrons (holes) of an electron-hole pair contributing to the spin susceptibility Eq. (S32), (a,c) for $\omega < \epsilon_F$ and (b,d) for $\omega > \epsilon_F$. Electron (or hole) energies lie between the chemical potential μ (solid black line) and $\mu + \omega$ (or $\mu - \omega$), indicated by the dotted green (or red) line. The frequency ω_{\max} , at which the LDOS is maximal, is indicated by the black dashed-dotted line.

change of two fermionic legs.

In equilibrium, we set

$$\begin{aligned} U_{ij}^{P(\sigma\bar{\sigma})} &= 2\text{Re } a^P(2\mu)_{(ij)}^{(\sigma\bar{\sigma})} \delta_{ij}, \\ U_{(ij)}^{X(\sigma\bar{\sigma})} &= 2\text{Re } a^X(0)_{(ij)}^{(\sigma\bar{\sigma})} \delta_{ij}, \\ W_{(ij)}^{D(\sigma\sigma)} &= 2\text{Re } a^D(0)_{(ij)}^{(\sigma\sigma)} \delta_{ij}. \end{aligned} \quad (\text{S29})$$

Note that in equilibrium, $a^P(2\mu)$, $a^X(0)$, and $a^D(0)$ are all real matrices.

In order to fully specify the flow, it remains to fix the initial conditions at large but finite Λ :

$$\Sigma_{ij} = \delta_{ij} U_i / 2, \quad (\text{S30})$$

$$\phi^X = \phi^P = \phi^D = 0. \quad (\text{S31})$$

S-III. THE FREQUENCY STRUCTURE OF THE SPIN-SUSCEPTIBILITY

In this section, we substantiate the claim of the main text that the characteristic frequency ω_{spin} of spin fluctuations is given by the distance between the chemical potential, μ , and the lower effective band edge, ω_{\max} . To do so, we consider the local non-interacting spin-susceptibility, defined in Eq. (3), which at zero tempera-

ture can be written as

$$\chi_{ii}^{U=0}(\omega) = 2\pi^2 \int_{\mu}^{\mu+\omega} d\Omega \mathcal{A}_i(\Omega) \mathcal{A}_i(\Omega - \omega). \quad (\text{S32})$$

Let us begin by analyzing its properties for a homogeneous tight-binding model with hopping τ and Fermi energy ϵ_F close to the lower band edge, i.e. $\epsilon_F = \mu + 2\tau \ll D, \omega \ll D$, where $D = 4\tau$ is the band width. This choice of ϵ_F most closely resembles the situation in the center of a QPC. $\mathcal{A}_i(\Omega)$ is zero for frequencies below the band edge, shows a divergence at the band edge and subsequently decreases monotonically with increasing frequencies [Fig. S1 (a,b)]. $\chi_{ii}^{U=0}$ essentially counts the number of available electron-hole excitations, where the electrons have an energy of $\Omega \in [\mu, \mu + \omega]$ and the holes an energy $\Omega - \omega \in [\mu - \omega, \mu]$ [Fig. S1 (a,b)].

Consider $\omega < \epsilon_F$ [Fig. S1(a)]. Then

$$\begin{aligned} \partial_{\omega} \chi_{ii}^{U=0}(\omega) &= -2\pi^2 \int_{\mu}^{\mu+\omega} d\Omega \mathcal{A}_i(\Omega) \mathcal{A}'_i(\Omega - \omega) \\ &\quad + 2\pi^2 \mathcal{A}_i(\mu + \omega) \mathcal{A}_i(\mu) > 0. \end{aligned} \quad (\text{S33})$$

Here, the prime denotes a derivative. Thus $\chi_{ii}^{U=0}(\omega)$ is a monotonically increasing function for $\omega < \epsilon_F$. This can be understood intuitively by considering the effects of an infinitesimal increase in ω : The first term in Eq. (S33) describes how, if the *electron* remains at energy Ω , the weight of the hole at energy $\Omega - \omega$ increases [$\mathcal{A}'_i(\Omega - \omega)$]. The second term in Eq. (S33) describes the appearance of additional electron-hole pairs.

For $\epsilon_F < \omega$ [Fig. S1(b)] Eq. (S33) is not useful, as the derivative of \mathcal{A} is ill-defined at the band edge. We thus rewrite Eq. (S32) as

$$\chi_{ii}^{U=0}(\omega) = 2\pi^2 \int_{\mu - \epsilon_F}^{\mu} d\Omega \mathcal{A}_i(\Omega + \omega) \mathcal{A}_i(\Omega), \quad (\text{S34})$$

where we have used the fact that \mathcal{A} vanishes for arguments below the band edge to restrict the range of integration. Using Eq. (S34) we obtain

$$\partial_{\omega} \chi_{ii}^{U=0}(\omega) = 2\pi^2 \int_{\mu - \epsilon_F}^{\mu} d\Omega \mathcal{A}'_i(\Omega + \omega) \mathcal{A}_i(\Omega) < 0. \quad (\text{S35})$$

For $\epsilon_F < \omega$, $\chi_{ii}^{U=0}(\omega)$ is thus monotonically decreasing. This can again be understood intuitively by considering the effects of an infinitesimal increase in ω : consider an electron-hole pair with fixed *hole* energy Ω . The weight of the electron states near $\Omega + \omega$ [described by $\mathcal{A}'_i(\Omega + \omega)$] diminishes, reducing the spin susceptibility.

The above analysis and Eqs. (S33) and (S35), together, lead to the following important conclusion: For the homogeneous system considered so far, $\chi_{ii}^{U=0}(\omega)$ exhibits a local maximum at an energy, ω_{spin} , that corresponds to the Fermi energy, i.e. to the distance between the chemical potential μ and the lower band edge ω_{\max} , $\omega_{\text{spin}} = \mu - \omega_{\max}$.

We now switch to a QPC geometry in the presence of interactions. The inhomogeneity of the QPC potential changes the divergence of the bare LDOS at the band bottom into a broadened peak, but leaves the other features of the LDOS qualitatively unchanged [compare Fig. S1(a) and (c) or (b) and (d)]. Within a Fermi liquid picture, where all of the above arguments still apply, albeit with renormalized parameters, we thus expect in the interacting QPC that $\omega_{\text{spin}} \simeq \mu - \omega_{\text{max}}$, where both ω_{spin} and ω_{max} are renormalized quantities.

S-IV. IMPLEMENTATIONAL DETAILS

The central region consists of $N = 61$ sites. We use ~ 1500 frequencies to sample the real frequency axis. One third of the frequencies is sampled exponentially in the region $|\omega| > 4\tau$, the rest is sampled homogeneously in the region $\omega \in [-4\tau, 4\tau]$. An additional 100 frequencies are included in windows of size $4T$ around μ and 2μ . In order to numerically perform the integrals, it is useful to map the real axis to a finite region. We thus represent $\omega \in \mathbb{R}$ in terms of the variable $\tilde{y} = y/\tau \in (-7, 7)$ via

$$\omega = \begin{cases} -2\tau \frac{(\tilde{y}+6)(1+\Lambda)}{(\tilde{y}+6)^2-1} - 6\tau, & \text{for } (\tilde{y} < -6) \\ -2\tau - \tau(\tilde{y}+2)^2/4, & \text{for } (-6 < \tilde{y} < -2) \\ \tau\tilde{y}\sqrt{\frac{4}{\tilde{y}^2} - \frac{\tilde{y}^2-4^2}{4\tilde{y}^2}}, & \text{for } (-2 < \tilde{y} < 2) \\ 2\tau + \tau(\tilde{y}-2)^2/4, & \text{for } (2 < \tilde{y} < 6) \\ -2\tau \frac{(\tilde{y}-6)(1+\Lambda)}{(\tilde{y}-6)^2-1} + 6\tau, & \text{for } (6 < \tilde{y}). \end{cases} \quad (\text{S36})$$

The structure of this substitution is chosen such that the van Hove divergence at the band edges is trivially integrated (i.e. the integral $\int d\omega(\omega \pm 2\tau)^{-1/2}$ is mapped to the integral $\text{const.} \times \int d\tilde{y}1$ for ω close to the band edges), while the large-frequency region is scaled with the flow parameter Λ and substituted such that the integral $\int d\omega\omega^{-2}$ (the most diverging integral that occurs) is mapped to the integral $\text{const.} \times \int d\tilde{y}1$ for $\omega \gg \Lambda$. For convenience, $y = \pm 2\tau, \pm 6\tau$ is mapped to $\omega = \pm 2\tau, \pm 6\tau$. Continuous frequency information is obtained by linearly interpolating in y -space.

The flow equation is solved with a 6th-order Runge-Kutta ODE solver with adaptive step size, while the integrals over internal frequencies are computed using Patterson sets. The integrals over internal frequencies are split into multiple intervals, such that a strong dependence on the internal frequency occurs near the integration boundaries, as the sampling is more dense there. The boundaries are determined by either the unsubstituted frequency of a Green's function or single scale propagator taking the value $\pm 2\tau, \mu, \mu \pm 10T, \pm(-2\tau + V_c)$ or $\pm 2\tau \pm \Lambda$, or by the argument of the P-channel (X-channel, D-channel) taking the value 2μ (0). The flow parameter used is not Λ , but rather $u := \log\left(\frac{\Lambda}{1+\Lambda}\right)$. This improves the dynamic choice of step size within the ODE-solver.

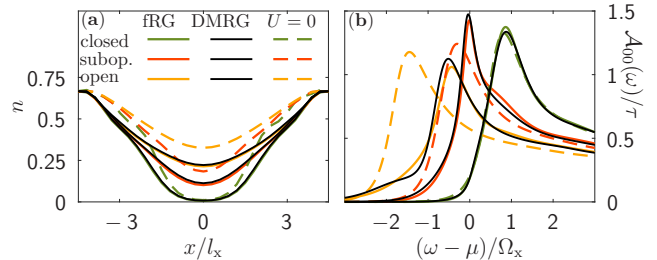


Figure S2. Comparison between Keldysh-fRG and DMRG results. (a) The local density as a function of position and (b) the LDOS as a function of frequency of a closed (green), subopen (red), and open (orange) QPC, computed without interactions (dashed lines), and with interactions (solid lines), using Keldysh-fRG (colored) and DMRG (black), respectively.

The flow starts at $\Lambda \approx 10^5$ and goes down to $\Lambda \approx 10^{-9}$. To minimize runtime, the Green's function and single scale propagator are computed at ~ 30000 frequencies, and a linear interpolation in y -space is used when either of them is required in an integrand. In equilibrium, the matrices appearing are symmetric under an exchange of sites. Further, the model considered here has a left-right parity symmetry. Both symmetries are exploited by using symmetric matrices to store the self-energy and the vertex, and by using a parity basis in the computation of the Green's function and the single scale propagator.

S-V. DMRG CALCULATIONS

The results in the main text are obtained using Keldysh-fRG, which is based on a perturbative ansatz. To verify the validity of the fRG data, we also employ density-matrix-renormalization-group (DMRG) calculations [33–35]. DMRG represents one of the most powerful quasi-exact numerical methods for describing one-dimensional quantum many-body systems regarding their static ground-state, dynamic, as well as thermodynamic properties. In particular, DMRG can treat fermionic systems with arbitrary interaction strength due to its non-perturbative character. Specifically, we have used DMRG to compute the local density n [Fig. S2(a)] and the LDOS [Fig. S2(b)], obtaining good qualitative agreement between our DMRG (black) and Keldysh-fRG (colored) results.

Below, we first elaborate on some peculiarities of our matrix-product-state (MPS) implementation [36], which could be of interest to practitioners, and then discuss the choice of model parameters used for this comparison.

A. DMRG details

The QPC model in Eq. (1) poses a particular challenge to DMRG since, in contrast to fRG, it is not possible to incorporate the non-interacting leads to the left and right of the interacting region by an additional term in the self-energy. Instead, a finite-size chain representation of both leads is necessary as a prerequisite to make the model accessible for DMRG. The simplest ansatz is to replace the semi-infinite leads by a finite-length tight-binding chain with open boundary conditions (OBC). However, this setup is not practicable as it requires to go to very large system sizes in order to avoid strong finite-size artefacts in physical properties in the interacting part of the QPC. Instead, we here employ the concept of smooth boundary conditions (SBC) [37, 38], which enable us to minimize finite-size effects in the interacting region of the QPC. Implementing SBC, the parameters of the non-interacting tight-binding chains are smoothly decreased to zero towards both ends of the chain to avoid having a sharp and rigid boundary as in the OBC setup. Thus for the interacting region of the QPC, the system's size is no longer fully determinable. SBC enable us to mimic very large leads with only $\mathcal{O}(10)$ sites.

In practice, we scale the Hamiltonian parameters in the non-interacting regions (which we label symmetrically by $I = 1, \dots, N_L$ for both the left and right lead; $I = 1$ corresponds to the left- or rightmost boundary, $I = N_L$ to the lead sites closest to the central region) with a smoothing function f_I such that $\tau_I = \frac{\tau}{2}(f_I + f_{I+1})$ and $\mu_I = \mu f_I$. Following Ref. [37], we choose $f_I = y(1 - I/[N_L + 1])$, and the smoothing function $y(x) = \frac{1}{2}(1 - \tanh \frac{x-1/2}{x(1-x)})$ for $0 < x < 1$, which interpolates between 1 at the edge of the central region and 0 at the boundary.

In this setup, we first determine the ground state of the QPC using standard DMRG formulated in terms of MPS. The LDOS $\mathcal{A}_i(\omega) = -\frac{1}{\pi} \text{Im} G_{ii}^R(\omega)$ is then determined using time-dependent DMRG [39]. To this end, we carry out two independent tDMRG runs to determine the retarded correlator in the time domain, $G_{ii}^R(t) = -i[\langle c_i^\dagger(t)c_i \rangle + \langle c_i(t)c_i^\dagger \rangle^*]$. The entanglement in the MPS increases linearly during the real-time evolution, thus the number of states D kept in simulation needs to be continuously increased to keep the numerical error constant. This implies that the simulation is bound to some maximum time T_{max} at which the simulation is no longer numerically feasible. A finite-time cutoff typically introduces artificial oscillations in the Fourier transform, requiring some artificial broadening to obtain a smooth and positive definite LDOS. However, we can avoid incorporating a broadening function by extending T_{max} to much larger times by means of linear prediction [40, 41]. The extrapolation scheme is expected to work for the present model since the correlator $G_{ii}^R(t)$ decreases exponentially over time scales smaller than the inverse mean

level spacing and larger than the lifetime of excitations in the central region.

We end this section with some technical notes. All DMRG calculations in this work are performed with the QSpace tensor library of A. Weichselbaum [42]. We studied a QPC with an interacting region consisting of $N = 31$ sites and two non-interacting regions to the left and right containing $N_L = 50$ sites each, yielding a total of $N_{\text{tot}}^{\text{DMRG}} = 131$ sites, whose parameters are tuned in terms of SBCs (see above). The DMRG ground-state calculation employs a two-site update keeping up to $D = 1600$ states. Convergence was typically reached after 10 to 40 sweeps, 40 being required particularly for an almost closed QPC, where the low particle density slows down convergence and the algorithm can get stuck in local minima during early iterations. In the tDMRG simulations we use a second-order Trotter-Suzuki decomposition with a time step $\Delta t = 0.05/\tau$ and adapt the number of states in the MPS dynamically by truncating all singular values smaller than $\epsilon_{\text{SVD}} = 5 \cdot 10^{-5}$. We stop the simulation when the number of kept states in the MPS exceeds $D = 4000$. In this setting, we typically reach time scales $T_{\text{max}} \cdot \tau = 60 - 65$ before applying linear prediction.

B. Choice of model parameters

Since DMRG solves a finite system, we need a way to estimate the 'optimal' system size: We extract the LDOS as a Fourier-transform of the real time Green's function, computed by DMRG. However, the resulting LDOS is only reliable if the Green's function is evolved up to time scales of the order of the traversal time t_{trav} , as at shorter times the low-energy quasi-particles have yet to leave the central region. This means that the system size must be chosen sufficiently large, such that the reflection time $t_{\text{refl}} \sim N_{\text{tot}}^{\text{DMRG}}/(2\tau)$ (the time until the first quasi-particles reflected at the boundary return to the center) is larger than the traversal time: $t_{\text{refl}} \gtrsim t_{\text{trav}}$. For the setup of the main text this yields $N_{\text{tot}}^{\text{DMRG}} \gtrsim 500$. Combined with the fact that we need to perform time-evolution up to the traversal time $t_{\text{trav}} \approx 250/\tau$, this would have required an unfeasible amount of resources in DMRG.

In order to reduce the traversal time, we shrink the system (i.e. reduce N) and make the QPC potential steeper (i.e. increase the curvature Ω_x): If the curvature is larger, a larger interaction is necessary to observe the same physics, as the LDOS is smeared out more. We have tried to compensate for this by choosing an appropriately larger interaction. Comparing Figs. 2(a) and S2(b), we see that the qualitative features of the fRG-LDOS are the same: There is a roughly constant energy-shift of the LDOS in the open region, in the sub-open region the LDOS peak is sharpened (the effective potential is

flatter) and pinned to the chemical potential, while the LDOS in the closed region is almost unaffected by interactions. Since the new parameters yield results that exhibit the same qualitative features as those shown in the main text, we consider them a reasonable proxy for a direct comparison between DMRG and Keldysh-fRG.

To be specific, the set of parameters used for this comparison is: $N^{\text{DMRG}} = 31$, $U^{\text{DMRG}} = 0.94\tau$, $V_c^{\text{DMRG}} = \{-1.69, -0.56, 0.56\}\Omega_x^{\text{DMRG}}$, $\mu^{\text{DMRG}} = -\tau$, and $\Omega_x^{\text{DMRG}} \approx 0.9\tau$. Since Ω_x is 3 times larger than in the main text, the traversal time should be reduced by a factor of roughly 3. We find $t_{\text{trav}} \approx 70/\tau$, and thus estimate $N_{\text{DMRG}}^{\text{tot}} \gtrsim 140$ (we use $N_{\text{DMRG}}^{\text{tot}} = 131$), which is still viable.

Finally, we remark that the choice of time t_{lp} , after

which linear prediction is applied, is a subtle issue: The linear prediction method does not capture any physics that happens at time scales $t \gg t_{\text{lp}}$ (this is an intended feature of the method, e.g. to mask finite-size effects). However, this implies that for $t_{\text{trav}} \gg t_{\text{lp}}$ there may exist times at which linear prediction appears stable (i.e. robust against variation of parameters used in linear prediction), while missing the finer details of the LDOS. This happens in our system for times $t_{\text{lp}} \sim 30/\tau$, and is generically to be expected in a system with multiple time scales. Once the largest time scale surviving the limit of infinite leads is reached (which in our case is t_{trav}), and provided that time scale is still much shorter than the inverse level spacing, linear prediction appears to yield reasonable long-time results.

4.3.1 Technical details of the DMRG implementation

The QPC model of [SBvD17] poses a challenge to the MPS setup. Therefore, we conclude this section with a few additional comments:

- Note that an almost closed QPC represents the hardest parameter regime for ground-state DMRG requiring a large number of sweeps (> 30). Poor convergence is caused by a combination of very low particle density in the interacting region and a high number of low-energy modes induced by the smooth boundary conditions.
- A symmetric MPS implementation incorporating $U(1)_{\text{spin}}$ and $U(1)_{\text{particle}}$ is strictly necessary in order to make the tDMRG simulations feasible on longer time scales. However, it turns out to be tricky to guess the correct particle number of the interacting ground state and obtain the symmetric MPS representation for a particular parameter set, for a number of reasons: (i) the noninteracting case typically does not represent a good starting point, since the total particle number can change drastically when interactions are turned on; (ii) generating the ground state in every particle sector and comparing the energy would be possible but requires $\mathcal{O}(100)$ DMRG runs; (iii) a DMRG calculation starting from some product state with the correct number of particles typically gets stuck in persistent local energy minima since the almost closed QPC prevents a proper particle redistribution in the two parts of the QPC.

To obtain the symmetric MPS representation of the QPC ground state in a finite amount of CPU time, we develop a slightly modified initialization procedure for the symmetric DMRG. First of all, we carry out a DMRG calculation without incorporating any symmetries. This yields the ground state with a somewhat reduced accuracy but containing almost the right amount of particles (typically deviating by ± 1 from the correct number). Now we project the non-symmetric MPS into a symmetric product state by borrowing ideas of our symmetric METTS implementation [BvdW15]. By definition, the resulting product state contains roughly the same amount of particles as the non-symmetric MPS, which are already distributed properly along the sites of the system. The symmetric product state is then evolved in imaginary time to generate some entanglement before feeding it back as initial state into the symmetric DMRG.

- Going forward, it should be easily possible to exploit time translational invariance [Bar13, KK16] to double the accessible time scale of the tDMRG in the QPC model at moderate additional costs.
- In contrast to fRG, tDMRG is not capable to evaluate the conductance of the QPC via the Meir-Wingreen formula [MW92], since boundary effects from the leads distort the non-local correlators at the edges of the interacting region. A promising alternative represents a quench scenario where we apply an initial bias to the leads. At $t = 0$, the bias is set to zero and particles will start moving from one lead through the contact into the other lead. The conductance can then be easily obtained from local current measurements in the middle of the contact. First steps into this direction indicate that one could potentially study large enough systems to shed light on some nonequilibrium properties of the 0.7 anomaly [Zen17].

Extending the range of two-dimensional tensor network techniques

Strongly correlated systems defined on two-dimensional lattices represent one of the most fascinating areas of condensed matter physics. The interplay of strong quantum fluctuations and geometric freedom in these systems induces a variety of exotic phenomena and yields new quantum states of matter, such as high- T_c superconductors [A⁺97, Dag94], frustrated magnets and spin liquids [Bal10, SB17], or topological insulators [HK10, QZ11]. Although the field continuously attracts a lot of attention, many details regarding the properties of these quantum many-body systems are still poorly understood. For instance, no consensus has reached regarding the origin of high- T_c cuprates, despite three decades of intense research.

Why do strongly correlated systems in 2D pose a particular challenge to theorists? The reason is strongly linked to the sources leading to the emergence of these exotic phenomena, namely the presence of strong quantum fluctuations and geometric freedom. These features cause many analytical and numerical approaches, which have been developed and successfully applied in other spatial dimensions, to fail in 2D. For example, mean-field theories work exceptionally well for many 3D systems but fail in two dimensions due to the presence of strong quantum fluctuations. Analytic approaches developed in 1D such as the Bethe-ansatz, which includes strong quantum correlations, has not yet been adapted to higher dimensions. Quantum Monte-Carlo is in principle capable to treat 2D systems. However, in the context of frustrated or fermionic 2D system, many formulations of QMC are severely limited by the sign problem, leading to an exponential increase of computational costs with system size. So far, attempts to beat the sign problem on a general level have not been successful.

Tensor network techniques represent a viable alternative to treat complex models of frustrated magnets or itinerant fermions in 2D. In particular, DMRG applied to two-dimensional clusters has provided us with some remarkable insight, for example, discovering the spin-liquid ground state of the Kagome Heisenberg model [YHW11, DMS12] or first observing the stripe states in the hole-doped t - J model [WS98]. More recently, also iPEPS earned some merit for the detailed study of the t - J model [CWVT11, CRT14], as well as for clarifying the spin-liquid nature of the spin- $\frac{1}{2}$ Kagome Heisenberg model [MCHW17, LXC⁺17]. In addition, a combined iPEPS and DMRG study supported by other numerical methods led to a consensus regarding the existence of stripe order in the hole-doped Hubbard model [ZCC⁺17].

Despite these success stories, tensor network approaches require substantial methodological advancement in order to be capable to tackle further open questions in the field and to directly relate to experimental work in real materials. One topic concerns the extension of the algorithms to dynamic observables such as spectral functions. Promising initial steps have already been taken in this direction, based on DMRG [HZOP16] and PEPS [VMVH15].

Finite-temperature calculations represent another important area of future research, particularly relevant to simulating experimental conditions. Little effort has been devoted up to now on the development of effective TN schemes for finite temperatures in 2D, with the exception of a few interesting studies of toy models based on iPEPS [LRG⁺11, CD14, CD15, CDO17]. In the following, we show for the first time that finite-temperature MPS algorithms, that up to now have only been applied to chain models, can be extended to two-dimensional systems as well [Sec. 5.1]. Analogous to 2D-DMRG, the MPS representation allows for an accurate and controlled description of clusters with moderate width. By minimizing finite-size effects and effectively dealing with long-ranged interactions in the imaginary-time evolution, we obtain results for the triangular Heisenberg model in excellent agreement with other state-of-the-art techniques. Moreover, we are even able to quantitatively determine the critical temperature of a finite-temperature phase transition in a frustrated lattice model.

Finally, the most difficult technical challenge concerns the treatment of complex fermionic multi-band models, e.g., highly relevant for many open questions in the context of high- T_c superconductivity and for the realistic description of real materials. Here we present the first fermionic iPEPS simulations that exploit a variety of non-abelian symmetries [Sec. 5.2]. In this way, we are able to substantially increase the performance of the algorithm allowing for the treatment of fermionic systems up to a bond dimension $D = 24$ on a square lattice. This sets the scene for a variety of complex 2D models becoming numerically accessible. In particular, we present some promising initial results for the two-band Hubbard model by incorporating both $SU(2)_{\text{spin}}$ and $SU(2)_{\text{flavor}}$ symmetries of the underlying Hamiltonian. Moreover, we also study a three-flavor Hubbard model featuring an $SU(3)_{\text{flavor}}$ symmetry, which recently has become accessible in the context of cold-atom experiments [SHH⁺14, HRS⁺16].

Our work in this chapter significantly advances 2D tensor network simulations in two directions. First of all, we introduce a powerful and controlled MPS framework for the finite-temperature calculations in 2D, many ideas of which can be directly adopted to other tensor network representations such as PEPS. Moreover, we present a very promising strategy to tackle complex fermionic multi-band models within the iPEPS framework. The first results of this approach represent an initial step towards the numerical solution of the two-band Hubbard model in two dimensions. Both of these methodological improvements open up numerous future research directions.

5.1 Matrix product state techniques for two-dimensional systems at finite temperature

The following article [BZWS17] illustrates for the first time that, analogous to 2D-DMRG, finite-temperature MPS techniques [Sec. 2.4.5] are viable for two-dimensional systems as well. Facing the challenge of strong entanglement growth under imaginary-time evolution, we develop a twofold strategy to minimize both finite-size effects as well as the accessible temperature: at high temperatures we rely on density-matrix purification in combination with a numerical linked-cluster expansion. At lower temperatures, inaccessible to purification, we employ the minimally entangled typical thermal state (METTS) algorithm on cylinders.

We demonstrate the capabilities of our approach in the context of the triangular Heisenberg model, obtaining excellent results for a large temperature regime. In addition, we illustrate that our method is able to quantitatively resolve the critical temperature of finite-temperature phase transitions in frustrated lattice models. This gives access to resolving the finite-temperature phase diagrams of many frustrated lattice models, which were previously out of reach for other methods. In general, we expect that this work paves the way to a more controlled treatment of finite-temperature effects in frustrated and fermionic 2D lattice models by means of tensor networks. We highlight that many ideas presented here are directly transferable to other tensor network techniques such as PEPS.

P7 *Matrix product state techniques for two-dimensional systems at finite temperature*

B. Bruognolo, Z. Zhu, S. R. White, E. M. Stoudenmire

submitted to SciPost Physics

Matrix product state techniques for two-dimensional systems at finite temperature

Benedikt Bruognolo^{1,2}, Zhenyue Zhu³, Steven R. White³, E. Miles Stoudenmire³,

1 Physics Department, Arnold Sommerfeld Center for Theoretical Physics and Center for NanoScience, Ludwig-Maximilians-Universität München, 80333 München, Germany

2 Max-Planck-Institut für Quantenoptik, Hans-Kopfermann-Str. 1, 85748 Garching, Germany

3 Department of Physics and Astronomy, University of California, Irvine, CA 92697, USA

August 24, 2017

Abstract

The density matrix renormalization group is one of the most powerful numerical methods for computing ground-state properties of two-dimensional (2D) quantum lattice systems. Here we show its finite-temperature extensions are also viable for 2D, using the following strategy: At high temperatures, we combine density-matrix purification and numerical linked-cluster expansions to extract static observables directly in the thermodynamic limit. At low temperatures inaccessible to purification, we use the minimally entangled typical thermal state (METTS) algorithm on cylinders. We consider the triangular Heisenberg antiferromagnet as a first application, finding excellent agreement with other state of the art methods. In addition, we present a METTS-based approach that successfully extracts critical temperatures, and apply it to a frustrated lattice model. On a technical level, we compare two different schemes for performing imaginary-time evolution of 2D clusters, finding that a Suzuki-Trotter decomposition with swap gates is currently the most accurate and efficient.

Contents

1	Introduction	2
2	Methods	3
2.1	Finite-temperature MPS techniques	3
2.2	Finite-size restrictions	5
2.3	Imaginary-time evolution of 2D clusters	6
3	Results	9
3.1	Triangular lattice Heisenberg model	9
3.2	J_1 - J_2 XXZ model on the square lattice	13
4	Conclusion	18
A	Numerical linked-cluster expansion	19

A.1	Basics of NLCE	19
A.2	Cluster groupings and order	20
A.3	Failure of statistical cluster solvers	21
B	Numerical details	22
B.1	Triangular lattice Heisenberg model	22
B.2	J_1 - J_2 XXZ model on square lattice	23
B.3	Statistical error bars	24
	References	24

1 Introduction

Two-dimensional strongly correlated electron systems are a major frontier of condensed matter physics. Even after decades of intense investigation many questions remain about the behavior of paradigmatic two-dimensional (2D) systems such as the kagome Heisenberg antiferromagnet [1, 2, 3, 4, 5] and the Hubbard model [6, 7]. Controlled and accurate numerical techniques are central for making progress. Recent advances in numerics have, for example, led to a consensus regarding the existence of stripe order in the underdoped Hubbard model [7].

Methods to access 2D finite-temperature physics are a key area of numerical development. Temperature-dependent properties can signal phase transitions, provide evidence for subtle ground-state scenarios, and of course allow comparisons to real experimental conditions.

Two very useful methods for computing thermal properties of strongly correlated electrons are quantum Monte Carlo (QMC) and series expansion techniques. Both can access large system sizes and a wide temperature ranges, yet encounter serious limitations. High-temperature series expansions often fail to converge at or below a thermal phase transition. QMC suffers from the sign problem, preventing its use for most frustrated magnets and models of itinerant fermions (though there are notable exceptions in special cases [8, 9, 10, 11]).

The seriousness of these problems makes tensor networks a compelling alternative. For example, the density matrix renormalization group (DMRG) is an algorithm for obtaining ground states in the form of a matrix product state (MPS) that is not affected by the sign problem. Following the success of MPS techniques, other families of tensor networks have been proposed that are better suited for 2D systems [12] and critical phenomena [13].

Finite-temperature extensions of tensor network techniques include the purification, or ancilla, method [14, 15, 16] and the METTS (minimally entangled typical thermal state) algorithm [17, 18]. (There are also transfer-matrix approaches for finite temperature using MPS [19, 20], though we do not discuss them further.) The purification method directly computes the thermal density matrix using imaginary time evolution techniques—the approach works well for high temperatures but the cost to reach lower temperatures grows rapidly. To address the limitations of the purification method, the METTS algorithm blends imaginary time evolution with Monte Carlo sampling, enabling a less costly pure-state formalism.

In this work we demonstrate that with MPS techniques we can obtain state of the art results for spin models in two dimensions over a wide range of temperatures, using the pu-

rification method for higher temperatures and METTS for lower temperatures. Some of the systems we study have a significant sign problem, making them out of reach of most Monte Carlo techniques. Though the approaches we use are not affected by the sign problem, they are of practical interest only if they scale to low enough temperatures and large enough system sizes to accurately estimate 2D behavior, as we show they do. We also study systems that undergo finite-temperature phase transitions, another challenge for which our techniques turn out to be well suited.

We review the methods we use in Section 2 before discussing our results. Our first set of results are for the spin- $\frac{1}{2}$ Heisenberg model on the triangular lattice in Section 3.1. This model has a severe sign problem [21, 22] and we are able to obtain results competitive with the few other methods able to treat it. In Section 3.2 we study a ferromagnetic XXZ model on the square lattice and obtain very accurate results for the critical temperature, both for a case where QMC results are available and for a case with additional frustrating second-neighbor interactions.

For those wishing to reproduce or extend our results, we have made our codes publicly available at: <https://github.com/emstoudenmire/finiteTMPS>

2 Methods

In this section we briefly review the two finite-temperature MPS algorithms we use in our simulations. We discuss the technical challenges for these MPS-based methods in the context of 2D systems. A major drawback of using MPS for 2D systems is their limitation to only modest system sizes in the direction transverse to the MPS path. We describe one way to minimize finite-size effects by using a numerical linked-cluster expansion. A key component of using the purification and METTS finite-temperature techniques with MPS is evolving MPS in imaginary time. This is challenging to do efficiently for 2D systems, and we discuss how to deal with the effectively further-neighbor interactions which necessarily arise.

2.1 Finite-temperature MPS techniques

Equilibrium thermal properties of quantum systems are fully encoded in the thermal density matrix

$$\hat{\rho} = \frac{1}{Z} e^{-\beta \hat{H}} \quad (1)$$

where Z is the thermal partition function and $\beta = 1/T$ the inverse temperature. Employing MPS techniques for imaginary time evolution, $\hat{\rho}$ can be directly computed by relying on the concept of purification. Or one can avoid purification and sample over a cleverly chosen set of pure states, the so-called METTS (minimally entangled typical thermal state). In this section we briefly review both of these MPS approaches.

Density-matrix purification.— Building on the ideas of purification, references [14, 15, 16] showed how to efficiently represent a thermal density matrix in an MPS framework. To this end, an auxiliary (or ancilla) space A is introduced as a copy of the physical Hilbert space P . The auxiliary sites can be interpreted as a heat bath thermalizing the physical sites. Using the construction of an enlarged Hilbert space $\mathcal{H} = P \otimes A$, it is possible to construct the thermal

density matrix from a pure state $|\psi_T\rangle$ by tracing out the auxiliary degrees of freedom:

$$\hat{\rho} = \text{Tr}_A |\psi_T\rangle\langle\psi_T|. \quad (2)$$

Starting at infinite temperature ($\beta = 0$), the purified state can be easily constructed as a product state of maximally entangled pairs of one physical and one auxiliary site each. To make a measurement at some finite temperature $T = 1/\beta$, one evolves $|\psi_0\rangle$ in imaginary time up to $\beta/2$. (The Hamiltonian used for time evolution is just the one defining the original problem and acts as the identity on the ancillary space.) An arbitrary static observable \hat{O} can then be evaluated by computing the overlap $\langle\psi_T|\hat{O}|\psi_T\rangle$, tracing out the auxiliary degrees of freedom.

The purification or ancilla approach works extremely well at high temperatures. But despite scaling polynomially with β , it becomes very costly in practice for temperatures well below the typical energy scales of the Hamiltonian.

METTS.– The minimally entangled typical thermal state algorithm (METTS) represents an alternative to purification [17, 18]. Instead of constructing the full density matrix, METTS generates a set of typical states $|\phi_\sigma\rangle$ satisfying

$$e^{-\beta\hat{H}} = \sum_{\sigma} P_{\sigma} |\phi_{\sigma}\rangle\langle\phi_{\sigma}|, \quad (3)$$

with P_{σ} denoting the probability of measuring the system for a given β in $|\phi_{\sigma}\rangle$. Starting from any orthonormal basis $\{|\sigma\rangle\}$, it can easily be shown that the following definition generates a set of states in agreement with typicality condition of Eq. (3),

$$|\phi_{\sigma}\rangle = \frac{1}{\sqrt{P_{\sigma}}} e^{-\beta\hat{H}/2} |\sigma\rangle, \quad P_{\sigma} = \langle\sigma|e^{-\beta\hat{H}}|\sigma\rangle. \quad (4)$$

Exploiting the freedom in the choice of the orthonormal basis $\{|\sigma\rangle\}$, the METTS approach starts from a set of classical product states of the form $|\sigma\rangle = |\sigma^1\rangle|\sigma^2\rangle\dots|\sigma^N\rangle$. These states represent the natural choice for a typical ensemble at infinite temperature, where the system should behave classically. Since their entanglement entropy starts out exactly zero and grows slowly during the imaginary-time evolution, they can typically be represented efficiently as MPS (hence the notion “minimally entangled”).

A thermal measurement of an arbitrary static observable O can be computed as

$$\langle\hat{O}\rangle_T = \frac{1}{Z} \sum_{\sigma} P_{\sigma} \langle\phi_{\sigma}|\hat{O}|\phi_{\sigma}\rangle. \quad (5)$$

Sampling the METTS ensemble randomly according to the probability distribution P_{σ}/Z , this expectation value can be evaluated by taking the ensemble average of $\langle\phi_{\sigma}|\hat{O}|\phi_{\sigma}\rangle$. To construct a sample, a Markov chain of product states $|\sigma\rangle$ is generated sequentially by the use of local measurements and then imaginary-time evolved to a specific temperature. We refer to Ref. [18] for details on the sampling algorithm and techniques to minimize autocorrelation effects.

Applicability.– Both methods are highly complimentary since they work best in opposite limits [23, 24]. Purification is highly accurate and efficient at high temperatures as it does not require any statistical sampling. However, the full thermal density matrix becomes much more costly to represent as a tensor network at low temperatures in comparison to the cost

of representing low-lying energy eigenstates or the pure states encountered in the METTS algorithm. This is specifically limiting for the 2D applications studied in this work, where the MPS representation of the density matrix quickly reaches the numerically feasible limits due to the additional entanglement in the system. Considering a typical 2D cluster of moderate size, we typically cannot reach temperatures significantly lower than the dominant energy scale (e.g. the spin coupling strength J) using purification.

In contrast, the METTS algorithm scales similarly to the ground state DMRG algorithm [18], allowing it to reach significantly lower temperatures. This feature particularly pays off in the context of 2D clusters, as it enables us to access relevant temperature regimes out of reach of purification. The METTS approach is less efficient than purification for higher temperatures, due to the extra sampling overhead. In Appendix B we present an example comparing the scaling of the MPS bond dimension with respect to temperature for both finite-temperature representations in the context of the triangular lattice Heisenberg model.

2.2 Finite-size restrictions

To understand the challenges of using MPS for 2D systems, it is helpful to recall the challenges of using the DMRG algorithm to compute a ground state MPS. In order to work with constant accuracy when using DMRG in 2D, the number of states kept in the MPS must be increased exponentially with respect to the width (transverse size) of the system. This limits the accessible system sizes and requires careful finite-size scaling. Nevertheless, DMRG has become a highly successful and competitive method for 2D systems mainly due to its flexibility, controllable accuracy, and access to the full many-body wavefunction.

Finite-temperature extensions of DMRG face the same system size restrictions. However, a non-zero temperature can often ease the finite-size limitations as correlation lengths are typically much shorter than at zero temperature. Therefore it often suffices to study narrow systems to extract information about the system’s properties in the thermodynamic limit. Here we employ two different strategies to minimize finite-size effects in our finite-temperature MPS simulations:

Purification plus NLCE.– The first approach combines density-matrix purification with the numerical linked-cluster expansion (NLCE). NLCE is a powerful method to calculate an extensive observable O of a lattice model directly in the thermodynamic limit, without having to perform calculations for the infinite system. Instead, NLCE employs measurements on finite-size clusters with open boundary conditions in both directions, while eliminating boundary and finite-size effects by a systematic resummation strategy [25, 26, 27]. In particular, we follow Ref. [28] and perform a modified NLCE procedure which takes only rectangular clusters into account and thus avoids the numerical bottleneck of computing cluster embeddings (see Appendix A for details). Using MPS based purification as finite-temperature cluster solver allows us to reach larger cluster sizes and higher expansion order than previously reported in the literature. Unfortunately, METTS is not a good candidate for a NLCE cluster solver because its errors are predominantly statistical, rather than systematic in nature (see Appendix A.3).

METTS on cylinders.– Our second scheme works analogously to most 2D DMRG calculations by taking open boundary conditions along the larger lattice direction (the length) and periodic boundary conditions along the smaller direction (the width). In this cylindrical setup one can first perform bulk-cylinder extrapolations based on the “subtraction trick” involving cylinders of various length [29]. The subtraction trick converges exponentially quickly once

the cylinder lengths exceed the correlation length. Then, if one reaches large enough cylinder widths, a second extrapolation can be performed to estimate properties in the thermodynamic limit. One advantage of using open boundaries along one direction is the possibility of adding boundary pinning fields which favor a particular symmetry-broken state in a parameter regime exhibiting spontaneous order. All of our METTS simulation are performed on cylinders.

2.3 Imaginary-time evolution of 2D clusters

One main ingredient of both finite-temperature algorithms introduced in Sec. 2.1 is an imaginary-time evolution that evolves the MPS starting from an infinite temperature state to a specific temperature. On a computational level, this represents the most expensive part of our calculations. Since we deal with various types of 2D clusters including systems with an enlarged Hilbert space in the purified setup, we include a discussion on the most important aspects. In particular, we focus on two schemes for MPS time evolution which are able to deal with long-ranged interactions of the Hamiltonian emerging from the mapping of the 2D cluster to a 1D chain. One approach is based on a combination of the Trotter decomposition and swap gates; the other uses a recently developed MPO approximation for the time evolution operator [30]. We conclude this section with an extended comparison of the two approaches in terms of accuracy and numerical efficiency.

Suzuki-Trotter with swap gates.— The simplest and most efficient setup to perform MPS time evolution for a 1D system with short-ranged interactions is the Suzuki-Trotter decomposition which splits the time-evolution operator into a product of local operators

$$e^{-\hat{H}\tau} \approx \prod_{\langle ij \rangle} e^{-\hat{h}_{ij}\tau}, \quad (6)$$

where $\hat{H} = \sum_{ij} \hat{h}_{ij}$. Suzuki-Trotter decompositions are in general very accurate approximations of the time-evolution operator, since they conserve important symmetries of the system dynamics [31]. The only error source originates from the non-commutativity of neighboring bond operators. The resulting so-called Trotter error can be controlled easily by choosing a small enough time step τ and using higher-order decompositions [31].

A Trotter-based time evolution is generally not applicable to systems with long-ranged interactions. However, a modified Trotter algorithm can be applied if interactions are restricted to two-body terms. To this end, one has to introduce the concept of swap gates. A swap gate switches the states of two identical sites and thus helps to modify the MPS in such a way that a non-local Trotter gate can be applied locally [18]. For each non-local bond operator $e^{-\hat{H}_{ij}\tau}$ the MPS is modified by a first set of swap gates so that site i is moved to the position of site $j - 1$. The bond operator can now be applied locally before a second set of swap gates moves site i back to its original position.

This scheme conserves the accuracy of the Suzuki-Trotter decomposition and, at the same time, can handle two-body interactions of any range. Nevertheless, its efficiency is strongly range-dependent. For the typical example of a rectangular 2D cluster considered in the following, the number of swaps scales roughly quadratically with the width of the system N_y . Since each additional swap requires an additional singular value decomposition computation, the method can become inefficient for wide systems.

MPO decomposition.— An alternative strategy relies on matrix-product-operator (MPO) approximations of the evolution operator $e^{-\hat{H}\tau}$ that can naturally include long-ranged interaction terms. An MPO-based time evolution is especially favorable for systems with different

types of long-ranged interactions, such as exponentially decaying terms which cannot be captured nicely in terms of two-site gates but which are encoded efficiently in the MPO representation of the Hamiltonian [32]. Although such systems are not considered in this work, an MPO-based approach could conceivably have better efficiency than the Trotter and swap gate approach when working on large 2D clusters. Hence we benchmark our Trotter scheme against the recently developed MPO-based scheme of Ref. [30].

An appealing feature of the approach of Ref. [30] is the enhanced error control in comparison to established MPO approximations, such as a simple Euler step or its Runge-Kutta and Krylov extensions. The key insight of Ref. [30] is to improve the simple Euler step by a local version of the Runge-Kutta stepper

$$1 + \tau \sum_x \hat{H}_x \rightarrow \prod_x (1 + \tau \hat{H}_x). \quad (7)$$

Using this approximation, the error remains constant with system size. In contrast an Euler stepper would incur an error per site that diverges for large systems. In addition, the Ref. [30] approach gives a very compact MPO representation making it appealing in terms of efficiency and implementation. The actual time evolution is carried out by applying the MPO to a MPS using standard tools, such as the fitting approach [12]. Note that one can combine two complex time steps to further reduce the scaling of the error per step to $\mathcal{O}(\tau^3)$. This leads to a second-order decomposition of the evolution operator which we use in our tests below.

Discussion.— In the following we compare the two schemes introduced above with respect to accuracy and numerical efficiency. The accuracy of the imaginary-time evolution is impaired by two error sources. On the one hand, the approximative decomposition of the full time-evolution operator introduces a finite time-step error. On the other hand, the accuracy is affected by the dynamical truncation of the MPS during the time evolution, which we control by adapting the cutoff parameter ϵ that limits the maximum discarded weight when truncating the MPS using a singular value decomposition [33]. These two error sources are not fully independent. Whereas a smaller time step decreases the effects of the decomposition error, it might increase the influence of the truncation error since more individual truncation steps are required during the time evolution. The numerical costs strongly depends on the total number of time steps as well. Fewer steps typically reduce the total computational time. In addition, the required MPS bond dimension might differ depending on the evolution scheme and time step leading to a slightly different cost scaling.

In our analysis we focus on a spin- $\frac{1}{2}$ antiferromagnetic XY model with nearest-neighbor interaction on a square-lattice cluster of size 5×5 with open boundary conditions. This cluster represents a nontrivial system with long-ranged interaction, yet it is still small enough to generate a quasi-exact reference state required for a proper benchmark procedure. Starting with a Neel-state at $\beta = 0$, we evolve the system in imaginary time to $\beta = 4$ and track the performance of both evolution schemes in terms of accuracy and numerical efficiency. The accuracy is monitored by calculating the overlap with respect to a quasi-exact reference state [34] after each time step τ for a cutoff $\epsilon = 10^{-10}$. Moreover, we track the CPU time required for each time step and the bond dimension m of the MPS during the evolution. We show the results in Fig. 1.

To our surprise, it turns out that the Trotter approach not only gives the more accurate results but also requires significantly less numerical resources. Studying the deviation from the exact state in Fig. 1(a), it becomes apparent that the Trotter approach is dominated by the truncation error. Reducing the time step τ by one order significantly decreases the accuracy

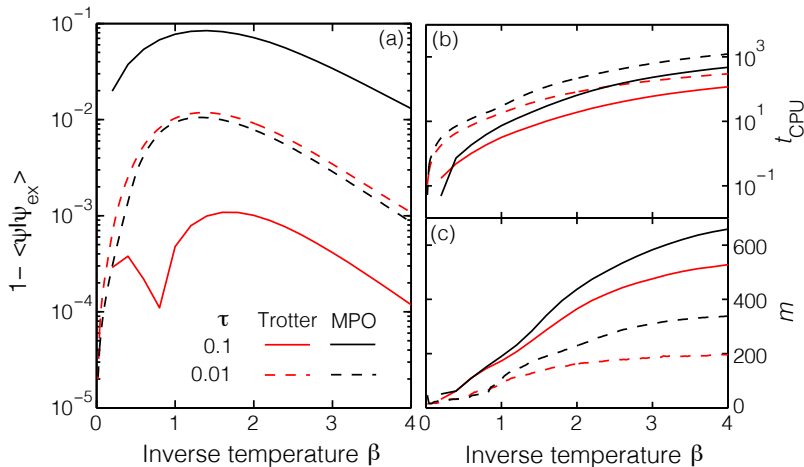


Figure 1: Comparison of MPO- and Trotter-based imaginary-time evolution for a spin- $\frac{1}{2}$ XY model on 5×5 square cluster with open boundary conditions.

due to the additional number of truncations. In contrast, the accuracy of MPO scheme strongly improves with a smaller time step indicating that the time step error represents the main error source. Nevertheless, the overall accuracy still remains roughly one order of magnitude larger than the Trotter approach with $\tau = 0.1$. At the same time, the MPO approach requires both significantly more CPU time and a larger bond dimension m , as shown in Fig. 1(b) and (c), rendering it less efficient than the Trotter scheme.

We conclude that the combination of a Trotter decomposition with swap gates currently represents the best choice for the purposes of this work, namely carrying out imaginary-time evolution for systems with long-ranged two-body interaction terms. At least the simple variant of the MPO decomposition of Ref. [30] employed here cannot meet the standards of the Trotter approach in terms of accuracy or efficiency. It may be that the MPO approximation misses some relevant contributions to the time evolution operator $e^{-\tau\hat{H}}$ that are included in the Trotter approximation. This could account for why the MPO approach requires smaller time steps to minimize the decomposition error. The more complex MPO variant of Ref. [30] might improve this behavior. However, due to its model dependent implementation we here refrained from testing it also. Moreover, the implementation of the second-order MPO decomposition requires complex numbers for imaginary-time steps. This increases the computational complexity in comparison to Trotter. We note that this is special to finite-temperature calculations. In the context of real-time evolution all time-evolution approaches require complex numbers, hence, the efficiency of the MPO approach might improve here.

Recent years have seen interesting developments regarding time evolution algorithms in systems with long ranged interactions. In addition to the two approaches discussed here, other suitable techniques include the time-dependent variational principle [35] or a recently introduced series-expansion thermal tensor network [36]. At the moment, these approaches coexist independently and, due to the inherent technical complexity, a practitioner typically picks the one most suitable to his problem and implementation framework. It remains an open question whether there exists a “best practice” approach amongst these schemes. Hence, a detailed benchmarking of these various time evolution techniques including different systems

and both real and imaginary time would be extremely helpful and is left for future work.

3 Results

Based on the MPS techniques introduced above, we present calculations for two frustrated lattice spin- $\frac{1}{2}$ systems in this section. First we focus on the antiferromagnetic Heisenberg model on the triangular lattice, illustrating that our MPS approach agrees with and extends results from other state of the art techniques to lower temperatures in the zero-field limit. In addition we also explore the system including a finite magnetic field. Moreover, we show how a METTS based approach can be used to detect a finite-temperature phase transition in a frustrated XXZ model on the square lattice. All calculations in this work are performed using the ITensor library [37]. To keep the discussion compact, we refer to Appendix B for further numerical details regarding the MPS parameters and setup.

3.1 Triangular lattice Heisenberg model

The antiferromagnetic spin- $\frac{1}{2}$ Heisenberg model (AFMH) on the triangular lattice, defined as

$$\hat{H} = J \sum_{\langle i,j \rangle} \hat{\mathbf{S}}_i \cdot \hat{\mathbf{S}}_j - h_z \sum_i \hat{S}_i^z, \quad (8)$$

represents a paradigmatic example of a frustrated lattice model (we assume $J = 1$ in what follows). It has been suggested as an effective description for several compounds such as $\text{Ba}_3\text{CoSb}_2\text{O}_9$ [38, 39], Cs_2CuBr_4 [40, 41] and, most recently, $\text{Ba}_8\text{CoNb}_6\text{O}_{24}$ [42, 43]. The combination of geometric frustration, reduced dimensionality and $S = 1/2$ degrees of freedom significantly enhances quantum fluctuations.

Without external magnetic field, $h_z = 0$, the ground state of the system exhibits coplanar, long-range magnetic order. The three spins in each triangle arrange themselves at 120° to one another in the same plane, forming a three-sublattice structure. For a finite magnetic field, the system features a broad magnetization plateau at $\frac{1}{3}$ of the total magnetization, where the spins order in a collinear, “up-up-down” configuration. Two coplanar phases surround the magnetization plateau transforming into a fully polarized state at very large fields.

At zero temperature, the model has been intensively studied by a number of methods, ranging from semi-classical approaches to extensive DMRG calculations pinning down the ground state phase diagram with high precision [45, 46, 47, 48, 49]. However, the finite-temperature regime still remains elusive since conventional QMC is impaired by the sign problem [21, 22]. In the zero-field limit, alternative approaches have proven very useful, such as high-temperature series expansions [50, 44, 51], conventional numerical cluster expansions [26], bold diagrammatic QMC [9], and Schwinger-Bosons [52]. Nevertheless, the limitation of all these methods in terms of accessible temperatures or system sizes leave room for improvement. In the following, we show that the combination of purification and NLCE, supported by additional METTS results on cylinders at lower temperatures, can be a competitive approach for determining the finite-temperature properties of the triangular AFHM.

Zero-field limit.– The ordered ground state of the triangular lattice AFHM at zero magnetic field breaks only the continuous $\text{SU}(2)$ symmetry of the Hamiltonian, as elaborated above. In this case spontaneous symmetry at finite temperature is prohibited by the Mermin-Wagner theorem [53], so that no phase transition can be observed at finite temperatures.

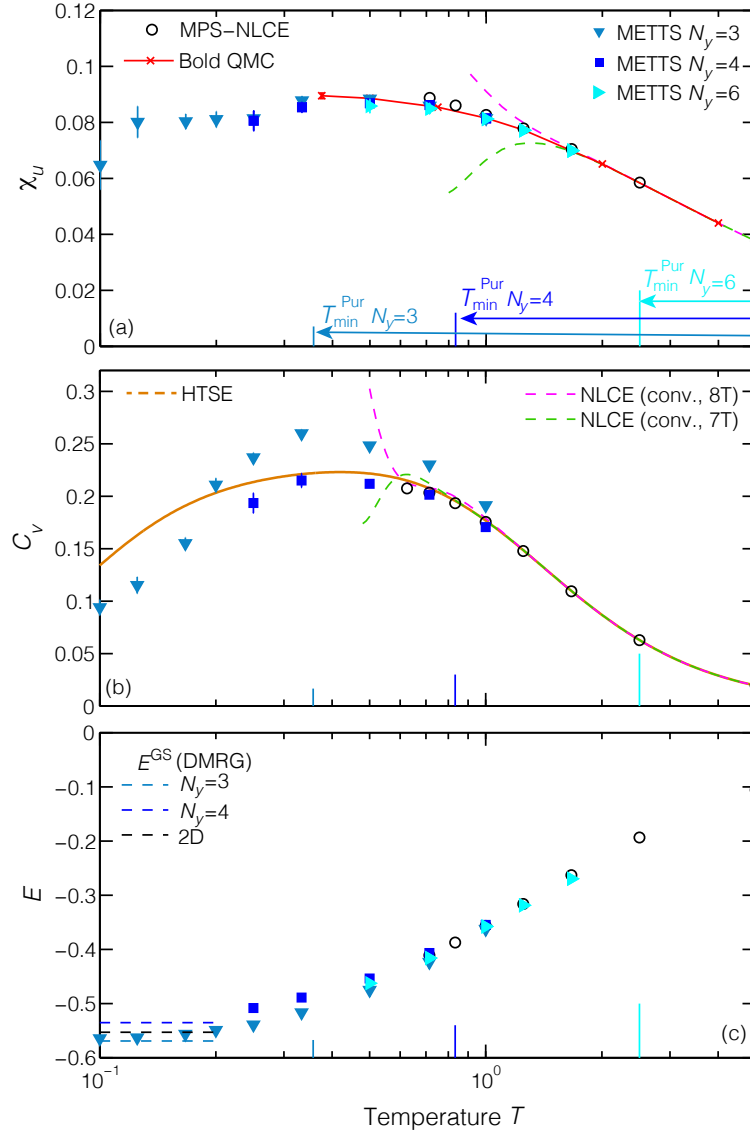


Figure 2: NLCE and METTS calculation of (a) uniform susceptibility χ_u , (b) specific heat C_v , and (c) energy density E (all per site) as a function of temperature for the triangular AFHM in the zero-field limit, $h_z = 0$. In comparison, we show results from high-temperature series expansion (HTSE) [44] for the specific heat, as well as bold diagrammatic QMC [9] and conventional NLCE [26] for the susceptibility. The colored ticks indicate the accessible temperature ranges when using density-matrix purification on width $N_y = 3, 4, 6$ cylinders while enforcing the same numerical accuracy as in the METTS calculation. This illustrates the importance of METTS for performing calculations at low temperatures (see Appendix B.1 for details).

Spin correlations remain short-ranged down to rather low temperatures (e.g. for $T = 0.25$ the correlation length is about two lattice spacings [50, 25]). This makes the model particularly suitable for our MPS techniques, which are primarily limited by system width. Our MPS calculations for this system employ a second-order Trotter decomposition with time step $\tau = 0.1$ and a truncation error cutoff $\epsilon = 10^{-10}$ for $N_y = 3, 4$, while for $N_y = 6$ we use a variable cutoff strategy, varying the cutoff from $\epsilon = 10^{-11}$ up to $\epsilon = 10^{-8}$ throughout different steps of the imaginary time evolution. The MPS-NLCE results are obtained on open clusters, whereas METTS is performed on long cylinders and finite-length effects are minimized via extrapolation. See Appendix B.1 for more details.

Our results for the zero-field case are presented in Fig. 2, where we study the finite-temperature properties of the triangular AFHM in terms of uniform susceptibility $\chi_u = (\langle \hat{\mathbf{S}}^2 \rangle_T - \langle \hat{\mathbf{S}} \rangle_T^2) / (3TN)$ [Fig. 2(a)], specific heat $C_v = (\langle \hat{H}^2 \rangle_T - \langle \hat{H} \rangle_T^2) / (T^2 N)$ [Fig. 2(b)], and energy density $E = \langle \hat{H} \rangle_T / N$ [Fig. 2(c)] per site, where $\hat{\mathbf{S}} = \sum_i \hat{\mathbf{S}}_i$. For the purpose of benchmarking, we compare our calculations with other state of the art techniques. This includes results from high-temperature series expansion (HTSE) [44] and conventional NLCE [26] in context of C_v , as well as bold diagrammatic QMC for χ_u [9].

Our MPS results show excellent agreement with the benchmark data, highlighting the complementarity of the two MPS-based strategies. First, we cover the high temperature regime shown in Fig. 3 down to about $T \sim 0.7$ with MPS-NLCE based on purification applied to cluster with a maximum size of 5×5 sites (black circles). We can observe that MPS-NLCE converges to significantly lower temperatures compared to conventional NLCE for quantities such as the susceptibility [Fig. 2(a)] since it can access larger cluster sizes. The resolution at high temperatures can easily be improved by using a smaller Trotter step, as illustrated in Fig. 3.

Lower temperatures are reached with METTS calculations on cylinders of width $N_y = 3$ (darker, downward triangular symbols), $N_y = 4$ (squares), and $N_y = 6$ (lighter, rightward triangles) shown in Fig. 2. The additional colored ticks along the temperature axis illustrate the minimum temperature accessible to purification on such cylinders with our resources, indicating that METTS algorithm is crucial for reaching the lowest temperatures shown. Cylinders of $N_y \leq 4$ turn out to be sufficient for estimating 2D properties down to rather low temperatures, depending somewhat on the specific property one is calculating. For χ_u , we find very good agreement with bold diagrammatic QMC down to the lowest temperature data currently available, about $T = 0.375$. For even lower temperatures down to $T = 0.25$, the results for $N_y = 3$ and $N_y = 4$ cylinders continue to agree, indicating that our $N_y = 4$ results for χ_u in Fig. 2(a) have very small finite-size effects.

Finite-size effects are clearly more significant for our C_v results Fig. 2(b). However, our $N_y = 4$ data is mostly in agreement with estimates of C_v based on high-temperature series calculations [44, 26]. We also show the energy per site in Fig. 2(c) to get further information about finite-size effects and to demonstrate that the lowest temperatures reached bring the system close to its ground state.

Finite magnetic field.— The triangular AFHM features four distinct magnetically ordered states at low temperatures for various values of an applied magnetic field [49]. The most striking state is the collinear, “up-up-down” configuration forming an extended magnetization plateau for $1.3 < h_z < 2.1$ at $\frac{1}{3}$ of the total magnetization. This plateau state is surrounded by two different states with co-planar order. In the high field region, $h_z > 4.5$, the system is fully polarized in the direction of the applied field. As some of these ordered phases spontaneously

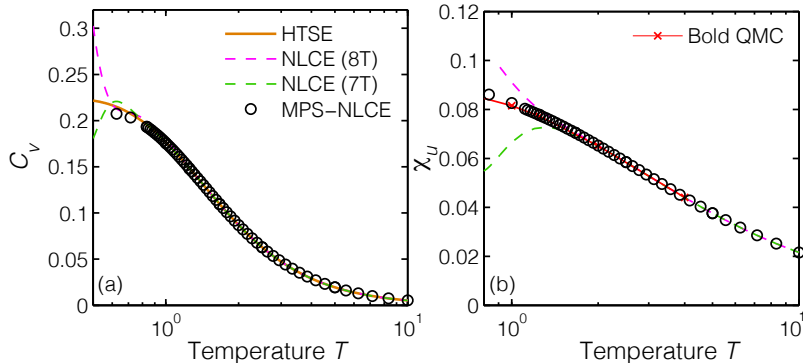


Figure 3: MPS-NLCE with smaller Trotter time step $\tau = 0.01$ illustrating excellent agreement with reference data at high temperatures.

break a discrete symmetry, they can persist for finite temperatures $T > 0$ and in such cases will be separated from the high-temperature paramagnetic phase by a finite-temperature phase transition.

Most theoretical studies of the triangular AFHM in an external magnetic field focus on the zero-temperature phases. The finite-temperature phase diagram has been explored by Monte-Carlo in the large- S limit [54] as well as in experimental AFHM in materials such as $\text{Ba}_3\text{CoSb}_2\text{O}_9$ [38] and Cs_2CuBr_4 [41].

Here we apply our MPS techniques to gather additional insight into the finite-temperature properties of the system. Unfortunately, we are not able to fully resolve the finite-temperature phase transition since, according to the experiments, the ordered phases should appear only for low temperatures $T < 0.25$. Our METTS sampling is numerically limited to temperature regimes of $T > 0.25$ on width $N_y = 4$ systems. However, an explicit study of T_c might be in reach employing a recently introduced, more efficient METTS sampling, that allows symmetry conservation even in the presence of a magnetic field [55]. This is left for future work.

For now we present MPS results for finite h_z in Fig. 4, which includes energy density E [Fig. 4 (a)], magnetization m_z [Fig. 4 (b)], specific heat C_v [Fig. 4 (c)], and susceptibility $\chi_z = (\langle \hat{m}_z^2 \rangle_T - \langle \hat{m}_z \rangle_T^2)/(TN)$ [Fig. 4 (d)] per site. We focus on three different field strengths, each representing a point in either one of the two distinct co-planar phases ($h_z = 1, 3$) or in the plateau phase ($h_z = 2$). Again the high-temperature regime is covered by our MPS-NLCE using purification (solid lines) while METTS is used at lower temperatures (squares).

The presence of long-range ordered states at finite-temperature can lead to stronger spin-spin correlations at higher temperatures if the system undergoes a continuous transition. This can clearly be seen in context of C_v and χ_z for which the NLCE breaks down (due to finite cluster size effects) at significantly higher temperatures in comparison to the zero-field case. This breakdown of MPS-NLCE is indicated by dashed lines in Fig. 4(c,d) showing the naive continuation of our MPS-NLCE procedure to lower temperatures for fixed maximum cluster size. It is unlikely that this is already a clear signature of the critical temperature T_c since we expect the phase transition to appear at significantly lower temperatures [38]. Moreover, the effect is most pronounced for strong magnetic fields at $h_z = 3$, whereas T_c should actually decrease compared to the plateau phase at $h_z = 2$.

Our $N_y = 4$ METTS results agree well with NLCE at high temperatures and can be pushed

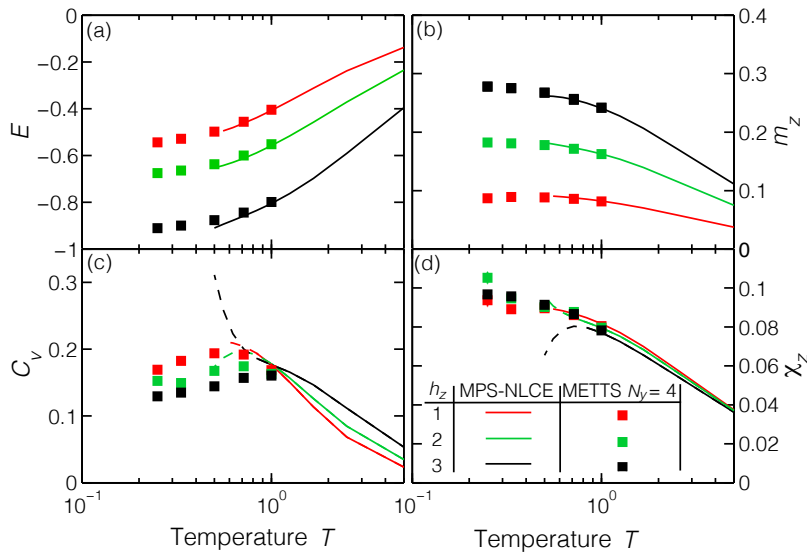


Figure 4: NLCE and METTS calculations of (a) energy density E , (b) magnetization m_z , (c) specific heat C_v , and (d) susceptibility χ_z (all per site) as a function of temperature for the triangular AFHM with finite magnetic field. The different field strengths include the two co-planar phases ($h_z = 1, 3$) and the plateau phase ($h_z = 2$).

to substantially lower temperatures than MPS-NLCE can reach for the same resources. An interesting feature appears in the METTS results for $h_z = 2$ where the magnetization already tends to saturate at $\frac{1}{3}$ of the total magnetization. This indicates that the system might be already ordered for the lowest temperature accessible, $T = 0.25$, in agreement with Ref. [38]. Nevertheless, we expect finite-width effects to be more pronounced in Fig. 4 than in the zero-field results shown in Fig. 2.

3.2 J_1 - J_2 XXZ model on the square lattice

In this section we show next that METTS is capable of accurately detecting a finite-temperature phase transition in lattice models with and without frustration, despite being limited to finite-size cylinders. This is a very appealing feature since the sign problem, often present in frustrated or fermionic systems, severely limits Monte Carlo techniques. Other powerful techniques such as high-temperature series expansion typically fail above or at the critical point, such that one has to rely on perturbative or mean-field approaches to determine the critical properties in such systems. While such approaches can work adequately on a qualitative level, they introduce significant quantitative errors such as in the determination of T_c . Our MPS scheme, which is neither limited by the sign problem nor by strong quantum fluctuations and interactions, could offer a valuable alternative to extract the exact location of the critical point in such models, assuming one can reach large enough system sizes for a particular problem of interest.

As proof of principle for our MPS approach, we consider a spin- $\frac{1}{2}$ J_1 - J_2 XXZ model on

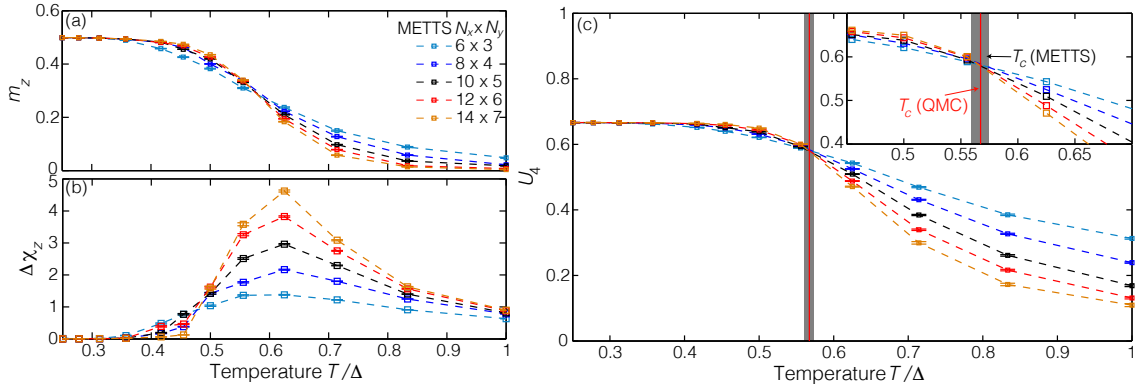


Figure 5: T_c estimate for non-frustrated spin- $\frac{1}{2}$ XXZ model on square lattice using METTS ($\Delta = 5$, $J_2/|J_1| = 0$). (a) Magnetization m_z , (b) susceptibility χ_z , and (c) fourth-order Binder cumulant U_4 as a function of temperature for different system sizes. Inset in (c) shows universal crossing point of Binder cumulants indicating the location of critical temperature $T_c/\Delta = 0.56 \pm 0.01$ (vertical shading) in excellent agreement with quantum Monte-Carlo calculation (vertical red line) [56].

the square lattice,

$$\begin{aligned} \hat{H} = & J_1 \sum_{\langle i,j \rangle} (\hat{S}_i^x \hat{S}_j^x + \hat{S}_i^y \hat{S}_j^y + \Delta \hat{S}_i^z \hat{S}_j^z) \\ & + J_2 \sum_{\langle\langle i,j \rangle\rangle} (\hat{S}_i^x \hat{S}_j^x + \hat{S}_i^y \hat{S}_j^y + \Delta \hat{S}_i^z \hat{S}_j^z), \end{aligned} \quad (9)$$

with ferromagnetic nearest-neighbor (NN) coupling $J_1 = -1$, antiferromagnetic next-nearest-neighbor (NNN) coupling $J_2 > 0$ and exchange anisotropy $\Delta > 1$ chosen in the following.

Non-frustrated model.— We first consider the non-frustrated nearest-neighbor XXZ model as a benchmark ($J_2 = 0$). In this case QMC is fully applicable and both ground-state and finite-temperature phase diagrams are well established [57, 58, 59]. Here we focus on the easy-axis regime $\Delta > 1$ where the spins in the system order ferromagnetically along the z -axis below some critical transition temperature T_c . The order parameter is given by the total magnetization per site $m_z = \langle \hat{S}^z \rangle / N$, with $\hat{S}^z = \sum_i \hat{S}_i^z$. This transition corresponds to a spontaneous breaking of the Z_2 symmetry of the Hamiltonian and belongs to the same universality class as the phase transition of the 2D Ising model.

In the following, we choose $\Delta = 5$ and assess whether we can detect the critical point with reasonable accuracy using METTS calculations on cylinders (see Appendix B.2 for numerical details). To this end, we employ the concept of a Binder cumulants [60], a method very commonly used in Monte Carlo studies to pin down the precise value of a critical point. Tensor network techniques have made use of Binder cumulants only very occasionally, and then only in the context of quantum phase transitions in 1D and quasi-1D systems [61, 62]. Here we show that the applicability can be straight-forwardly extended to thermal phase transitions in 2D models as well.

The Binder cumulant is a particularly useful quantity to study the critical point in systems with a known order parameter. For a system with Z_2 order parameter, such as (9), this

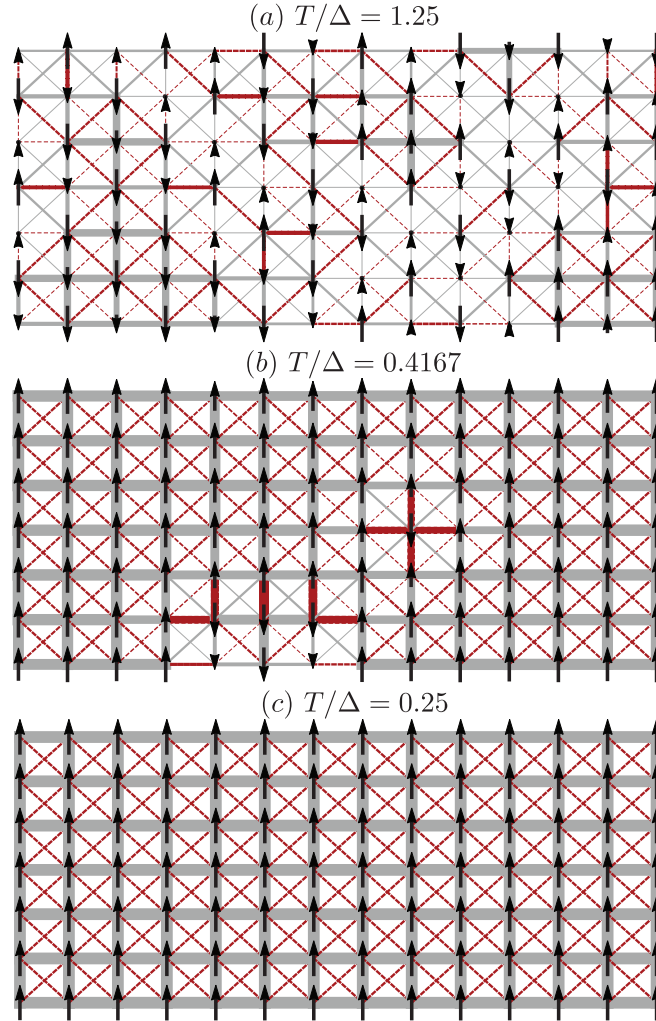


Figure 6: Snapshot of individual METTS in different phases of frustrated XXZ model ($\Delta = 5$, $J_2/|J_1| = 0.2$) on width $N_y = 7$ cylinder (a) in paramagnetic phase, (b) close to the phase transition, and (c) in ferromagnetically-ordered phase. The size of the arrows represent local measurements of $\langle \hat{S}^z \rangle$, and the widths of lines proportional to a bond measurement $J_{1/2} \langle (\hat{S}_i^x \hat{S}_j^x + \hat{S}_i^y \hat{S}_j^y + \Delta \hat{S}_i^z \hat{S}_j^z) \rangle$. Gray lines indicate a negative value of the bond measurement, while red lines correspond to positive bond measurements.

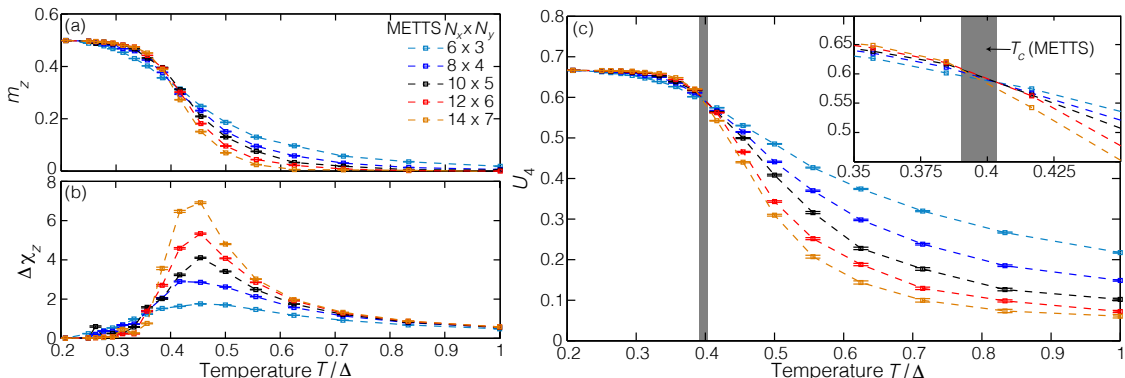


Figure 7: Same METTS-based T_c calculation as in Fig. 5 but for frustrated spin- $\frac{1}{2}$ XXZ model with next-nearest-neighbor interactions on square lattice ($\Delta = 5$, $J_2/|J_1| = 0.2$). Analogously to the non-frustrated case, U_4 enables us to precisely extract the value of $T_c/\Delta \approx 0.39 \pm 0.01$.

modified fourth order moment is defined as

$$U_4 = 1 - \frac{\langle (\hat{S}^z)^4 \rangle}{3\langle (\hat{S}^z)^2 \rangle^2}. \quad (10)$$

Note that the Binder cumulant can be obtained for other symmetry-broken orders as well, but the prefactors are typically different. The special feature of the Binder cumulant is its very distinct dependence on system size in the different phases as well as close to the phase transition. For $T > T_c$ in the disordered phase U_4 approaches zero with increasing system size, whereas it converges to a constant value $U_4 = \frac{2}{3}$ in the ordered phase for $T < T_c$. Close to the critical point the Binder cumulant is only weakly dependent on system size. Thus the curves of U_4 as a function of temperature, plotted for several system sizes, should all intersect at the critical temperature $T = T_c$. Due to the universality at the critical point, one can typically determine T_c very accurately on small systems without having to perform complex extrapolations to the thermodynamic limit. This makes the concept of Binder cumulants particularly appealing for MPS applications which are limited to modest system widths in 2D.

Fig. 5 shows our METTS calculations on cylinder with varying system sizes with constant aspect ratio (ratio of length to width is chosen 2:1). We set time step $\tau = 0.1$ and cutoff $\epsilon = 10^{-10}$ in all calculations and, in addition, apply pinning fields on the open boundaries of the system (see Appendix B.2 for more details).

While the precise critical temperature cannot be easily read off from the order parameter behavior [Fig. 5(a)], the maximum of susceptibility [Fig. 5(b)] gives already a first rough estimate of $T_c/\Delta \sim 0.6$. Studying the crossings of Binder cumulant obtained from calculations on different system sizes [Fig. 5(c) and inset], we obtain a much more precise estimate of $T_c/\Delta = 0.56 \pm 0.01$ which is indicated by the shaded region. This interval includes all line-segment crossings of U_4 and serves as a conservative error bar estimate for T_c . We are pleased to find this result in excellent agreement with QMC calculations [56], indicated by the vertical red line.

Frustrated model.— One of the attractive features of numerical approach is its straightforward adaptability to frustrated systems. As long as the states we encounter during imaginary-

time evolution have sufficiently low entanglement, we can straightforwardly treat the model with a finite antiferromagnetic NNN coupling $J_2 > 0$ that adds frustration. In this way, our METTS approach is a rare method that neither suffers from the sign problem nor contains a perturbative or mean-field ansatz and could become very helpful for studying finite-temperature transitions in frustrated systems.

In the following, we consider the Hamiltonian in Eq. (9) with $\Delta = 5$ (as before) and $J_2 = 0.2|J_1|$, which is small enough to preserve the ferromagnetic order at low temperatures. For the system with the additional J_2 interaction, we illustrate the physical properties of the system in the disordered phase, in the ordered phase, and close to the critical point in Fig. 6, showing individual METTS on a width $N_y = 7$ cylinder as “snapshots” of the different temperature regimes. In the paramagnetic phase at high temperatures, $T > T_c$, a typical METTS such as Fig. 6(a) is dominated by strong thermal fluctuations. As expected in a paramagnetic phase, we observe no indication of magnetic ordering, not even on the level of small clusters. Close to the critical temperature the METTS shown in Fig. 6(b) is already ferromagnetically ordered in most parts of the system. However, thermal fluctuations are still strong enough to flip individual spins or even small clusters, weakening the ferromagnetic order. For temperatures below the critical point, $T < T_c$, the ferromagnetic order is very strong, as illustrated by the METTS in Fig. 6(c).

Studying the independent METTS samples for different temperatures, one can notice another interesting yet intuitive effect. The temperature values requiring the most computational effort are in the paramagnetic phase very close to the phase transition. There the METTS are subject to thermal fluctuations which become long-ranged in the vicinity of the critical point, leading to large fluctuations in the local properties of the METTS and large sample variance. At lower temperatures the system orders ferromagnetically, breaking the Z_2 spin symmetry. The METTS in the ferromagnetic phase have relatively smaller fluctuations and, when collapsed, result in largely similar product states with most spins aligned. Empirically, we find that for these lower temperatures the sample variance is both smaller and the METTS are typically less entangled than for ensembles sampled just above the critical temperature. Therefore much less computational effort is required to get good accuracy.

Compared to the purification method, where the effort needed to reach lower temperatures is always strictly greater than for higher temperatures, in the above scenario of applying METTS within a low-temperature ordered phase we find that the METTS algorithm bypasses much of the numerical difficulties associated with the thermal phase transition. By this we mean that the algorithm adapts to the simpler low-temperature physics of an ordered phase, and does not require one to first deal with higher-temperature properties as a necessary precursor to obtaining low-temperature properties.

Turning again to the detection of T_c , we use the same procedure as for the non-frustrated case and the corresponding results are shown in Fig. 7. While the temperature dependence of the order parameter [Fig. 7(a)] and the susceptibility [Fig. 7(b)] again only allow rough estimates of the exact value of the critical temperature, the Binder cumulant [Fig. 7(c)] enables us to determine T_c much more precisely. Plotted as a function of temperature, the Binder cumulants approximately cross at an universal point indicating $T_c/\Delta \approx 0.39 \pm 0.01$ [see inset of Fig. 7(c)]. Again, the shaded region contains all line-segment crossings of U_4 and serves as a conservative error bar estimate.

Despite the small value of J_2 , we note that T_c decreases by almost 30% in comparison to the non-frustrated model since the J_2 couplings move the system closer to a regime where the ground state of the system is described by a stripy antiferromagnet. The ferromagnetic order

is expected to vanish for $J_2/|J_1| \approx 0.4$ in the isotropic model ($\Delta = 1$) [63]. The suppression of the thermal phase transition to lower temperatures is congruent with previous RG studies of Ref. [64] exploring the phase diagram of the antiferromagnetic version of Eq. (9), which also observed a significant decrease of T_c with increasing ratio J_2/J_1 .

Although an analysis of the full phase diagram of $J_2/|J_1|$ as a function of temperature is beyond the scope of this work, we emphasize that the results shown here do not represent an upper limit in terms of numerical feasibility. The typical MPS bond dimensions required to accurately simulate the width $N_y = 7$ systems are still small ($m < 120$) and handling the additional entanglement expected from increasing J_2 or decreasing Δ is definitely possible. In combination with the more efficient sampling routine of Ref. [55], the METTS-based scheme presented here offers a lot of potential to study thermal phase transition in frustrated lattice models without having to rely on perturbative approaches. Lastly, we note that calculations on the smaller clusters could have been carried out with density-matrix purification as well. But as METTS has much wider applicability to challenging systems, we refrained from using purification for this proof-of-principle study.

4 Conclusion

Despite much effort, the numerical treatment of strongly correlated electron systems in two dimensions remains a significant research challenge. Most methods to access finite-temperature physics of such systems are either limited to sign-problem-free models; cannot access very low temperatures; or fail in the vicinity of phase transitions. In this work we showed that tensor network techniques based on matrix product states are a compelling approach that can deal with all of these problems. And our approaches can be straightforwardly adapted to a very wide variety of systems beyond spin models and two-site interactions.

We employed a twofold strategy to deal with the system-size and temperature limitations of finite-temperature MPS techniques in the context of 2D systems. For high-temperatures we combined density-matrix purification with numerical linked-cluster expansions to get very accurate results for the thermodynamic limit. Since reaching low temperatures rapidly becomes prohibitive with purification, we applied the minimally entangled typical thermal state algorithm on cylinders to treat low-temperature regimes.

On a technical level, we elaborated on the treatment of finite-size effects in both finite-temperature MPS approaches. In this context, we note that NLCE could become an appealing companion to tensor network techniques on a more general level. By using a subset of possible clusters [28] and with recent progress in using NLCE for systems with long-ranged order [65], many other approaches such as ground-state DMRG and PEPS techniques could profit from the flexibility of the NLCE scheme. Another technical challenge we faced was the time evolution of 2D clusters within the MPS setup. We found that the combination of a Trotter decomposition with swap gates represents the best choice, currently, compared to a recently developed MPO scheme [30]. But MPO techniques will certainly continue to improve, and could quickly overtake the efficiency of the Trotter approach with the development of better algorithms, such as for applying an MPO to an MPS. Another approach could be to control costs or exploit additional parallelism by layering other types of Monte Carlo sampling on top of the METTS sampling; such an approach is explored for 2D systems in Ref. [66]. In the future it would be extremely helpful to MPS practitioners to establish whether there

exists a “best practice” approach among the various existing time evolution techniques for the treatment of long-ranged interactions.

As an application for our finite-temperature MPS techniques we treated the strongly frustrated spin- $\frac{1}{2}$ triangular Heisenberg antiferromagnet and established that our MPS techniques are competitive with other state of the art methods. We found that our MPS calculations are in excellent agreement with bold diagrammatic QMC and series expansions where results were available. We also studied the magnetic-field dependencies of different thermal properties. Furthermore, we showed that METTS is capable of treating finite-temperature phase transitions in the context of a frustrated spin- $\frac{1}{2}$ J_1 - J_2 XXZ model on the square lattice. This approach shows potential for controlled calculations of the phase diagrams of a wide variety of frustrated lattice systems.

Going forward, we expect that tensor network techniques will play an important role in understanding the finite-temperature properties in many two-dimensional frustrated systems. Although our results are already very promising, we have only taken a first step in this direction. With continually improving algorithms to produce and sample METTS, we expect the METTS approach to become an ever more powerful for studying 2D systems. For example, a recent work provides a framework for exploiting symmetries when producing METTS for any Hamiltonian with conserved quantum numbers [55]. Also the ideas presented here are directly transferable to other tensor networks. For example, a finite-temperature PEPS construction [67, 68] could replace MPS as the cluster solver in NLCE. As a natural tensor network ansatz for 2D systems, PEPS should also be useful for extending the METTS technique to lower temperatures and larger systems.

Acknowledgments We thank Sergey Kulagin and Marcos Rigol, who were kind enough to provide reference data for the triangular lattice Heisenberg model. We thank Norm Tubman for providing us crucial computing resources to obtain the low-temperature triangular lattice $N_y = 6$ data. We also thank Juan Carrasquilla, Lode Pollet, and Matthias Punk for helpful discussions. B.B. thanks Andreas Weichselbaum and Jan von Delft for their support of this research, as well as the tensor network group at UCI for their hospitality at the initial stages of this work. This work used the Extreme Science and Engineering Discovery Environment (XSEDE) [69], which is supported by National Science Foundation grant number ACI-1548562. This research was supported by the DFG through the Excellence Cluster “Nanosystems Initiative Munich”, SFB/TR 12, SFB 631 and by BaCaTeC Grant 15 [2014-2]. Z.Z., S.R.W., and E.M.S. were supported by the Simons Foundation Many-Electron Collaboration and by NSF grant DMR-1505406.

A Numerical linked-cluster expansion

For completeness, we present a brief summary of numerical linked-cluster expansion (NLCE) and the modified embedding scheme that has been used to obtain the MPS-NLCE results in Sec. 3.1.

A.1 Basics of NLCE

The key idea of NLCE is to obtain an extensive observable O directly in the thermodynamic limit, while using measurements on finite-size clusters and eliminating boundary and finite-size effects by a systematic resummation strategy [25, 26, 27]. To this end, the expectation

value of O per site can be represented by the sum of contributions of all different clusters, which can be embedded in the lattice \mathcal{L} ,

$$O(\mathcal{L})/N = \sum_c L(c) \times W_O(c). \quad (11)$$

Each specific cluster c contributes a certain weight $W_O(c)$ to the sum, which is multiplied by a combinatorial factor $L(c)$ defining the number of different ways to embed c on the lattice. The weights are defined recursively by

$$W_O(c) = O(c) - \sum_{s \subset L(c)} M(s)W_O(s), \quad (12)$$

with $O(c)$ being the observable of interest calculated on cluster c . The sum runs over all subcluster s that can be embedded into c and the combinatorial factor $M(s)$ indicates in how many different ways this can be achieved. Eq. (12) can be interpreted as a generalization of the inclusion-exclusion principle and ensures that double counting of clusters is avoided [70].

To perform an NLCE calculation, one generates all relevant cluster starting with the smallest one without subclusters ($W_O(1) = O(1)$) up to some maximum size and evaluates $O(c)$ on each cluster. By truncating Eqs. (11) and (12) at the maximum cluster size, one obtains an approximation of the expectation value O/N in the thermodynamic limit.

The quality of the result strongly depends on the correlation length in the system [70]. If the correlation length of the system is smaller than the maximum cluster size included, NLCE results show exponential convergence. This is reflected in the exponential decay of the weights $W(c)$ for clusters larger than the correlation length. Close to a phase transition or in an ordered phase at low temperatures, the correlations length typically exceeds the numerically accessible cluster size. In these cases, some properties show algebraic convergence (e.g. energy) while others (e.g. specific heat) might diverge and NLCE eventually breaks down. Even then, finite-size scaling or adapted summation techniques can help to extract useful information [26].

A.2 Cluster groupings and order

Conventional NLCE calculations include all possible connected clusters up to a certain number of sites or bonds. Generating and embedding all relevant clusters and subclusters poses a numerical challenge. In fact, it can be shown that the cluster embedding problem relates to an NP-complete graph embedding problem. This numerical bottleneck limits conventional NLCE approaches for zero-temperature properties to ~ 16 sites.

However, NLCE can be formulated in multiple ways in terms of the clusters one chooses to include. It possible to converge Eq. (11) with an alternative cluster definition, as long as this is done in a self-consistent way. In other words, it should still be possible to decompose each cluster c into subclusters s according to Eq. (12), all subclusters being constructed according to the same alternative definition.

Based on this idea, Ref. [28] introduced an alternative cluster grouping for square lattice geometries based on rectangular clusters only. This modified grouping scheme is illustrated in Fig. 8 for a few examples and it drastically reduces the complexity of the cluster embedding problem. To illustrate this, consider all clusters up to a maximum of 16 sites on a square lattice system with NN interactions only. Including all connected clusters, one ends up with

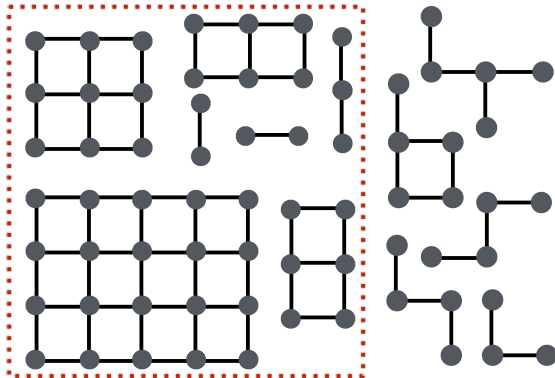


Figure 8: Example of clusters entering a NLCE calculation on the square lattice. The cluster grouping scheme of Ref. [28] only considers rectangular clusters (encircled red), significantly reducing the complexity of the cluster embedding problem.

$\mathcal{O}(10^8)$ clusters, whereas the restriction to rectangles reduces this number to a total of 27 clusters. Thus, the rectangular cluster grouping shifts the numerical bottleneck entirely to the cluster solver. Now the maximum expansion order of the NLCE is only limited by the size of cluster on which the observable $O(c)$ can still be measured. Employing this grouping scheme at zero temperature, Ref. [70] reached system sizes of ~ 50 sites based on Lanczos and DMRG cluster solvers in their NLCE calculations.

As discussed in the main part of this work, we combine NLCE with density-matrix purification as cluster solver and extend finite-temperature calculations previously performed by exact diagonalization. Following Refs. [28] and [70], we employ a rectangular cluster grouping in all calculations and perform the NLCE with a quadratic ordering scheme. This means that we include all clusters fitting inside the largest quadratic cluster considered, further reducing the number of clusters entering the calculation.

A.3 Failure of statistical cluster solvers

Measurements of an external quantity O performed with statistical approaches such as METTS or QMC include a statistical error scaling as $\delta O \sim \sqrt{\text{Var}[O]}/\sqrt{M}$ where M is the sample size. One is typically interested in the value of O in the thermodynamic limit but measurements have to be performed on finite-size systems with N sites with subsequent extrapolation $N \rightarrow \infty$. Standard finite-size scaling divides the value of the observable by N and extrapolates O/N as a function of system sizes. In this procedure the absolute value of the statistical error is obviously also reduced by the system size. In other words, a relative error $\delta O/O$ in the bare measurement of O on a cluster remains the same when computing O/N - a trivial statement.

To compute O/N in the framework of NLCE, the bare measurement $O(c)$ on each cluster c (not $O(c)/N(c)$!) enters the series in Eq. (11) multiple times. Hence, statistical fluctuations which may seem small compared to the bare value of $O(c)$ on a large cluster can become much more pronounced since the absolute error $\delta O(c)$ might not be small compared to O/N in the thermodynamic limit. This fact renders any statistical cluster solver for NLCE inapplicable.

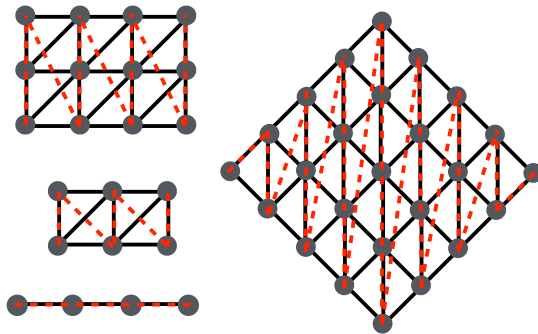


Figure 9: Example of clusters entering our rectangular-based NLCE scheme for the triangular Heisenberg lattice. The dashed red lines indicate the quasi-one-dimensional MPS path through the clusters. Rotating square clusters by 45° enables us to use an adapted MPS path that reduces the overall entanglement of the resulting MPS.

B Numerical details

Below we summarize additional numerical details of the MPS results presented in sections 3.1 and 3.2. All calculations are performed using the ITensor library [37].

B.1 Triangular lattice Heisenberg model

MPS-NLCE.— We employ standard density-matrix purification as finite-temperature cluster solver for the MPS-NLCE on the triangular lattice. Specifically, we rely on a second order Suzuki-Trotter decomposition to carry out the imaginary-time evolution with time step $\tau = 0.1$ and the truncation cut-off $\epsilon = 10^{-10}$. This results in a maximum bond dimension $m < 8500$ for $\beta = 1.4$ on largest cluster considered in our calculations (size 5×5). We always exploit U(1)-spin symmetry in the purified setup and use open boundary conditions in both directions.

To set up the NLCE with density-matrix purification on the triangular lattice, we employ the rectangular cluster grouping and perform the NLCE with a quadratic ordering scheme, as specified in Sec. A.2. A few examples of rectangular clusters entering the calculation are displayed in Fig. 9. The dashed red lines in Fig. 9 illustrate the choices of MPS paths through the cluster. We use an adapted path on square clusters, rotating them by 45° , to reduce the costs associated with representing an entangled 2D state as an MPS.

METTS.— For our METTS results we employ a second order Suzuki-Trotter decomposition with $\tau = 0.1$ and for the imaginary-time evolution set the truncation cut-off $\epsilon = 10^{-10}$ for width $N_y = 3$ and $N_y = 4$ systems and $\epsilon = 10^{-9}$ for $N_y = 6$ systems. All measurements are computed independently on length $N_x = 8$ and length $N_x = 16$ cylinders, before a bulk-cylinder extrapolations is used to minimize finite-length effects [29]. The METTS collapse into a product state is performed with a maximally mixed basis set [18]. In addition, for $h_z = 0$ we exploit the SU(2) spin rotation symmetry to implicitly rotate the basis states back into the \hat{S}^z basis after each collapse, allowing us to use a more efficient total- S^z conserving block-sparse representation for the time evolution. METTS sample sizes M vary between $M \approx 500$ for $T = 0.25$ on the width $N_y = 4$ cylinders to several thousand METTS for higher temperatures. We refrained from extrapolating the data as a function of the cylinder width

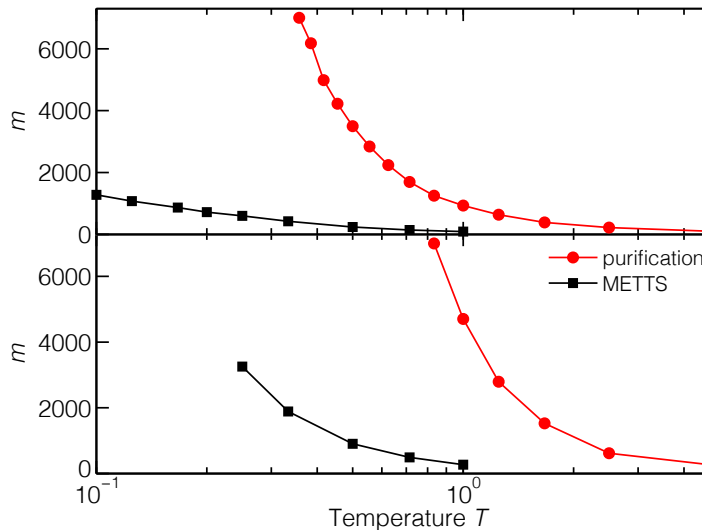


Figure 10: Maximum bond dimension m required by METTS (black) and density-matrix purification (red) for simulating the triangular AFHM on a cylinders of sizes (a) 16×3 and (b) 16×4 at various temperatures and zero magnetic field, using the numerical parameters specific in the text.

since the high amount of entanglement in the model limits us to width $N_y = 6$ systems.

To give some perspective on the numerical feasibility of the METTS calculations for the specified parameters, Fig. 10 displays the maximum bond dimension m required by METTS and density-matrix purification for two cylinders of sizes 16×3 and 16×4 at various temperatures and zero magnetic field. The METTS samples at high temperatures can be represented by MPS with small bond dimensions $m < 1000$, only the low-temperature samples on the width $N_y = 4$ cylinders require $m \geq 2000$ resulting in significant numerical effort (CPU times of several hours on four cores in order to generate single METTS). In these cases we made significant use of parallelizing the METTS sampling on numerous machines. With density-matrix purification applied to the same system, one is limited to temperatures $T_{\min}^{\text{Pur}} > 0.35$ on the width $N_y = 3$ and $T_{\min}^{\text{Pur}} > 0.8$ on the width $N_y = 4$ cylinders, respectively. For lower temperatures, we have to retain an unfeasibly large $m \gg 7000$ to keep the truncation error in the time evolution constant. The accessible temperature ranges for purification have been included as guide for the eye in Fig. 2 and illustrate the importance of the METTS algorithm to cover the low-temperature regime, where purification is no longer feasible.

B.2 J_1 - J_2 XXZ model on square lattice

All METTS calculations for the J_1 - J_2 XXZ model on the square lattice are performed with $\tau = 0.1$ and $\epsilon = 10^{-10}$. We typically have to obtain large sample sizes $M > 10000$ to converge the statistical error of the fourth order moment entering the Binder cumulant formula Eq. (10). Moreover, we perform measurements only in the middle half of the system and add a local pinning field $-\frac{\Delta}{2}\hat{S}_i^z$ on both ends of the cylinder to select one order parameter direction. The latter is of great importance, as calculations without pinning field can favor domain-wall formation on the cylinder that leads to ambiguous results and preclude the precise

determination of T_c .

B.3 Statistical error bars

The statistical error bars of the METTS calculations shown in Figs. 2, 4, 5, and 7 are derived using the standard error for energy density and magnetization. For more complex observables, such as specific heat, susceptibility and the Binder cumulant, we employ a resampling procedure via the bootstrap method. In this way, we properly take into account correlations between first, second, and fourth moments of a bulk observable [18]. Standard Gaussian error addition is employed in the context of the infinite-cylinder extrapolation.

References

- [1] S. Yan, D. A. Huse and S. R. White, *Spin-liquid ground state of the $S = 1/2$ Kagome Heisenberg antiferromagnet*, Science **332**(6034), 1173 (2011).
- [2] S. Depenbrock, I. P. McCulloch and U. Schollwöck, *Nature of the spin-liquid ground state of the $s = 1/2$ heisenberg model on the kagome lattice*, Phys. Rev. Lett. **109**, 067201 (2012).
- [3] Y.-C. He, M. P. Zaletel, M. Oshikawa and F. Pollmann, *Signatures of dirac cones in a dmrg study of the kagome heisenberg model*, arxiv:1611.06238 (2016).
- [4] H. J. Changlani, D. Kochkov, K. Kumar, B. K. Clark and E. Fradkin, *The mother of all states of the kagome quantum antiferromagnet*, arxiv:1703.04659 (2017).
- [5] H. J. Liao, Z. Y. Xie, J. Chen, Z. Y. Liu, H. D. Xie, R. Z. Huang, B. Normand and T. Xiang, *Gapless spin-liquid ground state in the $s = 1/2$ kagome antiferromagnet*, Phys. Rev. Lett. **118**, 137202 (2017).
- [6] J. P. F. LeBlanc, A. E. Antipov, F. Becca, I. W. Bulik, G. K.-L. Chan, C.-M. Chung, Y. Deng, M. Ferrero, T. M. Henderson, C. A. Jiménez-Hoyos, E. Kozik, X.-W. Liu *et al.*, *Solutions of the two-dimensional hubbard model: Benchmarks and results from a wide range of numerical algorithms*, Phys. Rev. X **5**, 041041 (2015).
- [7] B.-X. Zheng, C.-M. Chung, P. Corboz, G. Ehlers, M.-P. Qin, R. M. Noack, H. Shi, S. R. White, S. Zhang and G. K.-L. Chan, *Stripe order in the underdoped region of the two-dimensional hubbard model*, arxiv:1701.00054 (2017).
- [8] P. Henelius and A. W. Sandvik, *Sign problem in monte carlo simulations of frustrated quantum spin systems*, Phys. Rev. B **62**(2), 1102 (2000).
- [9] S. A. Kulagin, N. Prokof'ev, O. A. Starykh, B. Svistunov and C. N. Varney, *Bold diagrammatic monte carlo method applied to fermionized frustrated spins*, Phys. Rev. Lett. **110**, 070601 (2013), doi:10.1103/PhysRevLett.110.070601.
- [10] Y. Huang, K. Chen, Y. Deng, N. Prokof'ev and B. Svistunov, *Spin-ice state of the quantum heisenberg antiferromagnet on the pyrochlore lattice*, Phys. Rev. Lett. **116**, 177203 (2016), doi:10.1103/PhysRevLett.116.177203.

- [11] F. Alet, K. Damle and S. Pujari, *Sign-problem-free monte carlo simulation of certain frustrated quantum magnets*, Phys. Rev. Lett. **117**, 197203 (2016).
- [12] F. Verstraete and J. I. Cirac, *Renormalization algorithms for quantum-many body systems in two and higher dimensions*, eprint arXiv:cond-mat/0407066 (2004).
- [13] G. Vidal, *Entanglement renormalization*, Phys. Rev. Lett. **99**, 220405 (2007), doi:10.1103/PhysRevLett.99.220405.
- [14] M. Zwolak and G. Vidal, *Mixed-state dynamics in one-dimensional quantum lattice systems: A time-dependent superoperator renormalization algorithm*, Phys. Rev. Lett. **93**, 207205 (2004), doi:10.1103/PhysRevLett.93.207205.
- [15] F. Verstraete, J. J. Garcia-Ripoll and J. I. Cirac, *Matrix product density operators: Simulation of finite-temperature and dissipative systems*, Phys. Rev. Lett. **93**, 207204 (2004), doi:10.1103/PhysRevLett.93.207204.
- [16] A. E. Feiguin and S. R. White, *Finite-temperature density matrix renormalization using an enlarged hilbert space*, Phys. Rev. B **72**, 220401 (2005), doi:10.1103/PhysRevB.72.220401.
- [17] S. R. White, *Minimally entangled typical quantum states at finite temperature*, Phys. Rev. Lett. **102**, 190601 (2009), doi:10.1103/PhysRevLett.102.190601.
- [18] E. M. Stoudenmire and S. R. White, *Minimally entangled typical thermal state algorithms*, New J. Phys. **12**(5), 055026 (2010).
- [19] N. Shibata, *Thermodynamics of the anisotropic heisenberg chain calculated by the density matrix renormalization group method*, J Phys Soc Jpn **66**(8), 2221 (1997), doi:10.1143/JPSJ.66.2221.
- [20] X. Wang and T. Xiang, *Transfer-matrix density-matrix renormalization-group theory for thermodynamics of one-dimensional quantum systems*, Phys. Rev. B **56**, 5061 (1997), doi:10.1103/PhysRevB.56.5061.
- [21] T. Nakamura, N. Hatano and H. Nishimori, *Reweighting method for quantum monte carlo simulations with the negative-sign problem*, Journal of the Physical Society of Japan **61**(10), 3494 (1992), doi:10.1143/JPSJ.61.3494.
- [22] B. K. Clark and H. J. Changlani, *Stochastically projecting tensor networks*, arxiv:1404.2296 (2014).
- [23] B. Bruognolo, J. von Delft and A. Weichselbaum, *Symmetric minimally entangled typical thermal states*, Phys. Rev. B **92**, 115105 (2015), doi:10.1103/PhysRevB.92.115105.
- [24] M. Binder and T. Barthel, *Minimally entangled typical thermal states versus matrix product purifications for the simulation of equilibrium states and time evolution*, Phys. Rev. B **92**, 125119 (2015), doi:10.1103/PhysRevB.92.125119.
- [25] M. Rigol, T. Bryant and R. R. P. Singh, *Numerical linked-cluster approach to quantum lattice models*, Phys. Rev. Lett. **97**, 187202 (2006), doi:10.1103/PhysRevLett.97.187202.

- [26] M. Rigol, T. Bryant and R. R. P. Singh, *Numerical linked-cluster algorithms. i. spin systems on square, triangular, and kagomé lattices*, Phys. Rev. E **75**, 061118 (2007), doi:10.1103/PhysRevE.75.061118.
- [27] B. Tang, E. Khatami and M. Rigol, *A short introduction to numerical linked-cluster expansions*, Computer Physics Communications **184**(3), 557 (2013), doi:http://dx.doi.org/10.1016/j.cpc.2012.10.008.
- [28] A. B. Kallin, K. Hyatt, R. R. P. Singh and R. G. Melko, *Entanglement at a two-dimensional quantum critical point: A numerical linked-cluster expansion study*, Phys. Rev. Lett. **110**, 135702 (2013), doi:10.1103/PhysRevLett.110.135702.
- [29] E. Stoudenmire and S. R. White, *Studying two-dimensional systems with the density matrix renormalization group*, Annual Review of Condensed Matter Physics **3**(1), 111 (2012), doi:10.1146/annurev-conmatphys-020911-125018.
- [30] M. P. Zaletel, R. S. K. Mong, C. Karrasch, J. E. Moore and F. Pollmann, *Time-evolving a matrix product state with long-ranged interactions*, Phys. Rev. B **91**, 165112 (2015), doi:10.1103/PhysRevB.91.165112.
- [31] N. Hatano and M. Suzuki, *Finding exponential product formulas of higher orders*, In *Quantum annealing and other optimization methods*, pp. 37–68. Springer.
- [32] G. K.-L. Chan, A. Keselman, N. Nakatani, Z. Li and S. R. White, *Matrix product operators, matrix product states, and ab initio density matrix renormalization group algorithms*, The Journal of Chemical Physics **145**(1), 014102 (2016), doi:10.1063/1.4955108.
- [33] ϵ represents an upper bound for the sum squared discarded singular values of each SVD .
- [34] The reference state is generated using a second-order Trotter decomposition with a very small time step $\tau = 10^{-5}$ and an MPS cutoff of the order of double precision, $\epsilon = 10^{-16}$.
- [35] J. Haegeman, J. I. Cirac, T. J. Osborne, I. Pižorn, H. Verschelde and F. Verstraete, *Time-dependent variational principle for quantum lattices*, Phys. Rev. Lett. **107**, 070601 (2011), doi:10.1103/PhysRevLett.107.070601.
- [36] B.-B. Chen, Y.-J. Liu, Z. Chen and W. Li, *Series-expansion thermal tensor network approach for quantum lattice models*, Phys. Rev. B **95**, 161104 (2017), doi:10.1103/PhysRevB.95.161104.
- [37] <http://itensor.org> .
- [38] H. D. Zhou, C. Xu, A. M. Hallas, H. J. Silverstein, C. R. Wiebe, I. Umegaki, J. Q. Yan, T. P. Murphy, J.-H. Park, Y. Qiu, J. R. D. Copley, J. S. Gardner *et al.*, *Successive phase transitions and extended spin-excitation continuum in the $s=\frac{1}{2}$ triangular-lattice antiferromagnet $\text{Ba}_3\text{CoSb}_2\text{O}_9$* , Phys. Rev. Lett. **109**, 267206 (2012), doi:10.1103/PhysRevLett.109.267206.
- [39] Y. Shirata, H. Tanaka, A. Matsuo and K. Kindo, *Experimental realization of a spin-1/2 triangular-lattice heisenberg antiferromagnet*, Phys. Rev. Lett. **108**, 057205 (2012), doi:10.1103/PhysRevLett.108.057205.

- [40] T. Ono, H. Tanaka, H. Aruga Katori, F. Ishikawa, H. Mitamura and T. Goto, *Magnetization plateau in the frustrated quantum spin system Cs_2CuBr_4* , Phys. Rev. B **67**, 104431 (2003), doi:10.1103/PhysRevB.67.104431.
- [41] N. A. Fortune, S. T. Hannahs, Y. Yoshida, T. E. Sherline, T. Ono, H. Tanaka and Y. Takano, *Cascade of magnetic-field-induced quantum phase transitions in a spin- $\frac{1}{2}$ triangular-lattice antiferromagnet*, Phys. Rev. Lett. **102**, 257201 (2009), doi:10.1103/PhysRevLett.102.257201.
- [42] R. Rawl, L. Ge, H. Agrawal, Y. Kamiya, C. R. Dela Cruz, N. P. Butch, X. F. Sun, M. Lee, E. S. Choi, J. Oitmaa, C. D. Batista, M. Mourigal *et al.*, $\text{Ba}_8\text{CoNb}_6\text{O}_{24}$, Phys. Rev. B **95**, 060412 (2017), doi:10.1103/PhysRevB.95.060412.
- [43] Y. Cui, J. Dai, P. Zhou, P. Wang, T. Li, W. Song, L. Ma, Z. Zhang, S. Li, G. Luke *et al.*, *Experimental approach to the thermodynamics of the pure two-dimensional spin-1/2 triangular lattice antiferromagnet in $\text{Ba}_8\text{CoNb}_6\text{O}_{24}$* , arXiv preprint arXiv:1612.05217 (2016).
- [44] B. Bernu and G. Misguich, *Specific heat and high-temperature series of lattice models: Interpolation scheme and examples on quantum spin systems in one and two dimensions*, Phys. Rev. B **63**, 134409 (2001), doi:10.1103/PhysRevB.63.134409.
- [45] B. Bernu, C. Lhuillier and L. Pierre, *Signature of néel order in exact spectra of quantum antiferromagnets on finite lattices*, Phys. Rev. Lett. **69**, 2590 (1992), doi:10.1103/PhysRevLett.69.2590.
- [46] S. R. White and A. L. Chernyshev, *Neél order in square and triangular lattice heisenberg models*, Phys. Rev. Lett. **99**, 127004 (2007), doi:10.1103/PhysRevLett.99.127004.
- [47] D. J. J. Farnell, R. Zinke, J. Schulenburg and J. Richter, *High-order coupled cluster method study of frustrated and unfrustrated quantum magnets in external magnetic fields*, Journal of Physics: Condensed Matter **21**(40), 406002 (2009).
- [48] T. Tay and O. I. Motrunich, *Variational studies of triangular heisenberg antiferromagnet in magnetic field*, Phys. Rev. B **81**, 165116 (2010), doi:10.1103/PhysRevB.81.165116.
- [49] R. Chen, H. Ju, H.-C. Jiang, O. A. Starykh and L. Balents, *Ground states of spin- $\frac{1}{2}$ triangular antiferromagnets in a magnetic field*, Phys. Rev. B **87**, 165123 (2013), doi:10.1103/PhysRevB.87.165123.
- [50] N. Elstner, R. R. P. Singh and A. P. Young, *Finite temperature properties of the spin-1/2 heisenberg antiferromagnet on the triangular lattice*, Phys. Rev. Lett. **71**, 1629 (1993), doi:10.1103/PhysRevLett.71.1629.
- [51] W. Zheng, R. R. P. Singh, R. H. McKenzie and R. Coldea, *Temperature dependence of the magnetic susceptibility for triangular-lattice antiferromagnets with spatially anisotropic exchange constants*, Phys. Rev. B **71**, 134422 (2005), doi:10.1103/PhysRevB.71.134422.
- [52] A. Mezio, L. O. Manuel, R. R. P. Singh and A. E. Trumper, *Low temperature properties of the triangular-lattice antiferromagnet: a bosonic spinon theory*, New Journal of Physics **14**(12), 123033 (2012).

- [53] N. D. Mermin and H. Wagner, *Absence of ferromagnetism or antiferromagnetism in one- or two-dimensional isotropic heisenberg models*, Phys. Rev. Lett. **17**, 1133 (1966), doi:10.1103/PhysRevLett.17.1133.
- [54] L. Seabra, T. Momoi, P. Sindzingre and N. Shannon, *Phase diagram of the classical heisenberg antiferromagnet on a triangular lattice in an applied magnetic field*, Phys. Rev. B **84**, 214418 (2011), doi:10.1103/PhysRevB.84.214418.
- [55] M. Binder and T. Barthel, *Symmetric minimally entangled typical thermal states for canonical and grand-canonical ensembles*, arXiv preprint arXiv:1701.03872 (2017).
- [56] S. Göttel, S. Andergassen, C. Honerkamp, D. Schuricht and S. Wessel, *Critical scales in anisotropic spin systems from functional renormalization*, Phys. Rev. B **85**, 214406 (2012), doi:10.1103/PhysRevB.85.214406.
- [57] G. Rushbrooke and P. Wood, *On the high temperature staggered susceptibility of heisenberg model antiferromagnetics*, Molecular Physics **6**(4), 409 (1963), doi:10.1080/00268976300100461.
- [58] H. Takano and M. Suzuki, *Migdal-kadanoff renormalization group approach to the spin-1/2 anisotropic heisenberg model*, Journal of Statistical Physics **26**(4), 635 (1981), doi:10.1007/BF01010931.
- [59] S. Aplešnin, *A study of anisotropic heisenberg antiferromagnet with $s = 1/2$ on a square lattice by monte-carlo method*, physica status solidi (b) **207**(2), 491 (1998), doi:10.1002/(SICI)1521-3951(199806)207:2<491::AID-PSSB491>3.0.CO;2-G.
- [60] K. Binder, *Finite size scaling analysis of ising model block distribution functions*, Zeitschrift für Physik B Condensed Matter **43**(2), 119 (1981), doi:10.1007/BF01293604.
- [61] C. G. West, A. Garcia-Saez and T.-C. Wei, *Efficient evaluation of high-order moments and cumulants in tensor network states*, Phys. Rev. B **92**, 115103 (2015), doi:10.1103/PhysRevB.92.115103.
- [62] S. N. Saadatmand, B. J. Powell and I. P. McCulloch, *Phase diagram of the spin – $\frac{1}{2}$ triangular $J_1 - J_2$ heisenberg model on a three-leg cylinder*, Phys. Rev. B **91**, 245119 (2015), doi:10.1103/PhysRevB.91.245119.
- [63] Shannon, N., Schmidt, B., Penc, K. and Thalmeier, P., *Finite temperature properties and frustrated ferromagnetism in a square lattice heisenberg model*, Eur. Phys. J. B **38**(4), 599 (2004), doi:10.1140/epjb/e2004-00156-3.
- [64] J. R. Viana and J. R. de Sousa, *Anisotropy effects in frustrated heisenberg antiferromagnets on a square lattice*, Phys. Rev. B **75**, 052403 (2007), doi:10.1103/PhysRevB.75.052403.
- [65] D. Ixert and K. P. Schmidt, *Nonperturbative linked-cluster expansions in long-range ordered quantum systems*, Phys. Rev. B **94**, 195133 (2016), doi:10.1103/PhysRevB.94.195133.
- [66] J. Claes and B. K. Clark, *Finite-temperature properties of strongly correlated systems via variational monte carlo*, Phys. Rev. B **95**, 205109 (2017).

- [67] P. Czarnik and J. Dziarmaga, *Variational approach to projected entangled pair states at finite temperature*, Phys. Rev. B **92**, 035152 (2015), doi:10.1103/PhysRevB.92.035152.
- [68] P. Czarnik, M. M. Rams and J. Dziarmaga, *Variational tensor network renormalization in imaginary time: Benchmark results in the hubbard model at finite temperature*, Phys. Rev. B **94**, 235142 (2016).
- [69] J. Towns, T. Cockerill, M. Dahan, I. Foster, K. Gaither, A. Grimshaw, V. Hazlewood, S. Lathrop, D. Lifka, G. D. Peterson, R. Roskies, J. R. Scott *et al.*, *Xsede: Accelerating scientific discovery*, Computing in Science & Engineering **16**(5), 62 (2014), doi:doi.ieeecomputersociety.org/10.1109/MCSE.2014.80.
- [70] A. B. Kallin, E. Stoudenmire, P. Fendley, R. R. Singh and R. G. Melko, *Corner contribution to the entanglement entropy of an $o(3)$ quantum critical point in $2+1$ dimensions*, Journal of Statistical Mechanics: Theory and Experiment **2014**(6), P06009 (2014).

5.2 Fermionic iPEPS simulations with non-abelian symmetries

In the quest for understanding the underlying mechanism triggering strongly correlated phenomena such as high- T_c superconductivity in materials, we have to rely on powerful numerical approaches for complex fermionic many-body system working in two spatial dimensions. Quantum Monte-Carlo would be the ideal candidate for this challenge, however, the presence of the sign problem in these systems often restricts the applicability of QMC to special points in the phase diagram close to half filling. Amongst different tensor network methods, iPEPS represents the most promising alternative to QMC to successfully deal with complex systems of itinerant fermions. iPEPS techniques have seen rapid progress in recent years and have proven their competitiveness only recently in several applications to the single-band Hubbard and t - J model [CWVT11, CRT14, Cor16a, ZCC⁺17].

To answer many open questions in the field, however, the presence of intra-atomic Coulomb exchange or crystal field splitting is strictly required [IFT98, GdM13]. Thus it is necessary to go beyond effective single-band models and study multi-band generalizations of the Hubbard model. Due to the technical complexity of these systems and potentially also due to the small number of practitioners in the field, iPEPS has not yet been applied in this context. In this section, we introduce a promising strategy to numerically access fermionic multi-band systems by explicitly incorporating non-abelian symmetries in the iPEPS ansatz. In comparison to abelian symmetries, which by now are regularly applied in iPEPS simulations, non-abelian symmetries yield an additional compression of both the physical and virtual state spaces in the tensor network ansatz. This greatly enhances the efficiency and, in particular, allows for a substantial reduction of memory requirements (which very often represent the bottleneck for iPEPS calculations).

In the following, we present initial results obtained from our fermionic iPEPS ansatz with non-abelian symmetries for three different systems. First, we perform an $SU(2)_{\text{spin}}$ symmetric iPEPS simulation for the hole-doped t - J model, which reveals an intriguing connection of charge- and spin modulations in the stripe states [Sec. 5.2.2]. Moreover, we explore the properties of an orbital- and spin-degenerate version of the two-band Hubbard model on the square lattice, which only becomes accessible for iPEPS by exploiting $SU(2)_{\text{spin}} \otimes SU(2)_{\text{flavor}}$ symmetries [Sec. 5.2.3]. The non-abelian symmetries enable us to push the bond dimension up to $D = 24$, which yields excellent agreement with QMC benchmark data at half filling, and also enables us for the first time to study the hole-doped regime of this model. Finally, we also discuss initial results for a three-flavor Hubbard model featuring an $SU(3)_{\text{flavor}}$ symmetry. For all these cases, we explicitly incorporate the non-abelian symmetries in our iPEPS implementation using the QSpace library developed by Andreas Weichselbaum [Wei12a] [Sec. 5.2.4]. Before we dive into the discussion of the results, we also elaborate on a few technical details regarding the non-abelian iPEPS implementation in the next section.

5.2.1 iPEPS with non-abelian symmetries

All results presented in this section are based on the iPEPS algorithm which has been thoroughly introduced in Sec. 2.5. In particular, we employ both simple and full update combined with imaginary-time evolution [Sec. 2.5.4], and rely on a modified CTM scheme to perform the contraction of the iPEPS tensor network [Sec. 2.5.2]. The fermionic statistic is incorporated by means of the fermionization rules discussed in Sec. 2.6.

The special ingredient of our fermionic iPEPS implementation, that sets our work apart from that of other iPEPS practitioners, concerns the explicit incorporation of non-abelian symmetries, such as $SU(2)_{\text{spin}}$, $SU(2)_{\text{flavor}}$, and $SU(3)_{\text{flavor}}$, as well as combinations thereof with the fermionic \mathbb{Z}_2 parity symmetry in the particle sector. The non-abelian symmetries

are fully encoded in the QSpace tensor library [Wei12a], which automatically handles the symmetry-induced combination rules of both the reduced matrix elements and the Clebsch-Gordan space [Sec. 2.7]. This section sheds some light on technical details of the non-abelian iPEPS implementation.

Non-abelian iPEPS was pioneered by Ref. [LLW+15] for the case of the spin-1 Kagome Heisenberg antiferromagnet, which illustrated an $SU(2)_{\text{spin}}$ symmetric iPEPS representation in terms of a “projection” picture. Following ideas of $SU(2)$ invariant iPEPS representations for the spin- $\frac{1}{2}$ resonating valence-bond state [PSPGC12, PS13] and the spin-1 resonating AKLT state [LYC+14], the symmetric iPEPS tensors are generated from a set of virtual particles around each site that are projected into the local degrees of freedom of the corresponding site. Starting from such an $SU(2)$ invariant iPEPS, one only specifies the multiplet bond dimension D^* and lets the tensor optimization determine the relevant symmetry sectors on each bond dynamically. In practice, the numerically feasible values for D^* typically correspond to retaining an actual number of states D which lies out of reach of standard iPEPS calculations, incorporating abelian symmetries only.

In this section we discuss some important technical details of our non-abelian iPEPS implementation.

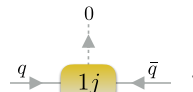
Global symmetry sector

Ref. [LLW+15] states that the projection picture is dense, as it can cover the full Hilbert space and generate any symmetry eigenstate. Whereas this is true for finite-size PEPS, we emphasize that, for translational invariant systems, the global symmetry label of the iPEPS is *always* constrained to the singlet sector in the case of non-abelian symmetries. This is conceptually similar to the case of abelian symmetries in iPEPS, where states are restricted to a global symmetry sector corresponding to the identity quantum number [BCOT11].¹ For abelian symmetries the identity quantum number can be associated with different symmetry sectors by appropriately relabeling the local symmetry sectors. The internal multiplet structure of different symmetry sectors prevents us from adopting this relabeling strategy in the case of non-abelian symmetries, so that, by construction, our iPEPS implementation represents a global singlet.

Arrow convention

In order to set up a symmetric iPEPS representation, we have to choose an “arrow convention” for all iPEPS tensors. In this way, we determine how the fusion rules apply to the different incoming and outgoing state spaces (i.e., which group of state spaces are fused into which according to Eq. (2.159)). Although the physical properties of the individual states are unaffected by this convention, there are good and bad choices from a technical perspective.

Especially during the CTM procedure it is often required, or at least beneficial with respect to the numerical efficiency (see discussion below), that two or more indices are fused together to form a thick bond index. The symmetry representation dictates that different indices should be all incoming or all outgoing in order to be combined (otherwise the symmetry fusion rules would no longer make sense). It is generically possible to revert the arrow direction of an index with the help of $1j$ symbols [Wei12a]. A $1j$ symbol represents

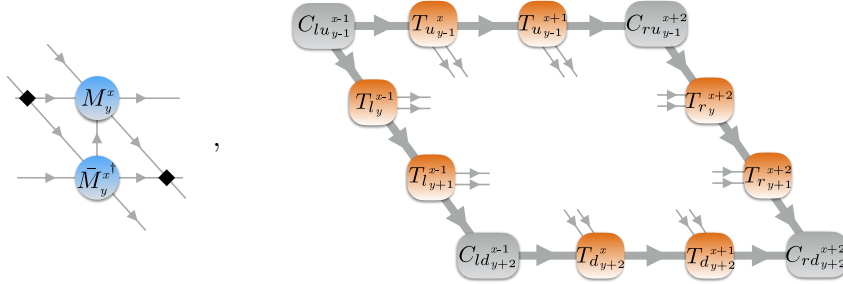
an object that fuses two quantum labels q, \bar{q} into a singlet:  .

¹The identity quantum number refers to the q label that, fused with another label q' according to the fusing rules of the specific symmetry, leaves q' invariant. Consider $U(1)_{\text{charge}}$ conservation as an example. Here the identity quantum number refers to $q = 0$, as it immediately follows that $q' + q = q'$.

Index reversion can be achieved by inserting an identity consisting of two $1j$ symbols on a bond and absorbing each into one of the neighboring tensors,

$$(5.1)$$

where the singlet index can simply be omitted in the end. For efficiency reasons, but also for compactness and readability of the code, we want to minimize the number of steps in the algorithm that involve reversing arrow directions by hand according to Eq. (5.1). To this end, we establish the following arrow convention for the M tensors as well as the corner matrices and transfer tensors,



Thus the quantum labels on all virtual bonds always “flow” from the upper left to the lower right corner of the tensor network. In particular, note that we have reverted the bond indices of $\bar{M}_y^{x\dagger}$ such that they point in the *same* direction as the corresponding indices of M_y^x . This greatly simplifies many fusion steps during the CTM procedure.

Effective contractions in the presence of non-abelian symmetries

An effective non-abelian iPEPS implementation requires a modified contraction pattern. The bottom line is that the ranks of the tensors involved in the various contraction pattern have to be kept minimal. Otherwise, the numerical effort will drastically increase, because of the significantly larger number of individual symmetry blocks involved in the contractions. The following section attempts to motivate this seemingly odd adaption and discusses some modifications to standard contraction orders, which have to be introduced.

As elaborated in detail in Sec. 2.7, abelian and non-abelian symmetries attach a multiplet quantum number q to each state; each physical or virtual index thus carries a set of these multiplet labels. This immediately yields a symmetric tensor with a sparse block structure. Each block is characterized by a set of incoming and outgoing multiplet labels obeying the symmetry fusion rules. The total number of symmetry blocks in an individual tensor can be roughly estimated by counting the number of different ways in which the incoming multiplet labels can be combined. This implies that a high-rank tensor contains a significantly larger number of blocks than a lower-ranked version of the same tensor, where some of the indices have been combined.

To be more specific, let us consider a simple example of an abelian charge symmetry and a rank-3 A tensor with two incoming quantum labels q, q' and one outgoing label q'' . The fusion rule restricts all blocks to satisfy $q + q' = q''$, which for $q'' = 0$ immediately leads to $q = -q'$. In the rank-3 representation of A there are typically numerous symmetry blocks,

e.g., $q = 1, q' = -1$ or $q = -2, q' = 2$, that can all be combined into $q'' = 0$. Fusing q and q' into a combined index Q and hence constructing a matrix representation of A , on the other hand, significantly decreases the number of these blocks. For instance, there is only a single block relating the incoming $Q = 0$ to the outgoing $q'' = 0$ sector. Obviously, the size of this single block exceeds the typical sizes of the many small symmetry blocks in the rank-3 representation. So why should we bother to introduce Q ? It turns out that, especially for high-rank tensors with many small symmetry blocks, the numerical costs of contracting a large number of tiny blocks drastically exceeds the effort necessary for contracting a single larger matrix. (Moreover, the latter can typically be efficiently parallelized by standard Lapack routines.)

Contracting high-rank tensors becomes even more expensive in the context of non-abelian symmetries, where the number of symmetry blocks can strongly increase due to the fact that the fusion of two multiplets can yield several different multiplets [Wei12a].

To illustrate the issue, we consider the example of an iPEPS calculation for the two-band Hubbard model [see Sec. 5.2.3] with $\mathbb{Z}_2 \otimes \text{SU}(2)_{\text{spin}} \otimes \text{SU}(2)_{\text{flavor}}$, retaining $D^* = 6$ multiplets on each bond. Already the rank-5 M tensors are complicated objects, however, the numerically most demanding tensors appear during the CTM coarse graining. Here, we typically have to deal with rank-6 or rank-7 tensors and it depends strongly on the implementation details whether the CTM procedure is still feasible. Let us focus on a typical rank-6 tensor appearing several times in a CTM step, which is obtained by contracting the following TN diagram,

(5.2)

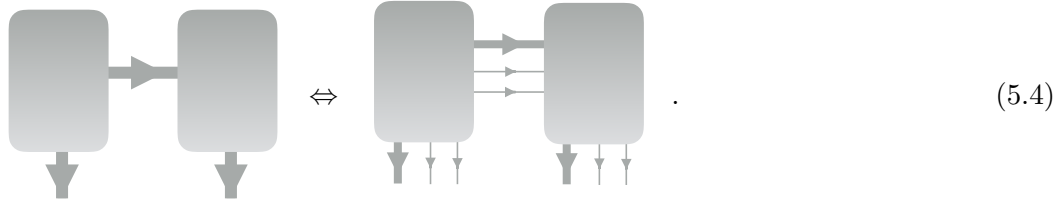
Each thin line corresponds to a single-layer bond index of dimension D^* , while the thick lines are environmental bond indices of dimension $\chi^* = 80$. In the form shown in Eq. (5.2), this tensor requires only 390 MB of memory for the reduced matrix elements compared to an estimated 883 GB without symmetries, which highlights the efficiency of the non-abelian symmetries. At the same time, it consists of about 430,000 (!) individual symmetry blocks. Of course, the sizes of the symmetry blocks are comparatively small, on average containing only 100 individual coefficients.

To reduce the rank of this tensor, it is possible to fuse the three indices pointing to the left and to the bottom, respectively. This yields a rank-2 matrix representation,

(5.3)

with size $28,000 \times 28,000$ on the multiplet level. The matrix only contains 37 symmetry blocks of larger size (on average, each block consists of 570,000 coefficients). Interestingly, the reduced matrix elements of the matrix require less memory (350 MB) than those of the rank-6 tensor above. To some extent, this can be attributed to overhead costs for organizing the long lists of symmetry blocks in the tensor. In addition, it indicates that the symmetry blocks in the matrix representation are extremely dense, containing only few zero-valued coefficients that can be omitted by decomposing the large symmetry blocks into many tiny ones in the rank-6 tensor.

Now how do the different representations perform in terms of contraction speed? To this end, we consider the next step of the CTM scheme, which requires forming the upper part of the environment in Eq. (2.99), by contraction the following tensor network, both in the rank-6 and rank-2 representation



The speed of the contraction vastly differs. Contracting both rank-2 objects results in 37 allowed contractions of individual symmetry blocks (exactly one per block) and can be achieved with QSpace in about one second of CPU time. In contrast, we had to terminate the contraction of the rank-6 tensors after four hours (!) of calculation time. In the latter case, there are 10^9 contractions which are allowed by symmetry. Although the effort for each of these contractions is minimal, having to process their vast number step by step leads to a drastic decrease of numerical efficiency.

This suggest a numerical speedup in the lower-rank representation by at least a factor $\mathcal{O}(10^4)$ (probably much more), which highlights the necessity to always minimize the rank of the tensors involved in the iPEPS contraction pattern. Note that any additional effort required for fusing pairs of indices (and sometimes also subsequent splitting them) comes with only subleading numerical costs, which can be completely neglected in comparison to the induced speedup.

In practice, one has to modify most contraction patterns in an iPEPS implementation with non-abelian and likely also abelian symmetries so that the rank of all tensors involved is kept minimal. In appendix A we illustrate these modifications for the example considered in this section: we show how to contract the full tensor network in Eq. (5.2) in the most efficient pattern, in order to end up with the matrix form shown in Eq. (5.3). With this technical prerequisite, we are now set to efficiently perform the iPEPS simulations with non-abelian symmetries. Initial results on three different fermionic models are presented in the following.

5.2.2 One-band t - J model

The discovery of high- T_c superconductivity has triggered intense research on the properties of the one-band t - J model on the square lattice, which is believed to capture some of the low-energy properties of cuprate materials [ZR88]. This model is derived from the Hubbard model (1.2) in the limit of strong interactions, where double occupancy is prohibited. The t - J Hamiltonian has the following form,

$$\hat{H}_{tJ} = -t \sum_{\langle ij \rangle \sigma} (\tilde{c}_{i\sigma}^\dagger \tilde{c}_{j\sigma} + \tilde{c}_{j\sigma}^\dagger \tilde{c}_{i\sigma}) + J \sum_{\langle ij \rangle} (\hat{S}_i \hat{S}_j - \frac{1}{4} \hat{n}_i \hat{n}_j) \quad (5.5)$$

with the fermionic operators $\tilde{c}_{i\sigma} = \hat{c}_{i\sigma}(1 - \hat{c}_{i\bar{\sigma}}^\dagger \hat{c}_{i\bar{\sigma}})$, spin operators \hat{S}_i , spin label $\sigma \in \{\uparrow, \downarrow\}$, and $\langle ij \rangle$ indexing all nearest-neighbor pairs of sites in the lattice. Moreover, we set $t = 1$ in the following.

Despite many analytical and numerical works, full consensus regarding the ground-state phase diagram of the t - J model has not been reached yet. Especially for low hole doping $\delta < 0.2$, there exist a number of competing low-energy states with different charge, spin, and superconducting orders. One category includes so-called stripe states, featuring charge- and spin-density waves [PR89, ZG89, Mac89, Sch89, WS98, WS99], where some of these states also exhibit coexisting d -wave superconducting order. Another potential candidate

for the ground state of the hole-doped t - J model is a superconducting state with uniform hole density [RCP⁺07, CFL08, CRT14]. Recently, large-scale iPEPS simulations on the t - J model demonstrated the extremely close competition of the uniform state and the vertical stripe state [CRT14], even for the largest accessible bond dimensions. Another recent work on the Hubbard model in a similar parameter regime pointed towards a striped ground state [ZCC⁺17]. Nevertheless, the underlying physical mechanism causing these intriguing ground-state properties remains illusive, and refined work in this direction is clearly necessary.

The t - J Hamiltonian (5.5) features an $SU(2)_{\text{spin}}$ symmetry and therefore represents an ideal first candidate for our non-abelian iPEPS approach. Incorporating the full spin symmetry in iPEPS has two effects in the context of this model: (i) with the increased numerical efficiency we can potentially reach larger bond dimensions than in an abelian setup; (ii) by construction, $SU(2)_{\text{spin}}$ symmetry suppresses antiferromagnetic (AF) order in the wavefunction. Switching the spin symmetry on and off, we can learn about the importance of AF ordering in possible candidates for the ground state wavefunction.

While point (i) has not been fully explored, yet, we illustrate the second benefit of fully controlling the emergence of AF order in the hole-doped t - J model for a specific coupling $J = 0.4$ in Fig. 5.1. Using both simple- and full-update simulations, we study the resulting low-energy wavefunctions on two unit-cell setups of different size. The first unit cell consists of 5×2 sites and requires 10 distinct iPEPS tensors; it was used in Ref. [CRT14] to bias the emergence of a striped ground state around $\delta = 0.1$ (where the cell has exactly a filling of half a hole per unit length per stripe). The second ansatz corresponds to a 2×2 unit cell requiring 2 distinct tensors, which represent the suitable setting for a uniform d -wave state.

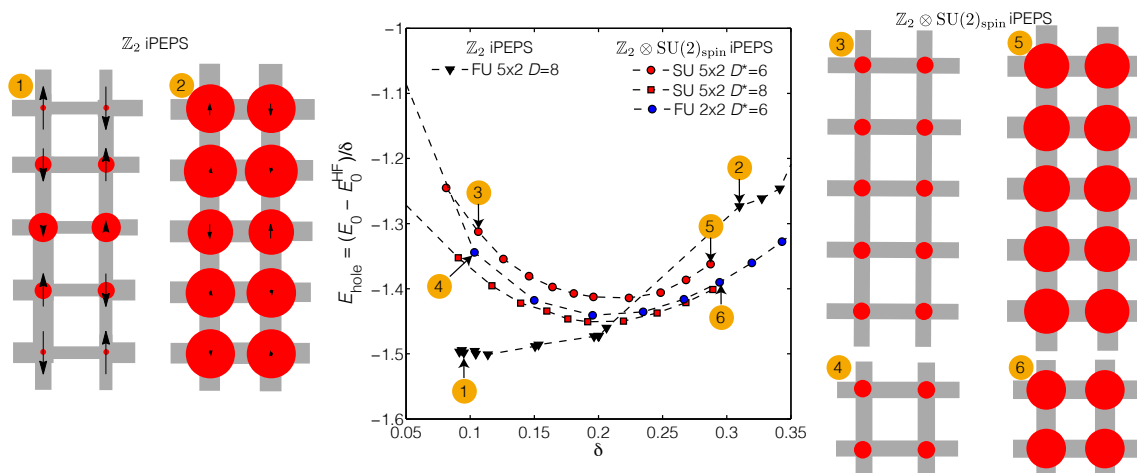


Figure 5.1: Non-abelian iPEPS results for the t - J model with $J = 0.4$, based on the QSpace tensor library. The panel in the center shows the energy per hole, E_{hole} , as a function of hole doping δ , obtained via both simple- and full-updated calculations on two different types of unit cells. Markers 1-6 in the panel point to individual iPEPS wavefunctions, where the hole doping per site is proportional to the diameter of the red dots, the length of the arrow indicates the magnitude of the magnetic moment, and the width of the bonds is proportional to their energy.

The panel in the center of Fig. 5.1 shows the energy per hole of the wavefunctions obtained from various iPEPS simulations as a function of the doping δ . The orange labels associate a specific energy with one of the iPEPS wavefunctions displayed next to the panel. The energy per hole is defined as $E_{\text{hole}} = (E_0 - E_{\text{HF}})/\delta$, where E_0 is the measured energy per site and $E_{\text{HF}} = -0.467775$ corresponds to the energy obtained by Sandvik [San97] at zero doping.

Comparing the energies of different calculations, we find that the $SU(2)$ -symmetric calculations (blue dots, red dots and squares) lead to energetically unfavorable wavefunctions for $\delta < 0.2$. In this parameter regime, the presence of AF order has a substantial impact

on the energy of the states [CRT14]. This is illustrated by the fact that energies of non-symmetric iPEPS simulations (black triangles) reach significantly lower energies than their SU(2) symmetric counterparts, despite having access to a smaller variational state space (the multiplet bond dimension $D^* = 8$ roughly corresponds to $D = 14$, while the non-symmetric simulations are restricted to $D = 8$).

A closer look at the individual iPEPS wavefunctions at $\delta = 0.1$ (labeled 1, 3, and 4) reveals further interesting information about what is going on. The non-symmetric state 1 clearly exhibits a modulation of charge-, spin- and superconducting order (the latter not shown) along the length-5 stripe. At the center site, hole doping is at a maximum whereas the local magnetization is strongly suppressed. This changes towards both ends of the stripe, where the AF order is enhanced while local hole doping decreases. This is in good agreement with the results of Ref. [CRT14], which also revealed that the charge and spin modulations are slightly suppressed towards larger values of $D = 14$ but, nevertheless, remain finite in the $D \rightarrow \infty$ limit. Switching on SU(2) symmetry on a 5×2 unit cell (wavefunction 3) immediately suppresses the AF order and, hence, the spin modulations.² In addition, it also has the rather surprising effect that charge modulations completely disappear as well. The resulting state no longer shows any characteristics of the stripe state and rather has the same structure as the uniform state obtained on a 2×2 unit cell at similar filling (wavefunction 4). This observation suggests that charge- and spin modulations in the stripe states are closely connected, a conclusion that is, to the best of our knowledge, new.

As expected, AF order is not relevant for the ground-state properties of the t - J model at larger doping $\delta > 0.2$. Here we find that the symmetric iPEPS simulations benefit from their enlarged variational space and the resulting wavefunctions have significantly lower energies than their non-symmetric counterparts. A closer look at the wavefunctions at $\delta = 0.3$ (labeled 2, 5, and 6) suggests that, at least in the 5×2 setup, the stripe states disappear. The non-symmetric iPEPS (wavefunction 2) only features remainders of charge- and spin modulations, and mostly resembles the uniform states (wavefunctions 5, 6) obtained from SU(2) symmetric iPEPS calculations.

In conclusion, by comparing symmetric with non-symmetric calculations, our initial study suggest that AF order becomes relevant for doping $\delta < 0.2$, regardless of the specific unit cell under consideration. This is supported by the energy minimum at doping $\delta = 0.2$ observed in all SU(2)-symmetric iPEPS simulations in Fig. 5.1. Going forward, we still need to unlock the full potential of the symmetric iPEPS implementation for the t - J model. In particular, it would be interesting to push the full-update simulations to larger multiplet bond dimensions $D^* = 8, 10$ and compare their results to the abelian iPEPS calculations by Ref. [CRT14]. Nevertheless, this initial study has already revealed some salient information about the ground-state properties, especially regarding the connection of charge- and spin modulation in the stripe states.

5.2.3 Two-band Hubbard model

Whereas the one-band Hubbard model already features important aspects of strongly correlated materials, such as the Mott insulator transition or the emergence of d -wave superconducting pairing, a number of fascinating phenomena emerge from the interplay of different electron orbitals which cannot be captured by an effective model with a single band. Both intra-atomic Coulomb exchange or the presence of crystal field splitting can give rise to a number of intriguing effects, such as, for example the existence of an orbital-selective Mott insulating phase, where only one orbital becomes insulating while the other retains its

²Note that we do not observe a breaking of the unit-cell symmetry, which would suggest that the AF order is only hidden by the SU(2) symmetry but still present (this happens for instance for the spin- $\frac{1}{2}$ Heisenberg model on the square lattice, or the two-band Hubbard model at half filling). Going forward, we also plan to verify the absence of AF order by measuring longer-ranged spin-spin correlators.

metallic properties [IFT98, TN00]. In order to understand this physics from a theoretical perspective, it is clearly necessary to go beyond a single-band system and study multi-band generalizations of the Hubbard model.

In addition to perspectives in strongly correlated materials, multi-band physics is also highly relevant for the description of high-symmetry models, such as $SU(N)$ Hubbard models or related Heisenberg models. These systems host fascinating new types of quantum states including exotic magnetically ordered phases, that are not only of general academic interest but recently have also become experimentally accessible in the context of cold atoms [SHH⁺14, HRS⁺16].

Fully understanding the physical properties of these system in two dimensions is highly nontrivial. First, the enlarged Hilbert space and strong electron-electron correlations pose a challenge to most numerical approaches. Second, one also has to deal with an enlarged parameter space that substantially adds to the complexity of these systems. For instance, the two-band Hubbard model with only nearest-neighbor interactions already contains up to four additional parameters in comparison to its single-band version. Therefore, wide regions of the phase diagram of these models remain blank spots and there is a compelling need for developing numerical methods that can faithfully deal with such systems in an unbiased way.

In this section, we demonstrate that fermionic iPEPS enhanced with non-abelian symmetries may represent a viable tool to deal with such complex multi-band systems in 2D, at least for scenarios where $SU(2)$ orbital symmetry is not broken. To this end, we focus on the repulsive two-band Hubbard model with spin- and orbital degeneracy on the square lattice. Its Hamiltonian is defined as

$$\hat{H}_{2\text{HB}} = -t \sum_{\langle ij \rangle, m, \sigma} (\hat{c}_{im\sigma}^\dagger \hat{c}_{jm\sigma} + \hat{c}_{jm\sigma}^\dagger \hat{c}_{im\sigma}) + \frac{1}{2} (U - \frac{3J}{2}) \sum_i (\hat{N}_i - 2)^2 - J \sum_i (\hat{\mathbf{S}}_i^2 + 2), \quad (5.6)$$

with hopping between nearest-neighbor sites $\langle ij \rangle$, spin index $\sigma \in \{\uparrow, \downarrow\}$, band index $m \in \{1, 2\}$, and the generalized occupation and spin operators, $\hat{N}_i = \sum_{m\sigma} \hat{n}_{im\sigma}$ and $\hat{\mathbf{S}}_i = \sum_m \hat{\mathbf{S}}_{im}$, respectively [GdM13]. The Hamiltonian (5.6) features both an $SU(2)_{\text{spin}}$ and $SU(2)_{\text{flavor}}$ symmetry which we exploit in our iPEPS implementation.

For the sake of simplicity, we consider only the case of $J = 0$ in this initial study and will address the effects of a finite Hund coupling elsewhere [BvdDW17]. The resulting Hamiltonian has the form,

$$\hat{H}'_{2\text{HB}} = -t \sum_{\langle ij \rangle, m, \sigma} (\hat{c}_{im\sigma}^\dagger \hat{c}_{jm\sigma} + \hat{c}_{jm\sigma}^\dagger \hat{c}_{im\sigma}) + \frac{U}{2} \sum_i (\hat{N}_i - 2)^2, \quad (5.7)$$

where the spin and flavor index are now, in principle, interchangeable, since all four fermionic species are degenerate leading to an $SU(4)_{\text{flavor}}$ symmetry. Again we consider $t = 1$ in the following.

To our knowledge, the phase diagram of this system is largely unknown away from integer filling. However, some interesting results are available for certain points in parameter space.

For instance, several studies based on a sign-problem-free determinant quantum Monte-Carlo method addressed the magnetic properties of the model at half filling (two fermions per site, $N = 2$) [CHWW13, WLC⁺14, ZCWW14]. Their findings support the existence of long-ranged antiferromagnetic (AF) order for a wide range of interaction strengths, starting with $U = 2$ or higher [WLC⁺14]. Interestingly, the AF order does not show a monotonic behavior with respect to U as it exhibits a maximum around $U \approx 8$ and then decreases towards larger interactions strengths. Note that the question regarding the persistence of long-ranged AF order in the limit $U \rightarrow \infty$ remains open. A previous QMC study of the corresponding Heisenberg model found no AF order but rather a potential gapless spin-liquid phase in this

regime [Ass05]. Another recent work based on variational QMC [TASB16] addressed the Mott transition of the half-filled Hubbard model, finding a critical coupling $U_c \approx 11$ for the band degenerate case (however, their ansatz is rather biased, as it only accounts for a non-magnetic solution).

In addition, a combined iPEPS and ED study focusses on the quarter-filled case ($N = 1$) in the infinite U limit, where Eq. (5.7) can be mapped on an $SU(4)$ symmetric Heisenberg model [CLP⁺11]. They find a rather curious Neel-like order with dimers alternating between pairs of flavors, which points towards a symmetry breaking of both $SU(4)$ symmetry and translational symmetry.

In this section, we present a first step towards a coherent iPEPS study of the full two-band Hubbard model (5.7) that, in addition to half- and quarter filling, also investigates arbitrary doping regimes. The main challenge for iPEPS in the context of such a two-band model is the strongly enlarged local Hilbert space. In total, we need to deal with four different flavors of fermions (two per band) resulting in a local dimension $d = 16$ per site, larger by a factor of four relative to the $d = 4$ in the one-band version.

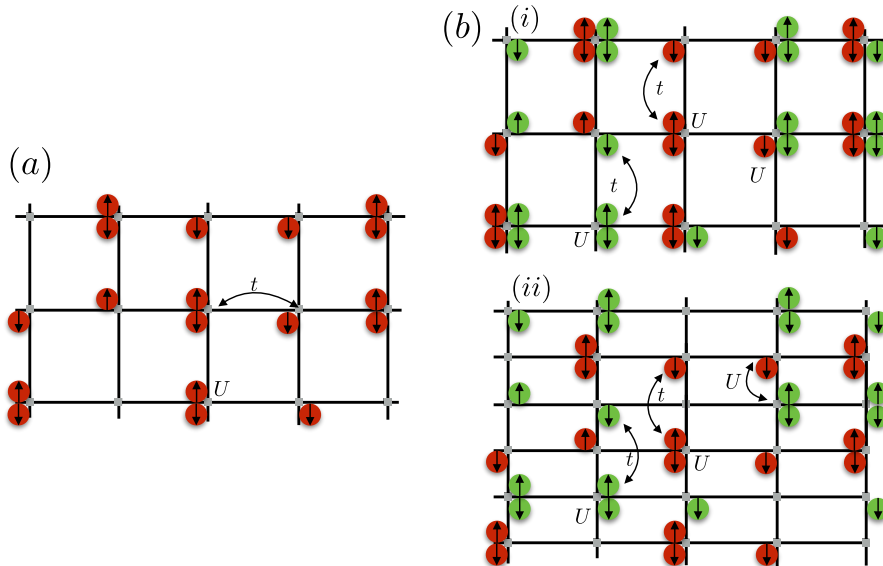


Figure 5.2: Illustration of (a) single-band and (b) two-band setups for a spinful Hubbard model. In the two-band setup (i) all four fermionic flavors are located on a single site, leading to an enlarged Hilbert space of $d = 16$. On the other hand, this setup allows for the incorporation of flavor symmetry. Setup (ii) avoids the enlarged local Hilbert space at the costs of introducing an additional set of sites, causing interaction terms to become longer-ranged.

To treat systems with such an enlarged local state space within iPEPS (or other TN approaches) one can follow two different strategies, illustrated in Fig. 5.2: (i) Either one stacks all different flavors of fermions on the same lattice site and tries to deal with the enlarged local state space. However, this is hardly feasible for standard iPEPS techniques, even when incorporating all abelian symmetries of the system; (ii) one introduces a new set of artificial sites for the fermions in the second band to reduce the local state space to $d = 4$. However, iPEPS then has to handle longer-ranged interactions and correlations in its ansatz.

Here we follow strategy (i) and perform simulations with an iPEPS implementation that exploits $\mathbb{Z}_2 \otimes SU(2)_{\text{spin}} \otimes SU(2)_{\text{flavor}}$ symmetry. In this way, the local state space gets compressed to an effective multiplet dimension of $d^* = 6$, while simultaneously enabling us to retain up to $D^* = 6$ multiplets on each virtual bond, which corresponds to an effective bond dimension of $D = 24$. In this way, we are able to run simple-update simulations for a wide regime of parameters, the results of which are presented in the following.

First of all, we focus on the case of half-filling ($N = 2$) where reference data from

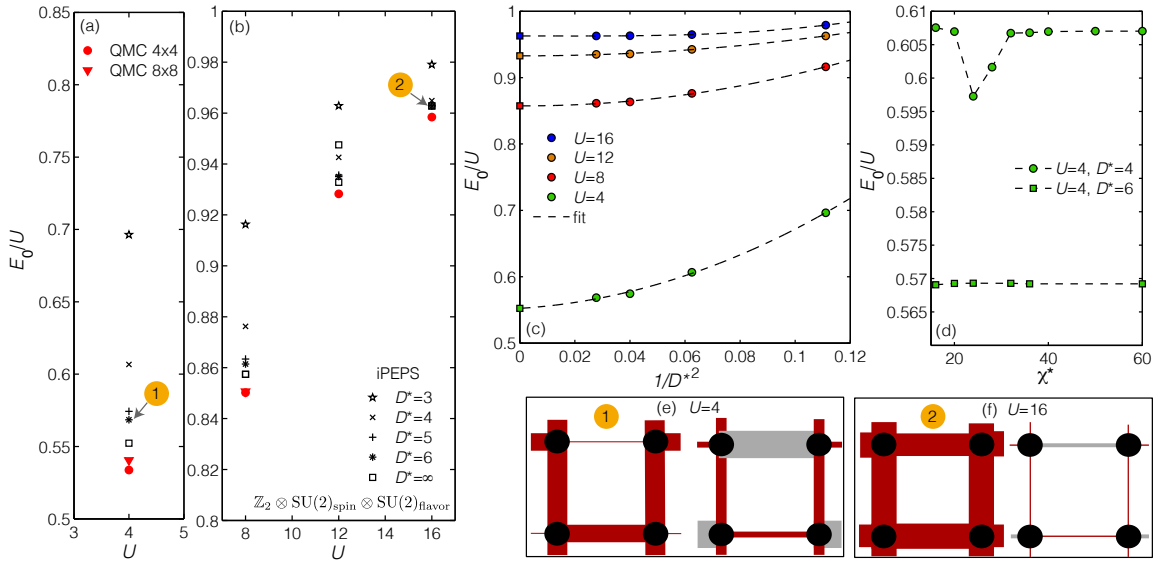


Figure 5.3: Non-abelian iPEPS results for the two-band Hubbard model at half filling ($N = 2$), based on the QSpace tensor library. Panels (a) and (b) display the normalized iPEPS ground-state energy per site (black symbols) as a function of U for various multiplet bond dimensions D^* , in comparison to QMC data (red symbols). The extrapolated iPEPS energies (black squares) are obtained from extrapolating the energies with $1/D^{*2}$, as illustrated in (c). The convergence of the energy with the environmental bond dimension χ^* is shown in (d), where the maximum $\chi^* = 60$ roughly corresponds to $\chi = 200$. Labels 1 and 2 in the panels (a) and (b) point to individual iPEPS wavefunctions shown in (e) and (f), where the filling per site and the bond energy $E_0^{(ij)}$ are proportional to the diameter of the black dots and the width of the bonds, respectively [red (gray) bond correspond to positive (negative) energies]. The additional figures to the right of the labeled wavefunctions depict the shifted bond energies $E_0^{(ij)} - (E_0/2)$ to better illustrate the breaking of translational invariance in the unit cell.

determinant projector QMC is available [Cai17]. The results of this analysis are summarized in Fig. 5.3. Panels (a) and (b) show the normalized ground-state energies per site obtained from a simple-update iPEPS simulation on a 2×2 unit cell for various bond dimensions $D^* = 3, 4, 5, 6$ as a function of the interaction strength. The extrapolated energies for $D^* \rightarrow \infty$ are determined by polynomial fits depicted in Fig. 5.3(c), and the convergence of our measurements with respect to the environmental bond dimension χ^* are shown in Fig. 5.3(d). Note that the QMC results are not free from finite-size effects, so we expect their energies in the thermodynamic limit to still increase to some extent. Nevertheless, we already find very good agreement (roughly 1% deviation) of our extrapolated energies with the QMC results, which confirms the reliability of our approach.

Following the work of Ref. [WLC⁺14] at half filling, we expect the presence of long-ranged AF order for all considered values of U in Fig. 5.3. Since our iPEPS is $SU(2)_{\text{spin}}$ invariant by construction, however, a direct measurement of the magnetization is not possible. Nevertheless, we expect that the symmetry-breaking AF order is somehow hidden in our iPEPS wavefunction. In the context of a spin- $\frac{1}{2}$ Heisenberg model, for example, we observed that the hidden AF order in the ground state leads to an artificial breaking of translational symmetry within the unit cell. Interestingly, we also observe such an effect in the iPEPS wavefunctions shown in Fig. 5.3(e) and (f), where the left figures illustrate the bond energies $E_0^{(ij)}$ and the right figures depict the shifted values $E_0^{(ij)} - (E_0/2)$, where E_0 represents the ground-state energy *per site*. In both cases, we clearly observe that a single bond carries a substantially reduced energy in comparison to the other three. This could signal the presence of AF order, which ultimately should be verified by studying long-ranged

spin-spin correlators. This is left for future research.

For completeness, table 5.1 gives examples of the relevant multiplet contributions encountered in iPEPS simulations upon increasing D^* at half filling.

D^*	$Q (\mathbb{Z}_2, \text{SU}(2)_{\text{spin}}, \text{SU}(2)_{\text{flavor}})$	D
3	$(1, 0, 0) \oplus (-1, 1, 1) \oplus (1, 2, 0)$	$1 + 4 + 3 = 8$
4	$(1, 0, 0) \oplus 2 \cdot (-1, 1, 1) \oplus (1, 2, 0)$	$1 + 8 + 3 = 12$
5	$(1, 0, 0) \oplus 2 \cdot (-1, 1, 1) \oplus (1, 2, 0) \oplus (1, 2, 2)$	$1 + 8 + 3 + 9 = 21$
6	$(1, 0, 0) \oplus 2 \cdot (-1, 1, 1) \oplus (1, 2, 0) \oplus (1, 0, 2) \oplus (1, 2, 2)$	$1 + 8 + 3 + 3 + 9 = 24$

Table 5.1: Typical multiplet configurations obtained from iPEPS simulations with varying multiplet bond dimension D^* at half filling. Here the $\text{SU}(2)$ S labels indicate a multiplet with spin or flavor of $S/2$.

In addition to the special case of a half-filled lattice, iPEPS is also able to treat parameter regimes of arbitrary filling N . We focus on small to intermediate interactions, $U = 4, 8$, and consider the case of finite hole doping $\delta = 2 - N > 0$ in the following, which has not been explored in detail by other methods so far. Fig. 5.4 illustrates our iPEPS results for various doping strengths, which we tune by means of a chemical potential term, $(\mu + \frac{3}{2}U) \sum_i \hat{N}_i$ (the additional prefactor guarantees that the half-filled case corresponds to $\mu = 0$). Figs. 5.4(a) and (c) display the normalized ground-state energies per site as a function of δ for $D^* = 5, 6$, whereas Figs. 5.4(b) and (d) show the filling N as a function of the chemical potential.

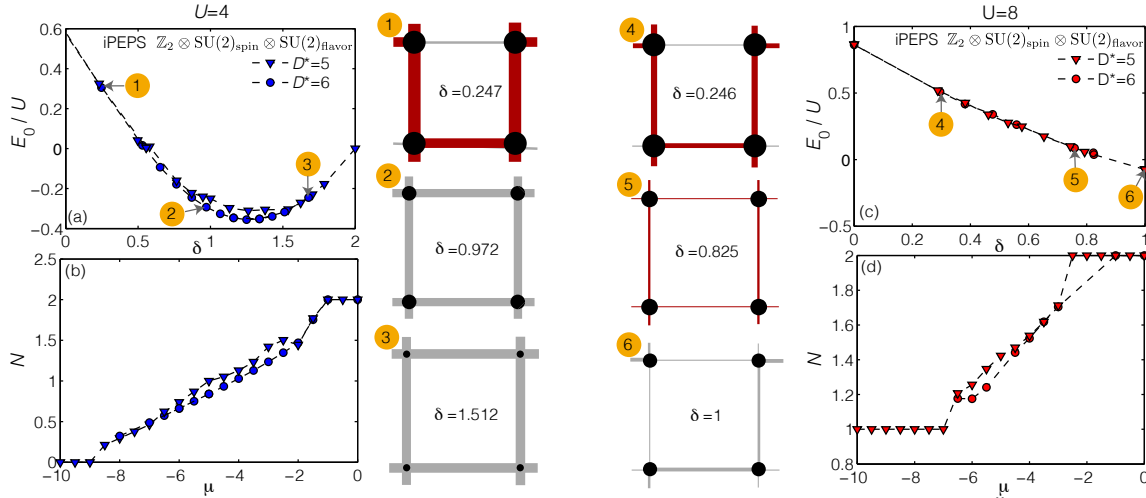


Figure 5.4: Non-abelian iPEPS results for the two-band Hubbard model away from half filling for $U = 4, 8$, based on the QSpace tensor library. Panels (a) and (c) display the normalized ground-state energy per site as a function of doping δ for multiplet bond dimensions $D^* = 5, 6$, whereas (b) and (d) show the filling N as a function of the chemical potential μ . Labels 1-6 in panels (a) and (c) point to individual iPEPS wavefunctions depicted in the center, where the filling per site and the bond energy are proportional to the diameter of the black dots and the width of the bonds, respectively [red (gray) bond correspond to $E_0^{ij} > 0$ (< 0)].

In the case of $U = 4$ we find an energy minimum for $\delta \approx 1.2$. In this regime, we still observe a significant dependence of the energy on bond dimension D^* , hinting at a strongly entangled ground state. From the results of the corresponding Heisenberg model at $\delta = 1$ [CLP⁺11], we additionally expect a dimerized order that cannot be captured properly by a 2×2 unit cell. Additional calculations on a 4×2 unit cell are currently ongoing and might yield wavefunctions with lower energy. Studying the individual wavefunctions (labeled 1, 2, and 3), we only observe a translational symmetry breaking in wavefunction 1 close to

half filling, where AF order potentially is still present. In contrast, the wavefunctions 2 and 3 around quarter filling and in the strongly hole-doped regime, respectively, have a very homogenous structure at $U = 4$.

The convergence of the ground-state energies appears significantly better at intermediate interaction strength $U = 8$, where deviations between iPEPS results with $D^* = 5$ and 6 are barely visible. At the same time, the wavefunctions 5 and 6 around quarter filling show stronger translational symmetry breaking than at $U = 4$. The underlying physical mechanism for this behavior is not clear, yet, but it could be a signal of emerging AF order around $\delta = 1$. Again, studying longer-ranged spin-spin correlators could shed some light on this hypothesis. Alternatively, one could also explicitly allow for symmetry breaking in the iPEPS by means of a simulation with abelian symmetries. However, this does not seem feasible in the current setup.

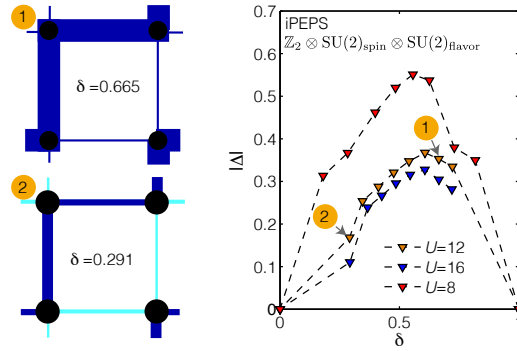


Figure 5.5: Generalized singlet-pairing amplitude $|\Delta|$ per site, measured in iPEPS wavefunctions with $D^* = 5$ as a function of the hole doping δ . $|\Delta|$ is obtained by averaging over the absolute value of Δ_{ij} for each bond in the unit cell. Labels 1 and 2 point to individual iPEPS wavefunctions, where the filling per site and the singlet-pairing amplitude are proportional to the diameter of the black dots and the width of the bonds, respectively [blue (cyan) bond correspond to $\Delta_{ij} > 0$ (< 0)].

In addition to antiferromagnetism, we also expect that superconducting order plays an important role in the two-band Hubbard model at finite hole doping. To check for the presence of d -wave superconductivity, we have measured a generalized singlet-pairing amplitude $\Delta_{ij} = \sum_m \frac{1}{\sqrt{2}} (\hat{c}_{im\uparrow} \hat{c}_{jm\downarrow} - \hat{c}_{im\downarrow} \hat{c}_{jm\uparrow})$. The results for different values of U and δ are displayed in Fig. 5.5. We find that, indeed, superconducting order is present at non-integer hole doping for all considered interaction strengths. Two effects that will require further attention in the future is the suppression of superconductivity at $\delta = 1$, and the fact that Δ decreases with increasing interaction strength. Also the individual values of Δ_{ij} show strong inhomogeneity within the unit cell, something which has not been observed in the one-band Hubbard model. It might be related to a tendency toward spontaneous symmetry breaking of the flavor symmetry that is conserved by construction in our iPEPS implementation, or to the fact that the actual ground state breaks translational symmetry in a different way. Simulations on different unit-cell geometries will shed light on this issue.

In conclusion, we have presented the first fermionic iPEPS simulation of the two-band Hubbard model that incorporates spin- and orbital $SU(2)$ symmetry explicitly in the TN ansatz. The excellent accuracy of our results found at half-filling encouraged us to explore also the hole-doped regime, where our initial results uncover a number of intriguing features. Going forward, much work remains to be done to fully understand the guiding mechanisms and phases in this regime. This includes the study of longer-ranged spin-spin correlators, the comparison to simulations on different unit cells and unveiling the dependencies of various quantities such as energy and d -wave pairing as a function of interaction strength and doping more carefully. Sticking to the model with $J = 0$, the efficiency of iPEPS could be further

enhanced by exploiting the full $SU(4)_{\text{flavor}}$ symmetry present in the Hamiltonian within QSpace [Wei12a]. After fully understanding the phase diagram in this parameter regime, it will be highly interesting to study the effects of finite Hund's coupling J on the emergence of superconductivity and other competing orders. Moreover, it would also be worthwhile to analyze whether abelian iPEPS simulations are numerically feasible in a modified setup [c.f. Fig. 5.2]. This would yield a different perspective on the ground-state properties of the model, especially in the context of spontaneous symmetry breaking.

5.2.4 Three-flavor Hubbard model

In addition to basic $SU(2)$ symmetries, QSpace [Wei12a] also provides a convenient framework for the incorporation of more complex non-abelian symmetries such as $SU(N > 2)$. To explore the potential of this feature within fermionic iPEPS, we consider a three-flavor Hubbard model with $SU(3)$ symmetric repulsive Coloumb interaction. Its Hamiltonian has the form,

$$\hat{H}_{SU(3)} = -t \sum_{\langle ij \rangle, m} (\hat{c}_{im}^\dagger \hat{c}_{jm} + \hat{c}_{jm}^\dagger \hat{c}_{im}) + \frac{U}{2} \sum_i (\hat{N}_i - 2)^2, \quad (5.8)$$

with flavor index $m \in \{1, 2, 3\}$ and $\hat{N}_i = \sum_m \hat{n}_{im}$ ($t = 1$). Although the Hamiltonian (5.8) is not naturally realized by the atomic configuration of any real material, this model, as well as other $SU(N > 2)$ realizations of the fermionic Hubbard model, currently attract a lot of attention in context of cold-atom experiments based on alkaline earth-like atoms such as ytterbium [SHH⁺14, HRS⁺16], where such systems have become directly accessible in highly controlled setups. $SU(N)$ symmetric systems feature a number of exotic phases and magnetic properties, that are of interest from a condensed matter perspective. In addition, they are also relevant for other fields, for example in the context of studying lattice gauge theories for quantum chromodynamics [BBD⁺13].

So far, little is known for the specific $SU(3)$ symmetric Hamiltonian (5.7) embedded in a 2D square lattice. Some work has been done for the weak to intermediate coupling limit, where one expects the emergence of a flavor density wave breaking the translational symmetry of the lattice [HH04]. At half filling in particular, it is expected that two flavors occupy the same lattice site whereas neighboring sites exclusively host the third flavor, such that a two-sublattice structure emerges. In the strong coupling limit and integer filling the model can be mapped on a $SU(3)$ Heisenberg model, which is believed to favor a three-sublattice order with finite magnetic moments [BCL⁺12].

Here we follow the strategy employed in the previous section and reduce the numerical complexity of the system (5.8) by incorporating the non-abelian $SU(3)$ symmetry in the fermionic iPEPS ansatz. To this end, the large local state space $d = 8$ can be compressed to $d^* = 3$ multiplets on the $SU(3)$ multiplet level and we can perform simple-update calculations with a multiplet bond dimensions up to $D^* = 6$. Again, the symmetry sectors are dynamically adapted during the optimization. We illustrate examples of the relevant multiplet contributions encountered in iPEPS simulations with varying D^* at half filling ($N = 1.5$) in table 5.2.

We perform iPEPS simulations on both 2×2 and 3×3 unit cells with two and three different tensors, respectively, to slightly bias the emergence of the two- and three-sublattice order expected from the predictions discussed above (although these state are expected to explicitly break the $SU(3)$ symmetry).

Figs. 5.6(a) and (b) summarize our initial results for the normalized ground-state energies per site as a function of filling N , at weak coupling $U = 1$ and intermediate to strong coupling $U = 6$, respectively. In the two cases, simulations on both unit-cell geometries surprisingly yield very compatible ground-state energies. Only in the half-filled case ($N = 1.5$) at $U =$

D^*	$Q (\mathbb{Z}_2, \text{SU}(3)_{\text{flavor}})$	D
4	$(-1, 00) \oplus (-1, 01) \oplus (1, 01) \oplus (1, 10)$	$1 + 3 + 3 + 3 = 10$
5	$(-1, 00) \oplus (-1, 11) \oplus (1, 01) \oplus (1, 10)$	$1 + 8 + 3 + 3 = 16$
6	$(-1, 00) \oplus (-1, 11) \oplus 2 \cdot (1, 01) \oplus (1, 10)$	$1 + 8 + 6 + 3 = 19$

Table 5.2: Typical multiplet configurations obtained from $\text{SU}(3)$ symmetric iPEPS simulations with varying multiplet bond dimension D^* at half filling. For details on the $\text{SU}(3)$ multiplet labels see Ref. [Wei12a].

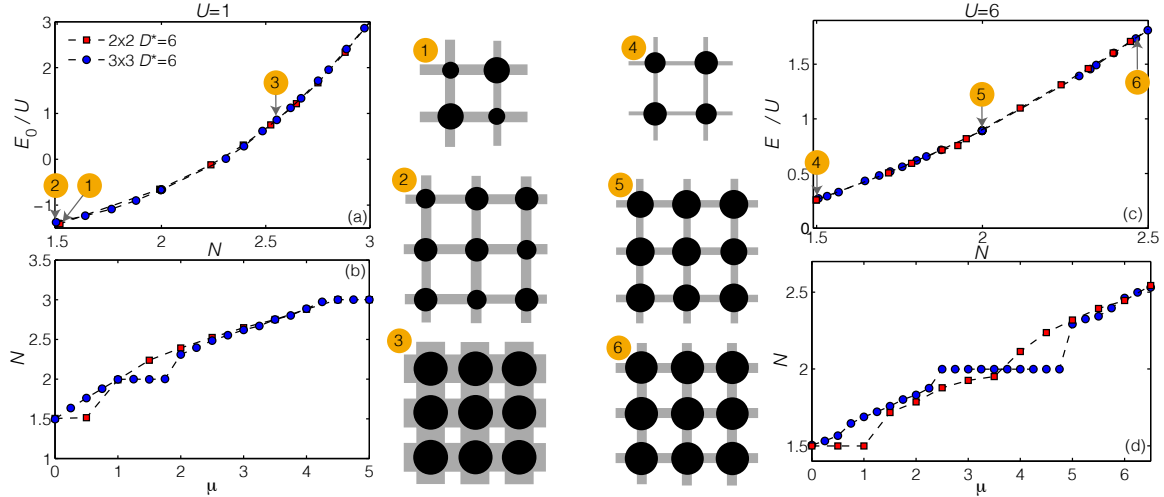


Figure 5.6: Non-abelian iPEPS results for the three-flavor Hubbard model for $U = 1, 6$, based on the QSpace tensor library. Panels (a) and (c) display the normalized ground-state energy per site as a function of filling N for iPEPS simulations on a 2×2 and 3×3 unit cell, whereas (b) and (d) show the filling N as a function of the chemical potential μ . Labels 1-6 in the panels (a) and (c) point to individual iPEPS wavefunctions depicted in the center, where the filling per site and the bond energy are proportional to the diameter of the black dots and the width of the bonds, respectively.

1 the 2×2 cluster gives a roughly 2-3% lower ground-state energy in comparison to its counterpart on the 3×3 unit cell. Interestingly, in both cases (wavefunction 1 and 2) we observe a strong translational symmetry breaking in the form of modulation of the occupancy on different sites. This is qualitatively in agreement with Ref. [HH04], that predicts a phase with two-sublattice order with single and double occupancy on neighboring sites. This is almost realized by wavefunction 1 shown in Fig. 5.6 with occupancies $N \approx 1.19$ and $N \approx 1.81$ on neighboring sites. The density modulation are substantially suppressed on the 3×3 unit cell, where we find two sites having the same occupancy $N \approx 1.58$ while slightly fewer particles occupy the third site $N \approx 1.32$. The density-wave modulation disappears both in the case of larger filling and stronger interaction, as illustrated by the wavefunctions 3,4,5, and 6 in Fig. 5.6.

Finally, we note that the occupancy is not a steadily increasing function of the chemical potential term, $(\mu + U) \sum_i \hat{N}_i$, which is used to modify the filling. This can be observed in Figs. 5.6(b) and (d), where the simulations on both unit cells exhibit plateau-like structures at fillings of $N = 1.5$ and $N = 2$, respectively. Typically this is a signature of Mott physics, which is to some extent also expected in the three-flavor model at $N = 2$ [GB09]. However, an artificial locking may also occur if the occupation inside a unit cell changes by integers (this effect is expected to depend on numerical details and should become less pronounced with increasing D^*). This can be observed for the plateau at $N = 1.5$ filling, which corresponds to an integer filling of the 2×2 unit cell. On the other hand, the $N = 2$ plateau is nearly

absent in this setup. The reason for this behavior still remains unclear.

Going forward, it would also be interesting to study the hole doped regime, where, according to [BCL⁺12], we should encounter a three-lattice substructure in the limit of strong interactions. Furthermore, we should be able to reveal additional information about the flavor order by studying (i) longer-ranged correlators and (ii) switching off the SU(3) in favor of two abelian U(1) symmetries and explicitly allowing spontaneous breaking of the flavor symmetry. We expect that iPEPS simulations should still be feasible in this setup for small bond dimensions $D < 10$.

Conclusion and outlook

In this thesis, we explored a set of intriguing topics in low-dimensional quantum many-body systems ranging from quantum criticality in impurity models, over spectral features of 1D spin- and electron materials, to the treatment of zero and finite-temperature properties in 2D lattice models for frustrated magnets and itinerant fermions. To account for the strong quantum correlations present in all of these systems, we employed unbiased tensor network techniques based on matrix product states (MPS) and projected entangled-pair states (PEPS). Here we present a summary of the main results of this thesis and address potential directions for future research.

Quantum criticality of bosonic quantum impurity models

In our MPS simulation of the two-bath spin-boson model we discovered exotic quantum critical properties. Our findings indicate that this system presents, in a sense, the simplest quantum model violating the quantum-to-classical correspondence. Moreover, we revealed universal properties of the quantum critical wavefunction in the one-bath spin-boson model such as a universal decay of entanglement between an impurity and its bath, that are likely to occur in other critical systems as well. In a subsequent work we proposed a new type of “open” Wilson chain (OWC) that successfully incorporates missing bath modes neglected in standard constructions. This enabled us to settle a long-standing open issue regarding the critical properties of the spin-boson model at finite temperatures.

Especially the OWC setup presents a promising basis for future research beyond the field of quantum criticality, as it is not limited to bosonic impurity models. For instance, it sets the scene for the controlled incorporation of dissipative effects in the Wilson chain setup required for studying nonequilibrium situations. In addition, the OWC construction paves the way to the solution of multi-channel impurity models with off-diagonal couplings relevant for multi-impurity models and dynamical mean-field theory (DMFT) applications involving spin-orbit coupling.

Our MPS techniques also have the potential to shed light on a number of open questions arising in different generalizations of the spin-boson model. In particular, the study of the Bose-Fermi-Kondo model [SRIS01, SRIS03] presents an interesting challenge from two different perspectives. First of all, MPS simulations could help to reach full consensus on the nature of the critical properties [GI05]. Second, the Bose-Fermi-Kondo model describes the local physics of the Kondo-lattice model in the DMFT context, an effective system relevant for certain types of heavy fermion materials [TUM⁺94, Hew97]. An MPS-based impurity solver could provide new insight into these systems by building on recently developed time-evolution algorithms for bosonic systems [BDV⁺15, SC16].

Spectral features of 1D quantum systems

Our work on spectral functions revealed new information about the effects of an applied magnetic field on the dynamical properties of the two spin- $\frac{1}{2}$ materials Cs_2CoCl_4 and $\text{Cu}_3(\text{CO}_3)_2(\text{OH})_2$ at zero and finite temperatures, which could guide potential inelastic neutron scattering experiments on the compounds in the future. Moreover, we proposed a symmetry-enhanced version of the minimally entangled typical states (METTS) algorithm and verified the validity of a perturbative functional RG approach for quantum point contacts.

On a technical, one important open question concerns the search for the most efficient spectral algorithm. Building on our initial study, which pointed out close similarities in the entanglement structure of an MPS subject to real-time evolution or Chebyshev expansion, it remains to be settled whether tDMRG or CheMPS presents the best choice.

Another topic that deserves further attention involves models with longer-ranged interactions. With new time-evolution techniques available [HCO⁺11, ZMK⁺15], studies of spectral functions in ladder systems [BKL⁺11, BLE⁺17] or in even more 2D-like setups [HZOP16, GVMP17] have become feasible and opens access to addressing truly new physics.

Finally, we expect that MPS tools can also provide viable insight into the nonequilibrium properties of interacting quantum point contacts. By studying quench scenarios, first steps into this direction have already been taken [Zen17].

Extending the range of two-dimensional tensor network techniques

In the context of 2D quantum systems, we demonstrated for the first time the viability and competitiveness of MPS algorithms at finite temperatures. Remarkably, our combination of density-matrix purification and METTS was not only able to access the finite-temperature phase diagram of the spin- $\frac{1}{2}$ triangular Heisenberg model for a wide range of temperatures, our METTS protocol also allowed for detecting the critical temperature of finite-temperature phase transitions in the presence of frustrated interactions. Moreover, we performed the first fermionic iPEPS simulation that exploited a variety of non-abelian symmetries, enabling the treatment of fermionic systems up to a bond dimension $D = 24$ on a square lattice. In this way, we demonstrated that complex models are becoming numerically accessible for iPEPS and presented promising initial results for the three-flavor and the two-band Hubbard model.

Going forward, our work on symmetry-enhanced iPEPS sets the scene for an unbiased numerical study of the full zero-temperature phase diagram of the two-band Hubbard model and related systems of comparable complexity [GdM13], with potential impact towards many fields which currently are at the heart of condensed matter physics, such as high- T_c superconductivity. Related topics include the study of other high-symmetry Heisenberg and Hubbard models featuring exotic magnetic properties, that have recently become experimentally accessible with cold atoms [SHH⁺14, HRS⁺16].

Finally, our work towards controlling finite-temperature properties with MPS techniques also opens many new directions. On a technical level, it would be highly beneficial to transfer our ideas to other tensor networks such as PEPS. For example, a finite-temperature PEPS construction [CCD12, CD14] could replace MPS as the cluster solver in numerical link-cluster expansions. Finite-size PEPS should also be useful for extending the METTS technique to lower temperatures and larger systems. Our work also represents an initial step towards uncovering new physics in various settings. Due to the lack of alternative approaches, there exists a vast number of open questions regarding the finite-temperature properties and the nature of finite-temperature phase transitions in frustrated systems, that could be answered with these tensor network techniques.

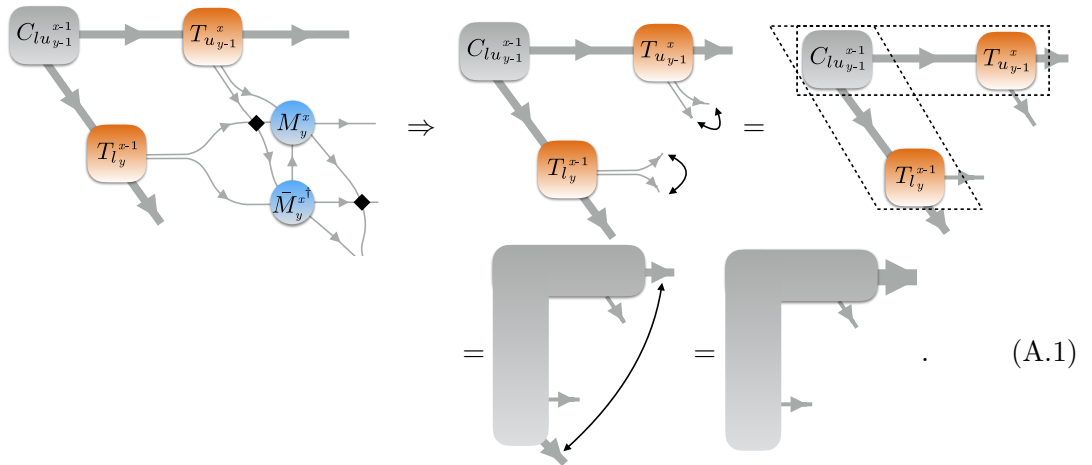
Appendix

Effective contractions in the presence of non-abelian symmetries

The common rationale for the effective implementation of contractions in the presence of non-abelian and also abelian symmetries is to minimize the number of open indices per tensor while always preserving the optimal cost scaling [see Sec. 2.5.2 for more details]. The optimal cost scaling already fixes the contraction order to the most extent. Given this contraction order, we then attempt to reduce the number of open indices per tensor to three or less in each individual step by fusing smaller indices together into larger ones.

Here we illustrate this approach explicitly for the example of contracting the full tensor network in Eq. (5.2) such that we end up with the matrix representation shown in Eq. (5.3).

First we fuse the two small bond indices of the transfer tensors not involved in this first contraction steps. Then we contract the corner matrix with the two transfer tensors. Subsequently, we combine the two environmental bond indices into one very thick index,



To retain the optimal cost scaling, we next apply the M tensor and its conjugate separately. To this end, we first have to split the two combined bond indices of the boundary tensor, then apply the first fermionic swap gate (black diamond), and thereafter refuse them in a different combination in line with the contraction order. At the same time, the bond indices

of M_y^x and $\bar{M}_y^{x\dagger}$ are combined correspondingly,

(A.2)

Note that we omitted drawing the second swap gate in Eq. (A.2) to simplify the diagram; it will be integrated into the tensor at a later step. We now absorb M_y^x and $\bar{M}_y^{x\dagger}$ into the big tensor and then split the bond indices once more

(A.3)

At this point, we need to reintroduce the second fermionic swap gate, which can now be absorbed directly into the big tensor. Then we reindex the indices in a different order and finally obtain the matrix representation shown in Eq. (5.3).

(A.4)

List of Figures

2.1	Illustration of subregion \mathcal{C} and \mathcal{D} required to obtain the entanglement entropy $S(\rho_{\mathcal{C}})$ in one- and two dimensions. The volume of region \mathcal{C} is given by L in 1D and by L^2 in 2D.	10
2.2	Example of square lattice cluster for 2D-DMRG calculation. The dashed red line indicates the quasi-one-dimensional MPS path through the cluster. . . .	30
2.3	Required MPS bond dimension for representing the purified density matrix in comparison to a METTS ensemble (maximum bond dimension of sample shown) illustrating complementary of both finite-temperature methods. (a) For the spin- $\frac{1}{2}$ triangular lattice Heisenberg model on a width-4 cylinder, METTS reaches significantly lower temperatures than accessible with purification (reprint from our publication [BZWS17]) (b) For simulating the finite-temperature dynamics of a spin- $\frac{1}{2}$ Heisenberg model on a 1D chain, METTS is able to reach longer time scales at low temperatures $T = 1/20$. Purification becomes more efficient at $T = 1/4$, where the MPS representation of the density matrix for times $t > 15$ requires a smaller bond dimension than a single METTS (bond dimension D is dynamically truncated in both cases according to the SVD spectrum; reprint from our publication [BvDW15]).	37
2.4	Evolution of the excitation over (a) time $\langle \hat{S}_j^z \hat{S}_0^z(t) \rangle$ and (b),(c) iteration order $\mu_n(j) = \langle \psi_0 \hat{S}_j^\alpha t_n \rangle$. Reprinted from our publication [BWvDG16].	43
2.5	(a) Local spectral function $\langle \hat{S}_0^z \hat{S}_0^z \rangle(\omega)$ obtained from tDMRG and CheMPS for the spin- $\frac{1}{2}$ model for Cs_2CoCl_4 with $N = 100$ spins directly at the phase boundary for $h = 1.56$ and $T = 0$. (b)-(d) Comparison of entanglement entropy S_{ent} , bond dimension D , and cumulative CPU time t_{CPU} . Reprinted from our publication [BWvDG16].	44
2.6	Illustration of 3x3 square cluster.	46
2.7	CTM coarse graining move to the left lattice direction: (i) extra unit cell is first inserted, and then column-wise integrated into the left part of the environment by performing two subsequent (ii) absorption and (iii) renormalization steps.	52
2.8	CTM coarse graining move to the top of the lattice: (i) extra unit cell is first inserted, and then row-wise integrated into the upper part of the environment by performing two subsequent (ii) absorption and (iii) renormalization steps (only first step is shown).	53

- 2.9 A unit cell of size 3×2 consists of six different M tensors (here denoted M, N, O, P, Q , and R). For each of the six relative coordinates in the unit cell, we have to obtain a 2×2 CTM representation (indicated by the solid and dashed squares, and explicitly illustrated for two examples). Therefore, the CTM scheme here requires storing 24 corner matrices and 24 transfer tensors in total. 57
- 5.1 Non-abelian iPEPS results for the t - J model with $J = 0.4$, based on the QSpace tensor library. The panel in the center shows the energy per hole, E_{hole} , as a function of hole doping δ , obtained via both simple- and full-updated calculations on two different types of unit cells. Markers 1-6 in the panel point to individual iPEPS wavefunctions, where the hole doping per site is proportional to the diameter of the red dots, the length of the arrow indicates the magnitude of the magnetic moment, and the width of the bonds is proportional to their energy. 216
- 5.2 Illustration of (a) single-band and (b) two-band setups for a spinful Hubbard model. In the two-band setup (i) all four fermionic flavors are located on a single site, leading to an enlarged Hilbert space of $d = 16$. On the other hand, this setup allows for the incorporation of flavor symmetry. Setup (ii) avoids the enlarged local Hilbert space at the costs of introducing an additional set of sites, causing interaction terms to become longer-ranged. 219
- 5.3 Non-abelian iPEPS results for the two-band Hubbard model at half filling ($N = 2$), based on the QSpace tensor library. Panels (a) and (b) display the normalized iPEPS ground-state energy per site (black symbols) as a function of U for various multiplet bond dimensions D^* , in comparison to QMC data (red symbols). The extrapolated iPEPS energies (black squares) are obtained from extrapolating the energies with $1/D^{*2}$, as illustrated in (c). The convergence of the energy with the environmental bond dimension χ^* is shown in (d), where the maximum $\chi^* = 60$ roughly corresponds to $\chi = 200$. Labels 1 and 2 in the panels (a) and (b) point to individual iPEPS wavefunctions shown in (e) and (f), where the filling per site and the bond energy $E_0^{(ij)}$ are proportional to the diameter of the black dots and the width of the bonds, respectively [red (gray) bond correspond to positive (negative) energies]. The additional figures to the right of the labeled wavefunctions depict the shifted bond energies $E_0^{(ij)} - (E_0/2)$ to better illustrate the breaking of translational invariance in the unit cell. 220
- 5.4 Non-abelian iPEPS results for the two-band Hubbard model away from half filling for $U = 4, 8$, based on the QSpace tensor library. Panels (a) and (c) display the normalized ground-state energy per site as a function of doping δ for multiplet bond dimensions $D^* = 5, 6$, whereas (b) and (d) show the filling N as a function of the chemical potential μ . Labels 1-6 in panels (a) and (c) point to individual iPEPS wavefunctions depicted in the center, where the filling per site and the bond energy are proportional to the diameter of the black dots and the width of the bonds, respectively [red (gray) bond correspond to $E_0^{ij} > 0$ (< 0)]. 222

- 5.5 Generalized singlet-pairing amplitude $|\Delta|$ per site, measured in iPEPS wavefunctions with $D^* = 5$ as a function of the hole doping δ . $|\Delta|$ is obtained by averaging over the absolute value of Δ_{ij} for each bond in the unit cell. Labels 1 and 2 point to individual iPEPS wavefunctions, where the filling per site and the singlet-pairing amplitude are proportional to the diameter of the black dots and the width of the bonds, respectively [blue (cyan) bond correspond to $\Delta_{ij} > 0$ (< 0)]. 222
- 5.6 Non-abelian iPEPS results for the three-flavor Hubbard model for $U = 1, 6$, based on the QSpace tensor library. Panels (a) and (c) display the normalized ground-state energy per site as a function of filling N for iPEPS simulations on a 2×2 and 3×3 unit cell, whereas (b) and (d) show the filling N as a function of the chemical potential μ . Labels 1-6 in the panels (a) and (c) point to individual iPEPS wavefunctions depicted in the center, where the filling per site and the bond energy are proportional to the diameter of the black dots and the width of the bonds, respectively. 224

Bibliography

- [A⁺97] Philip W Anderson et al., *The theory of superconductivity in the high- t_c cuprate superconductors*, vol. 446, Princeton University Press Princeton, NJ, 1997. See pages: [2](#) and [179](#)
- [ADP16] Fabien Alet, Kedar Damle, and Sumiran Pujari, *Sign-problem-free monte carlo simulation of certain frustrated quantum magnets*, Phys. Rev. Lett. **117** (2016), 197203. See page: [5](#)
- [AF09] A. Alvermann and H. Fehske, *Sparse polynomial space approach to dissipative quantum systems: Application to the sub-ohmic spin-boson model*, Phys. Rev. Lett. **102** (2009), 150601. See page: [4](#)
- [AKLT87] Ian Affleck, Tom Kennedy, Elliott H. Lieb, and Hal Tasaki, *Rigorous results on valence-bond ground states in antiferromagnets*, Phys. Rev. Lett. **59** (1987), 799–802. See page: [13](#)
- [AM05] Neil W Ashcroft and N David Mermin, *Solid state physics (holt, rinehart and winston, new york, 1976)*, Google Scholar **403** (2005). See page: [1](#)
- [And61] P. W. Anderson, *Localized magnetic states in metals*, Phys. Rev. **124** (1961), 41–53. See page: [25](#)
- [Arb12] Peter Arbenz, *Lecture notes on solving large scale eigenvalue problems*. See page: [28](#)
- [AS05] Frithjof B. Anders and Avraham Schiller, *Real-time dynamics in quantum-impurity systems: A time-dependent numerical renormalization-group approach*, Phys. Rev. Lett. **95** (2005), 196801. See page: [24](#)
- [Ass05] F. F. Assaad, *Phase diagram of the half-filled two-dimensional SU(n) hubbard-heisenberg model: A quantum monte carlo study*, Phys. Rev. B **71** (2005), 075103. See page: [219](#)
- [Bal10] Leon Balents, *Spin liquids in frustrated magnets*, Nature **464** (2010), no. 7286, 199–208. See pages: [2](#), [3](#), and [179](#)
- [Bar13] Thomas Barthel, *Precise evaluation of thermal response functions by optimized density matrix renormalization group schemes*, New J. Phys. **15** (2013), no. 7, 073010. See pages: [31](#), [39](#), [40](#), [44](#), and [178](#)
- [Bar17] Thomas Barthel, *One-dimensional quantum systems at finite temperatures can be simulated efficiently on classical computers*, arXiv preprint arXiv:1708.09349 (2017). See page: [35](#)

- [BB15] Moritz Binder and Thomas Barthel, *Minimally entangled typical thermal states versus matrix product purifications for the simulation of equilibrium states and time evolution*, Phys. Rev. B **92** (2015), 125119. See page: [37](#)
- [BB17] ———, *Symmetric minimally entangled typical thermal states for canonical and grand-canonical ensembles*, arXiv preprint arXiv:1701.03872 (2017). See page: [37](#)
- [BBD⁺13] D. Banerjee, M. Bögli, M. Dalmonte, E. Rico, P. Stebler, U.-J. Wiese, and P. Zoller, *Atomic quantum simulation of $U(n)$ and $SU(n)$ non-abelian lattice gauge theories*, Phys. Rev. Lett. **110** (2013), 125303. See page: [223](#)
- [BCBB⁺17] Zach Blunden-Codd, Soumya Bera, Benedikt Bruognolo, Nils-Oliver Linden, Alex W. Chin, Jan von Delft, Ahsan Nazir, and Serge Florens, *Anatomy of quantum critical wave functions in dissipative impurity problems*, Phys. Rev. B **95** (2017), 085104. See pages: [24](#), [27](#), and [104](#)
- [BCL⁺12] Bela Bauer, Philippe Corboz, Andreas M. Läuchli, Laura Messio, Karlo Penc, Matthias Troyer, and Frédéric Mila, *Three-sublattice order in the $su(3)$ heisenberg model on the square and triangular lattice*, Phys. Rev. B **85** (2012), 125116. See pages: [223](#) and [225](#)
- [BCOT11] B. Bauer, P. Corboz, R. Orús, and M. Troyer, *Implementing global abelian symmetries in projected entangled-pair state algorithms*, Phys. Rev. B **83** (2011), 125106. See pages: [77](#) and [212](#)
- [BCP08] Ralf Bulla, Theo A. Costi, and Thomas Pruschke, *Numerical renormalization group method for quantum impurity systems*, Rev. Mod. Phys. **80** (2008), 395–450. See pages: [4](#), [24](#), [25](#), and [26](#)
- [BDSW96] Charles H. Bennett, David P. DiVincenzo, John A. Smolin, and William K. Wootters, *Mixed-state entanglement and quantum error correction*, Phys. Rev. A **54** (1996), 3824–3851. See page: [9](#)
- [BDV⁺15] C. Brockt, F. Dorfner, L. Vidmar, F. Heidrich-Meisner, and E. Jeckelmann, *Matrix-product-state method with a dynamical local basis optimization for bosonic systems out of equilibrium*, Phys. Rev. B **92** (2015), 241106. See page: [226](#)
- [BGS⁺13] O. Breunig, M. Garst, E. Sela, B. Buldmann, P. Becker, L. Bohatý, R. Müller, and T. Lorenz, *Spin- $\frac{1}{2}$ xxz chain system cs_2cocl_4 in a transverse magnetic field*, Phys. Rev. Lett. **111** (2013), 187202. See page: [42](#)
- [BHS⁺13] Florian Bauer, Jan Heyder, Enrico Schubert, David Borowsky, Daniela Taubert, Benedikt Bruognolo, Dieter Schuh, Werner Wegscheider, Jan von Delft, and Stefan Ludwig, *Microscopic origin of the /‘0.7-anomaly/’ in quantum point contacts*, Nature **501** (2013), no. 7465, 73–78. See page: [164](#)
- [BKL⁺11] Pierre Bouillot, Corinna Kollath, Andreas M. Läuchli, Mikhail Zvonarev, Benedikt Thielemann, Christian Rüegg, Edmond Orignac, Roberta Citro, Martin Klanjšek, Claude Berthier, Mladen Horvatić, and Thierry Giamarchi, *Statics and dynamics of weakly coupled antiferromagnetic spin- $\frac{1}{2}$ ladders in a magnetic field*, Phys. Rev. B **83** (2011), 054407. See pages: [40](#) and [227](#)
- [BL14] Lars Bonnes and Andreas M Läuchli, *Superoperators vs. trajectories for matrix product state simulations of open quantum system: a case study*, arXiv preprint arXiv:1411.4831 (2014). See page: [31](#)

- [BLE⁺17] AK Bera, B Lake, FHL Essler, L Vanderstraeten, C Hubig, U Schollwöck, ATMN Islam, A Schneidewind, and DL Quintero-Castro, *Spinon confinement in a quasi one dimensional anisotropic heisenberg magnet*, arXiv preprint arXiv:1705.01259 (2017). See page: [227](#)
- [BLS⁺17] B. Bruognolo, N.-O. Linden, F. Schwarz, S.-S. B. Lee, K. Stadler, A. Weichselbaum, M. Vojta, F. B. Anders, and J. von Delft, *Open wilson chains for quantum impurity models: Keeping track of all bath modes*, Phys. Rev. B **95** (2017), 121115. See pages: [24](#), [26](#), [27](#), and [115](#)
- [BPE09] Thomas Barthel, Carlos Pineda, and Jens Eisert, *Contraction of fermionic operator circuits and the simulation of strongly correlated fermions*, Phys. Rev. A **80** (2009), 042333. See page: [69](#)
- [BPM12] Jens H. Bardarson, Frank Pollmann, and Joel E. Moore, *Unbounded growth of entanglement in models of many-body localization*, Phys. Rev. Lett. **109** (2012), 017202. See page: [34](#)
- [BS14] A. Braun and P. Schmitteckert, *Numerical evaluation of green's functions based on the chebyshev expansion*, Phys. Rev. B **90** (2014), 165112. See pages: [41](#) and [42](#)
- [BSW09] Thomas Barthel, Ulrich Schollwöck, and Steven R. White, *Spectral functions in one-dimensional quantum systems at finite temperature using the density matrix renormalization group*, Phys. Rev. B **79** (2009), 245101. See pages: [40](#) and [164](#)
- [BTV03] Ralf Bulla, Ning-Hua Tong, and Matthias Vojta, *Numerical renormalization group for bosonic systems and application to the sub-ohmic spin-boson model*, Phys. Rev. Lett. **91** (2003), 170601. See pages: [4](#) and [81](#)
- [BvDW15] Benedikt Bruognolo, Jan von Delft, and Andreas Weichselbaum, *Symmetric minimally entangled typical thermal states*, Phys. Rev. B **92** (2015), 115105. See pages: [31](#), [35](#), [37](#), [38](#), [42](#), [77](#), [147](#), [178](#), and [231](#)
- [BvDW17] Benedikt Bruognolo, Jan von Delft, and Andreas Weichselbaum, To be published (2017). See page: [218](#)
- [BWG⁺14] Benedikt Bruognolo, Andreas Weichselbaum, Cheng Guo, Jan von Delft, Imke Schneider, and Matthias Vojta, *Two-bath spin-boson model: Phase diagram and critical properties*, Phys. Rev. B **90** (2014), 245130. See pages: [24](#), [26](#), [27](#), [77](#), and [83](#)
- [BWvDG16] Benedikt Bruognolo, Andreas Weichselbaum, Jan von Delft, and Markus Garst, *Dynamic structure factor of the spin- $\frac{1}{2}$ xxz chain in a transverse field*, Phys. Rev. B **94** (2016), 085136. See pages: [27](#), [31](#), [35](#), [38](#), [42](#), [43](#), [44](#), [135](#), and [231](#)
- [BZH⁺03] László Borda, Gergely Zaránd, Walter Hofstetter, B. I. Halperin, and Jan von Delft, *Su(4) fermi liquid state and spin filtering in a double quantum dot system*, Phys. Rev. Lett. **90** (2003), 026602. See page: [24](#)
- [BZWS17] Benedikt Bruognolo, Zhenyue Zhu, Steven R White, and E Miles Stoudenmire, *Matrix product state techniques for two-dimensional systems at finite temperature*, arXiv preprint arXiv:1705.05578 (2017). See pages: [13](#), [30](#), [31](#), [32](#), [33](#), [35](#), [37](#), [77](#), [181](#), and [231](#)

- [Cai17] Zi Cai, Private communication (2017). See page: [220](#)
- [CC05] Pasquale Calabrese and John Cardy, *Evolution of entanglement entropy in one-dimensional systems*, Journal of Statistical Mechanics: Theory and Experiment **2005** (2005), no. 04, P04010. See page: [34](#)
- [CCD12] Piotr Czarnik, Lukasz Cincio, and Jacek Dziarmaga, *Projected entangled pair states at finite temperature: Imaginary time evolution with ancillas*, Phys. Rev. B **86** (2012), 245101. See page: [227](#)
- [CCX⁺17] Jing Chen, Song Cheng, Haidong Xie, Lei Wang, and Tao Xiang, *On the equivalence of restricted boltzmann machines and tensor network states*, arXiv preprint arXiv:1701.04831 (2017). See page: [8](#)
- [CD14] Piotr Czarnik and Jacek Dziarmaga, *Fermionic projected entangled pair states at finite temperature*, Phys. Rev. B **90** (2014), 035144. See pages: [180](#) and [227](#)
- [CD15] ———, *Variational approach to projected entangled pair states at finite temperature*, Phys. Rev. B **92** (2015), 035152. See page: [180](#)
- [CDO17] Piotr Czarnik, Jacek Dziarmaga, and Andrzej M Oleś, *Overcoming the sign problem at finite temperature: Quantum tensor network for the orbital e_g model on an infinite square lattice*, arXiv preprint arXiv:1703.03586 (2017). See page: [180](#)
- [CE06] M Cramer and J Eisert, *Correlations, spectral gap and entanglement in harmonic quantum systems on generic lattices*, New Journal of Physics **8** (2006), no. 5, 71. See page: [10](#)
- [CEVV10] Philippe Corboz, Glen Evenbly, Frank Verstraete, and Guifré Vidal, *Simulation of interacting fermions with entanglement renormalization*, Phys. Rev. A **81** (2010), 010303. See page: [69](#)
- [CFL08] Chung-Pin Chou, Noboru Fukushima, and Ting Kuo Lee, *Cluster-glass wave function in the two-dimensional extended $t-j$ model*, Phys. Rev. B **78** (2008), 134530. See page: [216](#)
- [CHWW13] Zi Cai, Hsiang-Hsuan Hung, Lei Wang, and Congjun Wu, *Quantum magnetic properties of the $su(2n)$ hubbard model in the square lattice: A quantum monte carlo study*, Phys. Rev. B **88** (2013), 125108. See page: [219](#)
- [CJV10] Philippe Corboz, Jacob Jordan, and Guifré Vidal, *Simulation of fermionic lattice models in two dimensions with projected entangled-pair states: Next-nearest neighbor hamiltonians*, Phys. Rev. B **82** (2010), 245119. See pages: [54](#) and [59](#)
- [CKN⁺16] Garnet Kin-Lic Chan, Anna Keselman, Naoki Nakatani, Zhendong Li, and Steven R. White, *Matrix product operators, matrix product states, and ab initio density matrix renormalization group algorithms*, The Journal of Chemical Physics **145** (2016), no. 1, 014102. See pages: [13](#), [21](#), [22](#), [24](#), and [33](#)
- [CLCL17] Bin-Bin Chen, Yun-Jing Liu, Ziyu Chen, and Wei Li, *Series-expansion thermal tensor network approach for quantum lattice models*, Phys. Rev. B **95** (2017), 161104. See page: [34](#)

- [CLP⁺11] Philippe Corboz, Andreas M. Läuchli, Karlo Penc, Matthias Troyer, and Frédéric Mila, *Simultaneous dimerization and $su(4)$ symmetry breaking of 4-color fermions on the square lattice*, Phys. Rev. Lett. **107** (2011), 215301. See pages: [219](#) and [221](#)
- [CM13] Philippe Corboz and Frédéric Mila, *Tensor network study of the shastry-sutherland model in zero magnetic field*, Phys. Rev. B **87** (2013), 115144. See pages: [45](#) and [59](#)
- [CM14] ———, *Crystals of bound states in the magnetization plateaus of the shastry-sutherland model*, Phys. Rev. Lett. **112** (2014), 147203. See page: [45](#)
- [COBV10] Philippe Corboz, Román Orús, Bela Bauer, and Guifré Vidal, *Simulation of strongly correlated fermions in two spatial dimensions with fermionic projected entangled-pair states*, Phys. Rev. B **81** (2010), 165104. See pages: [45](#), [49](#), [50](#), [51](#), [63](#), [69](#), [70](#), [71](#), [72](#), [73](#), and [74](#)
- [Cor16a] Philippe Corboz, *Improved energy extrapolation with infinite projected entangled-pair states applied to the two-dimensional hubbard model*, Phys. Rev. B **93** (2016), 045116. See pages: [45](#) and [211](#)
- [Cor16b] ———, *Variational optimization with infinite projected entangled-pair states*, Phys. Rev. B **94** (2016), 035133. See pages: [45](#) and [60](#)
- [CRT14] Philippe Corboz, T. M. Rice, and Matthias Troyer, *Competing states in the t - j model: Uniform d -wave state versus stripe state*, Phys. Rev. Lett. **113** (2014), 046402. See pages: [45](#), [48](#), [54](#), [179](#), [211](#), [216](#), and [217](#)
- [CV09] Philippe Corboz and Guifré Vidal, *Fermionic multiscale entanglement renormalization ansatz*, Phys. Rev. B **80** (2009), 165129. See pages: [69](#), [70](#), and [75](#)
- [CWVT11] Philippe Corboz, Steven R. White, Guifré Vidal, and Matthias Troyer, *Stripes in the two-dimensional t - j model with infinite projected entangled-pair states*, Phys. Rev. B **84** (2011), 041108. See pages: [45](#), [48](#), [56](#), [179](#), and [211](#)
- [Dag94] Elbio Dagotto, *Correlated electrons in high-temperature superconductors*, Rev. Mod. Phys. **66** (1994), 763–840. See pages: [2](#) and [179](#)
- [Dal14] Andrew J. Daley, *Quantum trajectories and open many-body quantum systems*, Advances in Physics **63** (2014), no. 2, 77–149. See page: [31](#)
- [Dav75] Ernest R. Davidson, *The iterative calculation of a few of the lowest eigenvalues and corresponding eigenvectors of large real-symmetric matrices*, Journal of Computational Physics **17** (1975), no. 1, 87 – 94. See page: [28](#)
- [DdSHMF⁺08] Luis G. G. V. Dias da Silva, F. Heidrich-Meisner, A. E. Feiguin, C. A. Büsser, G. B. Martins, E. V. Anda, and E. Dagotto, *Transport properties and kondo correlations in nanostructures: Time-dependent dmrg method applied to quantum dots coupled to wilson chains*, Phys. Rev. B **78** (2008), 195317. See page: [31](#)
- [DHR02] Matthew J. Donald, Micha Horodecki, and Oliver Rudolph, *The uniqueness theorem for entanglement measures*, Journal of Mathematical Physics **43** (2002), no. 9, 4252–4272. See page: [9](#)

- [Dir28] Paul AM Dirac, *The quantum theory of the electron*, Proceedings of the Royal Society of London. Series A, Containing Papers of a Mathematical and Physical Character **117** (1928), no. 778, 610–624. See page: [1](#)
- [DKSV04] A J Daley, C Kollath, U Schollwöck, and G Vidal, *Time-dependent density-matrix renormalization-group using adaptive effective hilbert spaces*, Journal of Statistical Mechanics: Theory and Experiment **2004** (2004), no. 04, P04005. See pages: [7](#), [13](#), [27](#), and [30](#)
- [DMDNS98] J. Dukelsky, M. A. Martn-Delgado, T. Nishino, and G. Sierra, *Equivalence of the variational matrix product method and the density matrix renormalization group applied to spin chains*, EPL (Europhysics Letters) **43** (1998), no. 4, 457. See pages: [13](#) and [27](#)
- [DMS12] Stefan Depenbrock, Ian P. McCulloch, and Ulrich Schollwöck, *Nature of the spin-liquid ground state of the $s = 1/2$ heisenberg model on the kagome lattice*, Phys. Rev. Lett. **109** (2012), 067201. See pages: [3](#), [8](#), [29](#), [79](#), and [179](#)
- [DTD⁺09] A. J. Daley, J. M. Taylor, S. Diehl, M. Baranov, and P. Zoller, *Atomic three-body loss as a dynamical three-body interaction*, Phys. Rev. Lett. **102** (2009), 040402. See page: [31](#)
- [ECP10] J. Eisert, M. Cramer, and M. B. Plenio, *Colloquium*, Rev. Mod. Phys. **82** (2010), 277–306. See pages: [8](#) and [10](#)
- [Eis13] J. Eisert, *Entanglement and tensor network states*, Autumn School on Correlated Electrons: Emergent Phenomena in Correlated Matter, Juelich (E. Pavarini, E. Koch, and U. Schollwöck, eds.), 2013, arXiv:1308.3318 [quant-ph]. See pages: [5](#), [7](#), [8](#), [9](#), [13](#), [14](#), [45](#), and [47](#)
- [EP07] Viktor Eisler and Ingo Peschel, *Evolution of entanglement after a local quench*, Journal of Statistical Mechanics: Theory and Experiment **2007** (2007), no. 06, P06005. See page: [34](#)
- [EV09] G. Evenbly and G. Vidal, *Algorithms for entanglement renormalization*, Phys. Rev. B **79** (2009), 144108. See page: [8](#)
- [EV15] ———, *Tensor network renormalization*, Phys. Rev. Lett. **115** (2015), 180405. See pages: [7](#), [45](#), and [49](#)
- [Eve17] G. Evenbly, *Algorithms for tensor network renormalization*, Phys. Rev. B **95** (2017), 045117. See pages: [7](#), [45](#), and [49](#)
- [EWN17] G. Ehlers, S. R. White, and R. M. Noack, *Hybrid-space density matrix renormalization group study of the doped two-dimensional hubbard model*, Phys. Rev. B **95** (2017), 125125. See page: [30](#)
- [FMNR01] W. M. C. Foulkes, L. Mitas, R. J. Needs, and G. Rajagopal, *Quantum monte carlo simulations of solids*, Rev. Mod. Phys. **73** (2001), 33–83. See page: [5](#)
- [FNW92] M. Fannes, B. Nachtergaele, and R. F. Werner, *Abundance of translation invariant pure states on quantum spin chains*, Letters in Mathematical Physics **25** (1992), no. 3, 249–258. See page: [13](#)
- [FW05] Adrian E. Feiguin and Steven R. White, *Finite-temperature density matrix renormalization using an enlarged hilbert space*, Phys. Rev. B **72** (2005), 220401. See pages: [7](#), [13](#), [27](#), [31](#), and [35](#)

- [GAS⁺13] Fabian Güttge, Frithjof B. Anders, Ulrich Schollwöck, Eitan Eidelstein, and Avraham Schiller, *Hybrid nrg-dmrg approach to real-time dynamics of quantum impurity systems*, Phys. Rev. B **87** (2013), 115115. See pages: [24](#) and [26](#)
- [GB09] E. V. Gorelik and N. Blümer, *Mott transitions in ternary flavor mixtures of ultracold fermions on optical lattices*, Phys. Rev. A **80** (2009), 051602. See page: [225](#)
- [GdM13] Antoine Georges, Luca de’Medici, and Jernej Mravlje, *Strong correlations from hunds coupling*. See pages: [211](#), [218](#), and [227](#)
- [Gel96] Martin P Gelfand, *Series expansions for excited states of quantum lattice models*, Solid state communications **98** (1996), no. 1, 11–14. See page: [5](#)
- [GI05] Matthew T. Glossop and Kevin Ingersent, *Numerical renormalization-group study of the Bose-Fermi Kondo model*, Phys. Rev. Lett. **95** (2005), 067202. See pages: [4](#) and [226](#)
- [GKKR96] Antoine Georges, Gabriel Kotliar, Werner Krauth, and Marcelo J. Rozenberg, *Dynamical mean-field theory of strongly correlated fermion systems and the limit of infinite dimensions*, Rev. Mod. Phys. **68** (1996), 13–125. See pages: [4](#) and [24](#)
- [GKSS05] Dominique Gobert, Corinna Kollath, Ulrich Schollwöck, and Gunter Schütz, *Real-time dynamics in spin- $\frac{1}{2}$ chains with adaptive time-dependent density matrix renormalization group*, Phys. Rev. E **71** (2005), 036102. See page: [34](#)
- [GLW08] Zheng-Cheng Gu, Michael Levin, and Xiao-Gang Wen, *Tensor-entanglement renormalization group approach as a unified method for symmetry breaking and topological phase transitions*, Phys. Rev. B **78** (2008), 205116. See pages: [7](#), [45](#), and [49](#)
- [GML⁺11] Emanuel Gull, Andrew J. Millis, Alexander I. Lichtenstein, Alexey N. Rubtsov, Matthias Troyer, and Philipp Werner, *Continuous-time monte carlo methods for quantum impurity models*, Rev. Mod. Phys. **83** (2011), 349–404. See page: [5](#)
- [GS00] Martin P. Gelfand and Rajiv R. P. Singh, *High-order convergent expansions for quantum many particle systems*, Advances in Physics **49** (2000), no. 1, 93–140. See page: [5](#)
- [GTV⁺14] Martin Ganahl, Patrik Thunström, Frank Verstraete, Karsten Held, and Hans Gerd Evertz, *Chebyshev expansion for impurity models using matrix product states*, Phys. Rev. B **90** (2014), 045144. See pages: [24](#), [26](#), [40](#), [41](#), and [42](#)
- [GVMP17] Matthias Gohlke, Ruben Verresen, Roderich Moessner, and Frank Pollmann, *Dynamics of the kitaev-heisenberg model*, arXiv preprint arXiv:1701.04678 (2017). See page: [227](#)
- [GWvDV12] Cheng Guo, Andreas Weichselbaum, Jan von Delft, and Matthias Voja, *Critical and strong-coupling phases in one- and two-bath spin-boson models*, Phys. Rev. Lett. **108** (2012), 160401. See pages: [4](#), [24](#), [26](#), and [81](#)
- [Hal83a] F. D. M. Haldane, *Nonlinear field theory of large-spin heisenberg antiferromagnets: Semiclassically quantized solitons of the one-dimensional easy-axis néel state*, Phys. Rev. Lett. **50** (1983), 1153–1156. See page: [3](#)

- [Hal83b] F.D.M. Haldane, *Continuum dynamics of the 1-d heisenberg antiferromagnet: Identification with the $o(3)$ nonlinear sigma model*, Physics Letters A **93** (1983), no. 9, 464 – 468. See page: [3](#)
- [Hal95] Karen A. Hallberg, *Density-matrix algorithm for the calculation of dynamical properties of low-dimensional systems*, Phys. Rev. B **52** (1995), R9827–R9830. See page: [38](#)
- [Has07] M B Hastings, *An area law for one-dimensional quantum systems*, Journal of Statistical Mechanics: Theory and Experiment **2007** (2007), no. 08, P08024. See page: [9](#)
- [HCD⁺16] Yuan Huang, Kun Chen, Youjin Deng, Nikolay Prokof'ev, and Boris Svistunov, *Spin-ice state of the quantum heisenberg antiferromagnet on the pyrochlore lattice*, Phys. Rev. Lett. **116** (2016), 177203. See page: [5](#)
- [HCO⁺11] Jutho Haegeman, J. Ignacio Cirac, Tobias J. Osborne, Iztok Pizorn, Henri Verschelde, and Frank Verstraete, *Time-dependent variational principle for quantum lattices*, Phys. Rev. Lett. **107** (2011), 070601. See pages: [34](#) and [227](#)
- [Hei28] W. Heisenberg, *Zur theorie des ferromagnetismus*, Zeitschrift für Physik **49** (1928), no. 9, 619–636. See page: [3](#)
- [Hew97] A.C. Hewson, *The Kondo problem to heavy fermions*, Cambridge Studies in Magnetism, Cambridge University Press, test, 1997. See page: [226](#)
- [HH04] Carsten Honerkamp and Walter Hofstetter, *Ultracold fermions and the $SU(n)$ hubbard model*, Phys. Rev. Lett. **92** (2004), 170403. See pages: [223](#) and [224](#)
- [HK06] Matthew B. Hastings and Tohru Koma, *Spectral gap and exponential decay of correlations*, Communications in Mathematical Physics **265** (2006), no. 3, 781–804. See page: [9](#)
- [HK10] M. Z. Hasan and C. L. Kane, *Colloquium*, Rev. Mod. Phys. **82** (2010), 3045–3067. See page: [179](#)
- [HKM15] Jad C. Halimeh, Fabian Kolley, and Ian P. McCulloch, *Chebyshev matrix product state approach for time evolution*, Phys. Rev. B **92** (2015), 115130. See page: [42](#)
- [HMS17] C. Hubig, I. P. McCulloch, and U. Schollwöck, *Generic construction of efficient matrix product operators*, Phys. Rev. B **95** (2017), 035129. See page: [22](#)
- [HMSW15] C. Hubig, I. P. McCulloch, U. Schollwöck, and F. A. Wolf, *Strictly single-site dmrg algorithm with subspace expansion*, Phys. Rev. B **91** (2015), 155115. See page: [29](#)
- [HOA99] Yasuhiro Hieida, Kouichi Okunishi, and Yasuhiro Akutsu, *Numerical renormalization approach to two-dimensional quantum antiferromagnets with valence-bond-solid type ground state*, New Journal of Physics **1** (1999), no. 1, 7. See page: [45](#)
- [HP17] Johannes Hausschild and Frank Pollmann, Private communication (2017). See page: [40](#)

- [HRS⁺16] Christian Hofrichter, Luis Riegger, Francesco Scazza, Moritz Höfer, Diogo Rio Fernandes, Immanuel Bloch, and Simon Fölling, *Direct probing of the mott crossover in the SU(n) fermi-hubbard model*, Phys. Rev. X **6** (2016), 021030. See pages: [180](#), [218](#), [223](#), and [227](#)
- [HS00] Patrik Henelius and Anders W. Sandvik, *Sign problem in monte carlo simulations of frustrated quantum spin systems*, Phys. Rev. B **62** (2000), no. 2, 1102–1113. See page: [5](#)
- [HS05] Naomichi Hatano and Masuo Suzuki, *Finding exponential product formulas of higher orders*, Quantum annealing and other optimization methods, Springer, 2005, pp. 37–68. See page: [31](#)
- [Hub63] John Hubbard, *Electron correlations in narrow energy bands*, Proceedings of the royal society of london a: mathematical, physical and engineering sciences, vol. 276, The Royal Society, 1963, pp. 238–257. See page: [2](#)
- [HWM⁺11] Andreas Holzner, Andreas Weichselbaum, Ian P. McCulloch, Ulrich Schollwöck, and Jan von Delft, *Chebyshev matrix product state approach for spectral functions*, Phys. Rev. B **83** (2011), 195115. See pages: [38](#) and [41](#)
- [HWvD10] Andreas Holzner, Andreas Weichselbaum, and Jan von Delft, *Matrix product state approach for a two-lead multilevel anderson impurity model*, Phys. Rev. B **81** (2010), 125126. See pages: [7](#), [24](#), and [26](#)
- [HZOP16] Yin-Chen He, Michael P. Zaletel, Masaki Oshikawa, and Frank Pollmann, *Signatures of dirac cones in a dmrg study of the kagome heisenberg model*, arxiv:1611.06238 (2016). See pages: [3](#), [29](#), [180](#), and [227](#)
- [IFT98] Masatoshi Imada, Atsushi Fujimori, and Yoshinori Tokura, *Metal-insulator transitions*, Rev. Mod. Phys. **70** (1998), 1039–1263. See pages: [2](#), [211](#), and [218](#)
- [Jec02] Eric Jeckelmann, *Dynamical density-matrix renormalization-group method*, Phys. Rev. B **66** (2002), 045114. See page: [38](#)
- [JOV⁺08] J. Jordan, R. Orús, G. Vidal, F. Verstraete, and J. I. Cirac, *Classical simulation of infinite-size quantum lattice systems in two spatial dimensions*, Phys. Rev. Lett. **101** (2008), 250602. See pages: [7](#), [45](#), [47](#), [49](#), [57](#), [59](#), [60](#), [61](#), [64](#), and [65](#)
- [JWX08] H. C. Jiang, Z. Y. Weng, and T. Xiang, *Accurate determination of tensor network state of quantum lattice models in two dimensions*, Phys. Rev. Lett. **101** (2008), 090603. See pages: [60](#), [61](#), and [62](#)
- [KBM12] C. Karrasch, J. H. Bardarson, and J. E. Moore, *Finite-temperature dynamical density matrix renormalization group and the drude weight of spin-1/2 chains*, Phys. Rev. Lett. **108** (2012), 227206. See page: [39](#)
- [KK16] D.M. Kennes and C. Karrasch, *Extending the range of real time density matrix renormalization group simulations*, Computer Physics Communications **200** (2016), 37 – 43. See pages: [39](#) and [178](#)
- [KmWW80] H. R. Krishna-murthy, J. W. Wilkins, and K. G. Wilson, *Renormalization-group approach to the Anderson model of dilute magnetic alloys. I. Static properties for the symmetric case*, Phys. Rev. B **21** (1980), 1003–1043. See page: [24](#)

- [KPS⁺13] S. A. Kulagin, N. Prokof'ev, O. A. Starykh, B. Svistunov, and C. N. Varney, *Bold diagrammatic monte carlo method applied to fermionized frustrated spins*, Phys. Rev. Lett. **110** (2013), 070601. See page: [5](#)
- [KSGG⁺11] Andrey V. Kretinin, Hadas Shtrikman, David Goldhaber-Gordon, Markus Hanl, Andreas Weichselbaum, Jan von Delft, Theo Costi, and Diana Mahalu, *Spin- $\frac{1}{2}$ kondo effect in an inas nanowire quantum dot: Unitary limit, conductance scaling, and zeeman splitting*, Phys. Rev. B **84** (2011), 245316. See page: [24](#)
- [KSH⁺06] G. Kotliar, S. Y. Savrasov, K. Haule, V. S. Oudovenko, O. Parcollet, and C. A. Marianetti, *Electronic structure calculations with dynamical mean-field theory*, Rev. Mod. Phys. **78** (2006), 865–951. See pages: [4](#) and [24](#)
- [KSVC10] Christina V. Kraus, Norbert Schuch, Frank Verstraete, and J. Ignacio Cirac, *Fermionic projected entangled pair states*, Phys. Rev. A **81** (2010), 052338. See page: [69](#)
- [KSZ05] C. Kollath, U. Schollwöck, and W. Zwerger, *Spin-charge separation in cold fermi gases: A real time analysis*, Phys. Rev. Lett. **95** (2005), 176401. See page: [31](#)
- [KTF⁺16] E. S. Klyushina, A. C. Tiegel, B. Fauseweh, A. T. M. N. Islam, J. T. Park, B. Klemke, A. Honecker, G. S. Uhrig, S. R. Manmana, and B. Lake, *Magnetic excitations in the $s = \frac{1}{2}$ antiferromagnetic-ferromagnetic chain compound $\text{BaCu}_2\text{V}_2\text{O}_8$ at zero and finite temperature*, Phys. Rev. B **93** (2016), 241109. See page: [42](#)
- [KW99] Till D. Kuehner and Steven R. White, *Dynamical correlation functions using the density matrix renormalization group*, Phys. Rev. B **60** (1999), 335–343. See page: [38](#)
- [LAB⁺15] J. P. F. LeBlanc, Andrey E. Antipov, Federico Becca, Ireneusz W. Bulik, Garnet Kin-Lic Chan, Chia-Min Chung, Youjin Deng, Michel Ferrero, Thomas M. Henderson, Carlos A. Jiménez-Hoyos, E. Kozik, Xuan-Wen Liu, Andrew J. Millis, N. V. Prokof'ev, Mingpu Qin, Gustavo E. Scuseria, Hao Shi, B. V. Svistunov, Luca F. Tocchio, I. S. Tupitsyn, Steven R. White, Shiwei Zhang, Bo-Xiao Zheng, Zhenyue Zhu, and Emanuel Gull, *Solutions of the two-dimensional hubbard model: Benchmarks and results from a wide range of numerical algorithms*, Phys. Rev. X **5** (2015), 041041. See pages: [3](#) and [8](#)
- [Lan50] C Lanczos, *An iteration method for the solution of the eigenvalue problem of linear differential and integral operators*, Journal of research of the National Bureau of Standards **45** (1950), 255–282. See pages: [4](#) and [28](#)
- [Lan59] LD Landau, *On the theory of the fermi liquid*, Sov. Phys. JETP **8** (1959), no. 1, 70. See page: [1](#)
- [LCBn14] Michael Lubasch, J. Ignacio Cirac, and Mari-Carmen Bañuls, *Algorithms for finite projected entangled pair states*, Phys. Rev. B **90** (2014), 064425. See pages: [45](#), [46](#), [67](#), and [68](#)
- [LCD⁺87] A. J. Leggett, S. Chakravarty, A. T. Dorsey, Matthew P. A. Fisher, Anupam Garg, and W. Zwerger, *Dynamics of the dissipative two-state system*, Rev. Mod. Phys. **59** (1987), 1–85. See pages: [4](#) and [81](#)

- [LHH⁺11] Christian Latta, Florian Haupt, Markus Hanl, Andreas Weichselbaum, Martin Claassen, Wolf Wuester, Parisa Fallahi, Stefan Faelt, Leonid Glazman, Jan von Delft, Hakan Türekli, and Ataç Imamoglu, *Quantum quench of Kondo correlations in optical absorption*, Nature **474** (2011), no. 7353, 627–630. See pages: [24](#) and [26](#)
- [LLW⁺15] Tao Liu, Wei Li, Andreas Weichselbaum, Jan von Delft, and Gang Su, *Simplex valence-bond crystal in the spin-1 kagome heisenberg antiferromagnet*, Phys. Rev. B **91** (2015), 060403. See pages: [45](#), [77](#), [80](#), and [212](#)
- [LN07] Michael Levin and Cody P. Nave, *Tensor renormalization group approach to two-dimensional classical lattice models*, Phys. Rev. Lett. **99** (2007), 120601. See pages: [7](#), [45](#), and [49](#)
- [LRG⁺11] Wei Li, Shi-Ju Ran, Shou-Shu Gong, Yang Zhao, Bin Xi, Fei Ye, and Gang Su, *Linearized tensor renormalization group algorithm for the calculation of thermodynamic properties of quantum lattice models*, Phys. Rev. Lett. **106** (2011), 127202. See page: [180](#)
- [LvDX12] Wei Li, Jan von Delft, and Tao Xiang, *Efficient simulation of infinite tree tensor network states on the bethe lattice*, Phys. Rev. B **86** (2012), 195137. See pages: [60](#) and [63](#)
- [LXC⁺17] H. J. Liao, Z. Y. Xie, J. Chen, Z. Y. Liu, H. D. Xie, R. Z. Huang, B. Normand, and T. Xiang, *Gapless spin-liquid ground state in the $s = 1/2$ kagome antiferromagnet*, Phys. Rev. Lett. **118** (2017), 137202. See pages: [3](#), [29](#), [45](#), and [179](#)
- [LYC⁺14] Wei Li, Shuo Yang, Meng Cheng, Zheng-Xin Liu, and Hong-Hao Tu, *Topology and criticality in the resonating affleck-kennedy-lieb-tasaki loop spin liquid states*, Phys. Rev. B **89** (2014), 174411. See page: [212](#)
- [LYCS17] Yoav Levine, David Yakira, Nadav Cohen, and Amnon Shashua, *Deep learning and quantum entanglement: Fundamental connections with implications to network design.*, arXiv preprint arXiv:1704.01552 (2017). See page: [8](#)
- [Mac89] Kazushige Machida, *Magnetism in La_2CuO_4 based compounds*, Physica C: Superconductivity **158** (1989), no. 1, 192 – 196. See page: [216](#)
- [Man91] Efstratios Manousakis, *The spin- $\frac{1}{2}$ heisenberg antiferromagnet on a square lattice and its application to the cuprous oxides*, Rev. Mod. Phys. **63** (1991), 1–62. See page: [3](#)
- [McC07] Ian P McCulloch, *From density-matrix renormalization group to matrix product states*, Journal of Statistical Mechanics: Theory and Experiment **2007** (2007), no. 10, P10014. See pages: [21](#) and [29](#)
- [McC08] Ian P McCulloch, *Infinite size density matrix renormalization group, revisited*, arXiv preprint arXiv:0804.2509 (2008). See page: [47](#)
- [MCHW17] Jia-Wei Mei, Ji-Yao Chen, Huan He, and Xiao-Gang Wen, *Gapped spin liquid with F_2 topological order for the kagome heisenberg model*, Phys. Rev. B **95** (2017), 235107. See pages: [45](#) and [179](#)
- [MG02] I. P. McCulloch and M. Gulacsi, *The non-abelian density matrix renormalization group algorithm*, Europhys. Lett. **57** (2002), no. 6, 852. See pages: [77](#) and [80](#)

- [MOL⁺99] J. E. Mooij, T. P. Orlando, L. Levitov, Lin Tian, Caspar H. van der Wal, and Seth Lloyd, *Josephson persistent-current qubit*, *Science* **285** (1999), no. 5430, 1036–1039. See page: [81](#)
- [MS85] R.A. Marcus and Norman Sutin, *Electron transfers in chemistry and biology*, *Biochimica et Biophysica Acta (BBA) - Reviews on Bioenergetics* **811** (1985), no. 3, 265 – 322. See page: [81](#)
- [MSS01] Yuriy Makhlin, Gerd Schön, and Alexander Shnirman, *Quantum-state engineering with josephson-junction devices*, *Rev. Mod. Phys.* **73** (2001), 357–400. See page: [81](#)
- [MW92] Yigal Meir and Ned S. Wingreen, *Landauer formula for the current through an interacting electron region*, *Phys. Rev. Lett.* **68** (1992), 2512–2515. See page: [178](#)
- [MZMP16] Johannes Motruk, Michael P. Zaletel, Roger S. K. Mong, and Frank Pollmann, *Density matrix renormalization group on a cylinder in mixed real and momentum space*, *Phys. Rev. B* **93** (2016), 155139. See page: [30](#)
- [NMGN04] Yukinobu Nishio, Nobuya Maeshima, Andrej Gendiar, and Tomotoshi Nishino, *Tensor product variational formulation for quantum systems*, arXiv preprint cond-mat/0401115 (2004). See page: [45](#)
- [NO96] Tomotoshi Nishino and Kouichi Okunishi, *Corner transfer matrix renormalization group method*, *Journal of the Physical Society of Japan* **65** (1996), no. 4, 891–894. See pages: [49](#), [51](#), and [54](#)
- [OHZ06] Jaan Oitmaa, Chris Hamer, and Weihong Zheng, *Series expansion methods for strongly interacting lattice models*, Cambridge University Press, 2006. See page: [5](#)
- [ON00] Kouichi Okunishi and Tomotoshi Nishino, *Kramers-wannier approximation for the 3d ising model*, *Progress of Theoretical Physics* **103** (2000), no. 3, 541. See page: [45](#)
- [OR95] Stellan Östlund and Stefan Rommer, *Thermodynamic limit of density matrix renormalization*, *Phys. Rev. Lett.* **75** (1995), 3537–3540. See pages: [13](#) and [27](#)
- [Orú14a] Román Orús, *Advances on tensor network theory: symmetries, fermions, entanglement, and holography*, *The European Physical Journal B* **87** (2014), no. 11, 280. See pages: [8](#), [45](#), and [77](#)
- [Orú14b] ———, *A practical introduction to tensor networks: Matrix product states and projected entangled pair states*, *Annals of Physics* **349** (2014), 117 – 158. See pages: [5](#), [45](#), and [47](#)
- [OSLH08] Peter P. Orth, Ivan Stanic, and Karyn Le Hur, *Dissipative quantum ising model in a cold-atom spin-boson mixture*, *Phys. Rev. A* **77** (2008), 051601. See page: [81](#)
- [OV08] R. Orús and G. Vidal, *Infinite time-evolving block decimation algorithm beyond unitary evolution*, *Phys. Rev. B* **78** (2008), 155117. See pages: [49](#) and [54](#)

- [OV09] Román Orús and Guifré Vidal, *Simulation of two-dimensional quantum systems on an infinite lattice revisited: Corner transfer matrix for tensor contraction*, Phys. Rev. B **80** (2009), 094403. See pages: [49](#), [51](#), and [54](#)
- [PBE10] Carlos Pineda, Thomas Barthel, and Jens Eisert, *Unitary circuits for strongly correlated fermions*, Phys. Rev. A **81** (2010), 050303. See page: [69](#)
- [PBT⁺15] Ho N. Phien, Johann A. Bengua, Hoang D. Tuan, Philippe Corboz, and Román Orús, *Infinite projected entangled pair states algorithm improved: Fast full update and gauge fixing*, Phys. Rev. B **92** (2015), 035142. See pages: [45](#), [49](#), [60](#), [66](#), [67](#), and [68](#)
- [PEDC05] M. B. Plenio, J. Eisert, J. Dreißig, and M. Cramer, *Entropy, entanglement, and area: Analytical results for harmonic lattice systems*, Phys. Rev. Lett. **94** (2005), 060503. See page: [10](#)
- [PF10] John B. Parkinson and Damian J.J. Farnell, *Quantum magnetism*, pp. 135–152, Springer Berlin Heidelberg, Berlin, Heidelberg, 2010. See page: [3](#)
- [PMV15] Ho N. Phien, Ian P. McCulloch, and Guifré Vidal, *Fast convergence of imaginary time evolution tensor network algorithms by recycling the environment*, Phys. Rev. B **91** (2015), 115137. See page: [49](#)
- [PR89] D. Poilblanc and T. M. Rice, *Charged solitons in the hartree-fock approximation to the large- u hubbard model*, Phys. Rev. B **39** (1989), 9749–9752. See page: [216](#)
- [PS13] Didier Poilblanc and Norbert Schuch, *Simplex F_2 spin liquids on the kagome lattice with projected entangled pair states: Spinon and vison coherence lengths, topological entropy, and gapless edge modes*, Phys. Rev. B **87** (2013), 140407. See page: [212](#)
- [PSPGC12] Didier Poilblanc, Norbert Schuch, David Pérez-García, and J. Ignacio Cirac, *Topological and entanglement properties of resonating valence bond wave functions*, Phys. Rev. B **86** (2012), 014404. See page: [212](#)
- [PWKH99] Ingo Peschel, Xiaoqun Want, Matthias Kaulke, and Karen Hallberg, *Density matrix renormalization: a new numerical method in physics: lectures of a seminar and workshop held at the max-planck-institut für physik komplexer systeme, dresden, germany, august 24th to september 18th, 1998*, Density-Matrix Renormalization, a New Numerical Method in Physics, vol. 528, 1999. See page: [13](#)
- [QZ11] Xiao-Liang Qi and Shou-Cheng Zhang, *Topological insulators and superconductors*, Rev. Mod. Phys. **83** (2011), 1057–1110. See page: [179](#)
- [Ram94] AP Ramirez, *Strongly geometrically frustrated magnets*, Annual Review of Materials Science **24** (1994), no. 1, 453–480. See page: [2](#)
- [RBS06] Marcos Rigol, Tyler Bryant, and Rajiv R. P. Singh, *Numerical linked-cluster approach to quantum lattice models*, Phys. Rev. Lett. **97** (2006), 187202. See page: [30](#)
- [RBS07] ———, *Numerical linked-cluster algorithms. i. spin systems on square, triangular, and kagomé lattices*, Phys. Rev. E **75** (2007), 061118. See page: [30](#)

- [RCP⁺07] Marcin Raczkowski, Manuela Capello, Didier Poilblanc, Raymond Frésard, and Andrzej M. Oleś, *Unidirectional d-wave superconducting domains in the two-dimensional t–j model*, Phys. Rev. B **76** (2007), 140505. See page: [216](#)
- [RFZ⁺05] A. Recati, P. O. Fedichev, W. Zwerger, J. von Delft, and P. Zoller, *Atomic quantum dots coupled to a reservoir of a superfluid bose-einstein condensate*, Phys. Rev. Lett. **94** (2005), 040404. See page: [81](#)
- [RP16] Roman Rausch and Michael Potthoff, *Multipions in the two-hole excitation spectra of the one-dimensional hubbard model*, New Journal of Physics **18** (2016), no. 2, 023033. See page: [42](#)
- [RPK⁺96] S. Ramasesha, Swapan K. Pati, H. R. Krishnamurthy, Z. Shuai, and J. L. Brédas, *Symmetrized density-matrix renormalization-group method for excited states of hubbard models*, Phys. Rev. B **54** (1996), 7598–7601. See page: [38](#)
- [Sac01] S. Sachdev, *Quantum phase transitions*, University Press, 2001. See page: [2](#)
- [San97] Anders W. Sandvik, *Finite-size scaling of the ground-state parameters of the two-dimensional heisenberg model*, Phys. Rev. B **56** (1997), 11678–11690. See page: [217](#)
- [SB17] Lucile Savary and Leon Balents, *Quantum spin liquids: a review*, Reports on Progress in Physics **80** (2017), no. 1, 016502. See page: [179](#)
- [SBvD17] Dennis H Schimmel, Benedikt Bruognolo, and Jan von Delft, *Spin fluctuations in the 0.7-anomaly in quantum point contacts*, arXiv preprint arXiv:1703.02734 (2017). See pages: [27](#), [31](#), [38](#), [77](#), [164](#), and [178](#)
- [SC16] Florian A. Y. N. Schröder and Alex W. Chin, *Simulating open quantum dynamics with time-dependent variational matrix product states: Towards microscopic correlation of environment dynamics and reduced system evolution*, Phys. Rev. B **93** (2016), 075105. See page: [226](#)
- [Sca06] D. J. Scalapino, *The 2d hubbard model and the high t c cuprate problem*, Journal of Superconductivity and Novel Magnetism **19** (2006), no. 3, 195–200. See page: [2](#)
- [Sch89] HJ Schulz, *Domain walls in a doped antiferromagnet*, Journal de Physique **50** (1989), no. 18, 2833–2849. See page: [216](#)
- [Sch05] U. Schollwöck, *The density-matrix renormalization group*, Rev. Mod. Phys. **77** (2005), 259–315. See pages: [7](#) and [27](#)
- [Sch11] Ulrich Schollwöck, *The density-matrix renormalization group in the age of matrix product states*, Ann. Phys. **326** (2011), no. 1, 96 – 192. See pages: [5](#), [13](#), [20](#), [21](#), [27](#), [29](#), [30](#), and [32](#)
- [SHH⁺14] Francesco Scazza, Christian Hofrichter, Moritz Höfer, PC De Groot, Immanuel Bloch, and Simon Fölling, *Observation of two-orbital spin-exchange interactions with ultracold su (n)-symmetric fermions*, Nature Physics **10** (2014), no. 10, 779–784. See pages: [180](#), [218](#), [223](#), and [227](#)
- [Shi97] Naokazu Shibata, *Thermodynamics of the anisotropic heisenberg chain calculated by the density matrix renormalization group method*, J Phys Soc Jpn **66** (1997), no. 8, 2221–2223. See page: [35](#)

- [SK86] G Sugiyama and S.E Koonin, *Auxiliary field monte-carlo for quantum many-body ground states*, Annals of Physics **168** (1986), no. 1, 1 – 26. See page: [5](#)
- [SLZZ09] Qian-Qian Shi, Sheng-Hao Li, Jian-Hui Zhao, and Huan-Qiang Zhou, *Graded projected entangled-pair state representations and an algorithm for translationally invariant strongly correlated electronic systems on infinite-size lattices in two spatial dimensions*, arXiv preprint arXiv:0907.5520 (2009). See page: [69](#)
- [SN97] Germn Sierra and Tomotoshi Nishino, *The density matrix renormalization group method applied to interaction round a face hamiltonians*, Nuclear Physics B **495** (1997), no. 3, 505 – 532. See page: [77](#)
- [SPV10] Sukhwinder Singh, Robert N. C. Pfeifer, and Guifré Vidal, *Tensor network decompositions in the presence of a global symmetry*, Phys. Rev. A **82** (2010), 050301. See page: [77](#)
- [SPV11] Sukhwinder Singh, Robert N. C. Pfeifer, and Guifre Vidal, *Tensor network states and algorithms in the presence of a global $u(1)$ symmetry*, Phys. Rev. B **83** (2011), 115125. See page: [77](#)
- [SRIS01] Qimiao Si, Silvio Rabello, Kevin Ingersent, and J Llewelun Smith, *Locally critical quantum phase transitions in strongly correlated metals*, Nature **413** (2001), no. 6858, 804–808. See page: [226](#)
- [SRIS03] Qimiao Si, Silvio Rabello, Kevin Ingersent, and J. Llewelun Smith, *Local fluctuations in quantum critical metals*, Phys. Rev. B **68** (2003), 115103. See page: [226](#)
- [SS16] E Miles Stoudenmire and David J Schwab, *Supervised learning with quantum-inspired tensor networks*, arXiv preprint arXiv:1605.05775 (2016). See page: [8](#)
- [Sto99] H. L. Stormer, *Nobel Lecture: The fractional quantum Hall effect*, Reviews of Modern Physics **71** (1999), 875–889. See page: [2](#)
- [SV12] Sukhwinder Singh and Guifre Vidal, *Tensor network states and algorithms in the presence of a global $su(2)$ symmetry*, Phys. Rev. B **86** (2012), 195114. See pages: [77](#) and [80](#)
- [SV13] ———, *Global symmetries in tensor network states: Symmetric tensors versus minimal bond dimension*, Phys. Rev. B **88** (2013), 115147. See pages: [77](#) and [80](#)
- [SW10] E M Stoudenmire and Steven R White, *Minimally entangled typical thermal state algorithms*, New J. Phys. **12** (2010), no. 5, 055026. See pages: [32](#), [35](#), [36](#), and [37](#)
- [SW12] E.M. Stoudenmire and Steven R. White, *Studying two-dimensional systems with the density matrix renormalization group*, Annual Review of Condensed Matter Physics **3** (2012), no. 1, 111–128. See pages: [13](#), [27](#), [29](#), and [30](#)
- [SWVC08] N Schuch, M M Wolf, K G H Vollbrecht, and J I Cirac, *On entropy growth and the hardness of simulating time evolution*, New Journal of Physics **10** (2008), no. 3, 033032. See pages: [34](#) and [49](#)

- [SWvD08] Hamed Saberi, Andreas Weichselbaum, and Jan von Delft, *Matrix-product-state comparison of the numerical renormalization group and the variational formulation of the density-matrix renormalization group*, Phys. Rev. B **78** (2008), 035124. See pages: [24](#) and [26](#)
- [SYvD⁺15] K. M. Stadler, Z. P. Yin, J. von Delft, G. Kotliar, and A. Weichselbaum, *Dynamical mean-field theory plus numerical renormalization-group study of spin-orbital separation in a three-band hund metal*, Phys. Rev. Lett. **115** (2015), 136401. See page: [24](#)
- [TASB16] Luca F Tocchio, Federico Arrigoni, Sandro Sorella, and Federico Becca, *Assessing the orbital selective mott transition with variational wave functions*, Journal of Physics: Condensed Matter **28** (2016), no. 10, 105602. See page: [219](#)
- [THC⁺11] Hakan E. Türeci, M. Hanl, M. Claassen, A. Weichselbaum, T. Hecht, B. Braunecker, A. Govorov, L. Glazman, A. Imamoglu, and J. von Delft, *Many-body dynamics of exciton creation in a quantum dot by optical absorption: A quantum quench towards kondo correlations*, Phys. Rev. Lett. **106** (2011), 107402. See pages: [24](#) and [26](#)
- [THP⁺16] Alexander C. Tiegel, Andreas Honecker, Thomas Pruschke, Alexey Ponomaryov, Sergei A. Zvyagin, Ralf Feyerherm, and Salvatore R. Manmana, *Dynamical properties of the sine-gordon quantum spin magnet cu-pm at zero and finite temperature*, Phys. Rev. B **93** (2016), 104411. See page: [42](#)
- [TMH⁺00] Simon Trebst, Hartmut Monien, Chris J. Hamer, Zheng Weihong, and Rajiv R. P. Singh, *Strong-coupling expansions for multiparticle excitations: Continuum and bound states*, Phys. Rev. Lett. **85** (2000), 4373–4376. See page: [5](#)
- [TMPH14] Alexander C. Tiegel, Salvatore R. Manmana, Thomas Pruschke, and Andreas Honecker, *Matrix product state formulation of frequency-space dynamics at finite temperatures*, Phys. Rev. B **90** (2014), 060406. See pages: [41](#) and [42](#)
- [TN00] Y Tokura and N Nagaosa, *Orbital physics in transition-metal oxides*, science **288** (2000), no. 5465, 462–468. See page: [218](#)
- [TRS13] Ronny Thomale, Stephan Rachel, and Peter Schmitteckert, *Tunneling spectra simulation of interacting majorana wires*, Phys. Rev. B **88** (2013), 161103. See page: [42](#)
- [TUM⁺94] Yoshinori Tokura, Akira Urushibara, Yutaka Moritomo, Takahisa Arima, Atsushi Asamitsu, Giyu Kido, and Nobuo Furukawa, *Giant magnetotransport phenomena in filling-controlled kondo lattice system: La_{1-x}sr_xmno₃*, Journal of the Physical Society of Japan **63** (1994), no. 11, 3931–3935. See page: [226](#)
- [TW05] Matthias Troyer and Uwe-Jens Wiese, *Computational complexity and fundamental limitations to fermionic quantum monte carlo simulations*, Phys. Rev. Lett. **94** (2005), 170201. See page: [5](#)
- [VC04] F. Verstraete and J. I. Cirac, *Renormalization algorithms for quantum-many body systems in two and higher dimensions*, eprint arXiv:cond-mat/0407066 (2004). See pages: [5](#), [7](#), [33](#), and [45](#)

- [VGRC04] F. Verstraete, J. J. Garcia-Ripoll, and J. I. Cirac, *Matrix product density operators: Simulation of finite-temperature and dissipative systems*, Phys. Rev. Lett. **93** (2004), 207204. See pages: [7](#), [13](#), [21](#), [27](#), [31](#), and [35](#)
- [VHCV16] Laurens Vanderstraeten, Jutho Haegeman, Philippe Corboz, and Frank Verstraete, *Gradient methods for variational optimization of projected entangled-pair states*, Phys. Rev. B **94** (2016), 155123. See pages: [45](#) and [60](#)
- [Vid04] Guifré Vidal, *Efficient simulation of one-dimensional quantum many-body systems*, Phys. Rev. Lett. **93** (2004), 040502. See pages: [7](#), [13](#), [27](#), [30](#), [32](#), and [62](#)
- [Vid07] G. Vidal, *Classical simulation of infinite-size quantum lattice systems in one spatial dimension*, Phys. Rev. Lett. **98** (2007), 070201. See pages: [5](#), [8](#), [49](#), and [62](#)
- [VMC08] F. Verstraete, V. Murg, and J.I. Cirac, *Matrix product states, projected entangled pair states, and variational renormalization group methods for quantum spin systems*, Advances in Physics **57** (2008), no. 2, 143–224. See pages: [13](#), [16](#), [20](#), and [21](#)
- [VMVH15] Laurens Vanderstraeten, Michaël Mariën, Frank Verstraete, and Jutho Haegeman, *Excitations and the tangent space of projected entangled-pair states*, Phys. Rev. B **92** (2015), 201111. See pages: [45](#) and [180](#)
- [Voj03] Matthias Vojta, *Quantum phase transitions*, Reports on Progress in Physics **66** (2003), no. 12, 2069. See pages: [4](#) and [81](#)
- [Voj06] Matthias Vojta, *Impurity quantum phase transitions*, Philosophical Magazine **86** (2006), no. 13-14, 1807–1846. See pages: [4](#) and [81](#)
- [VWPGC06] F. Verstraete, M. M. Wolf, D. Perez-Garcia, and J. I. Cirac, *Criticality, the area law, and the computational power of projected entangled pair states*, Phys. Rev. Lett. **96** (2006), 220601. See pages: [10](#) and [47](#)
- [VWS⁺05] F Verstraete, A Weichselbaum, U Schollwöck, JI Cirac, and Jan von Delft, *Variational matrix product state approach to quantum impurity models*, arXiv preprint cond-mat/0504305 (2005). See page: [24](#)
- [WA08] Steven R. White and Ian Affleck, *Spectral function for the $s = 1$ heisenberg antiferromagnetic chain*, Phys. Rev. B **77** (2008), 134437. See pages: [31](#), [38](#), [40](#), and [164](#)
- [WC07] Steven R. White and A. L. Chernyshev, *Neél order in square and triangular lattice heisenberg models*, Phys. Rev. Lett. **99** (2007), 127004. See page: [29](#)
- [Wei11] A. Weichselbaum, *Discarded weight and entanglement spectra in the numerical renormalization group*, Phys. Rev. B **84** (2011), 125130. See pages: [24](#) and [26](#)
- [Wei12a] Andreas Weichselbaum, *Non-abelian symmetries in tensor networks: A quantum symmetry space approach*, Ann. Phys. **327** (2012), no. 12, 2972 – 3047. See pages: [77](#), [78](#), [79](#), [80](#), [211](#), [212](#), [214](#), [223](#), and [224](#)
- [Wei12b] Andreas Weichselbaum, *Tensor networks and the numerical renormalization group*, Phys. Rev. B **86** (2012), 245124. See pages: [24](#), [26](#), [69](#), and [73](#)

- [Wei17] ———, Private communication (2017). See page: [56](#)
- [WF04] Steven R. White and Adrian E. Feiguin, *Real-time evolution using the density matrix renormalization group*, Phys. Rev. Lett. **93** (2004), 076401. See pages: [7](#), [13](#), [27](#), [30](#), [31](#), and [38](#)
- [WF08] Alexander Weiße and Holger Fehske, *Exact diagonalization techniques*, pp. 529–544, Springer Berlin Heidelberg, Berlin, Heidelberg, 2008. See page: [4](#)
- [WH93] Steven R. White and David A. Huse, *Numerical renormalization-group study of low-lying eigenstates of the antiferromagnetic $s=1$ heisenberg chain*, Phys. Rev. B **48** (1993), 3844–3852. See page: [8](#)
- [Whi92] Steven R. White, *Density matrix formulation for quantum renormalization groups*, Phys. Rev. Lett. **69** (1992), 2863–2866. See pages: [5](#), [7](#), [13](#), and [27](#)
- [Whi93] ———, *Density-matrix algorithms for quantum renormalization groups*, Phys. Rev. B **48** (1993), 10345–10356. See pages: [5](#), [7](#), [13](#), [27](#), and [29](#)
- [Whi05] ———, *Density matrix renormalization group algorithms with a single center site*, Phys. Rev. B **72** (2005), 180403. See page: [29](#)
- [Whi09] ———, *Minimally entangled typical quantum states at finite temperature*, Phys. Rev. Lett. **102** (2009), 190601. See pages: [7](#), [13](#), [27](#), [31](#), [35](#), and [36](#)
- [Wil75] Kenneth G. Wilson, *The renormalization group: Critical phenomena and the kondo problem*, Rev. Mod. Phys. **47** (1975), 773–840. See pages: [24](#) and [77](#)
- [WJMS15] F. Alexander Wolf, Jorge A. Justiniano, Ian P. McCulloch, and Ulrich Schollwöck, *Spectral functions and time evolution from the chebyshev recursion*, Phys. Rev. B **91** (2015), 115144. See pages: [42](#) and [43](#)
- [WLC⁺14] Da Wang, Yi Li, Zi Cai, Zhichao Zhou, Yu Wang, and Congjun Wu, *Competing orders in the 2d half-filled $SU(2n)$ hubbard model through the pinning-field quantum monte carlo simulations*, Phys. Rev. Lett. **112** (2014), 156403. See pages: [219](#) and [220](#)
- [WMPS14] F. Alexander Wolf, Ian P. McCulloch, Olivier Parcollet, and Ulrich Schollwöck, *Chebyshev matrix product state impurity solver for dynamical mean-field theory*, Phys. Rev. B **90** (2014), 115124. See pages: [24](#), [26](#), [41](#), and [42](#)
- [WN92] S. R. White and R. M. Noack, *Real-space quantum renormalization groups*, Phys. Rev. Lett. **68** (1992), 3487–3490. See page: [27](#)
- [WRVB09] André Winter, Heiko Rieger, Matthias Vojta, and Ralf Bulla, *Quantum phase transition in the sub-ohmic spin-boson model: Quantum monte-carlo study with a continuous imaginary time cluster algorithm*, Phys. Rev. Lett. **102** (2009), 030601. See page: [4](#)
- [WS98] Steven R. White and D. J. Scalapino, *Density matrix renormalization group study of the striped phase in the 2d $t - J$ model*, Phys. Rev. Lett. **80** (1998), 1272–1275. See pages: [179](#) and [216](#)
- [WS99] ———, *Competition between stripes and pairing in a $t - t' - j$ model*, Phys. Rev. B **60** (1999), R753–R756. See page: [216](#)

- [WV11] Ling Wang and Frank Verstraete, *Cluster update for tensor network states*, arXiv preprint arXiv:1110.4362 (2011). See page: [61](#)
- [WvD07] Andreas Weichselbaum and Jan von Delft, *Sum-rule conserving spectral functions from the numerical renormalization group*, Phys. Rev. Lett. **99** (2007), 076402. See pages: [13](#), [24](#), and [26](#)
- [WVS⁺09] A. Weichselbaum, F. Verstraete, U. Schollwöck, J. I. Cirac, and Jan von Delft, *Variational matrix-product-state approach to quantum impurity models*, Phys. Rev. B **80** (2009), 165117. See pages: [24](#) and [26](#)
- [WX97] Xiaoqun Wang and Tao Xiang, *Transfer-matrix density-matrix renormalization-group theory for thermodynamics of one-dimensional quantum systems*, Phys. Rev. B **56** (1997), 5061–5064. See page: [35](#)
- [XCQ⁺12] Z. Y. Xie, J. Chen, M. P. Qin, J. W. Zhu, L. P. Yang, and T. Xiang, *Coarse-graining renormalization by higher-order singular value decomposition*, Phys. Rev. B **86** (2012), 045139. See page: [45](#)
- [XJC⁺09] Z. Y. Xie, H. C. Jiang, Q. N. Chen, Z. Y. Weng, and T. Xiang, *Second renormalization of tensor-network states*, Phys. Rev. Lett. **103** (2009), 160601. See page: [45](#)
- [YHW11] Simeng Yan, David A. Huse, and Steven R. White, *Spin-liquid ground state of the $S = 1/2$ Kagome Heisenberg antiferromagnet*, Science **332** (2011), no. 6034, 1173–1176. See pages: [3](#), [8](#), [29](#), and [179](#)
- [ZCC⁺17] Bo-Xiao Zheng, Chia-Min Chung, Philippe Corboz, Georg Ehlers, Ming-Pu Qin, Reinhard M. Noack, Hao Shi, Steven R. White, Shiwei Zhang, and Garnet Kin-Lic Chan, *Stripe order in the underdoped region of the two-dimensional hubbard model*, arxiv:1701.00054 (2017). See pages: [3](#), [8](#), [29](#), [45](#), [179](#), [211](#), and [216](#)
- [ZCWW14] Zhichao Zhou, Zi Cai, Congjun Wu, and Yu Wang, *Quantum monte carlo simulations of thermodynamic properties of $SU(2n)$ ultracold fermions in optical lattices*, Phys. Rev. B **90** (2014), 235139. See page: [219](#)
- [Zen17] Qi-Bo Zeng, *Real-time evolution of the current through a quantum point contact*, Private communication (2017). See pages: [178](#) and [227](#)
- [ZG89] Jan Zaanen and Olle Gunnarsson, *Charged magnetic domain lines and the magnetism of high- T_c oxides*, Phys. Rev. B **40** (1989), 7391–7394. See page: [216](#)
- [ZHS⁺01] Weihong Zheng, Chris J. Hamer, Rajiv R. P. Singh, Simon Trebst, and Hartmut Monien, *Linked cluster series expansions for two-particle bound states*, Phys. Rev. B **63** (2001), 144410. See page: [5](#)
- [ZMK⁺15] Michael P. Zaletel, Roger S. K. Mong, Christoph Karrasch, Joel E. Moore, and Frank Pollmann, *Time-evolving a matrix product state with long-ranged interactions*, Phys. Rev. B **91** (2015), 165112. See pages: [33](#) and [227](#)
- [ZR88] F. C. Zhang and T. M. Rice, *Effective hamiltonian for the superconducting cu oxides*, Phys. Rev. B **37** (1988), 3759–3761. See page: [215](#)

- [ZV04] Michael Zwolak and Guifré Vidal, *Mixed-state dynamics in one-dimensional quantum lattice systems: A time-dependent superoperator renormalization algorithm*, Phys. Rev. Lett. **93** (2004), 207205. See pages: [7](#), [13](#), [27](#), [31](#), and [35](#)